REALISTIC FRP SEISMIC STRENGTHENING SCHEMES FOR INTERIOR REINFORCED CONCRETE BEAM-COLUMN JOINTS

DANIEL A. POHORYLES

UNIVERSITY COLLEGE LONDON

DEPARTMENT OF CIVIL, ENVIRONMENTAL AND GEOMATIC ENGINEERING

THESIS SUBMITTED FOR THE DEGREE OF

DOCTOR OF PHILOSOPHY IN EARTHQUAKE ENGINEERING

2016

DECLARATION OF ORIGINALITY

I, Daniel A. Pohoryles, confirm that the work presented in this thesis is my own. Where information has been derived from other sources, I confirm that this has been indicated in the thesis.

Signature …… Date ……

ABSTRACT

The observation, in recent earthquakes, of brittle collapses of reinforced concrete (RC) structures built before the introduction of detailed seismic design codes (pre-1970's), underlines the need for significant upgrades to the existing RC building stock. In particular, weak-column/strong-beam mechanisms and shear failures have potentially catastrophic impacts that could be addressed by repair and retrofit solutions.

In recent years, retrofits with fibre reinforced polymers (FRP) are becoming increasingly popular due to the benefits of corrosion resistance, high strength-to-weight ratio and reduced labour time. Experimental evidence for the efficiency of such schemes for joint strengthening can be found in the literature. An analysis of all available literature shows that the reduced scale of most tested specimens, as well as the omission of slabs and transverse beams in many studies, may lead to an unrealistic assessment of FRP retrofit schemes. In this study, pre-1970's full-scale interior beam-column joints with slab and transverse beams are hence tested under realistic conditions in order to propose and assess new and practical FRP retrofit solutions for seismic actions.

Three carbon FRP (CFRP) retrofit schemes with selective retrofit objectives are designed using outcomes from the literature and from calibrated finite-element models. The retrofit schemes are composed of a combination of FRP strengthening and selective weakening components to ensure failure of inadequately reinforced RC beam-column joints according to capacity design principles. The objectives of the schemes include the enhancement in lateral capacity and ductility, as well as changing the failure mechanism of the joint.

Results from full-scale cyclic tests on the CFRP retrofitted specimens are compared to the behaviour of a deficient specimen and a specimen designed to modern guidelines (EC8), highlighting the successful achievement of the respective retrofit objectives. To evaluate the effect of the realistic set-up, the results are also compared to specimens without slab and transverse beams, highlighting their importance. Finally, new design equations, to be used in conjunction with existing guidelines, are formulated to ease the practical adoption of the proposed retrofit scheme.

Keywords: *FRP; Seismic retrofit; Beam-column joint; Full-scale testing; Existing RC structures.*

ACKNOWLEDGEMENTS

First and foremost, I offer my sincere gratitude to my supervisor, Professor Tiziana Rossetto, for her continuous guidance and encouragement. Her enthusiasm and wisdom have motivated me and helped me to become a better researcher.

I am grateful to Dr Phillipe Duffour, my MSc supervisor, without whom I would have never started this PhD. I would also like to acknowledge my second supervisor, Professor Dina D'Ayala. I also would like to thank Dr Umut Akgüzel for his advice.

To my colleague and friend Jose Melo for his valuable input and assistance throughout the experimental campaign of this project. This study would not have been successful without his patience and hard work. To Professor Humberto Varum, who has guided me during my year in Portugal and has been a treasured mentor in this project.

I would like to thank Warren from the Concrete Laboratory at University College London, as well as all the staff at the Structures Laboratory at the University of Aveiro for their support during the experimental campaign.

I am lucky to have found great friends at UCL who have made me think and made me smile. I would like to thank my friends Arash, Aris, Lily, Palak, Sam and Stelios, without whom these three years at UCL would not have been so enjoyable and who were a cherished distraction from the often stressful times.

To Bamdad, Dragan, Enrico and Julian, for the many laughs, trips and good times. To Magda, Paul and Vincent, for their long-lasting friendship, moral support and many long conversations despite the distance. To Maria, Konstantina, Egli and George who have treated me like family.

I am deeply thankful to my parents, Sabine and Ronald, and step-parents, Liana and Enno, for their kindness and encouragement. The love and nurture, education and intellectual stimulation, I benefitted from during my upbringing, made me the person I am today. They have always been there for me and supported me throughout my studies.

To my grandparents, Ingrid and Norbert, whose love and care has been felt throughout my life. To my late grandparents, Milla and Herrmann, who must be proudly smiling down on me from heaven and have been a great inspiration to me.

Most importantly, I am eternally grateful for the support and love from my girlfriend Xenia throughout my studies and the many difficult times involved. I am thankful for her advice and help whenever I needed it. Your smile and kindness have motivated me. I would never have made it this far without you!

TABLE OF CONTENTS

LIST OF TABLES

LIST OF FIGURES

GLOSSARY OF TERMS

Symbols	Definition	Units
γ	Joint distortion	radians
γ_c	Softening descent function for concrete in CDP model	
γ_{Rd}	Design reduction factor in EC8 and CNR guidelines	
δ	Horizontal displacement at top of superior column	mm
δ_{ecc}	Eccentricity of the rod at the base of the superior column	mm
δ_u	Ultimate displacement	mm
δ_y	Yield displacement	mm
ε_t	Inelastic tensile strain	
ε_{fdd}	Effective maximum FRP strain	
$\varepsilon_{fdd,CNR}$	Effective maximum FRP strain predicted by the CNR guidelines	
$\varepsilon_{fdd,strand}$	Predicted effective strain in the FRP strands using the equations developed herein	
$\varepsilon_{FRP,max}$	Experimentally measured maximum FRP strain in the strands	
$\varepsilon_{u,FRP}$	FRP rupture strain	
θ	Rotation of section	°
λ_f	Confinement ratio from the CNR guidelines	
μ	Viscosity parameter in CDP model	
$\mu_{\Delta u}$	Ultimate displacement ductility	
ν	Poisson's ratio	
ρ_l'	Longitudinal steel ratio	%
ρ_w	Transverse steel ratio	%
ρ_{tot}	Total longitudinal steel ratio	%
σ_c	Compressive concrete stress	MPa
σ_t	Tensile concrete stress	MPa
σ_t (w)	Tensile stress at crack opening displacement 'w'	MPa
Γ_c	Stiffness recovery factors for load changes to compression	
Γ_t	Stiffness recovery factors for load changes to tension	
Δ	Horizontal storey drift at top of superior column	%
Δ_u	Ultimate drift	%
Δ_{max}	Drift at peak lateral load	%
Δ_y	Yield drift	%
Φ	Curvature of section	m^{-1}
Ψ	Dilation angle that corresponds to the concrete internal friction angle	°
b	Column width	mm
b_t	Distance between transducers	mm
b_c	Column width	mm
b_{eff}	Effective width of the beam according to EC8	mm
$b_{eff,sw}$	Effective width of the beam for selectively weakened slab	mm
b_f	Width of FRP sheet	mm
b'_f	Splayed-out width of FRP sheet	mm
d	Beam deflection	mm
d_{bl}	Longitudinal bar diameter	mm
d_{bw}	Transverse bar diameter	mm
d_c	Compressive degradation variable in CDP model	
d_t	Tensile degradation variable in CDP model	
f_a	Nominal axial compressive stress on the column	MPa

f_{b0}/f_{c0}	Ratio of initial equibiaxial compressive stress to initial uniaxial compressive stress	
f_{cd}	Design concrete compressive strength according to EC2	MPa
f_{ccd}	Confined concrete design strength, according to CNR guidelines	MPa
f_{ck}	Characteristic concrete compressive strength according to EC2	MPa
f_{cm}	Mean concrete strength from cylinder tests, according to EC2	MPa
f_{ct}	Concrete tensile strength	MPa
f_{fed}	Effective stress in the FRP	MPa
$f_{l,eff}$	Effective lateral confinement pressure, according to CNR	MPa
f_u	Ultimate steel strength	MPa
f_{uf}	Ultimate FRP strength	MPa
f_y	Steel yield strength	MPa
$f_{y,main}$	Yield strength of longitudinal steel reinforcement	MPa
$f_{y,trans}$	Yield strength of transverse steel reinforcement	MPa
h_b	Depth of beam	mm
h	Slice length	mm
h_c	Depth of the columns	mm
h_f	Thickness of the slab	mm
h_{strand}	Non-bonded, free length of the FRP	mm
$h_{protrusion}$	Protrusion of the strand	mm
j_d	Lever arm	mm
k_s	Geometric reduction factor for the confinement effect of rectangular columns	
l_c	Characteristic length of FE element	mm
n_f	Number of FRP layers	
p_t	Principal tensile stresses	MPa
r_c	Corner radius	mm
t_f	Thickness of FRP	mm
v	Normalised axial load	
v_{jh}	Horizontal shear stress	MPa
w_c	Crack opening at which stress can no longer be transferred	mm
x_i	Empirical variable to account for part of the splayed-out FRP not adequately bonded to the concrete surface at the transition to the plastic tubes	mm

A_f	Cross-sectional area of FRP	mm^2
C_b	Compression in beam	kN
DI_{HRC}	HRC Damage index according to Rossetto and Elnashai (2003)	%
E	Elastic modulus	GPa
E_c	Concrete elastic modulus	GPa
E_y	Young's modulus	GPa
E_f	FRP elastic modulus	GPa
E_{diss} *or* E_d	Cumulative dissipated energy	kNmm
F	Lateral load	kN
F_c	Lateral load from the horizontal hydraulic actuator	kN
$F_{deg,1\text{-}2}$	Inter-cycle strength degradation (1^{st} to 2^{nd} cycle)	%
$F_{deg,1\text{-}3}$	Inter-cycle strength degradation (1^{st} to 3^{rd} cycle)	%
F_l	Total lateral load	kN
F_{max}	Maximum applied lateral load	kN
F_u	Ultimate load (80% of maximum)	kN
G_{cl}	Crushing fracture energy	N/mm
G_f	Fracture energy	N/mm
K_p	Peak-to-peak lateral stiffness	kN/mm
K_c	Second stress invariant	kN/mm
K_i	Initial stiffness	kN/mm
L_b	Clear beam length	m
L_c	Column length	m

L_N	Length from the base of the superior column to the top of the rod	m
L_p	Length of plastic hinge	m
L_{p0}	Length of unconfined plastic hinge	m
L_{pc}	Length of plastic hinge due to the confinement effect for circular columns	m
M_l	Moment from lateral load	kNm
M_{ecc}	Moment from eccentric axial load	kNm
M_c	Moment in column	kNm
M_b	Moment in beam	kNm
$M_{b,hog}$	Beam hogging moment	kNm
$M_{b,sag}$	Beam sagging moment	kNm
$M_{c,sup}$	Superior column moment	kNm
M_{max}	Maximum experimentally recorded column moment	kNm
M_{Rc}	Column moment of resistance	kNm
$M_{Rc,FRP}$	Moment of resistance of FRP-retrofitted column	kNm
$M_{Rc,FRP,CNR}$	Moment of resistance of FRP-retrofitted column using the CNR equations	kNm
$M_{Rc,FRP,new}$	Moment of resistance of FRP-retrofitted column using the CNR equations with the modified FRP strand strain $\varepsilon_{fdd,strand}$	kNm
M_{Rb}	Beam moment of resistance	kNm
$M_{Rb,FRP}$	Moment of resistance of FRP-retrofitted beam	kNm
$M_{Rb,slab}$	Beam moment of resistance with slab	kNm
$M_{Rb,sw}$	Beam moment of resistance with weakened slab	kNm
M_{yield}	Yield moment	kNm
N1	First axial load of 425 kN	kN
N2	Second axial load of 25 kN	kN
R_{bl} and R_{br}	Reaction forces at the left and right beam support	kN
R_h	Horizontal resistance at the inferior column support	kN
S	Post-peak softening slope	kN/mm
T_b	Tension in the beam bars	kN
$V_{Rd,s}$	Steel contribution to shear resistance, according to EC2	kN
$V_{Rd,f}$	FRP contribution to shear resistance, according to CNR guidelines	kN
V_{jh}	Horizontal shear force in the joint	kN
V_{col}	Column shear force	kN
W_f	Full width of FRP sheet used for FRP strand	mm

Abbreviations	Definitions
ABAQUS	General purpose FEA product suite by Dassault Systemes
ACI	American concrete institute, here referring to ACI-440F guidelines
ACT	Actuator
ASCE	American Society of Civil Engineers
BT	Inadequate transverse reinforcement in beam
BLR	Inadequate beam longitudinal reinforcement
BA	Inadequate beam bar anchorage
CDP	Concrete damaged plasticity model
CF anchors	Carbon fibre anchors
CTR	Inadequate column transverse reinforcement
CNR	Italian Consiglio Nazionale delle Ricerche, here referring to CNR-DT-200.R1/2013 FRP guidelines
CP	Collapse prevention performance level (FEMA 356)
C3D8R	3D 8-node hexahedron (brick) solid finite elements in Abaqus
DCH	Ductility class high, according to EC8
DIC	Digital-image correlation
EC	Eurocodes
EC2	Eurocode 2 (CEN, 2008), European RC design guidelines
EC8	Eurocode 8 (CEN, 2004), European seismic guidelines
EcC	Eccentric column
FE	Finite element
FEM	Finite element modelling
FEMA	Federal Emergency Management Agency, U.S.
FRP	Fibre reinforced polymers (note the use of prefixes: C– Carbon, G- Glass, A-aramid, B- Basalt)
gs	Glued strands
ICSD	Inter-cycle strength degradation
IO	Immediate occupancy performance level (FEMA 356)
JTR	Inadequate joint transverse reinforcement
LC	Low concrete strength
LS	Life safety performance level (FEMA 356)
LSC	Lap-spliced column bars
MRF	Moment resisting frame
NSM	Near surface mounted
PB	Plain reinforcement bars
PED	Damaged specimen
PH	Plastic hinge
PHR	Plastic hinge relocation
RC	Reinforced concrete
REBA	Portuguese RC code (1967)
RP	Repair
RT	Retrofit
RT-A	Retrofit scheme A
RT-A-sw	Retrofit scheme A with selective weakening
RT-B	Retrofit scheme B
RT-B-sw	Retrofit scheme B with selective weakening
sw	Selective weakening
S4R	Four-node shell elements in Abaqus
TRM	Textile reinforced mortar
T3D2	2-node truss elements in Abaqus
UCL	University College London
WC/SB	Weak-column/strong-beam

1. INTRODUCTION

1.1. RESEARCH MOTIVATION AND SIGNIFICANCE

Despite significant technical advances in the field of structural engineering, extensive damage to the building stock was still observed in Taiwan, Ecuador and Italy during recent earthquakes (2016). These events are powerful reminders of the vulnerability of pre-existing structures and the threat they pose, particularly in metropolitan areas.

Reinforced concrete (RC) structures built before the introduction of modern seismic codes (pre-1970's or 80's[1]), were not designed with adequate seismic resistance and ductility (Hoffman *et al.*, 1992). These are found to constitute a disproportionally large fraction of damaged or collapsed buildings in post-earthquake field reports, as shown in Christchurch, New Zealand (Kam et al., 2011), Kocaeli, Turkey (Sezen et al., 2003) or Viña del Mar, Chile (Aranda et al., 2014). The susceptibility to seismic damage is deemed twice to three times as high for Greek buildings built prior to the introduction of major revisions to the seismic codes (Dritsos, 2005). Similar conclusions can be made for other Southern European countries (Kappos, 2007).

A World Bank report sees 865 million people globally exposed to a high seismic hazard (Dilley, 2005). With an increasingly dense urban population, this number is likely to have grown since. Vulnerable pre-1980's RC frames constitute a large proportion of the existing building stock in these earthquake-prone areas (Ghosh and Sheikh, 2007). As RC structures are mainly found in urban areas, many of these buildings have high occupancies. These buildings serve a broad range of uses, including residential and commercial buildings, but also critical structures such as hospitals and schools. In Greece, such structures constitute 30% of the building stock (Yakut, 2004) and house nearly half the population (Kappos and Panagopoulos, n.d.). In Turkey, up to 75% of the existing structures are RC frames (Smyth et al., 2004; Yakut, 2004). In the state of California, which presents the highest seismicity in the U.S., a recent report suggests that up to 17,000 non-ductile buildings "are vulnerable to sudden collapse and pose serious threats to life" (Comartin et al., 2011). In Taiwan, 55% of all school buildings are low-rise RC structures with unsatisfactory seismic performance (Chiu et al., 2013).

Overall this leads to a significant total risk composed of high exposure (population density), vulnerability (structural deficiencies) and hazard (high seismicity). It is hence not surprising that earthquake events result in high human and economic losses due to severe damage and partial or complete collapse of structures. Natural disasters worldwide have caused an estimated $192 billion annual losses over the last ten years (Swiss RE, 2016). In Turkey alone, damage on 70,000

[1] Depending on the introduction of adequate seismic guidelines in individual countries. Pre-1970s and pre-1980s are used interchangeably in this thesis.

buildings and collapse of a further 20,000 due to earthquakes, lead to losses up to $20 billion and an estimated 20,000 deaths in a decade (Smyth et al., 2004). Globally, over 900,000 people are estimated to have been killed by earthquakes over the last 25 years, corresponding to an average of 35,000 deaths a year (USGS, 2016). Over 75% of these are caused by the collapse of structures (Coburn and Spence, 2006).

With the large scale of existing structures not presenting adequate seismic resistance, demolition and rebuilding is not feasible. Instead, a number of studies have highlighted the lifetime economic and human benefits of retrofitting RC structures through cost-benefit analyses (Chiu et al., 2013; Smyth et al., 2004). A field investigation report after the 2009 L'Aquila, Italy, earthquake noted that significant damage and casualties could have been prevented by adequate retrofit of structures (Global Risk Miyamoto, 2009). Moreover, it predicts that similar failures are expected even for moderate earthquakes unless significant retrofit programs are put in place. The need for adequate, fast and economical retrofit solutions is of timely importance, as confirmed by the recent events in Central Italy in August 2016.

In particular, inadequate detailing of beam-column joints and improper hierarchy of strengths between framing members play a critical role in the poor seismic behaviour of pre-1980's RC structures. As a fundamental principle, premature failure of joints needs to be avoided in order for the framing members to reach their full capacity (Kappos and Penelis, 1996). Furthermore, in line with modern capacity design principles, weak-column/strong-beam mechanisms are to be prevented for an improved global structural behaviour (Fardis, 2009).

Following the significant repair and retrofit efforts in the aftermath of the 2009 L'Aquila and 2011 Christchurch earthquakes, fibre reinforced polymers (FRP) are considered as viable alternative strengthening materials to traditional concrete or steel jacketing. Their high strength-to-weight ratio and corrosion resistance make FRP particularly attractive as retrofit material (Ghosh and Sheikh, 2007). In addition, their application can be performed rapidly and without disrupting building occupancy, which can reduce down-time in businesses and the need of relocating inhabitants in residential properties (Bousselham, 2010).

In the field, FRP retrofits are most commonly implemented at component-level (beam or column). Significant experimental research to improve the behaviour of beam-column joint sub-assemblies can however be found in the literature. They include efforts on enhancing the shear capacity of unreinforced joints (e.g.: Ghobarah and Said, 2002; Ilki et al., 2011) and the retrofit of columns for an improved strength hierarchy (e.g.: Prota et al., 2004; Shiohara et al., 2009).

These studies highlight the effectiveness of FRP as retrofit material in terms of enhancing strength and ductility of RC beam-column joints and are building the foundation for future uses of FRP for global structural retrofit interventions. Still, the majority of studies are limited to testing scaled

specimens without slabs and transverse beams. Such specimens do not represent real structures adequately (ACI, 2014). Moreover, ignoring the effect of slabs and transverse beams in particular, significantly impacts the requirements and practical layout for flexural strengthening of weak columns and the shear strengthening of inaccessible interior joints.

To ensure the wider acceptance and practical implementation of suitable, fast and efficient retrofits to address the constant threat of inadequate seismic behaviour of existing RC frames, there is hence a significant need in developing, and testing, FRP retrofits for realistic RC structures.

1.2. RESEARCH AIM AND OBJECTIVES

The overall aim of this thesis is to determine a practical retrofit strategy using carbon FRP (CFRP) sheets for full-scale realistic pre-1970's beam-column joints to achieve an adequate seismic behaviour with respect to modern guidelines.

In order to answer the overall research aim, a comprehensive series of fourteen full-scale experimental tests presented in this thesis were organised and undertaken, and complemented by numerical modelling. The particular objectives of this work are:

1. to design and model three FRP retrofit and repair schemes with different strengthening aims for realistic full-scale beam-column joints with slabs and transverse beams, in accordance with recent FRP guidelines and outcomes of a detailed literature review;
2. to assess the influence of slab and transverse beams on the effectiveness of a retrofit scheme, both numerically and experimentally;
3. to test the effectiveness of the three FRP retrofit schemes in order to identify an optimal FRP retrofit design for realistic structures;
4. to develop a methodology for the retrofit to be potentially implemented in future applications.

The achievement of these objectives will contribute to the drafting of future guidelines, by enabling parametric studies calibrated on the high quality empirical data gathered from this study.

1.3. THESIS STRUCTURE

This thesis is organised in seven chapters. **Chapter 2** presents the theoretical background to this work and a literature review on the experimental research undertaken so far on the FRP retrofit of beam-column joints. This review aims to obtain an in-depth understanding of the state-of-the-art in FRP strengthening and to define unexplored areas of research.

Based on the identified gap in the current literature and available experimental data, **Chapter 3** presents the employed methodology and design of experiments. This includes a detailed

description of the test set-up, specimen and retrofit scheme design. To inform the design of the full-scale test specimens and retrofit schemes, finite element (FE) models of RC beam-column joints with different geometries and reinforcement detailing are also presented in this chapter. These are first validated on experimental data from small scale tests.

Chapter 4 describes the diagnostics used to evaluate the test results from the full-scale experiments. The results from the large scale experimental study undertaken at the University of Aveiro are then presented in **Chapter 5**. In **Chapter 6**, a detailed discussion of the experimental results from the fourteen tests is presented, assessing the relative effectiveness of the three retrofit schemes and evaluating the effect of slab and transverse beams.

Finally, **Chapter 7** presents the conclusions of the current work, an overview of avenues for future research and the list of publications stemming from this project.

Following the core of this thesis, six Appendices are presented, including a summary table of the experimental database used in the literature review (Appendix A), a list of publications stemming from this research (Appendix B), a description of existing design guidelines (Appendix C), the seismic action and reinforcement detailing calculations to Eurocode 8 (Appendix D), a description of preliminary RC beam experiments (Appendix E), as well as a detailed design methodology for the proposed retrofit scheme (Appendix F).

2. LITERATURE REVIEW

In this chapter the background of this thesis is presented. First, the theoretical background on RC beam-column joints and typical design deficiencies leading to brittle failures are discussed. Then, a detailed review of all previous research on FRP strengthened beam-column joints is presented. The various tested retrofit schemes are assessed in terms of their effectiveness and practical applicability to inform the design of improved retrofit schemes proposed in this thesis. At the end of this review, an analysis of a database of all studies is presented, addressing the type and geometry of set-ups, material properties and discussing the factors affecting the retrofit design.

2.1. BACKGROUND

Beam-column joints[2] in RC structures refer to the common regions of intersection between horizontal and vertical structural elements. Beam-column joints play a critical role in the cyclic behaviour of RC structures and as a fundamental principle, premature failure of joints needs to be avoided in order for the framing members to reach their full capacity. The design for RC joints in modern seismic codes is hence focussed on ensuring that the capacity of the joint is larger than that of the weakest member framing into it and that the load-bearing capacity of the column is not put at risk by potential strength degradation of the joint core (Kappos and Penelis, 1996).

Moreover, to ensure that the mechanism of seismic energy dissipation is not characterised by strong stiffness and strength degradation under cyclic loading, according to capacity design principles, an appropriate hierarchy of relative strengths of the members framing into the joints is also crucial. Modern seismic design guidelines aim to ensure beam hinging precedes column hinging mechanisms, as this allows for larger global structural displacements and hence higher ductility under seismic loading (Fardis, 2009).

To achieve a favourable global structural failure mechanism characterised by high ductility, it is hence important to look at the mechanics of joints, common design deficiencies and potential failure mechanisms of the joint area.

2.1.1. MECHANICS OF RC BEAM-COLUMN JOINTS

Beam-column joint regions under seismic loading are characterised by complex mechanical interactions (Hakuto et al., 2000). Under gravity loading, beams generally experience bending moments of the same sign at opposite faces of the beam-column joint. Under the action of the seismic forces on the other hand, beam bending moments are of opposite sign at either side of the joint core. Similarly, under lateral loading, there is a change of column bending moment from a

[2] In this thesis this region will be referred to as “reinforced-concrete beam-column joints”, “RC joints” or simply “joints”.

high value just above the joint to an equally high but opposite value just below the joint (Paulay and Priestley, 1992). This large local variation in moment means that the joints are subjected to large shear stresses as illustrated in Figure 2.1.

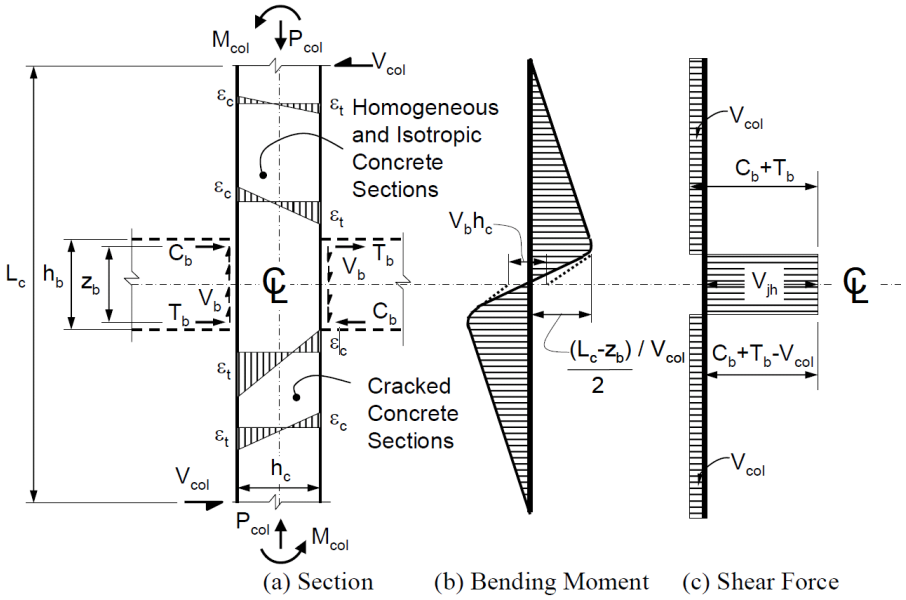

Figure 2.1. Moment and shear distribution in beam-column joints (Paulay and Priestley, 1992).

Joints can be considered to act through a system of two independent mechanisms of force transfer. On the one hand, forces are transferred from the beam and column bar to the core of the joint by bond and, on the other hand, forces are transferred from either side of the joint core through shear. Consequently, there are two main failure mechanisms: joint shear failure or bar anchorage failure.

As shown in Figure 2.1, loads from framing members can be idealised as tension, compression, and shear resultants acting on the joint. If no pull-out of the beam or column bars occurs, shear in the joint can be computed according to equation (2.1) as the maximum tensile force in the top bars of one beam plus the maximum compressive force in the top flange of the other beam. The shear force in the column above the joint is counter-acting this.

$$V_{jh} = T_{b1} + C_{b2} - V_{col} \tag{2.1}$$

Where V_{jh} is the horizontal shear force in the joint, T_{b1} the tension in the beam bars of beam 1, C_{b2} the compression in beam 2 and V_{col} the column shear force.

It is commonly assumed that this shear force in the joint core is resisted by the strut and tie mechanism (Park and Paulay, 1973):

1. Concrete in compression acts as a diagonal concrete strut between the compressive zones of beams and columns at the corners of the joint as shown in Figure 2.2(b). Bond stresses transferred from the beam bars to the joint also contribute to this.

2. Steel in tension acts as a truss extending over the entire core. This includes any horizontal hoops in the joint (if present), any vertical bars between the column corner bars and inclined concrete bars between shear cracks (Figure 2.2(c)).

As shown in Figure 2.2(a) diagonal tension cracking initiates in the joint core when the principal tensile stress in the joint exceeds the concrete tensile strength (Fardis, 2009). In many older structures, detailing is not adequate to prevent undesirable failure mechanisms. Common design deficiencies are presented in the next section.

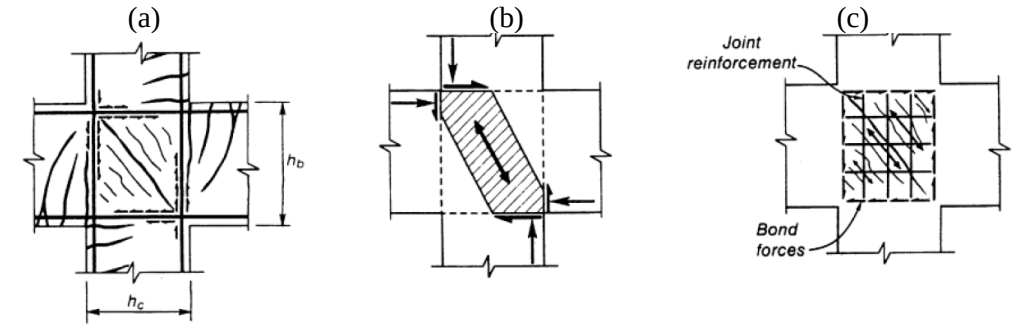

Figure 2.2. Interior beam-column joint crack patterns (a) and strut and tie mechanism (b) and (c) (adapted from Hakuto et al., 2000).

2.1.2. PRE-1970'S DESIGN AND TYPICAL DEFICIENCIES

Structures built in earthquake prone areas and designed before the introduction of modern seismic codes (pre-1970's or 80's) or to resist gravity loads only, typically have a number of deficiencies compared to the state-of-the-art in seismic design. These deficiencies are addressed by numerous authors (Beres et al., 1996; Bousselham, 2010; Pampanin et al., 2002) and can be summarised as follows:

- lower quality of materials,
- little or no transverse steel reinforcement in the joint cores, hence increasing the risk of preliminary joint shear failure,
- columns with a flexural capacity lower than that of beams, as the columns were not designed to resist any horizontal loads. Following the principle of capacity design it is however most favourable to achieve hinge formation in the beams, which allows for more energy dissipation with less local deformations and minimises the possibility for catastrophic collapse under strong earthquake loading,

- insufficient lap-splice length predominantly near plastic hinge regions of the columns or beams, which can lead to reduced capacities of the members,
- inadequate anchorage of beam bottom reinforcement, which can cause pull-out of the bottom beam bars and reduce the flexural capacity of beams,
- inadequate shear reinforcement spacing in beams and columns,
- location of lap-splices of column longitudinal reinforcement just above the floor level, where the moment caused by horizontal loading is largest.

2.1.3. OBSERVED FAILURE IN LABORATORIES AND THE FIELD

Under seismic loading, the presented deficiencies give rise to pre-mature and undesirable failure mechanisms. If the joint locally fails in a brittle manner or the hierarchy of strength of the members framing into the joint does not fulfil capacity design principles, a global ductile behaviour cannot be achieved. Due to the design deficiencies associated with pre-1970's structures, most existing structures cannot adequately resist earthquake loading. It is hence not surprising that joint shear failure has been identified as one of the critical mechanisms leading to strong damage and brittle failure of structures, both experimentally (Beres et al., 1992; Hakuto et al., 2000; Lehman et al., 2004) and in the field (Engindeniz et al., 2005; Kaplan et al., 2010; Ricci et al., 2011).

Typical cracking patterns of interior and exterior beam-column joints were recorded experimentally by Beres et al. (1992) and are shown in Figure 2.3. Strong diagonal cracking in the joint panel combined with a lesser extent of cracks through the beam and perpendicular to the column axis are observed. For beam-column joints tested experimentally without slab and transverse beams, shear failure of the joint is most commonly observed (Hakuto et al., 2000; Joh et al., 1988; Kazuhiro et al., 1991).

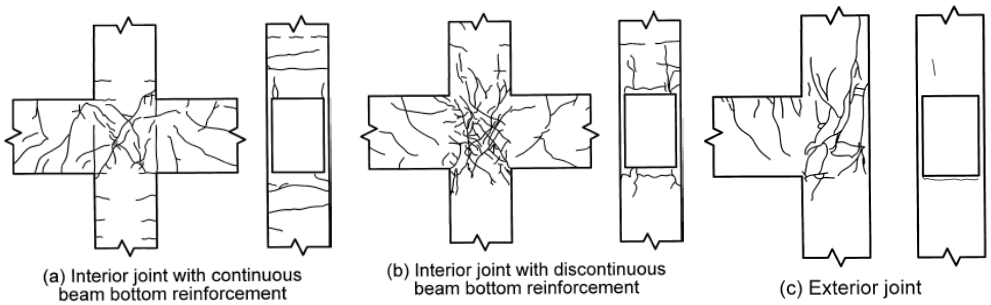

Figure 2.3. Typical cracking patterns for non-seismically detailed joints (Beres *et al.*, 1992).

When slabs and transverse beams are present, the capacity of the joint is however enhanced due to confinement (Kazuhiro et al., 1991) and the capacity of the beams in sagging and hogging are no longer symmetric, which can render columns the weakest link, causing flexural cracks to open at the column/joint interface. Of the few existing studies that include slabs and transverse beams, all indicate the significant effect of slabs on the behaviour of the specimens, however these studies

are either on scaled-down specimens (Kazuhiro et al., 1991), corner joints (Kam et al., 2010) or are seismically designed, hence containing significant joint reinforcement (Cheung et al., 1991).

In the field, joint shear failure (Figure 2.4(a)) and buckling of longitudinal bars lacking confinement at or near the joint (Figure 2.4(b)) are commonly observed after major earthquakes. These can lead to the catastrophic failure of RC structures observed in Kocaeli (Varum, 2003).

(a) (b)

Figure 2.4. Observed beam-column joint failures after the Kocaeli earthquake of 1999 – Source: (a) Varum, 2003; (b) Said and Nehdi, 2004.

For many pre-1970's RC buildings, the ratio of strength between the columns and beams framing into the joints is not adequate with respect to capacity design criteria. For such structures with a weak-column/strong-beam hierarchy, failures with column hinging are commonly observed, such as in L'Aquila, Italy in 2009 (Kaplan et al., 2010; Ricci et al., 2011) and Kocaeli, Turkey in 1999 (Sezen et al., 2003). In extreme cases this can lead to soft-storey collapses such as in Bingol, Turkey in 2003 (Doğangün, 2004) or most recently in Ecuador in 2016, as shown in Figure 2.5 (a). Soft-storey failures can however even be observed for moderate earthquakes, such as the one in Simav, Turkey in 2011 (Inel et al., 2013), as shown in Figure 2.5 (b).

(a) (b)

Figure 2.5 (a) Soft storey collapses in Ecuador 2016 (credit: Juan Cevallos) and (b) Simav, Turkey, 2011 (Inel et al, 2013).

Other failures attributed to inadequate detailing include column or beam shear failure. Beam hinging, in turn, is rarely observed in pre-1970's structures (Doğangün, 2004; Kaplan et al., 2010).

2.2. OVERVIEW OF STRENGTHENING METHODS

Due to the presented deficiencies, pre-1970's structures are hence at risk of failing prematurely by brittle failure mechanisms. The observed failures could often be prevented by appropriate interventions (Global Risk Miyamoto, 2009), as briefly discussed in this section.

The demolition and rebuilding of deficient structures is neither a sustainable nor economical solution, especially at large scale. A more economical solution is to retrofit deficient structural elements, which has been shown to be cost-efficient when looking at overall life-cycle costs (Chiu et al., 2013). Traditional retrofitting techniques, such as concrete or steel jacketing, addition of shear walls and epoxy repair, have proven effective and popular, as suggested in a detailed review by Thermou and Elnashai (2006). Yet, many of these schemes present practical issues, such as limited durability, adding weight and stiffness to structural elements, as well as being and labour intensive (Engindeniz et al., 2005).

In the last twenty years, the retrofit of RC joints with sheets of fibre reinforced polymers (FRP) is becoming increasingly popular. FRP sheet, as shown in Figure 2.6, is a composite material made of a polymer matrix (e.g. epoxy resin) reinforced with fibres, which usually are glass, carbon, basalt or aramid.

(a) (b)

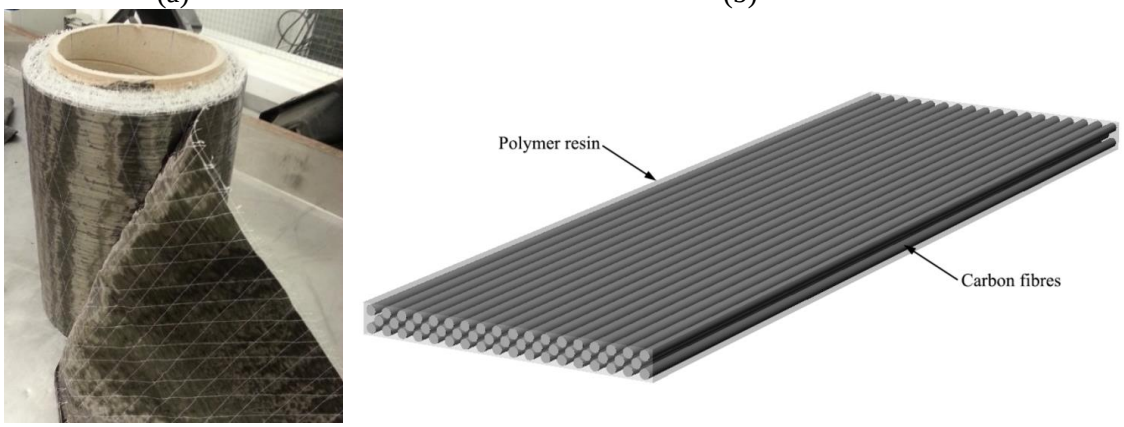

Figure 2.6. (a) Roll of CFRP sheet and (b) detail of the material (Mortezaei and Ronagh, 2012).

Compared to traditional retrofits, FRP does not increase the weight or stiffness of the members, but enhances their flexural or shear capacities. The typical strength of FRP is higher than that of steel while having a much lower density. Furthermore, from a life-cycle perspective, FRP jackets have a lower cost, as they are more durable and do not corrode (Ghosh and Sheikh, 2007). The application of FRP wraps can be performed rapidly and without disrupting the building occupancy, which is another major advantage, as it reduces the down-time in businesses and the need of relocating inhabitants in residential properties (Bousselham, 2010).

There are different types of FRP depending on the material used for the fibres. Carbon based CFRP has the highest strength while glass-fibre based GFRP can achieve higher strains, as shown in Figure 2.7.

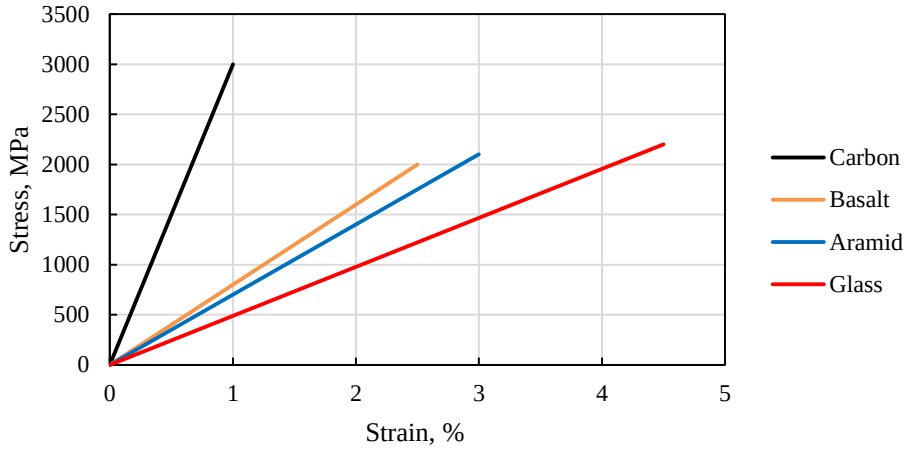

Figure 2.7. Comparison of typical dry fibre material properties.

GFRP is typically cheaper, still, based on a literature survey (Figure 2.8), CFRP is by far the most studied and used type of FRP and was chosen for this project as it is more commonly available.

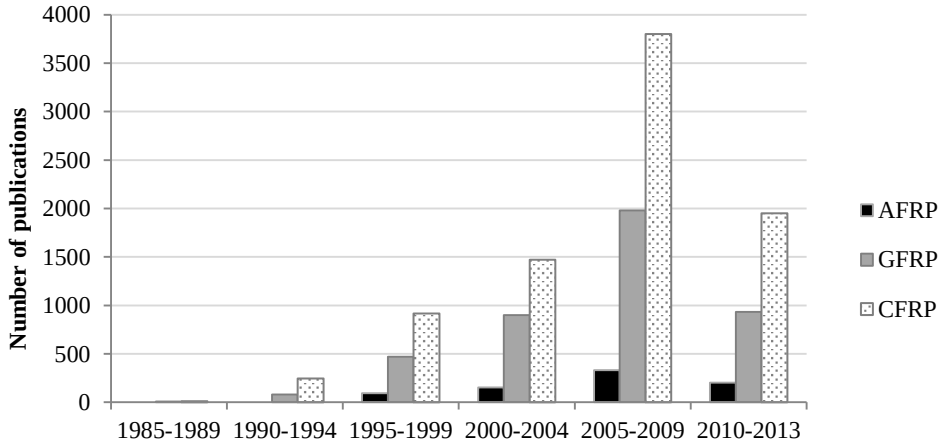

Figure 2.8. Survey on general academic publications on FRP types (source: google scholar).

The retrofit of RC beam-column joints with FRP often has different upgrade objectives that can be tackled selectively or together (Pantazopoulou et al., 2015). Sheets of FRP can be used to address common design deficiencies of pre-1970's structures by:

1. improving the shear capacity of under-reinforced joint panels,
2. improving the bond of beam bottom reinforcement bars with inadequate anchorage into the joint or enhancing the beam's flexural capacity to avoid shear failure
3. relocating the potential plastic hinge away from the column framing into the joint in order to fulfil capacity design principles.

Recently, an increasing number of applications of FRP retrofit in the field can be observed, for instance, after the 2009 Earthquake in L'Aquila, Italy. Figure 2.9 shows such an example from a hospital in L'Aquila where FRP was used to retrofit a column. These retrofits are usually for

individual members only. Furthermore, many research groups have provided experimental evidence for the effectiveness of FRP retrofit schemes for joint strengthening (Almusallam and Al-Salloum, 2007; Antonopoulos and Triantafillou, 2003; Engindeniz et al., 2008a; Ghobarah and El-Amoury, 2005; Pampanin et al., 2007; Realfonzo et al., 2014). A detailed review of the literature available on the FRP retrofit of beam-column joints is presented in the next section.

Figure 2.9. Example of FRP retrofit from L'Aquila (picture taken by the author)

2.3. REVIEW OF EXPERIMENTAL RESEARCH ON THE RETROFIT OF BEAM-COLUMN JOINTS WITH FRP

A review of the literature on FRP-retrofit schemes for non-seismically detailed RC beam-column connections under cyclic loading is carried out in order to identify the current state-of-the-art, identify avenues for the design of practically feasible retrofit solutions and potential gaps in the literature. A review of existing design guidelines for FRP retrofits can be found in Appendix C and in more detail in Pohoryles and Rossetto (2014).

Specimens with the typical pre-1970's design deficiencies discussed in Section 2.1.2 are the focus of this review. Research papers considering static loading are hence excluded and so are experimental specimens with modern seismic detailing. Furthermore, experimental work on bridge pier connections is excluded in this study as there are significant differences in terms of size, loading and desired response to seismic actions between buildings and bridges.

To facilitate a critical and systematic review of the literature a database of experimental work on the seismic FRP strengthening of RC beam-column joints in buildings is compiled. A summary of this database can be found in Appendix A. This work builds upon similar efforts by other researchers (Bousselham, 2010).

The experimental database contains information on the experimental campaigns and specimens tested by various research groups around the world. The recorded information includes the type

of deficiencies, the geometry and dimensions of specimens, the material properties (concrete, steel, FRP), the layouts of steel reinforcement, the FRP strengthening method (aim, type, number of layers, dimensions, application, surface preparation, presence and type of anchors), as well as information on the experimental set-up, loading, instrumentation and the available results of the experiments (load and displacement capacities, ductility, steel stress, FRP strains and others).

In the following sections the reviewed research is presented in terms of both strengthening objective, as well as joint geometry (i.e. exterior or interior joints with and without slab). The advantage of this organisation is to gain a deeper understanding of the aims of FRP retrofits for joints and how these are addressed by different research groups. The research is also grouped by authors as it is often difficult to compare different retrofit schemes and experiments directly. The proposed retrofit schemes are assessed in terms of their effectiveness, as well as their realistic practical applicability to real structures, as this forms a major objective of the present study.

2.3.1. SHEAR STRENGTHENING OF TWO-DIMENSIONAL EXTERIOR JOINTS

A number of research groups investigate similar retrofit strategies to shear-strengthen two-dimensional exterior joints without slabs or transverse beams. The results of this research avenue are summarised in this section.

2.3.1.1. GHOBARA'S GROUP AT MCMASTER UNIVERSITY.

The group at McMaster University led by Ghobarah proposed various retrofit schemes for the upgrade of two-dimensional (2D) exterior joints with joint shear deficiencies.

In a first study (Ghobarah and Said, 2002), two different retrofit layouts are presented with the aim of increasing the shear capacity of the joint panel only, without increasing the flexural capacities of the beam or columns framing into the joint. The two layouts are tested on full-scale exterior joints as shown in Figure 2.10 and Figure 2.11:

- U-wrap: bi-directional "U" shaped GFRP sheets of the same height as the joint, anchored with steel plates (specimen T1R) or not anchored (T4) are tested. This layout is also tested with additional FRP sheets extended above and below the joint on the column faces (T2R), with the objective of increasing its flexural capacity as well.

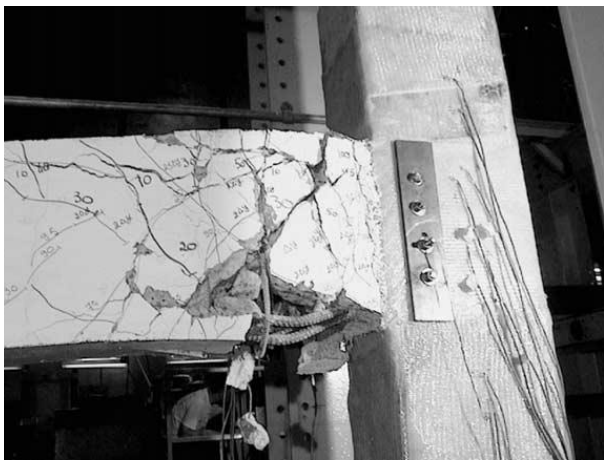

Figure 2.10. Failure mode of the U-wrapped specimen T2R (Ghobarah and Said, 2002).

- X-wrap: unidirectional GFRP sheets are wrapped diagonally around the joint in the direction of expected shear stress (specimen T9). The corners of the joint are fitted with equal leg steel angles with inclined plates in order to ease the application of the wrap.

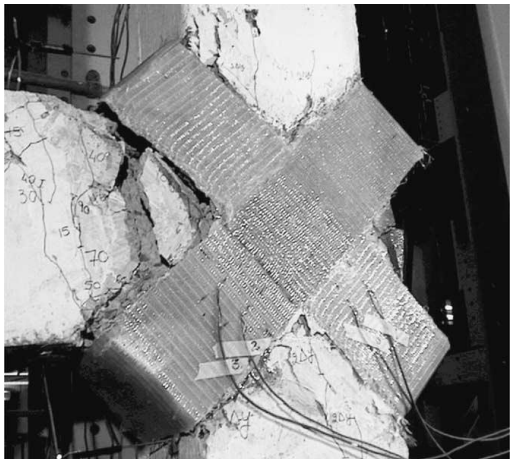

Figure 2.11. Failure mode of the X-wrapped specimen T9 (Ghobarah and Said, 2002).

It would appear that the first layout is more readily applicable in real situations with a slab present, as the diagonal FRP sheets would require cutting holes into the slab around the column. On the other hand, the first layout can only be applied to external joints with one beam framing into the joint, whilst the X-wrapped layout could be feasible for interior joints without transverse beams too. In both cases, however, the presence of transverse beams framing into the joint would make the application impossible or require significant changes in the set-up.

The effect of anchorage is also tested for the specimens with the U-wrapped retrofit layout. It is observed that the specimens with an anchor through the joint (T1R and T2R) performed better and that the performance of the non-anchored specimen (T4) is comparable to the control specimen. This is due to the non-anchored FRP debonding at an early stage and hence not contributing to the shear strength of the joint. For the anchored specimens T1R and T2R, the U-wrapped upgrade technique achieves the objective in delaying shear cracking and enhancing the ductility of the joint. For T1R the failure occurs ultimately in the joint, however at a much higher

ductility factor, nearly double of the control specimens. Failure is preceded by tearing of the single layer of FRP, which has not enough tensile capacity as compared to two layers used in T2R. For specimen T2R, for which the U-wrap is extended into the column, no shear cracking is observed in the joint area. The failure mechanism is changed to ductile flexural hinging in the beam compared to the joint shear failure observed in the control specimens. The highest displacement ductility and energy dissipation (five times that of the control specimen) are hence observed for T2R.

The X-wrap layout, on the other hand, proves effective initially, with cracks appearing in the beam first. However, the FRP debonds from the concrete due to these cracks and ultimately the joint fails in shear. The specimen still achieves an increase in ductility up to a factor of 5, similar to T2R. In terms of energy dissipation, the X-wrap scheme also achieves better results than T1R, corresponding to a threefold increase compared to the control specimens. The results would suggest that further layers of FRP combined with anchorage might make this strengthening layout viable. It is also important to note that the specimen strengthened with the X-wrap has an inferior concrete strength of 25 MPa as compared to 30.8 MPa for the other specimens.

In another study (Said and Nehdi, 2004), the successfully retrofitted specimens (T1R, T2R and T9) are also compared to a beam-column connection designed to modern code requirements, using the Canadian RC code (CSA A23.3, 1994). It is found that this level of performance is not achieved by any of the retrofit schemes. Particularly in terms of energy dissipation, the CSA designed specimen outperformed the best retrofitted specimen, i.e. T2R, with anchored U-wraps, by a factor of 2. Furthermore, in terms of displacement ductility (+20%) and lateral load (+11%), higher results are also observed for the specimen with seismic detailing.

Overall, both proposed layouts show promising results in enhancing the shear capacity of the joint. Ultimately, the importance of anchorage to avoid debonding is particularly highlighted by these experiments. Still, practical applicability of the schemes is limited to structures without slabs or transverse beams.

2.3.1.2. TRIANTAFILLOU'S GROUP AT THE UNIVERSITY OF PATRAS.

Triantafillou's research group at the University of Patras investigated the shear strengthening of under-designed exterior joints. In their experimental program, specimens are designed purposely to fail in shear and are strengthened with external CFRP or GFRP sheets, so as to test the contribution of FRP to the shear capacity of joints (Antonopoulos and Triantafillou, 2003). The design of the FRP intervention is based on earlier analytical work considering fundamental mechanics in the joint core, i.e. stress equilibrium and strain compatibility (Antonopoulos and Triantafillou, 2002).

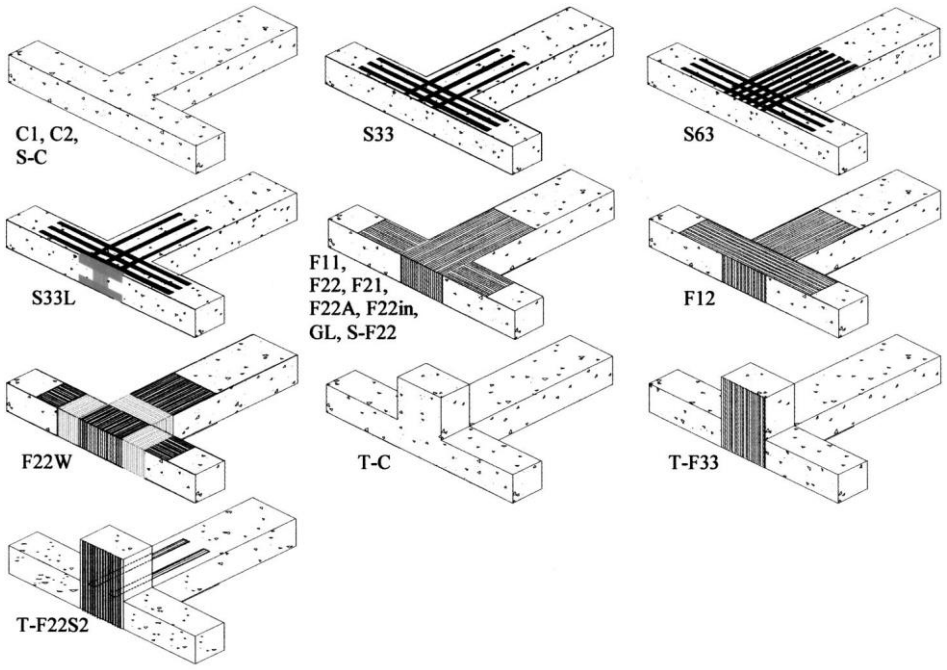

Figure 2.12. Strengthening schemes proposed by Antonopoulos and Triantafillou (2003).

As shown in Figure 2.12, in this study a total of 18 2/3-scale external beam-column connections are tested, including four control specimens and 14 retrofitted ones. The relative effectiveness of different FRP configurations and materials is tested by using strips rather than sheets for three specimens and GFRP rather than CFRP for another specimen. The use of different amounts of FRP layers allowed further comparisons to be made. One specimen is also tested for a higher axial load to investigate its effect on the shear capacity. Three of the specimens also have a stub transverse beam, while the rest are two-dimensional. Similarly, two joints are tested with one rebar for joint shear reinforcement, while all other specimens have none. Finally, the effect of anchorage is investigated by using perpendicular sheets of FRP as anchor for one sample and steel plates for another.

It is found that an increase in amount of FRP layers increases the strength and energy dissipation of the specimens, but not proportionally. Furthermore, stiffness degradation is also significantly reduced for retrofitted samples. In terms of number of FRP layers, compared to the base retrofitted sample (F11), doubling the amount of FRP in beams and columns (specimen F22), doubling the FRP in beams only (F21) and doubling the FRP in columns only are tested (F12). An increase in the number of horizontal layers of FRP is more effective in increasing the shear strength (and energy dissipation) of the joint, as F21 has a similar strength to F22, while F12 is only slightly stronger than F11.

An increased axial load in F22A, also leads to an increase in shear strength, i.e. a more efficient retrofit due to better confinement of the joint. Similar to other research groups, Antonopoulos and Triantafillou find that without anchorage, FRP debonding is always observed and leads to a less efficient retrofit. Specimen F22W, with perpendicular FRP wraps as anchorage of main FRP

sheets, achieves higher shear strength and energy dissipation than its unanchored counterpart (F22). This anchorage effect is even more pronounced for the specimens strengthened with strips rather than sheets (S33 and S33L). This is also illustrated by a comparison of strips and sheets as retrofit methods (S33L and F22), which shows that sheets are much more effective, attributable to reduced bond properties and hence anchorage for strips. Moreover, the presence of transverse reinforcement in the joint significantly reduces the effectiveness of the retrofit, indicating that a higher steel reinforcement ratio reduces retrofit effectiveness.

Finally, the presence of a transverse beam reduces the efficiency of the retrofit dramatically, as FRP cannot easily be applied to the joint panel on either side, highlighting that results of retrofit efficiency on planar specimens may not be transferrable to 3D-joints.

For specimen GL, designed as GFRP equivalent to F11 in terms of total elastic modulus of the jacket, the energy dissipation and shear strength are higher than for its CFRP equivalent. The reasons for this are not addressed by the authors. Looking at the experimental results, one hypothesis could be that the higher rupture strain of the GFRP jacket make it more efficient, as full fracture of one CFRP sheet is observed at 35 mm displacement in F11, but only slight ruptures in GFRP are observed in GL.

It is important to note, that while the strength of all retrofitted specimens is increased, the ultimate failure mechanism is still shear failure, albeit delayed, with diagonal cracking in the joint in all cases. Overall a number of factors are investigated, which is helpful when designing new retrofit schemes. Still, the scale, simple geometry and the specific retrofit layout are not fully representative of actual structures and the results may hence not be valid for full-scale joints with slabs and transverse beams, as confirmed by the different results for the tests with transverse beams.

2.3.1.3. KARAYANNIS AND SIRKELIS (2008).

Shear strengthening of exterior joints was also the objective of other work (Karayannis and Sirkelis, 2008), which included cyclic tests on 12 half-scale specimens retrofitted with CFRP. The effect of transverse shear reinforcement in the joint core is a main parameter investigated. As can be seen in Figure 2.13, the beams and columns are fully wrapped in CFRP sheets perpendicular to the members' axis. Furthermore, the joint core is strengthened by U-shapes. No additional anchorage is employed other than the perpendicular wrapping.

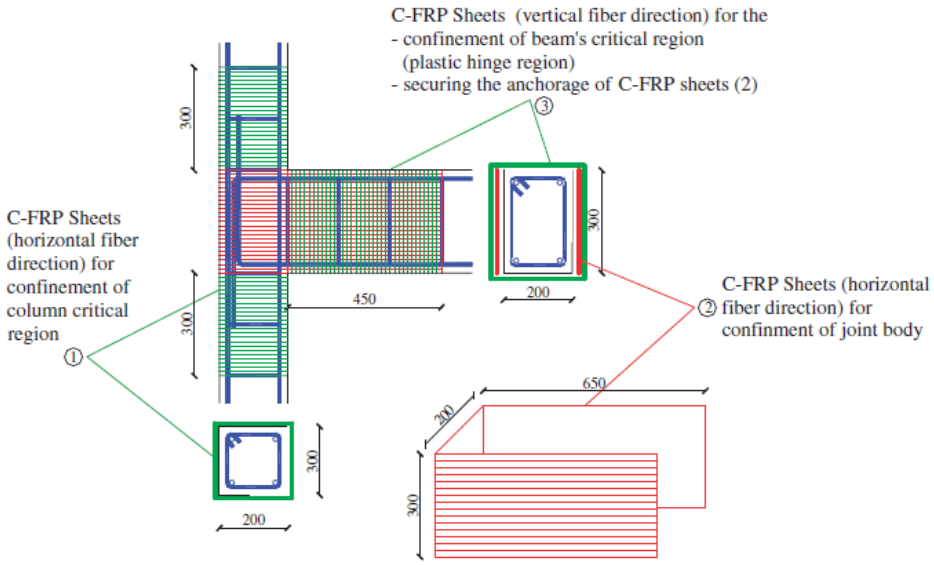

Figure 2.13. CFRP retrofit strategy suggested by Karayannis and Sirkelis (2008).

It is found that damage in specimens with transverse steel reinforcement is lower than for specimens without. The retrofit strategy is effective in strengthening the joint and relocating damage into the beam. However, the full wrap of beams and U-shapes in the joint would make the retrofit impossible to apply to structures with beams or slabs.

2.3.1.4. LE-TRUNG ET AL. (2010).

Le-Trung's group at Sejong University in the Republic of Korea tested seven shear deficient exterior joints strengthened with a variety of different CFRP retrofit set-ups (Le-Trung et al., 2010). The aim of the retrofits is to prevent shear failure in the joint with no transverse reinforcement, while ensuring a ductile beam flexural failure. The two main strategies are presented in Figure 2.14: An X-shaped configuration with fibres at 45° on three sides of the column (RNS-3 and RENS-4) and a T-shaped configuration with FRP sheets along two sides of the column and the beam (RNS-1, RNS-2, RNS-5, RNS-6).

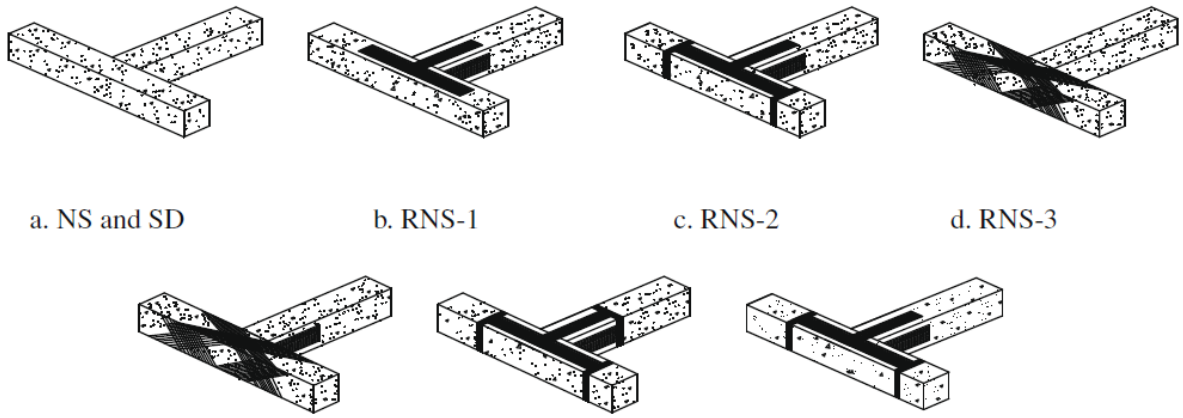

Figure 2.14. Six CFRP retrofit schemes by Le-Trung *et al.* (2010).

For both configurations L-shaped FRP sheets are placed at the corners between beams and columns to prevent slippage of the bars and delay crack opening. For the T-shaped configuration, anchorage strips at different locations (column-ends or beam-ends) are applied.

Overall it is found that all retrofits achieve an increase in lateral strength and ductility despite the lack of mechanical anchorage. The X-shaped configuration is more efficient in comparison to the other configuration. Moreover, delamination is observed for all specimens with the T-shaped configuration, while it is not observed for the X-shaped ones. Delamination is delayed for specimens with anchorage strips at the columns compared to the non-anchored specimen (RNS-1). For specimen RNS-5 with strip-anchorage for the beam L-shape, early debonding near the joint is observed compared to debonding near the beam-end. The presence of L-shaped strips at the corner achieves a delay in the flexural hinging of the beam for specimen RNS-4, however early debonding reduces its effectiveness at higher drift ratios.

It can be concluded that strip anchorage at the extremities of FRP sheets only is not sufficient to prevent debonding. Further strips, combined with mechanical anchorage are required. The X-shaped configuration is more efficient as the fibres are in the direction of principal stress and as the wrapping of the sheets creates better bond. However, both schemes would require significant changes to actual structures, with cuts through the slab around the column perimeters and potential removal of transverse beams, which would make the retrofit non-viable.

2.3.1.5. HADI AND TRAN.

Hadi and Tran (2014, 2015) proposed an unusual retrofit method for shear deficient exterior joints, in which FRP wrapping is preceded by the installation of glued-on concrete covers around the columns and joint to render square cross-sections circular. The aim of this scheme, presented in Figure 2.15, is to exploit the increased effectiveness of FRP wrapping in circular cross-sections.

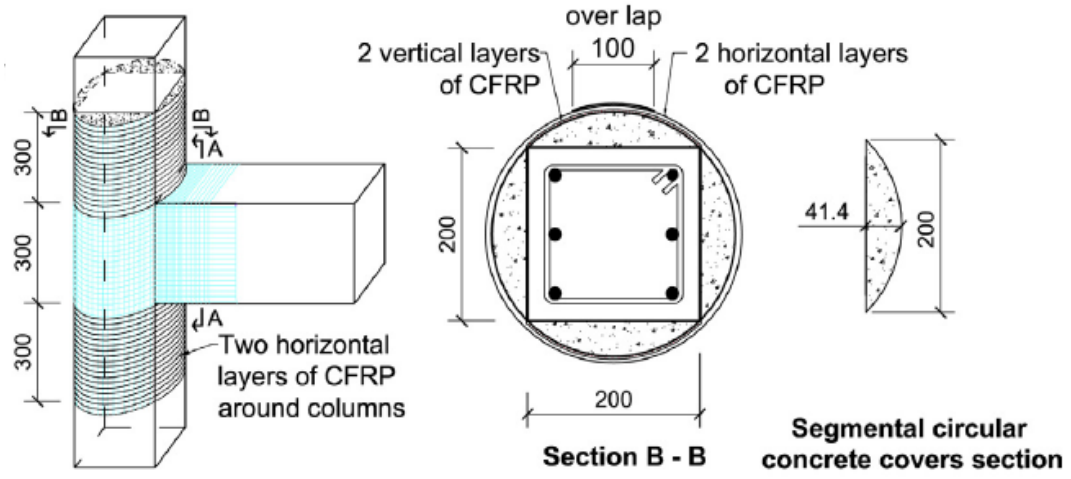

Figure 2.15. Proposed retrofit scheme for joint shear strengthening with segmental circular concrete covers and FRP by Hadi and Tran (2014).

Three specimens with different amounts of CFRP in the joint and columns (one, three and six layers) are tested. While the retrofits with lower amounts of FRP achieve delaying joint shear failure, only the specimen with six layers of FRP wrapping can successfully change the failure mechanism to ductile beam hinging. For all three specimens an increase in strength and ductility is observed compared to a control specimen, this is however not proportional to the amount of FRP used. Specifically, for the specimens with one (+84% increase in strength) and three layers (+116%), FRP rupture in the column and joint are observed, while for the specimen with six layers of FRP (+140%), no debonding or rupture is seen.

While the increase in strength employing this joint shear strengthening strategy is significant, it is highly impractical in real structures with transverse beams, walls or slabs present, which prevent the placement and continuity of the additional circular covers. Moreover, the effect of the additional concrete cover alone is not assessed by the authors of the study. This would however allow a better assessment of the effectiveness of the FRP intervention.

2.3.2. REPAIR SCHEMES FOR TWO-DIMENSIONAL EXTERIOR JOINTS

A number of studies investigate the effect of pre-damage on the effectiveness of FRP interventions. Four recent studies focussing on repairing exterior joints are summarised in this section.

2.3.2.1. AGARWAL ET AL. (2014)

A repair scheme consisting of cement grouting and GFRP U-wrapping was proposed for a pre-damaged exterior beam-column joint by Agarwal et al. (2014). One deficient full-scale specimen without joint shear strengthening is first tested to failure, before being repaired using five horizontal layers of GFRP on the joint panel. The GFRP is extended onto the beams and anchored by five layers of full-wraps around the beam.

Upon re-testing the repaired specimen, a reduction in initial stiffness is observed. Joint shear failure is not prevented, but only delayed up to debonding of the GFRP in the joint panel. The full strength of the control specimen is not recovered, with the repaired specimen achieving only 68% of the original capacity. An improvement in ductility up to 4.76 is however observed, corresponding to an increase of 43%.

Overall, despite a significant number of layers used for strengthening the joint, the behaviour of the repaired specimen is not improved compared to the original deficient joint. This can mainly be attributed to debonding of the GFRP sheets, which are not adequately anchored.

2.3.2.2. YURDAKUL AND AVSAR (2015)

Yurdakul and Avsar (2015) test the retrofit scheme proposed by Ghobarah and Said (2002), which is presented in Section 2.3.1.1, as a repair scheme for one full-scale deficient exterior joint specimen. The repair scheme uses two layers of X-shaped CFRP wraps in the joint region, as shown in Figure 2.16. The diagonal sheets (D) are anchored using full-wraps in the beam (A).

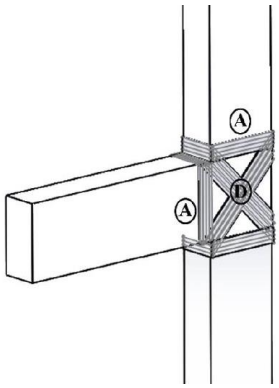

Figure 2.16. Joint shear repair scheme by Yurdakul and Avsar (2015).

After testing the control specimen to failure, the specimen is repaired and retested. A 28% reduction in initial stiffness is observed for the repaired specimen. Joint shear failure is again observed after debonding and subsequent rupture of the diagonal CFRP sheets, which is followed by spalling of the repair mortar. The repaired specimen does not reach the capacity of the original specimen, as a 25% reduction in maximum lateral force is observed.

It is suggested by the authors that a larger amount of FRP is required for repaired specimens compared to the proposed retrofit design by Ghobarah. However, inadequate anchorage is deemed the more crucial factor in this case as debonding is also observed in the initial study by Ghobarah, which is published 13 years prior.

In terms of practical applicability, while the authors claim the scheme is applicable to joints with floor slab and transverse beams, this is limited to retrofits of exterior joints, where at least one face of the joint is accessible.

2.3.2.3. BEYDOKHTI AND SHARIATMADAR (2016)

Beydokhti and Shariatmadar (2016) explored the effect of pre-damage on the effectiveness of CFRP-repair schemes for joint-shear deficient exterior joints. Four control specimens without transverse reinforcement, slab or transverse beams are initially tested to different damage levels according to FEMA 356 (immediate occupancy, life safety, collapse prevention and collapse). The specimens are then repaired in the joint using cement mortar first and then applying CFRP U-wraps according to the method proposed by Tsonos (2008).

As shown in Figure 2.17, next to the U-shape (2) for joint strengthening, one layer of vertical FRP is applied in the joint (3), as well as L-shapes in the corners for flexural retrofitting of beam and

column (1). For anchorage, only full wrapping at the beam/joint and column/joint interfaces is provided (4).

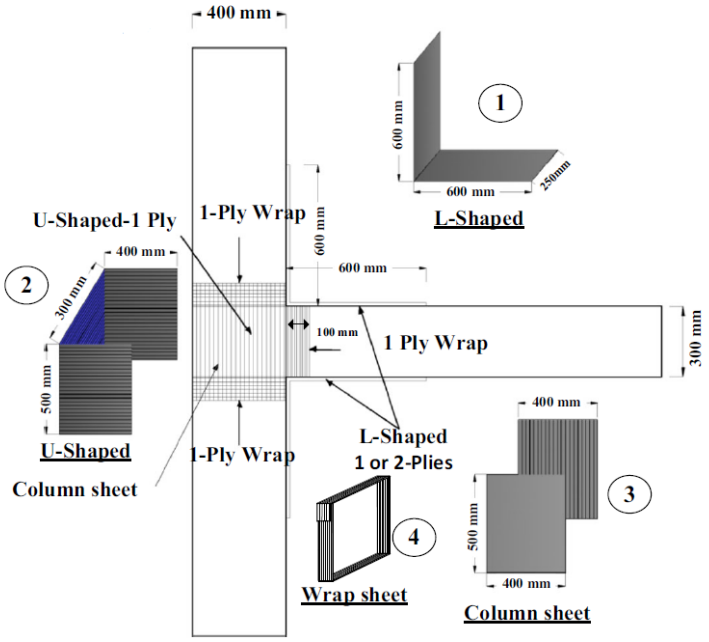

Figure 2.17. Repair scheme for exterior joints by Beydokhti and Shariatmadar (2016).

While the control specimens fail in joint shear, beam hinging is observed for the four repaired specimens. Despite adequate anchorage length according to the ACI 440.2R.08 guidelines (ACI, 2008a), due to the lack of additional anchors of the L-shapes, buckling and debonding of the beam-CFRP is observed, resulting in flexural failure of the beams at or near the joint-interface.

With increasing pre-damage levels, the authors observed an increasing deterioration of initial stiffness. For the two specimens with the lowest pre-damage, the strength of the control specimens is recovered, with a slight increase of 2.5% and 5.9% respectively. For the specimens damaged to near collapse and collapse damage states however, a reduction in strength of 19.5% and 15.3%, respectively, is obtained. These observations suggest that a full recovery of a severely damaged structures' performance is not achievable with the proposed repair scheme.

In terms of practical applications, the repair scheme is not achievable for structures with transverse beams, for which the joint is inaccessible. Furthermore, the study once again highlights the need for adequate anchorage. Providing adequate anchorage length or transversal wrapping of the longitudinal sheets is not sufficient when reaching high levels of drift.

2.3.2.4. GARCIA ET AL.

Three full-scale exterior joints with deficient joint shear capacity, inadequate column flexural capacity and beam bar anchorage were repaired with FRP after sustaining significant damage in an experimental program at the University of Sheffield (Garcia et al., 2012, 2014). The joint core was unreinforced in accordance with the common design practice in pre-seismic codes.

The three control specimens are first damaged by cyclic loading and then repaired by removing damaged concrete and replacing it with new concrete of nearly double the compressive strength. According to the authors, this is common repair practice in many Mediterranean countries. The joints are then rehabilitated with CFRP according to the scheme shown in Figure 2.18. The aim of the retrofit is to ensure an adequate beam hinging mechanism, by preventing brittle bar slippage and joint shear failures. The retrofit consists of U-wraps around the joint extending into the column (1), longitudinal FRP along the length of the column for flexural strengthening (3,4,5), as well as full confinement wraps of the column (6,7) and beam (2).

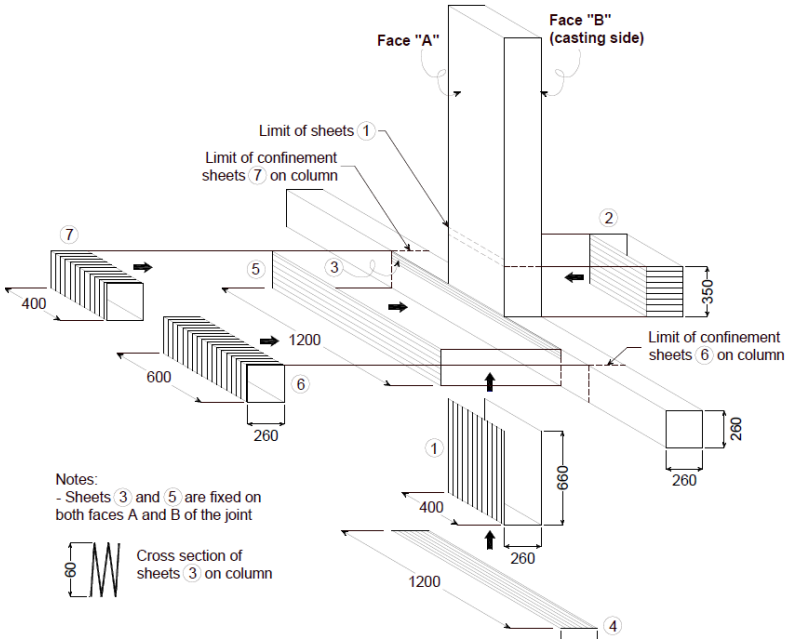

Figure 2.18. CFRP retrofit for beam bar anchorage by Garcia *et al.* (2012).

While the control specimens fail through extensive diagonal cracking and partial concrete spalling in the joint core, the CFRP-repaired joints fail instead by a more ductile combined beam and joint mechanism. While debonding is not observed, FRP rupture and significant damage are still observed in the joint core. Still, for the combined concrete repair and CFRP retrofit, a significant increase in load capacity up to 145% over the control specimens, and up to 69% over a specimen only rehabilitated with new concrete in the joint core, is achieved. The maximum increase capacity for the CFRP repaired joints corresponds to 85% of the shear strength required for ACI code-compliant RC joints (ACI Committee 352, 2002).

Finally, in practical terms, the lack of a slab makes the FRP retrofit easier than in real situation, which is also addressed by the authors who suggest that ensuring continuity of CFRP along the longitudinal column axis would require drilling slots in the slab. The potential presence of transverse beams is however not addressed.

2.3.3. SHEAR STRENGTHENING OF TWO-DIMENSIONAL INTERIOR JOINTS

2.3.3.1. MOSALLAM (2000)

Two half-scale interior joints retrofitted to improve joint shear capacity with GFRP and CFRP, respectively, were tested by Mosallam (2000). The joints are retrofitted with two layers of bi-directional sheets of FRP around beams, columns and joint, as well as diagonal straps around the joint (see Figure 2.19). The tested specimens with GFRP display a greater increase in ductility, due to its lower stiffness compared to CFRP. In terms of ultimate load, the results for both materials are identical. Next to significant practical considerations in terms of the retrofit layout and scale, the amount of FRP used would need to be increased as both retrofitted specimens experience delayed joint shear failure.

Figure 2.19. FRP retrofit of interior joints by Mosallam (2000).

2.3.3.2. D'AYALA ET AL (2003)

Three different retrofit strategies for different deficiencies were tested for interior joints by D'Ayala et al. (2003). The specimens were designed according to pre-seismic design codes and are characterised by either a weak-beam (WB) or a weak-column configuration (SB).

The FRP-layout W1 applied for the WB and SB configuration consists of L-strips at the corners of the joint to improve the capacity of the beam, and vertical and horizontal FRP sheets on the column and beam face, respectively, to increase the shear strength of the joint. All strips are anchored by perpendicular wraps at beams and columns. For the SB configuration, next to layout W1, two further layouts are proposed. The first, W2, consists of diagonal strips around the joint core to improve its shear strength combined with full wraps of beams and column. The second, W3, is similar to W2, but includes a continuous vertical strip to front and back faces of the column to further improve the shear capacity. Note that this scheme is applied for specimens with weaker concrete.

It is found that the diagonal wrapping layout is more effective than the orthogonal one (W1), not only because of the direction of fibres, but also because the joint is more confined at the corners.

For the specimens with weak columns, layout W2 achieved the highest improvement in terms of energy dissipation and reduction in stiffness degradation. Layout W1 is not successful in shifting the failure mode for the weak-column specimens. The non-occurrence of flexural hinging for configuration W3, with significant joint cracking despite strengthening, can be attributed to the lesser quality of concrete.

2.3.4. SHEAR STRENGTHENING OF CORNER JOINTS WITH SLABS OR TRANSVERSE BEAMS

2.3.4.1. TSONOS (2008)

The shear strengthening of corner joints with slabs and a (stub) transverse beam is investigated by Tsonos (2008). Three shear-deficient specimens are tested under cyclic loading in order to compare the relative effectiveness of CFRP and RC-jacket retrofits.

The FRP retrofit for one joint consists of 10 horizontal layers of FRP in the joint, nine vertical and seven horizontal layers to improve the flexural and shear capacity of the columns respectively. As shown in Figure 2.20, the joint FRP (1) is anchored with CFRP strips (2) fully wrapped around the beam through pre-drilled slots in the slab.

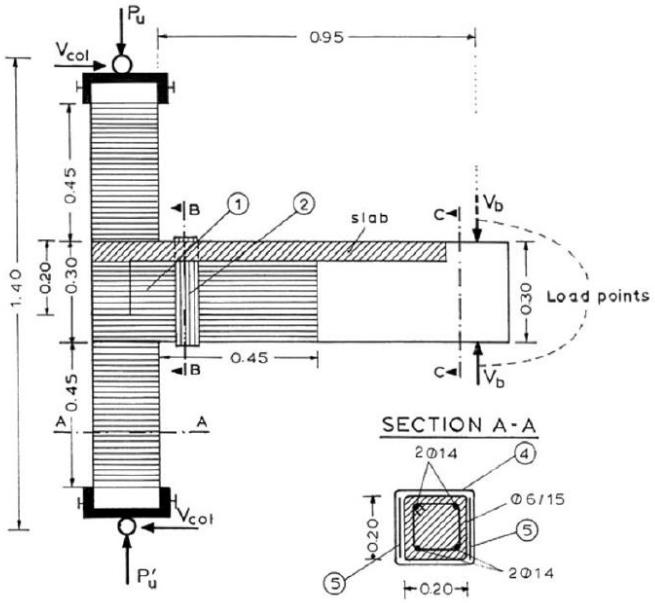

Figure 2.20. CFRP Retrofit by Tsonos (2008) for exterior joints with slabs.

By confining the joint with FRP, the ultimate strength of the assembly is improved by 70% and a more ductile beam hinging mechanism, is achieved. In comparison to the concrete-jacketed specimen, similar strength is obtained, but energy dissipation and stiffness of the concrete-jacketed specimen are greater.

The retrofit scheme takes into account realistic geometric constraints and is feasible for corner joints in real structures for which one face of the joint and column is accessible. Beam hinging is

achieved, however due to the lack of anchorage along the beam, damage with flexural cracks is concentrated at the beam-joint interface.

2.3.4.2. DEL VECCHIO ET AL.

Recently, two CFRP retrofit schemes for six shear-deficient full-scale corner joints with transverse beam are proposed as shown in Figure 2.21 (Del Vecchio et al., 2014, 2016).

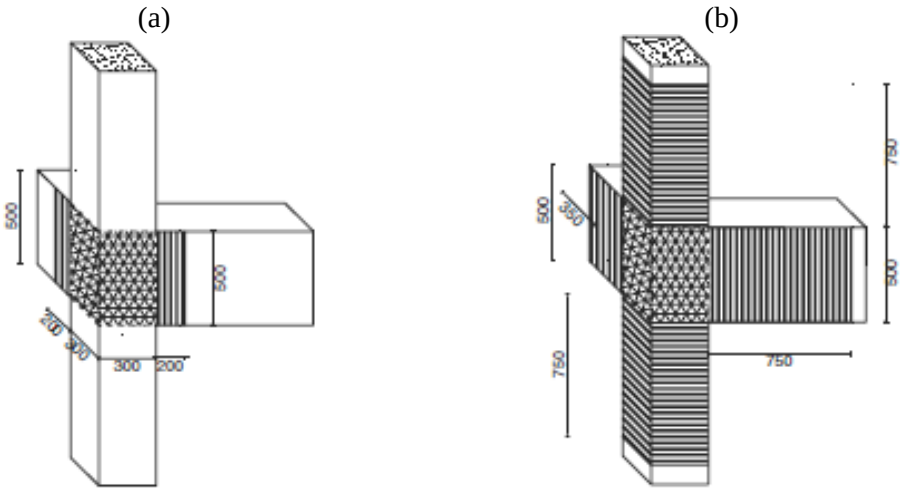

Figure 2.21. Retrofit layouts proposed by Del Vecchio et al. (2014) – (a) "light", (b) "strong".

The first scheme labelled "light" (a) consists of quadri-axial CFRP sheets in the joint panel and uniaxial FRP around the beam close to the joint (specimen FL1). Its aim is to avoid brittle joint shear failure without increasing the energy dissipation of the joint. The second scheme, "strong" (b), adds unidirectional sheets on columns and beams perpendicular to the member axes (FS1). The aim of this retrofit is not only to change the failure mechanism, but also to increase the energy dissipation of the joint. Quadri-axial CFRP is used for the joint panel, while unidirectional FRP is used for column and beams. A variation of this scheme with double the amount of FRP and with FRP extended to the top face of the beams is also tested (FS2).

For the "light" retrofit, premature debonding is observed, as well as crushing of concrete in the column above the joint. The latter demonstrates the need for FRP confinement of the column. It is observed that while the failure mode and ductility does not change for the "light" retrofit, the strength is increased by about 20%. For the "strong" retrofit, a large increase in ductility and strength is observed and this even more so for specimen FS2 with FRP on the top side of the beam. For specimen FS1, shear failure in the joint is not prevented, but only delayed. This is attributed to the amount of FRP present in the joint. For FS2, doubling the amount of FRP achieves preventing joint shear failure and moving the mechanism of failure to column flexural hinging.

This mechanism is not adequate in terms of capacity design either, highlighting that horizontal confinement wrapping alone is not enough to overcome a strong-beam/weak-column strength hierarchy and hence the need for column flexural strengthening in pre-1970's structures.

It is also noted that intermediate debonding of FRP occurs for all specimens, highlighting the need for further anchorage, which would lead to significant strength enhancement. Finally, an important observation is made in terms of the recorded strain values. Larger strains, close to the ultimate strain of the material are recorded by the authors, suggesting that the limits proposed by design guidelines (e.g. 0.4% strain) are conservative.

2.3.4.3. ILKI ET AL. (2011)

Another research group that focusses on shear strengthening of corner joints is that of Ilki at the Istanbul Technical University (Ilki et al., 2011). The research looks at strengthening corner beam-column joints with slab and transverse beams. The control specimen has a very low concrete strength (8.3 MPa) and is designed without joint shear reinforcement to represent a typical Turkish pre-1990's structure. The retrofit design consists of three layers of bidirectional CFRP placed on the free side of the joint and anchored using diagonal sheets of FRP wrapped around the beams (Figure 2.22).

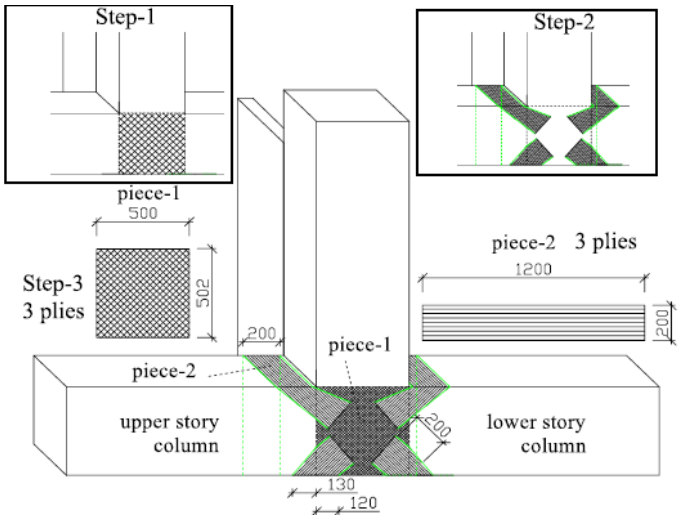

Figure 2.22. Joint shear strengthening scheme suggested by Ilki's group (2011).

In terms of practical aspects, the layout of the diagonal sheets (piece 2) is feasible for exterior joints, but the placement at the corners where there is already a higher stress concentration, may lead to premature debonding or rupture of the FRP sheets. In the tests, the sheets are not observed to debond, as the full capacity of the beam is not reached. It is found that, while the strength of the control specimen is limited by the joint shear capacity, for the strengthened specimen, beam bar slippage becomes the dominant mechanism. Joint shear failure is hence obverted, but no significant increase in strength is observed.

It is concluded by the authors that an FRP-only intervention does not suffice, but additional welding of longitudinal bars is also required to ensure the flexural capacity of the beams can be achieved. A test with welded beam bars indeed leads to a more ductile and dissipative beam-hinging failure (Ilki et al., 2011). Using FRP sheets in the bottom face of the beam is not

considered as an option. This could however lead to a better anchorage of the bottom bars, as proposed in the studies in the next sub-section.

2.3.5. BEAM STRENGTHENING

2.3.5.1. IMPROVING BEAM BAR ANCHORAGE

2.3.5.1.1. INTERIOR JOINTS

Two different strengthening schemes for preventing brittle beam failure mechanisms in interior beam-column joints are proposed by Mukherjee and Joshi (2005). The first scheme (a) uses L-shaped FRP sheets at the corners between beams and columns, while the second (b) uses a pre-cured CFRP strip along the top and bottom of the beams. A comparison of the two schemes can be seen in Figure 2.23. A total of ten 1/3-scale retrofitted joints are tested in this campaign. The specimens are classified as ductile and non-ductile depending on adequate or pre-seismic reinforcement detailing in terms of bar anchorage. Both groups have no transverse reinforcement in the joint. For each group, four different specimens are tested with scheme (a) and one with scheme (b). For scheme (a), the type of FRP used (CFRP and GFRP) as well as the amount of FRP (one or two layers) are varied.

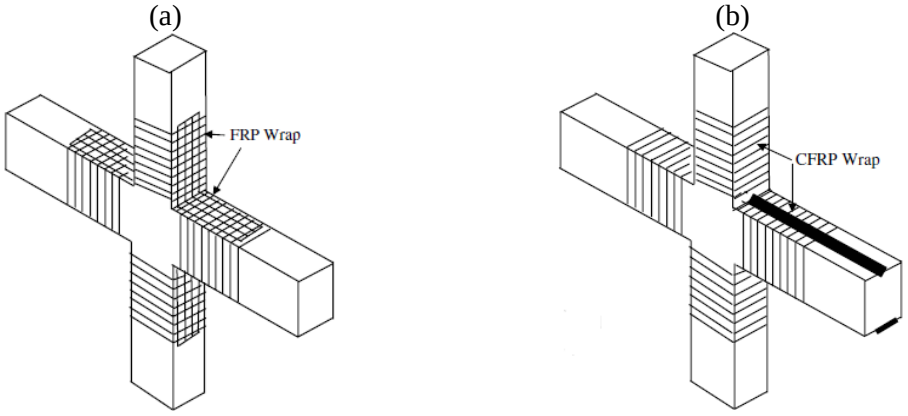

Figure 2.23. FRP retrofit schemes for interior joints proposed by Mukherjee and Joshi (2005).

For ductile specimens, the CFRP retrofitted specimens have higher strength but lower ductility than the GFRP retrofitted ones. The specimen with a CFRP strip (b) has the strongest gain in strength and ductility. For the non-ductile specimens, the difference between CFRP and GFRP retrofit are less pronounced and the GFRP retrofitted specimen actually achieves a larger strength increase. Retrofit (b) proves less efficient than retrofit (a) for two layers of FRP. In all cases the pull-out of the beam reinforcement seen in the control specimen is prevented.

Overall it can be seen that both retrofit methods and materials are effective and improved the behaviour of the joints. For low ductility joints, GFRP is proven more effective and this is attributed to its lower stiffness compared to CFRP.

2.3.5.1.2. EXTERIOR JOINTS

Ghobarah and El-Amoury (2005) present a retrofit scheme for improving the resistance to bond-slip of beam bottom bars in anchorage deficient exterior joints. The schemes used for anchorage deficient specimens consists of CFRP sheets placed along the bottom of the beam and continued along the interior face bottom column. Two joints (TB12 and TB11) are tested with different amounts of FRP sheets (2 and 4) and different anchorage systems (see Figure 2.24). While the anchorage system for TB12 consists only of a steel angle in the corner of joint, the anchorage for TB11 includes a curved concrete haunch in the corner, followed by a curved steel plate as anchorage, as well as four external steel rods as ties along the outside of the column. Both schemes can be deemed readily applicable in real structures, even with transverse beams and slab present.

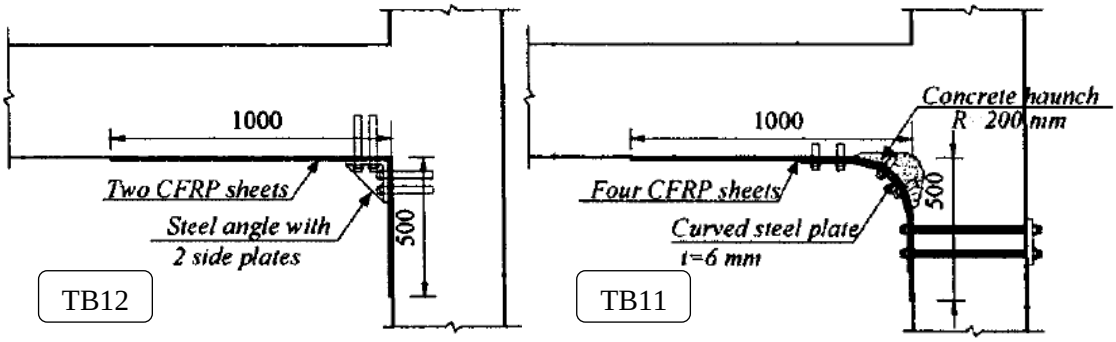

Figure 2.24. CFRP schemes for beam bar anchorage upgrade (Ghobarah and El-Amoury, 2005).

For the control specimen with anchorage deficiency, as expected, a very brittle behaviour with low ductility and rapid strength degradation is observed. For specimen TB12, the behaviour does not improve, with similar ductility and lower load capacity and energy dissipation than the control specimen. The poor behaviour is governed by the low strength of the expansion anchors of the steel angle and plates, causing a gap to the FRP sheets and hence de-bonding and fracturing of the sheets in the corner between beam and column. On the other hand, TB11 achieves its objective, as the additional external steel rods and the curved steel plate maintain the integrity of the retrofit scheme. The scheme is however not a pure FRP retrofit, but relies heavily on the deformation of the steel plate additionally dissipating a large amount of energy (nearly five times more). Overall a ductile flexural hinging mechanism is achieved, however the plastic hinge is observed to form very close to the face of the column.

2.3.5.1.3. PLAIN BARS

Russo and Pauletta test exterior RC joints with plain bars and inadequate beam bar anchorage (2012). The tested 2/3-scale and full-scale joints are designed in accordance with the design practice of the 50's and 60's in Italy, i.e. for gravity loads only. Three different retrofits are designed as shown in Figure 2.25.

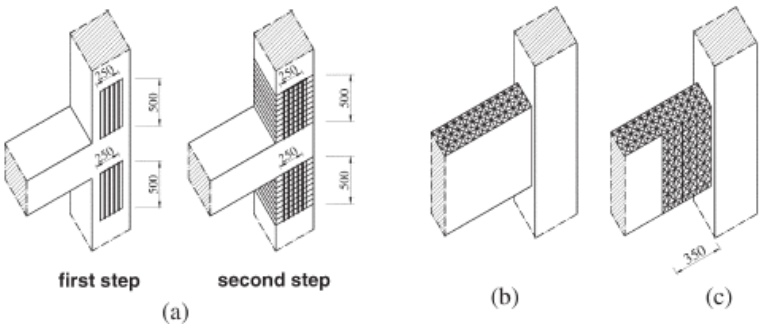

Figure 2.25. FRP retrofit for specimens with plain bars by Russo and Pauletta (2012).

From the control specimens with plain bars, it is found that beam bar slippage is the crucial mechanism, compared to experiments with ribbed bars, for which significant diagonal cracking in the joint is observed. The aim of the retrofit for specimens with plain bars is hence to prevent beam bar slippage. The method of retrofit applied involves steel-plate anchorage of the plain bars before application of CFRP wrapping. For all three retrofits, the wrapping is not applied in the joint panel to create a more realistic retrofit, as in actual buildings there would be transverse beams and cutting into these is deemed unrealistic by the authors.

Specimens with retrofit (a) fail in a ductile beam hinging mode instead of bar anchorage failure. This is however only attributable to the steel plate anchorage of the bars. The CFRP sheets provided do not contribute to the strength increase. Retrofit (b) and (c) provide a higher strength increase with FRP on the top face of the beam.

Overall the main contribution to the improved behaviour comes from the anchorage of the bars and not the FRP scheme, which is very labour extensive and invasive. No significant conclusions can hence be drawn for any future FRP retrofit schemes.

2.3.5.2. BEAM PLASTIC HINGE RELOCATION

Ronagh's research group at the University of Queensland, Australia, proposes to use CFRP wraps in order to relocate the plastic hinge (PH) in the beam away from the column face towards a location further along the beam (Mahini and Ronagh, 2007, 2011). The RC beam-column joint investigated by Ronagh's group is a 1:2.2 scaled model of a joint with non-ductile detailing typical for an 8-storey residential building in Brisbane, Australia. Scaling follows the similitude requirements of the Buckingham theorem (Noor and Boswell, 1992). Although most tests undertaken are static push-over tests, two specimens are also tested under cyclic loading.

The control specimen already presents a strong-column/weak-beam hierarchy, so the idea behind this strategy is to strengthen the beams near the joint to protect the beam/joint interface. The retrofit of RC beam–column joints, shown in Figure 2.26 (a), consists in bonding three layers of CFRP to the sides of the beam and around the back of the column, anchoring them with one layer of CFRP sheets placed along the length of the column. The latter also serve to improve the flexural behaviour of the column, which may be required after strengthening the beams.

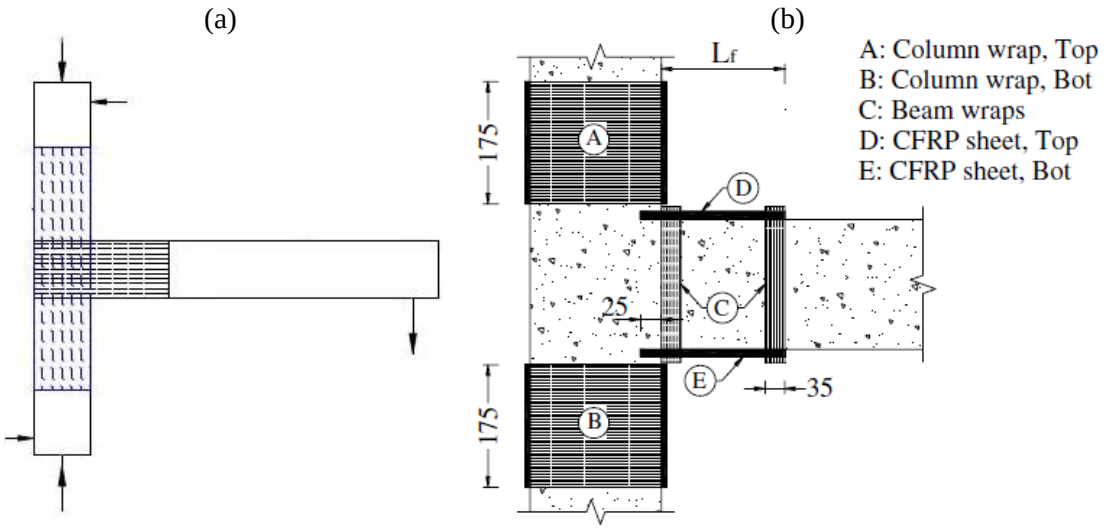

Figure 2.26. CFRP retrofit scheme for plastic hinge relocation in exterior joints: (a) Mahini and Ronagh (2011); (b) Eslami and Ronagh (2014).

For the control specimen the hysteretic behaviour shows severe pinching and stiffness degradation during cyclic loading. The specimen fails by spalling of the concrete followed by buckling of the beam reinforcement bars at the beam/joint interface. For the CFRP retrofitted specimen, first cracks are shifted away from the interface with the joint to the end of the FRP wrap in the beam. Large localised inelastic deformations are observed about 150 mm away from the column face, while the joint area remains elastic up to failure. The authors conclude that the CFRP retrofit of the beam web is effective in relocating the plastic hinge zone and providing a failure mechanism with more adequate energy dissipation. Again the geometry and retrofit scheme would not be reflective of most actual structures and the presence of a slab would increase the beam moment capacity, likely causing a column hinging mechanism in the control specimen.

An improved retrofit scheme for plastic hinge relocation within the beams of exterior joints by Ronagh's group (Eslami et al., 2013; Eslami and Ronagh, 2014) is presented in Figure 2.26 (b). Compared to the previous scheme, the joint area is left free from FRP, rendering the retrofit applicable to real structures with transverse beams. The thin beam FRP wraps in (C) are also realistically feasible if slots are drilled trough the slab. To achieve PH relocation, CFRP sheets (D) and (E) are extended along the beam top and bottom faces. While the specimens are designed for a weak-beam/strong-column mechanism, column wrapping is still provided to ensure the columns sustain the increased drift demand.

Three 1:2.85-scaled exterior joints are tested under cyclic loading, comparing a control specimen with two retrofitted specimens. The two schemes differ in PH strengthening lengths, with FRP applied along 175 mm (one beam depth) and 350 mm (two beam depths). Additional anchorage is provided by embedding the beam FRP sheets into a 25 mm deep groove in the concrete cover of the joint and its effect tested under monotonic loading.

For the control specimen, beam plastic hinging is observed, with significant damage at the beam/joint interface. For the retrofitted specimen without groove anchorage, no improvement in the specimen's behaviour is observed and PH relocation is not successful. With anchorage, the shorter beam FRP length achieves very satisfactory behaviour, with a concentrated PH forming right after the strengthening. This leads to a strength increase of 31% compared to the control specimen. With a longer strengthened length (two beam depths), the aim of PH relocation is not achieved. Instead, flexural cracks are observed near the beam/joint interface at high drift levels, which is attributed to the inadequate anchorage length (groove depth), limited to the concrete cover depth. While a higher increase in strength (45%) is still observed for this specimen, a steeper post-peak strength decrease is obtained, leading to a reduction in ductility by 36% compared to the control specimen.

Overall the second scheme for PH relocation is deemed a very adequate and successful solution that takes into account geometric challenges in real structures. Still, as only 2-D specimens are tested, the effect of a slab contributing to the beam moment capacity needs to be evaluated in real implementations.

2.3.5.3. EFFECT OF SPECIMEN SCALE

A comparative study for the FRP retrofit of beam-column joints for different sizes of members investigates the effectiveness of retrofit with specimen size (Choudhury et al., 2013). In the experimental campaign, six retrofitted exterior beam-column joint specimens with different beam and column dimensions (1/3-, 2/3 and full-scale) are tested under cyclic loading. The specimens are grouped in joints with beam weak in flexure and joints with beams weak in shear. While the amounts of FRP at different locations are varied depending on the deficiency, the global retrofit scheme remains the one shown in Figure 2.27.

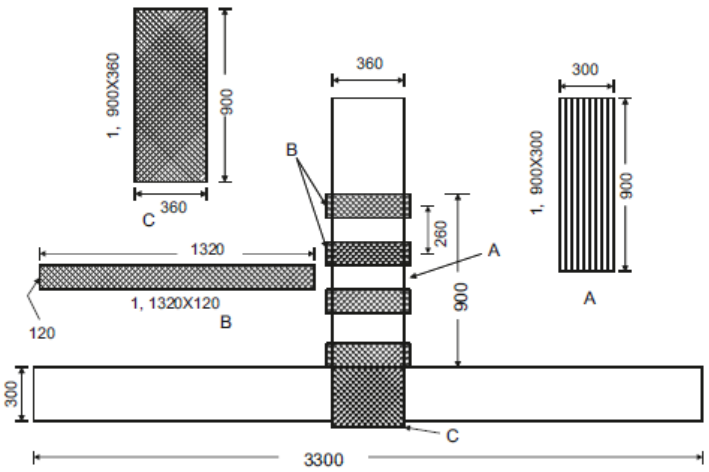

Figure 2.27. Retrofit scheme for exterior beam-column joints (Choudhury *et al.*, 2013).

Unidirectional CFRP sheets are used at the bottom of the beam to improve bar anchorage (A), bidirectional GFRP wraps (B) are used around the beam to improve its shear capacity and anchor the sheet (A), and bidirectional GFRP U-wraps are also used to strengthen the joint in shear (C).

For both deficiencies and retrofit schemes it is found that the percentage gain in ultimate load capacity due to FRP decreases with an increase in specimen size. The effect of the retrofit is hence the lowest for the specimens representative of real structures. Although the findings are based on a specific set-up and retrofit scheme, they still highlight that caution needs to be applied when inferring results based on scaled experimental set-ups, hence the need for more full-scale tests of FRP retrofitted joints.

2.3.6. SELECTIVE UPGRADES

One major advantage of FRP retrofitting is the possibility of a selective upgrade. By means of different retrofit architectures or different fibre angles, the effect of the retrofit can be tuned. In most cases, the aims of such retrofits are to improve the joint shear capacity, as well as improving the bond of the bottom beam bars and confinement or flexural capacity of the column.

2.3.6.1. EL-AMOURY AND GHOBARAH – COMBINED STRENGTHENING.

Further experimental work by Ghobarah's group looks into an improved strengthening scheme and design equations that provide the basis for the *fib* 35 (2006) guidelines (El-Amoury and Ghobarah, 2002). The exterior beam-column joint set-up and loading is the same as in the other experiments by the group (e.g.: Ghobarah and El-Amoury, 2005). Two joints are retrofitted with GFRP using a two-part selective retrofit scheme, shown in Figure 2.28, consisting of:

- Joint: U-wraps, similarly to aforementioned T2R (Ghobarah and Said, 2002).
- Upgrade of beam bar bond-slip capacity: unidirectional FRP placed along the beam bottom face and along the inside face of the bottom column.

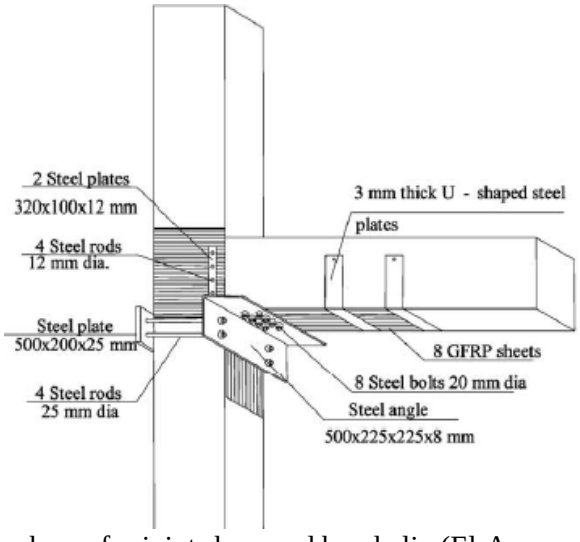

Figure 2.28. Retrofit scheme for joint shear and bond-slip (El-Amoury and Ghobarah, 2002).

Both retrofitted specimens have the same joint strengthening, but TR1 has only 4 layers of FRP along the beam, while TR2 has 8 layers. As evidence from past experiments and other researchers suggest, anchorage is provided to the sheets for all tests. The joint U-wraps are held by steel plates on either side connected by steel rods through the joint. The beam and column FRP is secured at

the corner using bolted steel angles. Furthermore, for one of the two specimens tested (TR2), two 3mm thick U-shaped steel plates are used to anchor the beam FRP towards the end of the beam.

For the control specimen, failure occurs due to severe shear cracking, as well as cracking in the beams caused by bond-slip of the bottom bars, ultimately leading to a lower load capacity. For the retrofitted joints, although the FRP sheets are reported to only reach about 25% of the design strain, higher energy dissipation and load carrying capacities are recorded. For specimen TR1 without additional anchorage of the beam FRP sheets, debonding of FRP followed by fracturing of the weld of the corner anchor ultimately leads to bond-slip of the beam bars. This, however, occurs at much higher values of drift and load then for the control specimen. For specimen TR2 with additional steel plate anchorage, no bond-slip is observed. The joint is reported to withstand much higher values of drift and load (52% higher than the control specimen) and ultimately fails in joint shear. Nevertheless, the behaviour of specimen TR2 is much more ductile than that of the control and TR1. TR2 is hence the more effective retrofit system, which is also indicated by the relative energy dissipation: while TR1 dissipates three times more energy than the control specimen, TR2 achieves nearly six times its energy dissipation.

2.3.6.2. AL-SALLOUM GROUP AT THE KING SAUD UNIVERSITY

Other efforts considering selective retrofit schemes for beam-column joints include the work of Al-Salloum's research group at the King Saud University in Saudi Arabia. The specimens tested are interior joints with two beams (Al-Salloum and Almusallam, 2007) and exterior joints with one beam framing into the joint (Alsayed et al., 2010). All specimens have the same overall element geometries and present a 60 mm deep slab of 600 mm width. No transverse beams are however included in the set-up.

Two different retrofit layouts using unidirectional CFRP are tested, as shown in Figure 2.29 for interior joint, with the aim of upgrading the shear strength and ductility of the seismically deficient joints. The first scheme (a) consists of wrapping both faces of the joint panel (U-wrap for the external joint), fully wrapping the column above and below the joint, and finally U-wrapping the beam(s), while the second (b) consists of the joint U-wrap only, but with steel bolts as anchorage. No reference is made as to why the first retrofit strategy does not include anchors. The amount of FRP required is calculated according to the method proposed by Ghobarah's group (El-Amoury and Ghobarah, 2002), and hence is in line with the *fib* 35 guidelines (fib, 2006). It is worth mentioning that scheme (b) is similar to in Ghobarah's U-wrap scheme (Ghobarah and Said, 2002), however, in this case, uni-directional CFRP sheets are used instead of bi-directional GFRP.

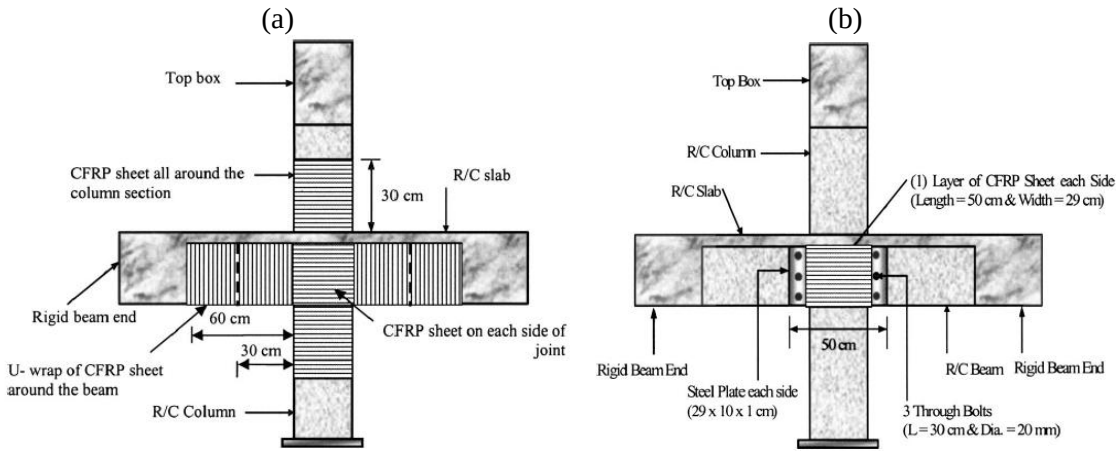

Figure 2.29 - Proposed retrofit layouts for interior joints (Al-Salloum and Almusallam, 2007).

For exterior joints undergoing quasi-static tests (Alsayed et al., 2010), it is observed that both CFRP retrofit schemes achieves to delay joint shear cracking and to make the joint generally stiffer against distortion. The increase in stiffness for scheme (a) is more pronounced than for scheme (b). However, as expected from other evidence in the literature, the specimen strengthened with layout (a) is less efficient in reducing the rate of stiffness degradation then layout (b) due to de-bonding and rupture of the FRP in the beam. With layout (b), the failure mode is shifted from joint shear failure, as observed in the control specimens, to a more ductile beam hinging mechanism. While the displacement capacity of the specimen strengthened with layout (b) is higher than that for (a), the peak lateral load is higher for specimen (a), as scheme (b) does not provide any strengthening of the beam or column.

For interior joints, very similar results are observed. Again the lack of mechanical anchors leads to bulging of the FRP in some locations. The strength of specimen (a) is slightly higher, as the joint and beams are strengthened, but retrofit (b) with less material and similar strength gain is more efficient. The aim of changing the failure mechanism is achieved and the study shows that strengthening of a joint at one location can substantially improve its strength and ductility, but will shift the location of damage, which needs to be assessed carefully beforehand (Al-Salloum and Almusallam, 2007).

Overall, it can be concluded that while scheme (b) is more efficient than (a) in terms of changing the failure mechanism and ductility, this seems to be mainly attributable to the fact that scheme (a) does not have any mechanical anchorage. It is also demonstrated that depending on the scheme used, different cyclic properties of the joint, such as peak load or ductility, can be enhanced selectively. Finally, as mentioned for other schemes, one constraint ignored by both retrofit designs is the presence of transverse beams, which would render them difficult or impossible to apply.

2.3.6.3. PANTELIDES ET AL. (2008)

Eight interior joints without slab and transverse beams are tested by Pantelides *et al.* (2008). The specimens are designed without transverse reinforcement and insufficient bottom beam bar anchorage and the proposed retrofit schemes have two different objectives, improving bar anchorage and joint shear strengthening.

The CFRP retrofit scheme consists of FRP wraps of the column for confinement, sheets along the bottom of the beam and along the sides of the beam through the joint, U- wraps for shear strengthening of the beams and two CFRP layers placed at an angle of 30° from the vertical in the joint region (see Figure 2.30).

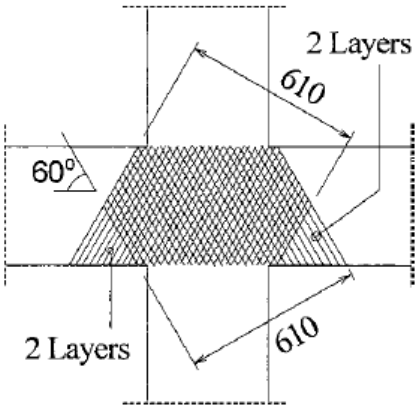

Figure 2.30. Joint shear strengthening with diagonal CFRP sheets (Pantelides *et al.*, 2008).

The angle of the fibres is determined based on earlier retrofit designs by the research group for 1/3 scaled T-joints (Gergely et al., 2000). To determine the amount of FRP required, first, the shear forces and stresses at the joint centre are calculated at the maximum storey shear. Then the principal stress and angle are calculated using Mohr's circle. Finally, the amount of FRP acting in tension along the principal axis is calculated to achieve a capacity of the joint that prevents cracking.

The retrofit can be adjusted depending on the relative strengths of the members framing into the joint, hence the tests are carried out for joints with stronger beams, assumed to fail in joint shear, and for joints with stronger columns, predicted to fail in beam bar anchorage. Ductile behaviour is achieved for all retrofitted specimens, but greater improvements are recorded for joints with joint shear deficiency.

In terms of practical implementation, the application of joint shear strengthening is limited to structures without transverse beams and would require cutting through the floors around the circumference of the column. Moreover, the scheme is focussed on specimens with a strong-column/weak-beam hierarchy of strengths, which are less frequently observed for pre-1970's structures, as emphasised in Section 2.1.3.

2.3.7. FLEXURAL COLUMN STRENGTHENING

To achieve an appropriate hierarchy of strength and a ductile beam hinging mechanism, flexural strengthening of columns is often required for pre-1970's structures. First flexural strengthening schemes for columns are presented, then their implementation within beam-column joint specimens is addressed.

2.3.7.1. COLUMN TESTS

In this section, the flexural strengthening of columns is discussed. Most studies on FRP strengthening of columns relate to the horizontal FRP wrapping or jacketing of RC columns, which is a well-documented method for enhancing the axial load capacity, shear capacity and ductility of columns (e.g.: Asaei et al., 2012; Belouar et al., 2013). Experimental evidence shows that FRP is more effective than typical concrete jacketing for increasing the ductility of RC columns (Bousias et al., 2006). FRP jacketing for confinement of RC columns is easy to apply and hence the most common use of FRP since the 1990's (Abbasnia et al., 2012; Motavalli and Czaderski, 2007). This is also because well-accepted and tested design equations in guidelines exist internationally, enabling engineers to use FRP in practical applications for real structures, as shown in Figure 2.9 for L'Aquila, Italy. Although most equations for FRP confinement of rectangular columns are based on modifying equations for circular columns using shape and confinement efficiency factors, these prove reasonably accurate and conservative (Ozcan et al., 2010; Rocca et al., 2008).

For flexural strengthening of columns, design codes recognise that horizontal FRP jacketing alone can however not be used, as FRP-strengthening with "fibres lying along the longitudinal axis of the member", as per cl. 4.5.1 (1) of the CNR guidelines (CNR, 2013) is required. In the same guidelines, adequate anchorage into the column base or beam-column is prescribed in cl. 4.2.2.4 (2). In the U.S., section 13.4.2 of the latest draft ACI guidelines for seismic strengthening with FRP (ACI, 2014), also recognises the need for continuity of vertical FRP through the joint to develop an adequate flexural capacity at the base and top of framing columns.

Compared to FRP jacketing, only a limited amount of studies on the flexural strengthening of RC columns exist. This is caused in particular by the difficulty of extending the externally bonded vertical FRP sheets beyond the column ends when floor slabs or column bases are present (Li et al., 2013). Anchorage into the column base or a connection between a lower and upper storey column is however crucial, as the maximum moments typically act at column ends.

2.3.7.1.1. NEAR-SURFACE-MOUNTED FRP

To achieve well-anchored column flexural strengthening, a number of studies investigate the applicability of NSM (near-surface-mounted) FRP. In NSM applications, FRP in form of bars or laminate strips is embedded into pre-cut grooves along the column and extended into the column base. For adequate bond, the grooves are then filled with epoxy resin or grout.

Barros' group at the University of Minho present tests on NSM retrofitted and repaired RC columns under cyclic loading and applied axial loading (Barros et al., 2006, 2008; Perrone et al., 2009). Four NSM CFRP laminate strips are applied in pre-cut slits along the length of the column and embedded into the column base in holes of 100 mm depth as shown in Figure 2.31. The retrofit and repair schemes are applied to the columns with two amounts of steel reinforcement, using four 10 or 12 mm diameter bars, respectively.

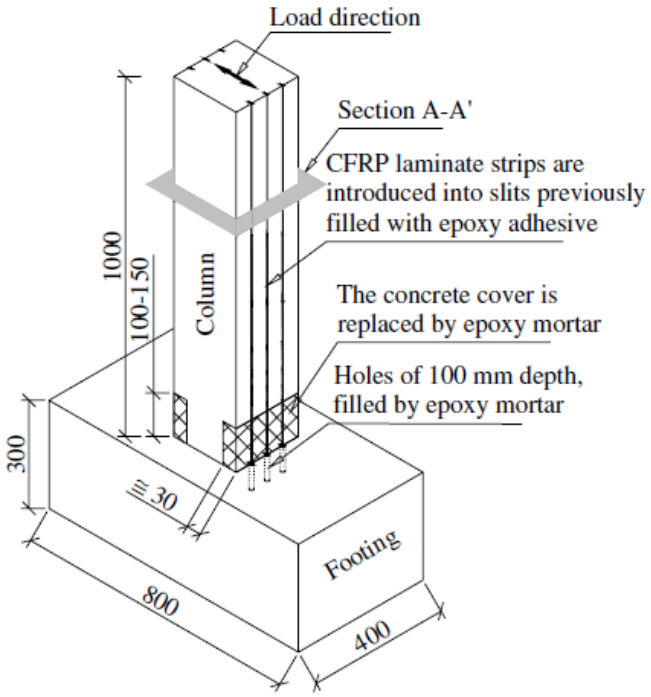

Figure 2.31. NSM flexural retrofit of RC columns (Barros et al, 2006).

In all cases the NSM retrofit improved the flexural capacity of the RC columns. This effect is found to be significantly larger for specimens with lower steel reinforcement ratio, with an increase in flexural capacity of 92%, compared to 34% for the specimens with larger amount of steel reinforcement. Furthermore, despite reaching large values of up to 1% FRP strain, the NSM laminate strips are not observed to debond during the tests. It is worth noting that no additional anchorage or wrapping of the NSM is required, highlighting the superior bond properties of NSM compared to externally bonded FRP.

Finally, in terms of energy dissipation, no significant improvements are recorded despite the increased flexural capacity, as larger pinching in the hysteretic loops is observed. The authors hence recommend additional horizontal FRP wrapping for a more dissipative behaviour.

A systematic research study on the cyclic behaviour of NSM retrofitted RC columns is conducted by Bournas and Triantafillou (2009), investigating the effect of NSM material (CFRP strips and GFRP or stainless steel bars) and additional local jacketing at the column ends. The confinement of the column ends is provided by TRM (textile-reinforced mortar) jackets. While an enhancement in flexural resistance up to 46% is obtained for all FRP retrofitted columns, it is found that without local jacketing, ductility and energy dissipation are not improved. This echoes the results obtained by Barros' group.

The need for combining NSM retrofit for flexural strengthening with jacketing for increased ductility is further confirmed by Li et al. (2013), testing three RC columns with NSM GFRP bars embedded into the base for flexural strengthening and using CFRP jackets for confinement. Without confinement, a reduced ductility is obtained, while the combined retrofit achieves significant strength (+51%) increase as well as an enhanced ductility (+15%).

Overall, while studies on the use of NSM for flexural strengthening of columns prove the feasibility of enhancing their moment capacity, additional confinement jacketing is required to ensure a ductile behaviour. Good anchorage to a column base can be accomplished, hence making full use of the FRP material without premature debonding. Still, their applicability is less practical in the case of beam-column joints, as achieving continuity between storeys through the joint region with NSM bars is hampered by the presence of transverse beams.

2.3.7.1.2. FRP ANCHORS

A study by Vrettos et al. (2013), provides an alternative to the use of NSM bars, using CFRP anchors to enhance the flexural resistance of RC columns subjected to seismic loading. The anchors are anchored into the column base in a similar fashion to NSM, as shown in Figure 2.32. The aim of this method is to transfer tensile forces from the vertical CFRP sheets that terminate at the column ends, into the column base. Three retrofitted columns are tested under cyclic loading with different amounts of FRP anchors. For all specimens, the FRP anchors are embedded in 250 mm deep holes in the column base. Using two thick anchor fans, a 35% increase in moment capacity is achieved. While debonding of the anchors is prevented, tensile rupture of the anchors is observed at the column ends. This is observed at a relatively low strains of 0.43% to 0.53%, which are similar to the maximum debonding strain (0.4%) used in many design guidelines (CNR, 2013). The authors of the study attribute this to the high concentration of stress at the base/column interface.

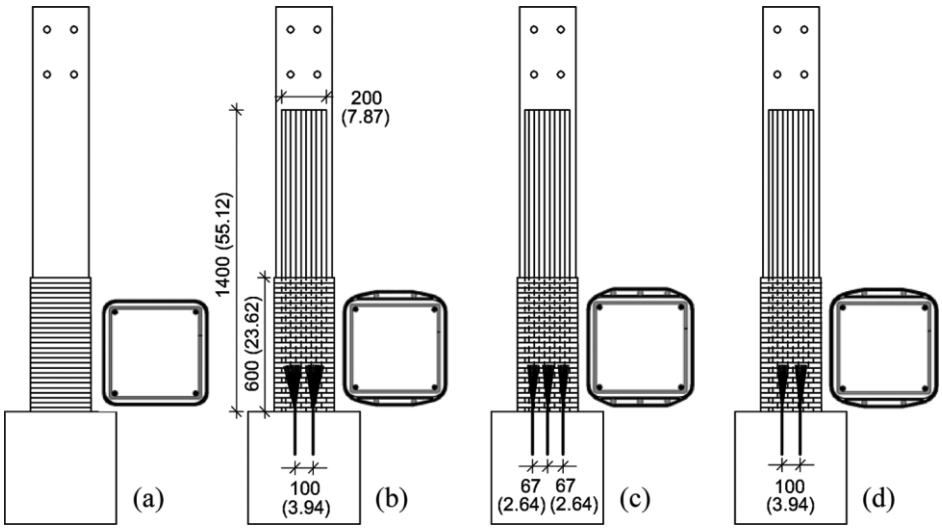

Figure 2.32. FRP anchors for flexural strengthening of RC columns (Vrettos et al., 2013).

More recently, a similar study on FRP anchors for flexural strengthening of columns is conducted by Bournas et al. (2015) on four ½-scale specimens under monotonic loading. While the amount of FRP anchor area is varied between specimens, the FRP anchors are embedded in 200 mm deep holes in the column base for all specimens. With an increased amount of anchor and vertical FRP area, a linearly increasing strength of the specimens is obtained. No comparisons to an unstrenghtened control specimen are however made. Again debonding is effectively prevented due to the anchors and failure is due to partial rupture of the anchors. While the same CFRP material as Vrettos et al. is used, larger FRP strains between 0.45% and 0.73% are observed, which is attributed to the monotonic loading in this study.

To conclude, in contrast to NSM bars, FRP anchors can be applied at the corners of columns, hence avoiding transverse beams in beam-column joints. It is hence conceivable to use double-headed FRP anchors at the corners of columns through holes in a slab to achieve continuity in strengthening. It is however important to consider the low rupture strain of these anchors under cyclic when fully embedded into the base.

2.3.7.2. INTERIOR JOINTS

2.3.7.2.1. NSM STRENGTHENING

A study by Prota et al (2004) looks at using near-surface mounted (NSM) CFRP rods in combination with horizontal FRP sheets to alter the hierarchy of strengths in interior joint sub-assemblies (Figure 2.33). Eleven cross-shaped interior joints are tested with three different levels of column axial load varying from values of 0.1 to 0.2 normalised axial load.

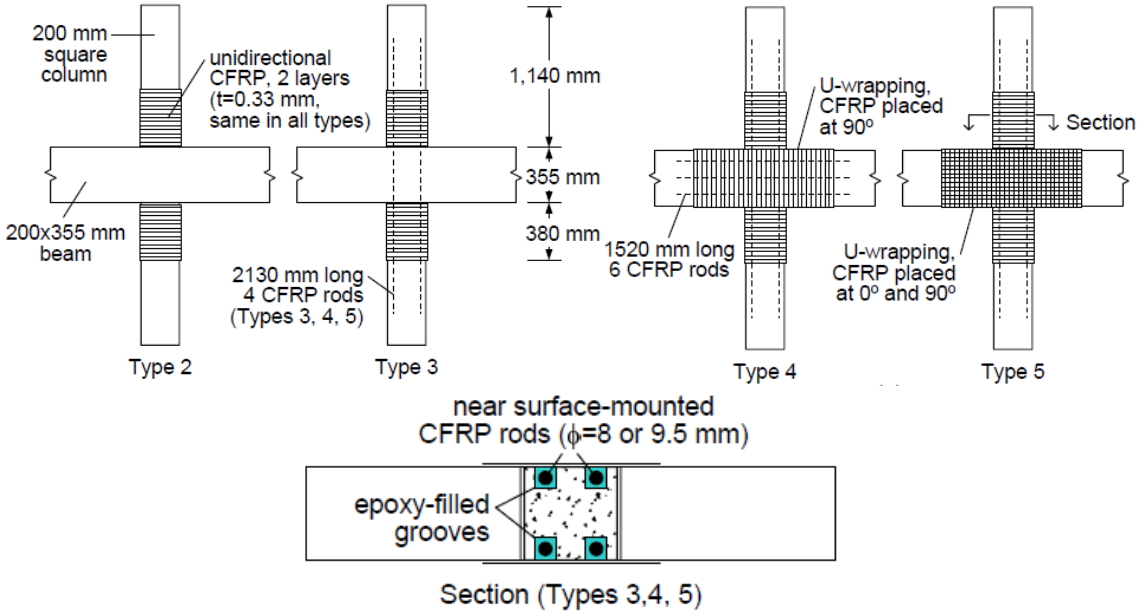

Figure 2.33. Interior joints retrofitted with CFRP sheets and/or NSM rods (Prota, 2004).

The first retrofit scheme, Type 2, consists of column confinement FRP wraps and aims to shift the failure initially from the column to the joint. The intended mechanism is however not observed as the failure is only moved from a compressive concrete crushing failure to a flexural hinging failure in the column for low column axial load. A low increase in strength of 7% with an 11% reduction in ductility is obtained. For a high axial load, a combined column-joint failure is observed, but significant flexural cracking is still noticed at the joint/column interface. The increase in strength is more pronounced with increased axial load (+33%) and an increase in ductility are observed.

Next, for specimen Type 3, CFRP bars are additionally placed in epoxy-filled grooves along the columns (NSM), serving as flexural reinforcement of the columns. This retrofit leads to a stronger flexural capacity of the columns, which do not fail, and joint shear failure is now observed for all three levels of axial load. While a significant strength-increase of 39% (low axial load) to 62% (high axial load) is obtained, due to the brittle failure mechanism, a reduction in ductility up to -14% is observed for Type 3 specimens.

As a next step, for specimen Type 4 the joint panel is also strengthened by horizontal CFRP rods and vertical CFRP U-wrapping along the beams and join. For Type 5, instead of horizontal CFRP rods, bi-directional U-wrapping is applied to the beams and joint. For both retrofits, the NSM bars are not applied continuously through the joint to account for the presence of a floor slab. The observed failure mechanism is a flexural failure of the columns at the column/joint interfaces where the NSM bars are terminated. Compared to Type 3, a slightly higher increase in strength of 37% (low axial load) and 83% (high axial load) is obtained, as well as a strong increase in ductility up to 73%.

An important outcome of this study is the need for flexural strengthening by means of longitudinal FRP, as confinement alone is not enough for weak gravity-designed columns. The flexural strengthening is however only effective if it is applied continuously through the joint, connecting both columns as for Type 3. Moreover, the assessment of the influence of axial load shows that an increase in axial load increases the strength enhancement of the FRP retrofits.

2.3.7.2.2. FRP STRIPS AT THE COLUMN CORNERS

A strengthening strategy for improving the strength of columns is proposed for interior joints by Lee et al. (2010). Three full-scale interior joints are tested, of which two are retrofitted with CFRP. The two retrofit schemes are shown in Figure 2.34. The first retrofit (a) consists of four layers of FRP strip along the corners of the column to ensure continuity and two perpendicular layers above and below the joint for shear strengthening. No anchorage is provided for this specimen. A second specimen is retrofitted similarly, but additional horizontal FRP is applied in the joint and anchored to the beams with steel-angles at all corners. The column FRP is also anchored using steel angles.

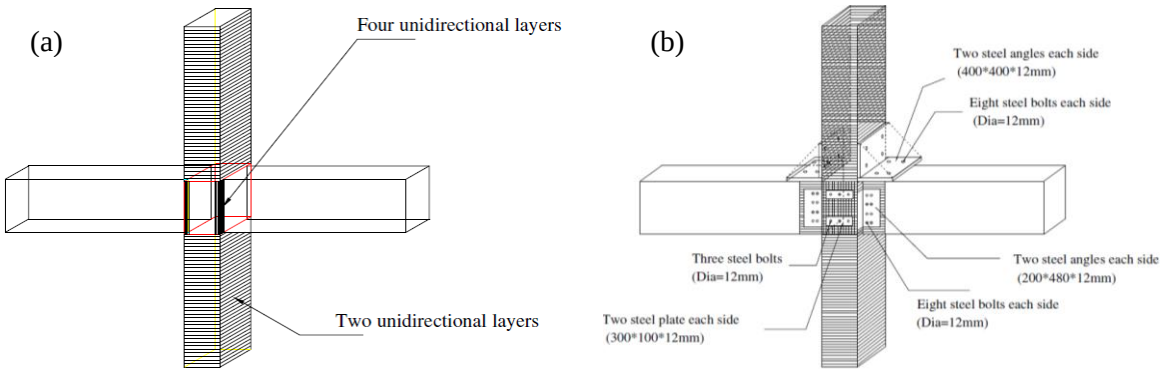

Figure 2.34. Column strengthening (Lee et al., 2010) – (a) without and (b) with steel angles.

The stiffness degradation is reduced for both specimens compared to the control specimen. For the unanchored specimen, however, no improvement is recorded in terms of failure mechanism or strength increase. For the specimen with anchorage, increased damage in the beams is observed, leading to a more dissipative failure mechanism with an increase in ultimate load capacity and energy dissipation of 36% and 90%, respectively. No CFRP debonding is observed for the specimen with anchorage, highlighting that anchorage is a requirement to ensure any strengthening strategy is effective.

2.3.7.2.3. L-SHAPED FRP

A recent study by Yu et al. (2016) on interior joint with slabs and transverse beams, addresses the need for flexural strengthening of columns for realistic weak-column/strong-beam specimens. The retrofit and repair schemes assessed in this study use externally bonded L-shaped FRP laminates as shown in Figure 2.35. Due to the ease of application, not requiring drilling through the slab, this method is widely used in China according to the authors.

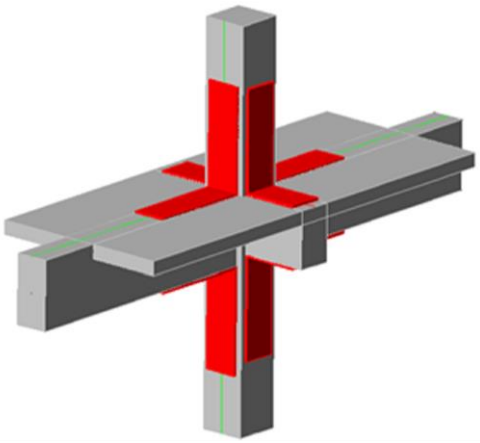

Figure 2.35. L-shaped column retrofit typically used in China (Yu et al., 2016).

To test the validity of this retrofit method, an experimental programme on ten half-scale interior joints is conducted. The retrofit is applied as a repair scheme to specimens with different extents of pre-damage, ranging from initial yielding of the column reinforcement to significant cracking. One specimen is retrofitted without pre-damage. The effect of FRP type is tested by splitting the tests in two groups of five specimens. The first group of specimens is strengthened with CFRP, while BFRP is used for the second group, which has a lower strength and stiffness, but a larger rupture strain. The effect of axial load is also investigated by testing two specimens with a lower axial load ratio (0.3 vs. 0.5).

The same retrofit layout is used for all specimens and includes full wrapping of the columns for anchorage and confinement, as well as U-shape wrapping on the beams to anchor the L-shapes. For the pre-damage specimens, epoxy crack-injection is applied before the FRP laminates.

Upon cyclic testing, ductile beam-hinging failure is observed for all of the strengthened specimens, indicating a successful reversal of the hierarchy of strengths. For the specimens with pre-damage, a reduction in initial stiffness is observed. This reduction is more pronounced for an increased extent of damage, confirming observations made in Section 2.3.2. However, the extent of pre-damage does not significantly influence the maximum obtained strength or ultimate drift of the repaired specimens. The increased axial load only leads to a slightly increased retrofit effectiveness (+3%).

With respect to the FRP type, a significant difference between CFRP and BFRP is observed. While the repair using CFRP achieves a strong increase in capacity (on average +23.8%), the repair with BFRP is less effective (+6.4%). In turn, the BFRP repair is more successful in increasing the ductility of the specimens, with an average increase of 44.3% compared to a 23% increase with CFRP. This observation echoes results for comparisons of CFRP with GFRP by other authors.

Overall the described repair schemes are effective and easily applicable to realistic RC frames. It is however worth noting that the obtained strain in both FRP materials is less than half the value

anticipated by guideline equations (ACI, 2008b). This results in a potentially dangerous over-estimation of the column flexural capacity by guideline equation for this type of retrofit. Yu et al. hence propose an improved strain calculation, applicable to L-shaped laminates, that proves more conservative and highlights the limitation of the retrofit by the effective strain in the laminates.

2.3.7.2.4. CFRP FAN-SHAPED ANCHOR STRANDS

A group at the University of Tokyo uses fan-shaped FRP anchors passed through all corners of an interior joint to improve its shear behaviour and ensure a beam-hinging failure mechanism (Shiohara et al., 2009). This retrofit strategy has the advantage of providing continuity of the longitudinal FRP sheets along the column, as well as contributing to the shear resistance mechanism of the joint. Compared to other retrofit strategies assessed in this review, Shiohara's retrofit is feasible even for interior joints with slabs and transverse beams, only requiring small holes drilled through the slab at the column corners.

The retrofit uses "CF anchors", a proprietary product available in Japan that consists of bundled CFRP strands with fan-shaped anchors on either end. The CF anchors are passed through plastic tubes at the corners of the column and anchored to the column faces, as shown in Figure 2.36, and thus provide vertical confinement and connect the flexural FRP in the columns through the joint.

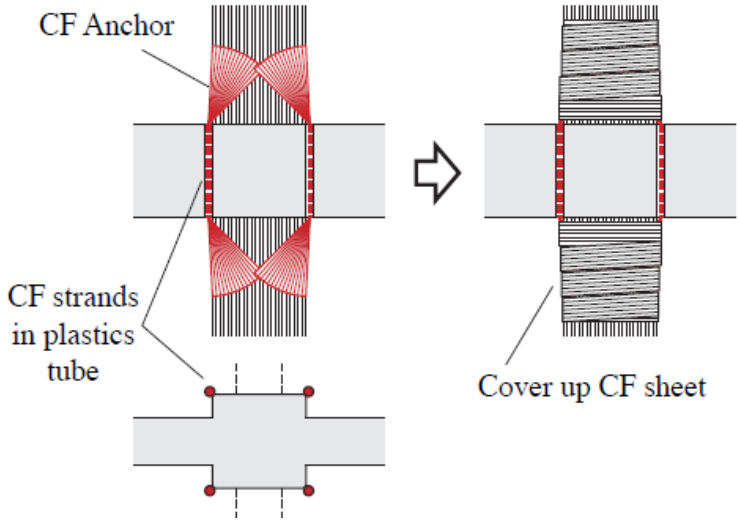

Figure 2.36. CFRP anchors in plastic tubes to strengthen interior joints (Shiohara et al, 2009).

Two retrofitted one-third scale interior joints with different beam geometry (rectangular and square cross-sections) are tested under cyclic loading. Despite the fact that the retrofit could be applied to joints with slabs and transverse beams, the tested specimens are simple 2D cross-shaped joints. The joint steel reinforcement consists of two transverse hoops and normal concrete strength is used. It is noted that no axial load is applied at the top of the column.

An increase in maximum story drift (+30%) and shear force (+6% and +13%, for the rectangular and square beams, respectively) are observed for the retrofitted specimens. In both retrofitted specimens, yielding of the column bars is prevented. In terms of failure mechanism, damage in

the joint core is not reduced. While the use of plastic tubes reduces the risk of rupture due to large localised stress at the joint/column interface (Vrettos et al., 2013), slippage of the CF strands is observed. This, in turn, means that energy dissipation is not improved.

It can be concluded that the idea of using vertical strands of FRP is readily applicable for all joint geometries and shows potential, in particular to increase the column flexural capacity. Nevertheless, the overall retrofit strategy needs improvement to be more effective. Moreover, the test set-up is not ideal, as the specimens are scaled, have no slab or transverse beams and no axial load is applied, rendering it highly unrealistic.

2.3.8. FULL CAPACITY DESIGN BASED RETROFIT STRATEGIES

In this section, retrofit strategies looking at modifying relative strength of beams, columns and joint according to capacity design principles are discussed. The control specimens present an inadequate strength hierarchy and the proposed retrofits aim to promote a beam-hinging mode.

2.3.8.1. GARCIA ET AL.

A further retrofit study by Garcia et al. is conducted on a one bay full-scale two-storey RC frame designed to pre-1970's RC guidelines (Garcia et al., 2010). The frame is repaired by strengthening all corner joints with CFRP sheets as shown in Figure 2.37. The columns are strengthened with one layer of vertical CFRP. For the interior column face, this layer is extended in an L-shape onto the slab and beams and anchored at the corners. One horizontal layer for joint shear strengthening is anchored using two thin strips fully wrapped around the beams through holes in the slab.

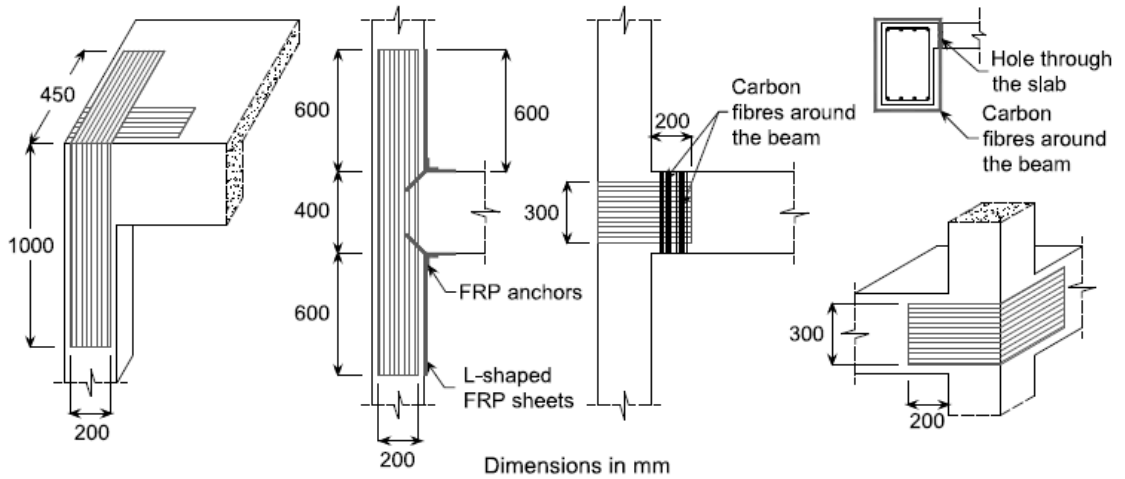

Figure 2.37. CFRP rehabilitation of corner joints in a full frame by Garcia et al. (2010).

While the control frame failed in a column-sway mechanism, the retrofit effectively changes the failure to a beam-sway mechanism. The vertical and L-shaped FRP sheets are hence successfully strengthening the weak column. The performance of the frame is improved from the Collapse Prevention to the Life Safety performance level with respect to definitions in FEMA 356 (1999).

Analytical modelling confirms the effectiveness of the retrofit scheme in promoting a more ductile failure mechanism for a further six real earthquake records.

2.3.8.2. ENGINDENIZ ET AL., 2008

Kahn's group at Georgia Tech investigate the feasibility of designing a CFRP retrofit for pre-1970's corner joints with slabs under bi-directional loading (Engindeniz et al., 2008a). The focus of the retrofit scheme lies on preventing brittle failure and promoting a beam hinging failure mechanism. The tested specimens are designed without shear strengthening, with lap-spliced column bars over the joint and a weak-column/strong-beam hierarchy, so as to break the principles of capacity design. Moreover, the anchorage of beam bottom bars into the joint is inadequate (no bend). The experimental programme also aims to compare the retrofit effectiveness for two specimens with different concrete strengths (33.9 compared to 15.4 MPa).

The results from control specimens indicate extensive yielding of column bars, joint shear cracking, as well as loss of anchorage of bottom beam bars. To prevent these brittle mechanisms, a two-step retrofit scheme, based on capacity design principles, is devised (Figure 2.38).

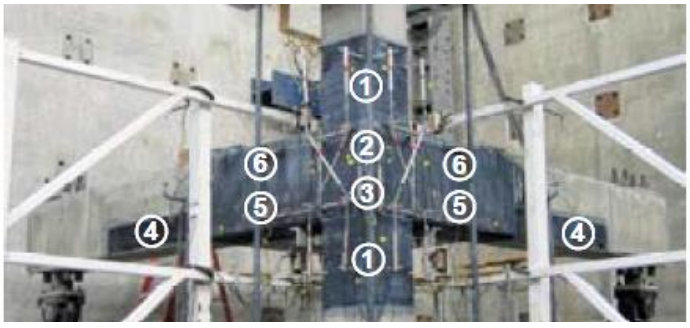

Figure 2.38. CFRP retrofit scheme by Engindeniz *et al.* (2008).

First the inner column corner is strengthened by removal of a 50 mm by 50 mm section of the column and a perforation of the slab of the same size, in which an additional M22 bar is placed and covered with a high strength polymer-modified cementitious mortar. The second step consists of a CFRP retrofit scheme that is adapted to account for differences in concrete strength between the two specimens. The amount of FRP layers is designed using the ACI-440F guidelines (2002).

Five layers L-shaped CFRP are applied around the joint panel, extending into the column, both perpendicular (3) and parallel (2) to the column axis. Then, five layers of CFRP strips are applied along the bottom of the beams to prevent beam bar slippage (4, 5). These strips are anchored with two layers of U-shaped sheets of FRP (6). Finally, the column is fully wrapped with two layers above and below the joint to improve ductility, as well as for anchorage of the sheets confining the joint area (1). One extra layer of FRP is placed above the joint for the specimen with lower concrete strength, to account for its lower shear capacity.

For both retrofitted specimens shear failure is prevented and a shear capacity compliant with modern codes is achieved. The specimen with stronger concrete achieves a more ductile beam

hinging failure mechanism with high energy dissipation and full use of the FRP, rupturing at 94% of its ultimate strain rather than debonding. The specimen with lower concrete grade experiences a significant reduction in stiffness (44% lower) and strongly reduced energy dissipation (37% lower), due to a less ductile hysteretic behaviour. This can be related to the specimen not achieving a beam hinging mechanism due to the lower concrete grade reducing the bond properties of the beam bars.

Overall the proposed multi-objective retrofit scheme is hence successful in preventing joint shear failure and promoting a more ductile mechanism. An important observation for real applications is that, for very low concrete strengths, a more invasive retrofit scheme with replacement of parts of the concrete is required to achieve a beam hinging failure.

2.3.8.3. PAMPANIN ET AL.

The retrofit design schemes proposed by Pampanin's group at the University of Canterbury follow the principles of performance-based design. It takes into account multiple performance levels based on specified limit states (Akguzel and Pampanin, 2009; Akguzel *et al.*, 2011). The aim of such retrofit strategies is to rearrange the existing sequence of events according to capacity design considerations and to provide a more favourable ductile failure mechanism. The retrofit hence pays particular attention to the global hierarchy of strength within the structure, as well as the local damage evolution in the joint sub-assembly. The hierarchy of strength and sequence of events for the retrofitted specimens is assessed in the M-N (moment – axial load) performance domain, proposed in earlier work (Pampanin et al., 2004).

2.3.8.3.1. TWO-DIMENSIONAL JOINTS

Initial work looks at retrofitting two-dimensional interior and exterior joints without slab that are designed for gravity loads only (Pampanin et al., 2004). The retrofit solution, consisting of a simple system of vertical and horizontal CFRP sheets, aims to protect the joint panel from a brittle shear failure mechanism with concrete spalling, which is observed for as-built specimens (Pampanin et al., 2002). Two layers of vertical CFRP are placed along the length of the column to enhance its flexural capacity and provide additional shear strength to the joint. For the exterior joint, an additional horizontal U-shaped laminate is applied to further increase joint shear strength wedge. Although no mechanical anchors are used, it is attempted to delay debonding of the laminates by wrapping them with smaller strips of FRP. Quasi-static testing of the joints shows that the retrofit successfully alters the hierarchy of strength and sequence of events, eliminating the brittle joint shear mechanism, but that debonding reduces the retrofit effectiveness.

2.3.8.3.2. CORNER JOINTS WITH TRANSVERSE BEAM

Following the work on two-dimensional exterior joints, the effect of bidirectional loading on three-dimensional specimens is investigated (Akguzel and Pampanin, 2007). The retrofit layout

is very similar to the one described in the previous study (Pampanin et al., 2004), but uses a different type of fibre (GFRP). To achieve a more realistic representation of actual structures, two corner joints are compared in the as-built and retrofitted case under uni- and bidirectional loading. No slabs are present in the tested specimens, but the 3D set-up contains a transverse beam. Despite additional confinement of a transverse beam in the 3D specimen, increased joint damage and faster strength degradation is observed. More importantly, the GFRP retrofit protects the joint panel from excessive damage, but proves more effective in the 2D specimen, with a complete relocation of damage away from the joint panel to the region of the beam at the end of the GFRP layer, resulting in a more ductile damage mechanism and hence a more stable hysteresis loop.

The capacity designed FRP retrofit scheme is assessed further with a second test program including ten 2/3-scaled corner joints (Akguzel and Pampanin, 2010). The GFRP scheme shown in Figure 2.39 again aims to promote a ductile beam-sway mechanism, by strengthening the columns (A) and protecting the joint panel from shear failure (B). Strengthening the beams near the joint (C, D) additionally seeks to force plastic hinging to occur further along the beam. The experiments look at the effect of varying the amount of FRP (1 or 2 layers) in the column, beam and joint, having one or no stirrup in the joint region, varying the axial load proportionally to the lateral load, as well as the effect of bidirectional compared to unidirectional lateral loading.

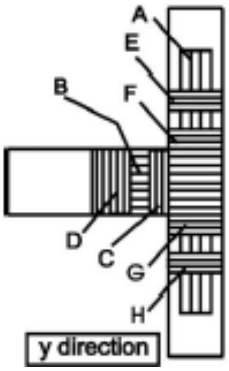

Figure 2.39. Basic scheme for exterior joints by Akguzel and Pampanin (2010).

Two different FRP layouts are tested, the first, R11, having one layer of FRP at each beam face (C, D in Figure 2.39) and one at the column faces (A), and a second, R21, with two layers at the beam faces and only one at the column faces. R21 is more effective than R11, as the shear strain in the joint is reduced from 0.76% (R11) to 0.25% (R21) at 3% drift, indicating higher shear strength. This is in line with earlier results by Triantafillou's group (Antonopoulos and Triantafillou, 2003). In turn, it is found that having one stirrup compared to none in the joint area improves the retrofit, as it maintains the integrity of the joint core and prevents the buckling of column longitudinal bars. Furthermore, for 3D retrofitted specimens, there is 10% additional stiffness degradation per drift level as compared to 2D specimens, confirming that bidirectional loading leads to faster strength degradation and that the FRP retrofit proposed is less effective for 3D joints, particularly when varying axial load. The improvement in behaviour for the retrofitted

3D joints is particularly limited by delamination and buckling of FRP sheets, suggesting that additional FRP, as well as improved anchorage, are needed for a more effective retrofit.

2.3.8.3.3. CORNER JOINTS WITH SLAB

More recently, a new set of experiments by Pampanin's group extends the research to two 2/3-scaled corner joints, of which one contains a slab (Akguzel and Pampanin, 2012a). This research represents one of few efforts globally that take into account the presence of a slab and transverse beams in the retrofit. This is particularly important as it renders the joint area difficult to strengthen and the FRP difficult to anchor.

The corner joints are detailed according to pre-1970s construction practice, with no transverse reinforcement in the joint and plain re-bars used throughout. A step-by-step GFRP retrofit scheme based on capacity design principles is displayed in Figure 2.40. First vertical FRP is applied to the column in order to improve its flexural capacity and to prevent wedge expulsion previously noticed. Then horizontal FRP is applied to the joint region to improve its shear strength. Vertical and horizontal L-sheets are then applied to the inside column and beam faces. The beams are then wrapped with a long sheet of FRP from the bottom face of the slab to the top face to improve the shear strength of beam and slab elements. Confinement of the column is provided and the sheets anchored with fan-shaped anchors. Compared to earlier schemes, the amount of FRP dowel anchors and L-shaped strips is increased. Finally, to reduce the contribution of the slab to the flexural capacity and stiffness of the beams, selective weakening cuts (step 8) are performed.

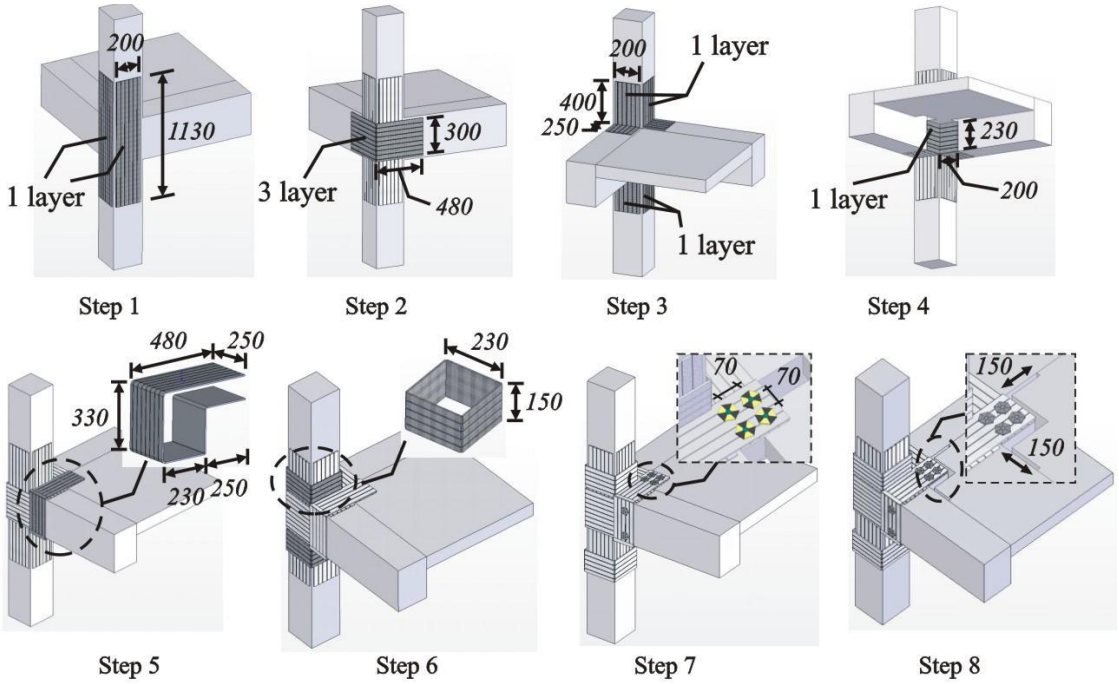

Figure 2.40. Improved GFRP retrofit of realistic corner joints (Akguzel and Pampanin, 2012b).

For anchorage, FRP dowels at the beam faces or through the slab are used, as shown in Figure 2.41, to address premature GFRP detachment. The FRP retrofit is effective in preventing joint

shear failure and transferring damage to the beams for the specimen without slab. Only minor damage is observed in the joint. No debonding occurs for the most part of the test and a strong increase in strength of 40% is obtained.

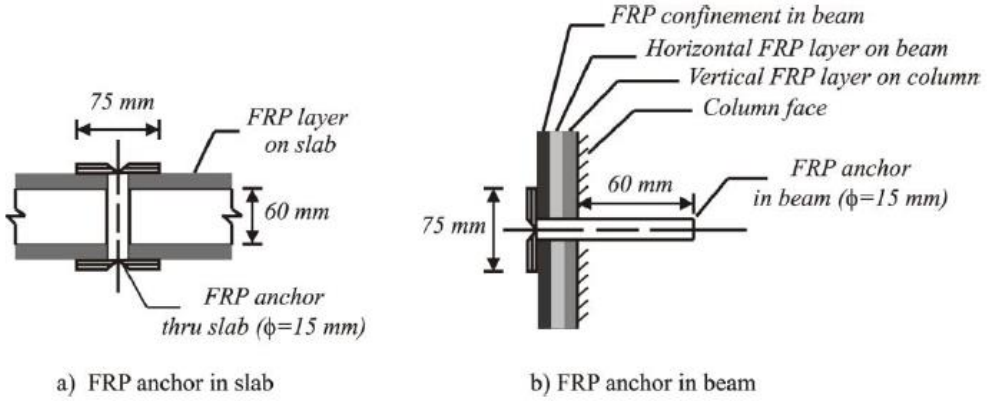

Figure 2.41. FRP dowel anchors (Akguzel et al, 2011).

Compared to the control specimen with slab, which is characterised by a very poor seismic performance, significant improvements are observed for the retrofitted specimen. Still, more damage is observed in the joint region compared to the specimen without slab. Some detachment of column FRP near the joint causes damage to be concentrated in the column/joint, leading to ultimate failure of the specimen. Despite the weakening cuts, beam hinging is not achieved for the specimen with slab. The increase in strength is however similar to the specimen without slab.

2.3.8.3.4. FULL FRAME

Finally, a global retrofit strategy for an 2/5-scale three-storey, two-by-one bay RC frame structure is tested on a shaking table at the University of Canterbury (Akguzel et al., 2011; Gallo et al., 2012). The retrofit strategy is applied for corner and exterior joints only and is equivalent to the one described previously, but including extended selective weakening of the slabs. Compared to an unstrenghtened frame, rather than shear failure, the retrofitted structure exhibits ductile beam hinging, suggesting the retrofit is effective. It is however observed that while the interventions improved the local behaviour, the global response of the structure is not significantly affected.

Overall, the research campaign by Pampanin's group provides a series of interesting approaches for the retrofit of joints with slabs and transverse beams. Important parameters such as three-dimensional geometry, anchorage and axial load are investigated. The retrofit schemes proposed are practical and readily applicable to realistic exterior and corner joints. Limited evidence on selective weakening of slabs for two specimens shows promise in enabling a beam-hinging mechanism for a retrofitted frame. The effect of scale discussed earlier is however not addressed, as all tested specimens are 2/3-scaled. Furthermore, the test on a full frame shows that the global behaviour of a structure may not be improved if only the exterior and corner joints are retrofitted, indicating the importance of retrofitting interior joints.

2.4. DATABASE OF EXPERIMENTS ON FRP-RETROFITTED JOINTS

Section 2.3 provides an overview of the main observations made in past experimental campaigns on the effectiveness of FRP strengthening of beam-column joints. In critiquing the literature, a number of issues have been highlighted, most importantly the lack of consideration of slabs and transverse beams in retrofit scheme proposals and the use of reduced scale specimens. These issues will need to be addressed by the experimental campaign presented later in this thesis.

A database of all the experiments found in the literature on the retrofit of beam-column connections was compiled as part of the literature review (see Appendix A). It is difficult to compare retrofit schemes across studies due to differences in terms of specimen geometry, materials, design deficiencies included, test set-up and loading. However, the database can inform this research in two ways. First, a statistical analysis of the database, and hence the composition of past experiments, highlights gaps in the available experimental data. Second, by assessing the interventions described in the literature, important observations for the design of practical retrofits can be derived. This includes strengthening aims and how to address them, factors affecting the effectiveness of the retrofit, as well as practical considerations such as anchorage design. The analysis of the outcomes informing the experimental campaign are discussed in the following sub-sections.

2.4.1. SPECIMEN CONFIGURATION

In order to assess any gaps in the literature in terms of joint geometry, the statistics on the configuration of the 249 tested specimens in the database of available experiments are shown in Table 2.1 below.

Table 2.1. Geometrical statistics of joints contained in database

		Joint type			Contains		Scale			
	Number	Interior	Exterior	Corner	Slab	Trans. Beam	Full	2/3	Half	1/3
Control	86	28%	57%	15%	14%	19%	41%	16%	15%	28%
Retrofitted	120	40%	48%	12%	8%	13%	34%	28%	15%	23%
Repaired	43	33%	63%	5%	33%	28%	47%	5%	28%	21%
Total	249	34%	54%	12%	15%	18%	39%	20%	17%	24%

As it can be seen, a majority of tested specimens is less than full-scale (61%) and without slab or transverse beams (82%). The literature review highlights that FRP retrofits are more effective for smaller specimens (Choudhury et al., 2013) and that slabs and transverse beams not only affect the behaviour of the specimen, but also present practical limitations for the application of FRP. Slabs and transverse are however typically present for most buildings with MRFs (Genesio et al., 2010; Lehman et al., 2004; Pampanin et al., 2002) and the issue of testing two-dimensional specimens is also addressed in the draft ACI 440-F guidelines (2014), where it is stated that "joints with beams framing into two opposite sides only, or into one side only, are not very common in

buildings". The statistics presented in Table 2.1 hence clearly highlight data gaps in the available literature and indicate further that experiments on realistic specimens need to be undertaken.

Moreover, in terms of joint type, a majority of retrofitted specimens tested are exterior joints (54%). Exterior joints often present a more critical need for retrofit due to the lack of confinement of the joint from four sides and lower axial force. As shown from the database, there is also a large interest in interior joints (34%), but less data is available. It is important to consider interior joints, as these often have higher shear stress in the joint core, with four beams with opposite moments at opposite sides of the joint. Moreover, retrofitting exterior joints alone while ignoring interior joints may not be sufficient to improve the global behaviour, as shown by limited experimental evidence on full frames (Akguzel et al., 2011; Gallo et al., 2012). In this research project, the retrofit of interior joints is hence investigated.

In terms of materials used, nearly 80% of all specimens are retrofitted with CFRP and the rest mostly with GFRP (18%) and limited studies on BFRP (<3%), which highlights the popularity of using CFRP as an effective material in RC retrofit. This can mainly be attributed to its higher strength and improved durability. Most studies (65%) use concrete with a mean strength of 20-30 MPa, as shown in Figure 2.42. Lower concrete strengths are often avoided as they are difficult to produce nowadays with modern materials. The majority of studies try to replicate concrete properties of pre-1970's three to four storey structures, hence values between 20 and 30 MPa seem to be a good balance between actual historic concrete strengths of pre-1970's structures and feasibility of producing the experimental specimens.

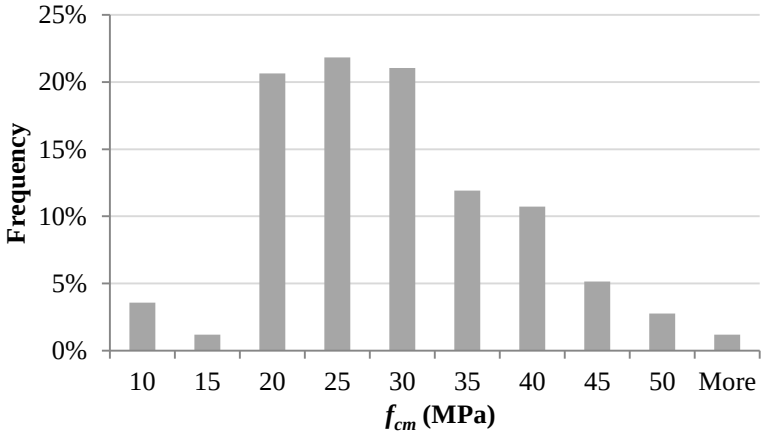

Figure 2.42. Values of f_{cm} used in experimental database.

2.4.2. TYPE OF DEFICIENCIES STUDIED

Clearly, a crucial factor for designing a retrofit is the identification and presence of a deficiency in the test specimens. All analysed research programmes test joints with pre-1970's design deficiencies, as discussed in Section 2.3. The statistics in terms of studied deficiencies are presented in Figure 2.43 below. It can be observed that most specimens (37%) do not contain any reinforcement in the joint (JTR). Inadequate beam bar anchorage (BA) and a weak-column/strong-beam mechanism (WC/SB) is also assessed by many groups (12% and 11%, respectively). An overlap of two or more deficiencies is usually the case and the percentage is not representative of the number of specimens with the relative deficiency.

Joint:
JTR - Inadequate joint transverse reinforcement

Column:
WC/SB - Weak-column/strong-beam
CTR - Inadequate column transverse reinforcement
LSC - Lap-spliced column bars
EcC – Eccentric column

Beam:
BT - Inadequate transverse reinforcement in beam
BLR - Inadequate beam longitudinal reinforcement
BA - Inadequate beam bar anchorage

Other:
LC - Low concrete strength
PB - Plain reinforcement bars
PED - Damaged specimen

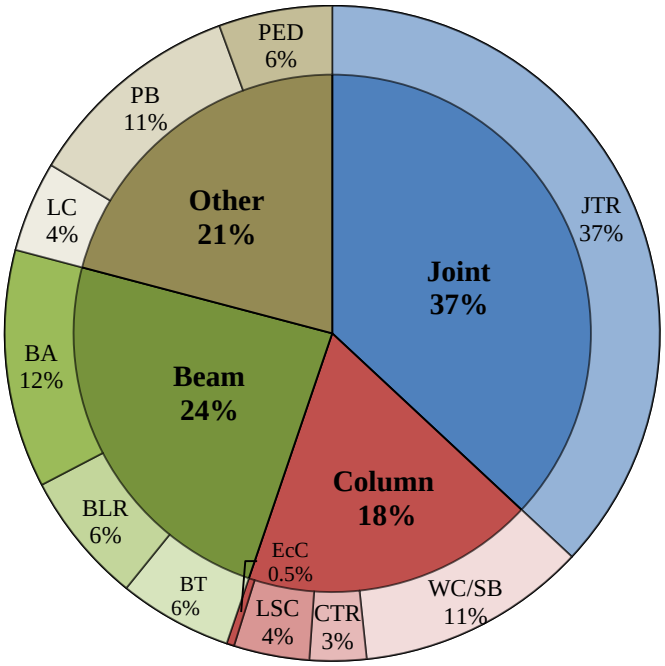

Figure 2.43. Type of design deficiency analysed for tested specimens reported in the literature.

A variety of types of deficiencies are hence studied in the literature for which different types of retrofit are needed. The next subsection addresses the objectives of the different studies and the FRP schemes typically used to achieve these specific strengthening aims.

2.4.3. RETROFIT OBJECTIVES

As it is observed from the literature review, a beam-column joint upgrade can have numerous objectives and FRP can be used to address these selectively. Depending on the relative capacities of the members, the objectives include increasing the flexural capacity of beams and column, improving the confinement and hence ductility of members, preventing slippage of the beam bars and increasing the shear capacity of the joint core. Increasing the stiffness and energy dissipation of specimens are however reported to be less efficient than traditional retrofit methods with RC jackets (Tsonos, 2008).

FRP sheets and strips are used in the following ways in past research studies:

- Joint shear strengthening by horizontal (e.g.: El-Amoury and Ghobarah, 2002), vertical (e.g.: Le-Trung et al., 2010) or diagonal FRP sheets (e.g.: D'Ayala et al., 2003) across unobstructed joint panels. No attempt to apply joint strengthening through transverse beams is presented in the literature, this is however crucial as it ignores their presence in real structures.
- FRP sheets along the column axis to increase its flexural capacity and avoid an unwanted column hinging failure mechanism, using straight sheets (Antonopoulos and Triantafillou, 2003), L-shapes (Akguzel and Pampanin, 2012b; Garcia et al., 2014; Yu et al., 2016), NSM (Hasan et al., 2016; Prota et al., 2004) or FRP anchors (Shiohara et al., 2009).
- FRP sheets wrapped fully around the column base to anchor the longitudinal FRP, but also to increase confinement and hence improve ductility (Akguzel and Pampanin, 2012b; Al-Salloum and Almusallam, 2007; Antonopoulos and Triantafillou, 2003; Del Vecchio et al., 2014; Engindeniz et al., 2008b; Shiohara et al., 2009).
- FRP sheets wrapped around the column for shear strengthening (Lee et al., 2010).
- FRP sheets along the bottom face of the beams (Engindeniz et al., 2008b) or L-shapes at the corner of the bottom of the beam framing into the bottom column (El-Amoury and Ghobarah, 2002; Ghobarah and El-Amoury, 2005) to prevent beam bar-slippage and cracks opening at the beam-joint interface.
- FRP U-wraps perpendicular to the beam axis to strengthen the beams in shear and to anchor the FRP sheets along the bottom (Akguzel and Pampanin, 2012b; Alsayed et al., 2010; Antonopoulos and Triantafillou, 2003; Engindeniz et al., 2008b).

Furthermore, it is crucial to set adequate performance targets for the retrofit schemes. Generally, these are set-out in terms of comparisons to modern seismically designed specimens. It is important to note that reaching the full capacity of modern structures is not required by retrofit and assessment guidelines such as Eurocode 8-3 (CEN, 2006) or ASCE 41 (ASCE, 2014). An appropriate target is to reach 75 to 80% of the capacity of seismically designed specimens. In the literature, retrofits reaching up to 85% of the modern Canadian RC code requirements (Ghobarah and Said, 2002) and 88% of the American RC code (Garcia et al., 2012) are reported.

The knowledge gained from this sub-section is used to inform the FRP retrofit of the specimens tested in this project. To design practical retrofit schemes, it is however also important to consider the factors that may affect the efficacy of the retrofit and these are discussed next.

2.4.4. FACTORS AFFECTING FRP RETROFIT

Based on the literature review, a number of factors that affect the effectiveness of the FRP retrofit, in terms of percentage increase in lateral load capacity and ductility, are summarised below.

- **Amount of FRP**: the amount of FRP increases the effectiveness of retrofits but not proportionally (e.g.: Antonopoulos and Triantafillou, 2003). Retrofits with one up to ten layers of FRP are tested in the literature (Tsonos, 2008).
- **Axial load**: Generally, it is found that an increase in axial load improves the effectiveness of the retrofit (Antonopoulos and Triantafillou, 2003; Prota et al., 2004). A varying axial load with lateral load however has an unfavourable effect on the retrofit efficacy (Akguzel and Pampanin, 2010, 2012a). Most studies only test one constant value of normalised axial load, with over 50% of these studies using values from 0.1 to 0.2, as shown in Figure 2.44, which is typical for lower storey columns. It is worth noting that nearly 15% of studies consider the highly unrealistic scenario with no axial load.

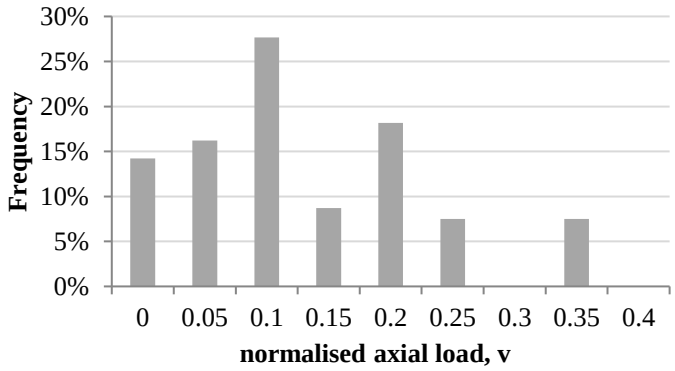

Figure 2.44. Statistics of normalised axial load in the experimental database.

- **Anchorage**: anchorage is always required to achieve a more effective retrofit and is discussed in detail in section 2.4.5.3. As shown in Figure 2.45, while most studies (65%) provide anchorage, a majority of this anchorage is provided by FRP U-wrapping or full-wrapping. Only 18% of studies employ adequate FRP or steel anchors.

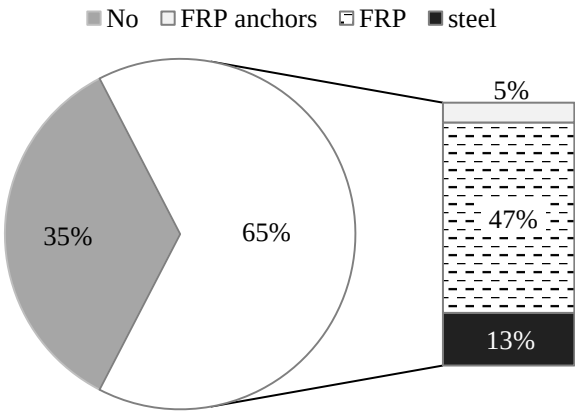

Figure 2.45. Statistics of employed anchorage solutions in the experimental database.

- **Angle of fibres**: As it would be expected, retrofits with fibres orientated in the angle of principal stress are more effective than strategies with horizontal and vertical sheets. However, diagonal sheets are difficult to place and FRP sheets with bi-directional fibres at 45° are much more expensive.
- **Strips vs sheets**: Based on limited available data, sheets are more effective than strips in increasing the lateral load capacity, but mainly because the bond characteristics of the latter are inferior (Antonopoulos and Triantafillou, 2003).
- **Type of FRP**: Generally speaking, CFRP has higher strength, but lower ultimate strain than GFRP. As expected, it is hence found that CFRP gives higher strength increase, but lower ductility (Mukherjee and Joshi, 2005). Furthermore, when using more layers of GFRP leading to an equivalent tensile strength to that of CFRP, retrofit is more effective in increasing ductility due to its higher ultimate strain (Antonopoulos and Triantafillou, 2003). Similarly, with respect to BFRP, Yu et al. (2016) find CFRP to be more effective in increasing the strength, but again less effective in terms of ductility. A variety of factors, including anchorage and retrofit layout may favour one material over the other.
- **Concrete strength**: It is found that for very weak concrete, FRP retrofit may not be viable without partial concrete replacement (D'Ayala et al., 2003; Engindeniz et al., 2008a).
- **Pre-damage**: Studies on repaired RC joints indicate that the extent of pre-damage affects the effectiveness of FRP repairs. For severely pre-damage joints, the strength of a non-repaired specimen may not be recovered (Agarwal et al., 2014; Beydokhti and Shariatmadar, 2016).
- **3D vs 2D set-up**: Transverse beams and slabs, but also of bi-directional loading, reduce the effectiveness of FRP retrofits (Akguzel et al., 2011). Recent studies (Kam et al., 2010; Park and Mosalam, 2013) show that the slab contributes to the moment capacity of the beams and hence has an influence on the failure mechanism, often promoting unwanted column hinging (Akguzel and Pampanin, 2012a). Importantly, the placement of sheets and anchorage are also largely affected by slab and transverse beams.
- **Effect of scale**: Scale can play a large role in the effect of the retrofit (Choudhury et al., 2013). Based on limited evidence, the larger the specimen, the less effective the retrofit.

The effect of scale and the presence of slab and transverse beams are deemed particularly important with respect to the lack of realistic specimen sizes and geometries tested in the literature (Table 2.1). The database of tests is hence analysed to assess the influence of these factors, as well as of pre-damage, on the increase in strength and ductility of retrofitted specimens.

The outcomes of this analysis are shown in Table 2.2. The analysis confirms the observations stated above, namely that specimens without slab and transverse beams (2D) present a higher effectiveness of FRP retrofit in terms of average strength increase (+45% compared to +26%). Scale has an effect too. However, this is less pronounced for the average strength increase (+44%

compared to +39% in full-scale), and reversed for ductility (+63% compared to +72%). Finally, repairs of pre-damaged specimens are not, as one would expect, less effective in increasing the load capacity than retrofits of existing structures (+44% compared to +42%). This may be attributed to the replacement of damaged concrete by stronger mortar, which is hence a recommended repair technique. All studies on repaired specimens also find a decrease in initial stiffness for repaired specimens, in terms of ductility, repaired specimens hence present a lower increase (+51% compared to +70%).

Table 2.2. Analysis of the literature database in terms of retrofit effectiveness.

	Geometry		Scale		Retrofit type	
	3D	2D	Full	Less than full	Repair	Retrofit
Number of specimens	27	128	59	96	37	117
Average Increase in Strength	26%	45%	39%	44%	44%	42%
Average Increase in Ductility	68%	65%	72%	63%	51%	70%

From this summary some important implications for the design of the experimental campaign and the used retrofit scheme arise. Firstly, a full-scale three-dimensional set-up should be tested in order to get data that accurately reflects real structures. Ignoring these effects will lead to an over-estimation of the effect of FRP retrofits and lead to easier applications and anchorage of FRP, hence not giving a correct picture on the practical applicability of the scheme.

Secondly, in terms of materials, CFRP should be used as it is the more effective and requires lower amounts of FRP due its higher stiffness. This means that practical applications of CFRP are more likely to be implemented, despite their higher cost, which is expected to reduce with time.

Thirdly, strips of FRP may be useful, particularly when they need to be passed through transverse beams, as they are less wide and need smaller cuts into the concrete. However, strips are more bond and anchorage critical. Embedding strips or bars into the concrete surface (NSM) or good anchor systems are hence required. Finally, anchorage is a crucial factor for all FRP interventions and needs to be provided. Anchorage and other practical observations are addressed in the next sub-section.

2.4.5. OTHER CRITICAL OBSERVATIONS

2.4.5.1. CONTINUITY OF FRP STRENGTHENING

FRP sheets or strips along the length of the column need to be provided to increase the flexural capacity of the columns. To be efficient, the strengthening should be applied along the effective length required and linked through the joint. This is often addressed by applying FRP sheets or NSM rods continuously from the superior to the inferior column through the joint (Antonopoulos and Triantafillou, 2003; Mahini and Ronagh, 2011). However, when a slab or transverse beam is

present, this is not possible for all sides of the column, as noted by several groups (Garcia et al., 2014; Prota et al., 2004) and would require cutting or drilling through these members. To date, only Shiohara et al. (2009) addressed this issue explicitly. The most recent draft ACI guidelines (ACI, 2014) suggests cut-outs and FRP applied along the corners of the column, as shown in Figure 2.46. Still, no detailed retrofit layout for interior joint specimens with continuous flexural strengthening for specimens with slabs and transverse beams has been tested in the literature. There is hence a clear need to determine a way of providing continuity and anchorage to the longitudinal FRP sheets on all column faces with minimal concrete removal.

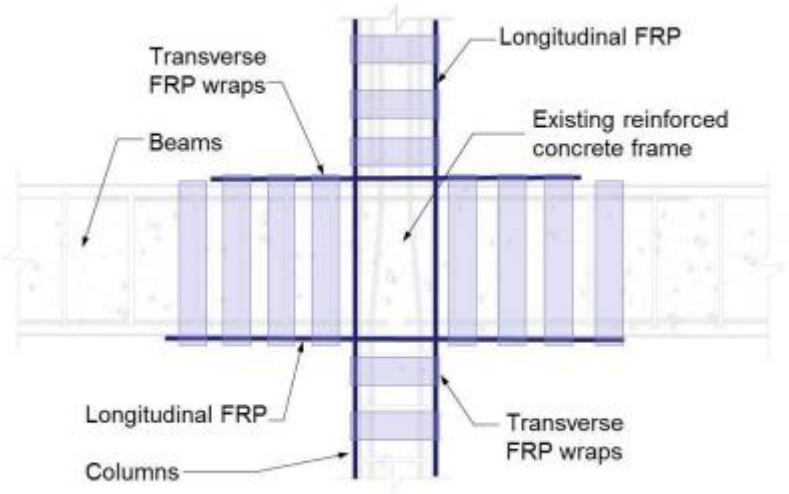

Figure 2.46. Conceptual retrofit according to ACI-440 F 2014 draft.

Similarly, the continuity and bond of FRP sheets applied to the bottom face of beams is of importance. This is mainly addressed by anchoring the sheets with U-wraps (Akguzel et al., 2011; Al-Salloum and Almusallam, 2007) or by continuing the sheets along the bottom column in an L-shape and providing anchorage at the corners (Ghobarah and El-Amoury, 2005). No efforts are however made to provide continuity through the joint, as shown conceptually in Figure 2.46.

2.4.5.2. SELECTIVE WEAKENING

For the few specimens tested with slab and transverse beams, a strong contribution of the slab to the beam moment capacity is observed. In practice, this contribution makes it difficult to achieve a beam-sway failure mechanism with an FRP retrofit scheme. To control the hierarchy of strength between columns and beams prior to retrofitting, Pampanin's group of the University of Canterbury, NZ (Pampanin, 2006) developed the selective-weakening technique (sw). This technique is a counter-intuitive seismic retrofit strategy for inadequately designed structures, developed with the aim of introducing capacity design principles into a pre-1970's structure. Following the concept, summarised in Figure 2.47, the structure is initially selectively weakened to provide a more ductile behaviour, which leads however to a reduced overall capacity (b). This is followed by a strengthening intervention (c) to increase the capacity of the structure.

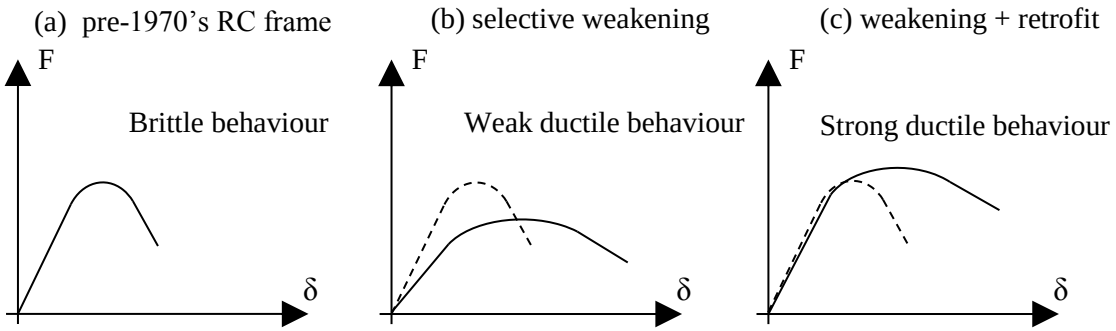

Figure 2.47. Conceptual illustration of a combined selective weakening and retrofit (adapted from Kam and Pampanin, 2008).

Preliminary experimental validation of the concept shows that the sw-strategy enables control over the failure mechanism and protection of members needed to achieve a ductile failure according to capacity design principles (Kam et al., 2009; Kam and Pampanin, 2009). The concept of a combined FRP and sw retrofitted has already been tested on one corner joint specimen with slab and transverse beam (Akguzel and Pampanin, 2012a). Cutting the slab reinforcement around the perimeter of beams in the joint area (sw) is found to be successful in reducing the hogging capacity of the beams considerably. This intervention allows a beam hinging mechanism to form and hence protecting the assembly from brittle joint or column failure mechanism. When considering specimens with realistic geometry, i.e. containing slabs and transverse beams, it is hence suggested to use slab weakening in combination with FRP strengthening.

2.4.5.3. NEED FOR ANCHORAGE

One major concern for the FRP strengthening of RC members, encountered by almost every research group, is the debonding of FRP sheets. This issue is particularly complex as debonding can occur through five different mechanisms (Au and Büyüköztürk, 2006): within the concrete cover, at the concrete/adhesive (epoxy resin) interface, within the adhesive, at the adhesive/FRP interface or within the FRP sheet (Figure 2.48).

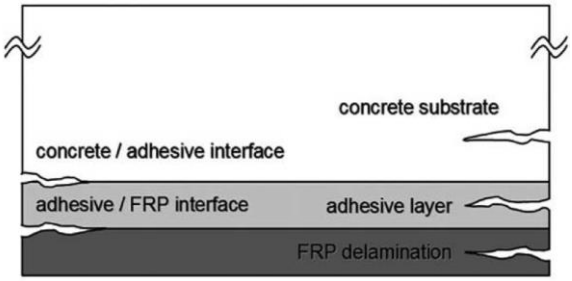

Figure 2.48. Different FRP debonding modes (Au and Büyüköztürk, 2006).

Premature debonding leads to an abrupt loss of capacity in retrofitted members and is classified as a brittle failure mechanism to be avoided. Reduced levels of FRP design strain are hence recommended in all major design guidelines.

Most research groups note that premature failure through FRP delamination or buckling occurs when the FRP sheets are not anchored appropriately. In some cases the lack of anchorage renders the retrofit useless (e.g.: Lee et al., 2010). This effect seems to be more pronounced for FRP strips than FRP sheets (Antonopoulos and Triantafillou, 2003). Simply tying sheets of FRP around the main FRP strengthening alone has shown little efficiency (Akguzel and Pampanin, 2010), while other anchorage methods are observed to have greater success:

- FRP dowel anchors or FRP fan-shaped anchors, prepared by twisting sheets of FRP and saturating them with epoxy before passing them through pre-drilled holes (Akguzel et al., 2011; Smith et al., 2011).
- Steel plates and rods (Al-Salloum and Almusallam, 2007; Ghobarah and Said, 2002).
- Steel angles in the corners between beams and column (El-Amoury and Ghobarah, 2002; Lee et al., 2010).
- U-shaped FRP anchors in combination with fan-shaped FRP anchors through slabs or beams (Akguzel and Pampanin, 2012b).
- U-shaped steel anchors (El-Amoury and Ghobarah, 2002).

A recent review of anchorage systems for FRP strengthening schemes (Kalfat et al., 2013) confirms the observations from this literature review. The main anchorage systems found in the literature include metallic anchors, FRP fan-shaped anchors, FRP U-shapes, fabric anchors and embedment into concrete. An analysis based on a large database of experimental results suggests that while metallic anchors are the most efficient, FRP-based anchors are less invasive, more practical to apply and can offer similar levels of anchorage. In particular, FRP anchors for flexural FRP strengthening sheets in beams are recommended. U-shaped anchors are deemed more efficient when inclined instead of perpendicular to the beam axis. Passing metallic anchors or FRP fan anchors through predrilled holes in beams or slabs in combination with U-shaped anchors is also suggested. Another recent study on FRP fan-shaped anchors for FRP sheets in columns shows a strong increase in tensile strain up to 75% of the rupture strain of the sheets due to the anchors (Bournas et al., 2015).

2.5. SUMMARY

This chapter provides the theoretical background to this thesis. The design deficiencies of concern for existing pre-1970's RC structures and their potentially catastrophic consequences are outlined. These comprise joint shear failures and non-ductile weak-column/strong-beam mechanisms, highlighting the crucial importance of the beam-column joint region on the failure mechanism of RC frames. As deficient RC structures form a large proportion of the existing building stock in many earthquake-prone countries, fast, efficient and cost-effective retrofit solutions are required. FRP materials are becoming increasingly popular for retrofitting RC members, as, compared to traditional retrofit materials, FRP benefits from its high strength-to-weight ratio, corrosion

resistance and reduced labour time. Still, to-date, most FRP retrofits in the field focus on the behaviour of individual members rather than on the global failure mechanism, which is dominated by the hierarchy of strengths in the beam-column joint region.

A review of the state-of-the-art of FRP retrofitting of beam-column joint subassemblies, presents numerous successful implementations that address various retrofit objectives. A detailed analysis of the proposed schemes and a compilation of a database of experiments allows a number of important conclusions to be drawn from this review.

Despite the large number of conducted studies, a strong bias towards scaled, cruciform test specimens is observed. The ease of construction and testing, as well as their less complex behaviour, have led to a majority of research groups to test these types of joints. A number of studies, however, highlight the important effect of realistic size and geometry of test specimens on FRP retrofit efficiency. For instance, it is shown that the effectiveness of retrofit reduces significantly for larger specimens.

The lack of slab and transverse beams in tested specimens is another shortfall identified in the analysis of the experimental database. Slabs are typically present in buildings with MRFs and are shown to influence the retrofit effectiveness, but also the failure mechanism of deficient specimens by increasing the beam moment capacity. Transverse beams, in turn, also influence the failure mechanism, by increasing the confinement and shear capacity of the joint. Moreover, ignoring these elements when assessing FRP, or other retrofit methods, additionally renders the joint region more accessible. This does not give a realistic picture of the practical challenges and feasibility of the schemes, including need for and placement of anchors.

The importance of realistic load conditions is also established, with a number of studies highlighting the effect of axial load on retrofit effectiveness. The lack of slabs and transverse beams, or inadequate loading conditions, hence affect the retrofit effectiveness, but also the failure mechanism, and ultimately the retrofit objective, for deficient joints. While joint shear failures are most commonly observed in the laboratory for cruciform interior joints, soft-storey failures caused by an undesirable weak-column/strong-beam hierarchy of strengths are more realistic for structures with slabs and transvers beams. The type of tested specimens hence leads to a focus on joint shear strengthening schemes that do not address other crucial mechanisms.

Indeed, a plethora of successful implementations of joint shear strengthening schemes have been presented. While sheets in the angle of principal stress are shown to be most effective, horizontal strengthening with FRP sheets is deemed most realistic. No study has however presented solutions for joint shear strengthening of interior joints in the presence of transverse beams.

To address other design deficiencies of pre-1970’s RC frames, such as the low flexural capacity of weak columns, a range of implementations are reported in the literature. These include NSM

bars, L-sheets and FRP anchors, which are, however, mostly tested on ground-floor columns. At beam-column joints, continuous flexural strengthening of columns through slabs and transverse beams is required. To achieve this, FRP anchors are deemed to be the most appropriate, as they can be passed through small holes at the corners of the columns. Such a solution has however yet to be tested for realistic specimens under adequate load conditions.

Beam plastic hinge relocation (PHR) is another application of FRP that shows potential in improving the seismic behaviour of structures. Limited studies show that strengthening the beam in the proximity of the joint allows a relocation of damage and plastic hinge formation away from the joint. This protects the joint from yield penetration and improves the dissipative behaviour of the specimen further. PHR has however not been tested in combination with flexural column strengthening. Moreover, anchorage of the FRP sheets at the beam/joint interface is a practical challenge that is not sufficiently addressed.

In general, anchorage is shown to be of outmost importance to ensure FRP retrofits are effective. Many research groups note that premature failure through FRP delamination or buckling occurs when the FRP sheets are not anchored appropriately. While most studies consider anchorage, an analysis of the experimental database indicates that simple FRP wrapping is the most common application. This solution is however not always effective, and a combination of FRP anchor fans and metallic anchors is instead suggested. A realistic specimen geometry is again of crucial importance, as it allows to assess practical obstacles to the placement of anchors and the full wrapping of members in the presence of slabs and transverse beams.

A final interesting observation from the literature is the effectiveness of repair schemes on pre-damaged specimens, which is shown to be significantly reduced compared to retrofits of undamaged or slightly damaged specimens.

Overall, while a number of successful retrofit schemes for improving the hierarchy of strengths in deficient joints is available in the literature, many practical concerns are not yet addressed adequately for realistic specimens. There is a clear need for further empirical research on retrofit designs taking into account realistic test conditions with representative axial loading, and full-scale specimens with slabs and transverse beams. This need will be addressed by an extensive experimental research program, allowing a fair assessment of the effectiveness of FRP retrofits and their practical applicability. The outcomes of the literature review will feed into the design of the experimental set-up, of the specimens and of the retrofit schemes presented in the next chapter.

3. METHODOLOGY AND DESIGN OF EXPERIMENTS

3.1. INTRODUCTION

In the previous chapter, the need for further empirical research on the FRP strengthening of realistic RC beam-column joints is established. Even though the literature encompasses a wide range of joint types and geometries, the majority of tested specimens are scaled exterior joints without slab or transverse beams (Table 2.1in Section 2.4). There is, hence, still a need for further empirical data, which will allow to validate and improve the design of seismic strengthening schemes for beam-column joints with FRP, and ease their practical implementation in the field.

The aim of this study is to design a realistic and practical retrofit solution for pre-1970's RC structures. To ensure all practical obstacles are considered in the retrofit design, a representative experimental set-up is of crucial importance. Therefore, a series of innovative experiments is designed following the methodology described in Figure 3.1. The rationale for the design of experiments is developed in this chapter and considers a number of important outcomes from the literature review, including:

- The need for full-scale testing of beam-column joints;
- The importance of realistic load conditions, in particular for axial loading, which affects the retrofit effectiveness;
- The importance of slabs and transverse beams affecting the failure mechanism, retrofit effectiveness and practical application of the retrofit; and
- The need for adequate anchorage, where fan-shaped FRP anchors, in combination with metallic anchors, are most effective.

As shown in Figure 3.1, first, typical design deficiencies of pre-1970's RC structures are identified from the analysis of the literature. A reinforcement design for full-scale beam-column joints including these deficiencies is created, and one control specimen is also designed to modern guidelines (Eurocode 8) for comparison (Section 3.2). The potential failure mechanism of the specimens is then evaluated using Eurocode 2 equations (Section 3.2.3) and detailed finite element (FE) models (Section 3.5). The FE study also allows for the significance of the slab and transverse beam contribution to be assessed before physical testing. The models are first calibrated on simpler small-scale beam tests to ensure their validity (Section 3.5.3).

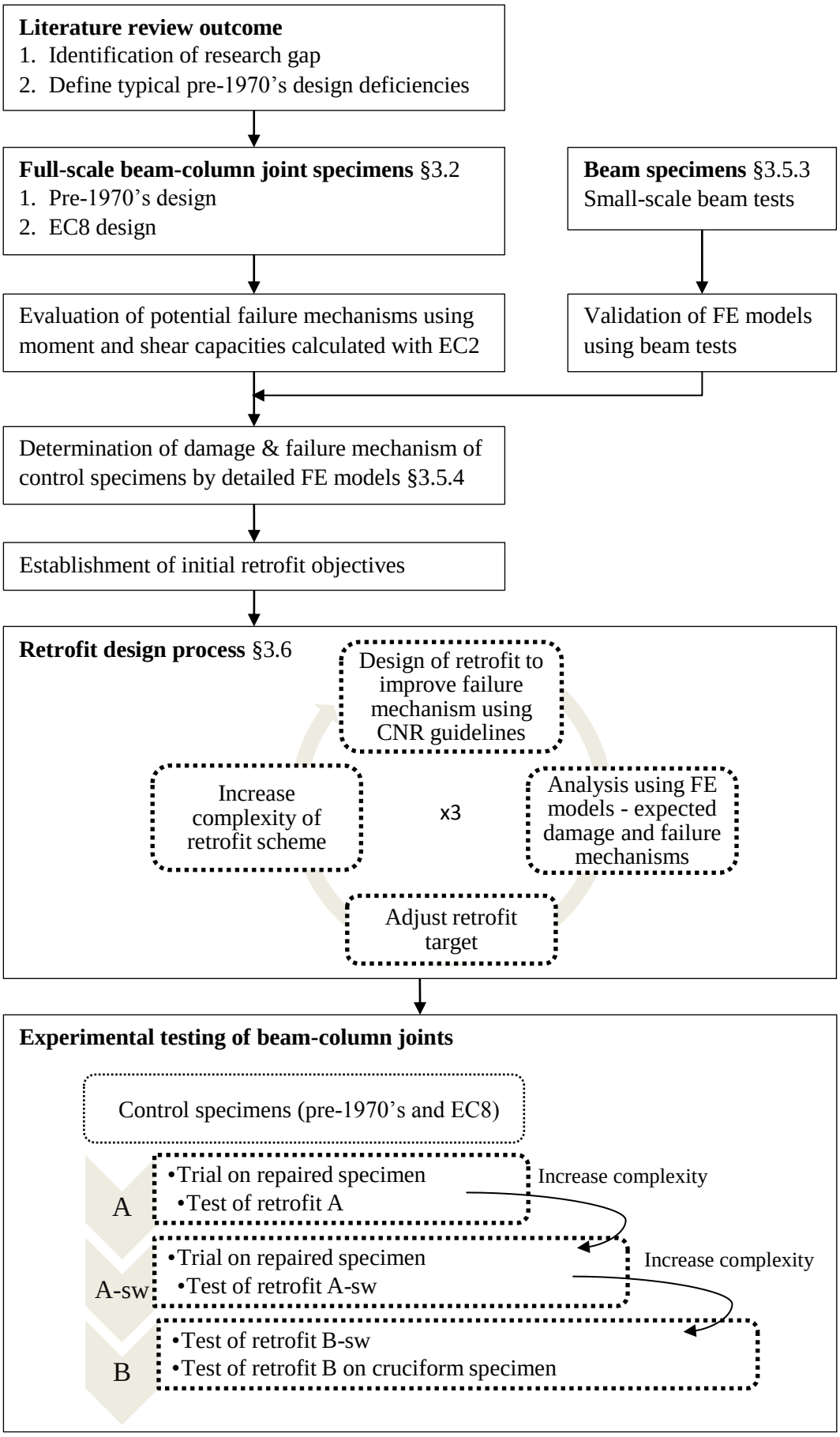

Figure 3.1. Methodology flowchart.

The determined failure mechanism is then used to identify a retrofit target, with the final aim of achieving an adequate ductile failure mechanism, in line with capacity design principles, with a capacity of 80% of the control specimen designed to EC8. To develop this FRP retrofit scheme, a systematic step-by-step design process, described in Section 3.6, is chosen. This involves fixing one parameter at a time and increasing the complexity of the retrofit design at each step, in order to isolate the effect of different elements in the schemes.

To warrant an informed decision in the design of the retrofits, and hence minimise the risk of wasting expensive and time-consuming experiments, the schemes are initially assessed by means of further FE models. Based on the results of the FE models, three retrofits are developed and first trialled as repair schemes before being tested experimentally on full-scale specimens under cyclic loading. The three schemes (A, A-sw and B-sw) address different targets in terms of seismic performance based on the identified gaps in the literature, including continuous flexural strengthening of columns and beams, as well as joint shear strengthening with adequate development and anchorage.

3.2. DESIGN OF EXPERIMENTS

To answer the research objectives of this study, in total, twelve full-scale beam-column joints, as well as two column-only tests, are carried out, as summarised in Table 3.1. Five of the tested specimens can be regarded as control specimens:

- C1 is considered the main control specimen and consists of an interior beam-column joint with transverse beam, slab and typical pre-1970's design deficiencies.
- C-noSLT, an interior joint with the same reinforcement as C1, but without slab and transverse beams, to address the objective of assessing the influence of these elements on the behaviour of the joint.
- C2, a specimen with the same dimensions as C1, but with an additional reinforcement bar in the bottom of the beam, to assess the case of a specimen with a more pronounced strong-beam/weak-column design.
- C1-sw, a specimen with the same dimensions and detailing as C1, but with 600 mm long selective weakening (sw) cuts in the slabs along the length of the beams, to assess the effect of selective weakening alone.
- C-EC8, a specimen with EC8 detailing, as a means of evaluating the performance of the retrofit schemes relatively to a new-built joint.

Seven strengthened specimens are tested, of which four correspond to the repair of the tested control specimens C0[3], C1, C2 and C-noSLT, and the other three corresponding to retrofits of undamaged specimens. Three different retrofit schemes are developed, and are described in full detail in Section 3.6. The first two retrofit schemes are initially tested as repair schemes of the pre-damaged control specimens in order to reduce the risk of errors in the retrofit design before testing them on undamaged specimens. This also allows for a comparison to be made on the effectiveness of FRP interventions on pre-damaged specimens, which is highlighted as a point of concern in the literature review. The last retrofit scheme (B) is also tested on a cruciform specimen to answer the research objective of understanding the effect of slab and transverse beams on the retrofit efficiency.

Table 3.1. List of test specimens

Name	Type	Description	Detailing	Slab & tr. beam
C-noSLT	Control	cross-shaped specimen	pre-1970s	No
C1	Control	main control specimen	pre-1970s	Yes
C2	Control	additional beam rebar	pre-1970s	Yes
C1-sw	Control	with selective weakening	pre-1970s	Yes
C-EC8	Control	designed to Eurocode 8	modern seismic	Yes
C0-RP-A-gs	Repair	repaired C0 with scheme A-gs	pre-1970s	Yes
C2-RP-A	Repair	repaired C2 with scheme A	pre-1970s	Yes
C1-RT-A	Retrofit	retrofitted with scheme A	pre-1970s	Yes
C1-RP-A-sw	Repair	repaired C1 with scheme A-sw	pre-1970s	Yes
C1-RT-A-sw	Retrofit	scheme A-sw	pre-1970s	Yes
C1-RT-B-sw	Retrofit	scheme B-sw	pre-1970s	Yes
C-noSLT-RP-B	Repair	repaired C-noSLT with scheme B	pre-1970s	No
C1-RT-A-sw-column	Retrofit	test of column of C1-RT-A-sw	pre-1970s	/
C1-RT-B-sw-column	Retrofit	test of column of C1-RT-B-sw	pre-1970s	/

[3] Specimen C0 has the same design as C1, but is not presented in this thesis due to issues with the experimental set-up during the testing of the specimen.

3.2.1. SPECIMEN GEOMETRY

The geometry of the interior joints with and without slab are shown in Figure 3.2 and Figure 3.3. The specimens are designed to represent real-scale interior beam-column joints in a four-storey RC moment resisting frame (MRF) structure. The superior and inferior columns represent a half-storey 1.50 m column with a square cross-section of 300 mm by 300 mm. Similarly, each main beam represents a 2.05 m half-span of a beam with a rectangular cross-section of 450 mm deep to 300 mm wide. For the specimens with slab, the slab is 1.95 m wide, with a depth of 150 mm, and the transverse beams are 825 mm long and have the same cross-sectional dimensions and reinforcement detailing as the main beams. Figure 3.4 shows the selective weakening cuts performed for all specimens with the name suffix '-sw'.

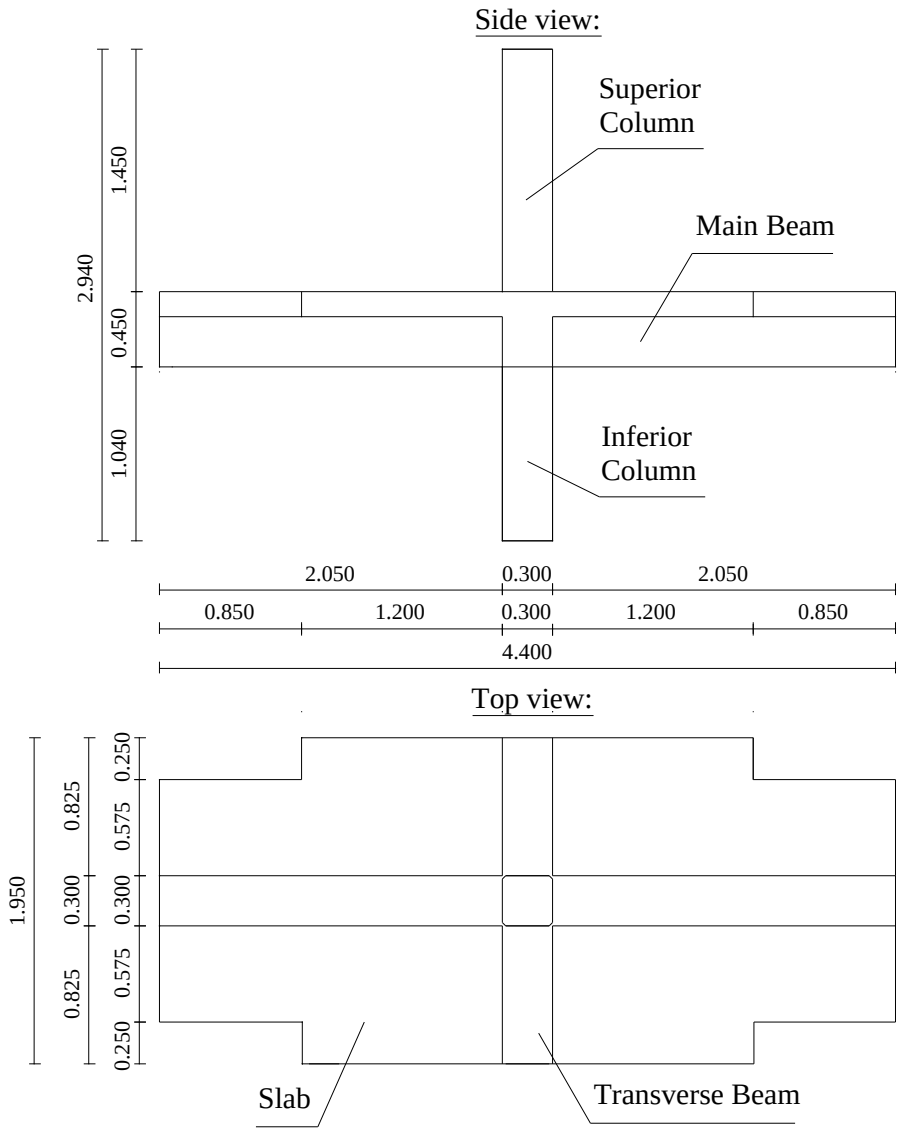

Figure 3.2. Beam-column joint specimens with slab and transverse beams (dimensions in m).

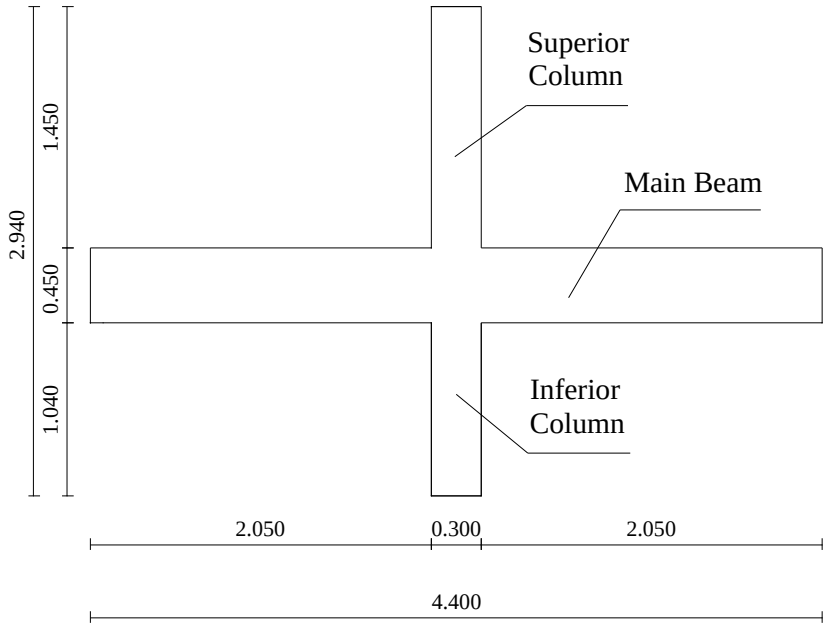

Figure 3.3. Beam-column joint specimen without slab and transverse beams (dimensions in m).

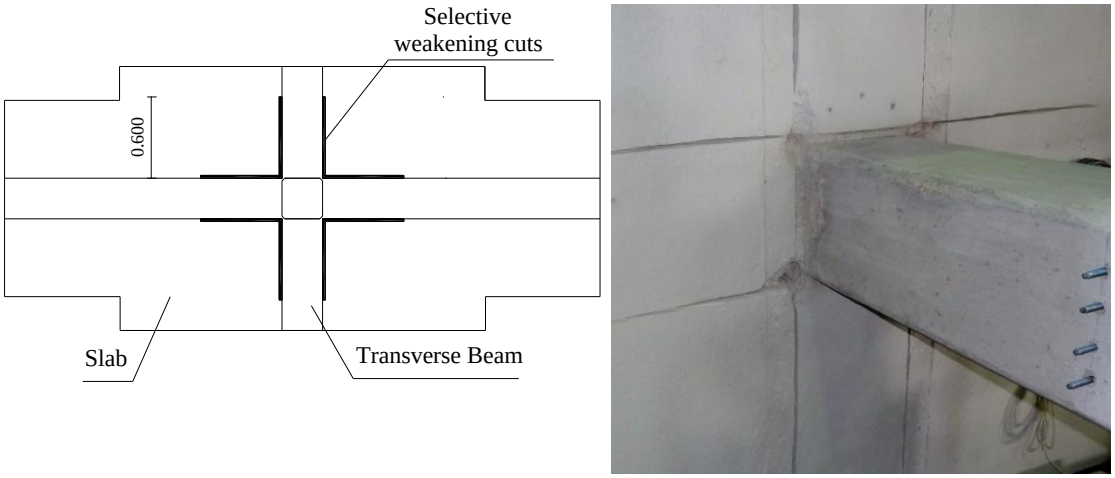

Figure 3.4. Selective weakening cuts for specimen C1-sw.

3.2.2. REINFORCEMENT DETAILING

Apart from specimen C-EC8, the steel reinforcement detailing of the specimens aims to reflect the common design deficiencies of a beam-column joint in a pre-1970's reinforced concrete residential building in Southern Europe. The limits given in the REBA (1967) Portuguese RC code are followed and a seismic factor for lateral load of 0.05 of axial load is chosen accordingly (zone C). This leads to a total base shear of 273 kN (corresponding to a normalised base shear of 0.05 of the building weight) for the REBA design of the model four storey RC structure. Only specimen C-EC8 is designed to Eurocode 8 for the high ductility class (DCH), with a pga of 0.36g (e.g. zone 3 in many Southern European countries) and ground type D (soft-to-firm cohesive soil). As expected, a much larger base shear of 1360.9 kN (normalised base shear of 0.18) is obtained for the four-storey model structure following the EC8 procedure. The reinforcement detailing

adopted in all specimens can be seen in the figures below and are summarised in Table 3.2. Detailed calculations of seismic loading and reinforcement detailing are provided in Appendix D.

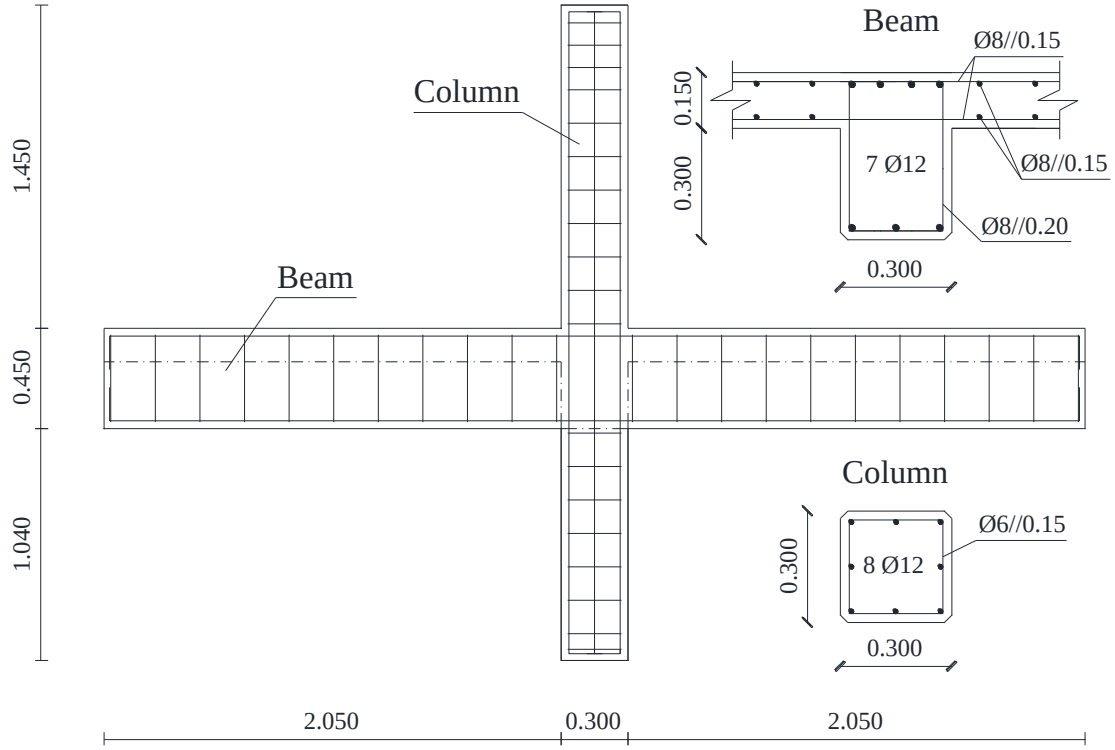

Figure 3.5. Full-scale beam-column joint specimen C1 reinforcement detailing (in m).

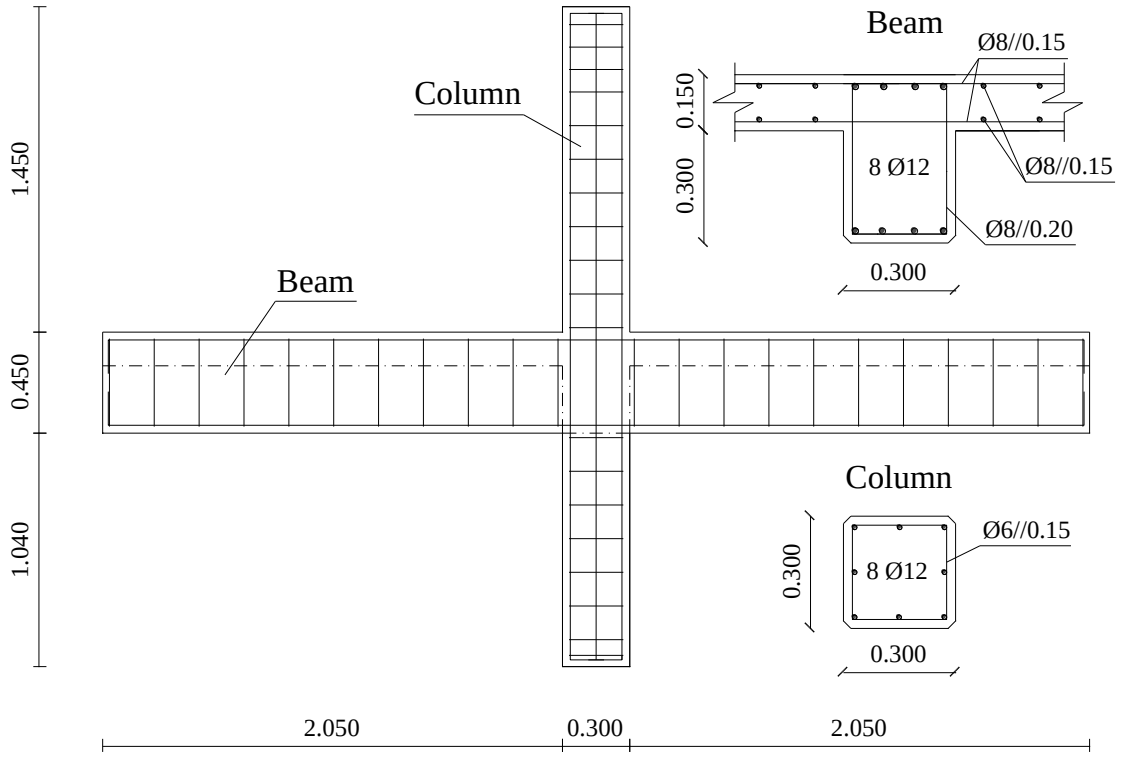

Figure 3.6. Full-scale beam-column joint specimen C2 reinforcement detailing (in m).

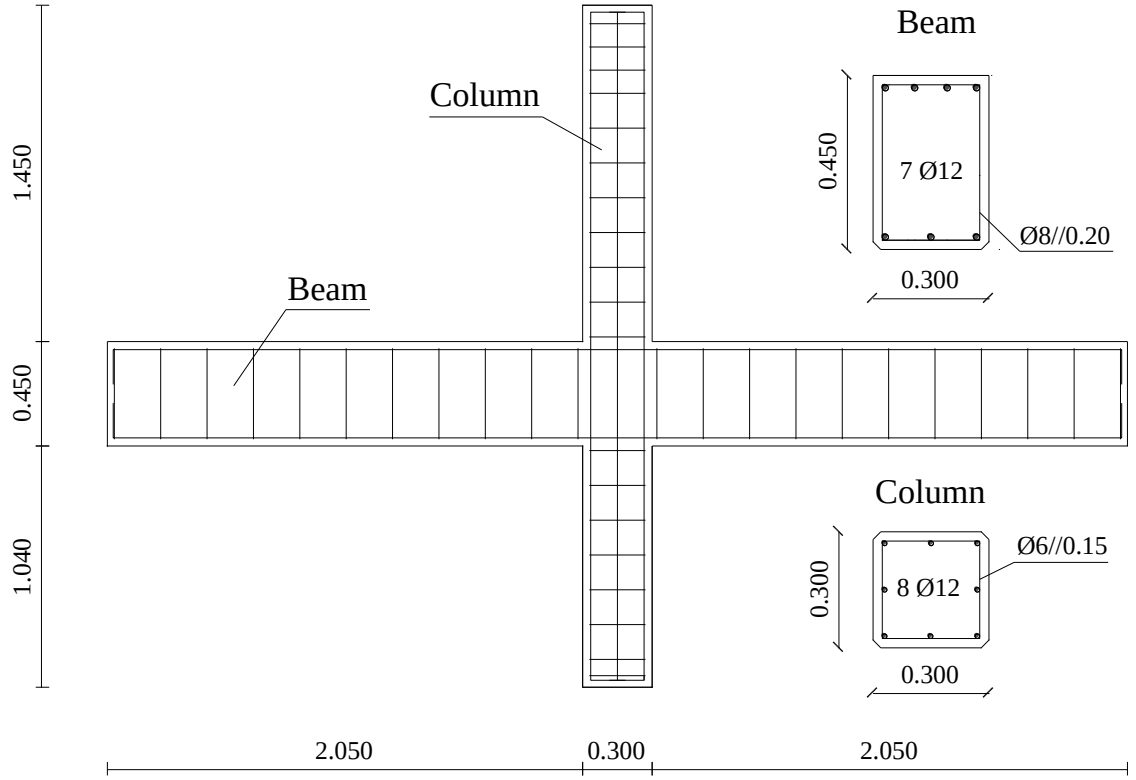

Figure 3.7. Reinforcement detailing for specimen C-noSLT without slab and transverse beam (in m).

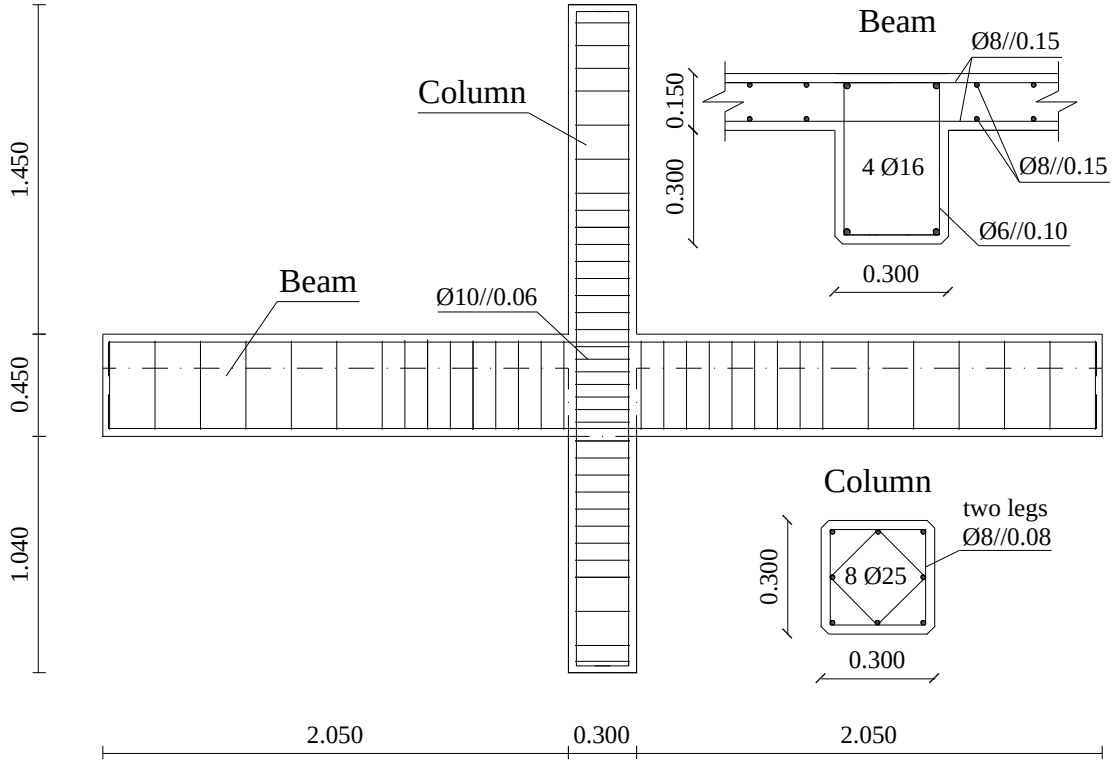

Figure 3.8. Full-scale beam-column joint specimen C-EC8 reinforcement detailing (in m).

Table 3.2. Summary of Reinforcement for Pre-1970's specimens

	Beams								Column					
	Main bars					Shear			Main bars			Shear		
	d_{bl}	top	ρ_l	bot	ρ_l'	d_{bw}	s	ρ_w	d_{bl}	#	ρ_{tot}	d_{bw}	s	ρ_w
	mm	#	%	#	%	mm	mm	%	mm			mm	mm	%
C1	12	4	0.34	3	0.25	8	200	0.17	12	8	0.01	6	150	0.13
C2	12	4	0.34	4	0.34	8	200	0.17	12	8	0.01	6	150	0.13
C-EC8	16	2	0.30	2	0.30	6	100	0.19	25	8	0.04	8	80	0.42

For the specimens designed to REBA (1967), the detailing adopted leads to a number of seismic deficiencies typical of pre-1970's designs. These deficiencies lead to brittle failure mechanisms that are related to the specimen's non-compliance with capacity design principles. The specimens present an inappropriate hierarchy of strengths with a lower flexural capacity of the columns than the beams (weak-column/strong-beam mechanism) and a low shear capacity of the joint. The latter is due to the lack of shear reinforcement in the joint, as well as a lack of confinement in the columns due to inadequate transverse reinforcement spacing. Note that for specimens C2 and C2-RP-A, the additional 12 mm bar in the bottom of the beam leads to a more pronounced weak-column/strong-beam strength hierarchy.

3.2.3. EVALUATION OF DESIGN MOMENT AND SHEAR CAPACITIES

To assess potential failure mechanisms and aid the design of the FRP retrofit schemes, the bending and shear capacities of the individual members of the control specimens are initially evaluated using design equations in modern European codes of practice.

For the control specimens without FRP strengthening, Eurocode 2 (CEN, 2008) and Eurocode 8 (CEN, 2004) were chosen to predict the relative moment and shear capacities of the beams, columns and joint. No factors of safety are applied in the equations to assess the capacities of the members. The characteristic and design concrete strength values of f_{ck} and f_{cd} are hence equal in all calculations and are determined from the mean value of six cylinder tests, f_{cm}:

$$f_{\mathrm{cm}} = f_{cd} \tag{3.1}$$

The mean concrete compressive strength of cylinder (Ø150 x 300 mm^2) samples, f_{cm}, is presented in Table 3.3 for the different specimens. Steel tensile tests are also performed and the mean yield strength of reinforcement steel, f_{ym}, and the mean ultimate tensile strength of reinforcement, f_{um}, are presented in Table 3.4 for six specimens of each of the different bar sizes used.

Table 3.3. Material properties for the control beam-column joint specimens.

Specimen	f_{cm} (MPa)
C-noSLT	29.6
C1	23.4
C2	31.5
C1-sw	26.0
C-EC8	32.7

Table 3.4. Steel tensile strength for all bar sizes used

Steel f_y / f_u (MPa)					
Φ25	Φ16	Φ12	Φ10	Φ8	Φ6
595/695	585/687	450/570	530/620	540/640	538/645

The column moment capacity is evaluated using the M-N interaction diagrams typically used for design (Arya, 2009). The use of these also allows to identify if potential failure occurs due to a failure of concrete in compression or steel in tension.

For the beam moment capacities, the procedure of EC2 as outlined in *Design of Structural Elements* (Arya, 2009) is followed. For the beam hogging moments, according to EC8 cl. 5.4.3.1.1(2), an effective width of the T-section, i.e. the slab, is considered for strengthened and unstrengthened specimens. For an internal joint with transverse beams, this effective width is the sum of the width of the beam and four times the thickness of the slab, h_f:

$$b_{\text{eff}} = b + 2 \cdot (4 \cdot h_f) = 1500\, mm \tag{3.2}$$

The top layer of slab reinforcement within the effective width is considered in calculating the hogging moment of the beams. For the specimens with selective weakening, the effective width is reduced to the part of the slab that is not cut, which corresponds to a length of $1.5 \cdot h_f$ (450 mm).

The shear strength of non-strengthened RC members is evaluated using the equations in cl. 6.2.3 of EC2, conservatively assuming only the steel contribution ($V_{Rd,s}$) with a value of the strut angle, θ, of 21.8°.

The flexural and shear capacities of the individual members for the control specimens are summarised in Table 3.5. The moment capacities of the column (M_c), as well as those of the beam in hogging ($M_{b,hog}$) and sagging ($M_{b,sag}$) are presented and so are the shear capacities of the beams ($V_{Rd,s,b}$), columns ($V_{Rd,s,c}$) and joint (V_j). The applied lateral loads required to reach the individual yield capacities are indicated in parentheses.

Table 3.5. Summary of calculated bending and shear capacities for the control specimens (equivalent applied lateral load in kN indicated in parentheses).

	C noSLT	C1	C2	C1-sw	C EC8
$M_{b,hog}$ (kNm)	-79.3 (40.5)	-149.8 (91.3)	-149.8 (91.3)	-114.5 (65.9)	-183.3 (115.4)
$M_{b,sag}$ (kNm)	59.5 (59.5)	61.7 (61.1)	82.4 (76.1)	61.1 (60.7)	95.1 (85.2)
M_c (kNm)	86.5 (67.8)	79.8 (62.6)	88.3 (69.3)	82.7 (64.9)	185.7 (145.6)
$\Sigma M_c / \Sigma M_b$	1.25	0.75	0.76	0.94	1.33
$V_{Rd,s,b}$ (kN)	250.4 (317.2)	250.4 (317.2)	250.4 (317.2)	250.4 (317.2)	281.7 (358.9)
$V_{Rd,s,c}$ (kN)	120 (120)	120 (120)	120 (120)	120 (120)	387.1 (387.1)
V_j (kN)	871.4 (113.7)	672.1 (87.7)	929.7 (121.3)	757.5 (98.8)	965.8 (126)

It can be seen in Table 3.5 that for the pre-1970's design control specimens C1, C2 and C1-sw the ratio of the column to beam moment capacities is lower than the recommended capacity design ratio of 1.3 in Eurocode 8. This indicates that flexural failure of the column is anticipated, as the column is the weakest member in flexure of the subassemblies. The shear capacity of all members is significantly larger than their moment capacity.

In the specimens with slab, the hogging moment capacity at the top of the beam, $M_{b,top}$, is much larger than the sagging moment capacity, $M_{b,bot}$, due to the contribution of the slab and the asymmetric reinforcement in the beam. The top of the beam is also much stiffer than the bottom due to the slab. Less rotation in the beams, and hence less cracking, are expected. Moreover, as explained in 3.3, the second axial load causes a constant hogging moment in the beams at the beam-column interface that counteracts the more critical sagging moment in the beam.

For C-EC8, the moment capacities satisfy capacity design criteria with a ratio of column to beam capacities exceeding 1.3 (1.33) and the failure is hence expected in the beams. For specimen C-noSLT without slab and transverse beams, despite the high apparent joint shear capacity due to the higher concrete strength of the specimen, failure in joint shear is likely due to a lack of confinement from transverse beams that is not captured well by the EC8 equation (Melo et al., 2015).

3.3. EXPERIMENTAL SET-UP

The quasi-static cyclic test set-up for full-scale RC beam-column joints is presented in this section. The tests were carried out in the Laboratory of Aveiro University (Portugal) from November 2014 to October 2015. To the best knowledge of the author, this corresponds to the first full-scale cyclic tests of realistic interior beam-column joints with slab and transverse beams, strengthened with FRP.

The loading set-up of the tests is shown in Figure 3.9 and pictures of the set-up and specimen in the laboratory are shown in Figure 3.10. A constant axial load (*N1*) of 425 kN is applied through external pre-stress rods, which are pin-jointed at the hydraulic actuator at the top of the superior column and the bottom support of the inferior column. This axial load is applied before the beam supports are fastened. The value of *N1* is calculated for a second storey column in a typical residential four-storey RC frame in Europe.

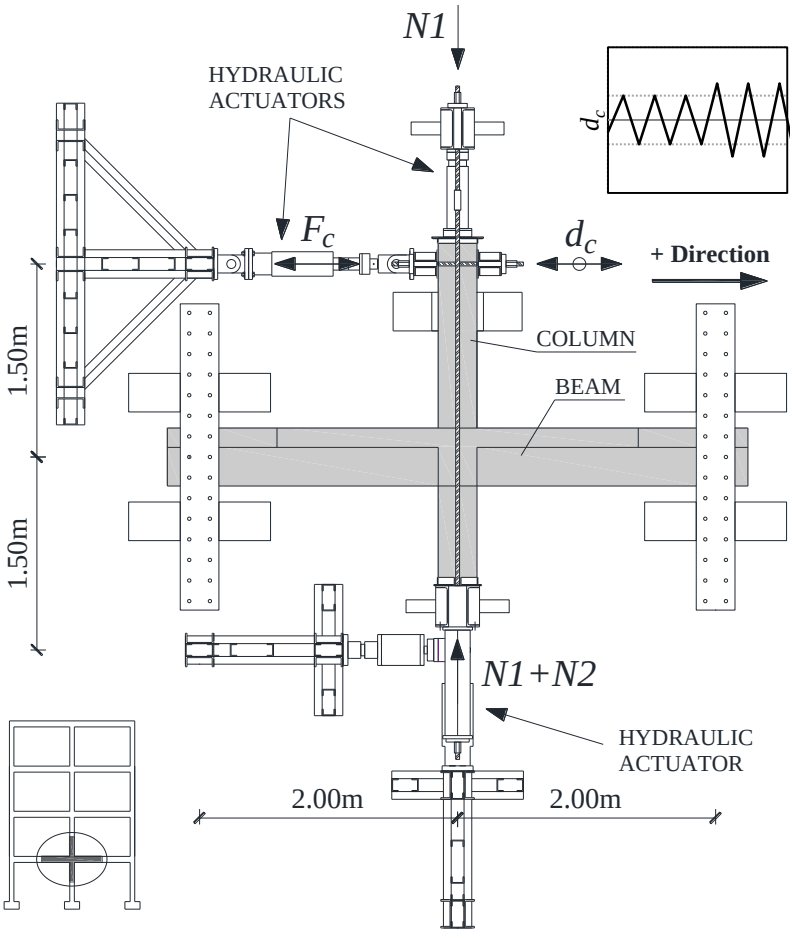

Figure 3.9. Test-set up with prototype structure and sample of loading protocol.

Figure 3.10. Pictures of the test set-up and specimen in the laboratory in Aveiro.

To induce a higher axial load in the first storey column, an additional axial load *(N2*) of 25 kN is applied at the inferior column. The second axial load is applied after beam supports are fastened so as to induce reaction forces in the beam supports, simulating moments from gravity loading, as shown in Figure 3.11.

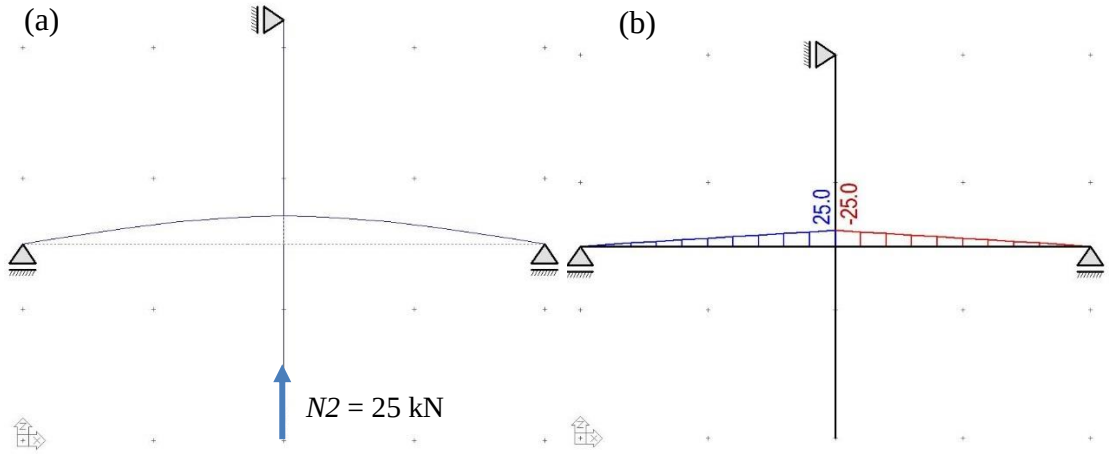

Figure 3.11. (a) Deflected shape and (b) moment diagram due to the second axial load (*N2*).

Using a hydraulic actuator, the lateral cyclic displacement (d_c) or drift (Δ) protocol shown in Figure 3.12 with three cycles per increment is applied at the top of the superior column, 1.5 m from the centre of the joint core. The drift values (in ± %) at each increment are: 0.1, 0.2, 0.3, then 0.5 up to 6.0 with 0.5 increments. The maximum lateral displacement at 6.0% drift is 180 mm. The rate of displacement application ranges from 0.1 in the first cycles up to 1.5 mm/second in the last cycles.

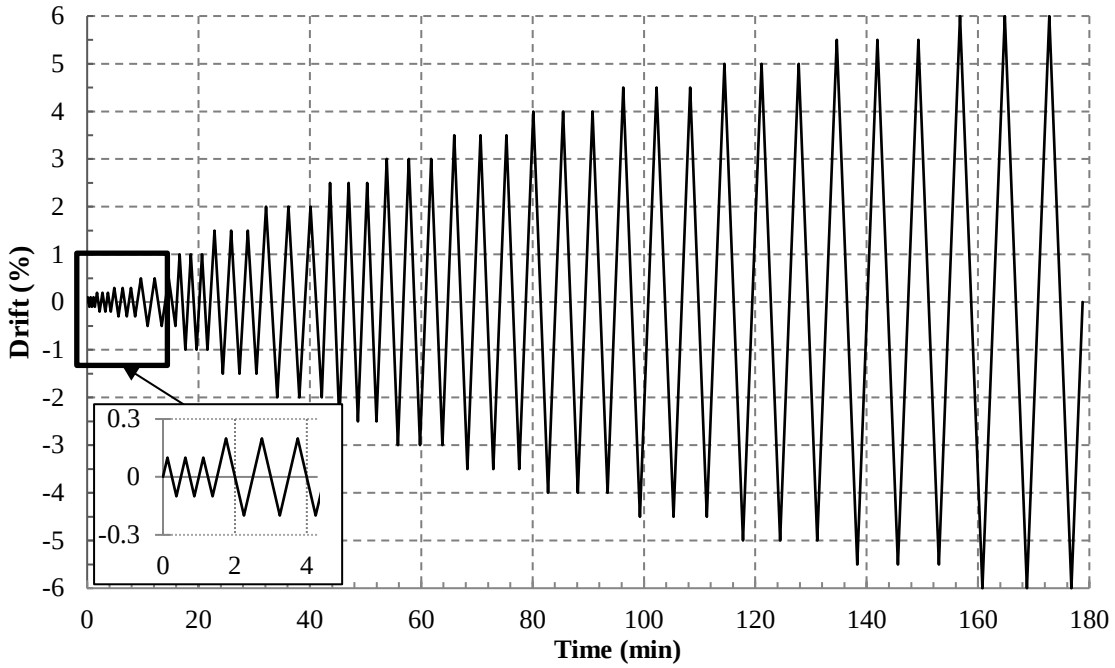

Figure 3.12. Applied displacement protocol for all experiments

Due to the use of pre-stressing rods for the axial load application of *N1*, an eccentricity of the applied axial load occurs at high drift levels. The lateral load effectively applied, F_l, needs to be calculated considering P-Δ effects from *N1*. This is done using the method described in the manual for the PEER structural performance database (Berry et al., 2004):

$$F_l = F_c + N1 \cdot \frac{\delta_{ecc}}{L_N} \tag{3.3}$$

Here, F_c is the applied lateral load from the horizontal hydraulic actuator, δ_{ecc} is the measured eccentricity of the rod at the base of the superior column of the specimen, and L_N the length from the base of the superior column to the top of the rod.

3.4. MONITORING

The general arrangement of the monitoring equipment is shown in Figure 3.13. The experiments are monitored using eight strain gauges (±0.6% accuracy) on the reinforcement (four on the superior column, one on the inferior column, two on the bottom beam bars and one on the top beam bars). In addition, one strain gauge on the top left FRP strand, 16 LVDT's (error < 0.025 mm), 28 rectilinear displacement transducers (error < 0.05 mm), four draw-wire position transducers (error < 0.5 mm), four inductive linear position sensors (error < 0.4 mm) and three pairs of cameras for stereoscopic 3D-digital-image correlation (DIC) are used to provide data on the deformation and damage evolution in the sub-assemblage. Despite being out of the scope of this thesis, due to the complicated set-up and high cost and effort associated with the experiments DIC data is collected to provide useful data for future research. In particular, the effective strain in the FRP material will be of interest. The DIC analysis is performed using the DaVis 8.2.3 software (LaVision), but not presented in this thesis.

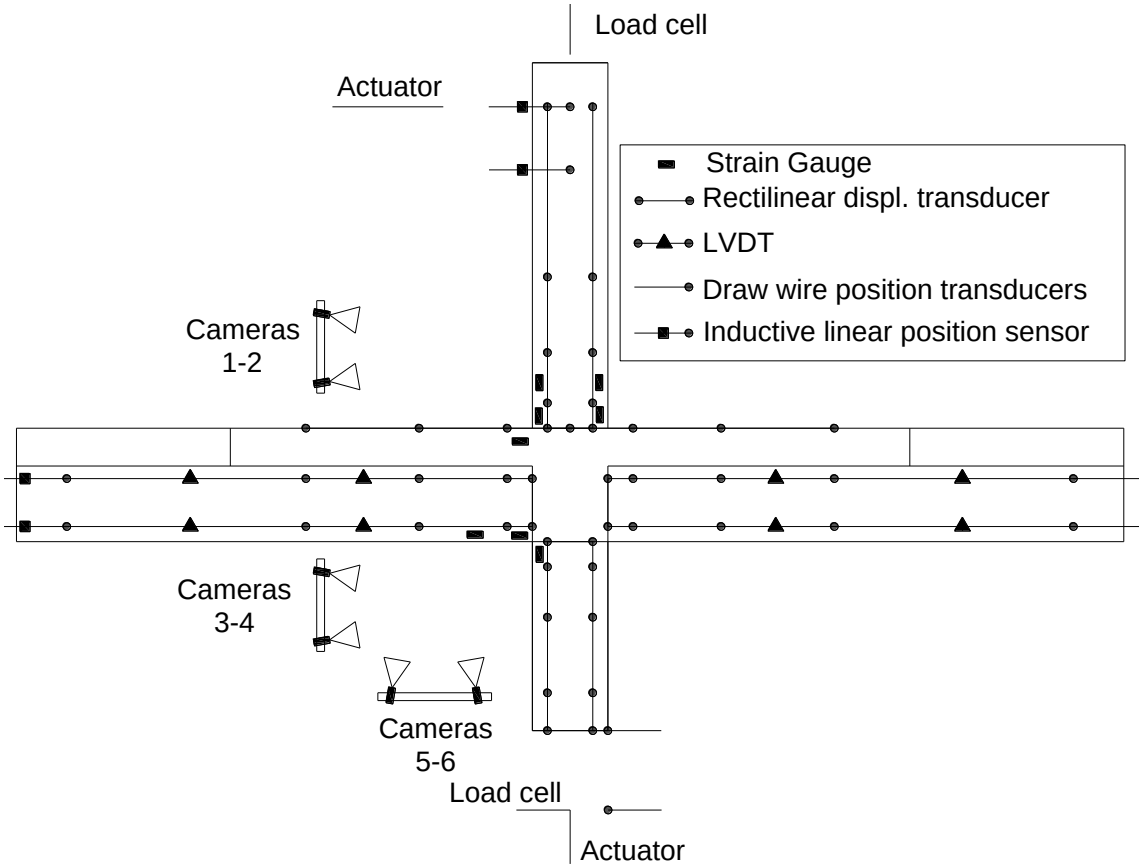

Figure 3.13. General arrangement of monitoring equipment for the beam-column joint tests.

Three different monitoring set-ups are used for the experiments due to changes in geometry and reinforcement detailing amongst the specimens tested. Figure 3.14 shows the set-up used for most specimens with slab and transverse beams. Figure 3.15 shows the set-up used for specimens without slab (C-noSLT; C-noSLT-RT-B) and Figure 3.16 shows the set-up used for specimen C-EC8.

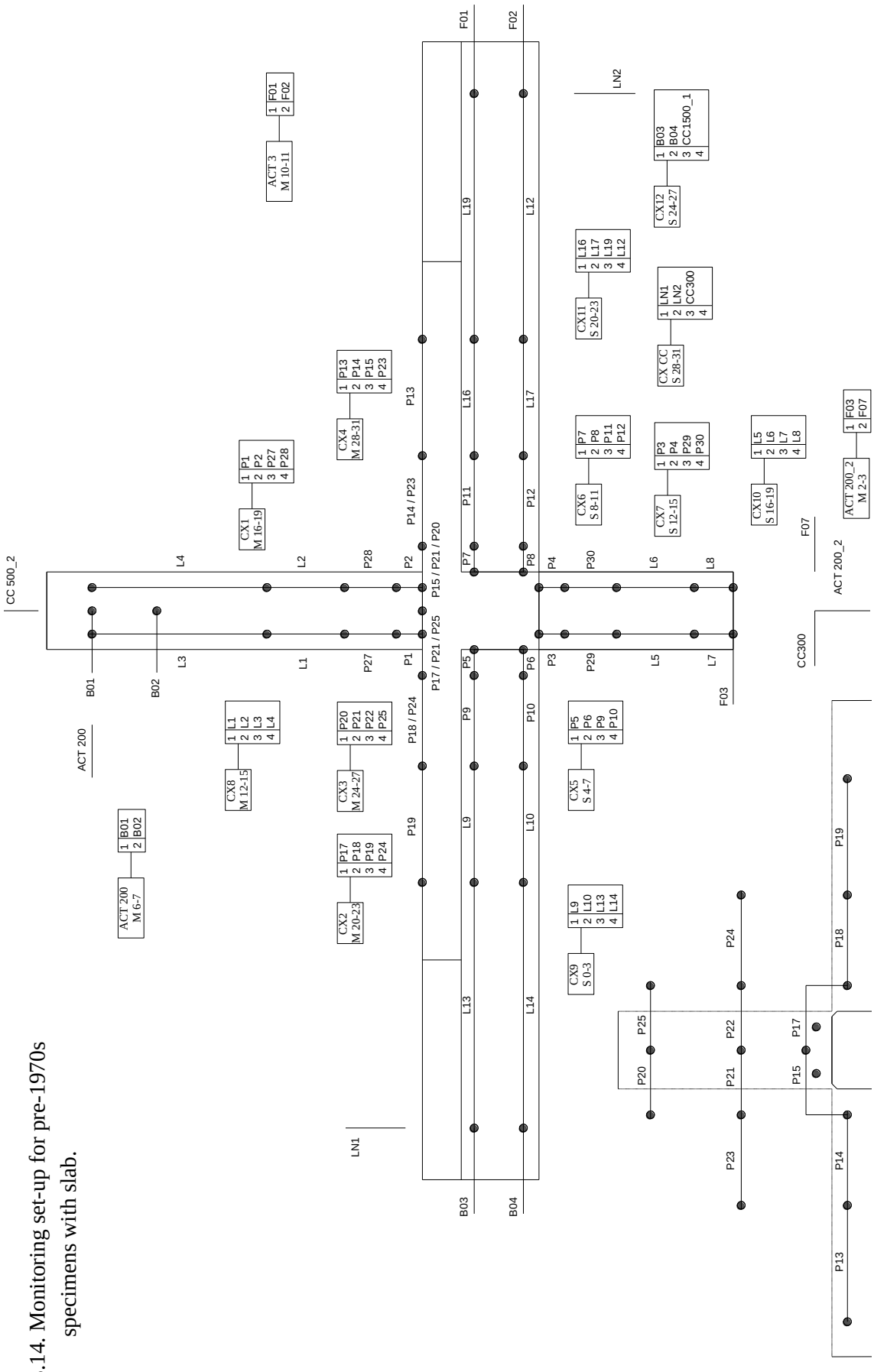

Figure 3.14. Monitoring set-up for pre-1970s specimens with slab.

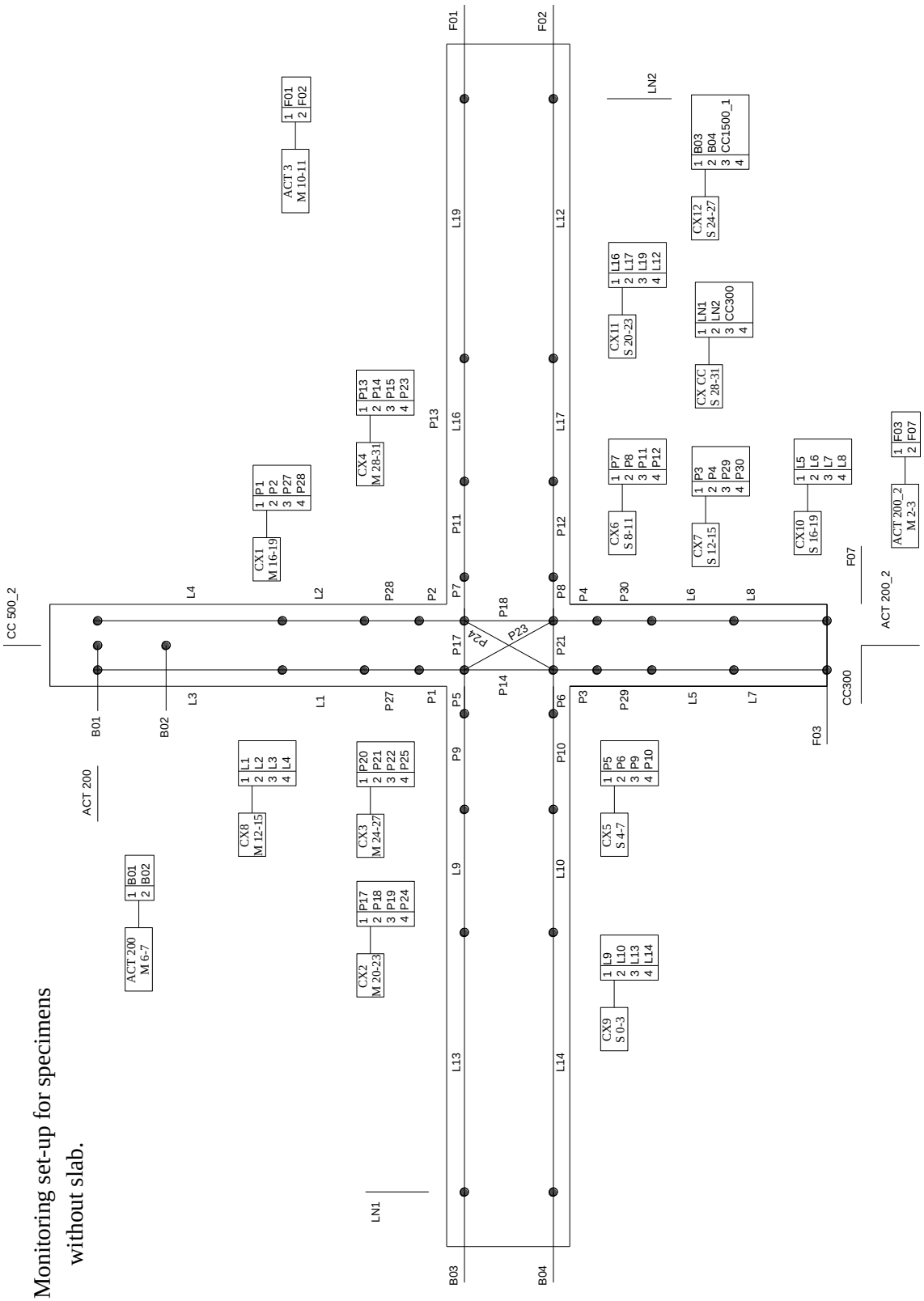

Figure 3.15. Monitoring set-up for specimens without slab.

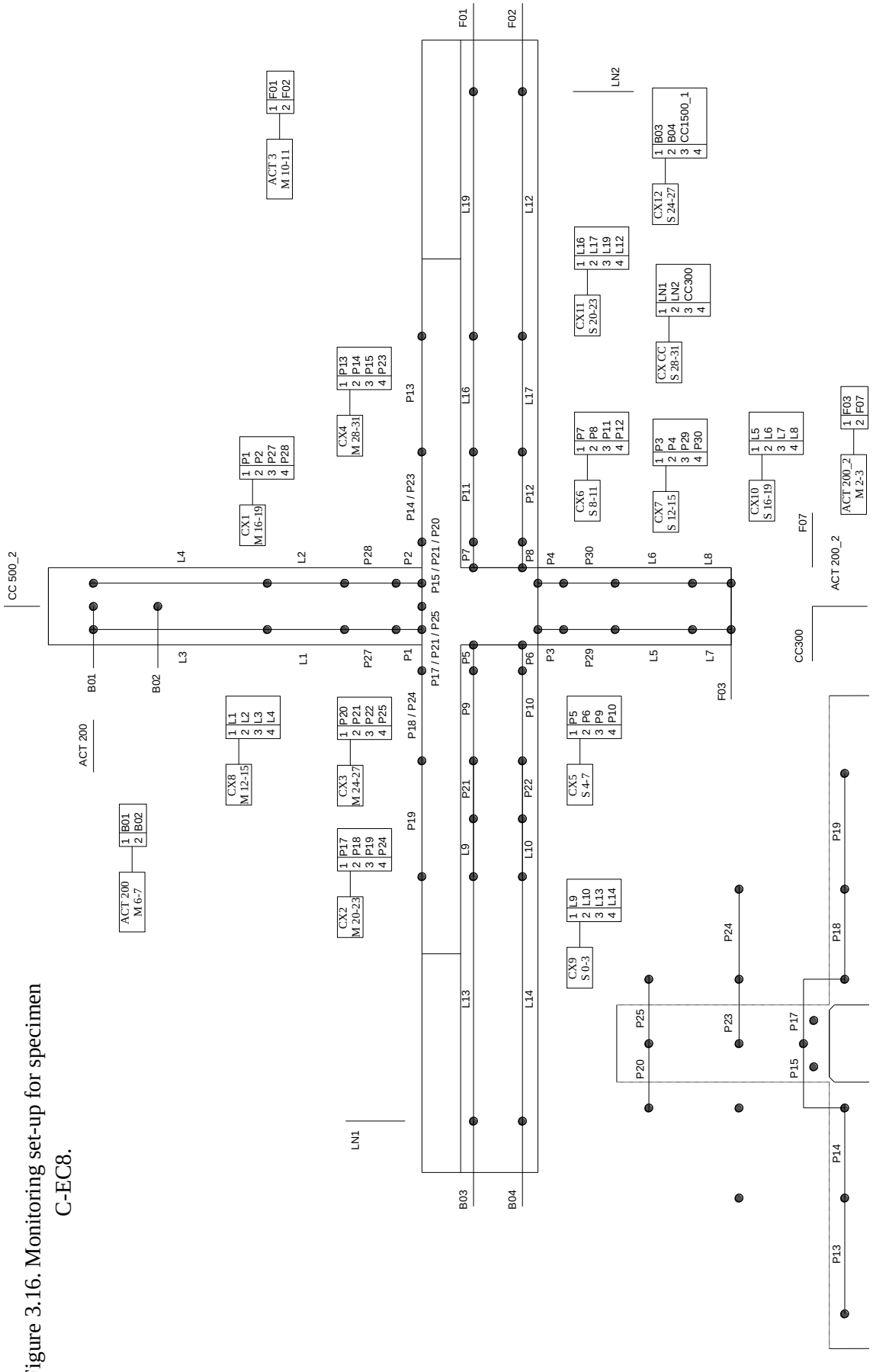

Figure 3.16. Monitoring set-up for specimen C-EC8.

3.5. NUMERICAL MODELS

"Essentially, all models are wrong, but some are useful" (Box and Draper, 1986)

3.5.1. INTRODUCTION

In order to design adequate retrofit schemes for the full-scale beam-column joint specimens, it is important to evaluate the deficiencies of the control specimens in detail. Next to the evaluation of expected moment and shear capacities from EC2 and EC8 presented in Section 3.2.3, detailed 3D nonlinear finite element (FE) models based on continuum mechanics are hence built in ABAQUS (2011) to assess the expected failure mechanism and location of damage in more depth. This information is useful to:

- Inform the specimen design, by determining the importance of the presence of slab on the failure mechanism and capacity of the beam-column joints.
- Inform the FRP retrofit design before physical testing, by assessing the location and mechanism of damage in the control specimens.

In this section the FE models and their results, as well as the theoretical background of the models, are presented. Numerical models are commonly used as a framework to predict the behaviour of structures. The complexity of models depends on the type of framework used and the objectives to be achieved. Computationally inexpensive, simple models are often used to get estimates about the overall behaviour of a structure or element. They are, however, limited in terms of recognising all deterioration or collapse modes and their interactions (López-Almansa et al., 2014). In contrast, detailed FE models with nonlinear material models lead to results that better represent the behaviour of the structures and are hence used here to inform the experimental testing programme. Some assumptions are however always required to reduce the computational effort and are presented along the description of the models. These approximations will, to some extent, introduce errors in the FE models. Prior to modelling the behaviour of the full beam-column joints, a series of strengthened and un-strengthened small-scale beam specimens is hence tested experimentally to validate the FE models (Section 3.5.3).

3.5.2. MATERIAL MODELS

3.5.2.1. CONCRETE DAMAGED PLASTICITY MODEL

In ABAQUS, three built-in models for concrete exist: the concrete smeared cracking in ABAQUS/Standard (Section 20.6.1 of the ABAQUS Analysis User's Guide), the brittle cracking model in ABAQUS/Explicit (Section 20.6.2), and the concrete damaged plasticity model in both ABAQUS/Standard and ABAQUS/Explicit (Section 20.6.3). The first two models are intended

to be used for monotonic loading only, while the third can be used for arbitrary or cyclic loading patterns. Moreover, the brittle cracking model is unsuitable for assessing concrete behaviour under both tension and compression in one model. For this project the concrete damaged plasticity model (CDP) model is therefore chosen for all simulations.

The CDP model, based on the Drucker–Prager strength hypothesis, was developed by Lubliner (1989) and later modified by Lee and Fenves (1998). It is a general capability model for analysing concrete elements under monotonic and cyclic loading. Material degradation through both, tensile cracking and compressive crushing modes can be defined using an isotropic damage model.

The uniaxial load cycle in the CDP model as presented in the ABAQUS theory manual is shown in Figure 3.17. Damage is associated to a reduction in elastic stiffness due to cracking or crushing characterised by degradation variables d_t and d_c, respectively. The concrete properties initial modulus of stiffness (E_0) and tensile and compressive stress-strain curves have to be defined. Γ_t (=0) and Γ_c (=1) are the stiffness recovery factors for load changes from compression to tension and tension to compression, respectively.

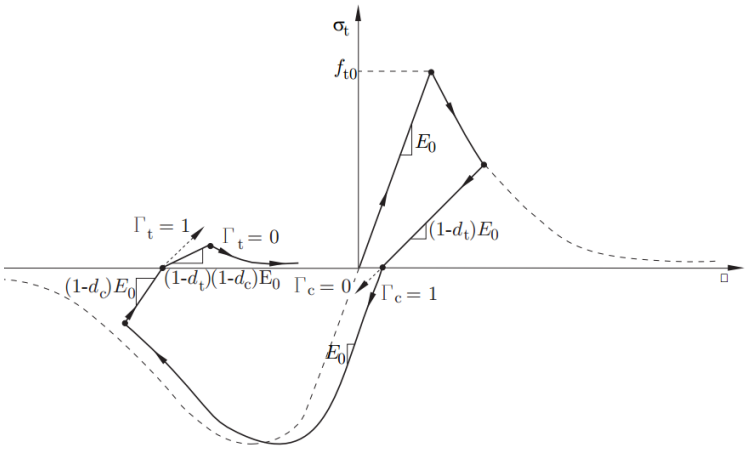

Figure 3.17. Uniaxial load cycle in CDP model (ABAQUS, 2011).

The concrete stress-strain curves used for all models have been described in detail in the literature (Krätzig and Pölling, 2004) and have been used by several researchers for RC members with good results (e.g. Birtel and Mark, 2006; López-Almansa et al., 2014; Luk and Kuang, 2012; Mark and Bender, 2010; Wang et al., 2012, amongst others).

3.5.2.1.1. CONCRETE IN COMPRESSION

The stress-strain of concrete in compression is modelled in three phases, a linear elastic part up to a stress f_{c0}, a non-linear hardening part up to the ultimate concrete strength f_{cu} (corresponding to the mean cylinder strength of the tested concrete sample, f_{cm}) and a softening part (the non-linear descending portion).

Phase 1: Linear elastic

In this region the stress-strain behaviour is linearly increasing and is defined by the initial stiffness E_c up to f_{c0}, where f_{c0} is defined as 40% of the failure strength f_{cm} in accordance with Eurocode 2 (CEN, 2008).

$$\sigma_c(1) = E_c\varepsilon \tag{3.4}$$

Where E_c can be reasonably accurately defined using the Eurocode 2 formulation:

$$E_c = 22(f_{cm}/10)^{0.3} \tag{3.5}$$

Phase 2: Hardening

The equation for this phase is similar to that in the fib-model code (fib, 1990) which was found to fit experimental data very well (Krätzig and Pölling, 2004).

$$\sigma_c(2) = \frac{\frac{E_{ci}\varepsilon}{f_{cm}} - \left(\frac{\varepsilon}{\varepsilon_{c1}}\right)^2}{1 + \left(\frac{E_{ci}\varepsilon_{c1}}{f_{cm}} - 2\right)\left(\frac{\varepsilon}{\varepsilon_{c1}}\right)} f_{cm} \tag{3.6}$$

Where, according to Eurocode 2, ε_{c1} is the strain of concrete taken as (CEN, 2008):

$$\varepsilon_{c1}(‰) = 0.7{f_{cm}}^{0.31} \tag{3.7}$$

and E_{ci} is defined as the secant modulus (fib, 1990):

$$E_{ci} = \frac{1}{2E_c}\left(\frac{f_{cm}}{\varepsilon_{c1}}\right)^2 - \frac{f_{cm}}{\varepsilon_{c1}} + \frac{3}{2}E_c \tag{3.8}$$

Phase 3: Softening

This phase is described by a decreasing function that takes into account the crushing fracture energy, G_{cl}, which is a material parameter, and a characteristic length, l_c. For the former a value between 10 and 25 kN/m can be taken for medium strength concrete (Vonk, 1993) and adjusted to fit experimental curves (Krätzig and Pölling, 2004). The characteristic length is dependent on the element geometry, and corresponds to the mesh size in the case of cubic elements. This approach using fracture energy, usually used for tensile cracking, was proposed in the early 1990's (Feenstra and de Borst, 1995).

$$\sigma_c(3) = \left(\frac{2 + \gamma_c f_{cm}\varepsilon_{c1}}{2f_{cm}} - \gamma_c\varepsilon + \frac{\gamma_c\varepsilon^2}{2\varepsilon_{c1}}\right)^{-1} \tag{3.9}$$

Where γ_c is the descent function that incorporates the ratio of G_{cl} and l_c:

$$\gamma_c = \frac{\pi^2 f_{cm} \varepsilon_{c1}}{2\left[\frac{G_{cl}}{l_c} - \frac{1}{2} f_{cm}(\varepsilon_{c1}(1-b_c) + b_c f_{cm}/E_c)\right]^2} \tag{3.10}$$

Where b_c is a constant factor linking corresponding plastic strains with inelastic strains (as shown in Figure 3.18) and takes values between 0 and 1. In this study b_c is taken as 0.7 based on experimental evidence on RC beams (Birtel and Mark, 2006).

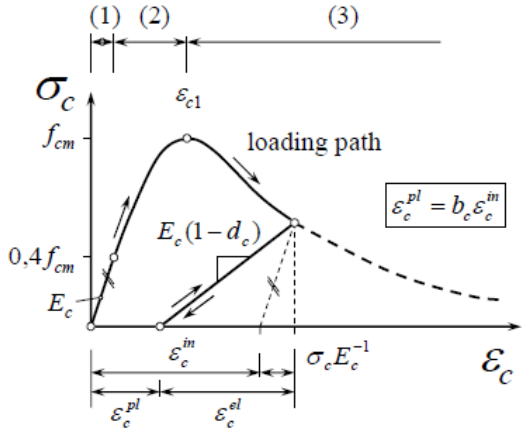

Figure 3.18. Stress-strain relationship for compressive loading from Birtel and Mark (2006).

The damage function for concrete, d_c, can be defined based on the relationship between inelastic and plastic strain with respect to Figure 3.18 (Birtel and Mark, 2006):

$$d_c = 1 - \frac{\sigma_c/E_c}{\varepsilon_c^{in}(1-b_c) + \sigma_c/E_c} \tag{3.11}$$

Where the inelastic strain is defined in the CDP model as:

$$\varepsilon_c^{in} = \varepsilon - \sigma_c/E_c \tag{3.12}$$

3.5.2.1.2. CONCRETE IN TENSION

The stress-strain relation for tensile loading consists of a linear part up to the tensile strength f_{ct} and a nonlinear descending branch, called tensile softening. This post-peak evolution of concrete tensile strength is an important aspect of the model as it implicitly controls the concrete-steel bond and load-transfer after cracking of the concrete section.

For the parts of the model without steel reinforcement, using a stress-strain relationship for tensile softening will introduce considerable mesh sensitivity according (Malm, 2009). To avoid this, it is preferable to use fracture energy or stress-crack opening laws. Bilinear crack opening laws by Hillerborg (1986) or exponential laws by Cornelissen (Reinhardt et al., 1986) and Hordijk (1992) are the most commonly used. Here, the law by Hordijk (1992) is used, as it is reported to be the

most accurate model (Malm, 2009). The relationship for the tensile stress, $\sigma_t(w)$, at crack opening displacement (w), normalised by the tensile strength of concrete, f_{ct}, is given by:

$$\frac{\sigma_t(w)}{f_{ct}} = \left[1 + \left(c_1 \frac{w}{w_c}\right)^3\right] e^{-c_2 \frac{w}{w_c}} - \frac{w}{w_c}(1 + {c_1}^3) e^{-c_2} \tag{3.13}$$

Where, w_c is the crack opening at which stress can no longer be transferred. For normal weight concrete, Reinhardt et al. (1986) propose values for material constants $c_1 = 3$ and $c_2 = 6.93$, and express w_c as a function of the fracture energy G_f, with $w_c = 5.14\, G_f/f_t$. The cracking energy can be determined from equation (5.1-9) of the CEB-fib model code (2010):

$$G_f = 73 {f_{cm}}^{0.18} \tag{3.14}$$

And f_{ctm} can be calculated according to EC 2 (CEN, 2008) as:

$$f_{ctm} = 0.3 {f_{cm}}^{2/3} \tag{3.15}$$

The principle of the fictitious crack model (Hillerborg, 1983) can be used to convert the crack opening law to a stress-strain relationship, by expressing the crack opening w as a product of the inelastic tensile strain, ε_t, and the characteristic length (i.e. mesh size):

$$w = l_c(\varepsilon_t - \sigma_t/E) \tag{3.16}$$

$$\varepsilon_t = \frac{w}{l_c} + \sigma_t/E \tag{3.17}$$

Accordingly, positive plastic strain in the analysis corresponds to initiation of cracking in the model (Obaidat *et al.*, 2010). Finally, the damage parameter for tension, d_t, can be found in the same way as for compression, with b_t, the ratio of plastic to inelastic tensile strain, taken as 0.1 (Birtel and Mark, 2006):

$$d_t = 1 - \frac{\sigma_t/E_c}{\varepsilon_t^{in}(1 - b_t) + \sigma_t/E_c} \tag{3.18}$$

3.5.2.1.3. FURTHER PARAMETERS OF IMPORTANCE

Finally, parameters for the yield function of the models have to be defined for the CDP model in ABAQUS. These parameters will not be described in detail but some information with regards to the choice of their values will be given here. A summary of the chosen values is given in Table 3.6. More detail on them and the theory behind the CDP model can be found in section 4.5.2 of the ABAQUS theory manual and the literature (Birtel and Mark, 2006; Jankowiak and Lodygowski, 2005).

Default values are given in the ABAQUS theory manual for some of the parameters. These are the flow potential eccentricity (e), the ratio of initial equibiaxial compressive yield stress to initial uniaxial compressive yield stress, f_{b0}/f_{c0}, and the ratio of the second stress invariant on the tensile meridian, K_c. Values for these constants can be obtained from experiments, but the default values have proven to be accurate and give good results in previous studies (Birtel and Mark, 2006; Jankowiak and Lodygowski, 2005; López-Almansa *et al.*, 2014; Sinaei *et al.*, 2012). Further parameters include the dilation angle ψ, that corresponds to the concrete internal friction angle, assumed between 36-40° according to an in-depth study by Kmiecik and Kaminski (2011), and a viscosity parameter, μ, which controls the influence of the hydrostatic stress on the yield/damage potential, for which a value of 0 is taken as default. Finally, the Poisson's ratio for concrete, v, is assumed to be 0.2 (CEN, 2008).

Table 3.6. Summary of chosen parameters for CDP model.

Parameter	E	f_{b0}/f_{c0}	K_c	ψ	μ	v
Value	0.1	1.16	2/3	36°	0	0.2

3.5.2.2. OTHER MATERIALS

To model the reinforcing steel material, it is assumed that the bars have approximately linear elastic behaviour defined by the Young's modulus at low strain. Past the yield strain, the plastic behaviour of the material including strain hardening is used. The values for the post-yield stress-strain curve are chosen to match the curves of real tensile tests of the steel rebars.

To model FRP, the elastic lamina material model is chosen with the material properties defined according to the tensile tests of FRP coupons.

3.5.2.3. ANALYSIS METHOD AND ELEMENT DISCRETISATION

To ensure convergence for nonlinear models, it is common to perform a quasi-static ABAQUS/Explicit analysis with a low loading rate in order to remove inertial effects (Section 6.2.5 of the ABAQUS Analysis User's Guide).

For all models, it was chosen to discretise concrete members with 3D 8-node hexahedron (brick) solid finite elements (C3D8R), the reinforcement bars by 2-node truss elements (T3D2) and the FRP as four-node shell elements (S4R). The relation between concrete and steel reinforcement in ABAQUS is typically defined by means of rebar or embedded elements, and the latter is used here. The concrete-FRP interaction is assumed to be a perfect bond and modelled as tied connections. The perfect bond assumption is sufficient for the purpose of using the numerical models to inform the design of experiments and strengthening solutions, because adequate anchorage solutions are to be used in the experimental tests. In future studies envisaged for the development of the experimental findings into design equations, more accurate modelling will be

required and it is envisaged to model the bond using cohesive elements, which have shown good results in the past (Chen et al., 2012).

Finally, the appropriate mesh size for the elements in the various models is determined based on a sensitivity analysis, looking for a convergence of peak force when decreasing the mesh size.

3.5.3. BEAM TESTS FOR MODEL CALIBRATION

As a first test and calibration, two RC beams were tested in the UCL concrete laboratory and modelled in Abaqus. Details of the beam tests can be found in Appendix E and are also published in Pohoryles et al. (2016). A brief summary of the tests is however provided here.

3.5.3.1. TEST SET-UP

Two T-beam specimens were tested under monotonic four-point bending at the concrete laboratory of University College London. The specimen geometry investigated is shown in Figure 3.19. The specimens consist of a control specimen (beam C) and a retrofitted specimen (beam FRP-1a). The reinforcement detailing was the same for both specimens. FRP was applied for flexural strengthening to the bottom face of beam FRP1-a, with U-strips for anchorage. The material properties are summarised in Table 3.7. This pilot study was carried out from May to July 2014.

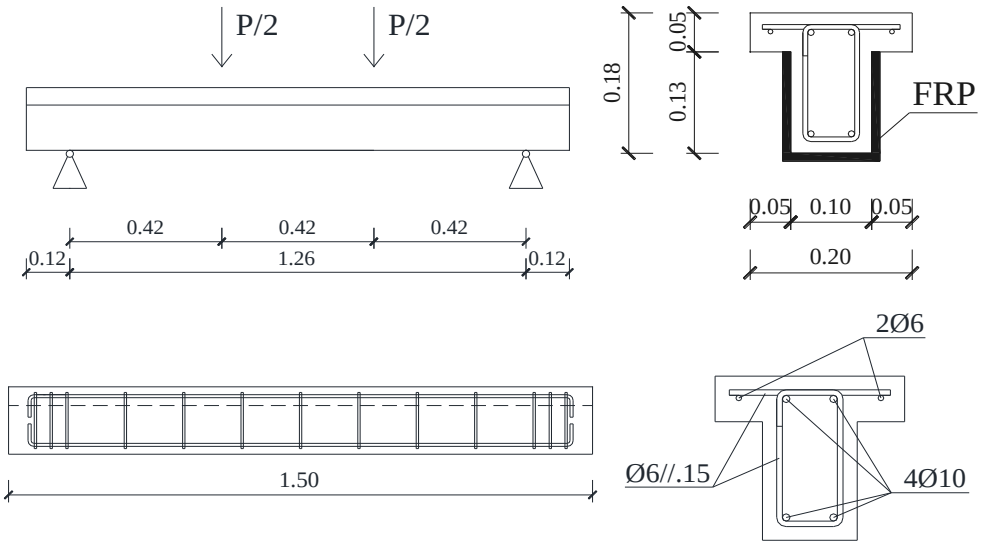

Figure 3.19. Beam specimens tested at the UCL concrete lab (dimensions in meters).

3.5.3.2. MODEL

Taking advantage of symmetry, an FE model is created for only a quarter of the beam and symmetric boundary conditions are applied along the mid-span and the centre line of the beam to reduce computational time. The model is shown in Figure 3.20 with a mesh size of 25 mm which is determined to be the most appropriate balance of accuracy (in terms of convergence of applied force) and runtime from a sensitivity analysis of different mesh sizes (100, 50, 25, 12.5 mm).

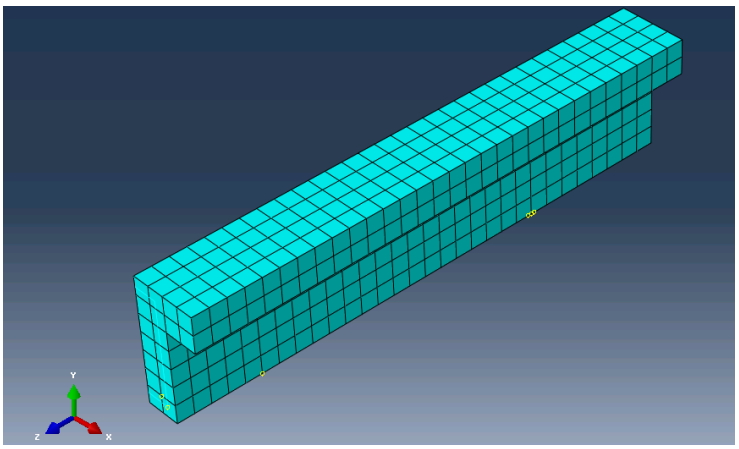

Figure 3.20. Quarter model of the control beam as modelled in Abaqus.

The concrete stress-strain curves and damage parameters shown in Figure 3.21 are determined according to the equations in Section 3.5.2 and used with the CDP model. The other material properties are summarised in Table 3.7.

Table 3.7. Material properties for beam FE-models.

f_{cm} (MPa)	$f_{y,main}$ (MPa)	f_u *(MPa)*	$f_{y,trans}$(MPa)	E_y (GPa)	f_{uf} (MPa)	E_f (GPa)
25	600	650	550	200	3300	195

(a) (b)

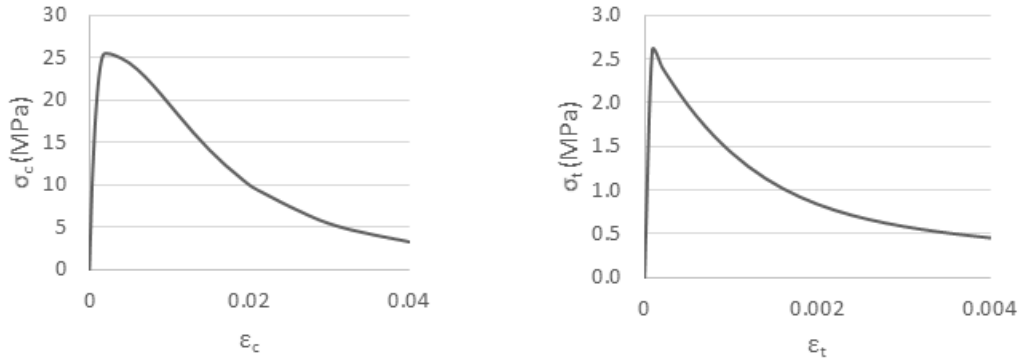

Figure 3.21. Compressive (a) and tensile (b) stress-strain relationships for the concrete model.

3.5.3.3. FE MODEL CALIBRATION

For the model, a displacement based loading is applied at the point of loading up to 25 mm at a rate of 0.1 mm/s. Mass scaling of a factor of 10^4 is found adequate to balance accuracy and run time of the FE model. The force-displacement plot for the FE model is compared to the experimental results in Figure 3.22. It can be seen that the maximum load in the FE model matches the experimental data very closely (+0.5%). A main difference in the two plots is however that the first change in stiffness occurs at very low deflection at about 5 kN in the experiment, whilst in the FE model the stiffness remains constant up to an applied load of about 15 kN. This difference in stiffness in the linear range is commonly reported in the literature for FE-models

(Ibrahim and Mahmood, 2009). It can be related to the bond between concrete and steel, which is assumed to be perfect (no slip) in the model, while some slip occurs in the experiments, slightly reducing composite action in the actual beams. Moreover, microcracks are produced by drying shrinkage. These reduce the stiffness of the actual beams, but are not simulated in the models.

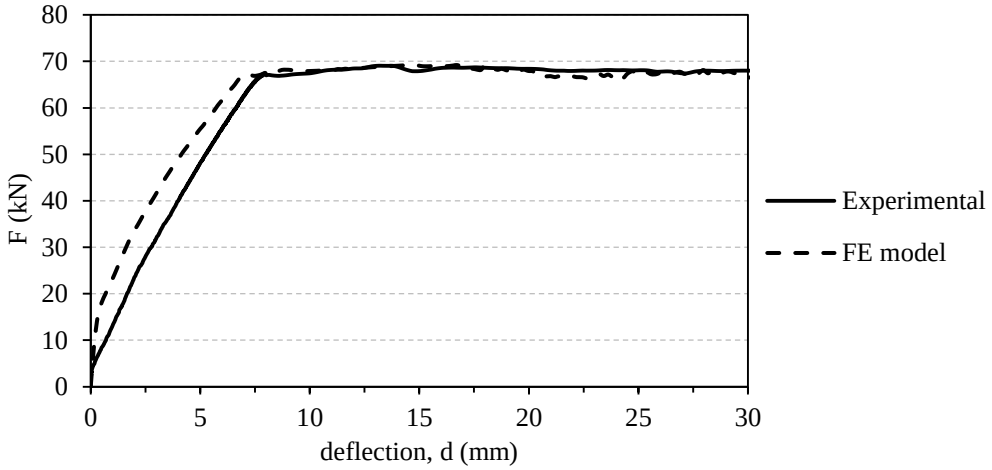

Figure 3.22. FE and experimental force vs mid-span deflection plots for the control beam.

The damage and cracking in the concrete is compared to the experiment. Figure 3.23 shows a comparison between plastic strain (PE) distributions obtained from the finite element analysis, corresponding to cracks according to the CDP model, and crack patterns from the experiments for the control beam. The cracks obtained in the experiments and in the simulations are similar, which indicates that the model can capture the main mechanisms of failure in the beams.

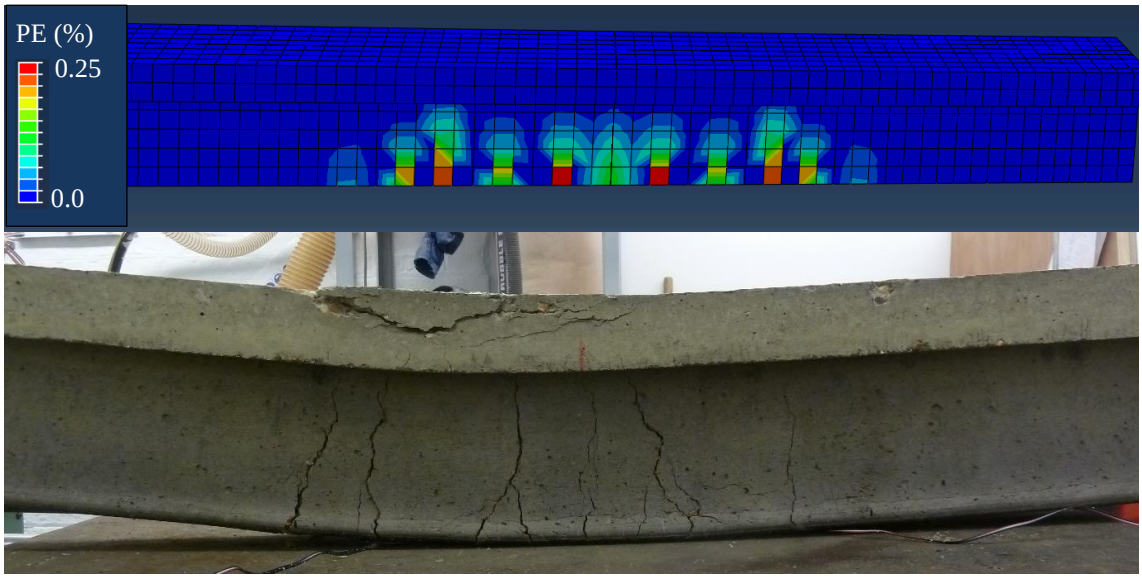

Figure 3.23. Comparison of cracking in the model and experiment for the control beam.

A second FE model represents the FRP strengthened beam A1 with one layer of FRP. The longitudinal strengthening sheet of 80 mm width is modelled with shell elements (S4R), as elastic lamina and perfect bond to the concrete is assumed. The transverse U-strips are also modelled, as

they provide shear strengthening. The results in terms of force-displacement response are shown in Figure 3.24. The predicted maximum load of 74 kN is slightly lower than the 76.5 kN in the experiments, but corresponds to a very close match (-3.22%). The drop in strength observed in the experimental data is much more sudden in the model, as FRP rupture is predicted. In the experiment this was not observed as concrete peeling occurred before the rupture strain could be reached. Similar observations in terms of stiffness can be made as for the control beam.

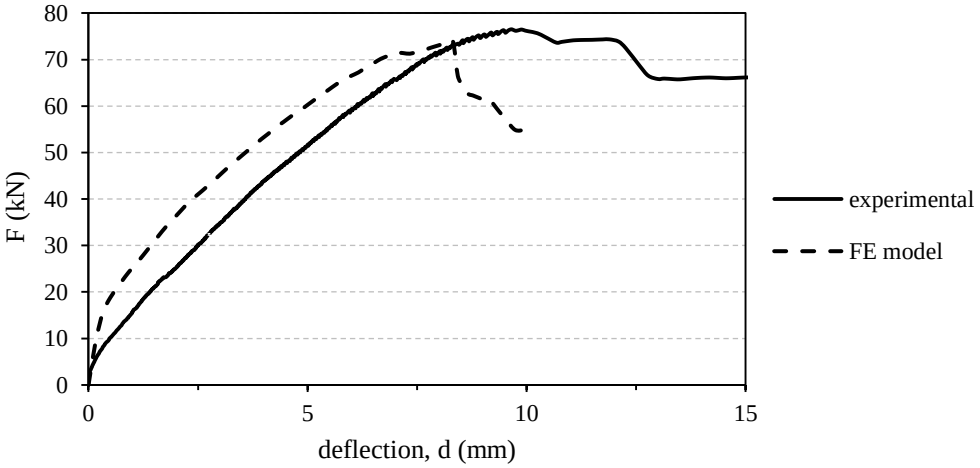

Figure 3.24. FE and experimental force vs mid-span deflection plots for the retrofitted beam.

When comparing plastic strains to the actual cracks in Figure 3.25, it can be seen that shear cracks in the experiment are well reproduced by the numerical model. By visualising the direction of the principle plastic strain on the right hand side of Figure 3.25, it can be seen that the high strains indeed correspond to diagonal crack opening.

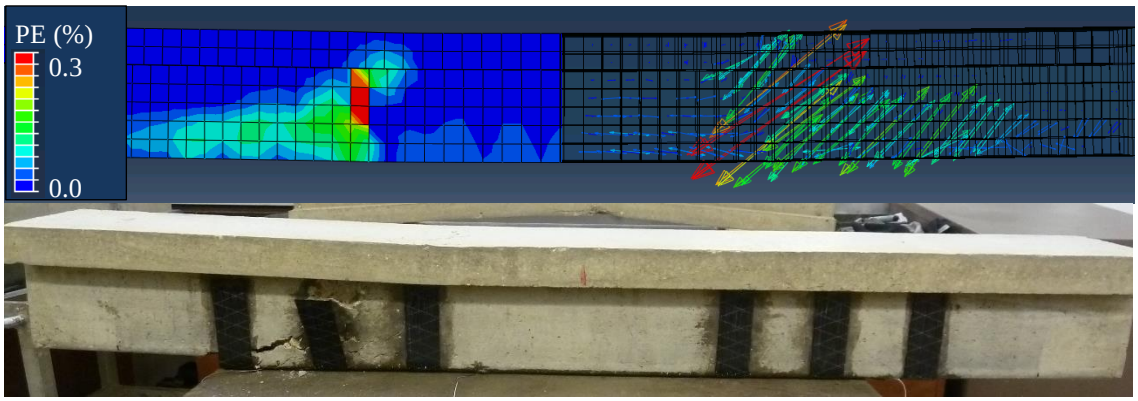

Figure 3.25. Comparison of cracking and direction of maximum plastic strain between model and experiment for the strengthened beam.

Overall it can be said that the models reproduce well the main behaviour of the two beams. The failure mechanisms and damage location, as well as the force-displacement curves match very well. In the next section, these models can hence be used, albeit adapted, to model the beam-column joints to be tested in the experimental campaign.

3.5.4. FULL-SCALE JOINT SPECIMENS

3.5.4.1. AIMS OF THE FE ANALYSIS

The finite element analysis presented in this section is seen as a tool to identify the effect of different geometrical properties to be tested as control specimens in the experimental programme and to inform the FRP retrofit strategies to be adopted.

First, four models of the as-built specimens without FRP are analysed. The parameters to be investigated are the presence of a slab in the assembly, the presence of transverse beams, as well as the effect of different reinforcement detailing (EC8 detailing).

The models reproduce the full reinforcement detailing and geometry of the actual specimens tested at the University of Aveiro, which are described in detail in Section 3.2. The FE model of the full-scale joint specimen with slab is shown in Figure 3.26.

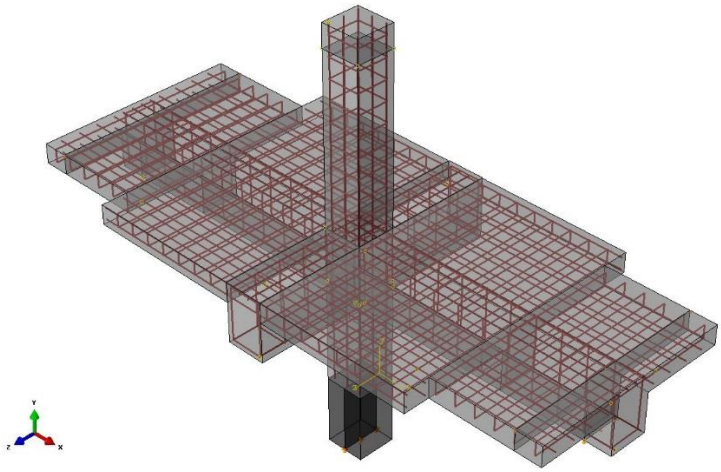

Figure 3.26. FE model of the full-scale beam-column joint specimen.

3.5.4.2. MODEL PARAMETERS

Taking advantage of symmetry, an FE model is created for only half the specimen, with symmetric boundary conditions applied along the centre-line of the main beams and columns to reduce computational time.

Based on a thorough sensitivity analysis looking at mesh size (100 to 12.5 mm), a mesh size of 50 mm is used for the analyses. This is determined to be the most appropriate to balance computational time and accuracy of results. While increasing the mesh size to 50 mm did not affect the force-displacement graphs, using a mesh size of 25 mm gives more details on cracking patterns and is hence used for better visualisation of some results.

Mass scaling, commonly used to make quasi-static analyses run more efficiently, is applied according to the ABAQUS user manual (chapter 11.6.1). This is achieved by artificially increasing the density of materials in the analysis while keeping the loading rate realistic. It is

important to consider however, that a quasi-static analysis corresponds to a dynamic analysis with negligible inertial effects and that changes in the mass will increase inertial forces. A scaling factor of 10^4 is determined to provide results that are not affected by inertial forces for the chosen loading rate. Increasing this factor, leads to local peaks in the force-displacement graphs to appear that can be associated to inertial effects.

Again, to reduce computational costs, rather than cyclic loading, an increasing displacement controlled load is applied at the top of the column, from 0 mm to 120 mm (4.0% drift), corresponding to the peak values expected in the experiments for the control specimens. At the top of the column, an axial pressure equivalent to the axial load used in the experiment (425 kN) is applied prior to the lateral displacement. The second axial load in the test set-up is not implemented in the model, as an attempt to do so results in an extremely unstable model under the selected quasi-static analysis method. As the FE models are only used as tools to assess the relative influence of certain parameters on the behaviour of the specimens, it is deemed that this simplification is acceptable, with a small difference being expected in maximum lateral loads predicted as compared to the experiments.

Finally, the loading rate is chosen to comply with a realistic duration which does not affect the results in terms of inertial effects. With this is in mind, a lateral loading rate of 0.5 mm/s is determined appropriate, leading to a total time of 250 s, with the first 10 s correspond to the application of the axial load only.

The same non-linear material models as for the T-beams described earlier are used, with the material properties initially assumed for the beam-column joints tested in Aveiro implemented in the models (see Table 3.8).

Table 3.8. Summary of material strengths used for the models.

f_{cm} (MPa)	$f_{y,main}$ (MPa)	f_u (MPa)	$f_{y,trans}$ (MPa)	E_y (GPa)
21	450	525	540	200

3.5.5. RESULTS

A variety of models of control specimens without FRP are developed in ABAQUS with different geometry and reinforcement detailing, as summarised in Table 3.9, in order to:

- Identify potential failure mechanisms of the control joints.
- Understand the effect of slab and transverse beams, often ignored in experimental campaigns, and determine if it is important to be included in experiments.
- Inform the retrofit strategy to be adopted (areas that need strengthening).

Table 3.9. Summary of FE models of control specimens.

Name	Description	Detailing	Transverse beam	Slab
C1	Main control specimen	pre-1970s	Yes	Yes
C-noSLT	Cruciform specimen	pre-1970s	No	No
C-noSL	Specimen with transverse beam	pre-1970s	Yes	No
C-EC8	Specimen designed to EC8	EC8	Yes	Yes

The developed models presented in this section, are assessed in terms of applied force against column tip displacement, as well as location of cracks (in terms of plastic strain according to the CDP model), location of steel yield and potential buckling. It is noted that some figures presented show the half-model, i.e. a cut through the centre line of the specimen.

The FE model of the control specimen C1, which consists of the full-scale beam-column joint with slab and transverse beams, is shown in Figure 3.26. This FE model provides a reference against which to compare the other specimen variations and is used to determine the areas to be strengthened in the experimental campaign. In this model, damage is concentrated in the superior column and the column/joint interface. Locations of plastic strain in concrete, corresponding to cracks and crushing in the CDP model, is shown in Figure 3.27 (a). Two large cracks can be seen at the tension face of the column, with one directly at the interface with the slab, and one at the level of the first transverse reinforcement.

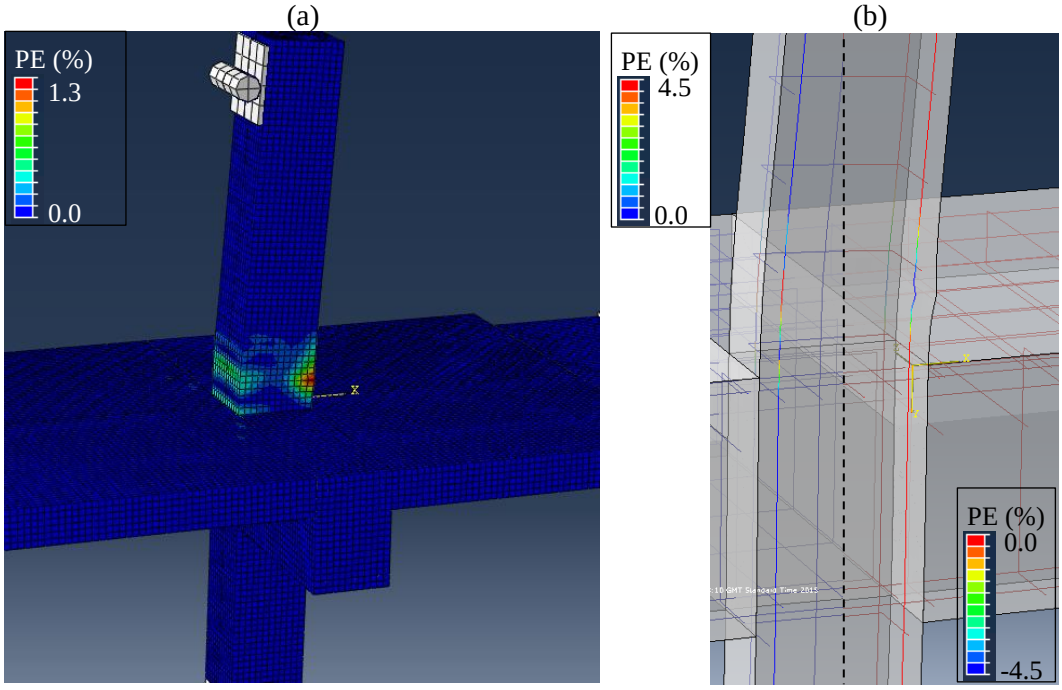

Figure 3.27. Control model C1 with slab (25 mm mesh): (a) Location of damage; (b) yield and buckling of column bars (cut through centre line).

Initial flexural cracking at the superior column is observed at a drift of 0.5%. This is followed by very local yielding of steel bars that is first observed in the corner column bars, just above the joint, at 1.25% drift when the plateau is reached in the force-displacement plot (see Figure 3.28). The plastic strain in the reinforcement at the maximum drift (4.0%) is shown in Figure 3.27 (b). At 2% drift the maximum lateral load (77.06 kN) is achieved as all three superior column bars in tension reach yield. Then, buckling of the longitudinal bars in the compression face of the superior column is observed, corresponding to the location of concrete crushing seen in Figure 3.27 (b). Yield in the beam bars is not observed.

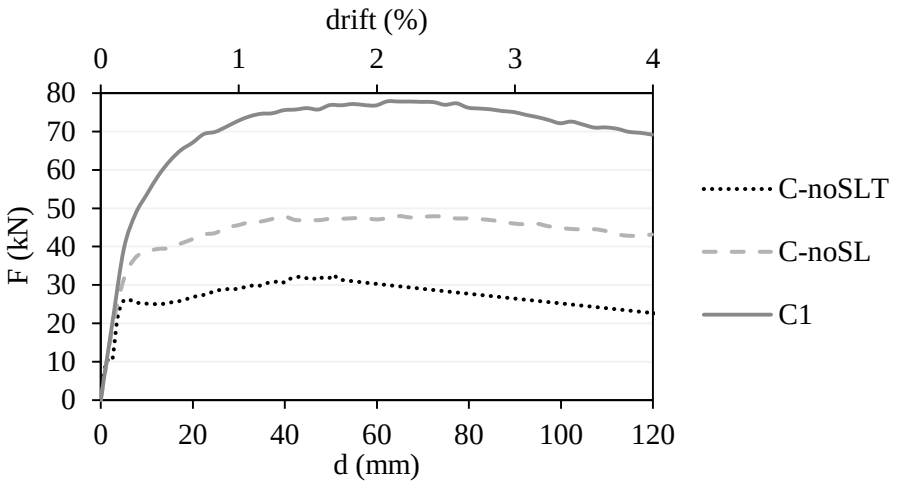

Figure 3.28. Force vs. displacement plot from FE models illustrating the effect of transverse beam and slab.

A strong-beam/weak-column mechanism is therefore predicted to occur in the control specimen, with a combination of plastic hinging in the column, just above the joint, and strong damage in the column due to concrete crushing at the slab interface.

3.5.5.1. EFFECT OF SLAB AND TRANSVERSE BEAM

The effect the slab has on the overall behaviour of the joint is assessed by comparing the control specimen FE model with an identical specimen without slab but with transverse beams. As shown in Figure 3.28, a much lower maximum lateral load of 48 kN (-38%) is observed and the initial stiffness is also slightly reduced. As shown in Figure 3.29 (a), no damage is observed in the columns. In turn, damage in the beams, with cracking close to the beam-joint interface, as well as in the joint core, with high strains in the diagonal of the joint, can be seen. Without slab, the capacity of the beam in hogging is reduced to a level similar to the sagging capacity and the beams, and the joint can rotate more. Close to symmetric yielding of the top and bottom beam bars is observed at a drift of 1.1%. Yielding then propagates along the length of the bars and into the joint core. In stark contrast to the control specimen with slab, no yielding is observed for the column bars, as the rotation of the column, and hence the demand, is reduced.

Next, the transverse beam is also removed to simulate the behaviour of a 'cruciform' specimen, which is usually tested in the literature. For this specimen an even lower capacity of 32.7 kN (-58%) is achieved (Figure 3.28), with damage primarily in the joint as shown in Figure 3.29 (b). The failure can be attributed to joint shear failure with diagonal cracking, which is in line with many observations from the literature for similar geometries. The maximum load is achieved at around 1.5% drift when the longitudinal beam bars yield in the joint core and high values of diagonal cracking strains in the joint core are observed.

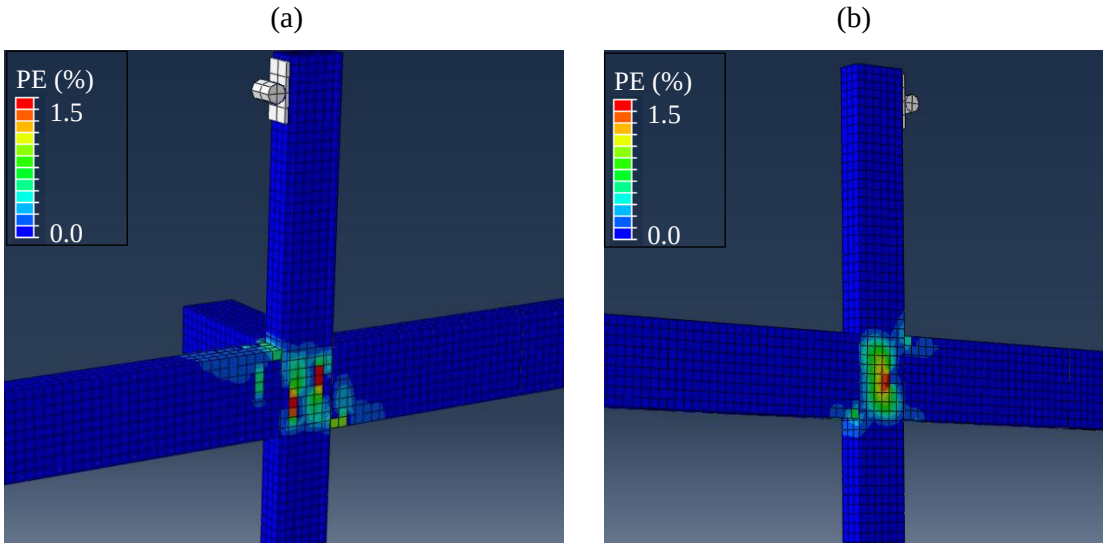

Figure 3.29. Damage location in model C-noSL (a) and cruciform model 3 C-noSLT (b) – cut through the centre line of the specimens.

The large difference in capacity and damage location between the three models highlights the importance of testing specimens with slab and transverse beams. Without slab and transverse beam, more damage is observed in the joint and beams as their rotation is less restrained. Less demand is imposed on the columns, which are consequently less damaged. Therefore, the slab and transverse beam not only present geometric obstructions when applying FRP, but also influence the FRP retrofit objectives: with the slab and transverse beams, the columns are the primary strengthening targets, whereas without these elements, the beams and the joint require strengthening. Furthermore, as FRP interventions have been reported to be more effective when the capacity of the joint is low (Antonopoulos and Triantafillou, 2003), this study indicates that for realistic specimens a less effective retrofit will be achieved as compared to weaker joints tested without slab and transverse beam.

3.5.5.2. EFFECT OF ADEQUATE REINFORCEMENT DESIGN

Here the control specimen model is compared to a joint with reinforcement detailing appropriate to modern seismic codes (Eurocode 8), as shown in section 3.2.2 for specimen C-EC8. The specimen presents adequate shear strengthening of the joint, higher flexural capacity of the column and an adequate spacing of the shear links. The aim of this model is to understand the

failure mechanism and strength that can be achieved for a modern specimen, which serves as a comparison to the retrofit schemes.

It is seen in Figure 3.30 that, as expected, with a larger moment capacity of the column, a strength of 128.6 kN, corresponding to a 67% increase compared to the control specimen is obtained. A larger initial stiffness is also observed for the Eurocode 8 specimen due to the increased column reinforcement. The post-peak softening for the specimen designed to Eurocode 8 is however more significant than for the control specimen.

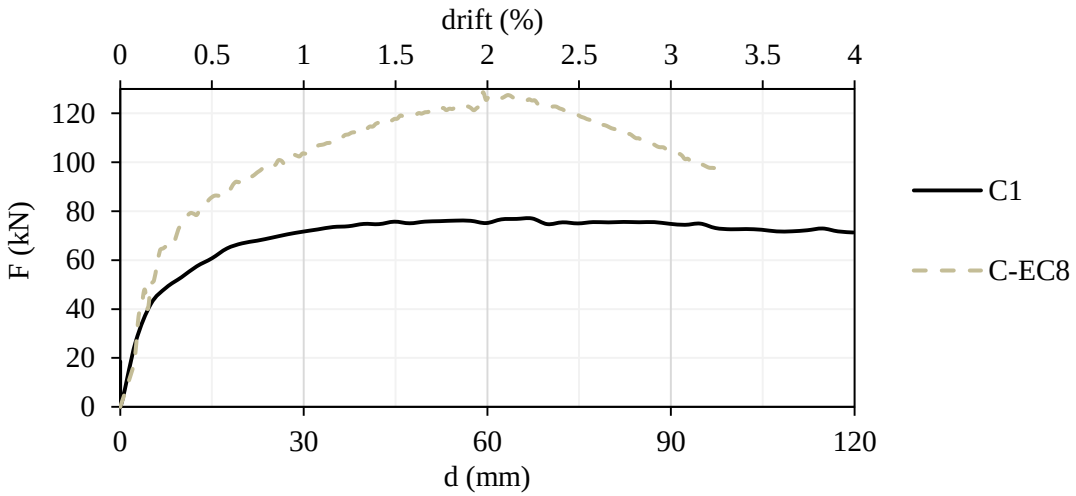

Figure 3.30. Force vs. displacement plot for the control and EC8 FE-models illustrating the effect of adequate seismic reinforcement design.

Due to capacity design, in the Eurocode 8 specimen damage is observed in the beam bottom face and the transverse beam-joint interface (Figure 3.31 (b)). Moreover, strong slab participation is also observed with crack formation in the slab top and bottom faces (Figure 3.31 (a)), parallel to the transverse beam/slab interface. Limited damage in the column/joint interface is seen.

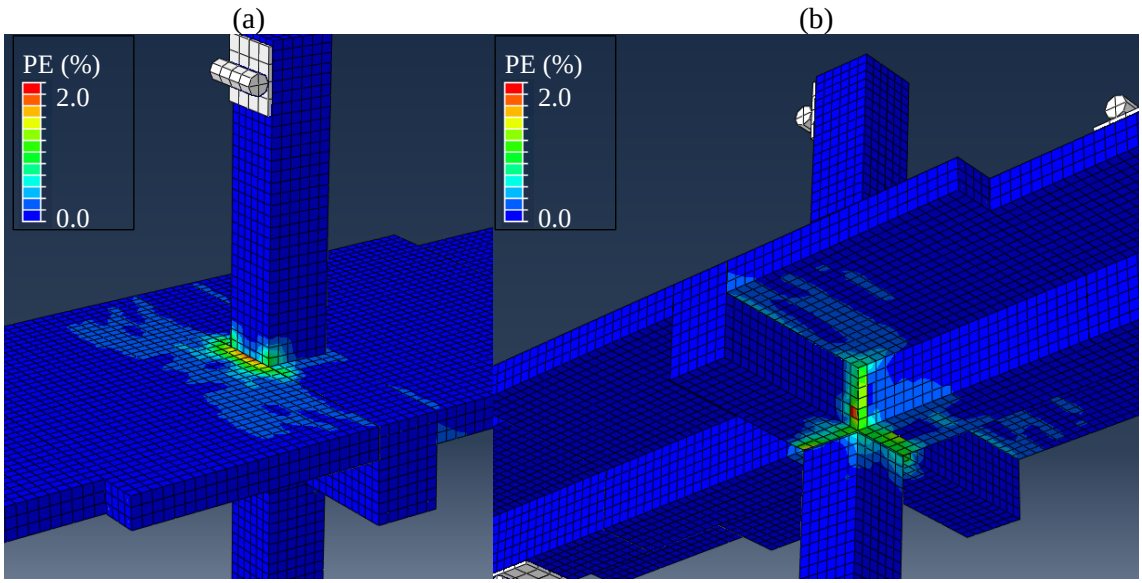

Figure 3.31. Damage in the model of specimen C-EC8 with seismic detailing: (a) top of slab and column; (b) beams and slab bottom face.

At the peak lateral load, yield is reached in the beam reinforcement bars, at the interface with the joint. The column rebars remain in the elastic range throughout the simulation. As shown in Figure 3.32, high tensile strains and yielding are observed in the top layer of slab reinforcement in hogging and the lower layer of slab reinforcement in sagging. The reinforcement outside the effective width calculated to EC8 also present large values of strain, which indicates that for an adequately reinforced specimen, the beam moment capacities is significantly enhanced by the slab reinforcement, and possibly more than anticipated by EC8 design.

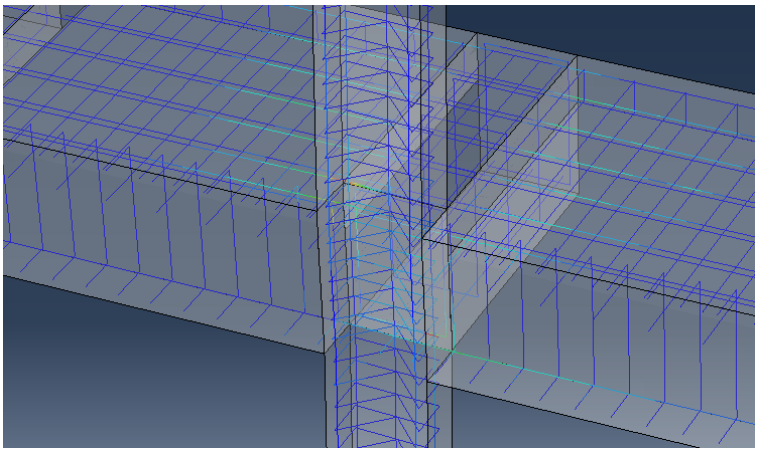

Figure 3.32. Strain in the reinforcement of the seismically designed specimen model.

3.5.6. SUMMARY OF OUTCOMES OF NUMERICAL MODELS

The results of numerical models of beams and beam-column joints were presented in this section. RC beams with and without FRP retrofit are modelled accurately with the non-linear material models employed in this study. The model is expanded to predict the behaviour and failure mechanism of the full-scale beam-column joint specimens tested in this project. The results of these models are summarised in Table 3.10 for the main beam-column joint models.

Table 3.10. Summary of results for the models of beam-column joints.

	C1	C-EC8	C-noSL	C-noSLT
Max Lateral load (kN)	77.1	128.6	48.0	32.7
Difference to control (%)	/	+67%	-38%	-58%

For the control specimen with slab and transverse beam (C1), the concentration of damage, combined with yielding of column bars and high rotation of the superior column, characterise an unfavourable failure mechanism. The FE analysis highlights that foremost strengthening of the column is needed to ensure a desirable failure mechanism is achieved.

The effect of slab and transverse beams, often ignored in experimental studies, is shown to be significant in terms of load capacity and failure mechanism. The different failure mechanism affects the design of FRP retrofit strategies, as the aim for retrofitting the specimens would be very different. While the control specimen with slab requires retrofitting of the column to increase

its confinement and flexural capacity, for the specimen without slab, instead, the first priority is retrofitting the joint.

The effect of reinforcement detailing is shown to be significant. Adequate seismic detailing is required to move damage away from the column and joint. To increase the strength of the specimen, in particular the column flexural and shear capacities need to be increased compared to the beam to avoid a strong-beam/weak-column mechanism observed for the control specimen.

3.6. FRP RETROFIT AND REPAIR SCHEMES

The strengthening schemes presented in this section are based on outcomes of the literature review, as well as the initial finite element study, which is used to identify the locations requiring strengthening. The numerical modelling of the control specimens presented in the previous section confirms the need for column strengthening, in order to prevent a brittle failure characterised by buckling and an inadequate hierarchy of strengths between the columns and beams. To achieve a better seismic behaviour, approaching that of C-EC8, three retrofit schemes, shown in Figure 3.33, are presented in this section.

The schemes are designed to take into account practical limitations and excessive removal of concrete, full wrapping of inaccessible members, ignoring slabs or transverse beams, are hence not considered. The first scheme (A) is the simplest design with FRP strengthening of the columns only. It aims to improve the strength of the specimen by increasing the moment capacity of the deficient columns and increase the global displacement capacity of the specimen by connecting the flexural strengthening of the superior and inferior columns. The second scheme (A-sw) aims to develop a more ductile beam hinging failure mechanism, in order to enhance the displacement ductility of the specimen further. This is done by selective weakening (sw) of the slab in addition to the flexural strengthening of the columns. Finally, scheme B-sw aims to increase strength and ductility of the specimen to achieve a behaviour comparable to specimens designed to modern design codes. This is the most intricate scheme including a combination of FRP strengthening of columns, beams and joint, as well as selective weakening of the slab.

While inspired by successful implementations in the existing literature, the proposed schemes are novel and innovative in many ways. The proposed retrofit schemes are the first to use FRP anchor strands for continuous flexural strengthening of columns on full-scale specimens with slabs and transverse beams. The design of RT-B-sw also includes the first effort of joint shear strengthening applied through transverse beams. Finally, flexural strengthening of beam for plastic hinge relocation using FRP anchor strands is proposed for the first time.

As a first step, existing FRP design guideline equations are used to determine the capacities of the retrofitted members. These equations are presented in Section 3.6.1. Then the detailed design including FE modelling is presented in Section 3.6.2.

Intervention	Objectives
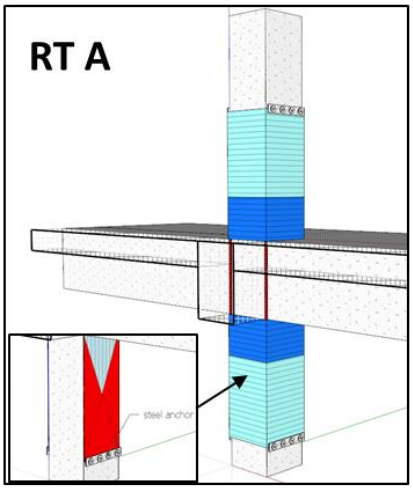 Strengthening of columns only	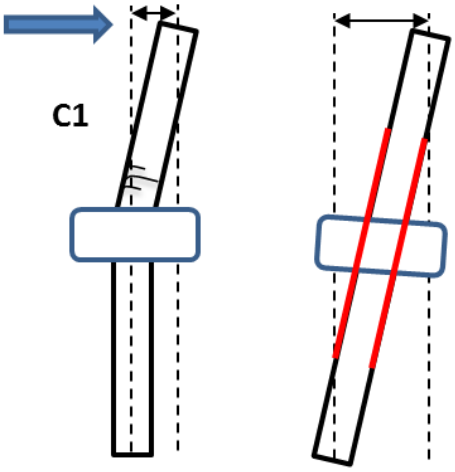 → Larger ultimate drift with failure in both columns
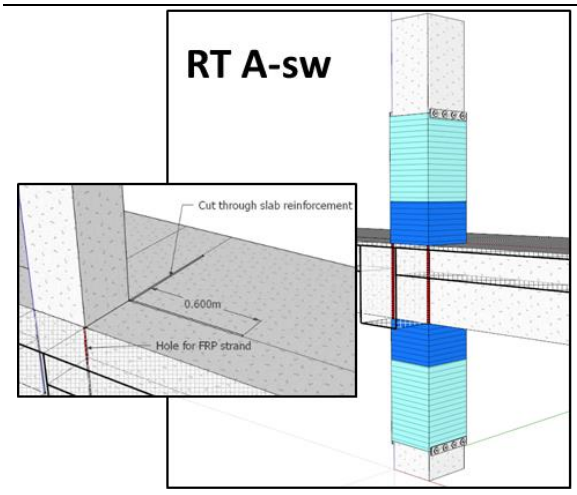 Strengthening of columns and selective weakening of slab	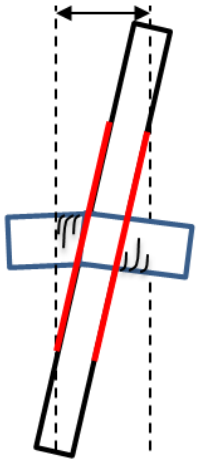 → Enhanced ductility with failure in beams, no strength enhancement
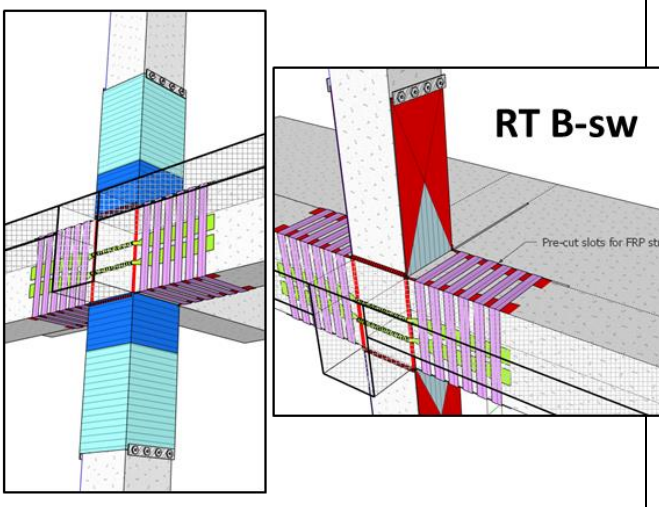 Strengthening of columns, beams and joint with selective weakening of slab	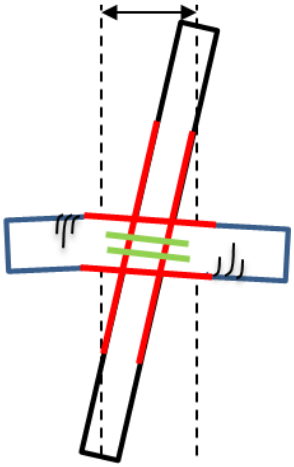 → Enhanced strength and ductility with failure in beams, plastic hinge forming away from the joint

Figure 3.33. Summary of three retrofit schemes and their performance objectives.

3.6.1. EVALUATION OF DESIGN MOMENT AND SHEAR CAPACITIES FOR STRENGTHENED MEMBERS

For the design of the three retrofit schemes presented in this work, the relative strength of the retrofitted members is evaluated using current guideline equations. The procedure followed is described in this sub-section.

For specimens strengthened with FRP, the Italian CNR-DT-200.R1/2013 (CNR, 2013) guidelines are deemed the most complete European guidelines, as shown in an initial study by Pohoryles and Rossetto (2014), which can be found listed in Appendix B. As for the control specimens, to evaluate the capacities, the factors of safety are set to unity and the material properties from material tests are used (Table 3.11).

Table 3.11. Material properties for the repaired and retrofitted beam-column joint specimens.

Specimen	f_{cm} (MPa)	f_{ccm} (MPa)
C0-RP-A-gs	27.6	30.0
C2-RP-A	31.5	34.4
C1-RT-A	23.8	25.5
C1-RP-A-sw	23.4	25.0
C1-RT-A-sw	22.0	23.3
C1-RT-B-sw	19.3	21.8
C-noSLT-RT-B	29.6	32.3

For the FRP strengthened column moment capacities, the method in Appendix E of the CNR guidelines is chosen, which gives the normalised moment capacity with respect to the normalised axial load. Equations 11.4 and 11.5 in the guidelines are equivalent to the equations behind the M-N interaction diagrams used for the EC2 design of the control specimens. Depending on the factors calculated in equations 11.6 and 11.7, the failure mode can be determined. Here differentiation is made between failure of concrete in compression (type 2), failure in tension, with FRP reaching its ultimate strain (governed by debonding rather than rupture), and yield of the steel bars (type 1a) or without yield of the steel bars (type 1b). The concrete strength for evaluating the FRP strengthened moment capacity is enhanced due to the confinement wraps. The increased confined concrete strength, f_{ccd}, equal to f_{ccm} is evaluated using equation 4.31 of CNR.

For the FRP strengthened beams, the equations in cl. 4.2.2 of the CNR guidelines are used. Just like the column design equations, the equations differentiate between three failure modes. The concrete failure mode is not critical in the design of the strengthened beams in C1-RT-B-sw and C-noSLT-RT-B.

The shear strength of FRP strengthened RC members, is evaluated according to equation 4.18 of the CNR guidelines. The total shear capacity is the sum of the steel contribution to the shear resistance, $V_{Rd,s}$, evaluated using the EC2 equation 6.8, and the FRP contribution to shear resistance, $V_{Rd,f}$, according to equation 4.19 of the CNR guidelines.

For all FRP retrofits, S&P C-240 CFRP sheet is used. The tensile strength is evaluated using characterisation tests performed according to the testing method in ISO/DIS 10406-2:2013. The parameters reported in Table 3.12 are $f_{u,FRP}$, $\varepsilon_{u,FRP}$, E_f and t_f, the ultimate strength, strain, elastic modulus and thickness of FRP, respectively.

Table 3.12. CFRP material properties.

Material	t_f (mm)	$f_{u,FRP}$ (MPa)	$\varepsilon_{u,FRP}$ (%)	E_f (GPa)
S&P C-240	0.223	3300	1.7	194.1

The relative bending and shear capacities of columns and beams for the retrofitted specimens are presented following the description of individual retrofit schemes.

3.6.2. DETAILED DESCRIPTION OF THE THREE RETROFIT SCHEMES

In this section, the detailed design of the three retrofit schemes (RT-A, RT-A-sw and RT-B-sw) compliant with current design recommendations (ACI, 2008b; CNR, 2013), is presented. The design of the retrofit schemes is based on observations from the literature (Pampanin and Akguzel, 2011; Shiohara et al., 2009), analysed in Chapter 2, and FE modelling, as well as recommendations in the latest draft of the ACI guidelines (ACI, 2014).

As the proposed experimental testing of the schemes is time-consuming and expensive, trial through numerical modelling is essential to reduce the risk of failed experiments, so as not to waste resources. In order to understand the influence of the different elements of the three retrofit schemes, FE models of the joints with FRP are presented with each retrofit scheme. Their outcomes are then used to identify a new retrofit objective for the design of the subsequent scheme. These FE models serve as a tool to investigate whether the theoretically assumed behaviour can be achieved and to understand the *relative* influence of the individual interventions. The models are using the same material models, element properties and model parameters as the models presented in Section 3.5. Again the full geometry and reinforcement detailing of the real test specimens are reproduced numerically. While serving a vital role in trialling the retrofit schemes, these models are however limited by the assumptions made in terms of loading arrangement, and material and bond models presented in Section 3.5. FE modelling can hence not substitute the need for empirical evidence to be gathered from the full-scale experiments.

3.6.2.1. REPAIR SCHEMES

As part of the design process for the retrofit schemes, the retrofits are first tested as repair schemes in the case of retrofits A and A-sw. For this reason, the control specimens C1 and C2 are repaired after having been tested to failure.

Next to serving as a test-bed for the retrofit schemes, their aim is also to investigate whether the heavily damaged specimens can be repaired and achieve similar performance as retrofitted specimens. As shown in Figure 3.34, the repair technique employed on specimens C1 and C2 consists of a two-step approach. The initial part of the repair of the damaged section is done following a tested procedure for RC columns (Rodrigues et al., n.d.). First, the buckled column bars are cut and the crushed concrete is removed from the damaged specimen. Then, new 250 mm long bars are welded onto the non-yielded ends of the existing bars and fresh high strength grout (ca. 40 MPa) is used to replace the removed concrete, according to current practice in Southern European countries (Garcia et al., 2012). After curing, the respective FRP retrofits, described in the following sections, are applied.

(a) (b)

Figure 3.34. Repair method: (a) Removal and replacement of damaged steel and concrete and (b) application of FRP retrofit.

3.6.2.2. RETROFIT A

The aim of scheme RT-A is to offer a simple and realistic solution to delay a brittle undesired column failure mechanism and increase the ductility of the specimen. Due to the presence of the slab and the geometry of the specimen, moving the failure mechanism to a flexural failure in the beam is a challenging task which is not the aim of this initial retrofit scheme.

3.6.2.2.1. DESCRIPTION OF RETROFIT A

To avoid the brittle failure mechanisms expected for the pre-1970's control specimens, it is deemed necessary to increase the shear capacity of the column, provide confinement to the column to avoid buckling of the column bars, as well as to increase the flexural capacity of the columns to delay a weak-column/strong-beam mechanism. In order to achieve adequate flexural

strengthening, it is of great importance to provide continuity in the vertical longitudinal FRP through the joint, as recommended by the latest draft ACI 440-F guidelines (ACI, 2014). This is a complex issue for interior joints with slab and has only been addressed by very few experimental campaigns (e.g. Shiohara et al. 2009).

By means of continuous strengthening, the columns above and below the joint are activated, which results in more symmetric behaviour of the two columns. This in turn leads to single-storey failure mechanisms to be avoided, as illustrated in Figure 3.33, enabling higher levels of drift to be achieved in a full structure. Another advantage of providing continuous flexural strengthening is a better development length and anchorage of the FRP sheets (Vrettos et al., 2013).

The main features of the retrofit for specimen C1-RT-A are shown in Figure 3.37. After surface preparation (roughening) of the concrete and rounding of the edges to a radius of 25 mm, a first layer of 250 mm wide CFRP sheet as column flexural strengthening is applied, extending 750 mm onto both columns. To provide continuity of the longitudinal column strengthening sheets through the joint, vertical FRP strands are used. These are inspired by previous efforts by Shiohara (2009), who used FRP anchor ropes at the corners of columns in beam-column joints. Rather than proprietary FRP anchors available in Japan, in this scheme 750 mm wide CFRP sheets, rolled into strands and glued together using epoxy are used (see Figure 3.35).

Figure 3.35. FRP “strand”: rolled FRP sheet passed through plastic tube.

As shown in Figure 3.36, the strands are passed through plastic tubes and then through holes in the slab at the corners of the columns and the ends are then splayed out and glued onto the columns to serve as fan-type anchors. They are then anchored on the inferior column by a steel plate and pre-stressed at the superior column.

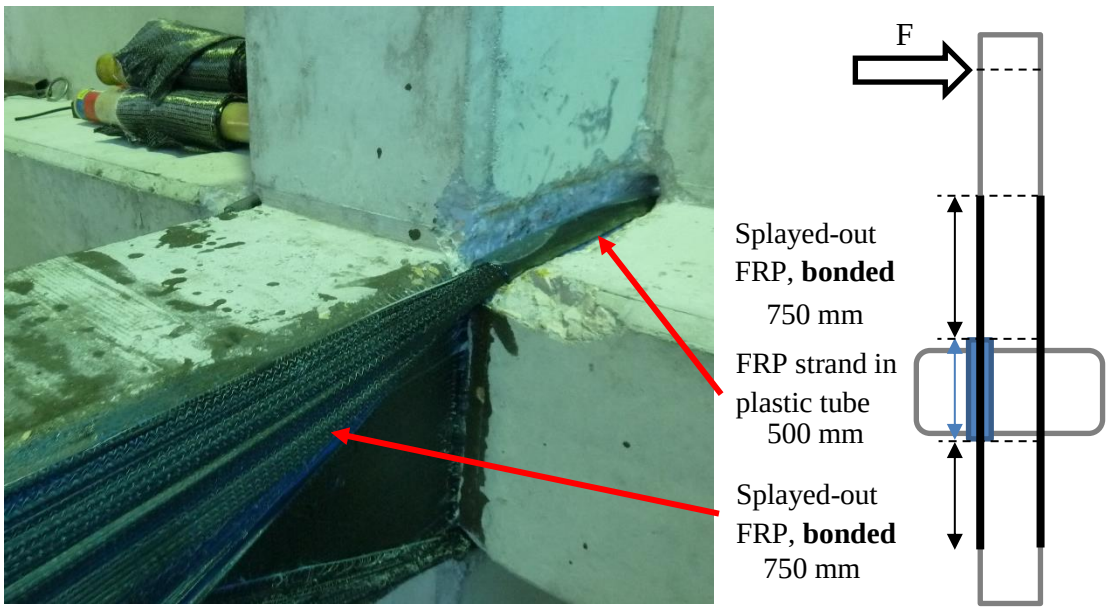

Figure 3.36. FRP strands passed through slab in tubes along joint region, and splayed-out onto column.

Following the evaluation process of moment and shear capacities for columns and beams in CNR-DT-200.R1/2013, the total equivalent amount of flexural strengthening required is evaluated as six layers of vertically applied CFRP sheet. As shown in Figure 3.37 (a), this is achieved by applying one layer of vertical FRP sheet on the concrete as base layer and two splayed-out FRP strands (six layers at an angle of about 10° from vertical axis). Next, as indicated in Figure 3.37 (b), horizontal column confinement wraps are applied to anchor the splayed-out strands, as well as to provide confinement and shear strengthening of the columns. Close to the joint, three layers of 250 mm wide confinement CFRP are applied. Further along the column, only two layers of 500 mm wide CFRP wrap are required. The expected moment and shear strengths of columns and beams for the specimens repaired (C2-RP-A) and retrofitted (C1-RT-A) with scheme RT-A are summarised in Table 3.14.

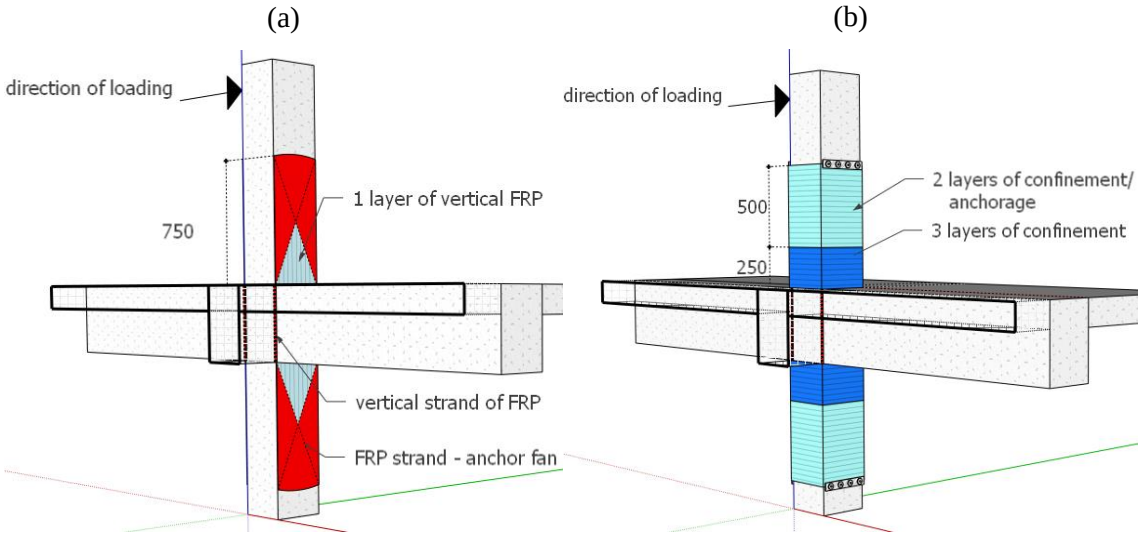

Figure 3.37. Dimensions of retrofit RT-A: (a) FRP strands; (b) FRP confinement wraps.

3.6.2.2.2. FE-MODEL

To understand the effect of retrofit RT-A, a full model including all features described above is created, as shown in Figure 3.38. To model the vertical FRP strands, unidirectional truss elements, with the same cross-sectional area as the applied sheets, are used.

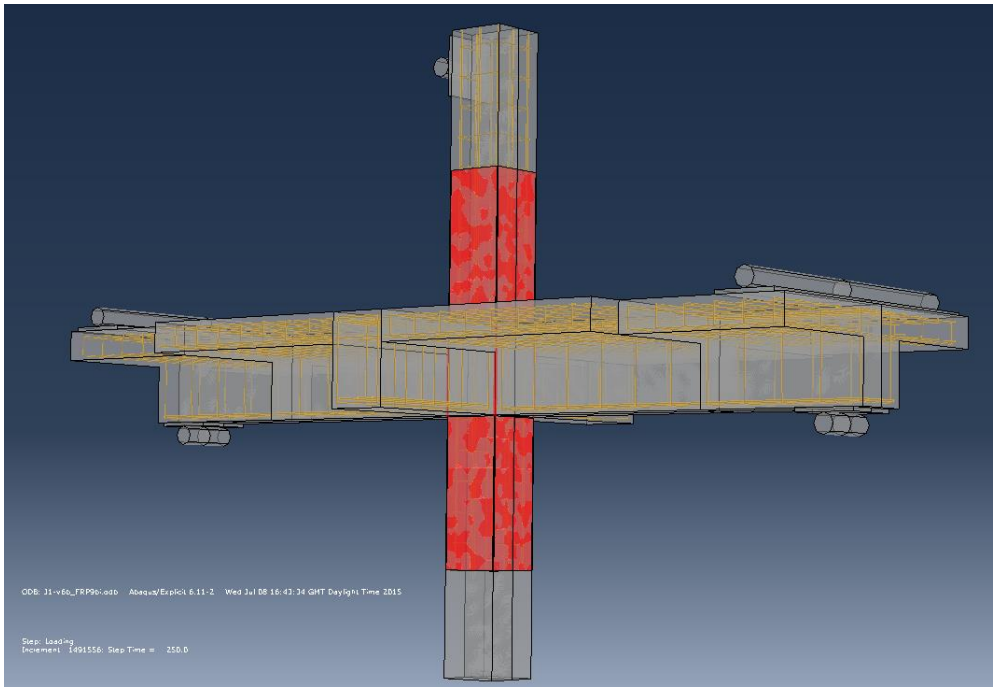

Figure 3.38. ABAQUS models of FRP retrofitted joint – FRP indicated in red.

As shown in Figure 3.39, the load capacity of the strengthened joint increases to 85 kN, corresponding to an increase of 10.3% compared to the control specimen. This increase is due to the enhanced column confinement and flexural capacity.

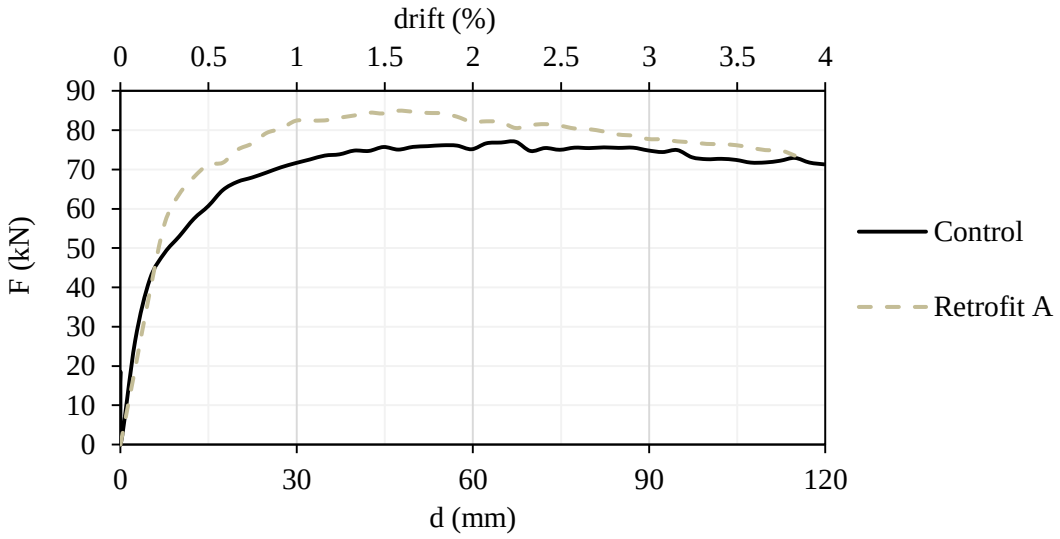

Figure 3.39. Force-displacement plot for the FE model of RT-A and the control specimen.

Damage is observed on the top of the slab, at the interface to the column (Figure 3.40 (a)), as well as at the bottom of the beam and transverse beam, at the interface to the joint (Figure 3.40 (b)).

Yielding of bars is observed mainly in the first shear links from the joint interface in all beams, as well as in the bottom beam bars at the joint interface.

(a) (b)

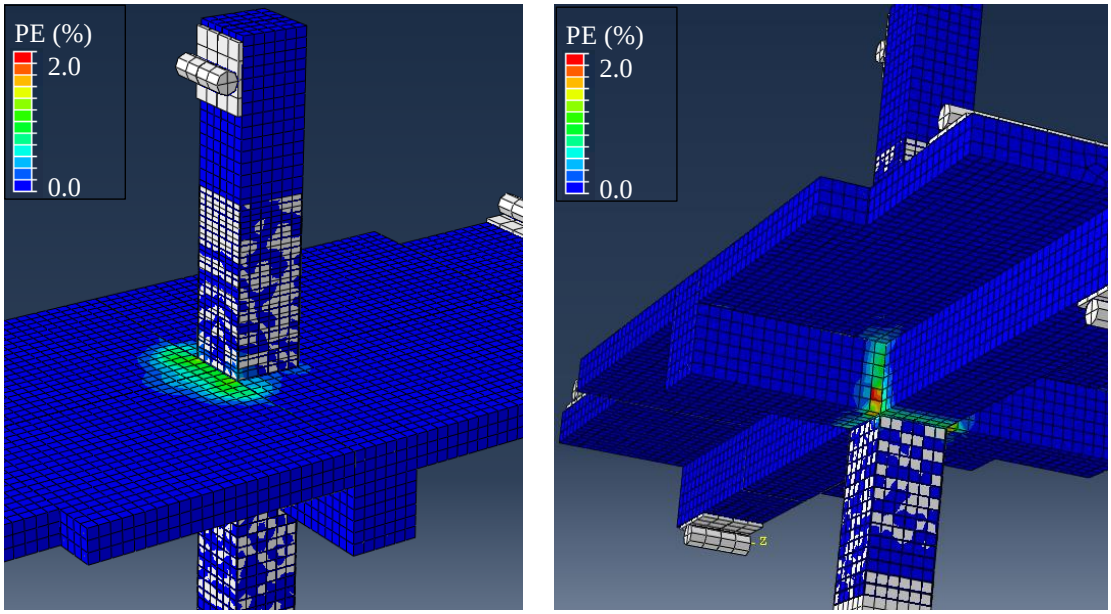

Figure 3.40. Damage in specimen RT-A: (a) top of slab; (b) bottom and transverse beam.

It can be observed from Figure 3.41, that the beam bottom bars yield at the interface to the joint, which corresponds to an improvement compared to the model of the control specimen. Yielding of the longitudinal column bars is however also observed at the column/joint interface, despite the FRP strengthening.

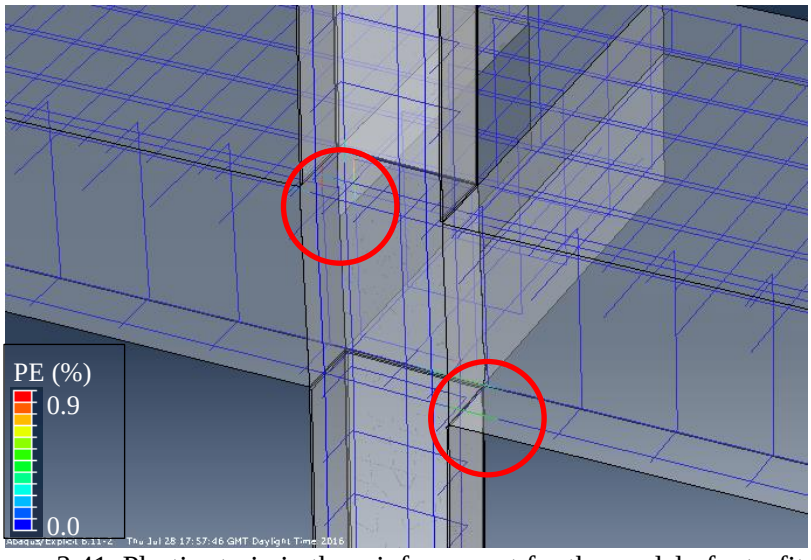

Figure 3.41. Plastic strain in the reinforcement for the model of retrofit A.

Overall the retrofit intervention on columns only (RT-A) presented in this section, seems to achieve its target of improving the column behaviour, eliminating the buckling of column bars and increasing the moment capacity. Higher rotation of the beams is also observed, leading to yield of the beam bars. Still the ultimate failure of the specimen is governed by the column, with the highest steel strain still observed in the column/joint interface.

3.6.2.3. REPAIR A-GS

This strengthening scheme is not a scheme of its own, but used as a validation test for the proposed retrofit scheme with strands passed through a plastic tube between the two columns. C0, a pre-damaged specimen with similar properties to C1, is repaired with retrofit scheme RP-A-gs (glued strands). This repair scheme is similar in application to retrofit A, but the FRP strands are bonded to the concrete along their entire length instead of being passed through a plastic tube for the length of the joint between the two columns.

3.6.2.4. RETROFIT A-SW

The second scheme (RT-A-sw) aims to improve the displacement ductility of the specimen. This is done by selectively weakening the slab in addition to strengthening the column as in RT-A, so as to ensure a ductile beam failure mechanism that follows capacity design principles. RT-A-sw hence aims to prevent the column-hinging mechanism observed for retrofit A in the FE models of Section 3.6.2.2.2. By reducing the strong contribution of the slab observed in the FE models in Section 3.5, a more symmetric rotation of the beams is expected, reducing demand on the columns. The addition of selective-weakening to the retrofit scheme is inspired by previous research (Akguzel and Pampanin, 2012a).

3.6.2.4.1. DESCRIPTION OF RETROFIT

For retrofit RT-A-sw, first, the slab concrete and reinforcement are cut along a length of 600 mm (two column depths) using a circular saw (Figure 3.42 (a)). After surface preparation (roughening) of the concrete and rounding of the edges to a radius of 25 mm, the same procedure as for retrofit RT-A is followed, as shown in Figure 3.42(b). However, only 4 layers of flexural strengthening are used in RT-A-sw (two 500 mm wide sheets) due to the weakening of the slab. The expected moment and shear strengths of columns and beams for the specimens repaired (C1-RP-A-sw) and retrofitted (C1-RT-A-sw) with scheme RT-A-sw are summarised in Table 3.14.

(a) (b)

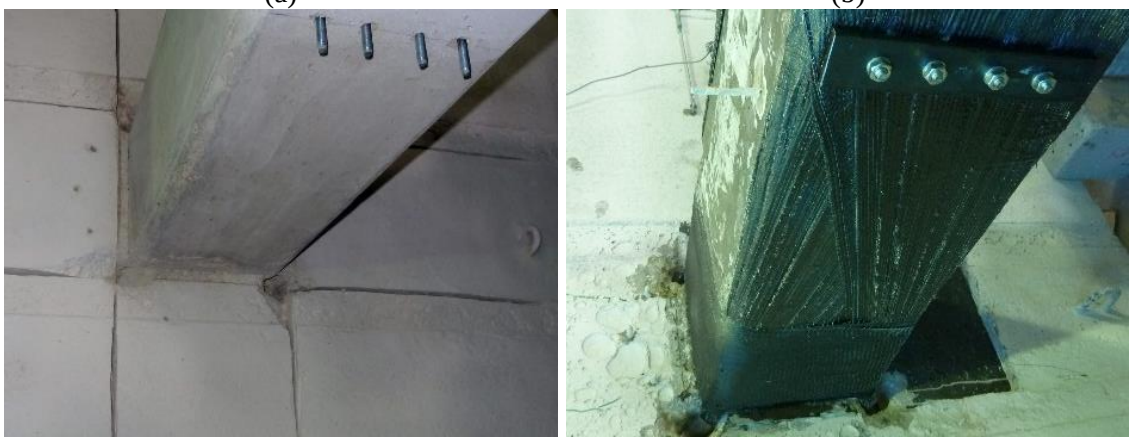

Figure 3.42. (a) Weakening cuts; (b) Applied FRP strands, anchors and layer of confinement.

3.6.2.4.2. FE-MODEL

For the design of retrofit A-sw, aiming to change the hierarchy of strengths, it is of critical importance to understand the behaviour of the beam and slab. For this purpose, as highlighted in Figure 3.43, the beam and slab *only* are modelled to look at the effect of selective weakening. This allows for a shorter computational time and a concentration on the behaviour of the beam.

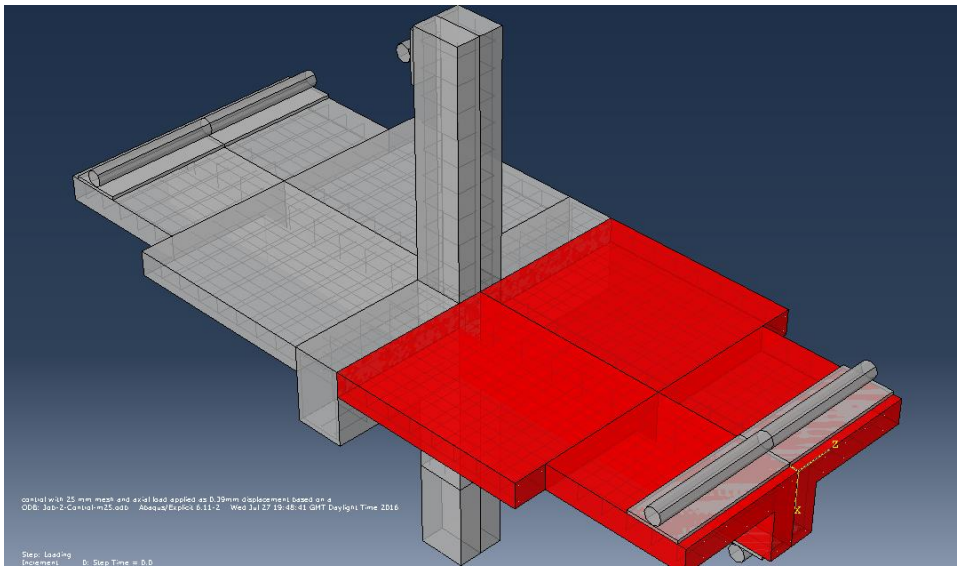

Figure 3.43. Parts of full specimen modelled for the beam and slab only model (shown in red).

For all slab and beam models, loading is applied via displacement control at 1.85 m from the fixed end (i.e. from the column), at the location of the beam supports in the full beam-column joint specimen. To investigate the behaviour of the beams, one full cycle of positive and negative displacement of 40 mm is applied at a loading rate of 0.1 mm/s. This is chosen to reach the maximum beam sagging moment and then the maximum beam hogging moment.

The selective weakening of the slab is applied by selectively removing the *fixed* boundary condition along the selective weakening cuts, as shown in Figure 3.44. Simulating the interface as *fixed* is a simplification that clearly does not hold true as cracks appear at the beam/column or slab/transverse beam interface. As mentioned previously, the FE models are only used as a tool to guide and verify the design of the retrofit strategy before expensive full-scale testing.

(a) (b)

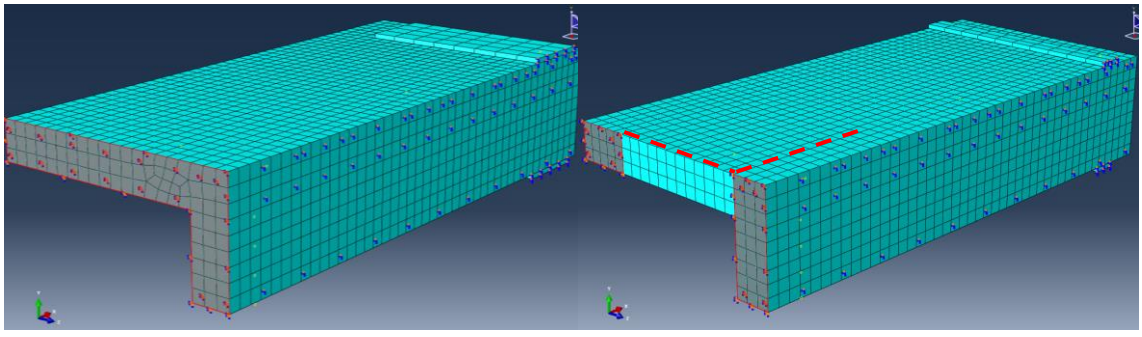

Figure 3.44. Fixed boundary condition at simulated slab-column interface for (a) non-weakened and (b) selectively-weakened specimen - red dotted line indicates selective weakening.

Two models are compared, one with and one without selective weakening of the slab. The first assessed model corresponds to the beam and slab of the control specimen, i.e. without weakening. Under positive loads, two cracks at the bottom beam face can be observed (Figure 3.45), within close proximity to the beam/joint interface. Some damage is also observed in the bottom face of the slab, with two slab bars reaching yield in sagging, as shown in Figure 3.46. The bottom beam bars are fully yielded within a localised plastic hinge length of about 100 mm.

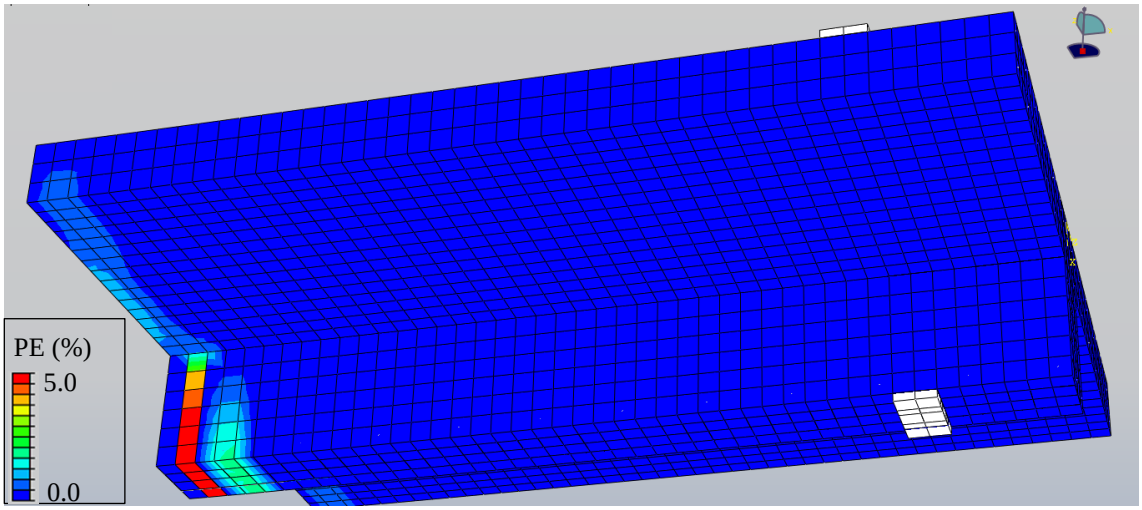

Figure 3.45. Plastic strain (cracks) for control specimen at maximum beam sagging moment.

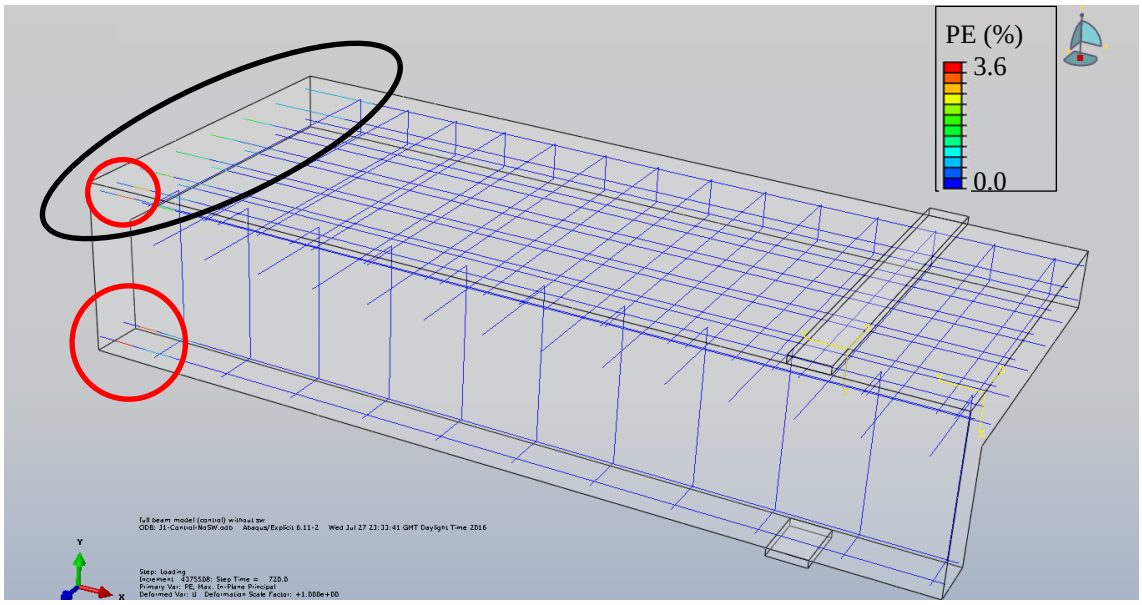

Figure 3.46. Plastic strain in steel reinforcement after maximum beam sagging and hogging moment in model of selective weakening (cut through centre line of beam). Yield in the beam bars indicated by red circle under sagging and by a black circle under hogging.

The results after the negative load cycle provide clear evidence for the strong slab contribution to the beam behaviour in hogging. As expected from EC8, the bars within the effective width of the t-section (4 h_f) contribute fully to the hogging moment capacity (Figure 3.46). This contribution of slab bars decreases with distance from the beam. However, it appears that the two bars outside the effective width also reach yield strain, albeit only at the final stages of the loading cycle. This

picture is completed by the cracking patterns in Figure 3.47, with a crack obtained all along the slab/transverse beam interface as well as multiple parallel cracks along the length of the slab.

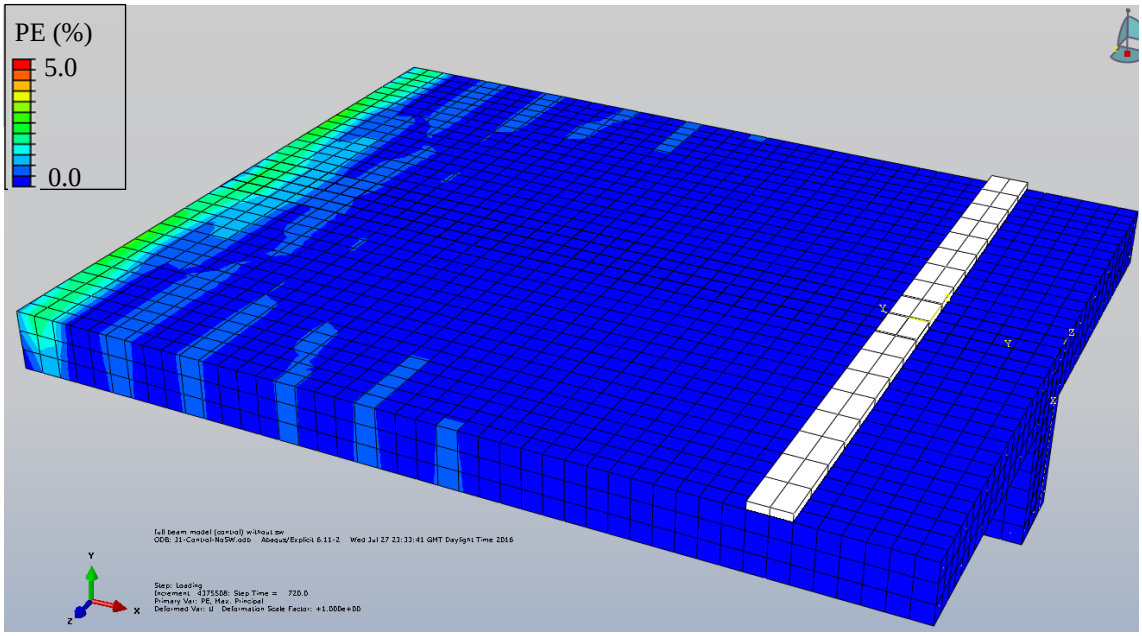

Figure 3.47. Plastic strain, indicating cracks and damage, in the top of the beam and slab after maximum applied hogging moment.

Next, the model of the beam with selectively weakened slab for specimen C1-RT-A-sw is assessed. As expected, and desired, the moment capacity of the specimen is reduced significantly by the weakening cuts. In hogging, a reduction of 34% of applied maximum load is obtained, while in sagging a reduction of 20% is indicative of the contribution of the slab in both loading directions. In terms of damage, with weakening, a large crack at the joint-beam interface is observed under sagging moment, with some minor damage also observed at the slab ends (Figure 3.48). The latter indicates that the slab also contributes slightly in sagging.

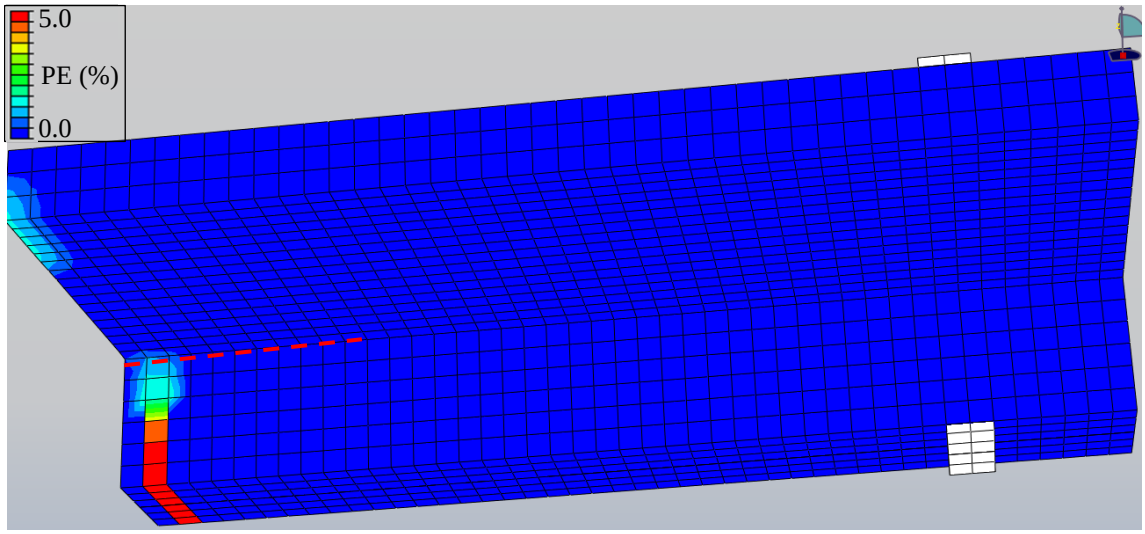

Figure 3.48. Plastic strain (i.e. cracks) in beam for selective weakening specimen at maximum beam sagging moment (red dotted line indicates extend of selective weakening).

Figure 3.49 indicates the plastic strain distribution in the beam and slab reinforcement after the full cycle of maximum sagging and hogging moment. It can be seen that yielding of the

reinforcement is only observed at the beam/joint interface, as well as at the four rebars in the non-weakened slab ends, with the rest of the beam remaining elastic. Similar observations can be made for plastic strain in the concrete.

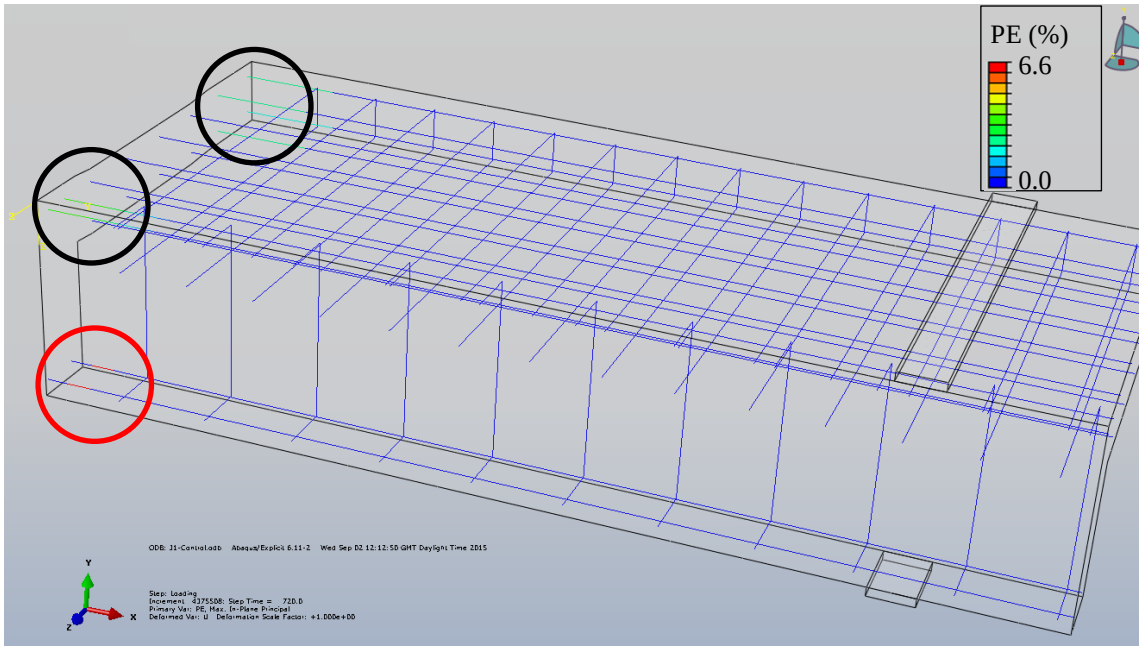

Figure 3.49. Plastic strain in steel reinforcement after applied maximum beam sagging and hogging moment in model of selective weakening (cut through centre line of beam). Yield in the beam bars indicated by red circle under sagging and by a black circle under hogging.

Overall, for both, the control and selectively weakened beams, a localised damage mechanism, with a plastic hinge right at the beam/joint interface is thus expected. Without weakening, the entire width of the slab contributes to the behaviour of the beam in hogging, leading to a considerable hogging moment capacity. The model with selective weakening shows its potential in reducing the contribution from the slab reinforcement. Only the four non-cut slab bars at either end contribute in hogging, which leads to a significant reduction in hogging moment capacity for the weakened beam and yield being observed in both, the top and bottom beam reinforcement.

3.6.2.5. RETROFIT B-SW

The objective of retrofit scheme B-sw is to achieve a similar performance to a structure designed to modern guidelines (C-EC8). In particular, the retrofit aims to increase the strength of the sub-assembly to reach a level close to 80% of C-EC8. To achieve greater energy dissipation and ductility, promoting the formation of a beam-sway mechanism with a plastic hinge (PH) forming in the beams, at one beam-depth (450 mm) from the beam-joint interface is proposed. This PH relocation distance is based on previous work by Eslami and Ronagh (2014).

3.6.2.5.1. DESCRIPTION OF RETROFIT

Following the design philosophy in Eurocode 8, FRP flexural strengthening of columns, as well as confinement and shear strengthening are applied to attain a strong-column/weak-beam

mechanism. As in retrofit A, to achieve continuous flexural strengthening through the slab and joint, vertical FRP strands are used to connect the bottom and superior column retrofit.

For the beams, the results from the FE-models for the control and selectively weakened specimens (Section 3.6.2.4.2) suggest that failure in the beams would occur near the joint for RT-A-sw. To enhance ductility and energy dissipation in RT-B-sw, PH relocation one beam-depth away from the joint interface is hence proposed. As illustrated in Figure 3.50, to achieve this, next to FRP strengthening, selective weakening of the slab is performed by means of cutting the slab reinforcement along 600 mm. The retrofit and weakening of the beam are designed according to the equations proposed in Appendix F, so as to achieve a weak section in zone (2) of Figure 3.50, in which the plastic hinge (indicated by PH) is anticipated. As shown by the three moment diagrams, the moment capacity in this section (2) is designed to be low enough to reach yield at this location before the beam/joint interface and the column/joint interface, hence preventing yield penetration into the joint core.

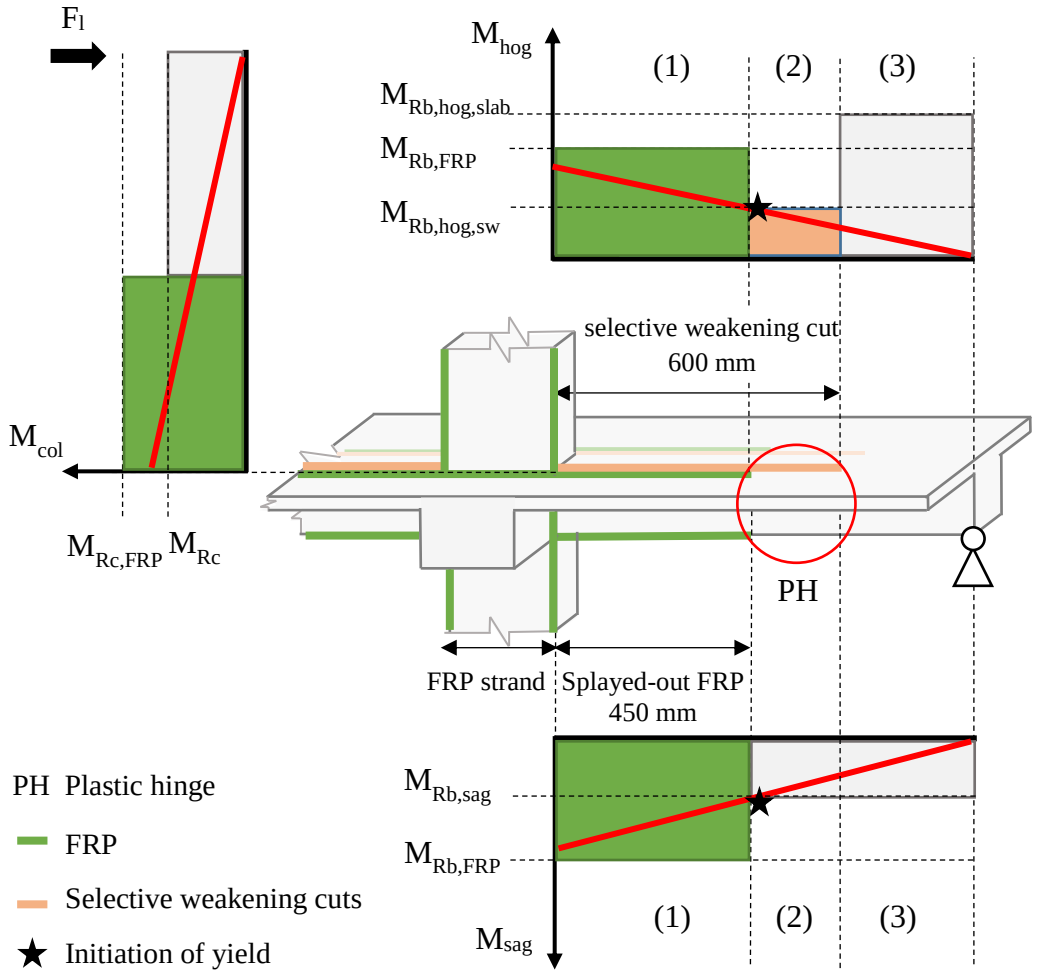

Figure 3.50. Conceptual design of Retrofit B-sw with moment diagrams for hogging (M_{hog}) and sagging (M_{sag}) with indication of the non-retrofitted capacities (M_{Rb}), with ($M_{Rb,slab}$) and without slab contribution ($M_{Rb,sw}$), as well as the retrofitted capacity ($M_{Rb,FRP}$).

To design the retrofit of the beams for PH relocation, existing equations for beam flexural strengthening in the CNR guidelines are used (cl. 4.2.2). These are however devised for rectangular sheets or laminates, and not for FRP strands used here. The strands are glued in the joint region and then splayed-out to the beam face, and for design an equivalent thickness and width of FRP with the same cross-sectional area as the FRP sheets is determined (Figure 3.51).

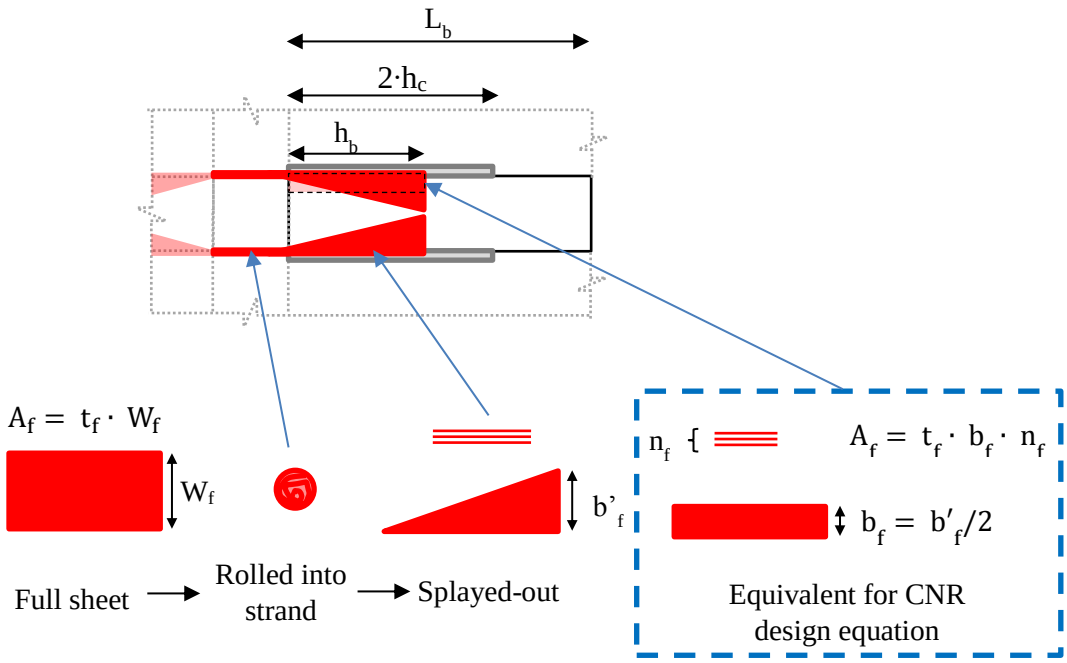

Figure 3.51. Equivalent width and thickness of FRP for beam strengthening.

The full design procedure suggested for retrofit B-sw is detailed in Appendix F and the step-wise application process is summarised in Figure 3.53. First, the relative strength of the retrofitted members is evaluated using current guideline equations in order to ensure the capacity of the retrofitted columns is higher than that of the beams in the desired plastic hinge zone by a factor greater than 1.3 (1.66 in this case). From this evaluation, summarised in Table 3.14, a total of six layers of vertical FRP over a length of 750 mm and three layers of horizontal wrapping are required for the columns to achieve their target strength.

Looking at Figure 3.53, as in retrofit A-sw, selective weakening cuts are first applied in the slab (Step 1). The vertical FRP is then applied, starting with a base layer (Step 2) and FRP strands to connect both columns (Step 3&4). The strands are mechanically anchored using steel anchors. Confinement and shear strengthening is applied as horizontal FRP wraps in Step 5.

The dimensions for the applied FRP in the beams and joint are shown in Figure 3.52. In Step 6, two 100 mm wide strips are applied as FRP strands at the top and bottom faces of the beams, through the joint area and along a length of 450 mm (zone 1) for PH relocation to zone 2. The continuous strengthening through the joint area also provides the required anchorage to develop PH relocation capability, similar to the anchorage grooves used by Eslami and Ronagh (2014).

The transverse strengthening of the beams (Step 7) consists of 50 mm wide strips spaced at 75 mm and is applied as full wraps through holes in the slabs.

Finally, as the specimen is designed to pre-seismic design codes, the joint shear capacity is very low. Strengthening of the joint is hence provided by means of horizontal FRP strands through its core. This consists of two 150 mm wide strips rolled-up and passed through holes at the transverse beam/joint interface (shown as part of Step 6). While many joint shear strengthening schemes with horizontal (e.g.: Ghobarah and Said, 2002) or X-wrapping (e.g.: Pantelides et al., 2008) have been tested in the literature, none have considered the presence of transverse beams explicitly. To the best knowledge of the author, this constitutes the first effort of joint shear strengthening in interior joints through transverse beams. These strands are then splayed out and extended for 300 mm onto the beams for anchorage. The joint FRP strands are not passed through plastic tubes and are hence bonded to the concrete as they are passed through the pre-drilled holes. All FRP sheets are additionally anchored using bolted steel plates to avoid end-debonding.

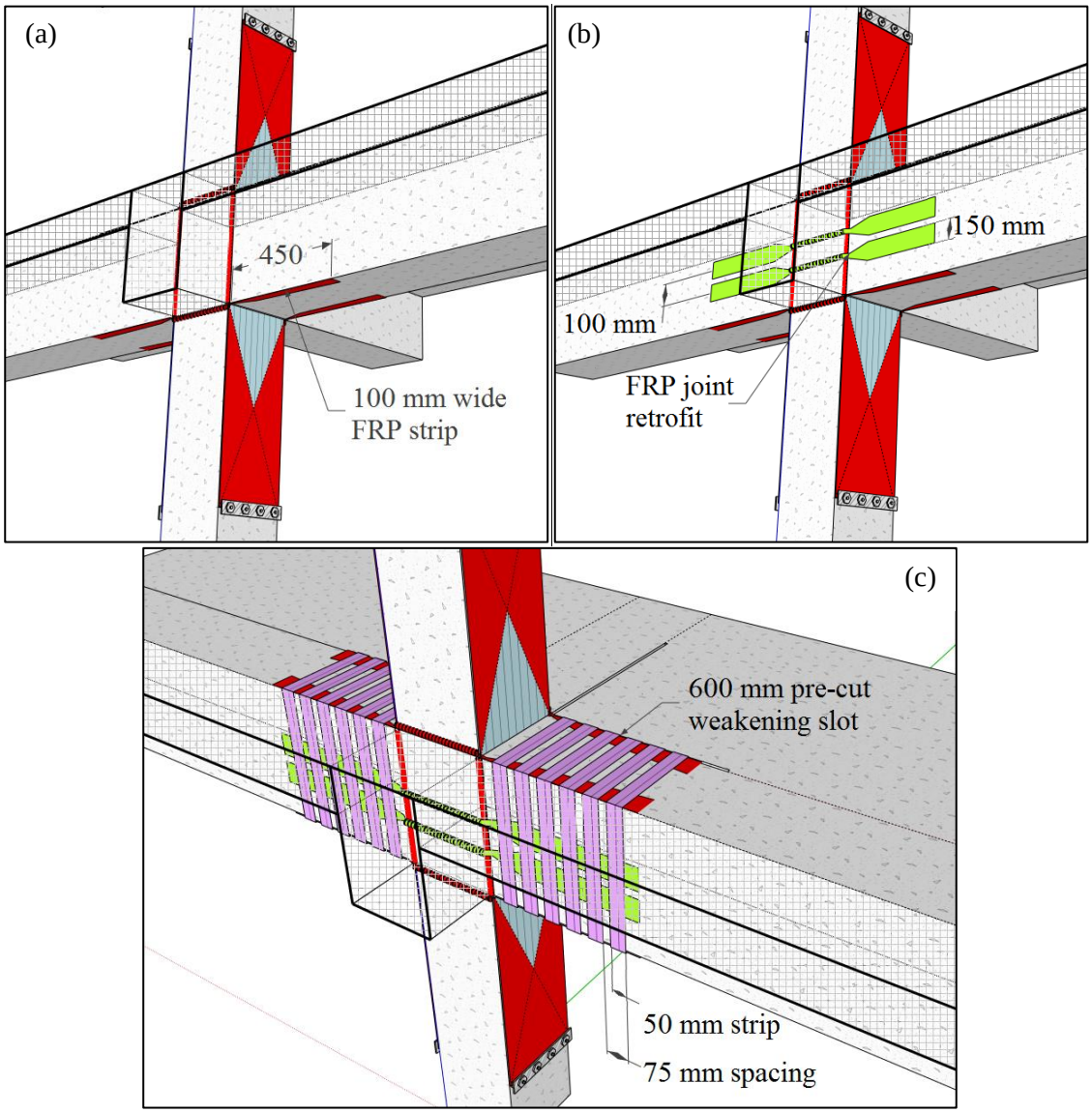

Figure 3.52. Dimensions of retrofit RT-B-sw: (a) Beam strands; (b) Joint strands; (c) Beam transverse strips.

Schematic of retrofit RT-B-sw

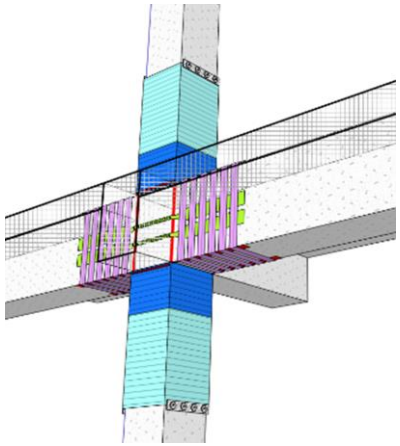

Step 1: Selective weakening cuts and holes for FRP strands

Step 2: Application of a base layer of FRP on the column

Steps 3 & 4: Application of FRP strands through slab, splayed out onto columns

Step 5: Column confinement and shear strengthening

Step 6: Strengthening of beams and joint with FRP strands

Step 7: Application of strips of FRP for shear strengthening and anchorage in beams; additional anchorage with bolted steel plates

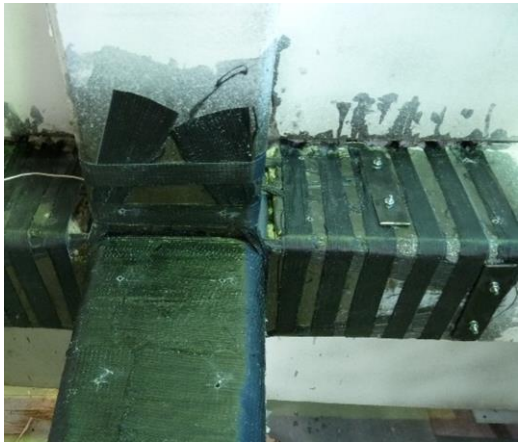

Figure 3.53. Step-wise retrofit of specimen C1-RT-B-sw.

3.6.2.5.2. FE-MODEL

The model of the beam with retrofit B-sw is shown in Figure 3.54. The selective weakening is again applied by excluding the cut part of the slab from the *fixed* boundary condition (see Section 3.6.2.4.2). The FRP is modelled as previously shown in section 3.5.3 for the small-scale beam, using shell elements with tied constraints (no debonding) and with the FRP strip dimensions from the retrofit B-sw design (100 mm wide by 450 mm long).

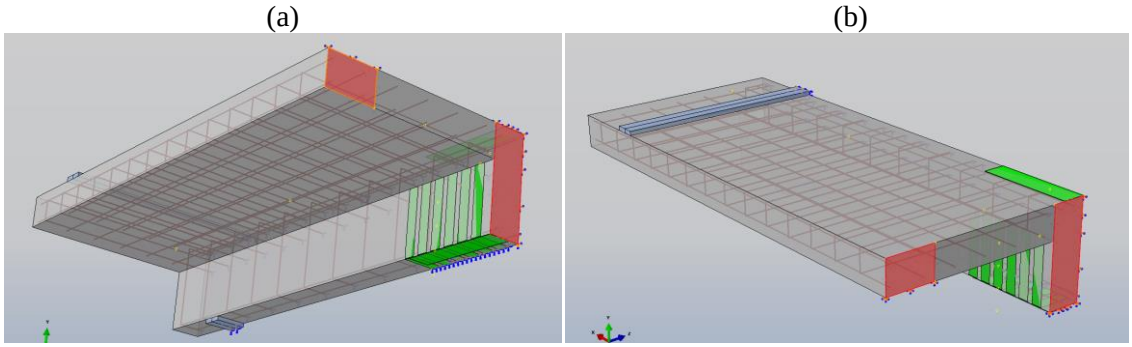

Figure 3.54. (a) Bottom and (b) top view of the retrofit B-sw beam model with weakened boundary conditions highlighted in red and FFRP strips in green.

Compared to the two previous models for the control specimen and retrofit RT-A-sw (Section 3.6.2.4.2), very different results are obtained for retrofit B-sw. Under sagging moment, as shown in Figure 3.55, a large crack (indicated by high plastic strain) is observed about 500 mm from the joint interface, i.e. in the desired plastic hinge location. This is followed by cracks in the beam/joint interface and further cracks in between. Some damage is also observed at the slab ends, indicating that the slab also contributes slightly in sagging.

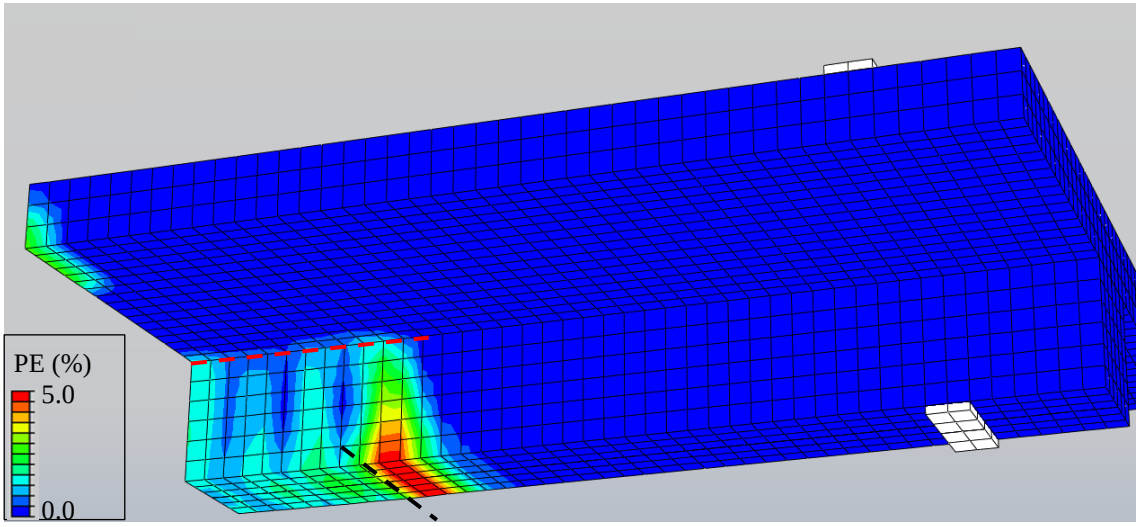

Figure 3.55. Plastic strain (i.e. cracks) in beam at maximum beam sagging moment (black dotted line indicates end of FRP; red dotted line indicates extend of selective weakening).

The observed location of cracking is coinciding with the observation of plastic strain in the rebars in Figure 3.56. It can be seen that yielding of the beam bars initiates in the desired plastic hinge zone, about 500 mm away from the joint interface, hence just after the end of the FRP strips, followed by yielding at the joint/beam interface.

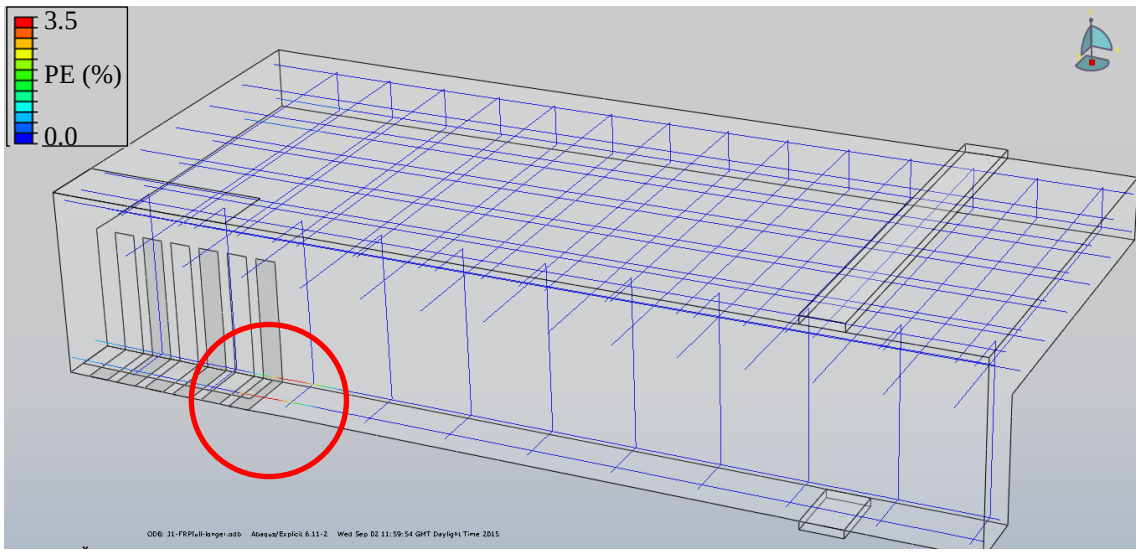

Figure 3.56. Plastic strain in steel reinforcement at maximum beam sagging moment in model of retrofit B-sw (cut through centre line of beam). Yield in the beam bars indicated by red circle.

After the sagging and hogging moment cycle, as shown in Figure 3.57, significant damage is additionally observed at the slab ends (i.e. where the slab is not weakened). Less significant damage is observed at the top of the beam, adjacent to the FRP strip. Similarly, yield of the four non-cut slab bars at either end of the slab is observed (Figure 3.58). Plastic strain in the steel reinforcement at beam/joint interface, as well as in the desired plastic hinge zone. Here, the plastic hinge length is much longer than for the previous specimens, with a spread of yield along a length of 400 mm.

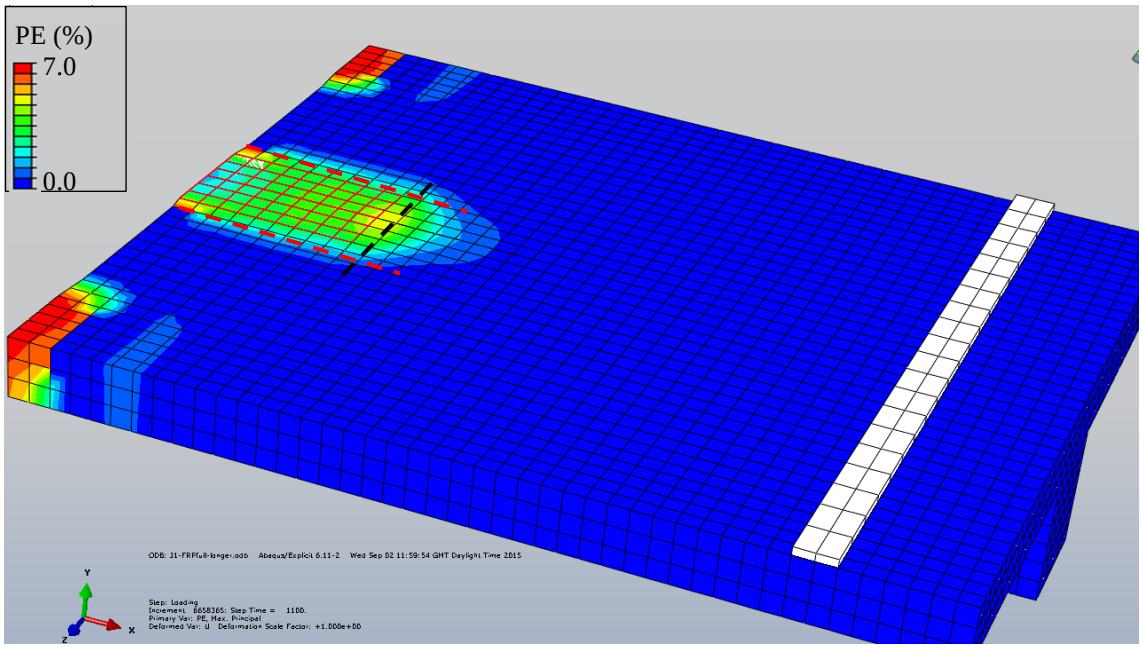

Figure 3.57. Plastic strain, indicating cracks and damage, in the top of the beam and slab after maximum applied hogging moment (black dotted line indicates end of FRP; red dotted line indicates extend of selective weakening).

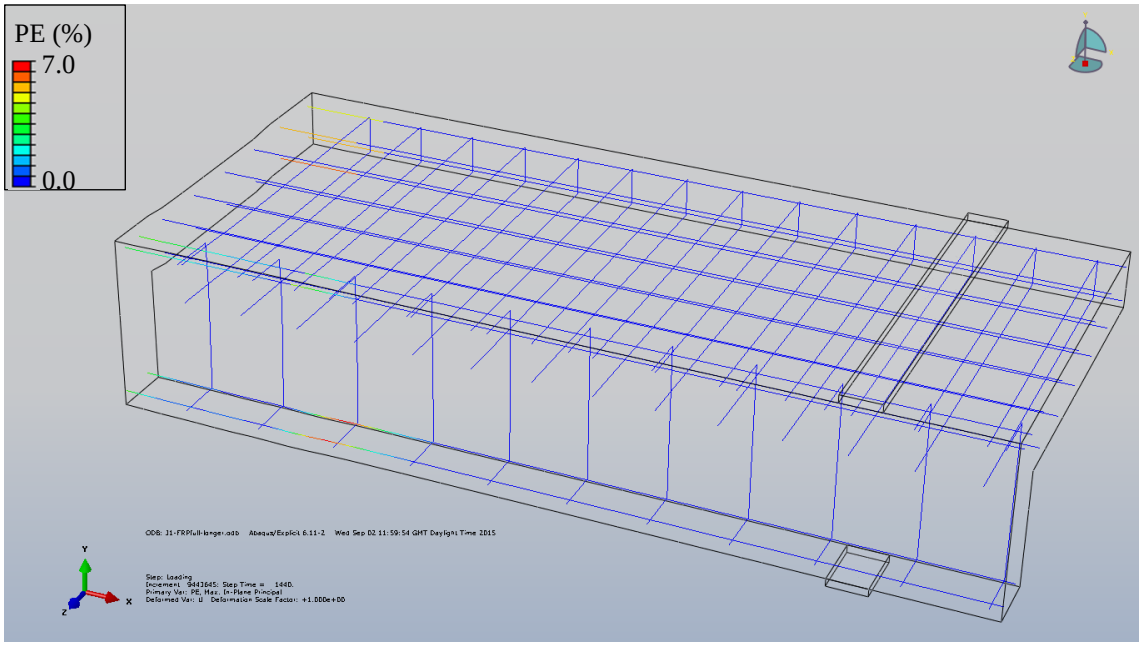

Figure 3.58. Total plastic deformations in steel reinforcement after maximum positive (beam sagging) and negative (beam hogging) load cycles (cut through centre line of beam).

To assess the influence of selective weakening (sw), as well as combined slab weakening and beam strengthening (FRP + sw), the moment-deflection graphs for the three FE models are compared in Figure 3.59. The main results in terms of maximum sagging and hogging moments at the beam/joint interface are summarised in Table 3.13.

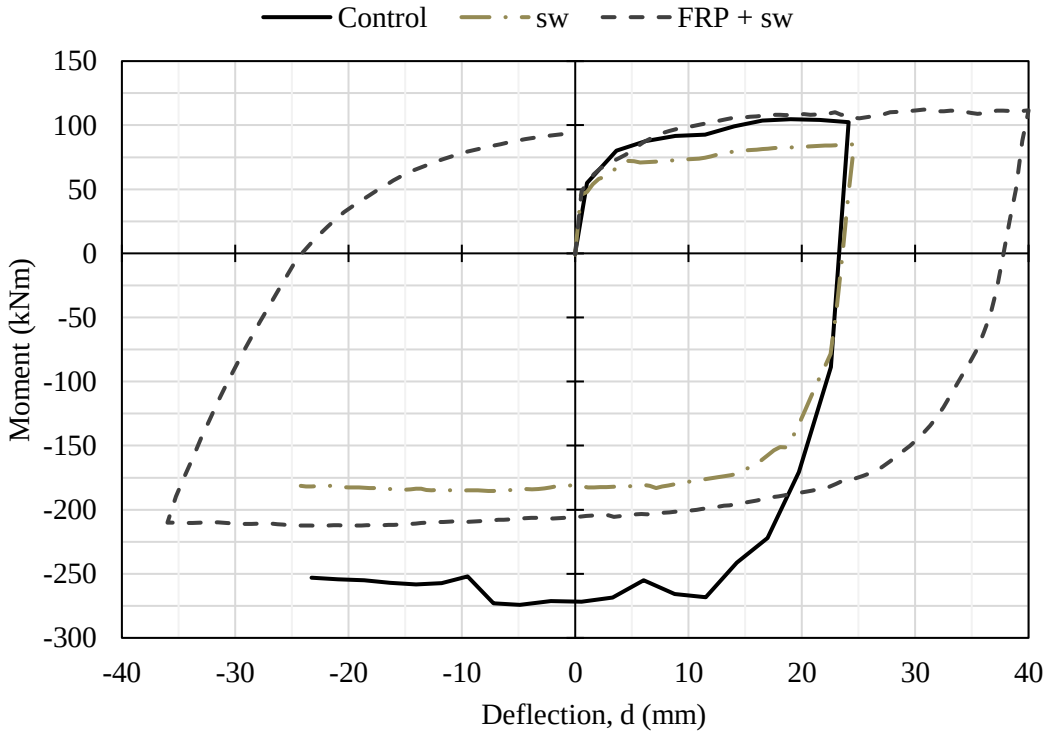

Figure 3.59. Moment-deflection curves for the three beam and slab models.

It can be observed that the control specimen presents the highest hogging and sagging moment capacities. The influence of selective weakening on the hogging moment capacity is significant, with a drop of 34% in capacity as the contribution of slab bars in tension is reduced. However,

the sagging moment capacity is also reduced by 20%. For the retrofit and weakening specimen, the aim of reducing the hogging moment capacity (-24%) while increasing the sagging moment capacity (+6%) at the beam/joint interface is achieved. In sagging, the influence of selective weakening is hence overcome by the FRP retrofit.

Table 3.13. Comparison of ultimate moments reached in beams for the three FE models (difference to control in parentheses).

	$M_{b,hog}$ (kNm)	$M_{b,sag}$ (kNm)
Control	-278.8	105.9
RT-A-sw	-185.37 (-34%)	85.05 (-20%)
RT-B-sw	-212.5 (-24%)	112.2 (+6%)

According to the results from FE modelling of retrofit B-sw, the plastic hinge can be successfully moved to the desired location, with yield and cracking initiating after the end of the applied FRP. An improved dissipative mechanism is observed for this specimen, with damage spread along the first 600 mm of the beams. After plastic hinge formation in the desired location, cracks and yielding of the bars are still observed at the beam/joint interface. This justifies the requirement for joint shear strengthening in retrofit B-sw to ensure the joint core is adequately protected.

3.6.2.1. RETROFIT B

The same retrofit scheme as RT-B-sw is also applied as a repair to specimen C-noSLT in order to evaluate the relative effectiveness of retrofit schemes for specimens with and without slabs and transverse beams. The same procedure is used for the retrofit shown in Figure 3.60.

Figure 3.60. Repair B of specimen C-noSLT.

3.6.3. EVALUATION OF DESIGN MOMENT AND SHEAR CAPACITIES

The expected moment and shear capacities for the FRP retrofitted joints calculated according to the CNR guidelines (retrofitted members) and Eurocode 2 (non-retrofitted members) are summarised in Table 3.14.

Table 3.14. Summary of calculated bending and shear capacities for the retrofitted specimens (equivalent applied lateral load in kN indicated in parentheses).

	C0-RP-A-gs	C2-RP-A	C1-RT-A	C1-RP-A-sw	C1-RT-A-sw	C1-RT-B-sw	C1-RT-B-sw (PH)	C-noSLT-RT-B
$M_{b,hog}$ (kNm)	-149.8 (91.3)	-149.8 (91.3)	-149.8 (91.3)	-114.5 (65.9)	-114.5 (65.9)	-138.1 (82.9)	-114.5 (65.9)	-125.2 (73.6)
$M_{b,sag}$ (kNm)	61.8 (61.2)	82.4 (76.1)	61.7 (61.1)	60.8 (60.5)	60.6 (60.3)	88.8 (80.7)	60.2 (60.1)	91.1 (82.4)
M_c (kNm)	146.6 (115)	153.1 (120.1)	147.4 (115.6)	144.6 (113.4)	142.8 (112)	144.8 (113.6)	144.8 (113.6)	148.6 (116.5)
ΣM_c / ΣM_b	1.39	1.32	1.39	1.65	1.63	1.28	1.66	1.37
$V_{Rd,s,b}$ (kN)	250.4 (317.2)	250.4 (317.2)	250.4 (317.2)	250.4 (317.2)	250.4 (317.2)	358.3 (461.1)	358.3 (461.1)	384.4 (495.9)
$V_{Rd,s,c}$ (kN)	311.1 (311.1)	323.6 (323.6)	297.7 (297.7)	296.2 (296.2)	290.8 (290.8)	279.5 (279.5)	279.5 (279.5)	317.7 (317.7)
V_j (kN)	808.7 (105.5)	929.7 (121.3)	685.5 (89.4)	672.1 (87.7)	625 (81.5)	607.7 (79.3)	607.7 (79.3)	947.4 (123.6)

3.7. SUMMARY

A detailed analysis of the literature in Chapter 2 has highlighted a number of gaps in the literature, notably the lack of tests on specimens with realistic size and geometry, which are to be addressed by an experimental study. To answer the specific aims of this thesis, a programme of fourteen full-scale tests is devised. The set of tests comprises specimens with and without slab and transverse beams, which are designed to pre-1970's guidelines, as well as Eurocode 8 for comparison. To conduct the experiments on full-scale specimens, a new experimental test set-up and adequate monitoring scheme is devised, including realistic loading and boundary conditions that are often not considered in the literature.

The design of experiments presented herein is justified by numerical testing to gain deeper understanding of potential design deficiencies of the realistic pre-1970's specimens. The FE models are calibrated on experimental results of previously tested RC beams.

Based on results from the numerical modelling of the control specimens, different retrofit objectives are defined. Three retrofit schemes with increasing complexity are developed in this study and are designed to address different objectives, as shown in Figure 3.33. The proposed retrofit schemes are compliant with current design recommendations (CNR, 2013) and the relative capacities of the strengthened members are evaluated by their design equations. The design methodology for the retrofit schemes again involves FE modelling to improve the confidence in the schemes before testing. The expected failure mechanism for each retrofitted specimen is used to inform the design of the next retrofit schemes, which are then adapted to a new retrofit objective to improve the global behaviour of the specimen. The main outcomes and innovations in the design of the three retrofit schemes are summarised below:

- Continuity of the longitudinal strengthening is required through the beam-column joint and this can be achieved by means of FRP anchor "strands". These strands are created from normal CFRP sheets in this study, corresponding to their first use in realistic specimens (all retrofits).
- For realistic specimens with slabs, a change in failure mechanism to comply with capacity design objectives can only be achieved by "selective weakening" of the slab, i.e. cutting through the slab reinforcement close to the joint. This does not affect the serviceability performance of the slab as the cuts are not in in a zone of high moments under gravity loading (retrofits RT-A-sw and RT-B-sw).
- Strengthening and confinement of the beams close to the joint is proposed for plastic hinge relocation within the beam and protection from plasticity spreading into the joint. To achieve this, FRP anchor strands are used for the first time in this study (retrofit RT-B-sw).

- Joint strengthening is required when increasing the overall lateral capacity of the specimens. The design of RT-B-sw includes the first recorded effort of joint shear strengthening applied through transverse beams.

To ensure that no valuable resources are wasted in the experimental campaign, next to the use of predictive FE models, the retrofits are initially trialled as repair schemes on pre-damaged control specimens. In the next Chapter, the diagnostics used to evaluate the performance of the retrofit and repair schemes is presented.

4. DIAGNOSTICS

A number of quantities are measured by the sensors presented within the experimental set-up. These include the value of lateral force (F_c, in kN), lateral displacement (δ, m), strain gauge measurements on rebars (ε_s) and the FRP strands ($\varepsilon_{FRP,strand}$). However, other parameters need to be derived from these measurements in order to compare the response of different specimens or of different components within one specimen, and to compare this study with the literature. Hence, this chapter presents the diagnostics used to analyse and compare results from the experiments in the following chapters.

4.1. LATERAL STOREY DRIFT

The value of drift is evaluated from the ratio of lateral displacement measured by sensor B01 (in m) and the sub-assembly storey height (3.0 m). Drift is presented as a percentage.

4.2. ENVELOPE OF FORCE-DISPLACEMENT CURVES

The envelope curves are created from the lateral force-displacement plots by joining the points at the end of the 1st cycle of each drift level. The applied lateral force, F_c, is measured in kN by the load cell in actuator ACT 200 at the top of the superior column. The maximum force is defined as the maximum value of F_c measured during the test.

4.3. MOMENTS

4.3.1. MOMENT IN COLUMNS

As shown in Figure 4.1, due to the nature of the axial load application of *N1* with pre-stressing rods, an eccentricity of the applied axial load occurs at high drift levels.

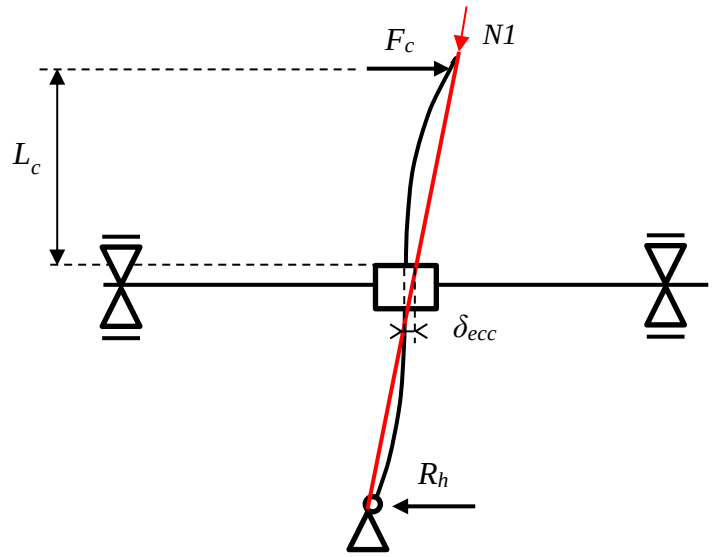

Figure 4.1. Schematic representation of the eccentricity in axial load application, δ_{ecc}, with pre-stressing rods (indicated in red).

The moment in the superior column, $M_{c,sup}$, is hence a combination of the moment M_l due to the lateral load, F_c, applied at the top of the column, and the moment M_{ecc} due to the eccentricity of axial load *N1*. The latter can be a significant contribution for large drift cycles and would also be present in a real structure undergoing large deformations. In the set-up, eccentricity of axial load was measured using string potentiometer F04 at the centre of the specimen, to measure the eccentricity of the steel rods used to apply the axial load. The moment due to eccentricity is evaluated using the method described in the manual for the PEER structural performance database (Berry et al., 2004), given by equation (4.1):

$$M_{ecc} = N_1 \cdot \delta_{ecc} \tag{4.1}$$

The total superior column moment is hence:

$$M_{c,sup} = M_l + M_{ecc} = F_c \cdot L_c + N_1 \cdot \delta_{ecc} \tag{4.2}$$

Where F_c is the applied lateral load from the horizontal hydraulic actuator ACT 200, δ_{ecc} is the measured eccentricity of the rod at the base of the superior column of the specimen, and L_c is the clear column height. *N1* is the applied axial load measured by the load cell in actuator CC 500_2.

For the inferior column, the moment is also evaluated as a combination of moment from the lateral force and the moment due to eccentricity, M_{ecc}, but the lateral force is found from the resistance, R_h, measured using the load cell CC300 at the base of the inferior column.

$$M_{c,inf} = M_{l,i} + M_{ecc} = R_h \cdot L_c + N_1 \cdot \delta_{ecc} \tag{4.3}$$

4.3.2. MOMENT IN BEAMS

The beam moments are evaluated as a function of the superior column moment and the moment due to the second axial load, *N2*, of 25 kN. At the joint, the sum of column moments and beam moments has to equate. The loading and reactions in the specimens are shown in Figure 4.2.

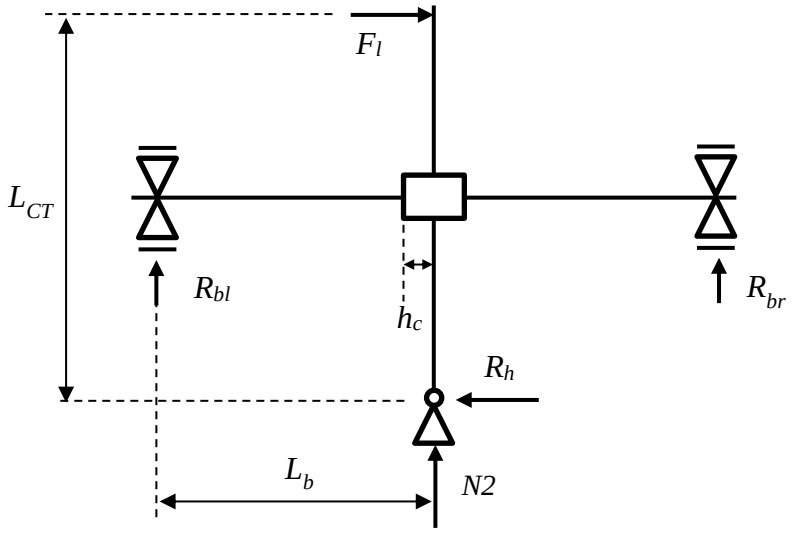

Figure 4.2. Loading and reactions for experimental set-up.

For vertical equilibrium:

$$R_{bl} + R_{br} = -N2 \ \therefore R_{bl} = -N2 - R_{br} \tag{4.4}$$

Where R_{bl} and R_{br} are the reaction forces at the left and right beam support, respectively, as shown in Figure 4.2. From equilibrium of moments, one can take the moments around the inferior column support:

$$F_l \cdot L_{CT} + R_{bl} \cdot L_b - R_{br} \cdot L_b = 0$$

$$\therefore R_{bl} - R_{br} = -\frac{F_l \cdot L_{CT}}{L_b} \tag{4.5}$$

Where F_l is the total lateral load applied at the superior column, including the effect of eccentricity, L_b the length between the beam supports and the centre of the joint (2.0 m), and L_{CT} the length between the lateral load application and the inferior column support (3.0 m).

Hence, substituting for R_{bl} from eq. (4.4) in eq. (4.5) and introducing the values of $N2$, L_b and L_{CT}, which are the same throughout all experiments:

$$\therefore -N2 - R_{br} - R_{br} = -\frac{F_l \cdot L_{CT}}{L_b}$$

$$\therefore 2 \cdot R_{br} = \frac{F_l \cdot L_{CT}}{L_b} - N2$$

$$\therefore R_{br} = \frac{F_l \cdot L_{CT}}{2 \cdot L_b} - \frac{N2}{2} = \frac{F_l \cdot 3}{4} - \frac{25}{2} = \frac{3}{4}F_l - 12.5 \tag{4.6}$$

And:

$$R_{bl} = -N2 - R_{br} = -25 - \left(\frac{3}{4}F_l - 12.5\right) = -\frac{3}{4}F_l - 12.5 \tag{4.7}$$

Then the moments at the beam/joint interface are simply found from the following equations, where h_c, the column cross-section height, is 0.3 m for all test specimens:

$$M_{bl} = R_{bl} \cdot (L_b - h_c/2) = \left(-\frac{3}{4}F_l - 12.5\right) \cdot 1.85 \tag{4.8}$$

$$M_{br} = R_{br} \cdot (L_b - h_c/2) = \left(\frac{3}{4}F_l - 12.5\right) \cdot 1.85 \tag{4.9}$$

4.4. JOINT SHEAR (SPECIMENS WITHOUT SLAB)

The joint shear force is determined based on equilibrium conditions and can be found from Equation (4.10), which is introduced in Section 2.1.

Joint shear is caused by the tension forces in the beam bars framing into the into the interior joint and the shear force from the column, V_{col}, in the opposite direction (i.e. the applied lateral load, F_c). The tension in the beam bars is found as the ratio of M_{b1} and M_{b2}, the moments in the beams on the left and right of the joint, with the lever arm, j_d, defined as 0.75 h_b (Bousselham, 2010):

$$V_{jh} = \frac{M_{b1}}{jd} + \frac{M_{b2}}{jd} - V_{col} \tag{4.10}$$

The shear stress in the joint core is commonly expressed as nominal shear stress or as principal tensile stresses. The horizontal shear stress (v_{jh}) in the joint can be calculated by equation (4.11), where V_{jh} is the horizontal shear force in the joint, calculated by equation (4.12); b_c is the width of the column; and h_c is the depth of the columns.

$$v_{jh} = \frac{V_{jh}}{b_c \cdot h_c} \tag{4.11}$$

Based on Mohr's circle, the principal tensile stresses (p_t) at the mid-depth of the joint core is found from equation (4.12). Here f_a is the nominal axial compressive stress on the column (equation (4.13). Note that compressive stresses are taken as negative.

$$p_t = \frac{f_a}{2} + \sqrt{\left(\frac{f_a}{2}\right)^2 + v_{jh}^2} \tag{4.12}$$

$$f_a = \frac{N}{b_c \cdot h_c} \tag{4.13}$$

The joint distortion in radians, γ, is determined from the displacement readings δ_{P23} and δ_{P24} in the diagonal transducers P23 and P24 of the joint, as shown in Figure 4.3.

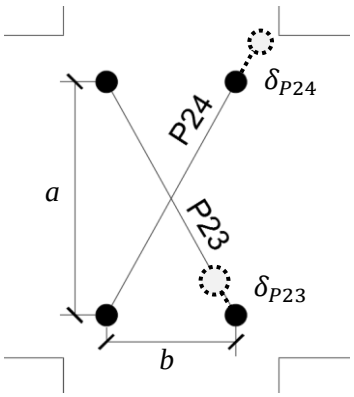

Figure 4.3. Transducers P23 and P24 used for the joint distortion calculation (dashed line indicates extension of transducer).

The equation of joint distortion is given as (Shiohara, 2001):

$$\gamma = \frac{\sqrt{a^2 + b^2}}{2ab}(\delta_{P23} + \delta_{P24}) \tag{4.14}$$

4.5. ROTATION AND CURVATURE

To assess the evolution of curvatures and rotation along the length of the columns and beams, each column and beam are divided into four lengths along the surface plane of the members, so-called 'slices', as shown in Figure 4.4.

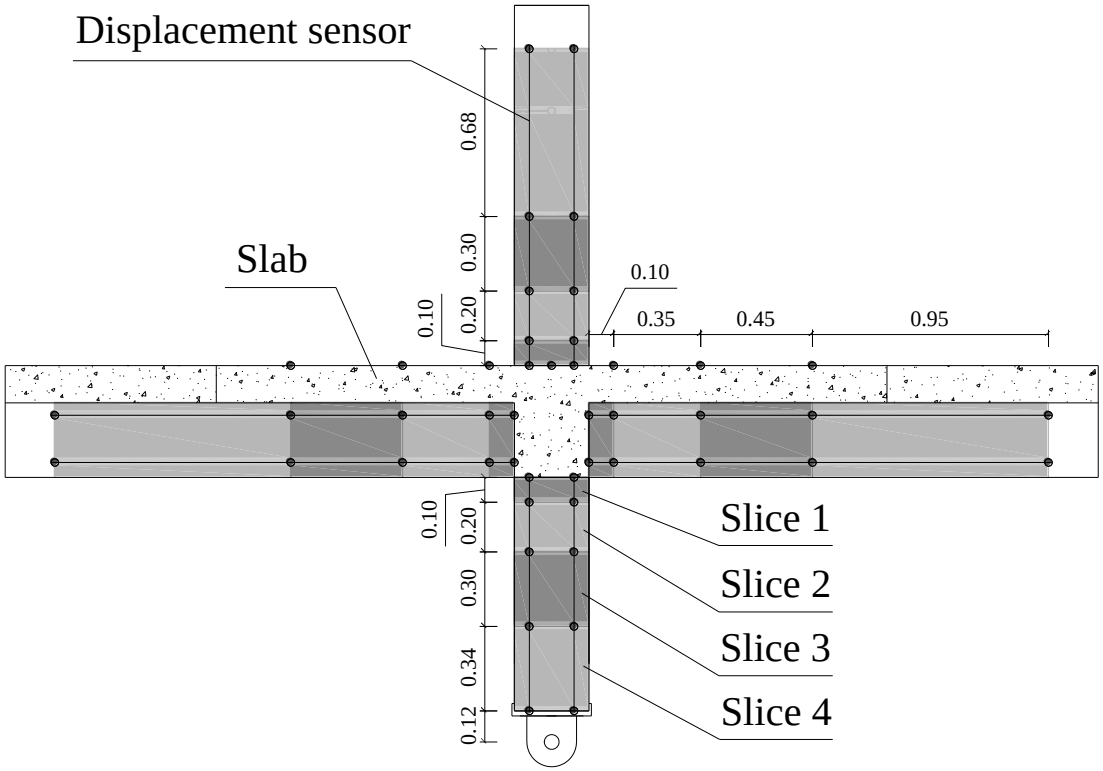

Figure 4.4. Details of 'slices' used for analysis of rotations and curvatures.

The rotation, θ, in each slice is evaluated by comparing the deformations, δ_i, of the two displacement transducers within the slice and dividing by the perpendicular distance between the two transducers, b_t. For example, for slice 3 of the superior column, transducers L1 and L2 are used as shown in Figure 4.5.

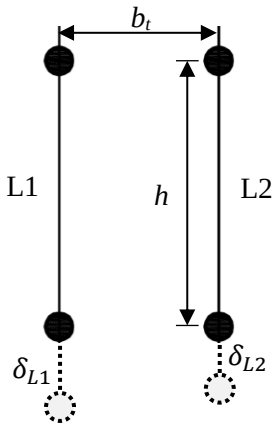

Figure 4.5. Transducers L1 and L2 used for the rotation and curvature calculation for slice 3, superior column (dashed line indicates extension of transducer).

For the same example, the rotation, θ, is then given by:

$$\theta = \frac{\delta_{L2} - \delta_{L1}}{b_t} \tag{4.15}$$

The curvature is then found by dividing the rotation by the slice length, *h*:

$$\varphi = \frac{\delta_{L2} - \delta_{L1}}{b_t \cdot h} \tag{4.16}$$

The curvature in each slice is an average curvature over the length of the transducers. The pairs of transducers, with reference to the monitoring schemes shown in Section 3.4 to calculate the rotation and curvature for each slice are summarised in Table 4.1.

Table 4.1. Summary of transducers used to evaluate rotations and curvatures in individual slices

Element	Slice	Slice length, *h*	Transducer pair	Distance between transducers, b_t	
		[mm]		With slab	Without slab
Left beam	1	100	P5 – P6	180	320
	2	350	P9 – P10	180	320
	3	450	L9 – L10	180	320
	3a and 3b for C-EC8 only	225 each	L9 – L10 and P21 – P22	180	320
	4	950	L13 – L14	180	320
Right Beam	1	100	P7 – P8	180	320
	2	350	P11 – P12	180	320
	3	450	L16 – L17	180	320
	4	950	L19 – L12	180	320
Superior Column	1	100	P1 – P2	180	180
	2	200	P27 – P28	180	180
	3	300	L1 – L2	180	180
	4	675	L3 – L4	180	180
Inferior Column	1	100	P3 – P4	180	180
	2	200	P29 – P30	180	180
	3	300	L5 – L6	180	180
	4	340	L7 – L8	180	180

4.6. ENERGY DISSIPATION

The global hysteretic energy dissipation of the specimens in units of kNm is defined as the area under the lateral force-displacement curves (see Figure 4.6).

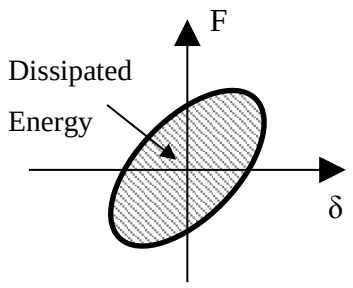

Figure 4.6. Schematic representation of global dissipated energy from force-displacement curve.

The cumulative dissipated energy, E_{diss}, is hence defined as the integral of the force displacement plot. Using the trapezoidal rule, this can be calculated from:

$$E_{diss} = \int_0^{\delta max} F(\delta).d\delta \cong \sum_0^{\delta_{i+1}=\delta max} \frac{(F_{i+1} + F_i)}{2} \times (\delta_{i+1} - \delta_i) \tag{4.17}$$

Where δ_i and F_i are the measured lateral displacement and applied force, respectively, at each level of displacement, i.

Energy dissipation is an indication of increased damage, as inelastic deformations lead to large energy dissipation. Higher dissipated energy developing over large drift levels is an indication of an improved, ductile, seismic behaviour (Kappos and Penelis, 1996). High energy dissipation at low levels of drifts, combined with a low value of ultimate drift is however an indication of damage at very early loading stages of the experiments. This in turn translates into a poorer seismic behaviour with significant damage occurring for smaller earthquakes.

The contribution of the individual members (beams, columns and joint) to the global energy dissipation, $E_{diss,member}$, is calculated from the moment-rotation curves at different sections along the length of the members. Each column and beam is divided into four slices, as shown previously in Figure 4.4. The moment and rotation at the centre of each slice is calculated assuming constant moment and rotation within each slice. As most of the inelastic deformations occur in the first two slices, that are smaller in length, this approximation is adequate. This method is common in the literature and good agreement is found in previous studies (Fernandes et al., 2011; Melo, 2014).

$$\begin{aligned} E_{diss,member} &= \sum_{slice\,=\,1}^{4} \int_0^{\theta max} M(\theta).d\theta \\ &\cong \sum_{slice\,=\,1}^{4} \sum_0^{\theta_{i+1}=\theta max} \frac{(M_{i+1} + M_i)}{2} \times (\theta_{i+1} - \theta_i) \end{aligned} \tag{4.18}$$

Where θ_i and M_i are the previously defined rotations and moments in the slice, respectively, at each level of displacement, i.

For specimens with slab, due to the experimental set-up containing transverse beams, the joint is not instrumented and the energy dissipated by joint deformations is hence approximated as the remainder between the difference of the global dissipated energy and the energy dissipated by columns and beams. For the specimens without slab and transverse beam, this approximation is verified by also calculating the energy dissipated from joint distortion (see Section 4.7).

To understand the evolution of the contribution of the individual members to the global energy dissipation, plots showing the proportion of dissipated energy for beams, columns and joint at the

end of the last cycle for every level of drift are produced. Following rules of capacity design, a better seismic behaviour is indicated by a higher proportion of beam participation.

4.7. ENERGY DISSIPATED BY JOINT DISTORTION (SPECIMENS WITHOUT SLAB)

For the two specimens without slab, C-noSLT and C-noSLT-RT-B, the energy dissipated in the joint is evaluated from the joint shear force and joint shear distortion calculated in section 4.4. The energy dissipated by the joint. $E_{diss,j}$ is then found from the area under the joint shear – joint distortion curve, i.e. the integral of this plot, which is approximated using the trapezoidal rule:

$$E_{diss,j} = \int_0^{\gamma max} V_{jh}(\gamma).d\gamma \cong \sum_0^{\gamma_{i+1}=\gamma max} \frac{\left(V_{jh_{i+1}} + V_{jh_i}\right)}{2} \times (\gamma_{i+1} - \gamma_i) \qquad (4.19)$$

Where γ_i and $V_{jh,i}$ are the previously defined joint distortion and horizontal joint shear force, respectively, at each level of displacement, *i*.

4.8. DUCTILITY FACTOR

The ability of a structure to dissipate energy by undergoing large plastic deformations is characterised by its ductility. In this study the ultimate displacement ductility, $\mu_{\Delta u}$, is chosen to characterise the global specimen ductility:

$$\mu_{\Delta u} = \frac{\delta_u}{\delta_y} = \frac{\Delta_u}{\Delta_y} \qquad (4.20)$$

Where δ_u and Δ_u are the ultimate displacement and drift of the specimen, respectively, and δ_y and Δ_y the yield displacement and drift of the specimen, respectively. This is represented graphically in Figure 4.7, with the yield and ultimate displacement points defined as in Sections 4.9 and 4.10.

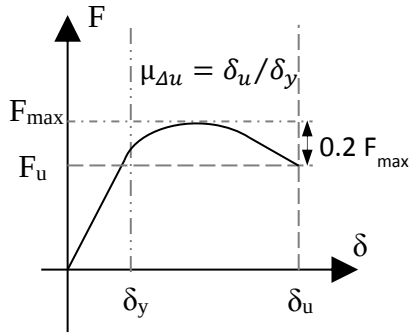

Figure 4.7. Schematic representation of displacement ductility from the force-displacement envelope curve.

4.9. YIELD DISPLACEMENT AND DRIFT

The ultimate displacement ductility is dependent on the value of the Δ_y, the yield drift. As indicated in Section 3.4, the strain gauges are placed near the interfaces of the members to the joint, hence at the locations of maximum moment and where yield of rebars is occurs first. In this study, yield drift for each element is hence defined as the first drift at which the measured strain at one of the strain gauge locations exceeds the yield strain ε_y of the longitudinal steel reinforcing bars (taken as 0.21% for the 12 mm rebars and 0.3% for the high strength 16 and 25 mm rebars used for C-EC8). To reduce the potential for physical errors due to inadequate strain gauge application, multiple strain gauges are applied in each member, as outlined in Section 3.4.

Using strain gauge readings is a commonly used experimental method for defining yield when adequate monitoring is used (e.g.: Engindeniz, 2008; Restrepo-Posada, 1992). While alternative methods for determining the yield displacement based on the force-drift envelope curves exist (e.g. using an equivalent elasto-plastic system with equal energy dissipation), the importance relies in using a consistent means of defining yield, and hence ductility, for all specimens.

The yield drift for beam and columns are also indicated on the plots of force vs. drift in Chapter 5. Following the rules of capacity design, it is desirable for yield of beam bars to occur before that of column bars. A higher value of yield drift for column bars is hence seen as an improvement when assessing the repair and retrofit interventions.

4.10. ULTIMATE DISPLACEMENT AND DRIFT

The ultimate drift, Δ_u, is defined according to Park et al. (1987) as the level of global drift after the maximum force (F_{max}) is reached in the specimen, at which the lateral force capacity of the specimens drops by 20%. Note that the ultimate point is extrapolated from the force-drift envelope to ensure consistency between the experiments. This is a commonly accepted definition of reaching the ultimate state (Fardis, 2009).

4.11. PEAK-TO-PEAK STIFFNESS

As shown in Figure 4.8, the peak-to-peak lateral stiffness, K_p, expressed in units of kN/mm, is defined as the slope of the line between the maximum positive and negative force ($F^+_{max,i}$ and $F^-_{max,i}$) at the first cycle of each level of displacement, i:

$$K_{p,i} = \frac{\left|F^+_{max,i}\right| + \left|F^-_{max,i}\right|}{\left|\delta^+_i\right| + \left|\delta^-_i\right|} \tag{4.21}$$

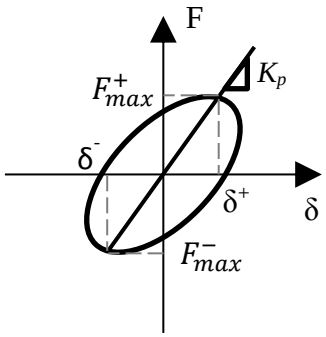

Figure 4.8. Schematic representation of the peak-to-peak stiffness calculation.

Plots of lateral stiffness against drift are used to highlight stiffness degradation with increased drift for the specimens. This diagnostic is used extensively in the literature (e.g.: Al-Salloum and Almusallam, 2007; Antonopoulos and Triantafillou, 2003; Pantelides et al., 2008; Realfonzo et al., 2014; Tsonos, 2008) and is an important parameter in evaluating the effectiveness of a retrofit. A lower rate of degradation in stiffness corresponds to a better seismic behaviour of the sub-assemblies, as loss of stiffness is not desirable. For pre-damaged and repaired specimens, a lower initial stiffness is expected and this is visualised using plots of peak-to-peak stiffness against drift.

4.12. POST-PEAK SOFTENING

The post-peak softening, *S*, is a characteristic of the behaviour of a structure after the maximum load, and is shown diagrammatically in Figure 4.9. The value of *S*, determined in units of kN/mm, is found from the slope between the maximum force, F_{max}, and the ultimate force, F_u, at their respective levels of lateral displacement. A higher softening is hence associated with a steeper strength reduction from F_{max} to F_u, and hence a lower residual strength for the structure at any level of drift.

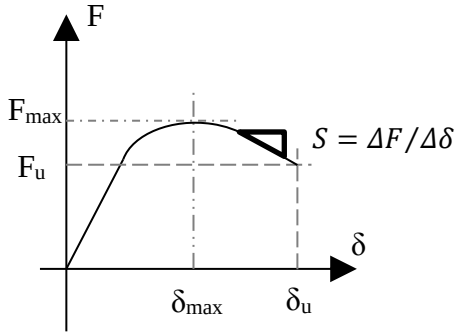

Figure 4.9. Schematic representation of the post-peak softening calculation from the force-displacement envelope.

4.13. INTER-CYCLE STRENGTH DEGRADATION

The strength degradation between cycles 1 and 2 ($F_{deg,1\text{-}2}$) and 1 and 3 ($F_{deg,1\text{-}3}$) is evaluated at each level of drift. This corresponds to the reduction in lateral load capacity at the end of each cycle. It is an important parameter to understand the seismic behaviour of the specimens, as in real

earthquakes structures undergo repeated cycles of load. A low reduction in strength upon repeated loading is hence desirable. Strength degradation is determined as a percentage of reduction from the 1st cycle and is plotted against increased drift levels. An average is taken between the values for loading in positive and negative directions. Strong reductions in strength between cycles are usually associated to brittle damage in the specimens, such as joint damage (Melo, 2014).

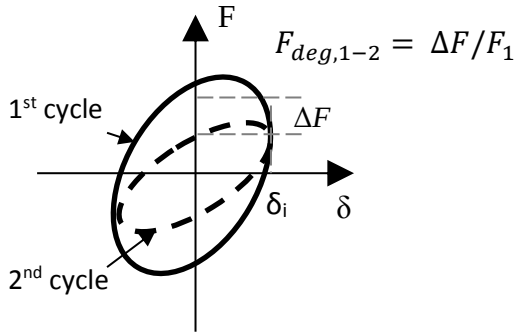

Figure 4.10. Schematic representation of the inter-cycle strength degradation calculation.

4.14. CRACKS

During the experiments, new visible cracks were marked on the concrete surface at the end of the third cycle of each drift level. The occurrence of first cracks in beams and columns, as well as at the interface to the joint are indicated on the plots of force vs. drift in the Chapter 5 and serve as a means of comparison between the specimens.

4.15. DAMAGE INDICES

As an additional diagnostic to evaluate the ability of the retrofit schemes to reduce or delay damage, the experimental observations are quantified using the HRC scale damage indices (DI_{HRC}) proposed by Rossetto and Elnashai (2013). Values of DI_{HRC} between 20 % and 49 % are defined as light damage, between 50% and 79% as moderate damage and between 70 % and 89% as extensive damage. Above 90% is considered a partial collapse. The relation between recorded physical observations of damage and the value of the indices can be summarised as:

- DI_{HRC} = 30% - observation of first cracks in any member
- DI_{HRC} = 50% - observation of flexural cracks in beams and columns
- DI_{HRC} = 60% - yielding in any member
- DI_{HRC} = 70% - initiation of spalling
- DI_{HRC} = 90% - ultimate drift.

5. RESULTS

5.1. INTRODUCTION

In this Chapter, results from twelve full-scale beam-column joint and two full-scale column tests are presented. The cyclic behaviour of the specimens is analysed based on the diagnostics introduced in Chapter 4.

First the detailed results for each control specimen are described individually. The global force-displacement behaviour, the occurrence of significant events such as cracking and spalling of the concrete, or yielding of the reinforcement bars, as well as the moment-curvature plots for the beams and columns are presented. The results are compared to the behaviour predicted by the design guidelines and to predictions from the FE models developed in Chapter 3. The latter is however only possible for the four specimens for which full FE models of the joints are available.

Next, the effect of the individual repair and retrofit schemes is addressed by comparison of the relevant diagnostics to the respective pre-1970's and EC8 control specimens. Finally, the outcomes of multiple tests are grouped thematically and compared amongst one another to address the effects of various parameters, such as the effect of slab, selective weakening or retrofit scheme.

5.2. CONTROL SPECIMENS

The results for five control specimens are presented in this section. The first four specimens are designed with typical pre-1970's deficiencies according to the Portuguese RC code (REBA, 1967). **C-noSLT** is the control specimen without slab and transverse beam, i.e. with the typically tested cross-shaped or cruciform geometry. **C1** is the control specimen with slab and transverse beam. This control specimen can be seen as the benchmark for all tests with slabs, as it has the same reinforcement detailing as all the retrofitted and repaired specimens apart from C2-RP-A. **C2** has the same geometry and reinforcement detailing as C1 apart from an additional bar in the bottom of the beams. This is the control specimen used for C2-RP-A. **C1-sw** is a control specimen with same detailing as C1 but with 600 mm long selective weakening cuts along the beams. Finally, **C-EC8** is a specimen with slab and transverse beam designed to modern seismic design guidelines (Eurocode 8) for a highly seismic zone.

A summary of the main results for all control specimens is presented in Table 5.1. A detailed description of the cyclic behaviour of the control specimens is provided. For all specimens the force-drift and moment-curvature figures are plotted with the same axes to enable an easier visual comparison. For specimen C-EC8 however, as much larger moments are observed, the limits of the axes are increased.

Table 5.1. Summary of experimental results for control specimens (difference to C1 in brackets).

Specimen	F_{max} (kN)	Main damage	Δ_y (%)	Δ_{max} (%)	Δ_u (%)	$\mu_{\Delta u}$	E_d (kN.m)	S (kN/mm)	K_i (kN/mm)	$F_{deg,1-2}$ (%)	$F_{deg,1-3}$ (%)
C-noSLT	45.16 (-28.4%)	Joint	0.67 (10.2%)	1.46	3.50	5.22 (44.4%)	31.82 (-0.8%)	-0.15 (-70.2%)	4.82 (-27%)	18.44 (-20.6%)	29.28 (-56.8%)
C1	63.08	Sup. column	0.65	1.27	2.34	3.62	32.08	-0.49	6.60	23.22	67.74
C2	66.71 (5.8%)	Sup. column	0.61 (-5.9%)	-1.46	2.52	4.14 (14.5%)	27.64 (-13.8%)	-0.39 (-20.4%)	5.95 (-9.9%)	7.46 (-67.9%)	14.58 (-78.5%)
C1-sw	67.47 (7%)	Sup. column	0.48 (-21.8%)	-0.96	1.85	3.89 (7.5%)	22.7 (-29.2%)	-0.4 (-18.4%)	7.71 (16.7%)	27.86 (20%)	67.53 (-0.3%)
C-EC8	123.88 (96.4%)	Columns, Beams	-0.89 (46.4%)	-3.45	-5.22	5.86 (61.9%)	172.28 (437.1%)	-0.47 (-5.8%)	7.18 (8.7%)	10.57 (-54.5%)	18.72 (-72.4%)

Note: Diagnostics defined in Chapter 4.

5.2.1. C-noSLT - Gravity Designed specimen without slab and transverse beam

5.2.1.1. Global parameters and failure mechanism

Specimen C-noSLT has the cross-shaped geometry that is typically tested in the literature. Due to the lack of joint reinforcement and lack of confinement of the joint by transverse beams, joint shear failure is often observed in the laboratory. As predicted by FE modelling in Section 3.5, large damage occurs in the joint region, with cracks noticeable along the beam and at the beam/joint interface (Figure 5.1). Limited cracking in the columns is observed, as the rotation of the column, and hence the demand, are low. The observed damage is characteristic of a joint shear failure, which is in line with observations from previous experiments (e.g.: Almusallam and Al-Salloum 2007; Shiohara 1998).

(a) (b)

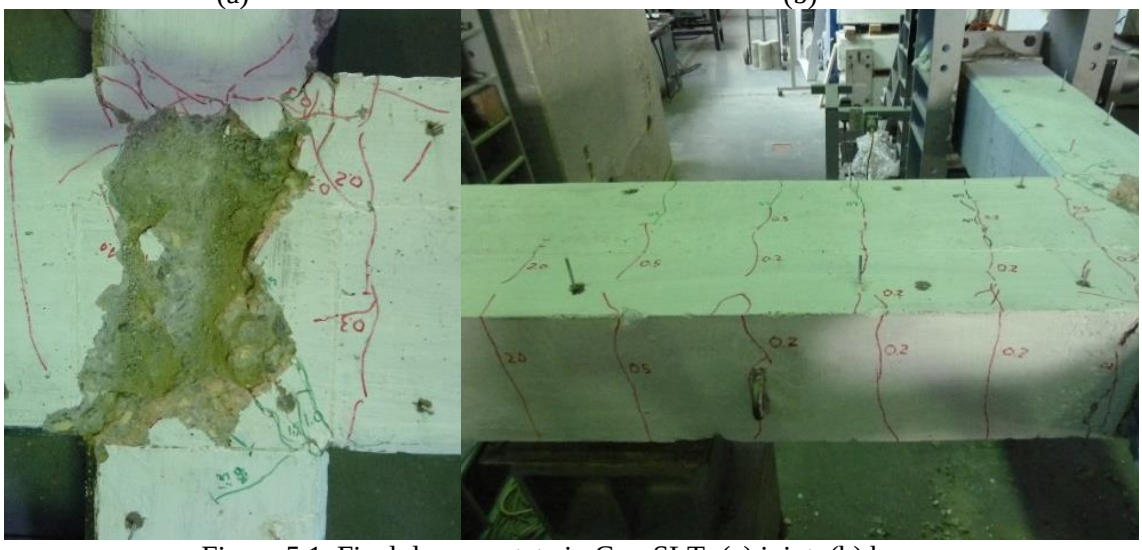

Figure 5.1. Final damage state in C-noSLT; (a) joint, (b) beam.

Figure 5.2 shows the lateral force-drift response for C-noSLT, with markers indicating different events that occur throughout the test. The maximum recorded lateral load is 45.16 kN, which is 28% larger than predicted by FE modelling. The higher capacity of the joint can partially be seen as a consequence of the second axial load increasing the confinement the joint in the physical experiment. As mentioned in Section 3.5, the second axial load is not included in the FE models. Still, the overall damage mechanism is well represented. Thin cracks are observed in the beams at very low drift cycles (0.2%) and yield of the top beam bars is observed at 0.67% drift. Yield occurs first in the top of the beams, as the hogging moment near the joint is larger than the sagging moments. This is due to the additional moment induced by the second axial load, which simulates the effect of gravity loading on the beams (see section 3.2). This result confirms the importance of simulating this realistic load condition and the effectiveness of the approach used in the experimental set-up to reproduce it.

Cracks in the joint and along the column become noticeable during the 1.0% drift cycles, just before the maximum lateral load is recorded at 1.46% drift. With increasing drift cycles, more damage in the joint is observed, with concrete crushing in the corners of the joint (4.0% drift) and cover spalling in the joint panel (4.5%) governing the ultimate failure

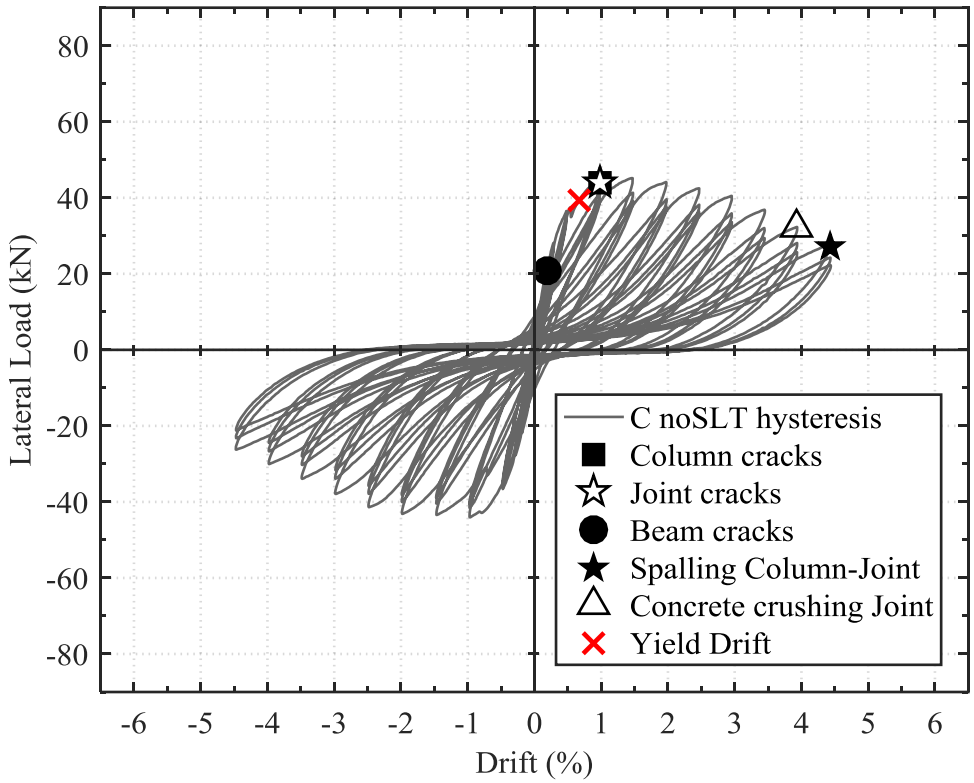

Figure 5.2. Force – drift response for specimen C-noSLT with important events markers.

Despite the joint failure, the ductility of the specimen is relatively large (5.2) with the ultimate force reached at 3.5% drift. The large ductility is a result of the low yield drift. As seen in Figure 5.2, the post-peak softening behaviour displays a modest slope of strength decrease after the maximum force. The energy dissipation of the specimen is dominated by the damage observed in the joint and beams, and a very low cumulative energy dissipation of 31.8 kNm is obtained, as shown in Table 5.1.

5.2.1.2. LOCAL BEHAVIOUR

5.2.1.2.1. MOMENT CURVATURE

Figure 5.3 displays the moment-curvature relationships for the columns and beams of specimen C-noSLT. The measurements of curvatures with potentiometers and LVDT's are in part affected by the damage in the concrete during the experiments, which explains some abnormalities in the curves (e.g. positive curvatures for negative moments in the superior column for one cycle). Overall the results are still useful and the coincidence of yield points with the reaching of moment plateaus confirm their reliability.

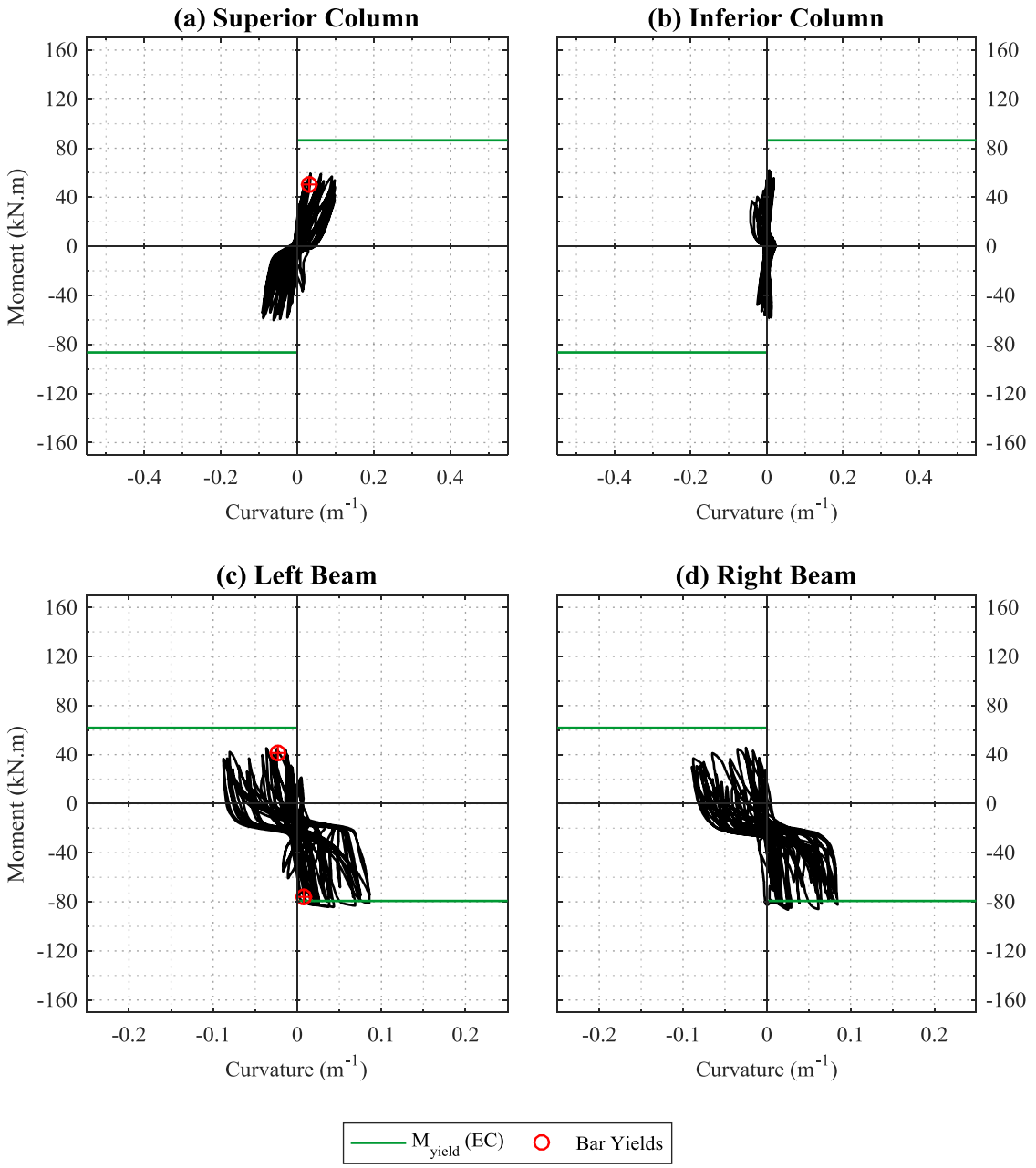

Figure 5.3. Moment Curvature behaviour in (a) superior and (b) columns, as well as the (c) left and (d) right beams for specimen C-noSLT, with indication of expected moment capacities (EC) and experimental yield points.

In Figure 5.3 (c) and (d) it can be seen that for both beams a symmetric rotation is observed, with maximum curvatures around ±0.075 m^{-1} for hogging and sagging in the left and right beam. This observation is consistent with the pattern of cracks on the beams. Yield of the bars is reached in hogging and sagging, with yielding coinciding with the calculated moment capacity from EC2. After yield, some extent of strain hardening is observed and the obtained difference in the expected moment capacity (+ 9.0%) is within the safety margin of 1.3 used for design. For the sagging moment however, yield of the bottom bars is observed at a lower moment than expected (-23.4%). This is similar for the superior column in Figure 5.3 (a), for which yield in the bar is observed despite low curvatures and not reaching the theoretical moment capacity. The reason for this is the lack of transverse reinforcement of the joint, with the beam and column longitudinal

bars hence providing resistance to the joint shear, thus reaching plasticity in the joint core. As the stress in the bars increases, plasticity then spreads outwards, yield is reached prematurely in the longitudinal bars at the column/joint and beam/joint interfaces where the strain gauges are placed. This is in line with observations from the FE study in Section 3.5, for which yielding of the beam and column bars within the joint is observed to spread outwards.

5.2.1.2.2. JOINT SHEAR DISTORTION

The behaviour of C-noSLT is pre-dominantly characterised by the low joint confinement leading to extensive damage in the joint panel. Looking at the principal stress versus joint shear distortion plot in Figure 5.4, significant joint shear strength degradation with increased distortion is observed. A large peak joint shear distortion of 0.065 rad is obtained. The maximum sustained tensile stress in the joint is 0.39 $\sqrt{f_c}$ in specimen C-noSLT.

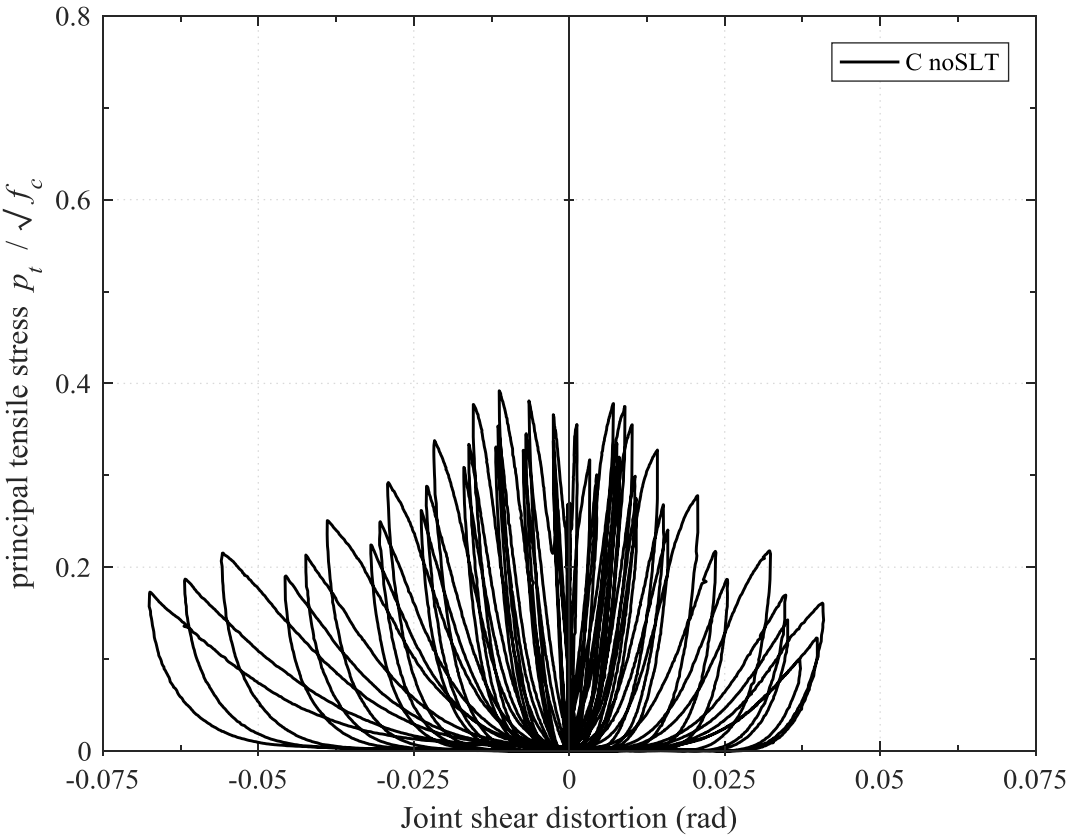

Figure 5.4. Principal tensile stress (normalised by concrete strength) against joint shear distortion for control specimen C-noSLT.

5.2.1.3. SUMMARY

Overall, the behaviour of the specimen without slab and transverse beam is dominated by the lack of confinement of the joint, leading to a low strength of the specimen. The joint significantly affects the specimen's behaviour, as indicated by a large level of joint shear distortion. The failure mechanism is similar to experimental observations found in the literature (e.g.: Mosallam 2000; Prota et al. 2004), as well as the prediction from FE modelling (Section 3.4).

5.2.2. C1 - GRAVITY-DESIGNED SPECIMEN WITH SLAB AND TRANSVERSE BEAM

5.2.2.1. GLOBAL PARAMETERS AND FAILURE MECHANISM

For the specimen with slab and transverse beams, designed to pre-1970's guidelines, C1, a brittle failure mechanism is observed. The behaviour is dominated by large rotation in the superior column, leading to localised plastic hinge formation, followed by concrete crushing and buckling of the superior column bars just above the column/slab interface. The final damage states in the superior column and the underside of the beam are shown in Figure 5.5. The experimental observations confirm the predictions from the FE models in Section 3.5. The type of failure mechanism observed can be described as a single-storey column failure, as no significant damage is observed in the rest of the specimen.

As shown in Table 5.1, a relatively low lateral capacity of 63.1 kN, combined with a very low ultimate drift (2.3%) and displacement ductility (3.6), are observed for the non-seismically designed control specimen. The inadequate seismic performance of the specimen is also characterised by a low cumulative energy dissipation (32.1 kNm) and significant post-peak softening, hence a low residual strength. The predicted lateral capacity from the FE-models is not achieved (-22%), which may be a consequence of the chosen model not being perfectly adequate for simulating the behaviour of substandard materials and reinforcement.

(a) (b)

Figure 5.5. Final damage state in C1: (a) superior column; (b) beam underside.

The lateral force-drift response of the specimen is presented in Figure 5.6 where the occurrence of cracking, spalling, buckling and yielding is also shown. Initial cracks are observed in the superior column during the 0.5% drift cycles. This is followed by yielding of the superior column bars at 0.65%. The peak lateral force of 63.1 kN is recorded at 1.27% drift. During the associated 1.5% drift cycle, two minor cracks in the beams, as well as in the slab are observed. The cracks in the slab are indicative of its contribution to the behaviour of the specimen. The cracks spread

along the entire width of the slab, perpendicular to the loading direction, with one crack along the transverse beam/slab interface and second parallel one, about 300 mm from the transverse beam.

The beam bars do not reach yield due to the limited rotation of the primary beams. After plastic hinge formation in the column, the ultimate state is reached suddenly at 2.34% drift. At this point, concrete crushing and buckling of the column bars just above the column/slab interface is observed, which can be attributed to the inadequate spacing of lateral reinforcement, and hence lack of confinement in the columns. This is also observed in the FE-models (Section 3.5).

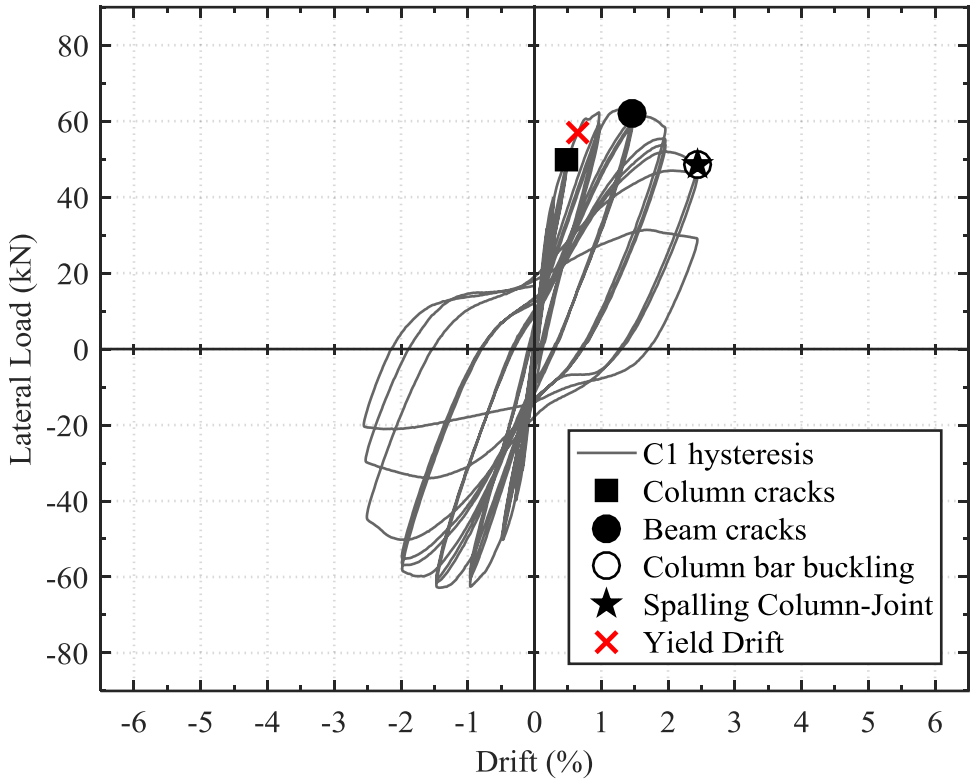

Figure 5.6. Force – drift response for specimen C1 with important events markers.

5.2.2.2. LOCAL BEHAVIOUR AND MOMENT CURVATURE

The moment-curvature curves for the beams and columns of specimen C1 are shown in Figure 5.7. The single-storey failure mechanism described in the previous paragraphs is confirmed by the inelastic response observed for the superior column and linear-elastic response of the other three members. For the superior column, curvatures up to 0.42 m^{-1} are measured, which are ten to twenty times larger than the curvatures in the inferior column and beams, respectively. Yielding of the column bars is recorded at moments coinciding with the anticipated capacities from Eurocode 2 (79.8 kNm). Again, due to strain hardening, the maximum moment in the column is slightly higher (+11.8%) than the capacity calculated using the yield strength of the bars. The over-strength factor is hence within the margins anticipated by EC8.

Failure of the inferior column is not observed as the increased axial load in lower storey columns leads to an enhanced confinement. As soon as the superior column bars yield, the deformation

imposed on the inferior column is reduced, which hence does not present large curvatures. The calculated sagging moment capacity of the beams is also reached, however, due to the highly asymmetrical sagging and hogging capacities, the curvature in the beams is limited and no yielding of the beam bars is observed.

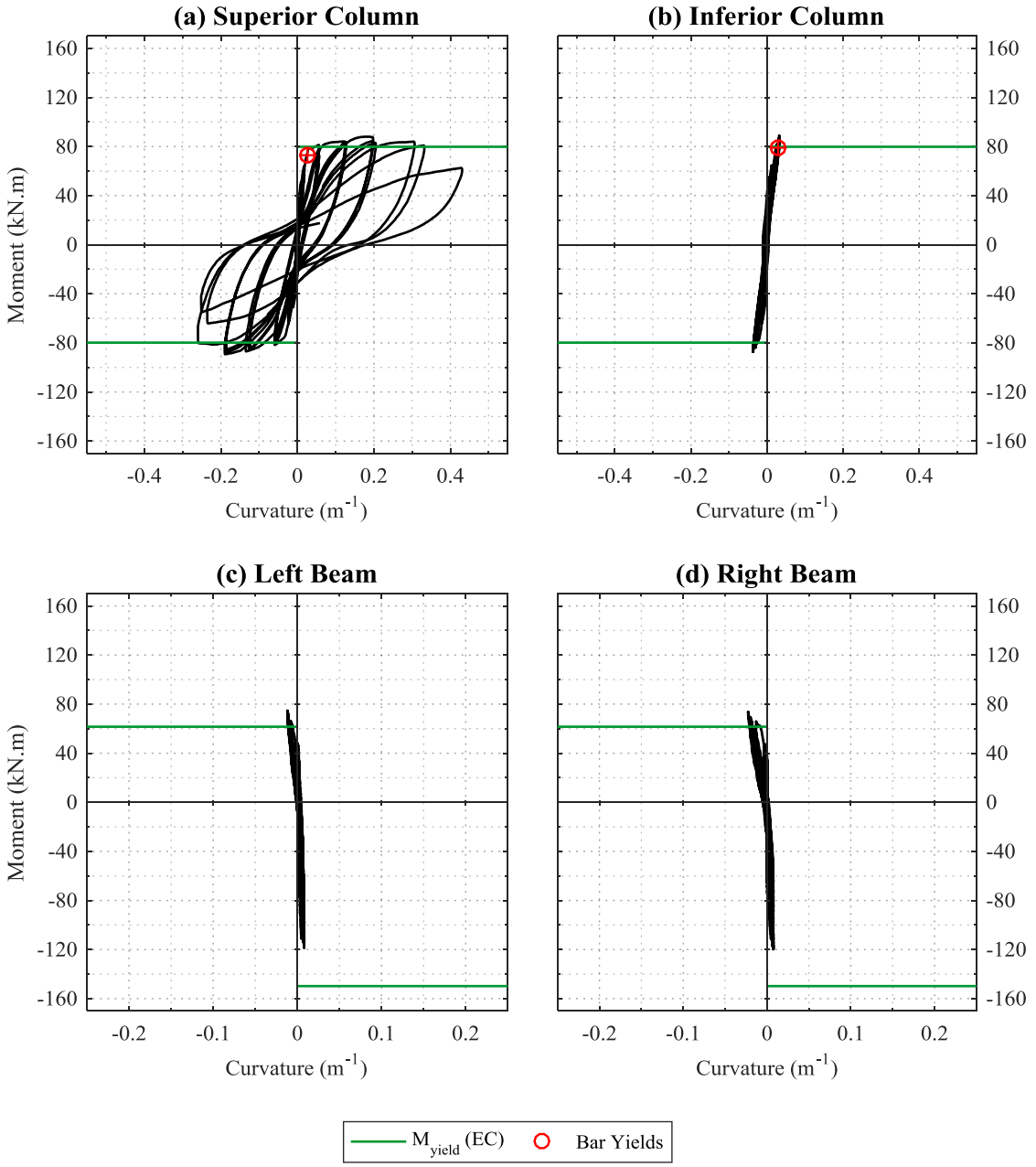

Figure 5.7. Moment Curvature behaviour in (a) superior and (b) inferior columns, as well as (c) left and (d) right beams for specimen C1, with indication of expected moment capacities (EC) and experimental yield points.

5.2.2.1. SUMMARY

Overall the behaviour of specimen C1 is characterised by isolated damage in the superior column, with buckling of the column bars, leading to an undesirable non-ductile failure mechanism with limited energy dissipation. Unlike specimen C-noSLT, the joint does not dominate the specimen's behaviour. The observed failure is similar to results from FE modelling presented in Section 3.5.

5.2.3. C2 - CONTROL SPECIMEN WITH ADDITIONAL BEAM REINFORCEMENT

5.2.3.1. GLOBAL PARAMETERS AND FAILURE MECHANISM

The behaviour of C2, a second deficient specimen with pre-1970's reinforcement, is similar to C1, with large deformation of the top column and very limited rotation of the joint, inferior column and beams. A slightly higher peak lateral strength of 66.7 kN (+5.8% compared to C1) is achieved for C2. Damage and cracking are mainly confined to the plastic hinge zone of the superior column, as shown in Figure 5.8 (a). In turn, as seen in Figure 5.8 (b), unlike C1, only one crack is observed in each beam and one crack on the slab, parallel to the transverse beam. This can be seen as a consequence of the increased beam reinforcement for C2.

(a) (b)

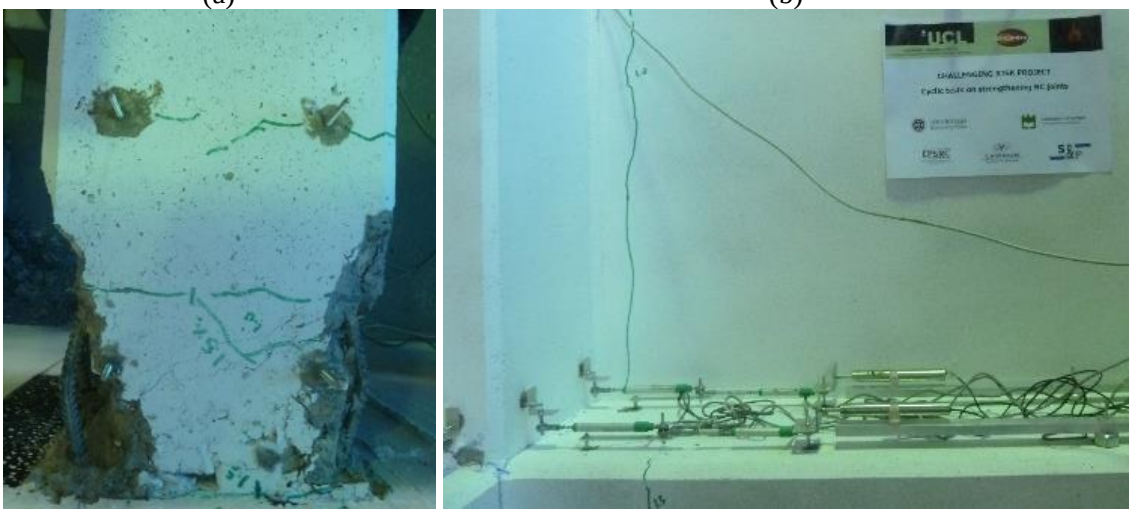

Figure 5.8. Final damage state in C2; (a) superior column, (b) beam underside.

The lateral force-drift response for C2 is shown in Figure 5.9. As it can be seen, cracks are first observed in the superior column at a drift of 0.5%. This is followed by yielding of the longitudinal reinforcement above the joint at a yield drift of 0.61%. One crack in the beam and slab is observed at 1.5% drift, however, no yield of the beam reinforcement is noted. The peak force of 66.7 kN is recorded at -1.46% drift, when some spalling of the concrete cover in the column is observable. The ultimate failure of the specimen after plastic hinge formation is reached at 2.5% drift, followed by buckling of column bars just above the column/joint interface in the first cycle of 3.0% drift. This corresponds to a moderate ultimate displacement ductility of 4.1 for C2.

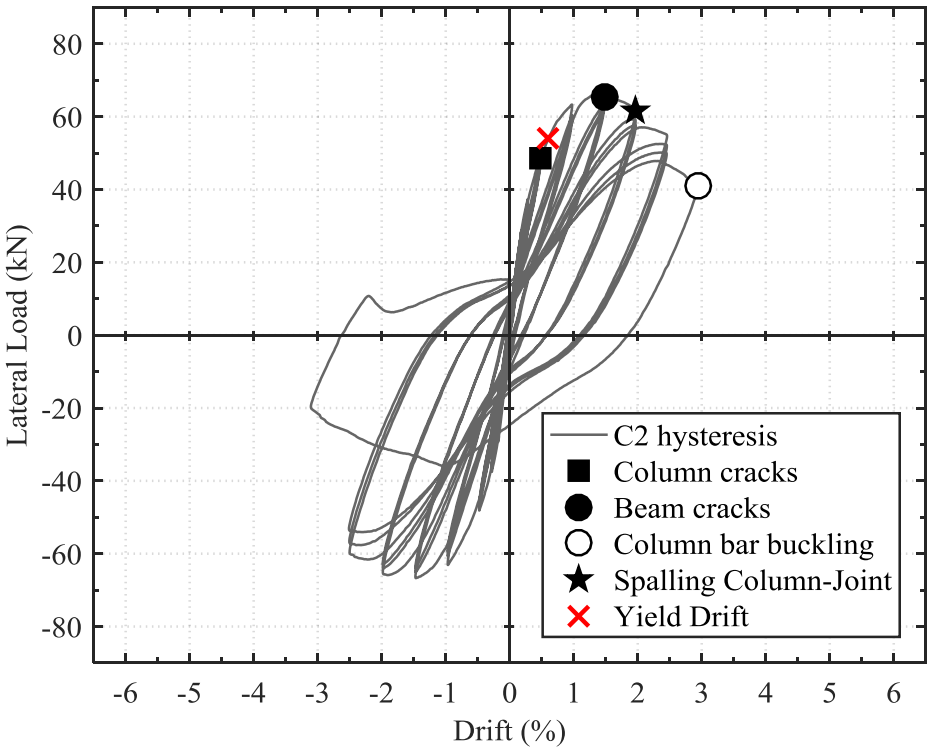

Figure 5.9. Force – drift response for specimen C2 with important events markers.

5.2.3.2. LOCAL BEHAVIOUR AND MOMENT CURVATURE

In the moment-curvature plots in Figure 5.10 it can be seen that the inferior column and the beams remain in the elastic range, while the superior column reaches a moment-plateau, close to the anticipated moment capacity of 88.3 kNm. Some limited strain hardening is observed and the maximum moment in the column is 93.4 kNm (+5.8%). The observed curvatures, and hence rotations, in the beams and inferior column remain very low, which consequently results in the non-ductile single-storey failure of the superior column seen for C2. Compared to C1, a slightly increased curvature of the inferior column is observed, this is due to the larger imposed drift of 3.0% compared to 2.5% for C1 at the end of the experiment.

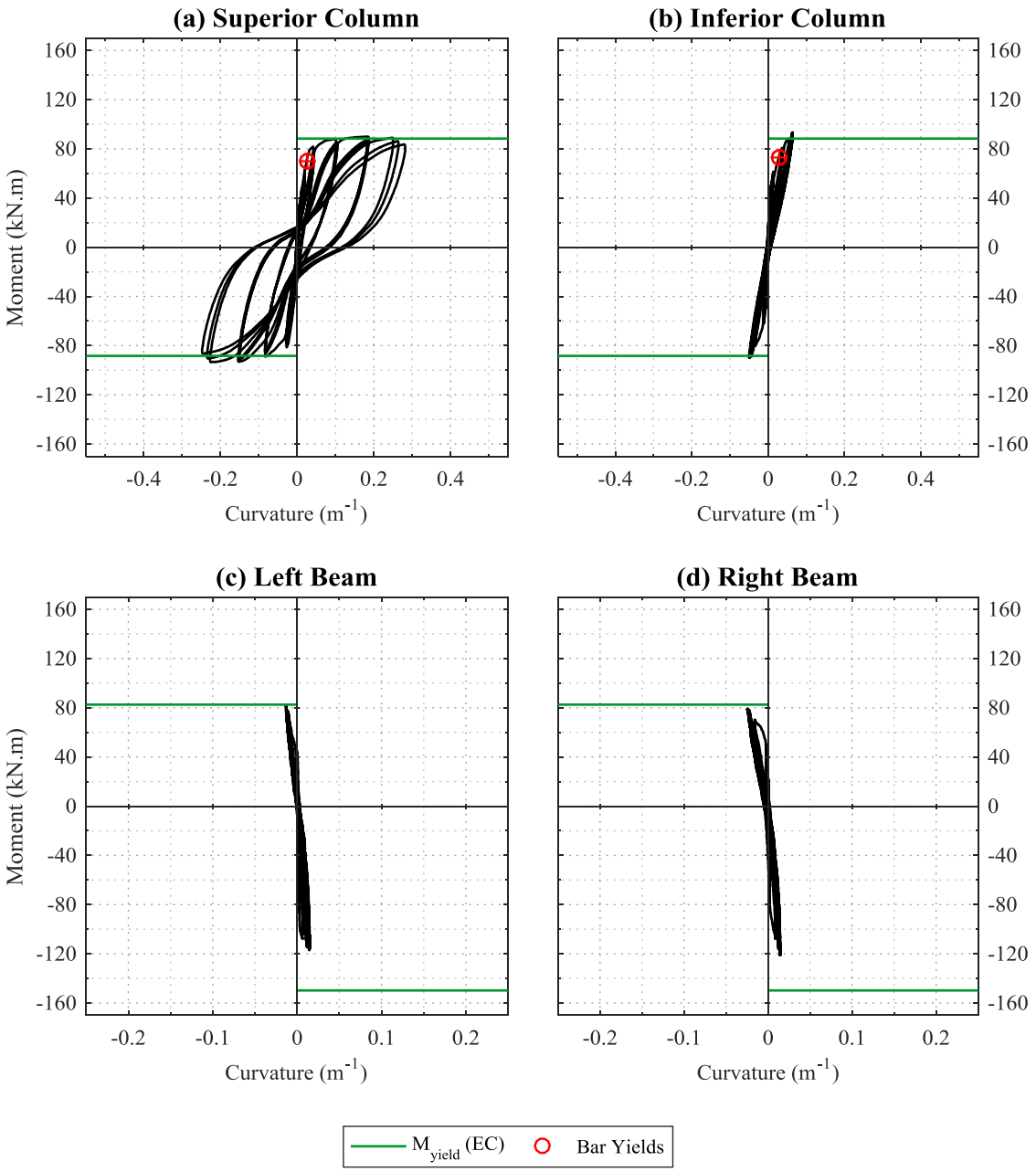

Figure 5.10. Moment Curvature behaviour in (a) superior and (b) inferior columns, as well as (c) left and (d) right beams for specimen C2, with indication of expected moment capacities (EC) and experimental yield points.

In the beams, the moment capacity is not reached and the observed rotation in the beams remains low as shown in Figure 5.10 (c) and (d). Overall, the increased beam reinforcement adds to the inadequate strong-beam/weak-column hierarchy of strengths, leading to a pronounced single-storey failure of the superior column for specimen C2.

5.2.3.3. SUMMARY

Overall the behaviour of specimen C2 is characterised by the isolated failure of the superior column with buckling, leading to an undesirable non-ductile with limited energy dissipation. The additional beam reinforcement limits the rotation of the beams further.

5.2.4. C1-SW - GRAVITY-DESIGNED SPECIMEN WITH SLAB AND TRANSVERSE BEAM AND SELECTIVE WEAKENING

5.2.4.1. GLOBAL PARAMETERS AND FAILURE MECHANISM

Specimen C1-sw is the control specimen with selective weakening (sw) cuts in the slab. Despite sw, the failure of specimen C1-sw is similar to C1, which is characterised by a single-storey failure, dominated by large deformation of the superior column, with limited rotation of the joint, inferior column and beams. Compared to the specimen without slab and transverse beams, it is noticed that the confinement of transverse beams alone is sufficient to prevent joint shear failure.

A slightly larger peak lateral force of 67.5 kN (+7% vs. C1) is achieved when the moment capacity of the superior column is reached. The final damage state for C1-sw is shown in Figure 5.11, highlighting that damage is confined to the plastic hinge zone of the superior column (a), with minor visible cracks in the inferior column and a single crack at the beam/joint interface (b).

(a) (b)

Figure 5.11. Final damage state in C1-sw; (a) superior column, (b) beam underside.

The lateral force-drift response of the specimen with indications of the occurrence of cracking, spalling, buckling and yielding is shown in Figure 5.12. First cracks in the superior and inferior columns become noticeable during the 0.5% drift cycles. This is also when yielding of the reinforcement bars is first observed in the longitudinal column reinforcement above the joint, with a yield drift of 0.48%. Further flexural cracks along the length of the columns are noticed with increasing drift levels. A crack along the transverse beam/slab interface is observed at 0.5% drift at the end of the weakening cuts, confirming the anticipated contribution of the slab bars in the non-weakened region. At higher drift levels (1.0%), the crack extends along the entire weakening cut. For the beam bars, yield is also observed at 0.74% drift for the bottom reinforcement. The peak lateral force is recorded at -0.96% drift. After plastic hinge formation in the column, the ultimate state is reached at 1.85% drift, with concrete crushing and spalling, as well as buckling of the column bars just above the column/joint interface. Significant post-peak softening is again observed for this specimen. The ultimate displacement ductility is 3.9 for C1-sw.

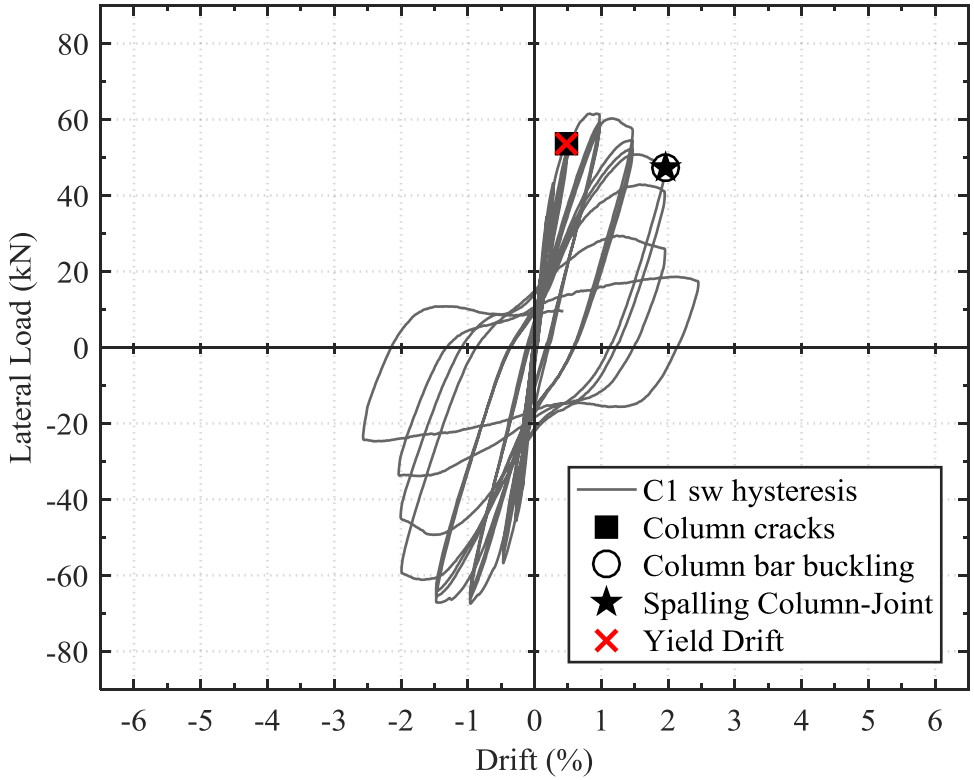

Figure 5.12. Force – drift response for specimen C1-sw with important events markers.

5.2.4.2. LOCAL BEHAVIOUR AND MOMENT CURVATURE

In Figure 5.13, the moment-curvature plots for the columns and beams of specimen C1-sw are shown. For the superior column in Figure 5.13 (a) very large curvatures are observed as the column bars yield and a plateau is reached in the moment curvature curve. The maximum moment observed in the column is 94.6 kNm, corresponding to an over-strength factor of 1.14 (+14.4%) compared to the calculated moment capacity, which is within the margin expected for strain hardening. For the inferior column, the behaviour remains linear.

Due to the removal of most of the slab contribution, the calculated hogging moment capacity is reduced for C1-sw. As can be seen in Figure 5.13 (c) and (d), the expected moment capacities in hogging and sagging are reached in the beams, but the curvatures remain very low, with a quasi-linear moment-curvature relationship. Yielding is however observed for the bottom beam bars. The ratio of observed maximum moment to the expected moment is 1.11 and 1.30 for the hogging and sagging moment, respectively. This observation confirms the anticipated contribution in hogging of the non-weakened ends of the slab, as the moment capacity calculation includes the influence of two non-cut slab bars on each side. In sagging a larger over-strength is observed, as it is also seen in the FE models of Section 3.5. This can be due to the bottom slab bars in the non-weakened slab section contributing in tension to the sagging moment capacity.

Overall, Figure 5.13 confirms the observed failure mechanism and shows that a single storey failure mechanism is reached, despite the slab weakening. Joint shear failure observed for the specimen without slab and transverse beams is prevented by the confinement due to the transverse

beams, which is unaffected by the sw cuts. The columns are hence still the weakest members in the sub-assembly, and the capacity of the superior column is reached before that of the beams.

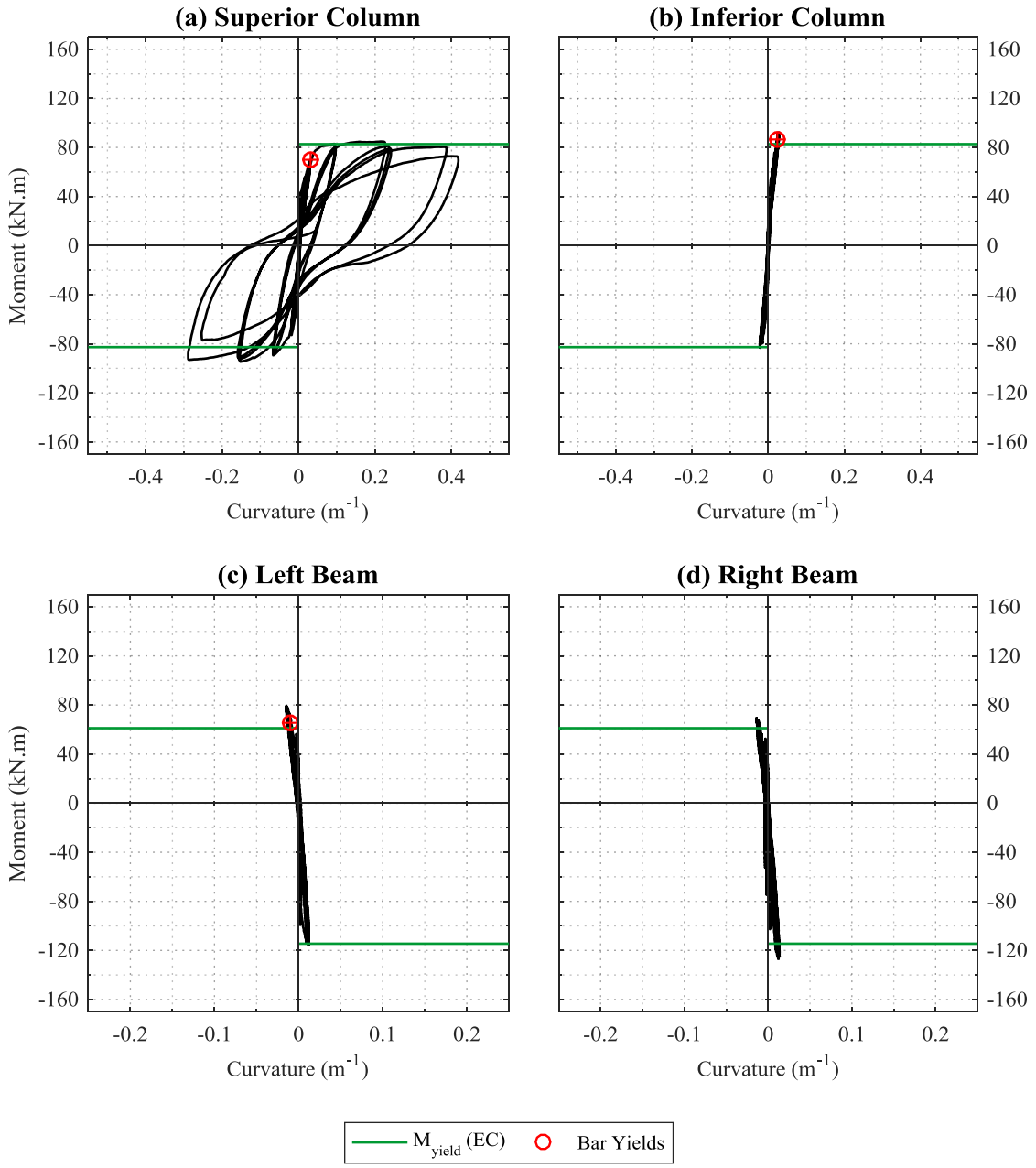

Figure 5.13. Moment Curvature behaviour in (a) superior and (b) inferior columns, as well as (c) left and (d) right for specimen C1-sw, with indication of expected moment capacities (EC) and experimental yield points.

5.2.4.3. SUMMARY

Overall the selective weakening of the slab alone does not lead to a change in the hierarchy of strengths for specimen C1-sw compared to C1. The confinement of the joint by transverse beams compared to specimen C-noSLT is sufficient to prevent joint shear failure. An isolated failure of the superior column is hence observed, leading to an undesirable non-ductile with limited energy dissipation.

5.2.5. C-EC8 - SPECIMEN DESIGNED TO MODERN SEISMIC GUIDELINES (EUROCODE 8)

5.2.5.1. GLOBAL PARAMETERS AND FAILURE MECHANISM

For the control specimen designed to Eurocode 8, C-EC8, as expected, a more ductile cyclic performance is observed compared to C1. As shown in Table 5.1, a very high strength of 123.9 kN (+96.4 vs C1) and a large ductility of 5.9 (+61.9%) are recorded for C-EC8. It can be seen in Figure 5.14 that cracks are spread over a large area of the beams, slab and columns, leading to a more dissipative failure overall. At the ultimate state, concrete crushing is observed at the base of the superior column and the top of the inferior column.

(a) (b)

Figure 5.14. Final damage state in C-EC8; (a) superior column, (b) beam underside.

Moreover, a very high dissipated energy (172.3 kNm, +437.1% vs C1), with modest post-peak softening and inter-cycle strength degradation are observed as a consequence of the improved seismic detailing. Overall, an improved seismic performance is observed, which is in line with the predictions from FE modelling in Chapter 3 and the obtained maximum lateral force is close to the predicted value of 128.6 kN (-4%).

The lateral force-drift response for specimen C-EC8 is presented in in Figure 5.15. The occurrence of cracking, spalling and yielding is also indicated. Flexural cracks in the columns are noticeable from 0.3% drift, while cracks in the beams are only observed in the 1.0% drift cycles. Still, the high reinforcement ratio of the column and joint ensure that yielding occurs first in the reinforcement bars at the bottom of the beam (0.89% drift).

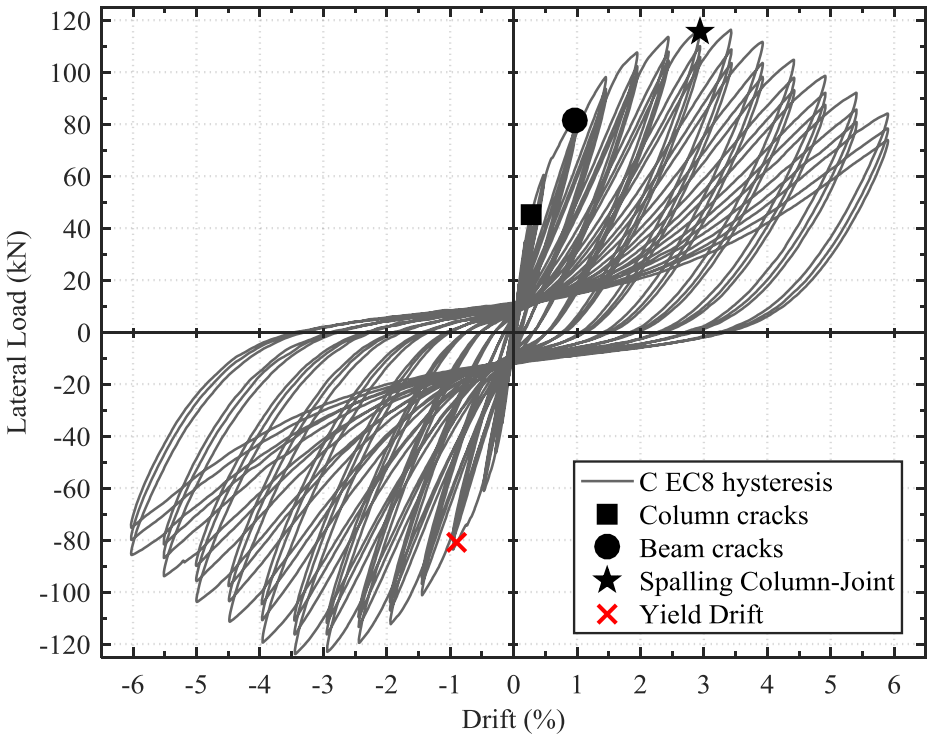

Figure 5.15. Force – drift response for specimen C-EC8 with important events markers

As shown in Figure 5.16, a large number of cracks is also observed in the slab and transverse beams. For the slab, five parallel cracks are seen in the top and bottom surface. However, the first noticeable crack at 1.5% drift originates at the end of slab away from the joint and then further extends towards the column, as indicated by the dark blue lines. The shape of this crack resembles the observed cracks in the transverse beams. In the transverse beams, torsional cracks (marked in dark red) are observed at 2.0% drift, leading to cracks around a wedge at the transverse beam/joint interface. This is similar to observations by Kam et al. (2010) and Cheung et al. (1991a). The reason for these torsional cracks is the difference in boundary conditions at the two ends of the transverse beam. The beam-end away from the joint is free to translate in the direction of loading, while the joint-end is fixed and hence contributes in resisting the rotation of the sub-assembly. This is representative of real structures, in which the mid-span of beams is not as restricted as the beam-ends. These cracks are not observed for the other control specimens, as the rotation of slab and joint are much lower, hence inducing less torsion in the transverse beams.

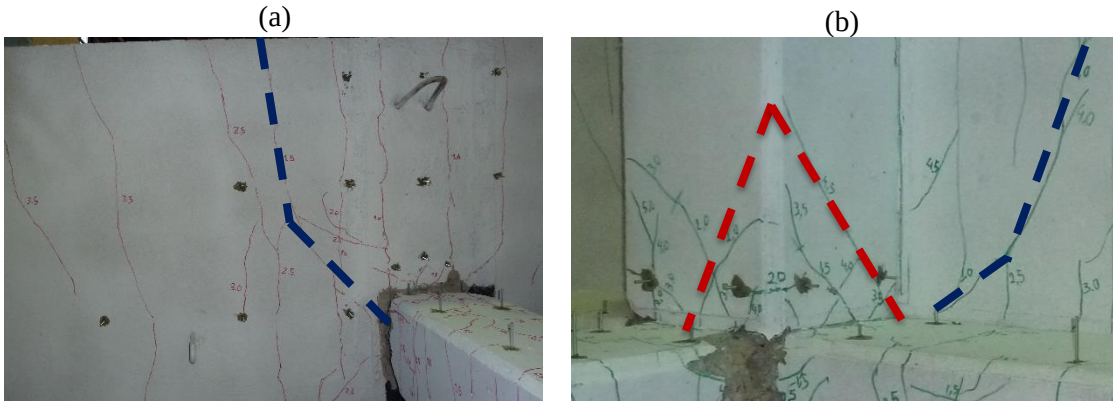

Figure 5.16. (a) cracks in the slab, (b) torsional cracks in transverse beam (red) and slab (blue).

Overall, rotation and damage in the columns is symmetric in the inferior and superior columns and no buckling is observed, corresponding to a significant improvement compared to C1. The peak force is reached at -3.45% drift, at which cover spalling is seen at the column/joint interfaces. With increased crushing at the superior column base and the top of the inferior column, strength degradation is observed, and the ultimate force is reached at 5.2% drift, corresponding to a ductility of 5.8

5.2.5.2. LOCAL BEHAVIOUR AND MOMENT CURVATURE

The contribution of the slab in the specimen's behaviour is highlighted by the final damage state. On the one hand, a large number of cracks are observed over the entire surface of the slab. On the other hand, despite implementation of capacity design, concrete crushing at the column/joint interfaces is observed for C-EC8. This ultimately causes failure of the specimen.

In the design, the ratio of the column moment capacities to the beam moment capacities, $\Sigma M_{Rc} / \Sigma M_{Rb}$ is 1.33, which should be a sufficient margin to induce failure in the beams, even when accounting for strain hardening. Looking at the moment-curvature in Figure 5.7, however, it becomes apparent that the actual moment reached in the columns (162.8 kNm) is lower than the expected 185.7 kNm (-12.3%).

The difference in moment capacity of the columns can be accounted for by an error in manufacturing of the specimen. When measuring the cross-section, it is noted that the actual dimensions of the column are not 300 by 300 mm, but rather 290 by 285 mm. Although the difference of 0.75 cm on either side of the column does not seem significant, due to the high reinforcement ratio and small cross-section dimensions with respect to the longitudinal reinforcement, a re-assessment using the M-N curves from EC2 show that failure is now expected in compression, at a lower applied moment of 172.5 kNm. This is closer to the obtained value (-5.9%) and is in line with the observed failure mechanism with spalling of the concrete in compression and no measured yielding of the main bars.

This alone, is, however, not responsible for the change in hierarchy of strengths, as the $\Sigma M_{Rc} / \Sigma M_{Rb}$ ratio remains sufficiently large (1.2) when taking the experimental column moment capacity into account. The more significant issue is encountered for the beams. The moment capacity of the beams is significantly larger than expected for the specimen, which ultimately leads to the strong-beam/weak column mechanism. For the sagging moment, the beam reaches a moment 56% higher than anticipated. The equations in Eurocode 8 take into account a potential over-strength from strain hardening of 1.3 and a higher over-strength of the beam bars can be excluded, as confirmed by the material tests presented in Table 3.3. Hence the increased sagging moment capacity is attributed to a larger proportion of the slab concrete contributing in compression than anticipated from the EC 8 equations. A larger effective width of slab raises the neutral axis, which

is in line with observations from the numerical modelling presented in Section 3.5, where it appears that the bottom row of slab bars act in tension under sagging moment, hence increasing the sagging moment capacity further.

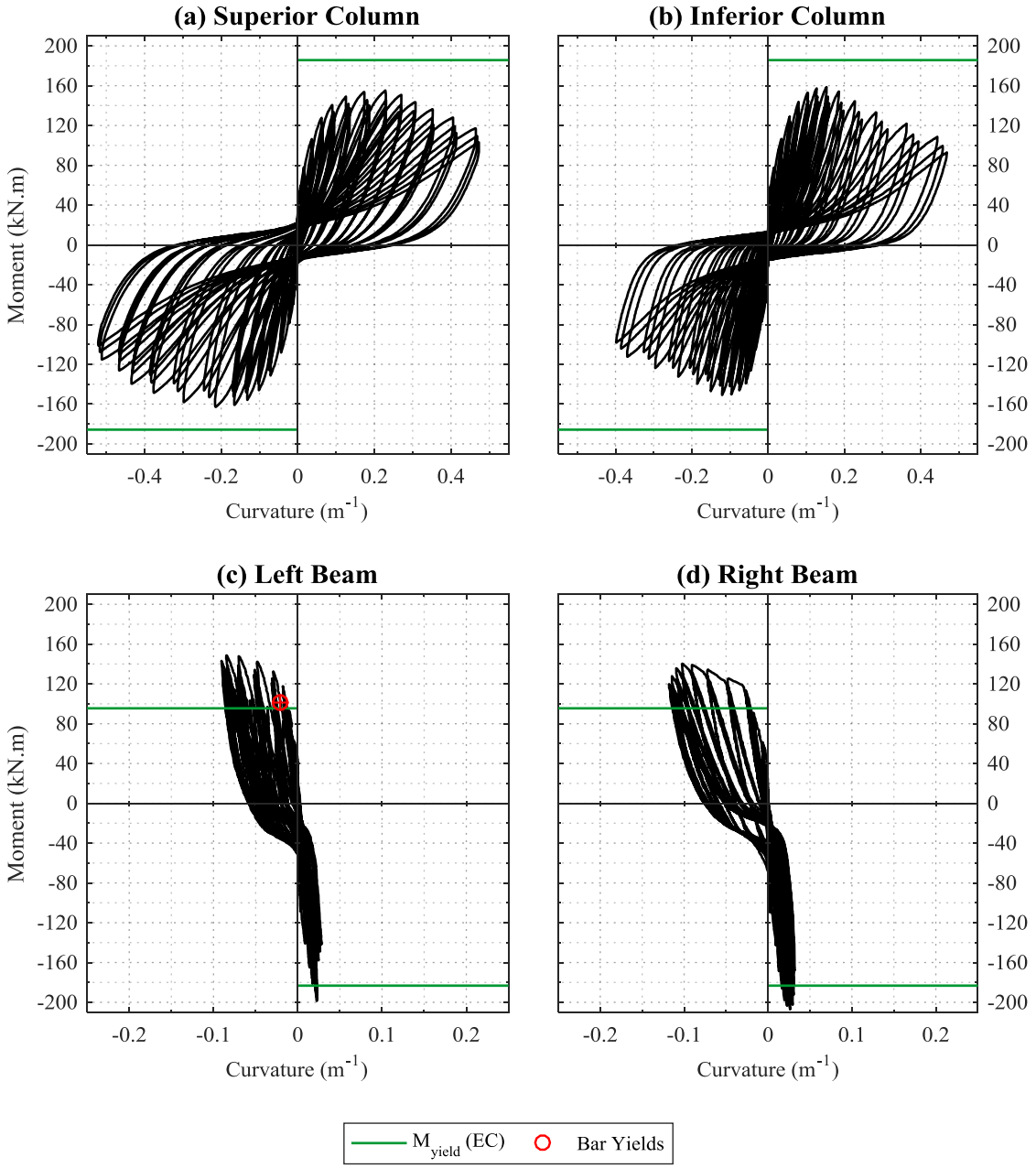

Figure 5.17. Moment Curvature behaviour in (a) superior and (b) inferior columns, as well as (c) left and (d) right beams for specimen C-EC8, with indication of expected moment capacities (EC) and experimental yield points.

For the hogging moment, the reason for the discrepancy cannot be attributed to the overstrength of the rebars, as the moment-curvature relation still exhibits a linear behaviour. Instead, a stronger slab reinforcement contribution than anticipated by the Eurocode 8 design equations is likely the reason for the underestimated hogging moment capacity. As shown in Figure 5.17, the beams remain elastic in hogging and indeed the experimental hogging yield moment capacity of the beams is at least 13.0% larger (the moment capacity is not reached experimentally) than anticipated by Eurocode 8 equations. This observation echoes results by Cheung et al. (1991b)

for which a capacity 39% higher than that calculated using seismic guidelines was observed for a specimen with slab. It is worth noting that for specimen C-noSLT, without slab, for which the hogging moment is reached, the prediction from EC8 is accurate (+9%). In the numerical model, high strains in the slab longitudinal bars along the entire width of the slab are observed. A longer effective width of the slab, i.e. the T-section of the beam, (830 mm, i.e. 5.5 times the thickness of the slab) hence contributes to the moment capacity of the beam than what is anticipated in section 5.4.3.1.1 of Eurocode 8 (i.e. 4 times the thickness of the slab). Including the entire slab, a moment capacity of 206.2 kNm is obtained, compared to the 183.3 kNm obtained when following EC8. This leads to an underestimation of the beam hogging capacity of only 0.5%.

The experimental evidence presented here-in is however not sufficient to make final conclusions on the adequacy of effective width calculations. The effective width of slab contributing to the beam moment capacity may be reduced in the more realistic case of bi-directional loading or within a full frame, which is not considered here.

5.2.5.3. SUMMARY

For C-EC8, a behaviour characterised by large strength and ductility is observed. Increased damage along the beams and the slab are observed as anticipated by FE modelling. The strong contribution of the slab and high over-strength of the beams in sagging and hogging, however, lead to an unexpected hierarchy of strength, with a concrete crushing failure in the columns at the ultimate state.

5.3. RETROFIT AND REPAIR

The results for three retrofitted and four repaired specimens are presented in this section. All specimens are designed with typical pre-1970's deficiencies according to the Portuguese RC code (REBA, 1967). The repaired specimens were initially tested only to trial the retrofit schemes, however, interesting results in terms of the effect of pre-damage and the consistency of retrofit effectiveness are observed and the results of these specimens are hence also presented in detail. Retrofitted specimens are specimens strengthened with FRP without any pre-damage, while repair specimens are heavily pre-damaged, as they correspond to control specimens initially tested to failure. The repair and retrofit procedures are described in detail in section 3.6.

The nomenclature of the specimens indicates what control specimen the retrofit is compared to ('C1' or 'C2'), whether the specimen is repaired ('RP') or retrofitted ('RT'), as well as which FRP strengthening scheme is applied ('A' or 'B'). The suffix '-sw' indicates selective weakening, while the suffix 'gs' indicated strands glued in the joint region.

C0-RP-A-gs is the first prototype specimen used to investigate the importance of the FRP strands and plastic tubes through the slab and joint.

C2-RP-A, corresponds to the repair according to scheme A of the heavily pre-damaged control specimen **C2** that has the same geometry and reinforcement detailing as C1 apart from an additional bar in the bottom of the beams.

Specimens **C1-RT-A, C1-RT-A-sw** and **C1-RT-B-sw** are retrofit specimens with the same reinforcement detailing and geometry as C1, the control specimen with slab and transverse beam.

C1-RT-A is retrofitted to scheme A, which aims to strengthen the columns only, to achieve a mechanism of failure including both columns.

C1-RT-A-sw is instead retrofitted with scheme A-sw, which includes selective weakening. The aim of this scheme is to ensure a higher ductility by increasing damage and rotation in the beams.

C1-RP-A-sw corresponds to the pre-damaged specimen C1 repaired with the same FRP strengthening and slab weakening intervention.

C1-RT-B-sw is retrofitted to scheme B, which aims to combine the effects of the first two retrofit schemes, hence enhancing the column strength significantly and inducing larger rotations and damage in the beams by selective weakening. The scheme also uses local retrofit of the beams near the beam/joint interface to ensure the plastic hinge is moved further along the beam. The joint is also retrofitted to avoid damage to the joint core.

Finally, **C-noSLT-RP-B** corresponds to the repaired control specimen without slab and transverse beam, i.e. with the typically tested cross-shaped geometry. The retrofit applied corresponds to scheme B, hence the same retrofit as in **C1-RT-B-sw**. This specimen is used to understand the role of slab and transverse beams on the effectiveness of a retrofit scheme.

A summary of the main results for all strengthened specimens is presented in Table 5.2. A detailed description of the cyclic behaviour of the repaired and retrofitted specimens is given. The results are compared to the respective control specimen and the design equations from CNR-DT-200.R1/2013 (CNR 2013). For all specimens the force-drift and moment-curvature figures are plotted with the same axes to facilitate visual comparison.

Table 5.2. Summary of experimental results (difference to C1 in brackets, apart from C-noSLT-RP-B, for which difference to C-noSLT is given)

Specimen	F_{max} (kN)	Main damage	Δ_y (%)	Δ_{max} (%)	Δ_u (%)	$\mu_{\Delta u}$	E_d (kN.m)	S (kN/mm)	K_i (kN/mm)	$F_{deg,1-2}$ (%)	$F_{deg,1-3}$ (%)	$\varepsilon_{FRP,max}$ (%)
C1-RT-A	87.71 (39.1%)	Both columns	-0.83 (36.4%)	-3.46	-5.25	6.32 (74.6%)	93.84 (192.5%)	-0.33 (-33.6%)	6.91 (4.6%)	10.86 (-53.2%)	20.26 (-70.1%)	0.14
C2-RP-A	89.67 (34.4%)	Both columns	1.29 (111.7%)	2.95	4.78	3.71 (-10.4%)	82.29 (197.7%)	-0.33 (-17%)	3.94 (-33.8%)	13.33 (78.7%)	23 (57.8%)	0.14
C1-RT-A-sw	71.61 (13.5%)	Beams, Joint	0.78 (27.6%)	-2.46	5.19	6.69 (84.9%)	94.53 (194.7%)	-0.17 (-66%)	6.39 (-3.2%)	13.92 (-40.1%)	24.36 (-64%)	n.m.
C1-RP-A-sw	76.8 (21.8%)	Beams, Joint	0.95 (55.7%)	2.46	5.84	6.16 (70.2%)	101.82 (217.4%)	-0.15 (-69.3%)	4.66 (-29.4%)	10.59 (-54.4%)	17.57 (-74.1%)	0.12
C1-RT-B-sw	86.86 (37.7%)	Beams, Columns	0.95 (55.7%)	3.43	6.50	6.86 (89.6%)	111.57 (247.8%)	-0.19 (-61.8%)	5.65 (-14.5%)	8.87 (-61.8%)	15.67 (-76.9%)	0.08
C-noSLT-RP-B	67.83 (50.2%)	Beams	-1.06 (57.3%)	-2.44	-2.98	2.82 (-45.9%)	19.22 (-39.6%)	-0.83 (464.6%)	3.84 (-20.4%)	6.07 (-67.1%)	8.57 (-70.7%)	0.09
C0-RP-A-gs	77.86 (23.4%)	Inf. Column	-0.96 (48.6%)	-1.45	-3.54	3.68 (1.8%)	69.19 (115.7%)	-0.3 (-39.3%)	3.9 (-40.9%)	11.38 (-51%)	14.6 (-78.4%)	n.m.

Note: Parameters defined in Chapter 4.

5.3.1. C0-RP-A-GS

As a first validation test of the retrofit schemes, C0[1], a pre-damaged specimen with similar properties to C1, was initially repaired with retrofit scheme RP-A-gs. This repair scheme is similar in application to retrofit RT-A, but the FRP strands are bonded to the concrete along their entire length instead of being passed through a plastic tube for the length of the joint between the two columns.

5.3.1.1. GLOBAL PARAMETERS AND FAILURE MECHANISM

The failure mechanism and observed damage are shown in Figure 5.18. As can be seen in Figure 5.18 (a), the FRP strand ruptured at the inferior column/joint interface. The failure mechanism is then governed by the behaviour of the inferior column, for which a large crack at the interface to the joint is observed. The overall failure mechanism is summarised by the schematic in Figure 5.18 (b).

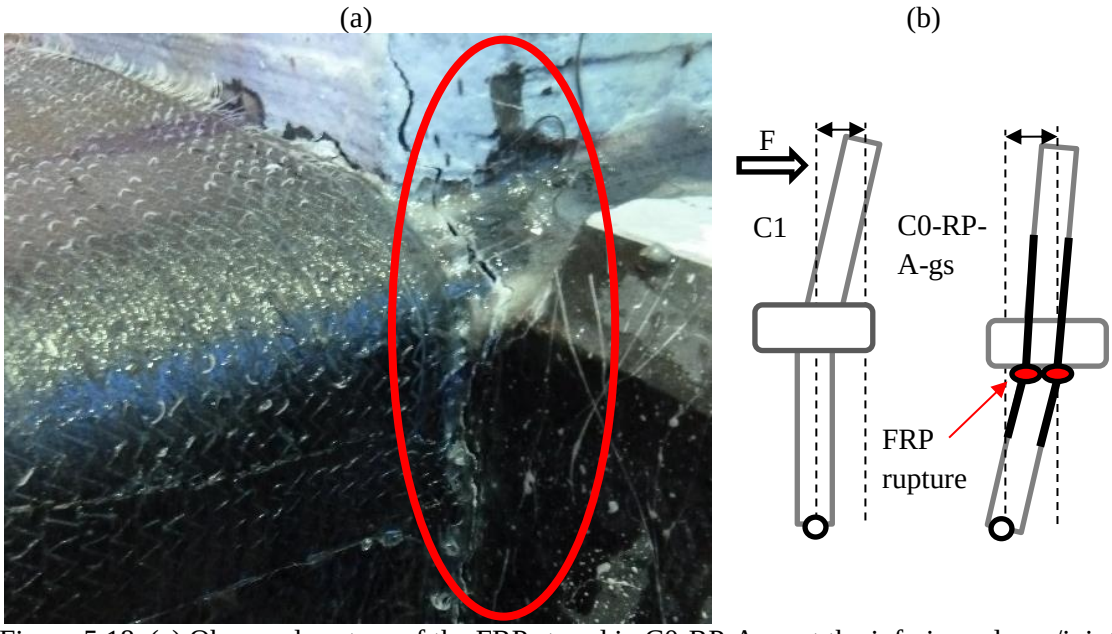

Figure 5.18. (a) Observed rupture of the FRP strand in C0-RP-A-gs at the inferior column/joint interface and (b) schematic global mechanism.

The effect of the retrofit is very limited as the strands rupture at a very early stage at a drift of -1.28%, as shown in the hysteresis plot in Figure 5.19. As the contribution of the FRP strand to the moment capacity of the column is reduced when the strand ruptures, a clear drop in strength is observed for C0-RP-A-gs at the rupture drift (Figure 5.20). The maximum lateral load of 77.9 kN recorded for the specimen is larger than for C1 (+23.4%), as the FRP strands are still intact at this point.

[1] Specimen C0 has the same design as C1, but is not presented in this thesis due to issues with the experimental set-up during the testing of the specimen.

Due to FRP confinement, the yield drift in the column occurs at a higher drift of 0.96% for C0-RP-A-gs with respect to C1 (+48.6% larger). Despite an increase in ultimate drift, the ductility of the specimen is hence similar to C1 (3.7, +1.8%). As buckling of the column reinforcement is prevented by the horizontal FRP wraps, the post-peak softening (-39.3% vs C1) and maximum inter-cycle strength degradation (-51% and -78% for $F_{deg,1\text{-}2}$ and $F_{deg,1\text{-}3}$, respectively) are significantly improved.

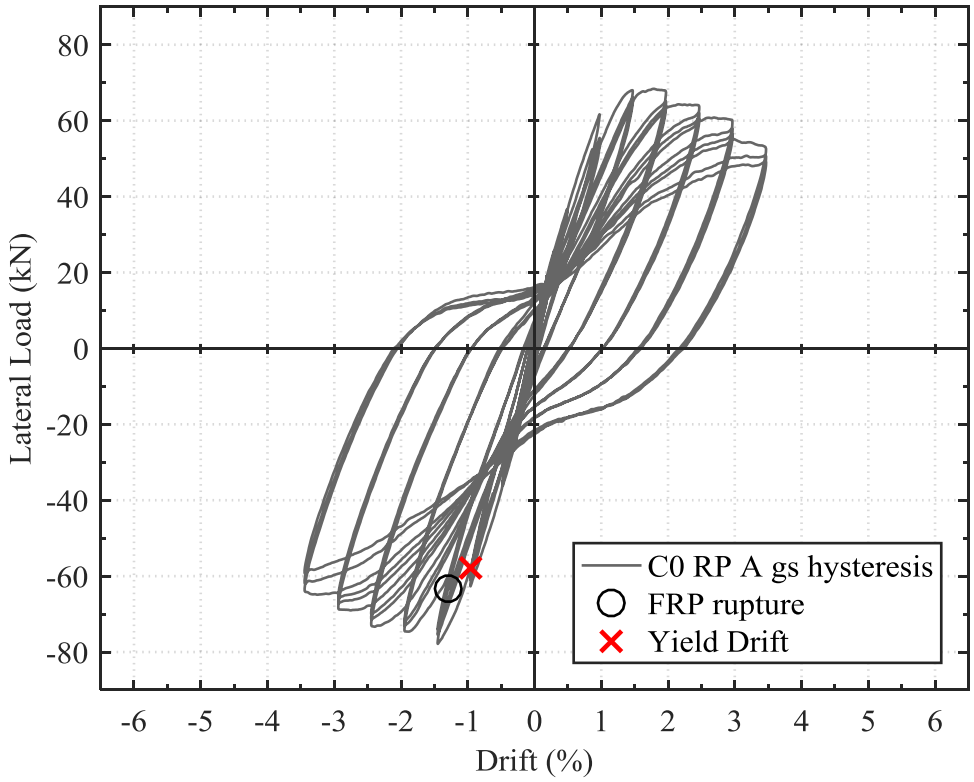

Figure 5.19. Force – drift response for specimen C0-RP-A-gs with important events markers.

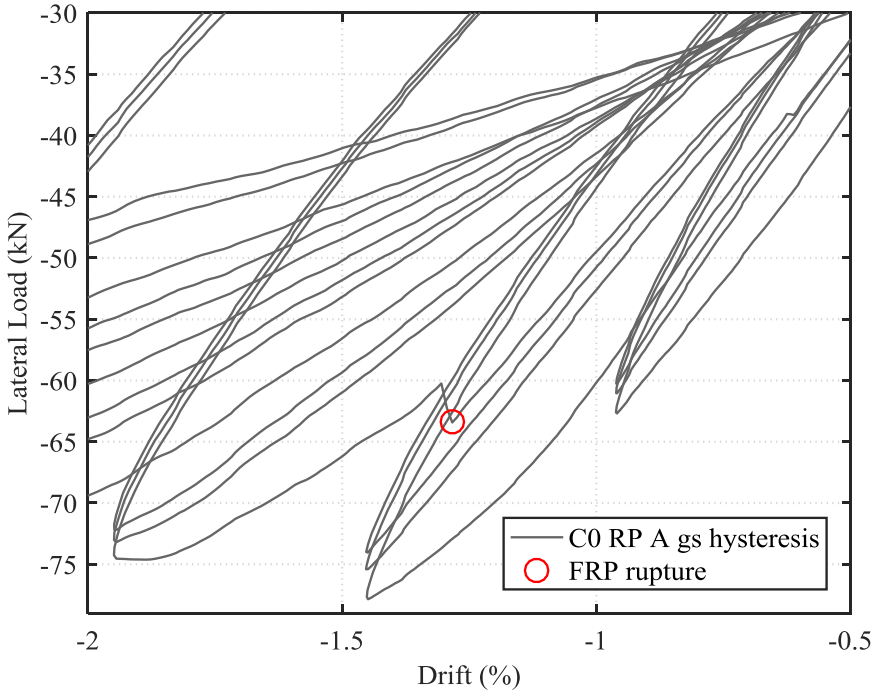

Figure 5.20. Drop in lateral load as the first FRP strand ruptures in the column/joint interface.

5.3.1.2. LOCAL BEHAVIOUR AND MOMENT CURVATURE

The moment-curvature plots for specimen C1-sw are presented in Figure 5.21. It can be seen that the superior column and beams present a quasi-linear behaviour throughout the test. Instead, the inferior column displays a significant non-linear behaviour, highlighting the observation of a single-storey failure.

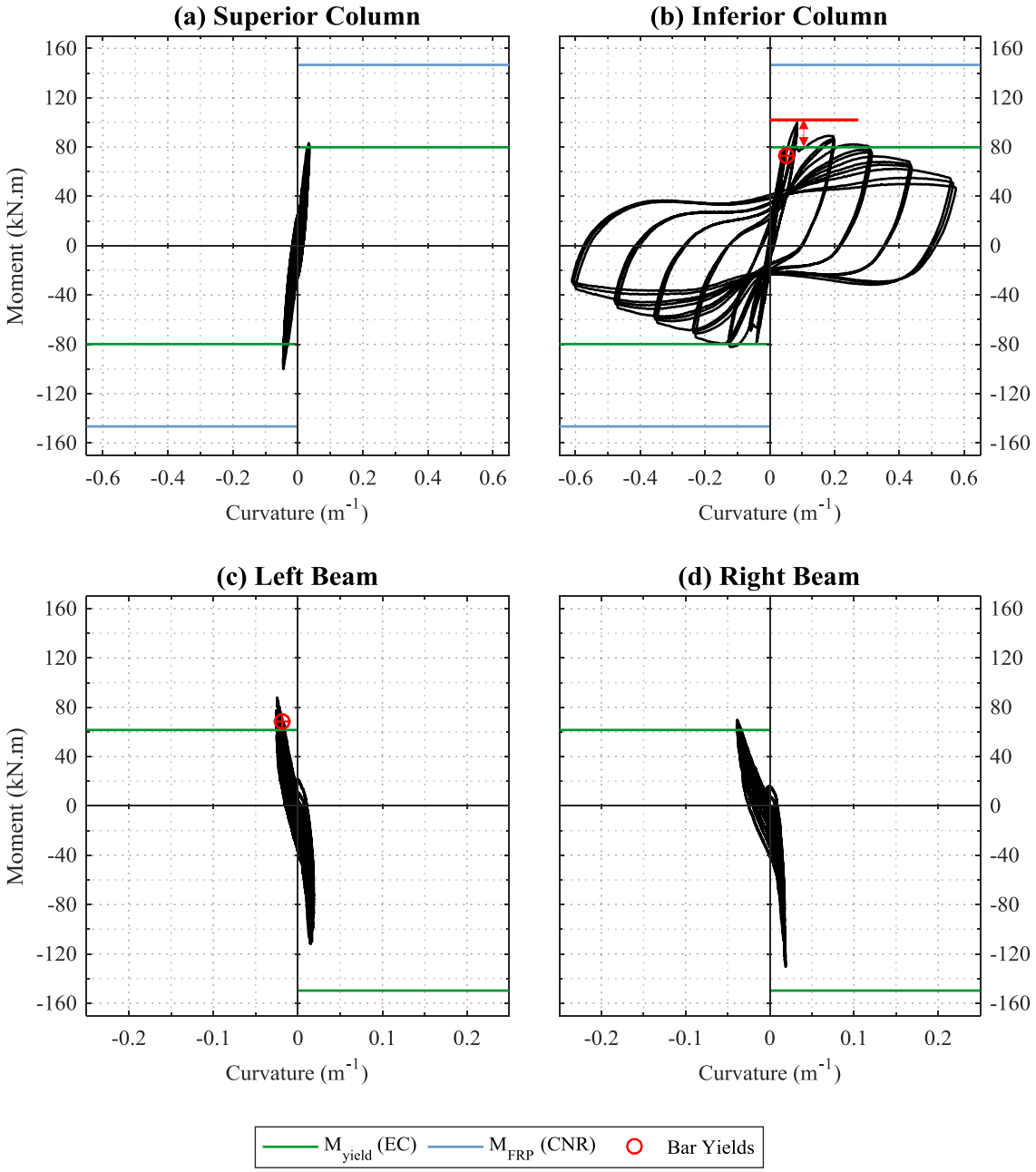

Figure 5.21. Moment Curvature behaviour in (a) superior and (b) inferior columns, as well as (c) left and (d) right beams for specimen C0-RP-A-gs, with expected moment capacities (EC for unstrenghtened and CNR for retrofitted members) and experimental yield points.

The effect of the FRP strand rupture in the inferior column is very clearly illustrated by Figure 5.21 (b). At first, the moment in the inferior column increases up to 100 kNm, beyond the expected moment for the non-retrofitted section (green line). Due to highly localised stress in the FRP at the transition between the splayed-out FRP on the column and the rolled FRP strand bonded to the concrete along the joint region, the FRP then ruptures suddenly (red line). As soon as the FRP strand ruptures at the inferior column/joint interface, a significant drop in the moment capacity is seen (indicated by the red arrow). The moment drops to the level expected for a non-retrofitted section (82 kNm), highlighting that without the strand contribution, the moment capacity at the column/joint interface, i.e. in slice 1, is reduced, despite the FRP along the rest of the column remaining intact. The effect of the FRP strand rupture is illustrated conceptually in Figure 5.22. This observation proves the importance of the strands in providing continuous strengthening along the columns and through the slab.

The effect seen is similar to observations made by Vrettos et al. (2013), who tested ground floor columns with splayed FRP anchors anchored into the base and recorded an increase in strength of 17% up to a sudden rupture of the FRP anchors, followed by a similar behaviour to the control specimen, with no improvement in ductility.

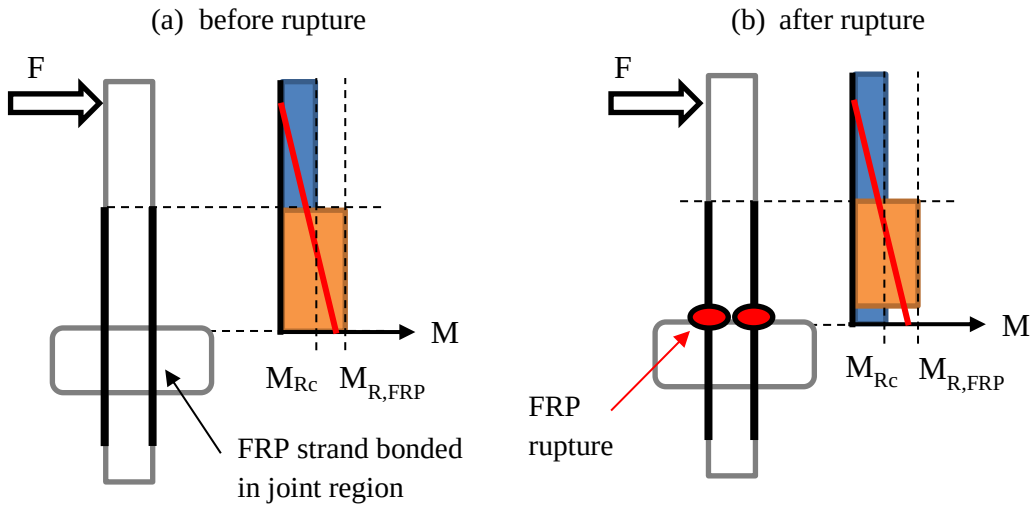

Figure 5.22. Schematic representation of the applied moment (red line) and with retrofitted, $M_{R,FRP}$, and non-retrofitted, M_{Rc}, moment capacities before (a) and after (b) FRP strand rupture.

5.3.1.3. SUMMARY

For C0-RP-A-gs, the effect of the FRP retrofit is suddenly lost at a low level of drift as the FRP strand ruptures under very high localised stress at the inferior column/joint interface. A non-ductile failure of the inferior column is then observed with a large crack opening at the interface to the joint. Apart from an improved softening behaviour due to the horizontal FRP wrapping preventing buckling, the retrofit after rupture of the strand provides no significant improvement compared to C1. This demonstrates the importance of providing continuous column strengthening through the slab and joint region to avoid failure at the column/joint interfaces.

5.3.2. C1-RT-A – RETROFIT A

5.3.2.1. GLOBAL PARAMETERS AND FAILURE MECHANISM

Figure 5.23 shows that for C1-RT-A the final damage state is characterised by a very pronounced crack at the slab/column interface (a), but with some cracks at the beam/joint interface and along the length of the beam (b). The observed damage echoes the results from FE modelling presented in Section 3.7.3. Throughout the test, no rupture or significant debonding of FRP is observed. The maximum FRP strain recorded in the strands is 0.11%.

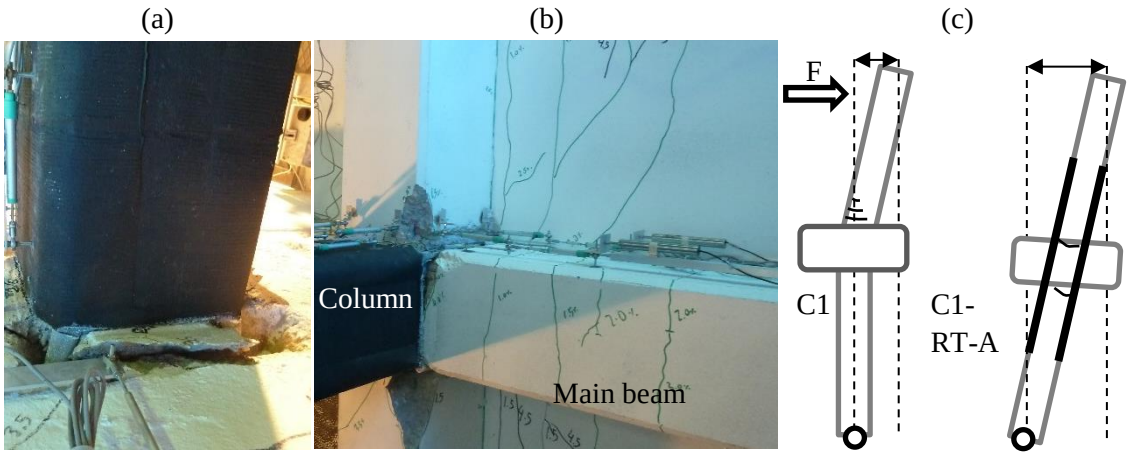

Figure 5.23. Observed damage in C1-RT-A (a) Damage at column/slab interface and (b) damage and cracks in the main and transverse beams; (c) schematic global mechanism.

For specimen C1-RT-A, large cracks at the slab-column and joint/inferior column interfaces are observed. The failure mechanism ultimately involves both columns, eliminating the single-storey mechanism of C1, as shown conceptually in Figure 5.23 (c). As a consequence, a higher value of drift is necessary to achieve the same curvature in the columns. Compared to the control specimens, yield is delayed significantly (0.83% drift, +36.4% compared to C1), as shown in Table 5.2.

Compared to control specimen C1, a number of other observations can be made suggesting that the intervention has positive effects on the local and global behaviour of the specimens. Firstly, the force-drift envelope, shown in Figure 5.24, indicates a larger lateral strength of 87.7 kN (+39.1% compared to C1). This lateral load capacity is well captured by the FE models in Section 3.6 (+3%). It also highlights that the FRP retrofit does not affect the initial stiffness, K_i, of the specimen significantly (+4.6%). Buckling of the column bars is successfully prevented due to the FRP confinement wraps, and the post-peak softening behaviour is hence considerably improved (-33.6% in slope compared to C1).

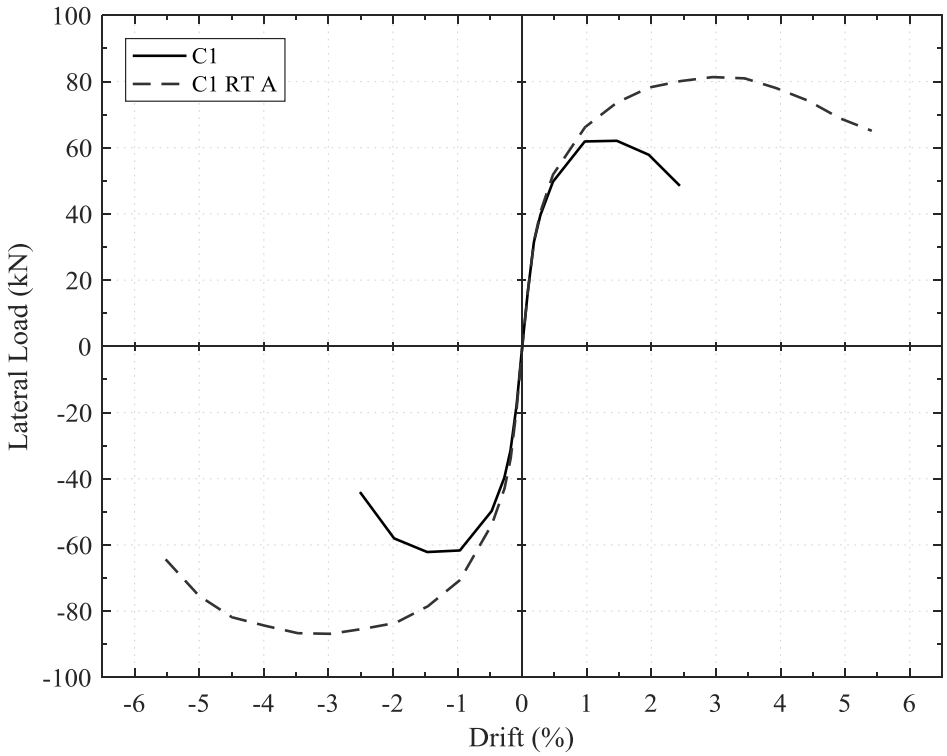

Figure 5.24. Force-drift envelope for specimens C1 and C1-RT-A.

With the reduced softening slope, a much larger ultimate drift compared to C1 is consequently obtained, leading to a large ductility of 6.32 (+74.6%). The larger ductility is attributed to a combination of increased confinement of the column through the FRP wraps and the aforementioned failure mechanism involving both columns rather than a single column, with quasi-symmetric rotation of the superior and inferior columns throughout the test.

The progression of damage in the specimen is highlighted by the force-drift hysteresis plot in Figure 5.25. Overall, a behaviour associated with a large strength and moderate softening after the peak lateral load can be observed. Compared to the hysteresis plot for C1 (Figure 5.6), a stronger pinching effect is noticeable for C1-RT-A. The increased pinching can be associated to the free movement of the FRP strands through the plastic tubes placed along the joint region, i.e. a ‘slippage’ of the FRP strands in the non-bonded region. Compared to steel jacketing, for which large hysteresis loops are observed due to plastic deformation of the steel, FRP retrofits have the drawback that the retrofit material itself is not ductile.

First cracks are observed in the inferior column/joint interface at 0.5% drift. Two initial cracks in the top of the slab, perpendicular to the direction of loading, are also observed at 0.5%. The first running along the top of the transverse beam, and a second parallel crack at a distance of 150-200 mm away from the transverse beam. At 0.8% drift, yield is observed in the superior column bars, but also in the bottom beam bars. This is shortly followed by yielding of the inferior column bars at 0.9% drift. At 1.0% a first crack in the beam is observed at the beam/joint interface, with a second crack around 200 mm away from the joint. The cracks in the top of the slab are now replicated on the bottom of the slab, with two visible parallel cracks in the bottom of the slab.

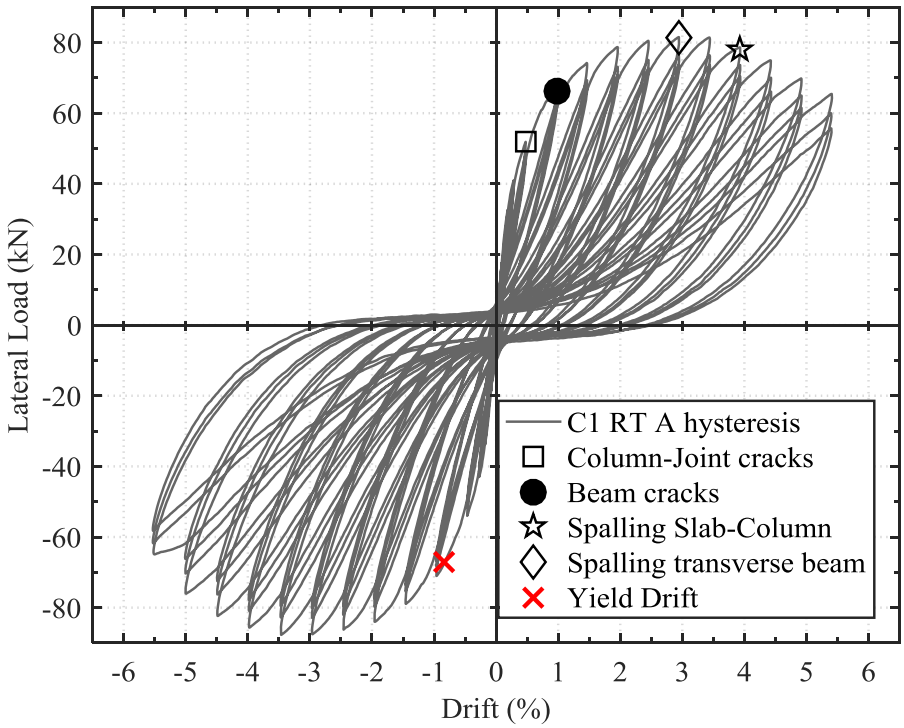

Figure 5.25. Force – drift response for specimen C1-RT-A with important events markers.

At 1.5% drift, a diagonal crack in the bottom of the slab, as well as some torsional cracks in the transverse beams are noticeable. These cracks become wider at larger drift values, with concrete starting to break away at the corner of the transverse beam at 3.0% drift. The damage in the transverse beam, seen in Figure 5.23 (b), can be described as a wedge of concrete breaking off, associated with the same torsional mechanism as described for C-EC8. The cracks in the column/joint interfaces open significantly with increasing levels of drift.

At 3.5% drift, the peak force of 87.7 kN is reached. After this point the longitudinal FRP on the columns debonds locally in proximity of the column/joint interface. This can be related to concrete crushing underneath the FRP wrap, which is observed at the end of testing when the FRP jacket is removed (Figure 5.26). This observation also explains the rather strong post-peak softening observed for the specimen. At 4.0% drift the crack along the column/slab interface opens fully, as shown in Figure 5.23. No other flexural cracks underneath the FRP can however be observed along the length of the column as shown in Figure 5.26, indicating a highly localised failure in the column/joint interface. Between 4.0% and 5.0% the concrete wedges appearing in the transverse beams fully break off. The strength of the specimen reduces with increased concrete crushing in the column/joint interface and the ultimate state is reached at -5.25% drift.

Figure 5.26. C1-RT-A superior column damage visible after removal of the FRP jacket.

5.3.2.2. LOCAL BEHAVIOUR AND MOMENT CURVATURE

Looking at the moment curvature behaviour for the columns of specimen C1-RT-A in Figure 5.27, a major difference to the control specimen becomes apparent. Rather than a linear elastic behaviour of the inferior column, as seen for C1, due to the FRP strands, the inferior column is activated, leading to quasi symmetric rotation of both columns. Similar peak curvatures are hence observed (0.44 m^{-1}), and yield is recorded in the rebars of both columns. This confirms further that the failure mechanism involving both columns presented in Figure 5.23 (c) is indeed obtained.

The large lateral load observed for this specimen can be ascribed to an increase in moment capacity of the columns compared to the 89.2 kNm in C1 due to the FRP strands. For both columns an increased moment capacity is observed due to the retrofit, with a maximum moment of 115.5 kNm, corresponding to a 29.4% higher capacity than for C1. This increase is however 21.6% lower than the expected moment capacity of 147.4 kN calculated using the CNR guidelines.

The absence of flexural cracks along the length of the column suggests that the splayed-out FRP bonded along the column is sufficient to increase its moment capacity. The large cracks observed at the joint-column interfaces, however, indicate that where the FRP strand is not bonded to concrete, but instead passed through a plastic tube and hence free to move, the contribution of the FRP to the moment capacity is reduced. In this section, the strain of the non-bonded strand is controlled by the relative elongation of the superior and inferior column, rather than the tensile strain in the fully bonded FRP. As this observation is shared for all retrofit specimens, this lower-than-expected moment is addressed in more detail in section 6.1 of the Discussion chapter.

Due to the higher capacity of the retrofitted columns, the beam rotation under sagging moment is also observed to increase, leading to larger curvatures and damage in the bottom face of the beams, which are not observed in C1. The effect of the slab and asymmetric reinforcement detailing can be readily observed. As shown in Figure 5.27 (c) and (d), the sagging moment capacity is reached and the bottom beam bars yield. The curvature in the beam in hogging is however limited due to the high strength and stiffness of the slab, with a maximum curvature in hogging (+0.015 mm^{-1}) nearly ten times lower than that in sagging (-0.13 mm^{-1}). The beam exhibits a linear behaviour in hogging and no yielding is recorded. This non-symmetric behaviour of the beams limits their damage and hence failure is not governed by beam failure.

Furthermore, for the beams is that the maximum sagging moment of 97.4 kNm in the beams exceeds the prediction of 61.7 kNm by 57.8%. The overstrength (1.58) is much larger than the expected overstrength factor of 1.3 for strain hardening considered in the EC8 design formulas. As for specimen C-EC8, the reason for this may be found in the contribution of the bottom slab reinforcement in sagging due to a larger effective width of slab participating.

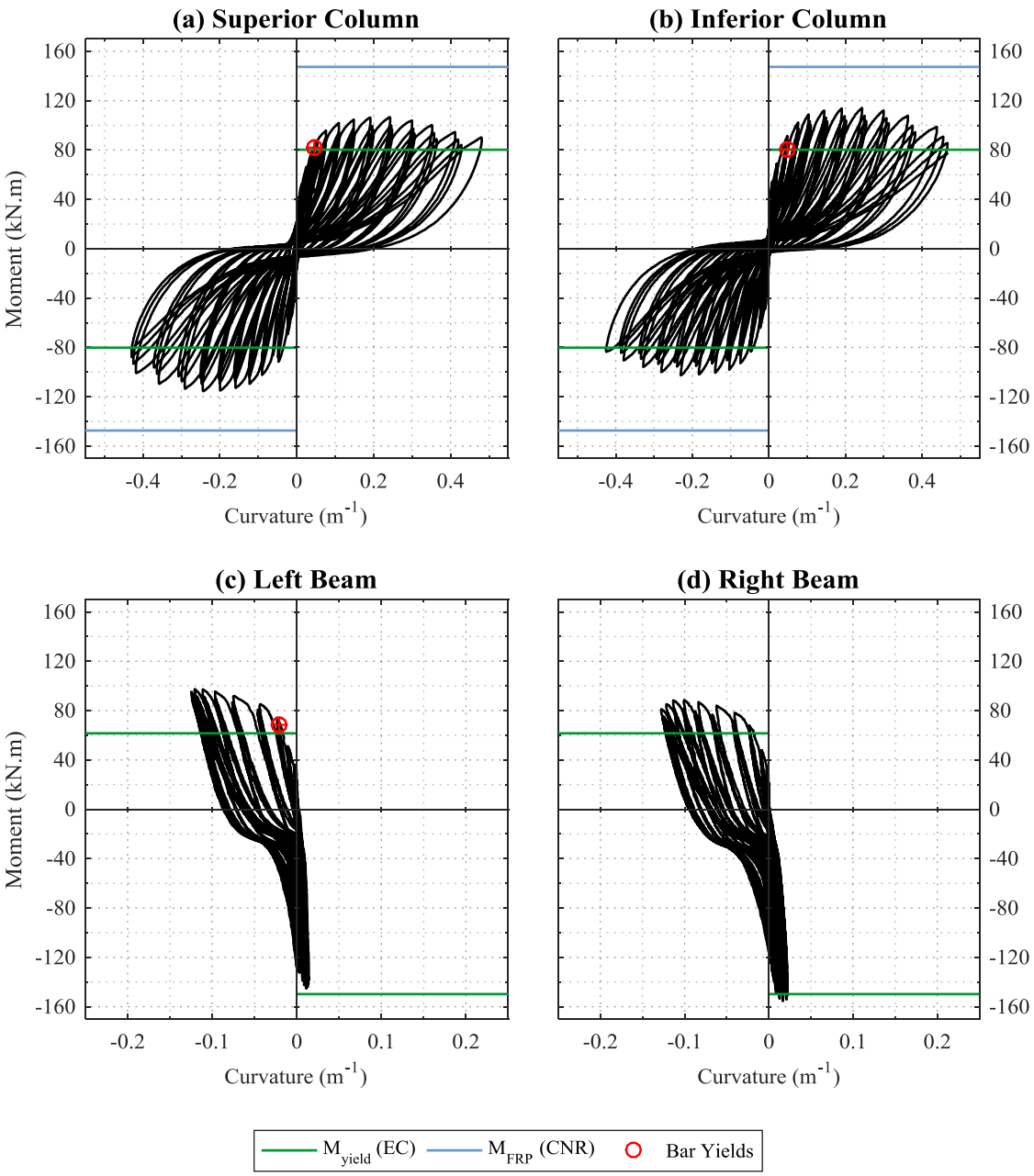

Figure 5.27. Moment Curvature behaviour in (a) superior and (b) inferior columns, as well as (c) left and (d) right beams for specimen C1-RT-A, with expected moment capacities (EC for unstrenghtened and CNR for retrofitted members) and experimental yield points.

5.3.2.3. SUMMARY

Overall, the aims of retrofit RT-A in increasing the strength of the specimen by increasing the moment capacity of the columns, and increasing the ductility by increasing the rotation of the inferior column, are achieved. The results obtained are similar to the observed failure mechanism in the FE model presented in Section 3.6.2.2. The yield drift of the retrofitted specimen is also delayed compared to the control specimen, indicating a better behaviour for more moderate drift levels. A strong contribution of the slab to the beam behaviour, inhibiting significant rotation of the beams, is observed, hence causing failure at the column/joint interfaces. The retrofit alone therefore does not redress the unfavourable strong-beam/weak-column global failure mechanism.

5.3.3. C2-RP-A – REPAIR OF SPECIMEN C2

5.3.3.1. GLOBAL PARAMETERS AND FAILURE MECHANISM

For specimen C2-RP-A with pre-damage, similar observations in terms of the overall behaviour and failure mechanism can be made as for C1-RT-A. As shown in Figure 5.28 (a), the behaviour of C2-RP-A is governed by significant cracks at the joint-column interfaces. Again, rupture of the FRP strands is not observed and a maximum strand strain of 0.14% is recorded (+22.1% vs C1-RT-A).

(a) (b)

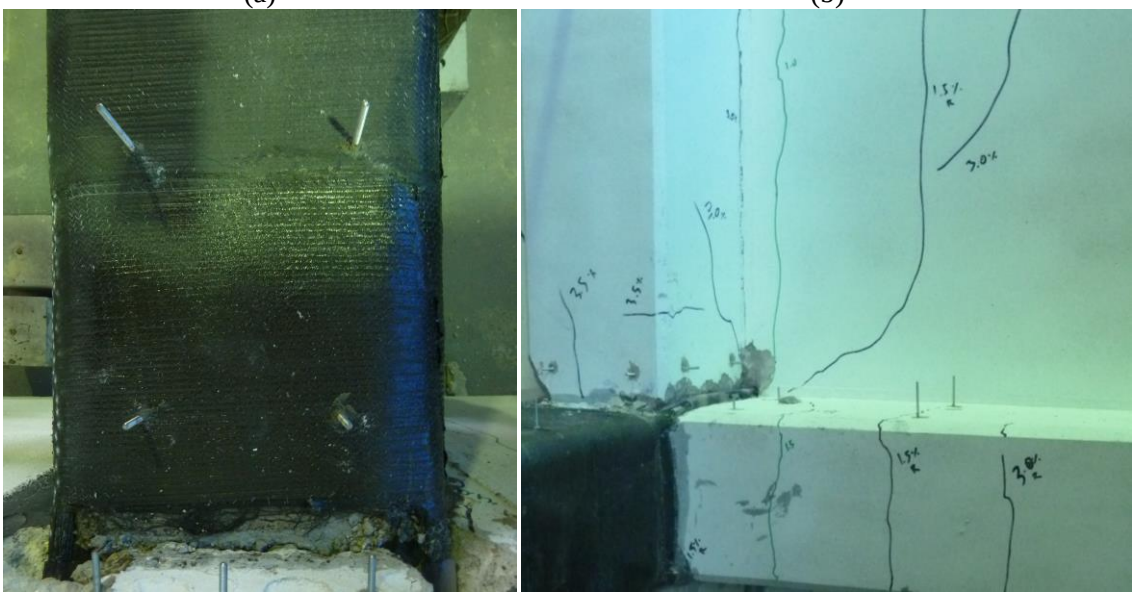

Figure 5.28. Final damage in specimen C2-RP-A: (a) large crack at superior column/joint interface; (b) cracks in bottom of beam and slab.

Few cracks in the beam and slab are observed, as shown in Figure 5.28 (b), but these are less severe than seen in C1-RT-A. The additional beam reinforcement leads to a more pronounced weak-column/strong-beam hierarchy of strengths for C2-RP-A, similar to the observations for control specimen C2 compared to C1.

For C2-RP-A a peak lateral force of 89.7 kN is achieved, corresponding to an improvement of +34.4% with respect to the control specimen C2. This increase in strength is only marginally lower than that for the C1-RT-A. Looking at Table 5.2, the post-peak softening behaviour is very similar to C1-RT-A and the improvement with respect to C2 is again not very large (-17%).

Moreover, despite an increased value of ultimate drift, a reduction in ductility is observed compared to the control specimen (-10.4%). This can be explained by a relatively large yield drift (1.29% drift), which is a consequence of the significantly reduced initial stiffness of the specimen (-33.8 % compared to C2), as shown in Figure 5.29. The initial stiffness is also the main difference for the repaired specimen, as it is nearly half of that of the retrofitted specimen C1-RT-A (-42.9%). This observation is in direct correlation with the pre-cracked concrete in the columns, seen in

Figure 5.30. A further consequence of the pre-damage is an increased inter-cycle strength degradation compared to C2 and C1-RT-A.

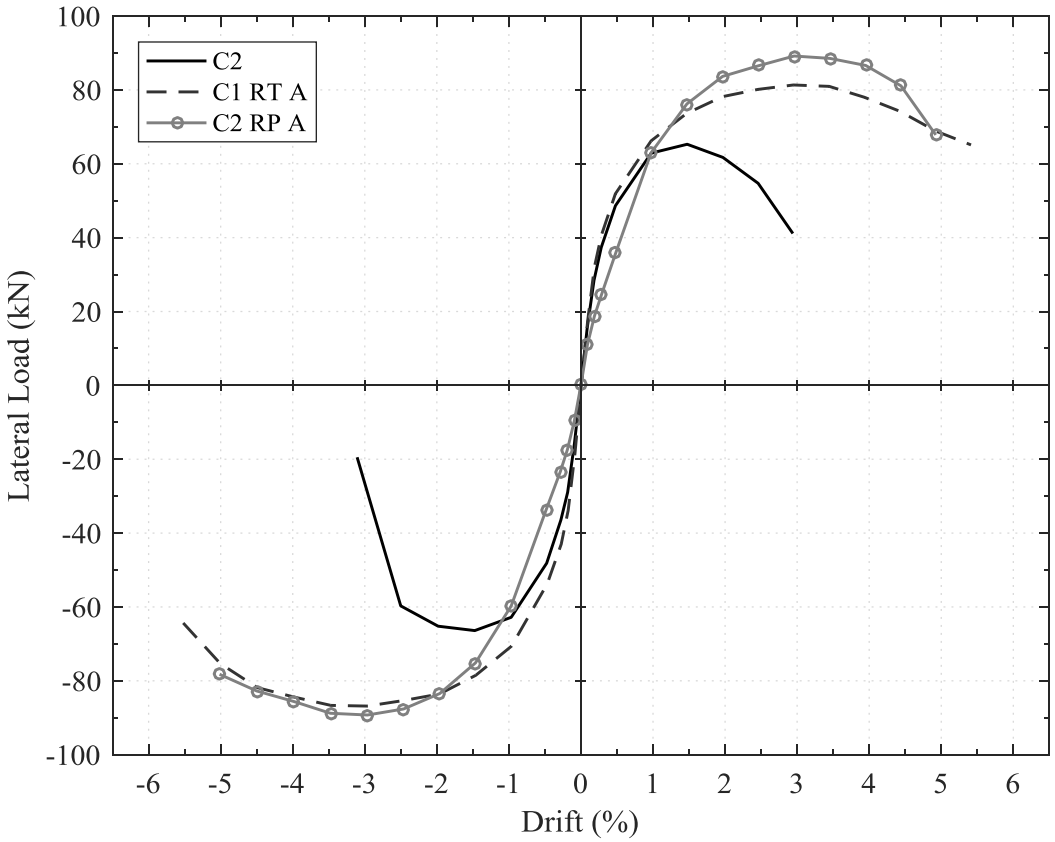

Figure 5.29. Comparison of the force displacement envelopes for C2, C2-P-A and C1-RT-A.

(a) (b)

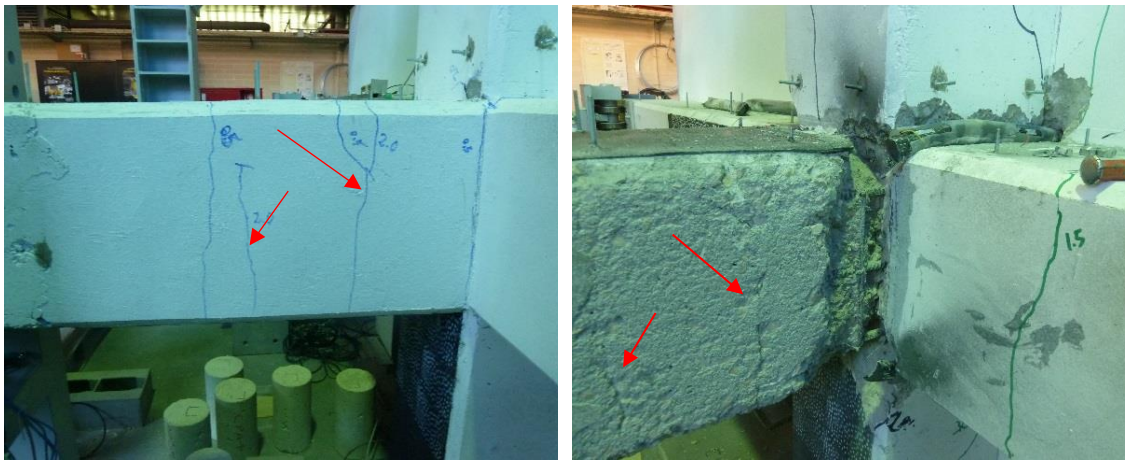

Figure 5.30. Cracks in inferior column: (a) before repair in C2; (b) after removal of FRP in tested C2-RP-A, with no new visible cracks in column (pre-cracks indicated by red arrows).

At 2.5% drift some debonding of the FRP jacket near the column/joint interfaces is observed. At 3.0% drift the peak lateral force is recorded. As for C1-RT-A, torsional cracks in the transverse beam appear at this stage, with concrete wedging initiating at 3.5%. The spalling of the concrete wedge in the transverse beams is however less significant than for C1-RT-A, as it can be seen in

Figure 5.30 (b). Finally, at the ultimate state, crushed concrete appears to escape from the FRP jacket, indicating spalling at the column/joint interface.

After removal of the FRP jacket (Figure 5.30 (b)), localised spalling is confirmed. Moreover, apart from the crack at the joint interface, no new cracks in the column are observed, as highlighted by the comparison of column cracks for C2 and C2-RP-A Figure 5.30 (a) and (b). This shows that the FRP applied along the column length is sufficient and that the failure is dominated by the behaviour at the column/joint interface.

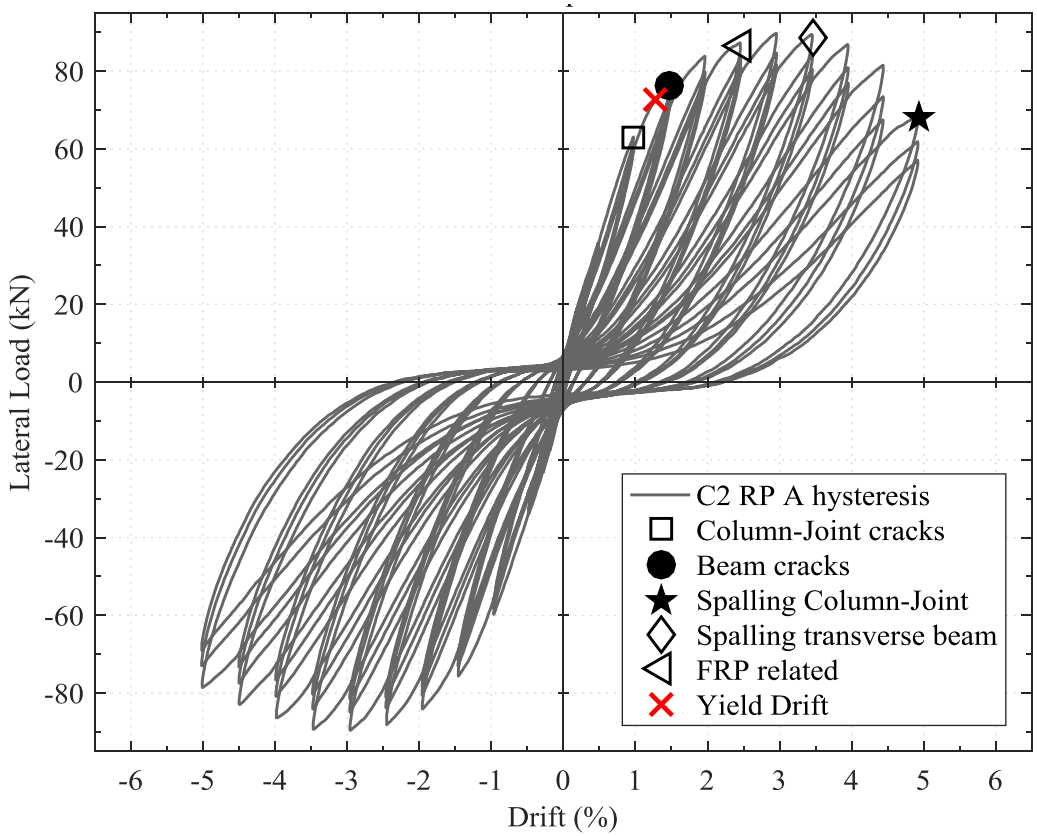

Figure 5.31. Force – drift response for specimen C2-RP-A with important events markers.

5.3.3.2. LOCAL BEHAVIOUR AND MOMENT CURVATURE

The moment-curvature diagrams for specimen C2-RP-A are shown in Figure 5.33. Again the behaviour of superior and inferior columns is quasi-symmetric and yield is observed in both columns, which confirms that the non-ductile single-storey failure for C2 is prevented by the repair and strengthening. The behaviour of the columns shown in Figure 5.33 (a) and (b) is similar to specimen C1-RT-A, with similar peak curvatures (0.44 m^{-1}) and a similar maximum column moment of 116.8 kNm (+1.1%). The column moment is 23.7% lower than the calculated capacity using the CNR guidelines. While no new cracks in the column are observed, the large cracks at the column/joint interfaces indicate localised failure, which is again addressed in more detail in section 6.1.

The large increase in column moment capacity also leads to a significant increase in dissipated energy compared to C2 (+197.7%). As the behaviour of C2-RP-A and C1-RT-A is dominated by large column deformations, the difference in energy dissipation at the same level of drift, shown in Figure 5.33 (a), is minimal between repair and retrofit specimens.

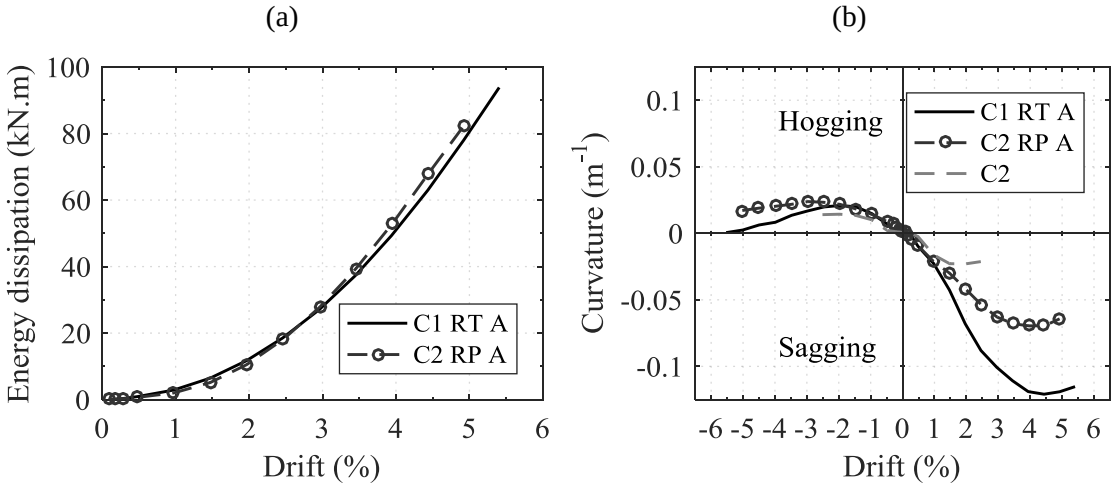

Figure 5.32. Comparison of specimens C1-RT-A and C2-RP-A; (a) Energy dissipation and (b) beam curvature against drift.

As for C1-RT-A, due to the higher capacity of the retrofitted columns, the rotation in the beams is observed to also increase compared to C2, leading to larger curvatures and damage in the beam bottom face as shown in Figure 5.33 (b). Failure is however not reached in the beam, and this can be explained by the slab providing a high stiffness and added capacity to the top of the beam, limiting its rotation in hogging. It can be seen in Figure 5.33 (b) that while the beam rotation in sagging nearly triples compared to C2 (+199.8%), in hogging the difference is less important (+72.8%).

The effect of the additional beam reinforcement in C2-RP-A is however highlighted by the significant difference that can be noticed for the beams in Figure 5.32 (c) and (d). While the beam behaviour in sagging is non-linear for specimen C1-RT-A, both beams present a nearly linear elastic behaviour for C2-RP-A. As shown in Figure 5.32 (b), a lower maximum beam sagging curvature (-0.07 compared to -0.13 m^{-1}) is hence observed for C2-RP-A. This is due to the larger sagging moment capacity as a result of the additional beam bar (+34.1% compared to C1-RT-A) and explains the reduced number of cracks in the beams for C2-RP-A.

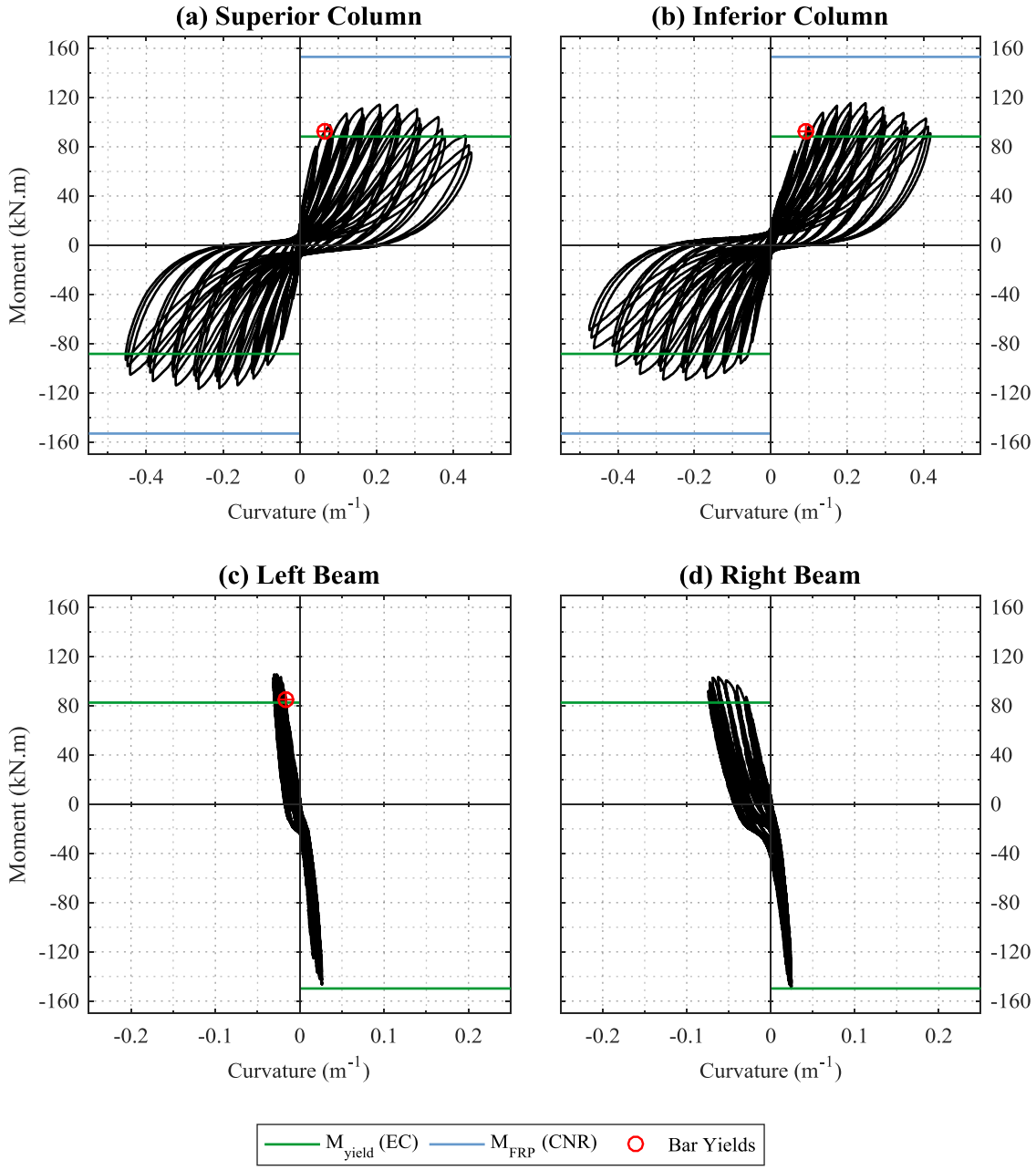

Figure 5.33. Moment Curvature behaviour in (a) superior and (b) inferior columns, as well as (c) left and (d) right beams for specimen C2-RP-A, with expected moment capacities (EC for unstrenghtened and CNR for retrofitted members) and experimental yield points.

5.3.3.3. SUMMARY

It is shown that the failure mechanism for C2-RP-A is similar to the retrofitted specimen C1-RT-A. The repair scheme successfully improves the global and local behaviour of the beam-column joint. Delayed yielding and no buckling of the column bars is observed, demonstrating the effectiveness of the FRP confinement wraps. Despite significant damage in C2, for C2-RP-A, an improved dissipative behaviour with increased capacity is achieved in the repaired specimen, showing that the repair method is successful. The ductility and initial stiffness of the repaired specimen are however significantly reduced.

5.3.4. C1-RT-A-SW - RETROFIT A WITH SELECTIVE WEAKENING

5.3.4.1. GLOBAL PARAMETERS AND FAILURE MECHANISM

For the specimen retrofitted to scheme A with selective slab weakening, C1-RT-A-sw, the final damage state is shown in Figure 5.34. As expected, a change in hierarchy of strengths is observed, with more damage occurring in the beams and an improved cyclic behaviour being achieved as compared to C1 and C1-sw. Figure 5.34 (a), highlights that no cracks along the column are detected after removal of the FRP. As predicted by FE-modelling in Section 3.7.3, significant cracking along the beams is observed in Figure 5.34 (b). Moreover, some cracks in the joint are noticeable after removal of the transverse beams (Figure 5.34 (c)). Throughout the test no significant debonding or rupture of the CFRP is observed.

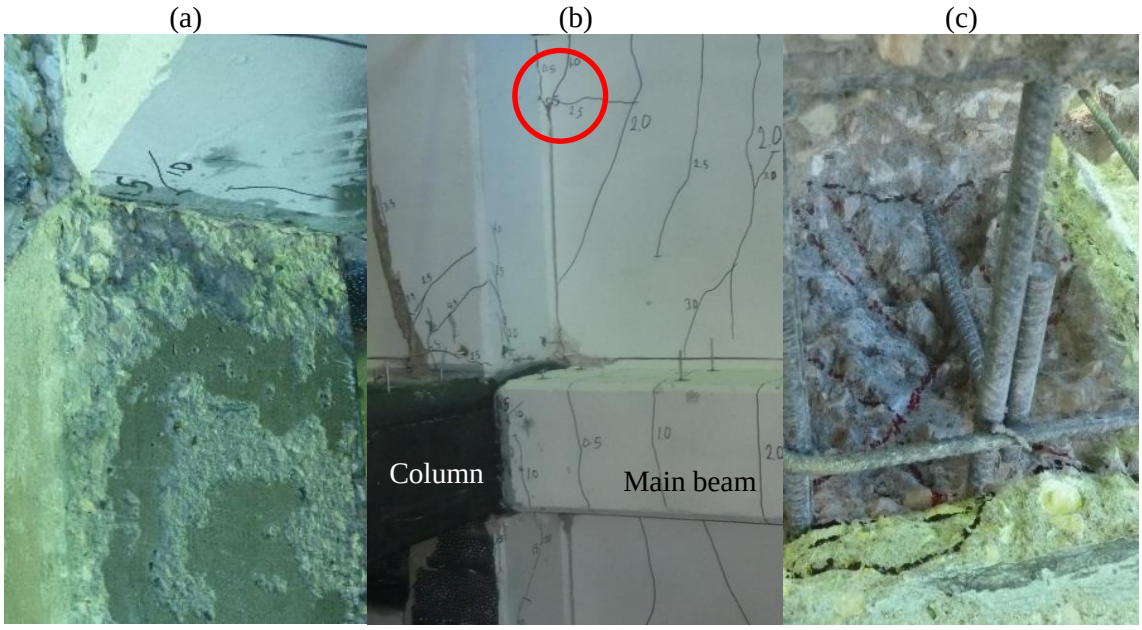

Figure 5.34. Final damage state in C1-RT-A-sw: (a) No cracks in column after removal of FRP; (b) significant cracks in main and transverse beam; (c) damage in joint visible after removal of transverse beam.

As shown in the comparison of force-drift envelopes in Figure 5.35, the increase in lateral load resistance is less significant for C1-RT-A-sw (+13.5 % vs C1) then for C1-RT-A (+39.1%). Compared to the control specimen C1, significant increase in displacement ductility is however observed for C1-RT-A-sw (6.69, +84.9% vs C1), which is larger than that achieved in C1-RT-A (6.32, +74.6%). Due to the prevention of column bar buckling, it can also be observed that the post-peak softening is drastically improved compared to C1 (-66%) and that this improvement is more significant than for C1-RT-A. In terms of dissipated energy C1-RT-A-sw provides the same increase as C1-RT-A (+194.7% vs C1), despite having a lower lateral load resistance.

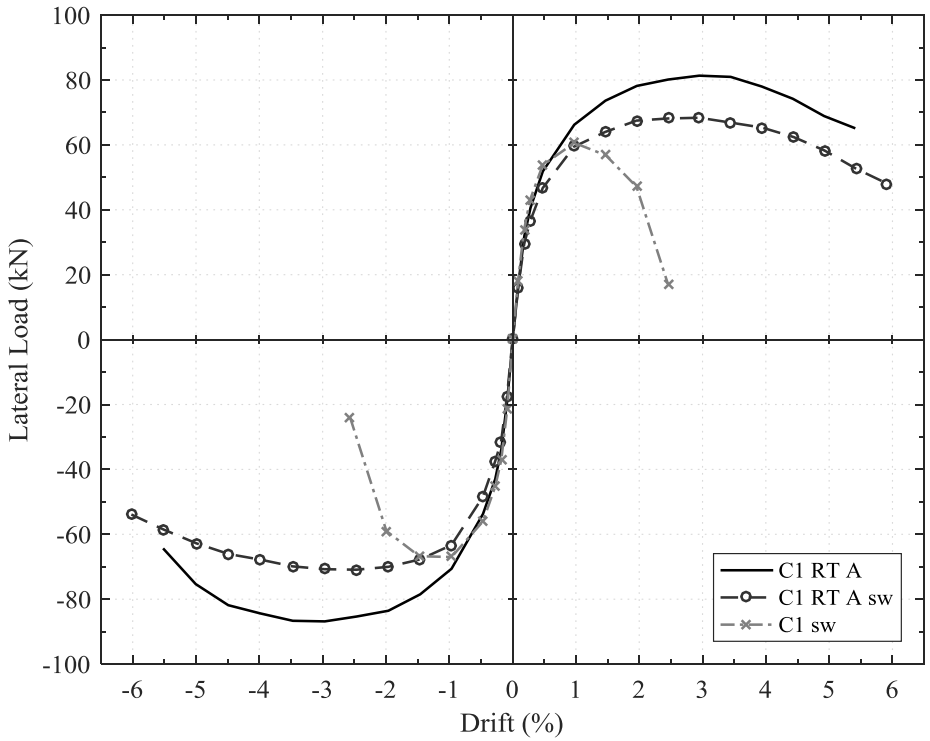

Figure 5.35. Comparison of the force-drift envelope for C1-RT-A-sw with C1-RT-A and C1-sw.

The development of damage in specimen C1-RT-A-sw is shown in Figure 5.36, indicating the occurrence of cracks, yielding and concrete spalling. At first, cracks in the beam are observed in the bottom face at lower drift levels (0.5% drift) compared to C1-RT-A (1%). Yield is then recorded at 0.78% drift (+27.6% vs C1) in the column bars. This is followed by yield in the bottom beam bars at 1.24 % drift and in the top beam bars at 1.89% drift. The first cracks in the columns are observed at the column/joint interface at 1.5% drift.

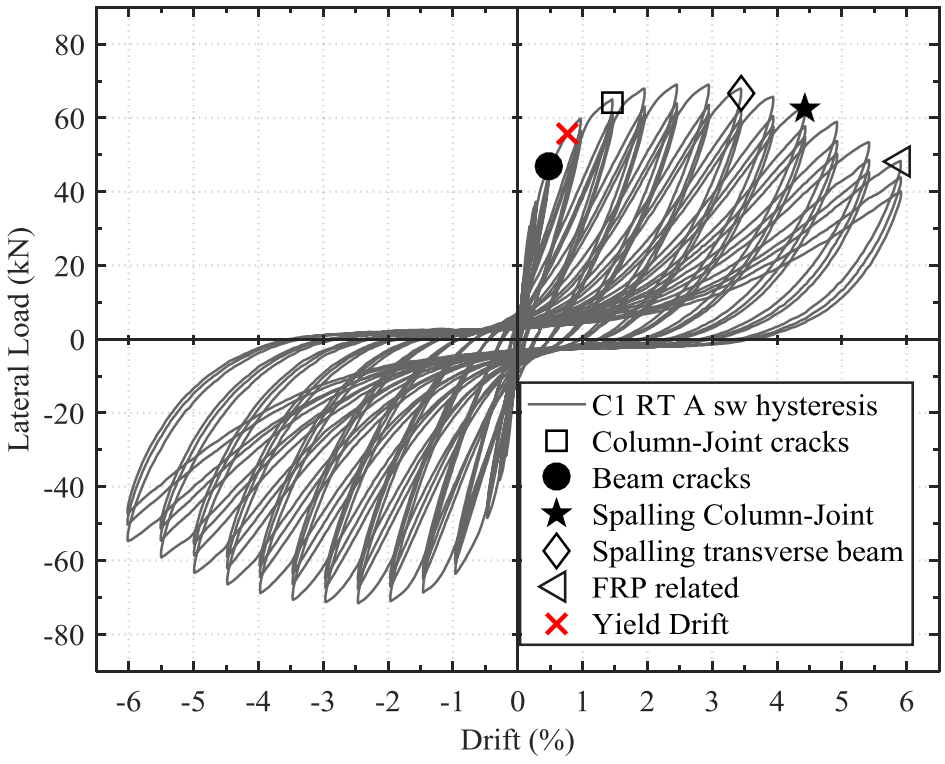

Figure 5.36. Force – drift response for specimen C1-RT-A-sw with important events markers.

As a consequence of the selective weakening, increased rotation of the beams is observed, leading to a larger number of cracks in the bottom of the beam. At 2.0% drift, five parallel cracks with a spacing of ca. 200 mm are observed in Figure 5.34 (b). In particular, the crack at the beam/joint interface is observed to open more significantly with increasing drift cycles than for C1-RT-A. This crack is observed to extend along the length of the slab/transverse beam interface indicated by the red circle in Figure 5.34 (b). After reaching the maximum force, at 2.5% to 3.0% drift, cracks in the beam top face are also noticed. The observation of cracks in the slab between 2.0% and 3.0% drift indicates slab participation, however not to the extent of specimen C-EC8.

In the transverse beams, torsional cracks (marked in dark red in Figure 5.37 (a)) are first observed at 1.5% drift, leading to cracks around a wedge at the transverse beam/joint interface. The cracks extend fully at 2.5% and two wedges finally break off at 3.5% on one side of the transverse beams. The observed spalling is more significant than for specimens C-EC8 and C1-RT-A. The torsional cracks are caused by the difference in rotation at the two ends of the transverse beam (joint end and free end). An increased rotation in the main beams, with associated greater joint deformation (as shown in Figure 5.34 (c)), explains the importance of the observed wedging. Again, these cracks are not observed for the other control specimens, as the rotation of slab and joint are much smaller, hence inducing less torsion in the transverse beams.

(a) (b)

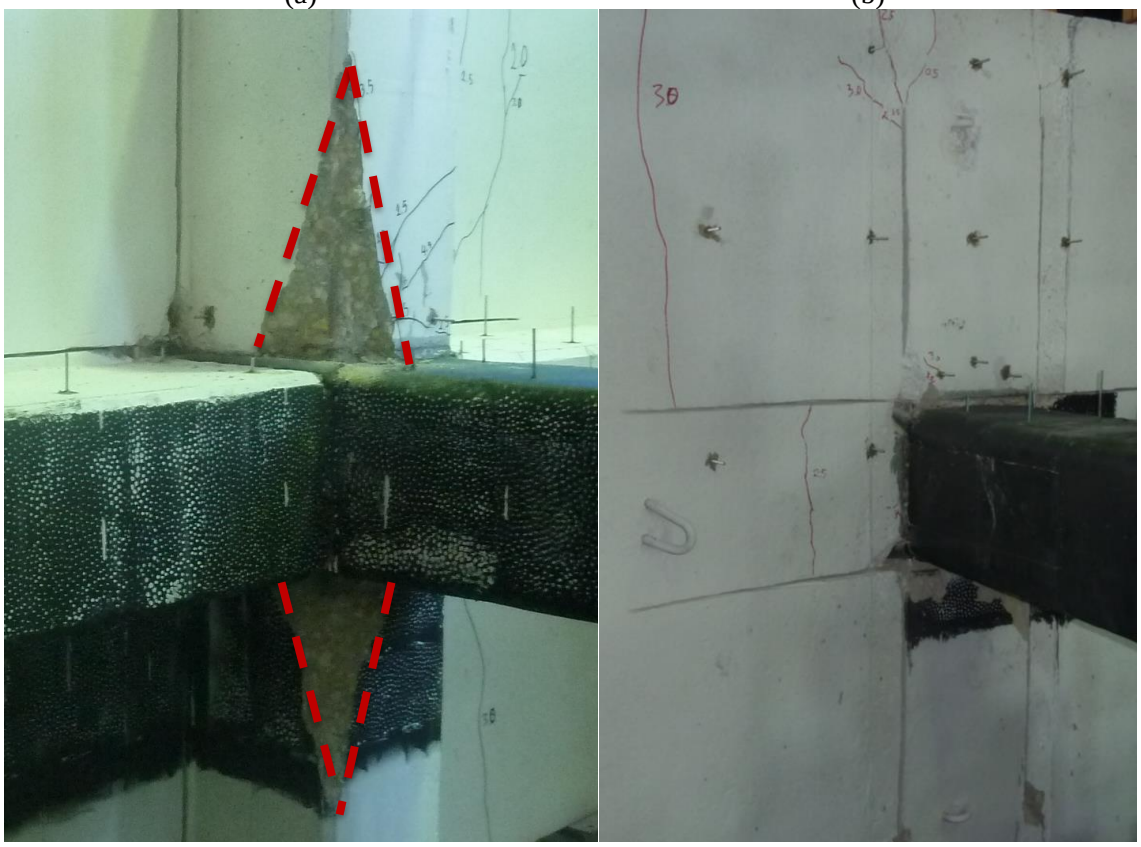

Figure 5.37. (a) Damage in the transverse beam with concrete wedge spalling indicated in red; and (b) cracks in the top of the slab for specimen C1-RT-A-sw.

In the post-peak softening regime, the cracks at the beam/joint interfaces are observed to open significantly. At 4.5% drift, concrete crushing is observed underneath the FRP wraps in the superior and inferior columns, leading up to the ultimate state at 5.2% drift. In the last drift cycles at 6.0% drift, debonding in the FRP column wrap near the joint interface is observed.

5.3.4.2. LOCAL BEHAVIOUR AND MOMENT CURVATURE

Looking at the moment-curvature diagrams in Figure 5.38 (a) and (b) for C1-RT-A-sw, the non-linear behaviour of both columns indicates that the single-storey failure in the control specimens is prevented. It is apparent that the expected column moment capacity of 142.8 kNm is not reached in both columns.

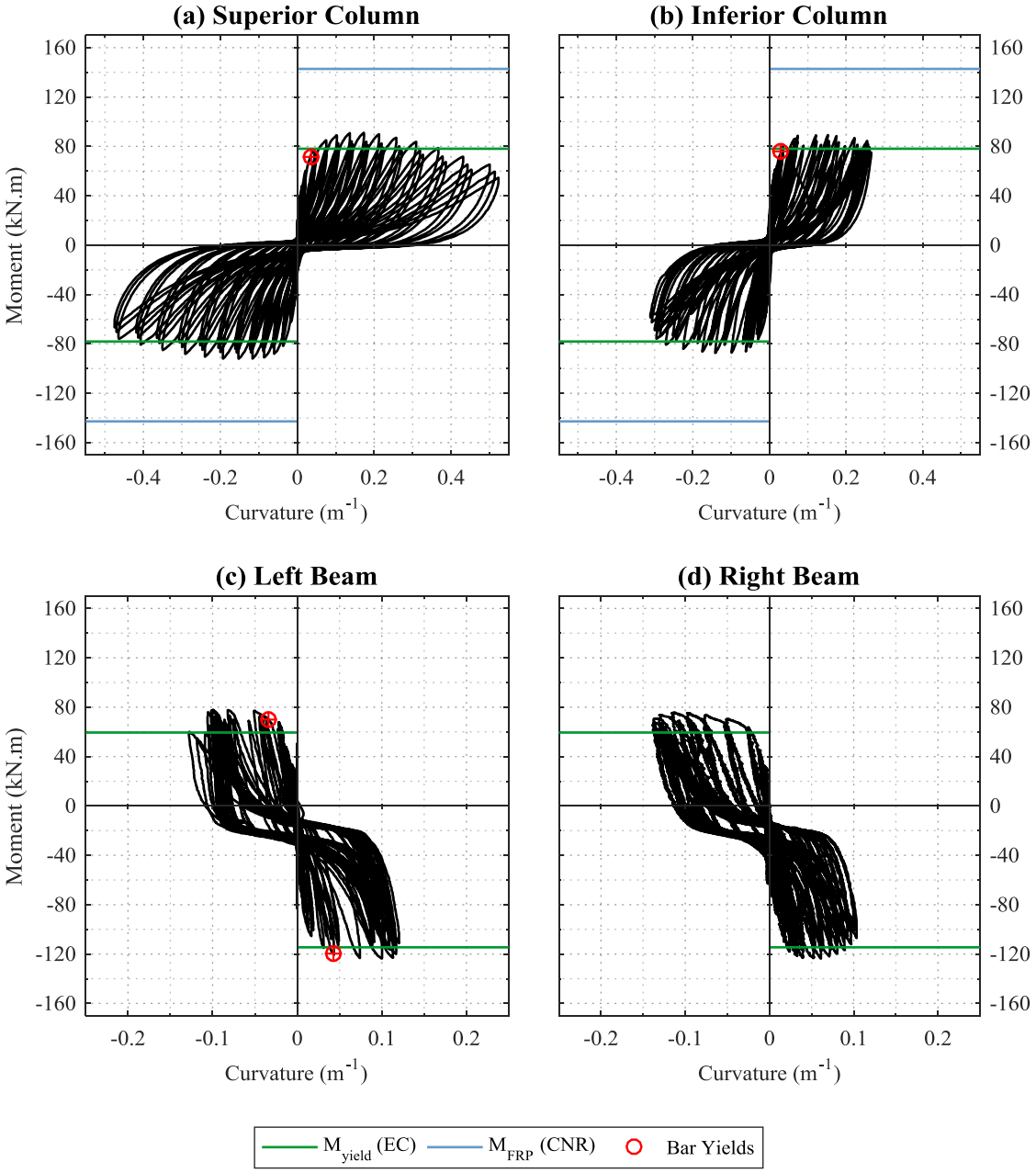

Figure 5.38. Moment Curvature behaviour in (a) superior and (b) inferior columns, as well as (c) left and (d) right beams for specimen C1-RT-A-sw, with expected moment capacities (EC for unstrenghtened and CNR for retrofitted members) and experimental yield points.

The maximum moment obtained in the columns is 92 kNm, hence 35.6% lower compared to the prediction using the CNR guidelines. The increase in capacity compared to control specimen C1 is only 3.1%. It is again observed that large cracks occur at both column/joint interfaces without cracks along the rest of the columns. As for C1-RT-A, this suggests a local failure where the FRP strands are not bonded to the concrete and develop less strain than anticipated (see Section 6.1). Moreover, as shown in Figure 5.38, lower column curvatures are recorded for C1-RT-A-sw compared to C1-RT-A. In particular for the inferior column, peak curvatures are reduced by 42.1%, explaining the occurrence of cracks at the column/slab interface at higher drift levels.

An increased beam participation in the behaviour of C1-RT-A-sw can also be observed in the moment-curvature diagrams in Figure 5.38. As seen in Figure 5.38 (c) and (d), the beam behaviour is fully non-linear with yielding of bars and the plateau in moment capacity reached in hogging and sagging. Due to the selective weakening cuts, the reduced hogging moment capacity of 123.7 kNm is reached in both beams. The maximum moment is 8.0% larger than the calculated capacity, and is hence within the expected margin for strain hardening. The observed sagging moment capacity of 77.9 kNm is also within this safety margin (+28.5%).

The effectiveness of the retrofit with selective weakening is particularly demonstrated by the increased sagging and hogging beam rotations of -0.14 m^{-1} and 0.1 m^{-1}, respectively (Figure 5.39).

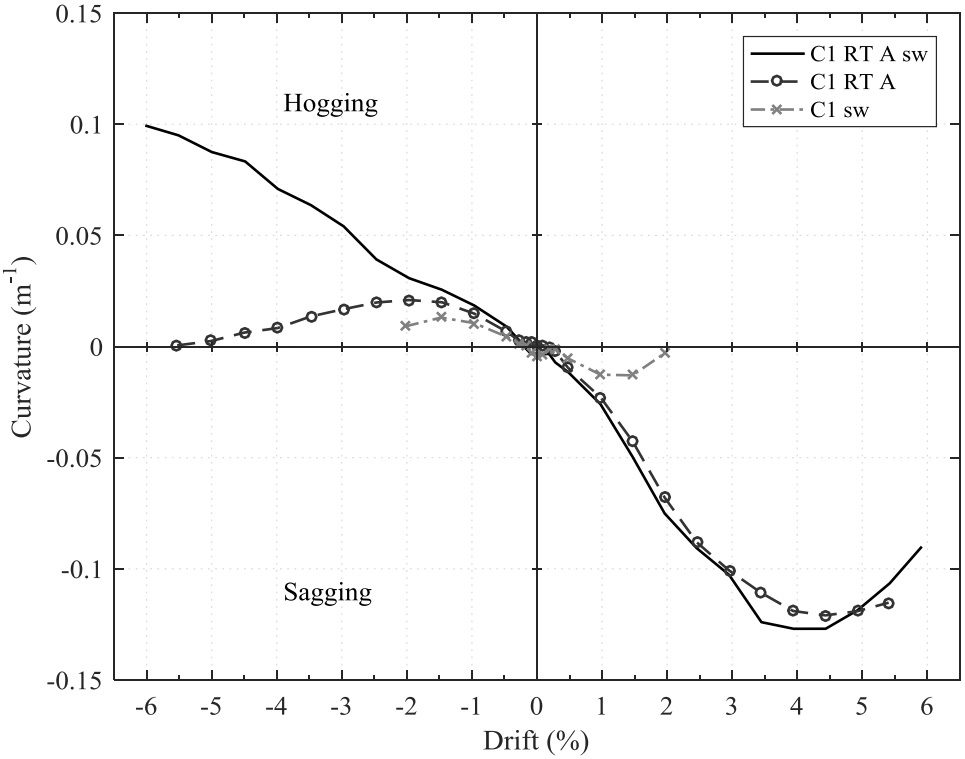

Figure 5.39. Beam curvature vs drift for C1-RT-A-sw compared to C1-RT-A and C1-sw.

While the five-fold increase in rotation in sagging compared to C1-sw is significant, it is similar to that observed for C1-RT-A. In hogging, however, a much larger, thirteen-fold increase in

rotation is observed. Overall, a more symmetric rotation of the beams in positive and negative drift directions, and hence a larger beam participation to the global behaviour are observed.

5.3.4.3. SUMMARY

Overall, the cyclic behaviour of C1-RT-A-sw is very ductile and dissipative, with a more appropriate hierarchy of strengths than for the specimens retrofitted without selective weakening. Significant damage and rotation in the beams is observed, with a decrease in moment capacities of the beams in line with results from FE-modelling. Due to the low strength of the weakened beams, however, only a small increase in lateral load capacity compared to C1 is observed. Moreover, the anticipated retrofitted column moment capacity is not reached and a large crack at the column/slab interface is observed.

5.3.5. C1-RP-A-SW – REPAIR OF SPECIMEN C1 WITH SCHEME A AND SW

5.3.5.1. GLOBAL PARAMETERS AND FAILURE MECHANISM

For the repair-specimen with selective weakening, C1-RP-A-sw, the ultimate damage state is similar to the one observed for the retrofitted specimen C1-RT-A-sw. As shown in Figure 5.40, a significant crack is observed at the joint-column interfaces, but, after removal of the FRP jacket, no cracks are observed along the length of column, indicating a highly localised column failure at the interface to the joint. No debonding or rupture of the FRP is observed throughout the test, with a maximum FRP strain in the strands of 0.12%.

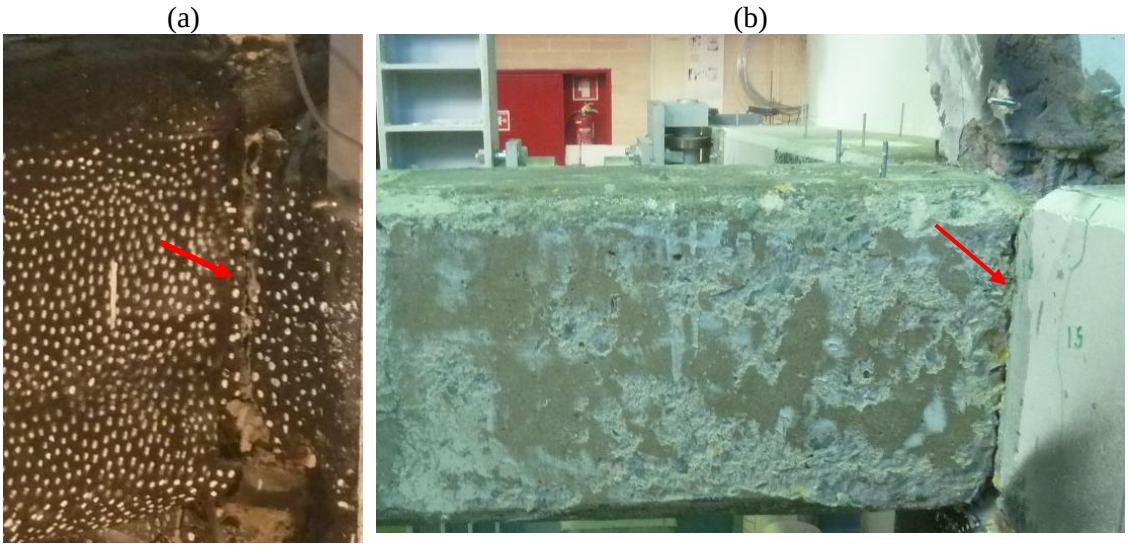

Figure 5.40. (a) Crack at superior column/joint interface; (b) crack at inferior column/joint interface and absence of cracks along column for C1-RP-A-sw, after removal of FRP jacket.

As can be seen in Figure 5.41, damage is spread along the beams, with a large crack at the beam/joint interface and three further cracks in the first 400 mm of the beam. The crack at the interface also runs along the entire slab width, through the selective weakening cuts and the non-weakened section (see inset of Figure 5.41 (a)).

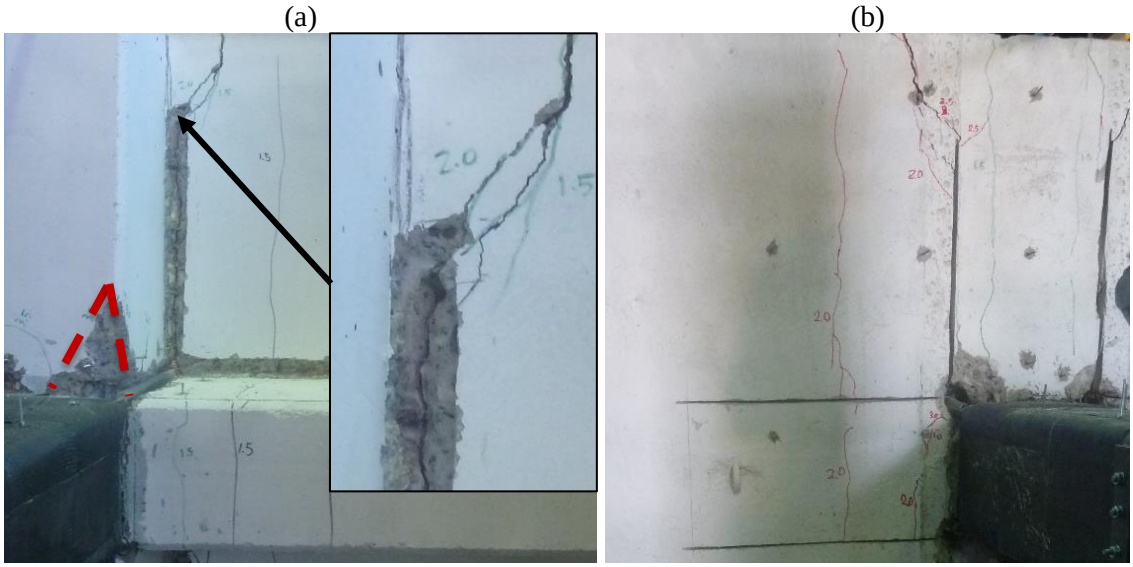

Figure 5.41. Final damage state in C1-RP-A-sw with significant cracks in beams and slab and concrete wedging due to torsion in transverse beams: (a) view from inferior column, with transverse beam wedging in red (inset: zoom on crack); (b) view from superior column.

Looking at Table 5.2, for specimen C1-RP-A-sw a modest increase in strength compared to C1 is observed (+21.8%). Due to the pre-damage, similarly to C2-RP-A, a lower initial stiffness is obtained (-29.4%), leading to a higher yield drift and hence a less significant increase in ductility for the repaired specimen compared to the retrofitted specimen (-9% vs C1-RT-A-sw). As shown in Figure 5.42, the softening behaviour is significantly improved compared to the control specimens C1 (-69.3%) and C1-sw (-62.4%), and is similar to that of the retrofit specimen C1-RT-A-sw. The increase in dissipated energy compared to C1 is more than three-fold (+217.4%), and hence larger than for C1-RT-A and C1-RT-A-sw.

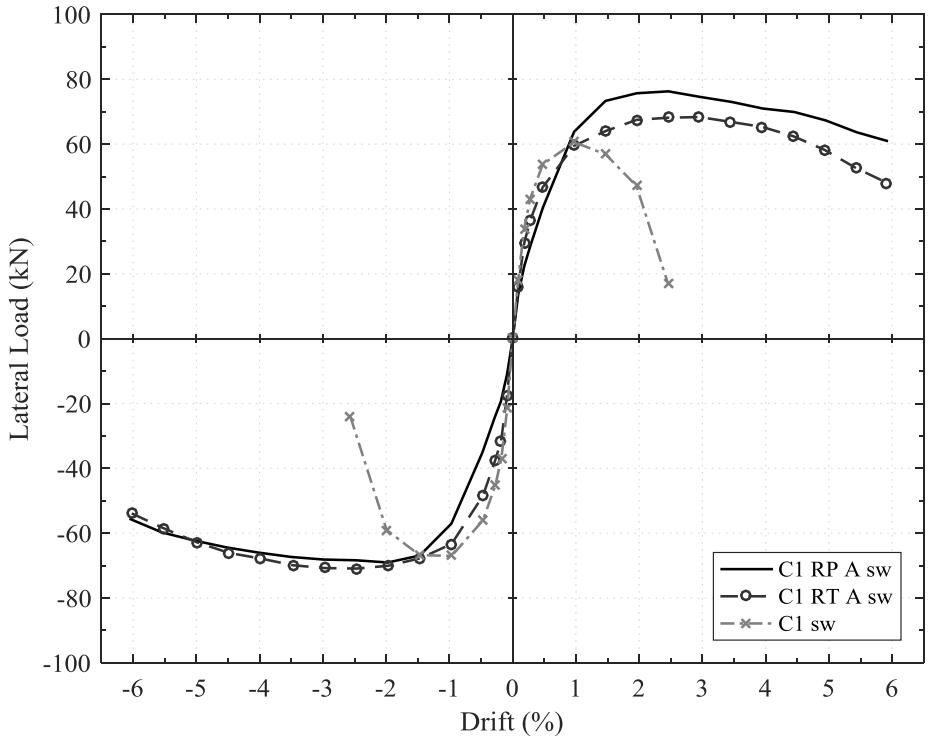

Figure 5.42. Comparison of force-drift envelope for C1-RP-A-sw with C1-RT-A-sw and C1-sw.

Figure 5.43 shows the development of damage in the specimen on the force-drift hysteresis plot. As for C1-RT-A-sw, cracking is first observed in the beams, but due to the decrease in stiffness, cracks are observed at a slightly higher drift of 1.0%. At this level of drift, yield is observed in the inferior and superior column bars, again preceding yield in the beam bars. For this specimen, yield is also observed in the top beam bars (1.5% drift) before the bottom beam bars (1.9%). Column/joint interface cracks become visible at 1.5% drift.

Three further cracks along the bottom face of the beams are also observed at 1.5% drift. At 2.0% drift, the crack along the beam/joint interface opens significantly and extends all the way along the slab, following the selective weakening, as shown in Figure 5.41 (a). A second crack on the slab, about 200 mm parallel to the transverse beams is also observed at this drift.

The maximum lateral force is reached at 2.46% drift, with significant crack opening of the column and beam/slab interfaces, which is identical to C1-RT-A-sw. After the peak lateral load, mainly expansion of the cracks at the beam/joint interface is observed, with cracks at the corners of the transverse beam appearing. These torsional cracks again lead to the formation of a concrete wedge breaking away from the transverse at 4.0% drift. As can be seen in Figure 5.41 (a), this wedge is less significant than for C1-RT-A-sw. Some crushing in the top face of the transverse beam is also observed (Figure 5.41 (b)) between 4.5 and 5.0% drift. The ultimate drift is finally reached at 5.84%, which is significantly larger than for C1 (+149%) and slightly higher than of C1-RT-A-sw (+12%).

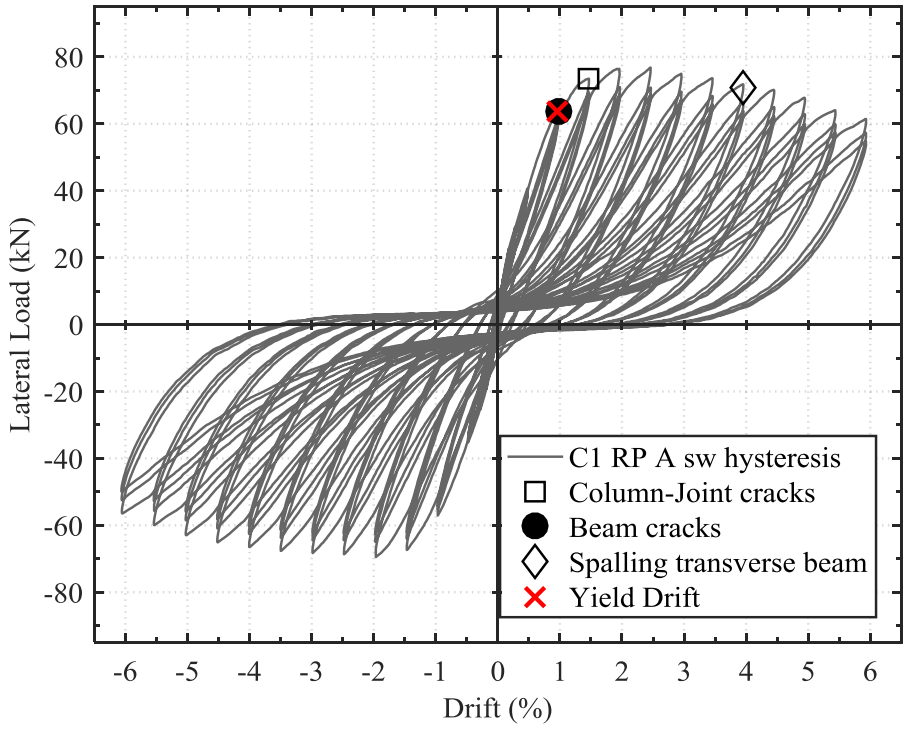

Figure 5.43. Force – drift response for specimen C1-RP-A-sw with important events markers.

5.3.5.2. LOCAL BEHAVIOUR AND MOMENT CURVATURE

Figure 5.44 displays the moment-curvature diagrams for the two columns and beams of C1-RP-A-sw. Similar observations to C1-RT-A and C1-RT-A-sw can be made for the columns in Figure 5.44 (a) and (b), with a non-linear behaviour of both columns indicating the retrofit successfully activates the inferior columns, eliminating the single-storey failure of the control specimens. Despite a higher FRP strand strain of 0.12% (+8% compared to C1-RT-A), the column moment capacity of 97.0 kNm is lower than for C1-RT-A (-16.0%), as the amount of FRP is reduced for C1-RP-A-sw. Again, the column moment capacity is lower than the predicted value from the CNR guidelines (-32.9%), as local failure at the column/joint interfaces is observed.

As for C1-RT-A-sw, increased beam curvatures are obtained for C1-RP-A-sw in Figure 5.44 (c) to (d). It appears, however, that the two beams do not behave in the same way. While the left beam displays a symmetric curvature in hogging (+0.151 m^{-1}) and sagging (-0.149 m^{-1}), the right beam reaches much larger curvatures in sagging (-0.23 m^{-1}) and remains close to elastic in hogging. This observation is related to the maximum superior column moment being about 10% larger in the positive drift direction than in the negative direction. The reason for this could be errors in the repair process, e.g. a difference in concrete cover. A slightly lower cover on either side of the column would increase the moment capacity in one direction, hence explaining the higher maximum moment, as well as the observation of lower superior column curvature in the positive direction (+0.41 m^{-1}) than in the negative direction (-0.58 m^{-1}).

Overall, the lateral force applied in the positive drift direction is hence larger, which is confirmed by looking at Figure 5.42, causing a larger sagging moment and lower hogging moment in the right beam.

Despite the asymmetry of applied loading, for both beams, the moment capacity in hogging and sagging is reached. In hogging, the maximum moment is 130.2 kNm, hence 13.7% larger than expected and in sagging, it is 82.5 kNm, 35.7 % higher than expected. While the hogging moment is well within the expected overstrength from strain hardening, the overstrength in sagging moment is slightly higher than the expected 1.3.

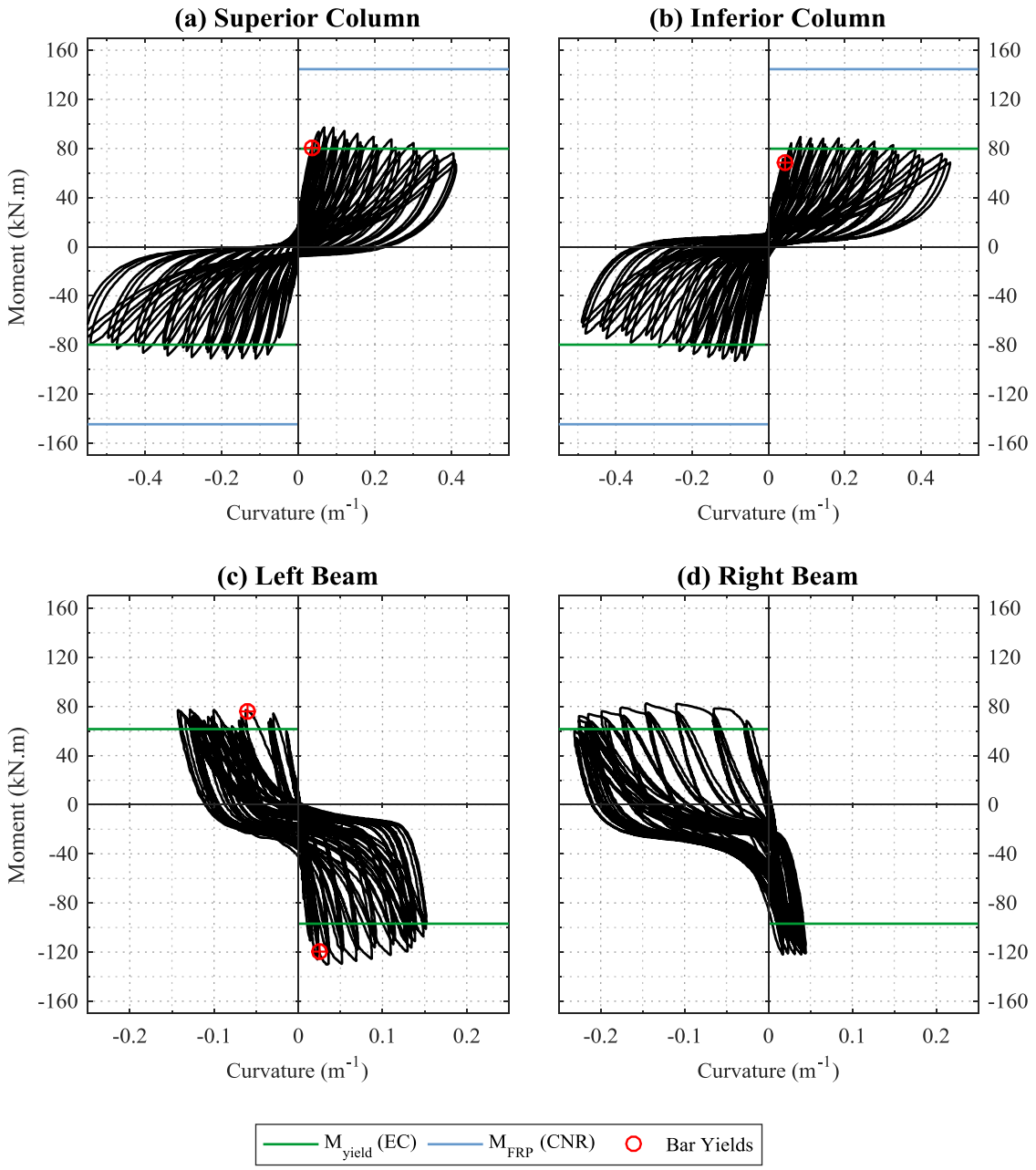

Figure 5.44. Moment Curvature behaviour in (a) superior and (b) inferior columns, as well as (c) left and (d) right beams for specimen C1-RP-A-sw, with expected moment capacities (EC for unstrenghtened and CNR for retrofitted members) and experimental yield points.

5.3.5.3. SUMMARY

Overall, the cyclic behaviour of C1-RP-A-sw is similar to the respective retrofit specimen. An increased beam participation due to the selective weakening of the slab is observed, leading to a very ductile and dissipative failure. Again, only a small increase in lateral load capacity compared to C1 is obtained as a large crack at the column/slab interface is observed and the anticipated column moment capacity is hence not reached. Compared to C1-RT-A-sw, despite significant pre-damage, the repair scheme successfully achieves an improved dissipative behaviour with increased capacity. As for the other repair specimen, C2-RP-A, ductility and initial stiffness of the repaired specimen are however reduced compared to the retrofit.

5.3.6. C1-RT-B-SW - RETROFIT B WITH SELECTIVE WEAKENING

5.3.6.1. GLOBAL PARAMETERS AND FAILURE MECHANISM

The aim of the combined retrofit and selective weakening scheme RT-B-sw is to achieve a strength increase up to 80% of C-EC8, with a similar failure mechanism and ductility. This target is to be achieved despite the design deficiencies and the significantly lower concrete strength for C1-RT-B-sw (19.3 MPa) compared to C-EC8 (32.7 MPa).

As shown in Figure 5.45, the envisaged hierarchy of strengths from the retrofit design and FE model in Section 3.7.3 is confirmed, with damage spread along the length of the beams and slab as shown in (b), starting from the envisaged plastic hinge zone, away from the joint. It can also be observed that the concrete wedging mechanism in the transverse beams seen for the other retrofit specimens is successfully avoided for C1-RT-B-sw. No damage or FRP rupture along the columns for the retrofitted specimen are seen in Figure 5.45.

(a) (b)

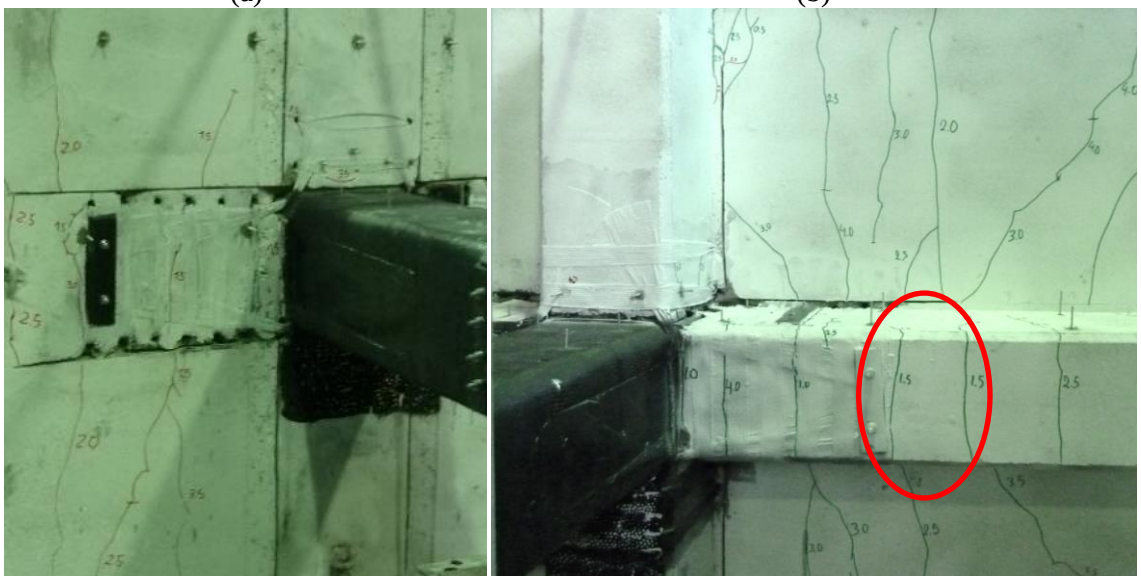

Figure 5.45. Final damage state in C1-RT-B-sw; (a) column and slab, (b) beam underside. Envisaged plastic hinge zone circled in red.

Despite no damage along the columns and no debonding of the longitudinal FRP being observed, crack opening is noticed at the column/joint interfaces as shown in Figure 5.46 (a). The continuous FRP strengthening of the columns allows a symmetrical rotation of superior and inferior columns, which hence prevents the brittle single-storey failure observed for C1. No debonding of the FRP is observed throughout the test, while partial rupture in the beam FRP strand, shown in Figure 5.46 (b) is noticed towards the end of the test (at 5.0% drift). The maximum recorded strain in the vertical FRP strands is significantly lower than the debonding or rupture strain (0.08%).

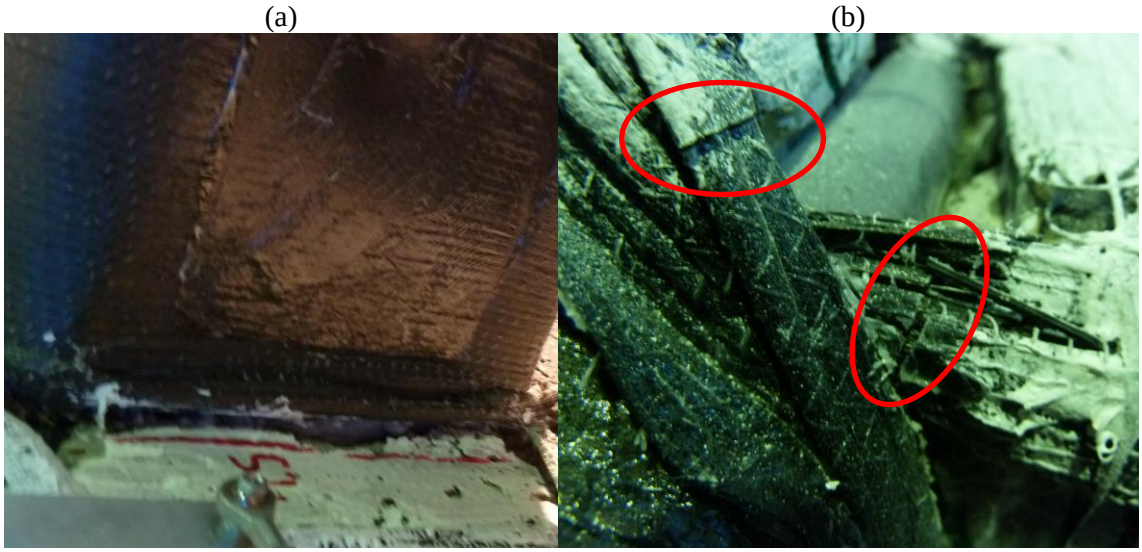

Figure 5.46. Detailed damage for specimen C1-RT-B-sw: (a) crack at the superior column/joint interface; (b) partial rupture of CFRP strands in main and transverse beam highlighted in red.

In terms of the global force-drift response in Figure 5.47, the performance of C1-RT-B-sw presents a significant improvement compared to C1, with a similar performance to the target 80% of C-EC8. Rather than the target, 70.1% of the strength of C-EC8 is achieved by the retrofitted specimen. Still, this corresponds to a significant strength increase of 37.7% with respect to C1, despite a lower concrete strength than the two control specimens.

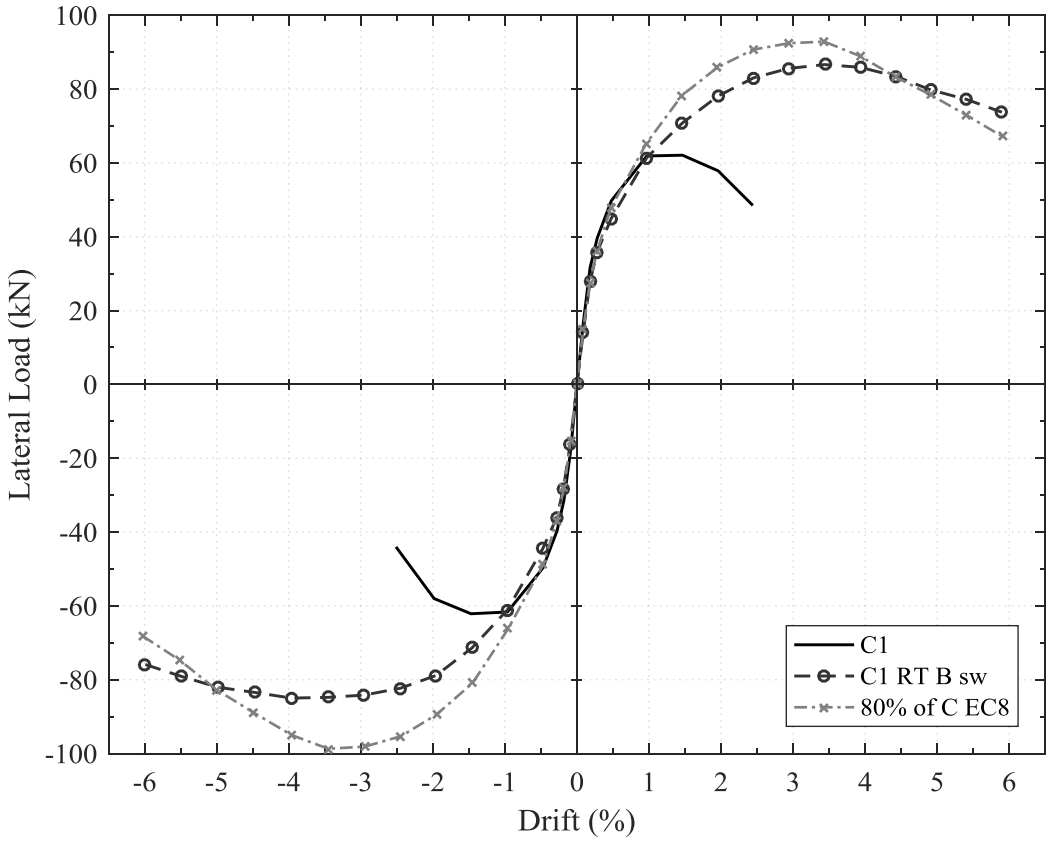

Figure 5.47. Force-drift envelope for C1-RT-B-sw compared to specimens C1 and C-EC8.

A more ductile failure mechanism, with damage in the beams starting from the predicted plastic hinge zone (450 mm away from the beam/joint interface), is observed. As can be seen in Table 5.2, the ductile failure is confirmed by the largest ductility of all specimens being recorded for C1-RT-B-sw (6.9, +89.6% compared to C1).

As shown in the hysteresis plot for C1-RT-B-sw in Figure 5.48, not only is the largest ductility observed, but a large yield drift of 0.95% is also observed (+46% compared to C1) as a consequence of the strengthening intervention. This, in turn, is favourable as it reduces the need for repair in the case of small earthquakes. Moreover, due to the strong increase in lateral load capacity and ductility, the behaviour of retrofitted specimen C1-RT-B-sw is highly dissipative, with a total cumulative energy dissipation of 111.6 kNm (+247.8% vs C1), which is close to 75% of specimen C-EC8 at its ultimate drift. The lowest inter-cycle strength degradation (-61.8% compared to C1) and a strongly improved post-peak softening (-61.8%) are also observed for C1-RT-B-sw, indicating a significantly improved performance under cyclic loading and improved residual strength, respectively.

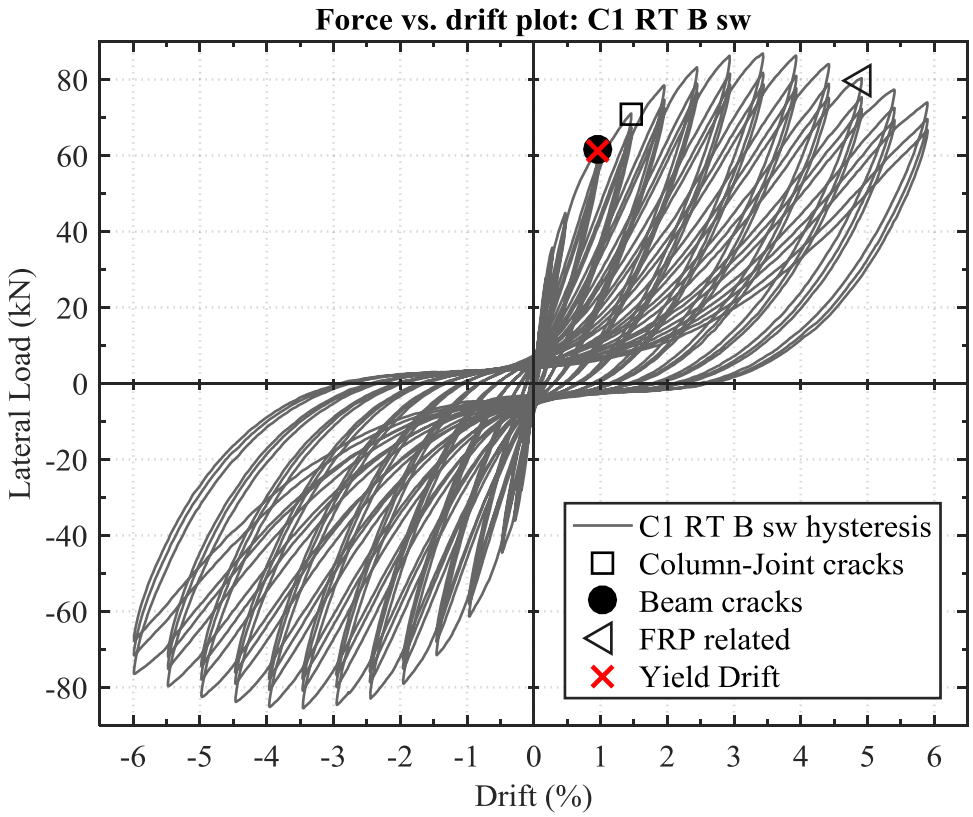

Figure 5.48. Force – drift response for specimen C1-RT-B-sw with important events markers.

The progression of damage shown in Figure 5.48 highlights the late onset of yielding (0.95% drift) and cracking (1.0% drift) in the beams. First cracks in the beams are observed in the bottom beam face about 300 mm from the joint, with two further cracks appearing at 450 mm and 600 mm from the joint interface in the next drift cycle (1.5%). At 1.5% drift, three cracks are also visible in the top face of the beam and slab.

At 1.5% drift, a crack at the column/joint interface becomes apparent. With increasing drift levels, a larger opening of the cracks is observed. At 2.0% drift, the first crack in the slab bottom face, perpendicular to the main beam axis, is observed about 600 mm from the transverse beams (indicated in blue in Figure 5.49). This is followed by two further parallel cracks at the slab/transverse beam interface and 300 mm from the interface at 2.5% drift. At 2.5% drift, further cracks in the top of the slab are also noticed at the same location as the cracks in the bottom face of the slab. In the beams, further cracks at 2.5% drift, about 900 mm from the joint are observed. These cracks extend into the slab at 3.0% drift. At 3.0% and 3.5% drift, diagonal cracks in the slab bottom face are observed, originating from the end of the selective weakening cuts along the main beams (red in Figure 5.49). At 4.0% drift the cracks in the slab extend fully across the width of the slab and a last crack in the beams, around 100 mm from the beam/joint interface is seen.

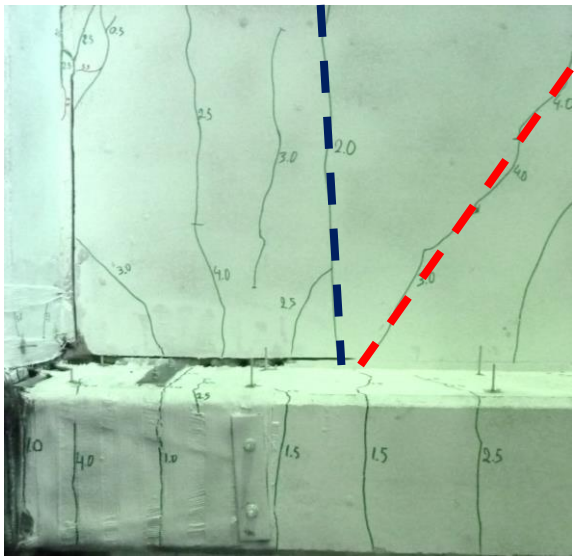

Figure 5.49. Observed cracks in the slab underside for specimen C1-RT-B-sw.

At 5.0% drift, a first partial rupture of the main beam FRP strand is observed. The rupture is not in tension but rather due to a shear mechanism where the strand is in touch with the transverse beam FRP strand. At 5.5% drift, partial rupture of the transverse beam FRP strand is also observed.

Overall cracking in the beams and slabs extends further than for any other specimen including C-EC8. Compared to retrofits RT-A and RT-A-sw, due to the strengthening of the transverse beams in RT-B-sw, no torsional cracks in the transverse beams and hence no diagonal cracks at the slab/transverse beam interface are observed. Moreover, due to the joint strengthening, no damage in the joint core is observed after removal of the transverse beams. The FRP strips in the joint reach a maximum strain of 0.12%, indicating that they are indeed activated.

5.3.6.2. LOCAL BEHAVIOUR AND MOMENT CURVATURE

The moment curvature plots for C1-RT-B-sw are shown in Figure 5.50 (a – d). As a common observation to all retrofits, the behaviour of the superior and inferior columns is symmetric, with

both columns reaching similar maximum curvature (0.45 m^{-1}). The single-storey mechanism of the control specimen is hence not observed. The maximum moment in the columns is 112.9 kNm (+26.5% vs C1), hence not reaching the anticipated value of 144.8 kNm from the CNR equation (-22.1%). The observation of large cracks at the column/joint interfaces again suggests local failure where the FRP in plastic tubes and not bonded to concrete, as discussed in section 6.1.

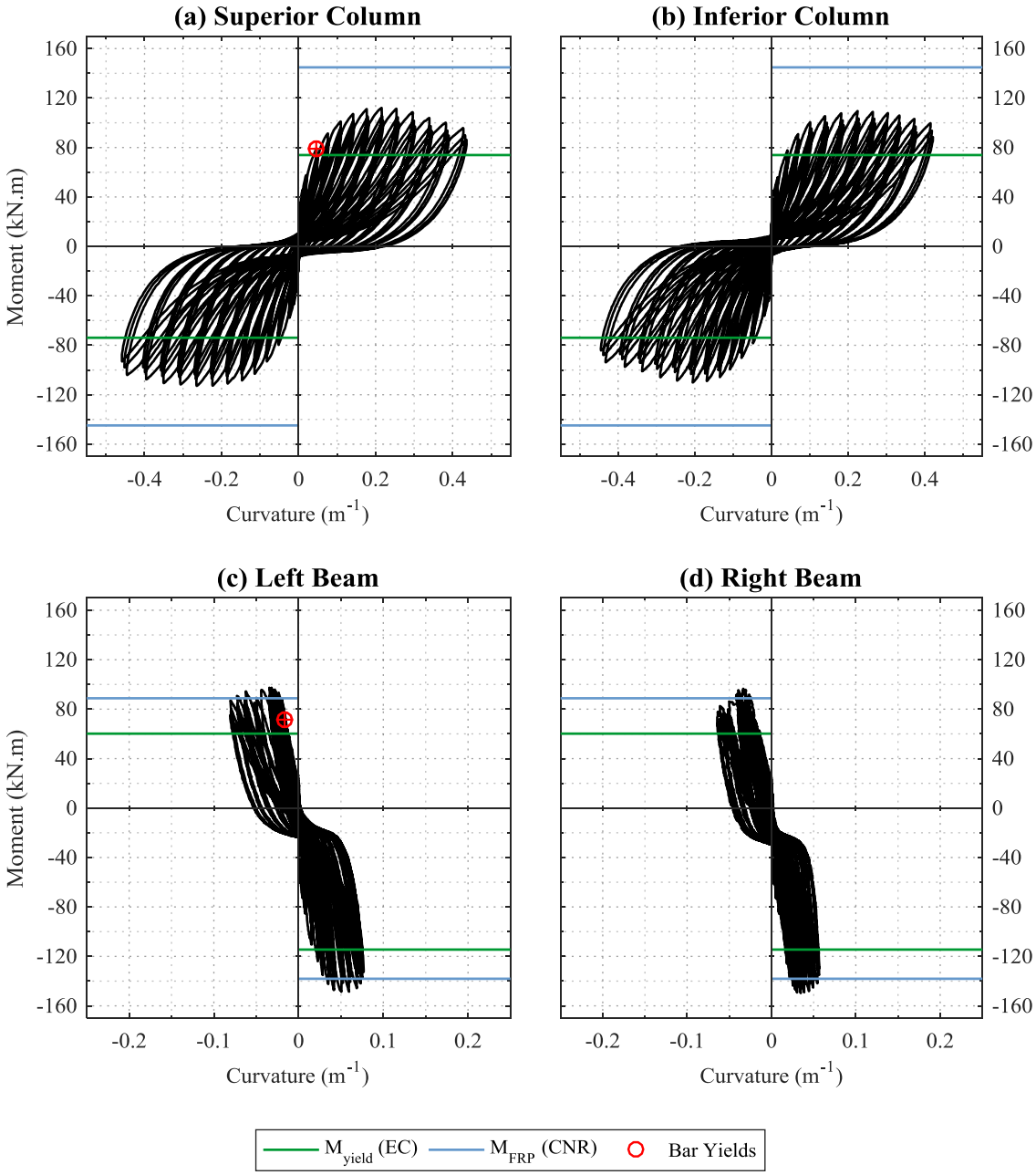

Figure 5.50. Moment Curvature behaviour in (a) superior and (b) inferior columns, as well as (c) left and (d) right beams for specimen C1-RT-B-sw, with expected moment capacities (EC for unstrengthened and CNR for retrofitted members) and experimental yield points.

As shown in Figure 5.46, increased damage in the beams is observed due to a stronger participation of the beams in the failure mechanism, with a nonlinear behaviour in sagging and hogging observed in in Figure 5.50 (c & d). This observation is a direct consequence of the selective weakening of the slab, with the beams able to rotate symmetrically in hogging (0.077

m^{-1}) and sagging (-0.081 m^{-1}). The rotations in hogging and sagging are less pronounced than for C1-RT-A-sw, but still 9 and 3.5 times larger than for the control specimen C1, respectively. Looking at the blue lines in Figure 5.50 (c & d), the moment capacity calculations from the CNR guidelines give a good estimate of the actual maximum moments in the beams. In sagging a value of 97.3 kNm, 9.6% larger than the calculated capacity, is obtained, while in hogging a value of 149.7 kNm, 8.4% larger than expected is observed. In both cases, the over-strength is lower than the accounted for strain-hardening factor of 1.3.

An important aspect of the retrofit design in RT-B-sw is the formation of a local weakness along the beam, about 450 to 600 mm from the joint interface, i.e. in slice 3. Figure 5.51 shows the moment curvature relationship in this part of the beam for specimens C1-RT-B-sw in comparison to control specimen C1-sw. The plot highlights that a plastic hinge is indeed formed in slice 3, with a non-linear behaviour of the beam in sagging and hogging that is not observed for any other specimen.

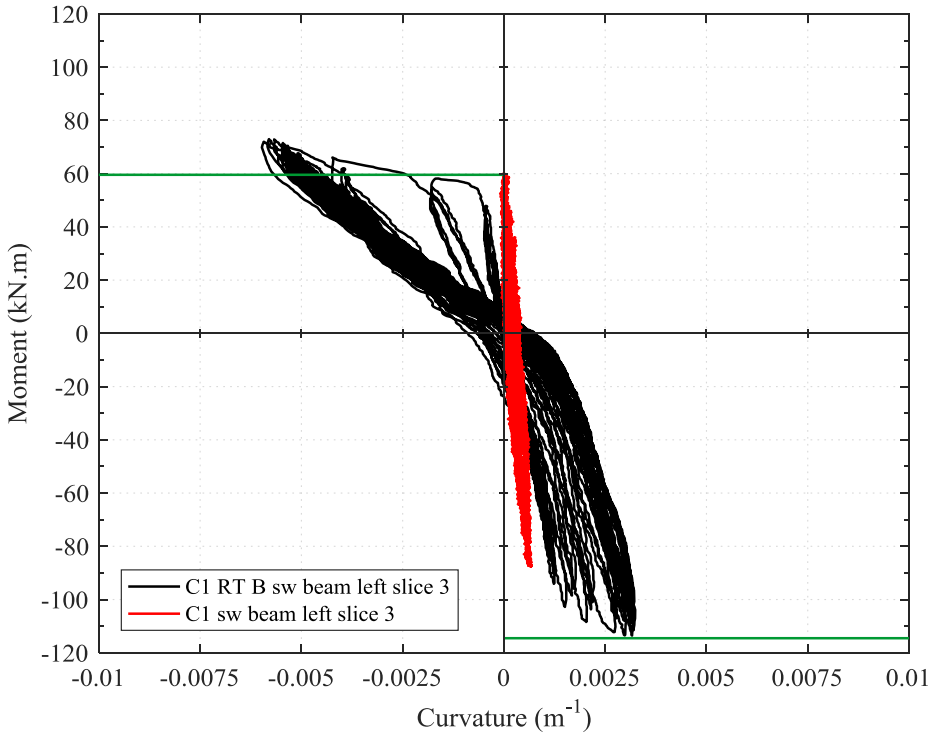

Figure 5.51. Comparison of moment-curvature in slice 3 for C1-RT-B-sw and C1-sw.

5.3.6.3. SUMMARY

For retrofit specimen C1-RT-B-sw a very ductile behaviour with high lateral load bearing capacity is observed. The failure mechanism is again dominated by a large crack in the column/joint interface. However, significant damage and rotation of the beams is also observed, with a plastic hinge forming away from the joint, as anticipated by design and FE modelling. This leads to a very dissipative failure mechanism with strongly improved post-peak softening and strength degradation even compared to C-EC8.

5.3.7. C-noSLT-RP-B – Repair B for specimen C-noSLT

5.3.7.1. Global parameters and failure mechanism

The final full-scale beam-column joint experiment presented is the test of the cruciform specimen C-noSLT without slab and transverse beam, repaired to scheme B. As shown in Figure 5.52, with the absence of the slab and transverse beams, damage in the beams (a & b) and joint (d) is much more pronounced. The failure of the specimen is entirely governed by the large crack opening under hogging observed in the beams, causing loss of anchorage of the beam FRP strengthening, about 500 mm from the joint interface (a). No damage or FRP debonding are observed in the columns.

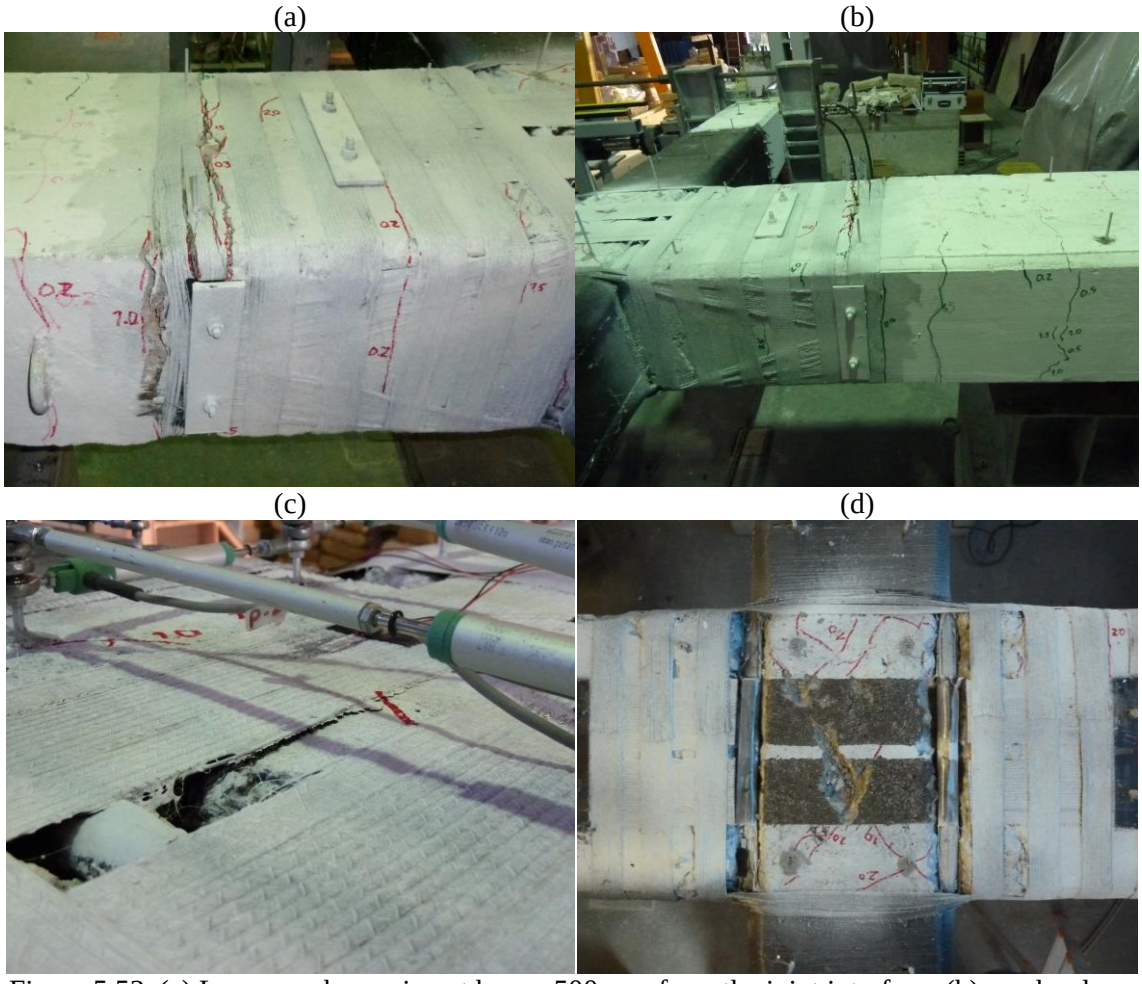

Figure 5.52. (a) Large crack opening at beam, 500 mm from the joint interface; (b) cracks along the beam bottom face; (c) slight debonding of the joint FRP at 1.5% drift; (d) after removal of FRP, diagonal cracks at the surface of the joint panel for specimen C-noSLT-RP-B.

In Figure 5.53 the force-drift envelope of C-noSLT-RP-B compared to its control specimen is shown. For the repair specimen, a very large lateral load capacity increase (+50.2%), but very low ductility of 2.8 corresponding (-45.9% compared to C-noSLT) are obtained. The low ductility can be explained by a sudden drop in capacity at -3% drift when the large crack in the top of the beam leads to a failure of the mechanical anchor. This may be avoided by better anchor placement. As

a consequence, the strain in the horizontal FRP is lost and the strength of the specimen reduces strongly. Looking at Table 5.2, the brittle failure is also marked by a significantly sharper softening slope (+456.6% vs C-noSLT) and a reduced energy dissipation of 19.2 kNm (-39.6%).

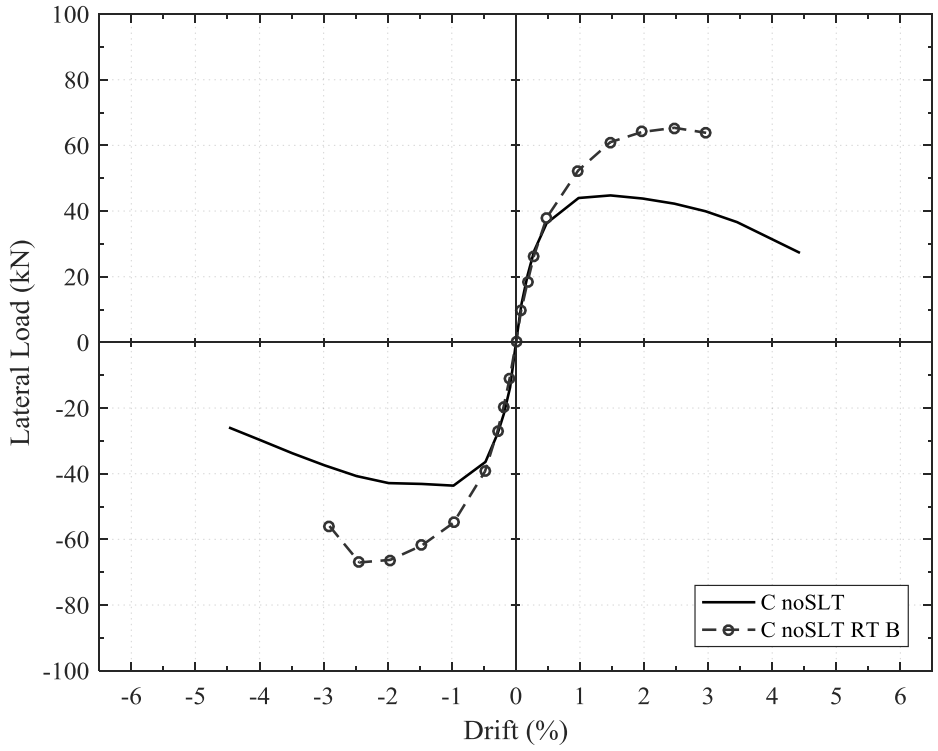

Figure 5.53. Force-drift envelope for C-noSLT-RP-B compared to C-noSLT without slab.

The progression of damage, displayed on the hysteresis curve in Figure 5.54, indicates cracking in the beam at very low drift levels (0.2%). The first cracks are observed at 250 mm from the beam/joint interface, with further cracks observed at the end of the horizontal FRP in the anchorage area, 500 mm from the joint, in the 0.3% drift cycle. At 0.5% drift, a crack further along the beam, about 900 mm from the joint is observed. At 1.0% drift, the crack at the mechanical anchor becomes larger and yield in the top beam bars is observed at -1.0% drift.

Diagonal cracks below the joint-shear strengthening, as well as at the joint/beam interfaces are also noticeable at 1.0% drift. At 1.5% drift, the diagonal cracks in the joint lead to some FRP debonding in the joint panel. At 2.0 % drift, further cracks along the top and bottom of the beams are observed and the crack at the anchor appears to open significantly, extending nearly through the entire depth of the beam. Finally, at -3.0% drift, the ultimate state is reached, with a sudden drop in capacity after anchorage of the horizontal beam FRP strips is lost. indicated by a red arrow in Figure 5.54.

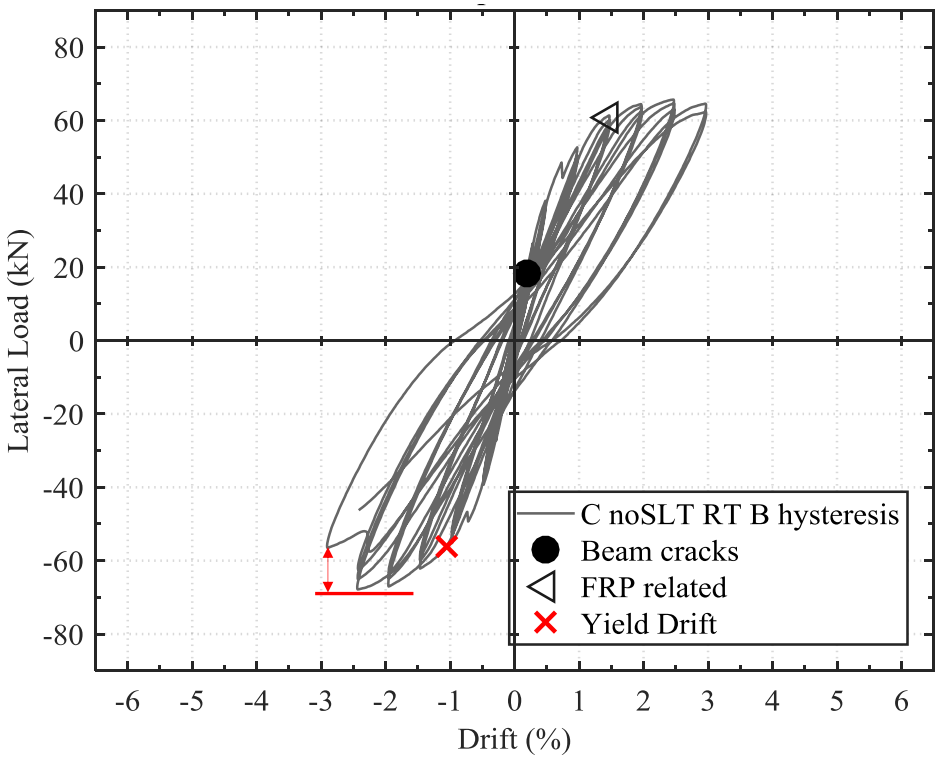

Figure 5.54. Force – drift response for specimen C-noSLT-RP-B with important events markers (drop in strength indicated by red arrow).

5.3.7.2. LOCAL BEHAVIOUR

5.3.7.2.1. MOMENT CURVATURE

In terms of local behaviour, clear differences between the retrofitted cruciform specimen and the specimen with slab can be observed. The moment-curvature relationship for both columns in Figure 5.55 (a & b) remains linear-elastic throughout the test. The beams, as shown in Figure 5.55 (c & d), remain elastic in sagging, but reach plastic behaviour in hogging. The maximum observed hogging moment of 123.5 kNm is 11.2% higher than the calculated capacity, which is again within the anticipated over-strength.

The observed curvature in hogging in slice 1 is still limited (0.06 m^{-1}), as the failure of the specimen occurs in slice 3. However, as the formation of the large crack also occurs at the location of the transducer anchorage, hence no meaningful curvature data is available in this slice.

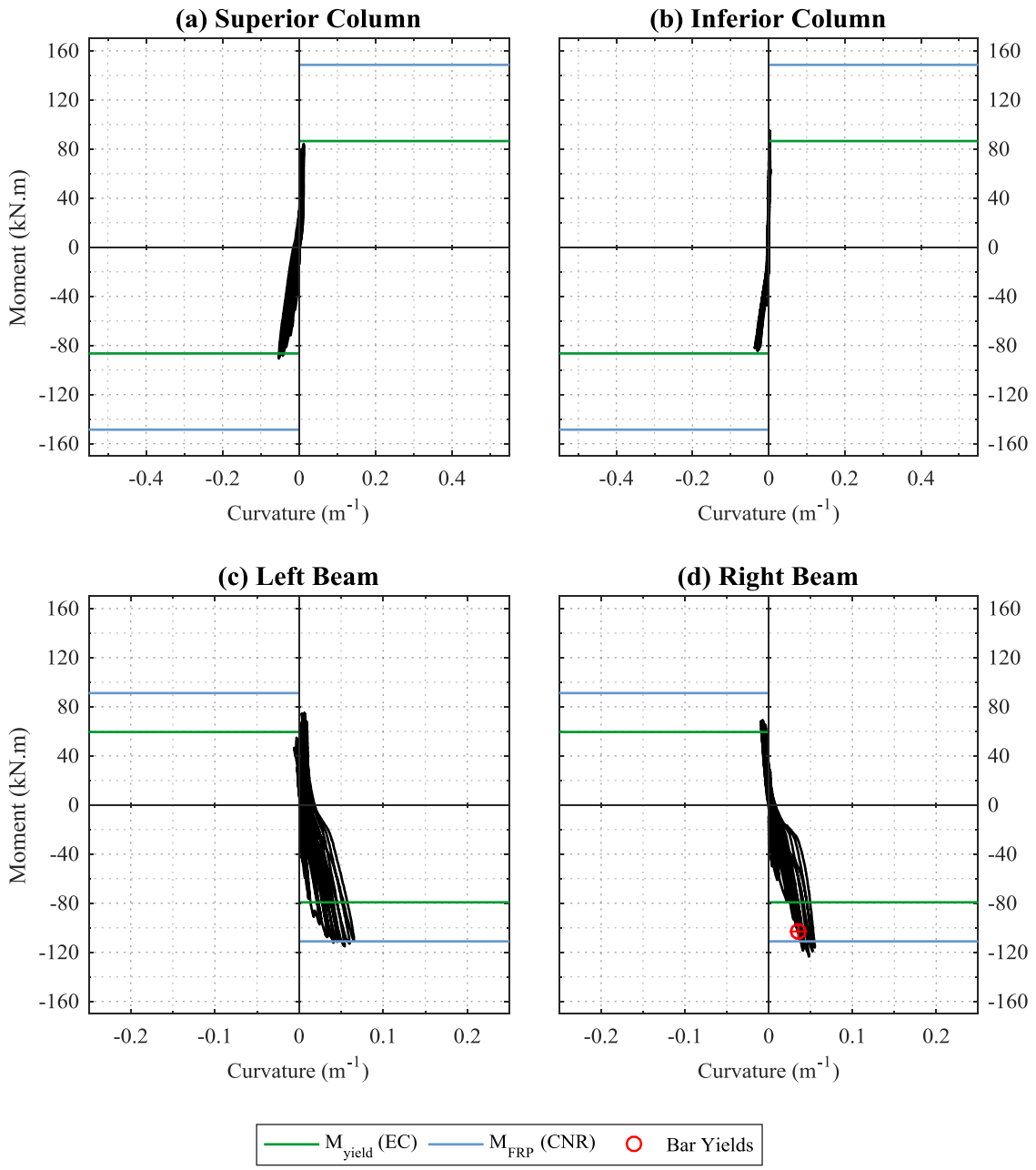

Figure 5.55. Moment Curvature behaviour in (a) superior and (b) inferior columns, as well as (c) left and (d) right beams for specimen C-noSLT-RP-B, with expected moment capacities (EC for unstrenghtened and CNR for retrofitted members) and experimental yield points.

5.3.7.2.2. JOINT SHEAR DISTORTION

In terms of joint shear damage, the behaviour of C-noSLT-RP-B is significantly improved compared to C-noSLT. This can be attributed to the two FRP strips in the joint, for which a large maximum strain of 0.46% is recorded at the ultimate drift level. This value is nearly four times larger than for C1-RT-B-sw (0.12%). Looking at the principal stress against joint shear distortion plot in Figure 5.56, it becomes apparent that the FRP strengthening is successful. For specimen C-noSLT, joint shear strength degradation with increased distortion is observed while for C-noSLT-RP-B, the joint remains elastic. Compared to C-noSLT, the joint shear distortion is also significantly reduced (-75%), indicating an improved behaviour. Moreover, the FRP strips permit

the joint to sustain larger tensile stress, reaching 0.72 $\sqrt{f_c}$ compared to the lower maximum value of 0.39 $\sqrt{f_c}$ in specimen C-noSLT (+84%).

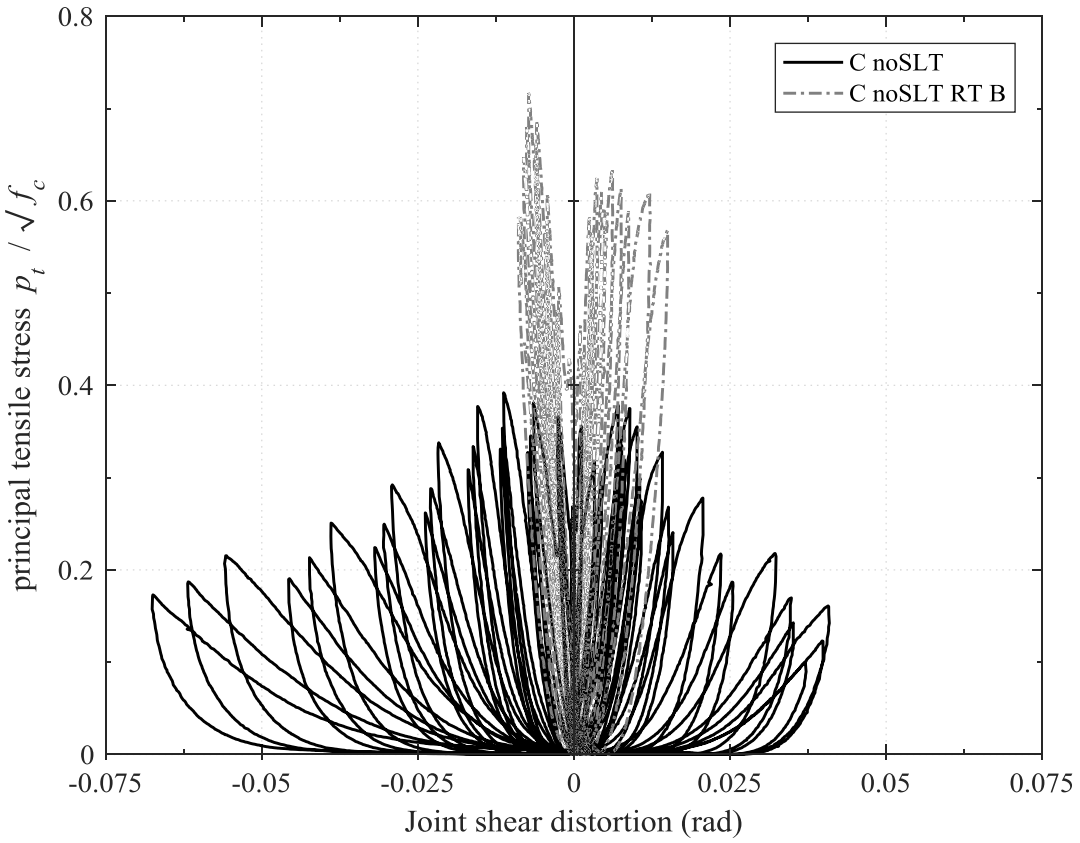

Figure 5.56. Principal tensile stress (normalised by concrete strength) against joint shear distortion for C-noSLT-RP B compared to control specimen C-noSLT.

5.3.7.3. SUMMARY

Overall, the behaviour of the repaired specimen C-noSLT with scheme B is characterised by a very large increase in strength, but a very low ductility. The low ductility is a result of the large localised damage in the beams causing sudden anchorage failure at the end of the horizontal beam FRP. Despite the significant increase in lateral load bearing capacity, the repaired specimen hence presents an undesirable brittle failure, with significant post-peak softening and low energy dissipation. Finally, the joint shear behaviour is significantly improved by the retrofit, indicated by limited cracking and reduced joint shear distortion.

5.4. COLUMN TESTS

Two column-only tests are carried out where the beams and slabs are fixed in the set-up and not allowed to move. These experiments serve to test if the actual capacity of the retrofitted columns is larger than the capacity obtained during the beam-column joint tests. Two amounts of longitudinal FRP are used for the retrofits, with vertical FRP strands made of four and six layers of FRP sheet for C1-RT-A-sw and C1-RT-B-sw, respectively.

The results for the two column-only tests are displayed in Figure 5.57. It can be seen that the moment capacities of the columns are 60.6% and 47.5% larger than for the columns within the full beam-column joint tests for C1-RT-A-sw and C1-RT-B-sw, respectively. The obtained maximum moments are also very close to the expected values from the CNR guidelines. For C1-RT-A-sw, a maximum moment of 147.7 kNm is recorded, which is 3.5% larger than the anticipated moment from the CNR guidelines. For C1-RT-B-sw, for the column-only test a moment of 166.4 kNm is obtained, 15.0% larger than expected.

In both cases, it is hence shown that the actual moment capacity of the columns is larger than for the beam-column joint tests. This leaves room for speculation as to why a reduced capacity with a single crack forming at the joint/column interfaces is obtained initially. An explanation and suggested equations for improved moment capacity calculations are presented in the next sub-section (6.1).

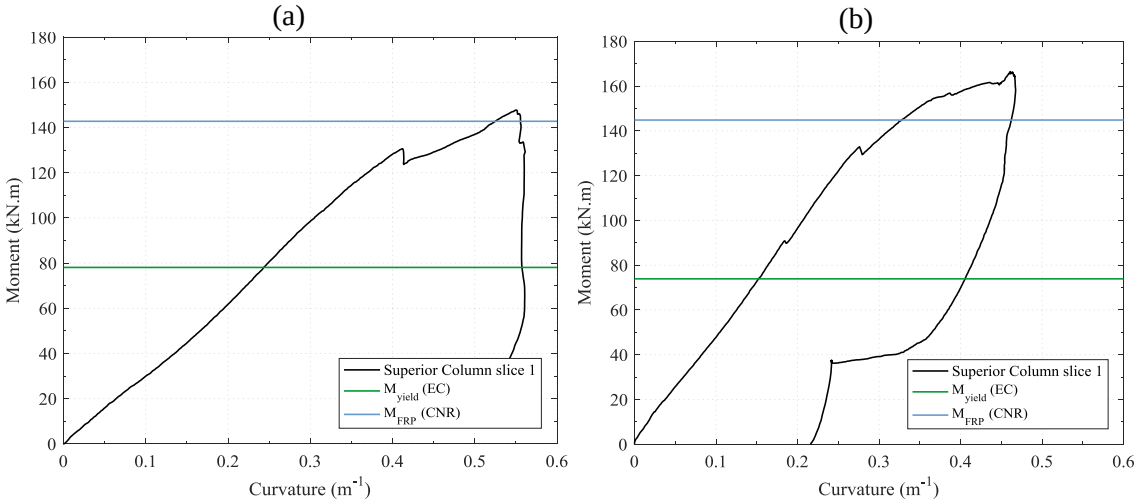

Figure 5.57. Moment curvature diagrams for column-only tests with indication of expected moment capacities (EC for unstrenghtened members and CNR for retrofitted members): (a) C1-RT-A-sw; (b) C1-RT-B-sw.

5.5. SUMMARY

A total of twelve full-scale RC beam-column joint and two column-only experiments are conducted to evaluate the relative effectiveness of three retrofit schemes and the effect of a realistic geometry on the seismic behaviour of RC structures.

In line with observations from the literature and FE modelling, joint shear failure is observed for the cruciform beam-column joint specimen without slab and transverse beam. In turn, the pre-1970's design control specimens with slab present a non-ductile behaviour with a single-storey failure of the superior column, characterised by a high level of post-peak softening, stiffness degradation and inter-cycle strength degradation at the ultimate state. A specimen designed to modern guidelines instead presents a much larger strength and ductility without rebar buckling and symmetric rotation of the two columns, with significant damage in the beams and slab.

Three retrofit schemes are designed to improve the deficient control specimen's behaviour by addressing the deficiencies selectively. First, retrofit RT-A is designed to increase the ultimate drift of the specimen. It successfully prevents buckling and connects the behaviour of the inferior and superior columns through longitudinal FRP strands. The observed behaviour is hence more ductile, with increased rotation of both columns and strongly increased lateral load bearing capacity. Still failure is ultimately governed by column hinging.

Next, retrofit RT-A-sw instead aims to increase the ductility of the specimen by enhancing the rotation of the beams through selective weakening of the slab, as well as connecting the superior and inferior column with FRP strands. The observed behaviour provides similar energy dissipation to that of RT-A, despite a lower lateral load capacity, due to a more ductile behaviour and significantly increased beam participation.

Finally, retrofit RT-B-sw aims to exploit the benefits of RT-A and RT-A-sw, providing a significant increase in strength and ductility. For the retrofitted specimen C1-RT-B-sw, indeed an improved seismic behaviour is observed. A strength enhancement to 70% of the EC8 specimen is achieved despite significant reinforcement detailing deficiencies and a very low concrete strength. The ductility enhancement is the largest of all retrofit specimens, as not only the single-storey and buckling failure mechanisms are prevented, but also spread-out damage is induced in the beams, starting in the anticipated plastic hinge zone, away from the joint. The resulting ductile failure mechanism is highly dissipative, reaching 80% of the energy dissipation of C-EC8 at the same level of ductility. Moreover, the post-peak softening, strength and stiffness degradation are all significantly reduced, even compared to the specimen designed to EC8.

A summary of all experimental results is given in Table 5.3.

Table 5.3. Summary of experimental results
(difference to C1 in brackets; apart from C2-RP-A for which C2 is the control, and C-noSLT-RP-B, for which difference to C-noSLT is given)

Specimen	F_{max} (kN)	Main damage	Δ_y (%)	Δ_{max} (%)	Δ_u (%)	$\mu_{\Delta u}$	E_d (kN.m)	S (kN/mm)	K_i (kN/mm)	$F_{deg,1-2}$ (%)	$F_{deg,1-3}$ (%)	$\varepsilon_{FRP,max}$ (%)
C-noSLT	45.16 (-28.4%)	Joint	0.67 (10.2%)	1.46	3.50	5.22 (44.4%)	31.82 (-0.8%)	-0.15 (-70.2%)	4.82 (-27%)	18.44 (-20.6%)	29.28 (-56.8%)	/
C1	63.08	Sup. column	0.65	1.27	2.34	3.62	32.08	-0.49	6.60	23.22	67.74	/
C2	66.71 (5.8%)	Sup. column	0.61 (-5.9%)	-1.46	2.52	4.14 (14.5%)	27.64 (-13.8%)	-0.39 (-20.4%)	5.95 (-9.9%)	7.46 (-67.9%)	14.58 (-78.5%)	/
C1-sw	67.47 (7%)	Sup. column	0.48 (-21.8%)	-0.96	1.85	3.89 (7.5%)	22.7 (-29.2%)	-0.4 (-18.4%)	7.71 (16.7%)	27.86 (20%)	67.53 (-0.3%)	/
C-EC8	123.88 (96.4%)	Columns, Beams	-0.89 (46.4%)	-3.45	-5.22	5.86 (61.9%)	172.28 (437.1%)	-0.47 (-5.8%)	7.18 (8.7%)	10.57 (-54.5%)	18.72 (-72.4%)	/
C1-RT-A	87.71 (39.1%)	Both columns	-0.83 (36.4%)	-3.46	-5.25	6.32 (74.6%)	93.84 (192.5%)	-0.33 (-33.6%)	6.91 (4.6%)	10.86 (-53.2%)	20.26 (-70.1%)	0.14
C2-RP-A	89.67 (34.4%)	Both columns	1.29 (111.7%)	2.95	4.78	3.71 (-10.4%)	82.29 (197.7%)	-0.33 (-17%)	3.94 (-33.8%)	13.33 (78.7%)	23 (57.8%)	0.14
C1-RT-A-sw	71.61 (13.5%)	Beams, Joint	0.78 (27.6%)	-2.46	5.19	6.69 (84.9%)	94.53 (194.7%)	-0.17 (-66%)	6.39 (-3.2%)	13.92 (-40.1%)	24.36 (-64%)	n.m.
C1-RP-A-sw	76.8 (21.8%)	Beams, Joint	0.95 (55.7%)	2.46	5.84	6.16 (70.2%)	101.82 (217.4%)	-0.15 (-69.3%)	4.66 (-29.4%)	10.59 (-54.4%)	17.57 (-74.1%)	0.12
C1-RT-B-sw	86.86 (37.7%)	Beams, Columns	0.95 (55.7%)	3.43	6.50	6.86 (89.6%)	111.57 (247.8%)	-0.19 (-61.8%)	5.65 (-14.5%)	8.87 (-61.8%)	15.67 (-76.9%)	0.08
C-noSLT-RP-B	67.83 (50.2%)	Beams	-1.06 (57.3%)	-2.44	-2.98	2.82 (-45.9%)	19.22 (-39.6%)	-0.83 (464.6%)	3.84 (-20.4%)	6.07 (-67.1%)	8.57 (-70.7%)	0.09
C0-RP-A-gs	77.86 (23.4%)	Inf. Column	-0.96 (48.6%)	-1.45	-3.54	3.68 (1.8%)	69.19 (115.7%)	-0.3 (-39.3%)	3.9 (-40.9%)	11.38 (-51%)	14.6 (-78.4%)	n.m.

6. DISCUSSIONS

In this chapter, the results presented in Chapter 5 are discussed and analysed in more detail. The results obtained reveal that the three steps of the proposed retrofit (A, A-sw and B-sw) achieve their respective targets overall. Still, a number of unresolved questions are raised by the observations and are further explored in this chapter. This will allow to ultimately answer the research question of this thesis, as to whether a practical retrofit strategy using CFRP sheets can be devised for full-scale deficient beam-column joints to achieve an adequate seismic behaviour.

A common observation amongst the strengthened specimens is that the moment capacity of the columns is lower than anticipated by the CNR guideline equations. The influence of the FRP strands and the impact of continuous strengthening of the columns through plastic tubes in the joint section is hence discussed initially (Section 6.1). An adaptation of the CNR design equations is offered to adequately estimate the contribution of FRP strands to the moment capacity of columns. This ultimately satisfies the objective of devising a methodology for the retrofit to be potentially implemented in future applications.

The effect of pre-damage and the consistency of retrofit effectiveness observed in the experiments is also presented in more detail (Section 6.2). The difference between repair and retrofit is assessed and the outcomes are discussed in terms of practical considerations.

The objective of assessing the influence of slab and transverse beams on the effectiveness of a retrofit scheme is then addressed is Section 6.3. The experiments highlight the overstrength of beams for both, retrofitted and control specimens. The effect of reinforcement detailing and geometry of the specimens is hence discussed, with particular emphasis on the observed under-estimation of the effect of slab and transverse beams. The effect of selective weakening is also considered (Section 6.4).

The effectiveness of the three retrofit schemes is also critically compared to evaluate their relative benefits and to assess whether an effective retrofit scheme for realistic beam-column joints can be designed to achieve the initially outlined targets (Section 6.5). Finally, as practical retrofit solutions for realistic structures are particularly emphasised in this thesis, practical aspects and considerations for the future implementation of the retrofit schemes are also discussed (Section 6.6).

Note: A number of comparative plots for all specimens referred to in this section can be found at the end of this Chapter.

6.1. THE EFFECT OF THE FRP STRANDS

6.1.1. MOMENT CAPACITY OF THE COLUMNS

For all strengthened specimens, the observed moment capacity for the retrofitted columns is lower than the expected values from the CNR guideline equations. The increase in flexural strength of the columns is highly dependent on the strain in the strands, but the practical implementation of the strands violates the assumptions of the complete bond of FRP sheets in the CNR guidelines.

Figure 6.1 illustrates the moment distribution and failure at the maximum load for the retrofitted specimens schematically. The absence of flexural cracks along the length of the column in zones (ii) and (iii) for all retrofitted specimens indicates that the contribution of the splayed-out FRP, which is bonded onto the column, is sufficient to withstand the applied moment in this section. The capacity in zone (iii) is governed by the non-retrofitted RC section. In zone (ii), the moment capacity corresponds to a retrofitted section with FRP bonded onto concrete, as calculated using the CNR guidelines. At the interface to the joint (zone i) however, the FRP strand is not bonded to concrete, but instead passed through a plastic tube, and hence free to move. In this section, corresponding to slice 1 in the analysis, large cracks are observed (e.g. Figure 5.28). Here, the contribution to the moment capacity by the FRP is controlled by the strain of the non-bonded strand, which, in turn, is governed by the relative fixed-end rotation of the superior and inferior columns. The FRP strands can hence be said to act passively, i.e. as they are free in the joint area, there is slippage and they are activated by increased rotation of the columns, which means yield of column bars will still occur. This slippage of FRP strands is also observed by Shiohara (2009).

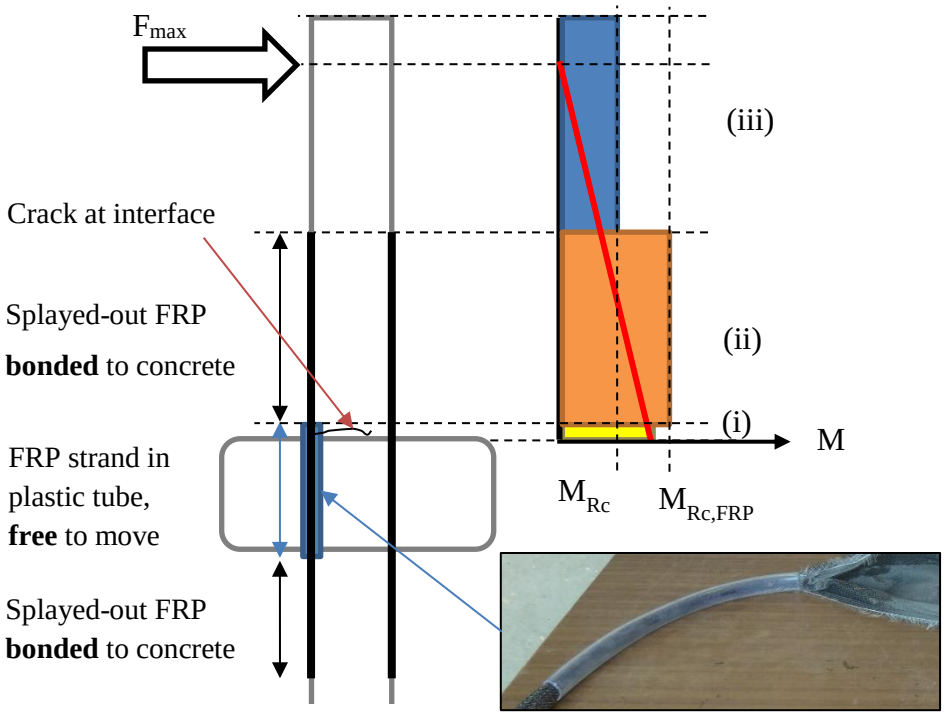

Figure 6.1. Schematic representation of the moment capacity along the length of the superior column in all retrofits.

Clearly, the higher tensile strain is in the strands, the more the FRP strands contribute to the moment capacity of slice 1. Lower strain in the FRP in this section than the predictions from the CNR guidelines, as the FRP is free to move, may hence explain why the moment reached in the column is lower than initially expected.

To obtain the highest strain possibly in the FRP strands, these would need to be anchored in a relatively fixed position. In the case of the two column-only tests, the strands are de-facto anchored to a fixed position, as the inferior columns are prevented from rotating. The largest moments are hence obtained for the two column-only tests and the CNR guideline equations hold true, predicting conservative values 3.5% and 15.0% lower than the experimental values. A large rotation of the superior column with absence of inferior column rotation, as observed for the column-only tests, leads to a higher strain in the strands and hence a larger contribution to the moment capacity.

In the case of the full beam-column joint specimens, if anchored along the entire height of the joint, as for C0-RP-A-gs, premature rupture is observed. This is because a very high local strain between the glued section in the joint area and the splayed-out section in the columns is obtained. The moment capacity of the retrofitted columns at the interfaces to the joint is governed by the strain in the FRP strands. As the strand ruptures for C0-RP-A-gs, the moment capacity in the column/joint interface is immediately observed to drop to the level of a non-retrofitted column, as the ruptured strands no longer contribute to the flexural capacity in zone (i). This observation is schematically illustrated in Figure 5.22.

The drop in capacity after rupture confirms the importance of the strands in providing continuous strengthening along the columns and through the slab. Without strands, the columns reach their non-retrofitted moment capacity at the joint-column interface, making the retrofit of the rest of the column also ineffective. The retrofit of the entire length of the column, including continuity through the slab, is hence required to ensure the capacity of the joint-column interface is enhanced and formation of a crack at the interface is prevented.

For the other retrofitted beam-column joint specimens, the strands are fully free between the two columns and the strain in the strand is governed by the relative elongation of the superior and inferior columns. In the positive drift direction, the left side of the superior column is in tension, while the left side of the inferior is in compression, and vice-versa. The strain in the strands is thus a trade-off between the tensile and compressive strain in the two columns at any given point.

In Table 6.1, the peak strain values in the strands are compared to the expected strain values from the CNR guidelines for fully bonded FRP sheets (CNR equation 4.7). In Figure 6.2, the strain evolution at the peak drifts in the FRP strands are presented. The readings from strain gauges placed on the FRP strands are shown. Note that for specimen C1-RT-A-sw no strain gauge

recordings are available due to a technical error. It can be seen that the strain in the strands reaches a plateau for all specimens, which is lower than the expected FRP strain for fully bonded FRP on concrete members according to the CNR equations (Table 6.1). The lower values of FRP strain confirm the hypothesis that the FRP strands in the plastic tubes reach lower strain values and hence lead to a lower moment capacity at the column/joint interface.

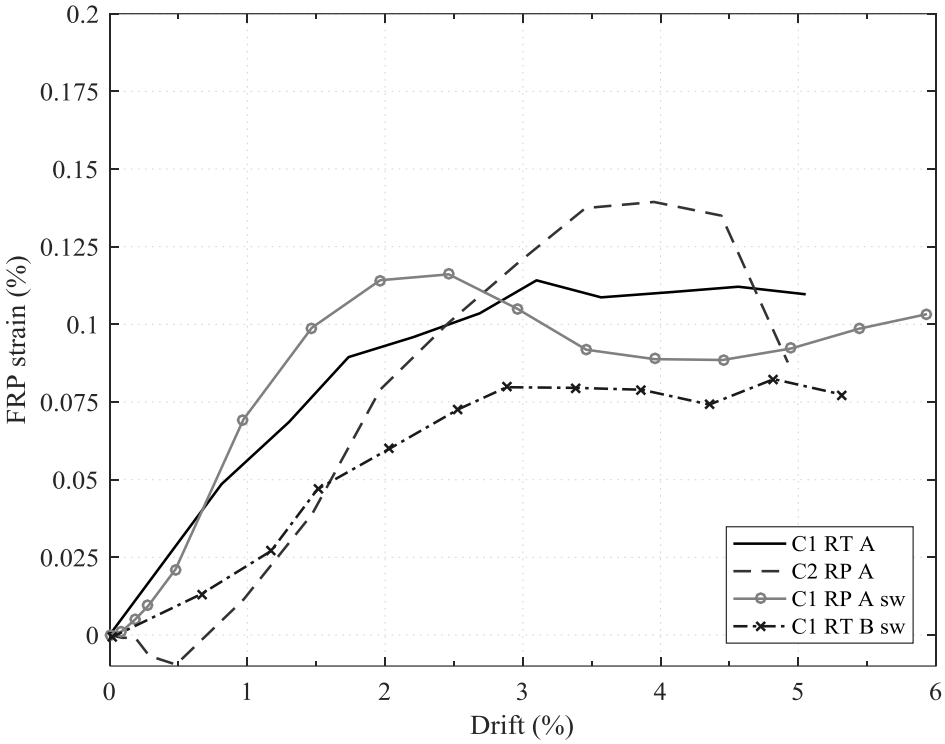

Figure 6.2. Envelope of FRP strains at peak positive drift for left-hand-side FRP strands for the retrofitted beam-column joint tests.

From Table 6.1, it can be observed that the experimental strain values in the FRP strands are indeed much lower than the predicted values. The CNR predicted FRP strain based on fully bonded FRP sheets, $\varepsilon_{fdd,CNR}$, are therefore on average double compared to the experimental values of strain, $\varepsilon_{FRP,max}$ (+105%). This echoes observations by Yu et al. (2016) for L-shaped laminates for column strengthening.

Table 6.1. Comparison of FRP strains predicted by the CNR guidelines for bonded FRP sheets and FRP strains measured in the FRP strands.

	Experimental strain $\varepsilon_{FRP,max}$ (%)	CNR strain $\varepsilon_{fdd,CNR}$ (%)	$\varepsilon_{fdd,CNR}/\ \varepsilon_{FRP,max}$
C1-RT-A	0.114	0.212	1.85
C2-RP-A	0.139	0.240	1.72
C1-RT-A-sw	/	0.250	/
C1-RP-A-sw	0.116	0.257	2.21
C1-RT-B-sw	0.082	0.198	2.40
Average			2.05

An alternative formulation of the CNR equations is therefore proposed here in order to take into account the lack of bond of FRP strands in the joint section. As illustrated in Figure 6.3, the effective strain in the FRP fibres, ε_{fdd}, calculated according to eq. 4.6 of the CNR guidelines, applies only to the splayed-out, and hence bonded, section of the FRP. Between the superior and inferior column, as the FRP strands are placed in plastic tubes and not bonded, it is hence necessary to determine the equivalent effective strain $\varepsilon_{fdd,strands}$ in this location.

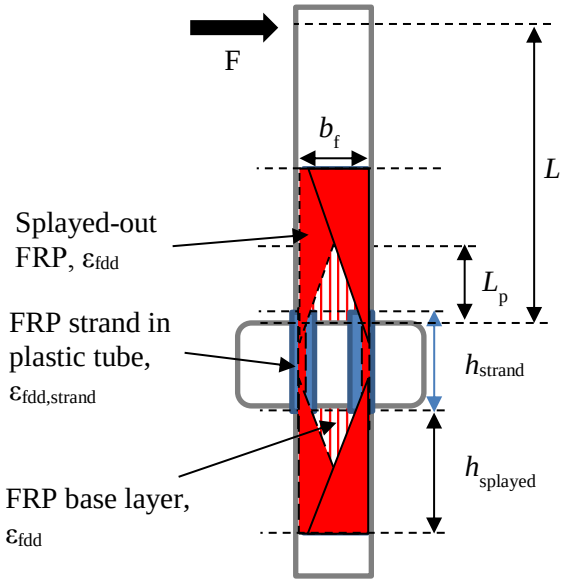

Figure 6.3. Definition of geometric parameters for the FRP strands in the tubes and splayed-out.

First, the non-bonded, free length of the FRP, h_{strand}, is defined as the height of the beam plus the protrusion of the strand, $h_{protrusion}$, on either side, to allow for the length of the plastic tubes not finishing exactly at the joint-column interface:

$$h_{strand} = h_b + 2 \cdot h_{protrusion} \ (mm) \tag{6.1}$$

For the experiments presented in this thesis an average of ca. 30 mm is measured for $h_{protrusion}$, but its value will depend on the practical application on site.

With no debonding, it is assumed that at the level of maximum moment in the column, the effective maximum FRP strain, ε_{fdd}, will be fully developed along the plastic hinge length, L_p. The length of the FRP confined plastic hinge can be determined using well-tested equations proposed by Jiang et al. (2014):

$$L_p = L_{p0} + \left(\frac{2r_c}{b}\right)^{0.72} \cdot L_{pc} \tag{6.2}$$

Where L_{p0} is the unconfined plastic hinge length determined according to the well-established equation by Paulay and Pristley (1992):

$$L_{p0} = 0.08L + 6\,d_b \tag{6.3}$$

With L, the column shear span, and d_b being the bar diameter of the longitudinal steel.

Finally, L_{pc} is the plastic hinge length due to the confinement effect for circular columns, reduced by the $k_s = \left(\frac{2r_c}{b}\right)^{0.72}$ factor, dependent on the corner radius, r_c, and the column width, b, to account for square column geometries:

$$\begin{cases} L_{pc} = 3.028\,\lambda_f & when\ \ 0 \le \lambda_f < 0.1 \\ L_{pc} = \left(0.51 - 2.3\,\lambda_f + 2.28\,{\lambda_f}^2\right)L & when\ \ 0.1 \le \lambda_f < 0.5 \end{cases} \quad (6.4)$$

With λ_f defined as the confinement efficiency factor, calculated as in cl. 4.5.2 (7) of CNR-DT 200 R1/2013:

$$\lambda_f = f_{1,eff} / f_{cd} \quad (6.5)$$

Based on the plastic hinge length, the strain in the strand is then determined by calculating the fixed end deformation along the plastic hinge from the effective strain in the bonded FRP, ε_{fdd}, and dividing this by the free length of the FRP in the plastic tube, i.e.:

$$\varepsilon_{fdd,strand} = \frac{(\varepsilon_{fdd} \cdot L_p)}{h_{strand} + 2\,x_i} \quad (6.6)$$

As illustrated in Figure 6.4, x_i is an empirical variable to account for part of the splayed-out FRP not adequately bonded to the concrete surface at the transition to the plastic tubes. Values between 15 and 25 mm are measured here and an average value of 20 mm is suggested.

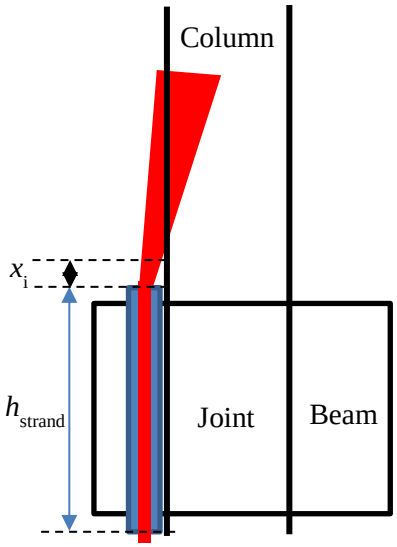

Figure 6.4. Schematic representation of empirical factor x_i.

As shown in Table 6.2, the predicted strains using the new equation for the strands, $\varepsilon_{fdd,strand}$, are much closer to the experimental values (+10%) than the values of strain previously determined using the CNR equations, $\varepsilon_{fdd,CNR}$ (+105%).

Table 6.2. Comparison of experimental FRP strains and values predicted by the CNR guidelines and the new equations for FRP strands.

	Experimental strain $\varepsilon_{FRP,max}$ (%)	CNR strain $\varepsilon_{fdd,CNR}$ (%)	New predicted strain $\varepsilon_{fdd,strand}$ (%)	$\varepsilon_{fdd,strand}/\varepsilon_{FRP,max}$
C1-RT-A	0.114	0.212	0.123	1.075
C2-RP-A	0.139	0.240	0.124	0.892
C1-RT-A-sw	/	0.250	0.140	/
C1-RP-A-sw	0.116	0.257	0.148	1.273
C1-RT-B-sw	0.082	0.198	0.095	1.159
Average				1.10

Using the experimental strain values in the CNR guideline equations, the moment capacities for the column/joint interface (slice 1) are re-evaluated. These new values ($M_{Rc,FRP,new}$) are presented in Table 6.3. For all specimens, the re-calculated moment capacities are significantly improved compared to the initial assessment using the CNR design strain ($M_{Rc,FRP,CNR}$). On average the moment capacities evaluated with the real strain values are 7% higher than the real moment capacities, while for the initial assessment, values 38% higher are obtained. The values of $M_{Rc,FRP,new}$ lie within 10% of the predictions, apart from C1-RP-A-sw (+19%), which had significant pre-damage.

Table 6.3. Comparison of actual maximum moment (M_{max}) to predicted moments with experimental strains ($M_{Rc,FRP,new}$) and from the CNR guidelines ($M_{Rc,FRP,CNR}$).

	$M_{Rc,FRP,new}$ (kNm)	$M_{Rc,FRP,new}/M_{max}$	$M_{Rc,FRP,CNR}/M_{max}$
C1-RT-A	120.4	1.04	1.28
C2-RP-A	126.3	1.08	1.31
C1-RT-A-sw	/	/	1.55
C1-RP-A-sw	115.0	1.19	1.49
C1-RT-B-sw	111.2	0.99	1.28
Average		1.07	1.38

As the moment capacities obtained using the experimental strain values are very close to the experimentally obtain maximum moments in the columns, the validity of the CNR equations to determine the retrofitted moment capacities of columns is hence confirmed. The modified design methodology for retrofit B-sw in Appendix F is based on the CNR equations to enable ease of implementation, but improved with new effective strain equations to account for realistic implementation of the proposed FRP strand retrofits.

6.1.2. BEAMS AND JOINT

Another innovation in the proposed retrofit design came from the strengthening of beams and joint using horizontal FRP strands in retrofit B-sw. The modified method for calculating the amount of FRP required for the beams (described in Section 3.6.) is confirmed, as the moment capacity of the retrofitted beam-ends is correctly estimated using the CNR guideline equations (+8.4%). The reason for this is that, unlike the columns, the assumption of full bond is true for the beam strands, as no plastic tubes are used in the joint regions.

For the joint strengthening using FRP strands, no numerical assessment can be made, as no joint shear cracks are observed for retrofit RT-B-sw. It can however be said, that the intervention is successful as no debonding or rupture of the joint FRP is observed.

Still, it is not possible to draw any further conclusions, as results are only available for one specimen, highlighting the need for further experimental or numerical work to validate the design methodology for joint and beam strengthening.

6.2. THE EFFECT OF INITIAL DAMAGE

In Chapter 5, the results for a number of repaired specimens is presented. Although showing similar trends to retrofitted specimens in terms of strengthening objective achievement, they display significant differences in terms of initial stiffness and ductility improvement that can be achieved. Here, the effect of initial damage is hence assessed by comparing the two repair specimens C2-RP-A and C1-RP-A-sw with the respective retrofit specimens.

In terms of repair and retrofit effectiveness, no significant differences are observed when it comes to the peak lateral force, however, a significant reduction in initial stiffness is observed for all repair specimens. For specimen C2-RP-A, the reduction in initial stiffness is -33.8 % compared to C2, and, similarly, for C1-RP-A-sw, a lower initial stiffness than C1 is obtained (-29.4%). This observation is in direct correlation with the pre-cracked concrete in the columns, seen for both repair specimens, and is in line with previous observations in the literature (Agarwal et al. 2014; Beydokhti and Shariatmadar 2016; Yurdakul and Avşar 2015).

The reduced stiffness in turn leads to a higher value of yield drift for both repair specimens. As a consequence, reduced ductility of the repaired specimens compared to the respective retrofits is obtained, with a decrease of 39.0% for C2-RP-A and 10.4% for C1-RP-A-sw. Finally, damage in the specimens is also observed at slightly higher drift for the repair specimens compared to the retrofit specimens.

Furthermore, in terms of practical implementation of repair schemes, quality control for repairing damaged concrete is shown to be crucial. For specimen C1-RP-A-sw, for instance, a difference in concrete cover for the repaired column leads to an asymmetric capacity in the two loading

directions. In a full frame, such errors can affect the behaviour of the structure and can lead to premature failure in one direction of loading. Errors in repair are hence important to consider in putting forwards guidelines on repairing specimens.

Overall, for all repaired specimens an improved dissipative behaviour with increased load capacity is achieved. Unlike previous observations in the literature, for which the strength of the control specimens is not recovered (Agarwal et al. 2014; Beydokhti and Shariatmadar 2016; Yurdakul and Avşar 2015), the proposed repair method can be successfully applied despite significant initial pre-damage, up to failure of the control specimens.

6.3. THE EFFECT OF SLAB AND TRANSVERSE BEAMS

6.3.1. CONTROL SPECIMENS

To assess the effect of slab and transverse beams, the behaviour of the control specimen C1, with slab and transverse beam, and the cross-shaped specimen C-noSLT are compared.

The importance of including slabs and transverse beams is first and foremost seen in the failure mechanism. For the control specimen without slab and transverse beam, C-noSLT, a very different failure mechanism and damage pattern are observed. Damage is observed mainly in the joint region, with some cracking along the beam and very limited cracking in the columns. This is in stark contrast to the column failure observed for C1, with limited rotation of the beams and damage concentrated in the column, just above the joint.

This difference in failure mechanism is of grave importance as it affects the retrofit design and objectives. Retrofit designs that cater for cruciform specimens like C-noSLT need to focus on joint shear strengthening, while in reality, post-earthquake field studies indicate that weak-column failures are mainly observed for interior RC joints (Yu et al. 2016). Due to the additional hogging capacity from the slab reinforcement, as well as increased joint confinement in interior joints from the transverse beams, failure mechanisms such as the one observed experimentally for C-noSLT are highly unrealistic for real structures. To simulate actual seismic damage to interior beam-column joints, set-ups with a slab and transverse beams are hence required.

The effect of the slab is clearly highlighted by the evolutions of curvatures at the beam to joint interface shown in Figure 6.5. In the case of C-noSLT the beam rotation is not limited by the slab and a symmetric curvature evolution is observed between positive and negative cycles (imposing sagging and hogging in the right beam, respectively). Without the slab, the hogging and sagging moment capacities of the beam are similar, allowing the beams and joint to rotate. For C1, in turn, overall a much lower maximum hogging curvature in the beams is recorded (- 90.2% vs C-noSLT). The rotation of the beams is also highly asymmetric, with curvatures in sagging of the beams three times larger than in hogging.

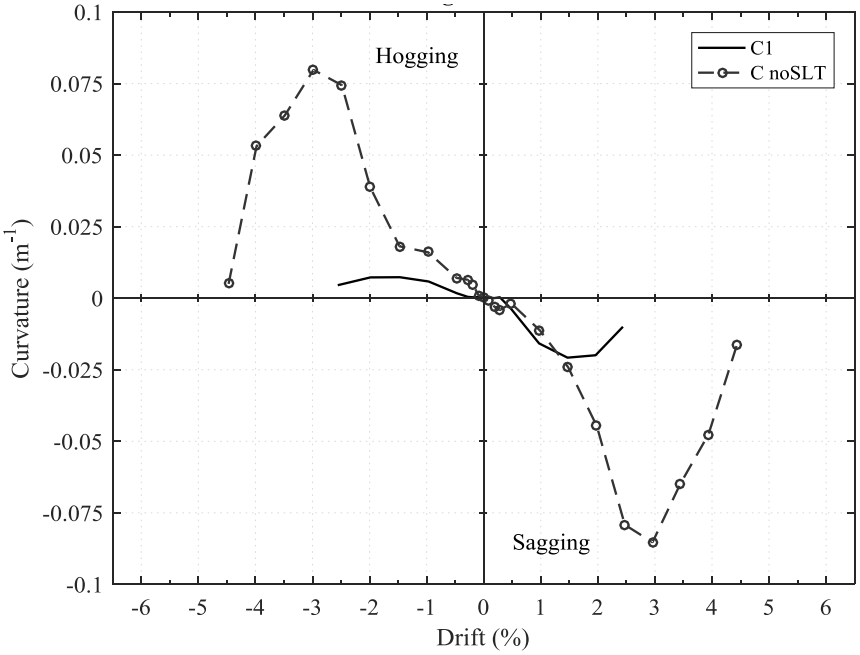

Figure 6.5. Comparison of the experimental beam curvatures close to the joint interface (slice 1) for C1 and C-noSLT versus level of drift (%).

Looking at the at the contribution to the total energy dissipation by individual members in Figure 6.17, for the control specimen with slab 80% of the total energy dissipation is dissipated by the columns and only 1.5% can be attributed to the beams. For the specimen without slab, this is drastically different, with the column contribution reduced to 11.5 %, with 20.4% of the total energy dissipated by the beams and the majority of energy dissipated by the joint (68.1%).

The influence of slab and transverse beam on the behaviour of the control specimens is also seen in terms of global force-drift envelope and energy dissipation (Figure 6.6). Specimen C-noSLT displays a more ductile response (+44.4% vs C1), but with a much lower peak force (-28.4%) and a decreased energy dissipation (-0.8%). The increase in ductility is a direct consequence of the reduced yield drift. Due to the removal of the slab contribution, yielding is observed in the beams, and this leads to a lower yield drift of 0.59% (-9.2% compared to C1). As shown in Table 5.1, the initial stiffness of the specimen without slab is also much lower (-27%).

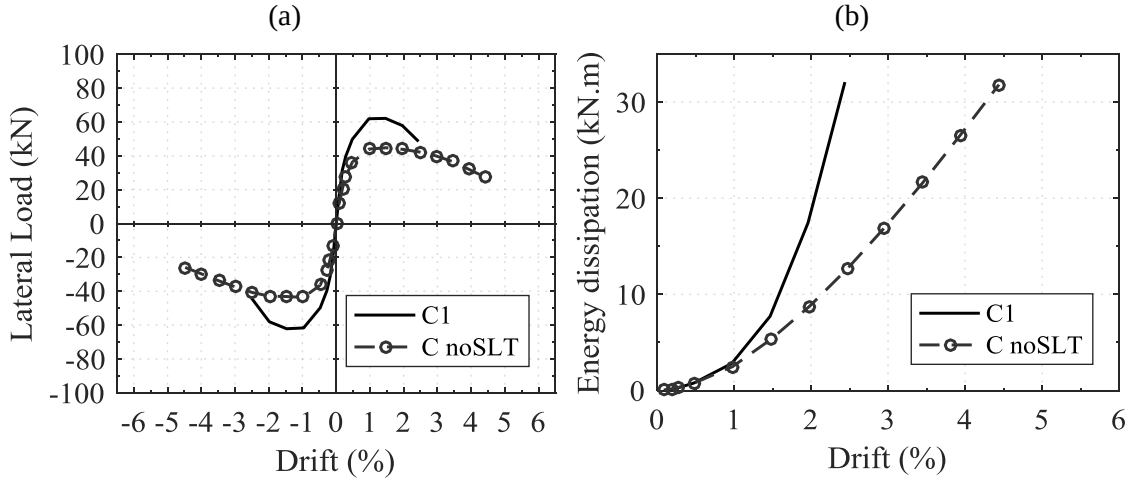

Figure 6.6. (a) Force-drift envelope and (b) energy dissipation vs drift for C1 and C-noSLT.

Overall, the importance of testing specimens with slab and transverse beams is highlighted by the experimental results. The failure mechanism of the specimen without slab is shown to be very different to the one with slab, which in turn plays a crucial impact on the retrofit design, in terms of retrofit aim and need for weakening the slab.

6.3.2. LARGER SLAB CONTRIBUTION THAN ANTICIPATED

When testing specimens with slab, it is also observed that the moment capacities of the T-beams are actually higher than the calculated capacities using the Eurocode equations, even when considering the overstrength factor for strain hardening. This is noticed for specimens C-EC8, C0-RP-A-gs and C1-RT-A, for which the maximum beam sagging moments are over 50% larger than the calculated capacities[2]. The reason for this can be found in an increased slab contribution, with a larger effective width possibly required in the EC8 equations. The contribution of bottom slab bars in tension would then also be needed to be considered.

The observations are in line with limited experimental observations from other experimental work and echoes the critique of Paulay (1986), which called for a higher beam overstrength factor of 2.0-2.5 rather than the lower values seen in EC8. To confirm these observations however, the mechanisms involved need to be investigated further by means of a thorough numerical parametric study and further experimental evidence. The effect of bi-directional loading is not considered in this study and may play an important role in determining the real contribution of the slab to the overall beam and joint behaviour (Cheung et al. 1991b; Engindeniz et al. 2008). This is however not the scope of this thesis, but can be seen as avenue for future research.

6.3.3. TORSIONAL CRACKS IN THE TRANSVERSE BEAMS

Next to the effect of the slab, it is also noticed that the presence of transverse beams leads to increased damage in the specimens. For specimens with increased joint and beam rotation, torsional cracks in the transverse beams, leading to triangular wedges of concrete spalling off are observed. The cracks are reciprocated in the slab, with an angled crack in the top and bottom surface, as shown in Figure 5.16. The observed torsional cracking is similar to observations by Kam et al. (2010) and Cheung et al. (1991a). Torsional cracks appear due to a difference in support conditions at the two ends of the transverse beam. At the end away from the joint is free to translate in the direction of loading, while at the interface to the joint, the beam is connected to the joint and slab, which resists the rotation of the sub-assembly. These cracks are hence only observed for specimens with significant rotation of beams and joint, hence inducing more torsion in the transverse beams.

[2] In terms of hogging moments, similar results are expected, however the hogging moment is not reached for any specimen with full slab participation.

6.3.4. RETROFIT EFFECTIVENESS

A major outcome of the literature review presented in Chapter 2 is that the effectiveness of retrofits may be overestimated when testing unrealistic configurations without slab and transverse beams. The statistical analysis of the compiled literature database presented in section 2.2.4 highlights that for specimens without slab and transverse beams, on average, a 45% strength enhancement is obtained by FRP retrofitting. For specimens with slab and transverse beams, however, this is reduced to an average strength enhancement of 26%. Clearly, the comparison is not fully valid, as a variety of geometries and retrofit schemes are tested, making an objective one-to-one comparison impossible.

To objectively test the hypothesis that specimens without slab render retrofits more effective, specimens C1-RT-B-sw and C-noSLT-RP-B are compared in terms of strength increase, but also in terms of failure mechanism and strength degradation. The two specimens are retrofitted to the same procedure, with the same amount of FRP applied in both cases.

In terms of increase in lateral load capacity, as shown in Figure 6.7, the increase in strength due to retrofit B is 37.7% with slab and 50.2% without slab. The difference in effectiveness is hence less pronounced than it is found from the analysis of the literature database, but it is still significant.

Looking at Table 5.1, for specimen C-noSLT-RP-B a reduction in performance in terms of ductility and softening behaviour is observed. This can however mainly be associated to the loss of strengthening in the beams after crack formation underneath the anchorage system.

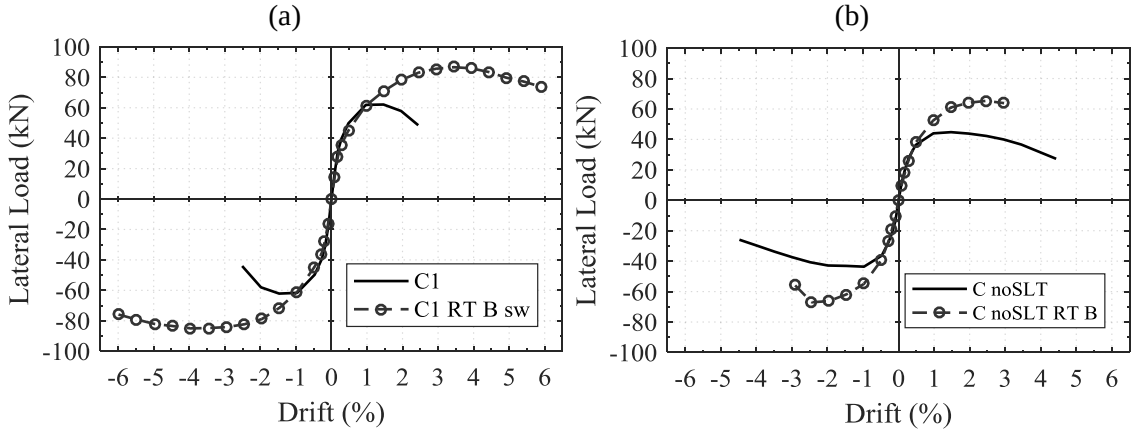

Figure 6.7. Comparison of force-displacement envelopes for (a) C1 and C1-RT-B-sw; and (b) C-noSLT and C-noSLT-RP-B.

In terms of increasing the beam participation in the failure mechanism, the retrofit of the specimen without slab is more effective. Due to the very different hierarchy of strength for the respective control specimens, for the specimen without slab, no column damage is observed. Ensuring failure by a beam-sway mechanism in C-noSLT-RP-B, is hence easily achieved by retrofitting the joint appropriately to eliminate joint shear failure. Indeed, very strong damage in the beams is

observed, with a large strength increase up to the failure of the anchorage system. For the specimen with slab however, moving the failure mechanism to the beam is very difficult, as the slab prevents rotation of the beams. Selective weakening is hence required, leading to strongly increased beam damage and rotation, but not without cracking at the column/joint interface.

The effectiveness of inducing beam failure is further highlighted by looking at the contribution to the total energy dissipation by individual members in Figure 6.17. For C1-RT-B-sw, the beam participation to the total energy dissipation is increased from 1.5% in C1 to 14.4%, hence by 12.9 pp. In turn, for C-noSLT-RP-B, the increase is much larger (31.8 pp), from 20.4% in C-noSLT to 52.2% in C-noSLT-RP-B. This increase is mainly achieved by reducing joint shear deformation in C-noSLT-RP-B, while for C1-RT-B-sw, the contribution by the column is reduced.

In terms of inter-cycle strength degradation, as shown in Figure 6.18 and Figure 6.19, C-noSLT performs particularly badly. The very high strength degradation observed is mainly related to the increased damage in the joint. It is hence seen that for C-noSLT-RP-B, the values of $S_{deg,1\text{-}2}$ (-67.1%) and $S_{deg,1\text{-}3}$ (-70.7%) are effectively reduced by preventing joint shear failure. For specimen C1-RT-B-sw, the improvement compared to C1 is similar, as for C1 very large strength degradation in the last cycle is observed due to column bar buckling, which is prevented by the retrofit.

6.4. THE EFFECT OF SELECTIVE WEAKENING

In order to assess the retrofit schemes objectively, the isolated effect of selective weakening is assessed by comparing the results for specimens C1 and C1-sw.

When looking at the behaviour of specimen C1-sw, it can be observed that selective weakening of the slab alone does not significantly alter the specimen's behaviour. The same failure mechanism is observed as for control specimen C1 without weakening cuts. The contribution of the remaining slab reinforcement outside of the weakening cuts (two bars on each side), as well as the confinement provided by the transverse beams lead to a behaviour of C1-sw more similar to that of C1 rather than C-noSLT, the specimen without slab and transverse beams. Looking at Figure 6.17, the contribution to the total energy dissipation is very similar to C1, with a similarly low beam contribution (2.3%) compared to C1 (1.5%).

Still, due to the reduction in slab contribution, yielding in the bottom beam bars is observed, which is not observed in C1. The slight increase in strength (+6.96 %) and ductility (+7.47%), shown in Figure 6.8 (a), may be attributed to selective weakening, however, C1-sw also presents a higher concrete strength of 26 MPa then C1 (23.4 MPa). As shown in Table 5.1, a similar post-peak softening behaviour and strength degradation between cycles is also recorded. However, as shown in Figure 6.8 (b), a reduction in total cumulative dissipated energy is observed (-29.2% compared to C1), possibly due to reduced damage in the slab and hence a removal of the slab contribution.

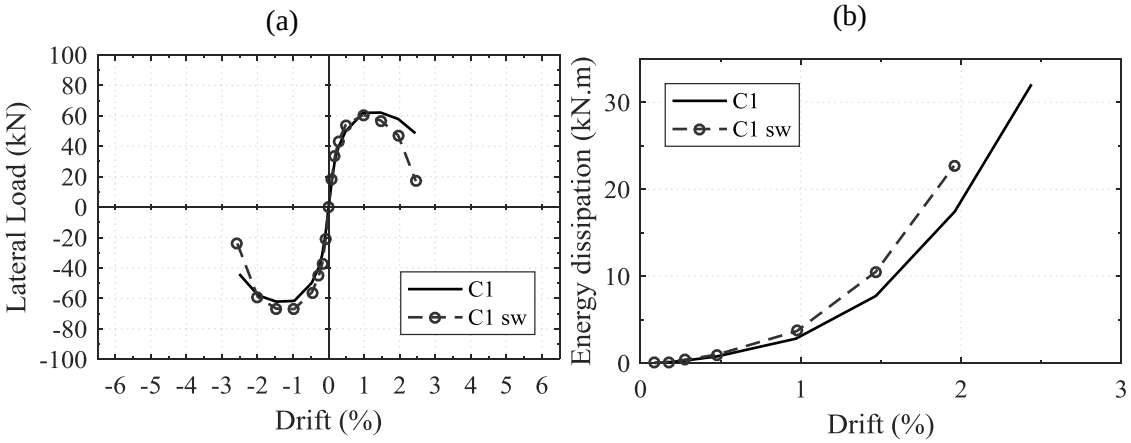

Figure 6.8. (a) Force-drift envelope and (b) energy dissipation against drift for C1 and C1-sw.

Overall, the hierarchy of strength is unchanged by the cuts in the slab, as the columns remain the weakest members in the sub-assembly. Joint shear failure, observed for the cruciform specimen, is prevented by the confinement provided by the transverse beams. To achieve a more appropriate hierarchy of strength, in addition to the slab weakening, column strengthening is hence required.

6.5. COMPARISON OF THE THREE RETROFIT SCHEMES

In this sub-section, the effect of the three proposed retrofit schemes is compared in terms of the metrics discussed in Chapter 4.

6.5.1. LATERAL FORCE CAPACITY

First, in terms of force-drift shown in Figure 6.9, retrofits RT-A and RT-B-sw are most effective in enhancing the lateral load capacity. For both retrofits, an increase in strength close to 40% compared to C1 is observed, leading to a capacity close to 70% of the EC8 specimen. This is slightly lower than the designed-for capacity (80% of EC8), but a substantial increase in strength in comparison to other efforts in the literature for specimens with slab (26% average strength increase). For retrofit RT-A-sw, for which the beams are not strengthened, only a 13.5% increase in strength is observed. Shiohara (2009) observed a 12.8% improvement for interior joints without slab and transverse beams, which are also retrofitted with vertical FRP strands, indicating that with selective weakening similar performance to cruciform specimens is obtained. However, due to the better hierarchy of strengths in retrofit RT-A-sw ($\mu_{\Delta u}$ = 6.7), it is slightly more successful in enhancing the ductility of the specimen than retrofit RT-A ($\mu_{\Delta u}$ = 6.3). With the plastic hinge relocation in the beams, retrofit RT-B-sw is achieving the highest ductility of 6.9.

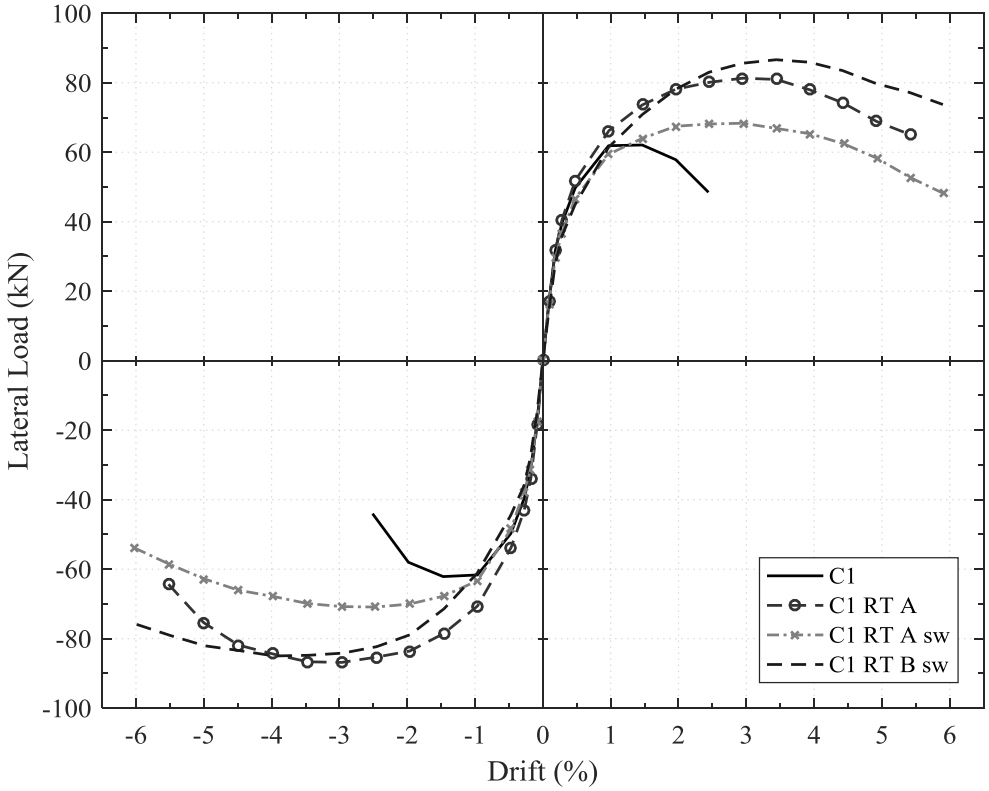

Figure 6.9. Force-displacement envelopes for the control specimen C1 and the three retrofit specimens.

From Figure 6.9 it also becomes apparent that the post-peak softening behaviour of the retrofits with selective weakening are superior to RT-A. For all retrofits, a better softening behaviour than

the control specimens C1 (-490 kN/m) and C-EC8 (-470 kN/m) are obtained. The softening is large for the control specimens as buckling and crushing failures are observed, respectively. For RT-B-sw, a softening stiffness of -190 kN/m is obtained, corresponding to an improvement in softening of 62% compared to the control specimen C1. The softening behaviour is slightly better with retrofit RT-A-sw, with a softening stiffness of -170 kN/m (-66% vs C1). Finally, for retrofit RT-A without selective weakening, the softening is still improved compared to C1 (330 kN/m, -33.6%), but nearly double that of RT-A-sw. This means that for retrofits with selective weakening a larger residual strength after the lateral force peak are hence obtainable.

6.5.2. DAMAGE AND FAILURE MECHANISM

In terms of damage and failure mechanism, for all three retrofits, compared to the control specimens, buckling of the superior column bars and the single-storey failure mechanism are prevented. From the three retrofit specimens, cracking and yielding are delayed to the highest drift levels for RT-B-sw, making it easier to repair in case of less significant earthquakes.

This observation is particularly highlighted when looking at the damage evolution for the retrofitted specimens and control specimens C1 and C-EC8, presented in Figure 6.10. The definition of damage indices proposed by Rossetto and Elnashai (2003) is used here, and the physical observations associated to the damage indices is presented within the figure. For comparison, the performance levels for concrete frames in FEMA 356 (1999) are also indicated.

At low drift levels, the retrofitted specimens present a similar performance, with consistently less damage than the control specimens. For all tested specimens, moderate damage is reached for drift levels below 1.0%. Limited yielding is observed for all specimens, which is in line with the definition of the IO (immediate occupancy) performance level of FEMA 356. Moderate to extensive damage with spalling is observed for drift levels above the 2.0% drift, hence complying with the drift limit for the LS (life safety) performance level. Here, all three retrofits outperform the two control specimens. While RT-A displays similar performance to C-EC8, RT-A-sw and RT-B-sw reach moderate to extensive damage at significantly higher drift levels.

Finally, it can be observed that for C1 extensive damage up to partial collapse is reached around 2-2.5% drift, hence not meeting the 4.0% drift limit prescribed in FEMA 356 for collapse prevention (CP). This is expected for a specimen designed to pre-1970's guidelines. In turn, all retrofitted specimens and C-EC8 reach their ultimate point (partial collapse) after 4.0% drift, and hence present adequate behaviour with respect to the limits in FEMA 356. While retrofits RT-A and RT-A-sw show a similar performance to C-EC8, retrofit RT-B-sw clearly outperforms them, reaching the ultimate drift around 6.5 %.

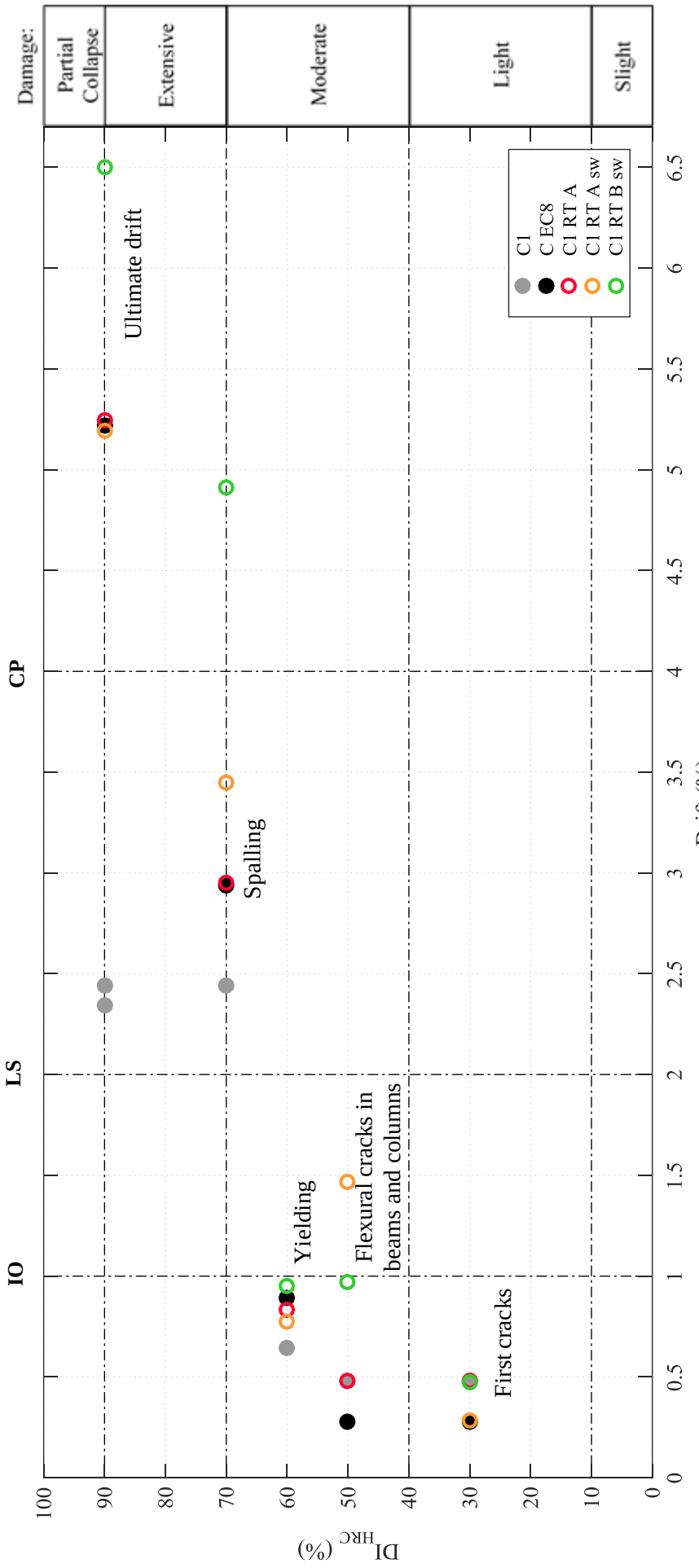

IO = Immediate occupancy; LS = Life Safety; CP = Collapse Prevention - according to FEMA 356 (1999).

Figure 6.10. Evolution of damage in terms of the HRC damage index for all retrofitted specimens compared to control specimens C1 and C-EC8.

The three retrofit schemes are also judged in their ability to move damage to the beams. As shown in Figure 6.11, for retrofit RT-A the lowest curvatures along the beams are observed, while for the retrofits with selective weakening, RT-A-sw and RT-B-sw, much larger and symmetric curvatures in hogging and sagging are recorded together with significant damage along the beams.

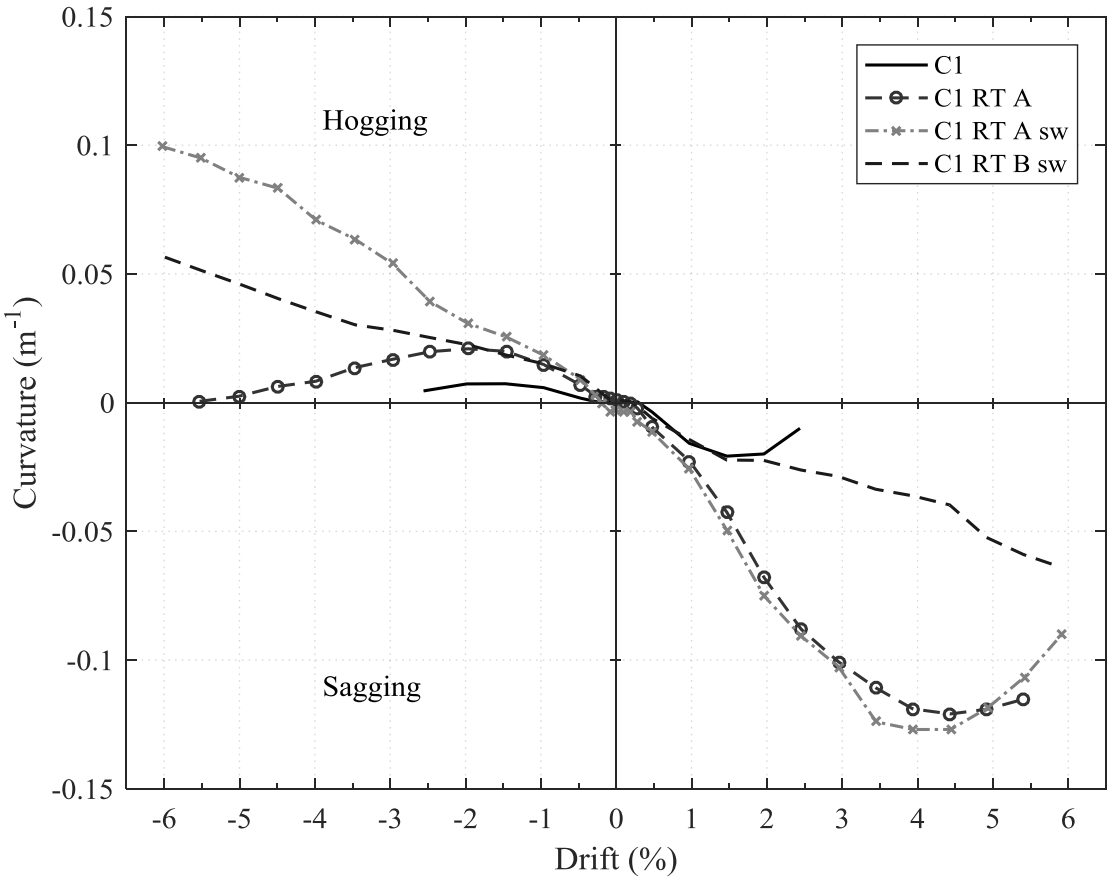

Figure 6.11. Curvatures in slice 3 for the right beams for the three retrofitted specimens compared to control specimens C1 and C-EC8.

Damage is most spread-out along the beams for retrofit RT-B-sw, with initial cracks forming about 500 mm from the joint, while for retrofit RT-A-sw, cracking initiates at the beam/joint interface. This is similar to observations from FE-modelling presented in Section 3.6. For retrofit RT-B-sw the aim of relocating the plastic hinge and damage 500 mm away from the joint of the beam is indeed achieved, with the highest curvatures in hogging and sagging recorded in slice 3, as shown in Figure 6.12. The curvatures recorded are about three times higher than for retrofit RT-A-sw.

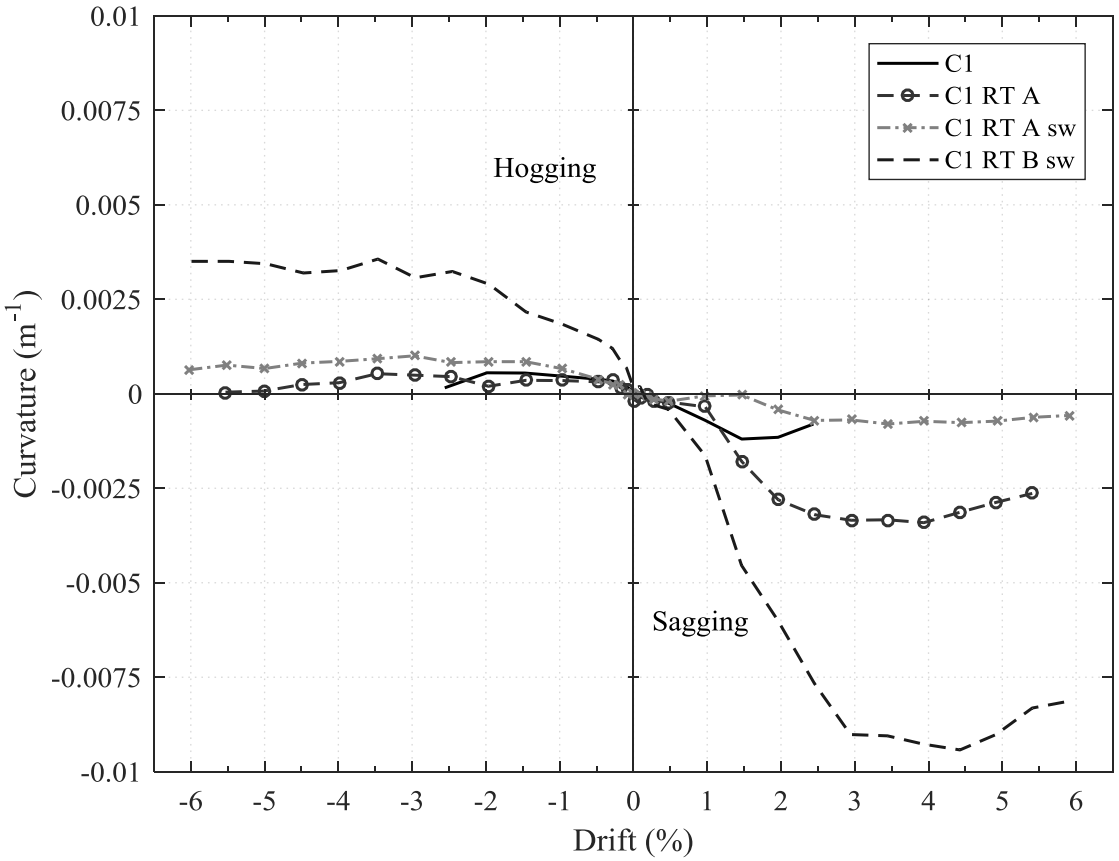

Figure 6.12. Curvatures in slice 3 for the right beams for the three retrofitted specimens compared to control specimens C1 and C-EC8.

Overall, the beams are however most effectively activated for specimen C1-RT-A-sw, and this is also highlighted by the plots of relative contribution to the total energy dissipation in Figure 6.17. For the control specimens over 80% and for C1-RT-A and C1-RT-B-sw over 70% of the total energy dissipation is dissipated by the columns. This is significantly reduced to 50 % in C1-RT-A-sw, with 26% of the total energy dissipated by the beams and 24% by the joint, slab and transverse beams.

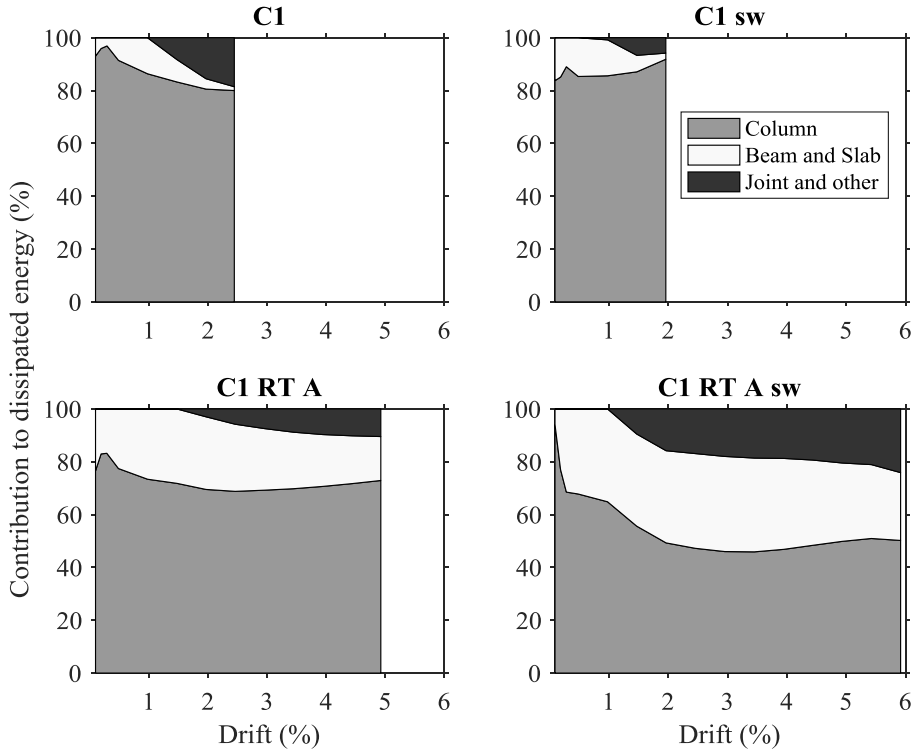

Figure 6.13. Contribution to total energy dissipation by individual members for specimens C1, C1-sw, C1-RT-A and C1-RT-A-sw.

Still, a comparison of the energy dissipation plots at component level in Figure 6.14 highlights the adequate performance of specimen C1-RT-B-sw, with a similar behaviour to C-EC8 obtained. For C1, only 2.4% of the total cumulative energy is dissipated by the beams and slab, while for C-EC8 (12.4%) and C1-RT-B-sw (14.4%) a more significant proportion of the total energy dissipation is due to the beams.

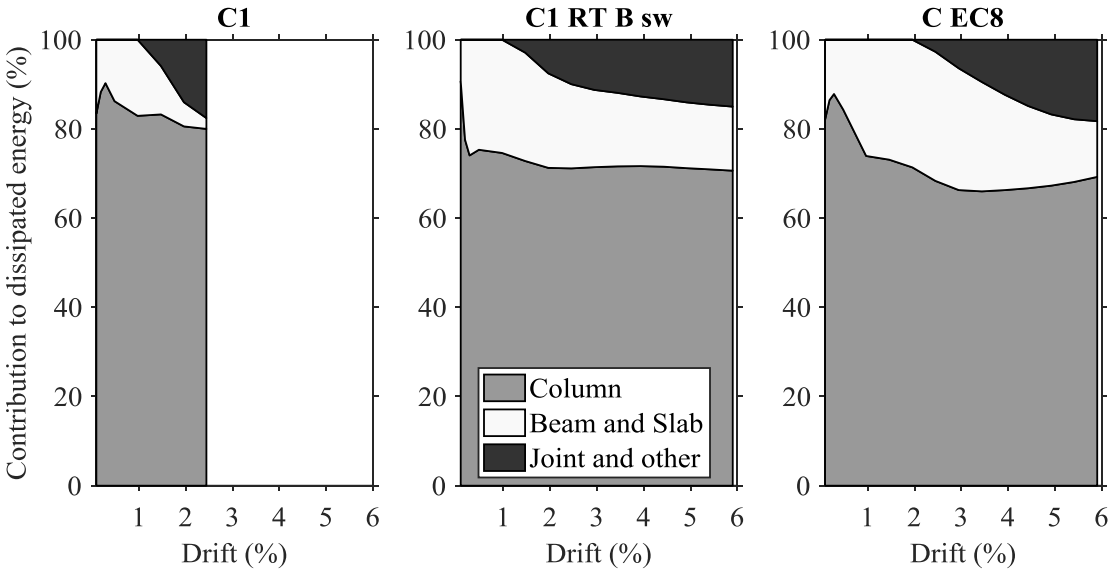

Figure 6.14. Contribution to total energy dissipation by individual members for specimens C1, C1-RT-B-sw and C-EC8.

Furthermore, for retrofit RT-A and RT-A-sw, significant damage due to torsional forces in the transverse beams is observed. This is effectively prevented by the FRP placed in the first 450

mm of the beams in RT-B-sw. Similarly, damage in the joint observed for C1-RT-A-sw is effectively prevented by the joint shear strips in retrofit RT-B-sw.

Overall, in terms of damage and failure mechanism, RT-B-sw is hence the most advantageous, requiring the least repair in moderate earthquakes and performing well in relocating damage away from the joint. Still, retrofits RT-A and RT-A-sw achieve their respective targets and provide improved behaviour compared to the control specimens.

6.5.3. DISSIPATED ENERGY

As shown in Figure 6.15 (a), the total cumulative energy dissipation against drift highlights that the retrofit specimens are significantly more dissipative then the control specimen C1. With retrofits RT-A (93.8 kNm) and RT-A-sw (94.5 kNm), similar levels of energy dissipation are reached, corresponding to an increase of nearly 200% compared to C1. For retrofit RT-B-sw (111.6 kNm), the increase is even larger (+247.8 %), reaching about 65% of the dissipated energy of the EC8 specimen (172.3 kNm) at the maximum drift level.

The displayed plot in Figure 6.15 (a) however shows the results for the specimens up to the maximum drift level tested, which, for some specimens, is larger than the ultimate drift (80% drop in strength). Instead, a fairer comparison can be made when looking at the plot of dissipated energy against ductility in Figure 6.15 (b). The evolution of energy dissipation now follows a similar path for the control specimen and the retrofit specimens at low levels of ductility. It can be observed that for retrofit RT-B-sw at the same level of ductility, the dissipated energy is about 20% higher than for RT-A and close to 40% larger than for RT-A-sw. The retrofit also reaches similar levels to the targeted 80% at the maximum ductility of the specimen designed to EC 8.

From the three retrofits, RT-B-sw is hence also the most dissipative, nearly reaching the target performance of 80% of EC8 at equivalent ductility levels.

6.5.4. STIFFNESS DEGRADATION

The improved ductile and dissipative behaviour of the specimen retrofitted to RT-B-sw, with delayed onset of cracking and yielding, is also reflected in the degradation of peak-to-peak stiffness shown in Figure 6.16. In Figure 6.16 (a), the peak-to-peak stiffness in absolute terms is compared, highlighting the large initial stiffness (7.2 kN/mm) for the control specimen designed to Eurocode 8 compared to a 20% lower stiffness for retrofit RT-B-sw (5.7 kN/mm). For means of assessing the degradation in stiffness more objectively, the peak-to-peak stiffness values are divided by the initial stiffness, K_i, for each specimen in Figure 6.16 (b).

It can be observed that the evolution of stiffness degradation for the retrofit RT-A-sw is similar to the control specimen C1. For RT-A, the improvement is marginal, while for RT-B-sw a better performance, close to C-EC8 is observed.

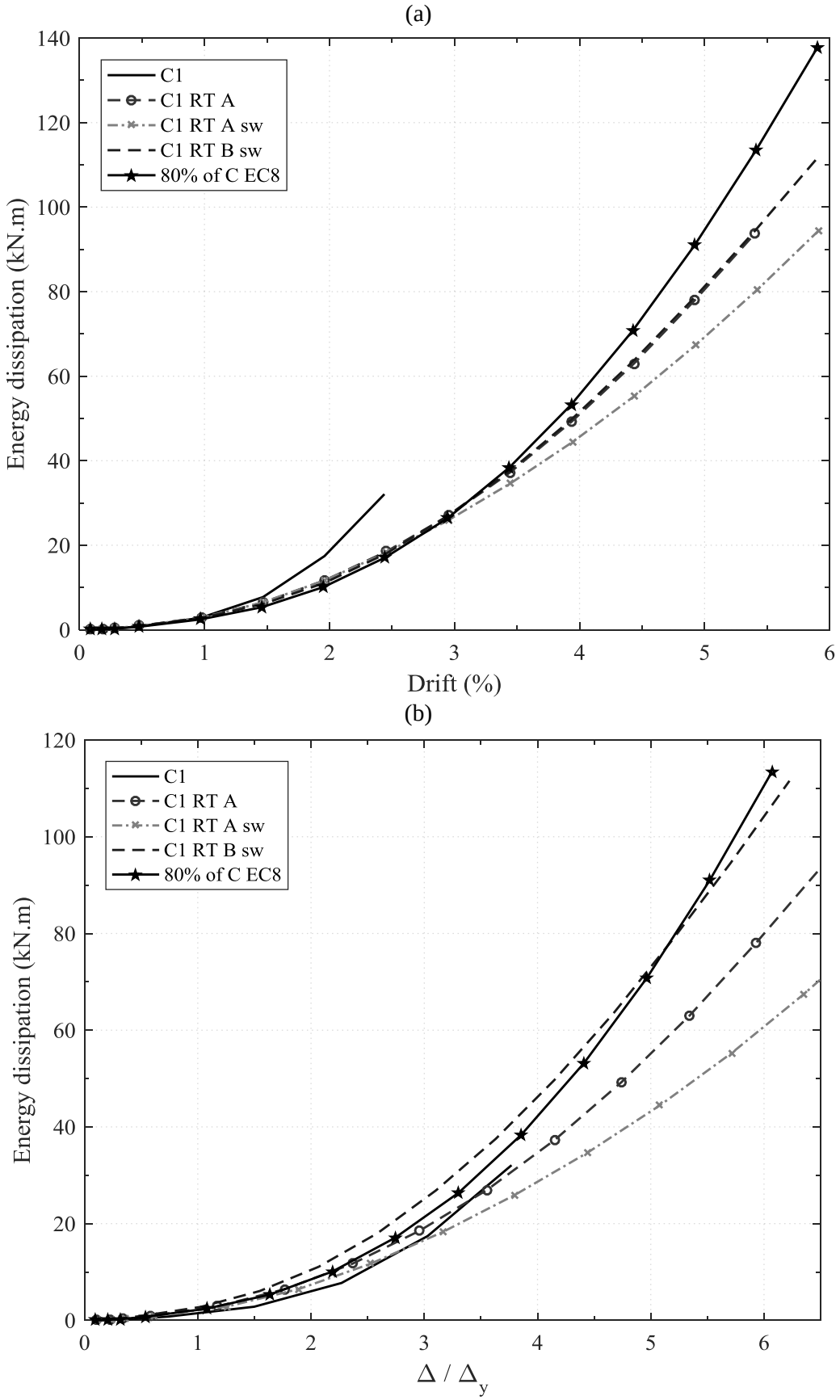

Figure 6.15. Cumulative energy dissipation against drift (a) and against ductility (b) for the three retrofit specimens compared to control specimens C1 and C-EC8.

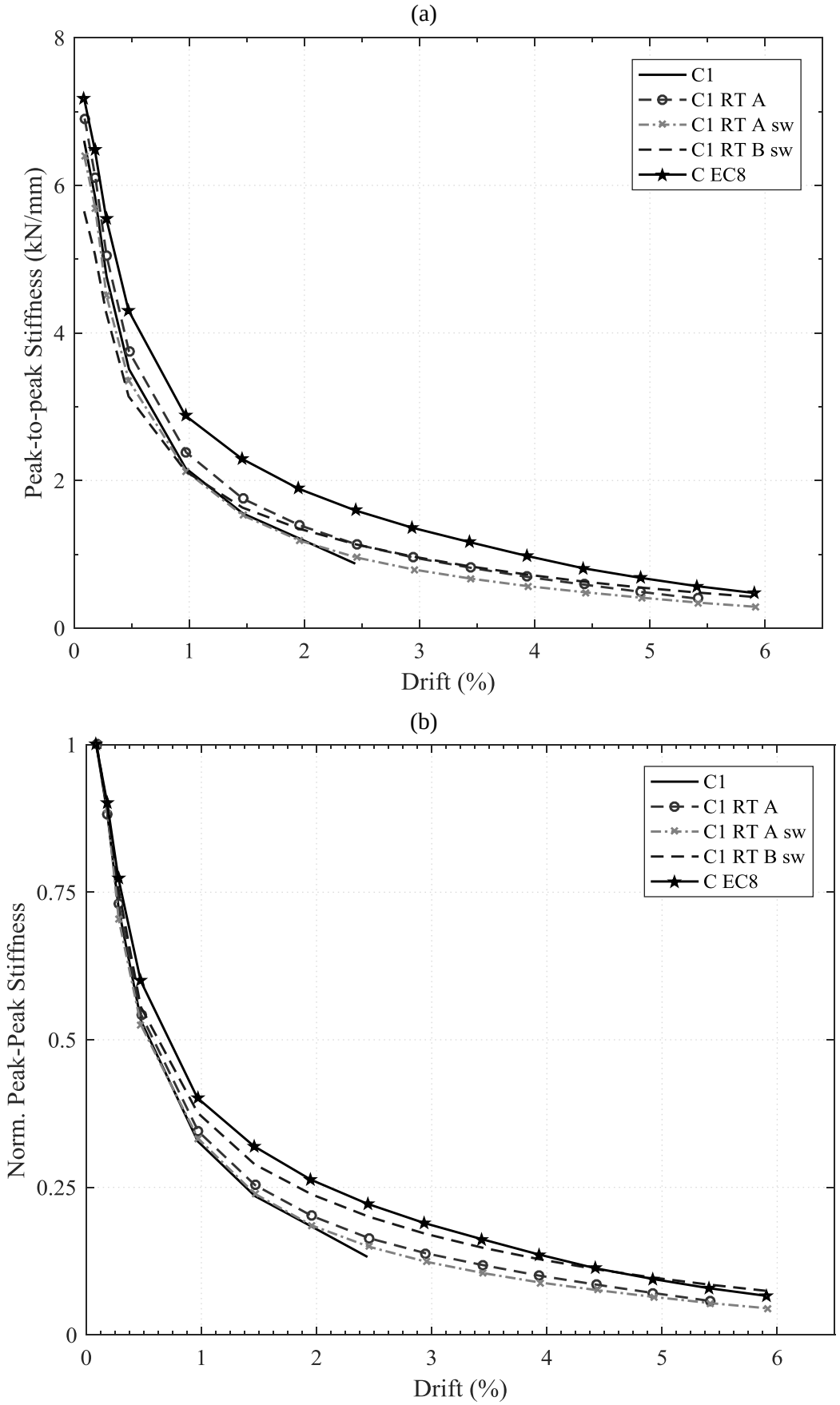

Figure 6.16. (a) Absolute and (b) normalised stiffness degradation against drift for the three retrofit specimens compared to control specimens C1 and C-EC8.

6.5.5. INTER-CYCLE STRENGTH DEGRADATION

Finally, the last metric to assess the performance of the retrofits is the inter-cycle strength degradation (F_{deg}) between the first and second, as well as the first and third cycles, shown in Figure 6.18 and Figure 6.19, respectively. The F_{deg} is a diagnostic indicating the resilience of a specimen to repeated loading, which is of crucial relevance in real earthquake events. With increased level of drift, increased damage reduces the specimens' ability to perform consistently under repeated loading, as shown by the generally increasing F_{deg} values with drift for all specimens.

For the control specimens, relatively low F_{deg} values are observed at low drift values, but at the ultimate drift, due to the observed column bar buckling, very high values of $F_{deg,1\text{-}2}$ (above 25%) and $F_{deg,1\text{-}3}$ (above 65%) are obtained.

For the retrofit specimens, no sudden increase to high values of strength degradation is observed. When comparing the three retrofit specimens, it can be observed that for RT-A, similarly to C-EC8, the $F_{deg,1\text{-}2}$ remains constant around 10% after 2% drift, while it increases up to 15% for RT-A-sw. The best performance is again obtained with retrofit RT-B-sw, for which a maximum strength degradation of 8.9% is obtained.

After the third cycle, the strength degradation increases for all specimens, with C1-RT-A ($F_{deg,1\text{-}3}$ = 20.3%) and C-EC8 (18.7%) again performing similarly, while C1-RT-A-sw displays the largest strength degradation (24.4%). The performance of retrofit RT-B-sw remains consistently good, with a slowly increasing $F_{deg,1\text{-}3}$ up to 15.7%.

Analysis of inter-cycle strength degradation hence shows that retrofit B-sw is the most effective at reducing strength degradation upon repeated cycling, even outperforming the specimen designed to modern guidelines.

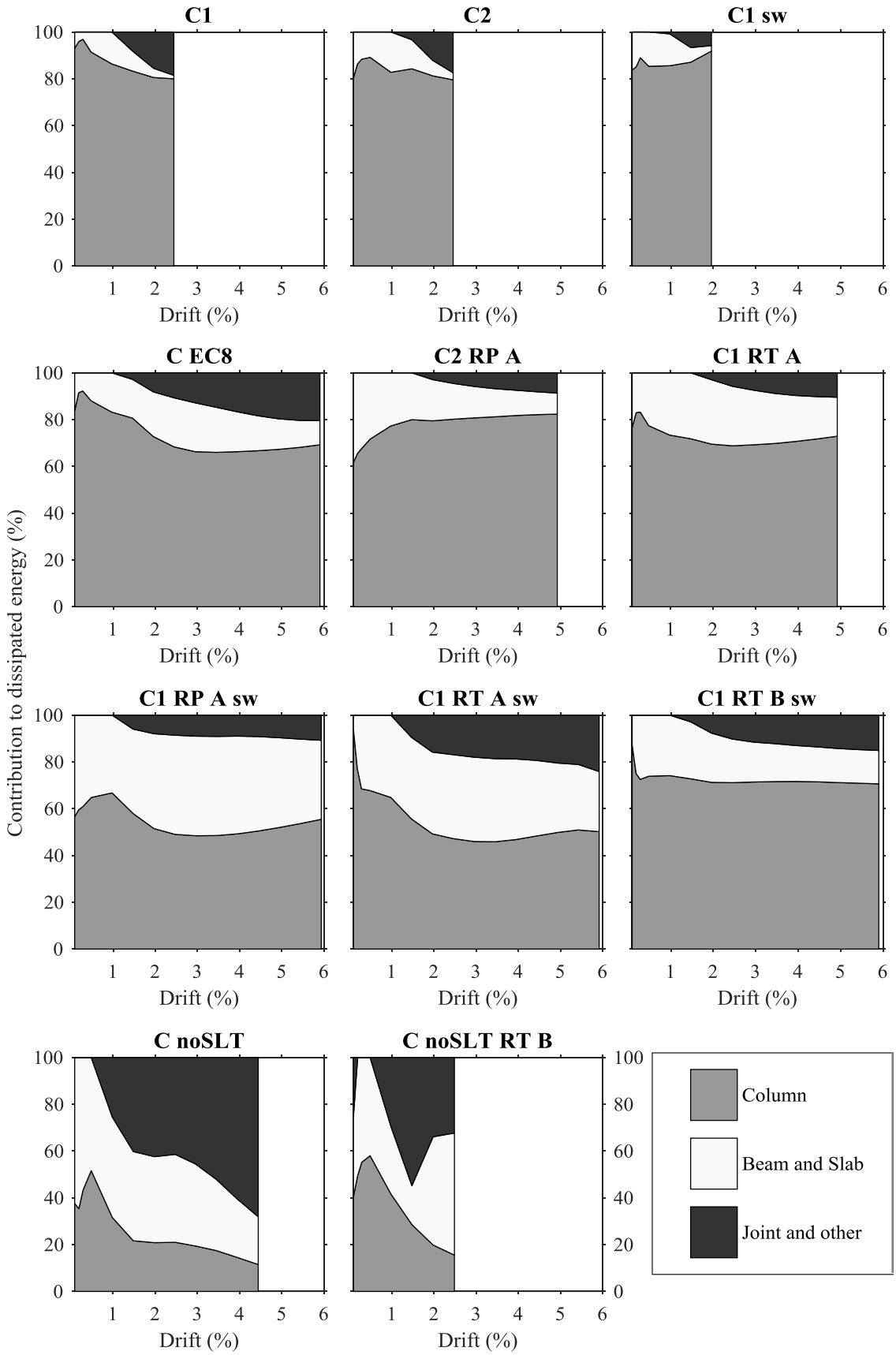

Figure 6.17. Contribution to total energy dissipation by different members against drift for all specimens.

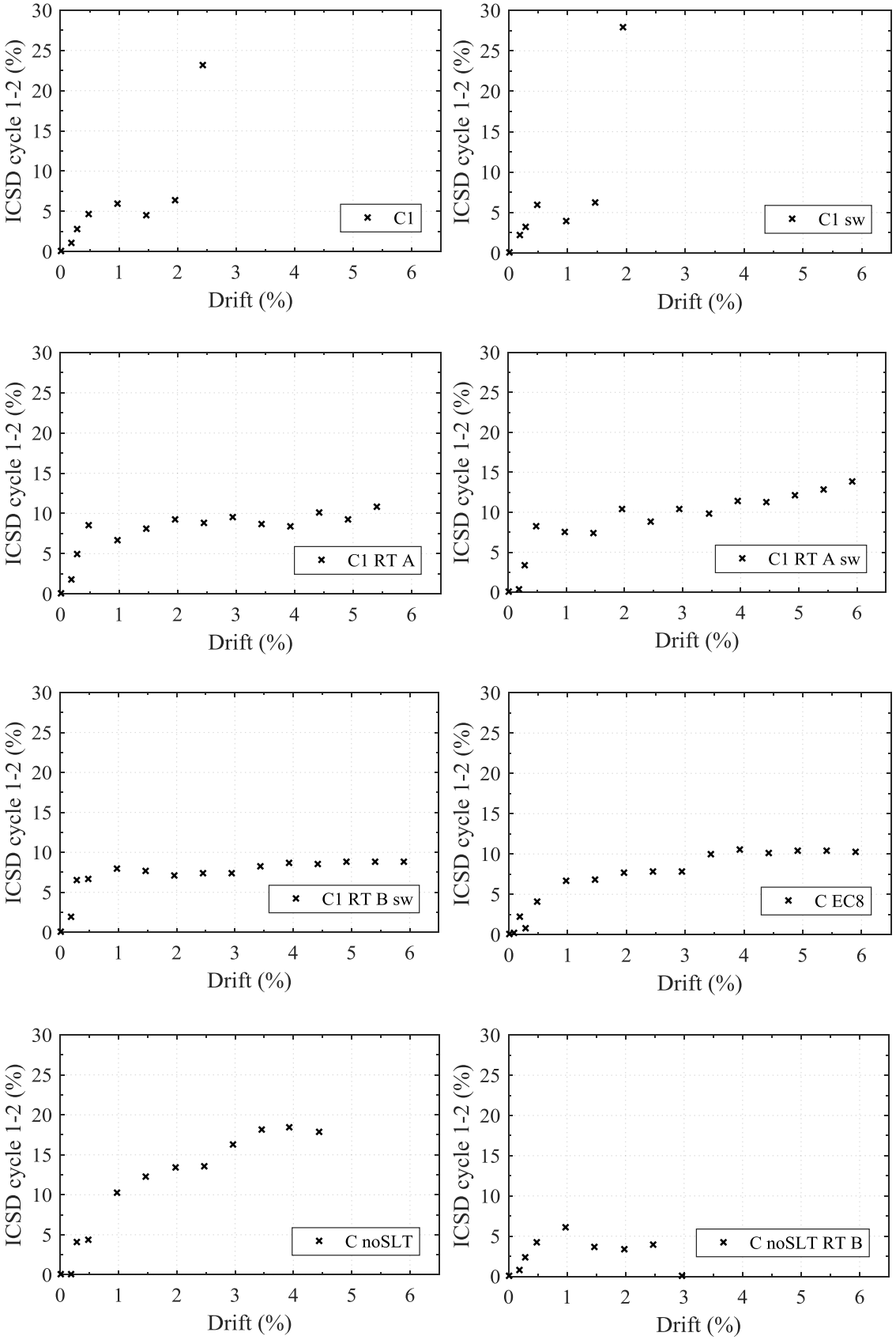

Figure 6.18. First to second cycle strength degradation plots for retrofit and control specimens.

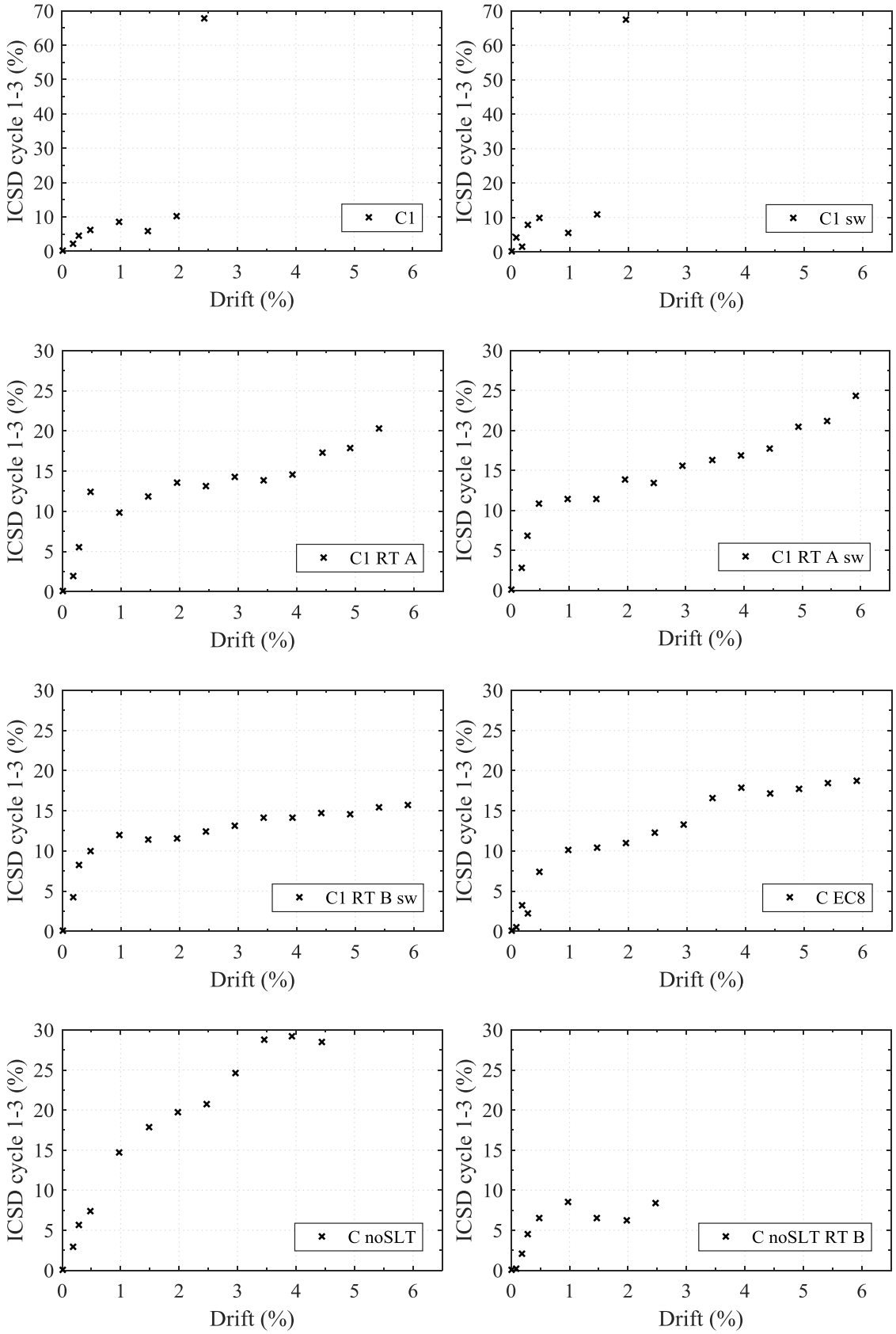

Figure 6.19. First to third cycle strength degradation plots for retrofit and control specimens.

6.6. PRACTICAL CONSIDERATIONS AND IMPLEMENTATION

A critical objective of the work presented in this thesis is to design efficient retrofit solutions that are also practical for use in real structures. To ensure the retrofit design are applicable to real buildings, realistic specimens are hence used in order to ensure practical obstacles to the implementation of the FRP schemes are considered.

Testing realistic specimens with slabs and transverse beams is shown not only to be important in terms of different retrofit effectiveness (Section 6.3.4), but also in terms of retrofit objectives (Section 6.3.1) and potential overlooked damage, such as torsional cracks (Section 6.3.3).

It is important that realistic specimen geometry and configuration were used in the experiments to be able to prove the practical implementation of the FRP retrofit, including the need for cuts and anchorage. The proposed retrofit schemes satisfy the practical requirements of not being excessively invasive, as only small holes need to be drilled at the column corners. The selective weakening cuts are feasible too, as shown by their actual implementation in the laboratory. Moreover, tests on the control specimen with selective weakening cuts indicate that the behaviour of the slab is not compromised by the intervention.

The proposed retrofit schemes only use easily available materials, such as CFRP sheets. Compared to other schemes (e.g.: Shiohara et al. 2009), no specialised products are required that may not be available in many countries. Furthermore, the additional anchors are simple steel plates that can be manufactured in any workshop, hence again not limiting their implementation.

The repair schemes also use commonly used methods, such as welding of new steel rebars and replacing damaged concrete, which facilitates the implementation in the field, making use of already existing skills in the work force.

In general, the proposed strengthening does not require further training than other FRP retrofits. While the retrofit may be more labour intensive and intrusive than simple FRP jacketing of single elements, it is still maintaining all the advantages of FRP retrofits compared to traditional methods, such as RC or steel jacketing, in terms of weight, labour time or corrosion resistance.

Furthermore, important observations for future guidelines are made in the experiments, for instance, with regards to the effective strain calculations for FRP strands. This is only observed due to the realistic test set-up, and for tests with similar FRP anchors tested on column bases, much larger strain are reported (Vrettos et al. 2013).

The effective strain calculation, as well as the design philosophy are an adaptation of equations within the existing CNR guidelines. This means the retrofit is easier to integrate within an existing and approved framework, facilitating the potential for future implementation. Still, further work is required to eventually implement the proposed retrofits in real structures. This includes

additional numerical work, based on the FE models presented in this thesis, but expanding to assess further parameters, such as different geometries, reinforcement and loading conditions. Ultimately, a full-scale shaking table test of a realistic structure retrofitted to scheme RT-B-sw would allow a final validation of the scheme, ensuring all potential interactions are considered.

6.7. SUMMARY

A detailed analysis and discussion of the results from the experimental study is presented in this chapter. The three FRP retrofit schemes with selective retrofit objectives are generally effective in achieving their respective targets. The effectiveness of the suggested retrofits is critically compared with respect to a number of retrofit targets. A summary of this evaluation of the retrofit and repair schemes is presented in Table 6.4. For comparison, the evaluation of the Eurocode 8 specimen is also presented. The objectives used for assessment of the schemes are based on representative diagnostics for typical retrofit applications (Chapter 4). The ranking system from negative effect (–) to a highly positive effect (***) is defined by the relative improvement (in %) of the relevant diagnostic compared to the control specimens.

The table echoes the main findings of the experimental programme, namely that in terms of increasing strength, retrofits RT-A and RT-B-sw are similarly effective, but that looking at promoting damage in the beams, and hence increasing ductility, RT-A-sw is most effective.

Table 6.4. Summary evaluation of all retrofits.
Evaluation of positive effect from low (*) to high (***), no effect (o) and negative effect (-).

Specimen	Increased ductility	Increased strength	Improved softening	Increased Energy dissipation	Increased beam damage	Average
C-EC8	**	***	o	***	**	**
C0-RP-A-gs	o	*	**	*	o	*
C1-RT-A	**	**	**	**	*	**
C2-RP-A	-	**	*	**	*	*
C1-RT-A-sw	***	*	***	**	***	**1/2
C1-RP-A-sw	**	*	***	***	***	**1/2
C1-RT-B-sw	***	**	***	***	**	***
C-noSLT-RP-B	-	***	-	-	***	*

As seen in Table 6.4, for all retrofits, improved ductility and softening is observed, which is in part due to the effectiveness of FRP confinement wrapping of the columns in delaying yield of the column bars and preventing buckling. Moreover, the use of FRP strands passed through tubes between the columns successfully prevents the single-storey failure observed for the control specimens, hence delaying damage in the columns and improving the ductility of the specimens further. This effect is not observed when the column strands are glued to the concrete in the joint region and hence rupture. An early brittle failure for C0-RP-A-gs causes its low retrofit effectiveness in terms of ductility, strength and energy dissipation shown in Table 6.4.

While passing the strands through plastic tubes ensures that rupture is prevented, it also means that 'slippage' of the FRP strands in the non-bonded region is observed for all three retrofits. This, in turn, leads to lower strain in the FRP strands than in the bonded regions, where the FRP is splayed-out onto the columns. A localised weakness at the column/joint interfaces, with a significant crack for all retrofitted specimens, is hence observed. This weakness eventually causes the ultimate failure. Increased pinching in the hysteresis loops for the retrofit specimens is also observed as a consequence.

While an improved seismic performance is observed for all retrofitted specimens, the full moment capacity of the columns is not reached as a result of the lower than expected strain in the non-bonded FRP strands. This explains why full relocation of the ultimate failure to a beam-only mechanism is not achieved. In terms of lateral capacity, the enhancement is hence also lower than expected, which leaves room for improvement for a re-designed retrofit scheme that takes into account a factor for determining the actual strain in the FRP strands.

The FRP strain calculations from the CNR guidelines need to be adapted for the use with the suggested column retrofits with FRP strands in this thesis. Based on the results presented in this thesis, the suggested equations in Section 6.1 for modifying the strain calculations, are accurate and can be used in conjunction with the existing CNR guideline equations to predict the moment capacities of retrofitted RC columns. For the beams and joint, as the FRP strands are bonded throughout, the CNR guideline equations only require slight modification to account for geometrical differences between rectangular FRP strips and the splayed out FRP strands. Again, this observation is only based on limited evidence and requires further empirical and numerical validation.

Looking at Table 6.4, a number of other conclusions from the experimental program can be derived. In terms of repair and retrofit effectiveness, no significant differences are observed when it comes to the strength of the specimens, however, a significant reduction in initial stiffness is observed for all four repair specimens. This, in turn, leads to a higher value of yield drift, and hence a reduced ductility of the repaired specimens.

The importance of testing specimens with slab and transverse beams is also highlighted by the experimental results. For the control specimens, a very large contribution of the slab dictates the hierarchy of strengths, causing a column hinging failure which is not compatible with capacity design. The failure mechanism of the specimen without slab, for which a joint shear failure is observed instead, is shown to be very different to the one with slab. This, in turn, has a crucial impact on the retrofit design, both, in terms of retrofit aim and need for weakening the slab.

It is also shown that weakening of the slab alone is not sufficient to change the hierarchy of strength and, thus, to increase damage and rotation of the beams. In a combined retrofit and selective weakening system, however, the contribution of the slab can be effectively reduced, making a symmetric behaviour in hogging and sagging possible. This ultimately allows a transfer of damage to the beams, leading to a stronger beam participation for specimens C1-RT-A-sw, C1-RP-A-sw and C1-RT-B-sw than for C1-RT-A and C2-RP-A.

When comparing the effectiveness of retrofit layout B for the specimens with and without slab, a higher strength increase is observed for the cruciform specimen C-noSLT-RP-B. This confirms the hypothesis made after analysing the existing literature: tests on cruciform-specimens may hence overestimate the effectiveness of retrofit schemes. Still, in terms of ductility and softening behaviour, retrofit B is less effective for the specimen without slab, which may however be a consequence of the pre-damage in C-noSLT-RP-B.

Overall, retrofit RT-B-sw can be seen to achieve a good balance between retrofits A and A-sw. It is the most effective in terms of increasing lateral load capacity, ductility and post-peak softening. It therefore achieves a very good seismic performance by all relevant diagnostics, and even outperforms the EC8 specimen in many cases. It is envisaged that the proposed retrofit is easily applicable in the field, as it does not require excessive removal of material and only uses readily available materials (FRP sheets). The design is also based on existing design guidelines (CNR), modified to take the behaviour of the FRP strands into consideration, which would ease its future adoption into guidelines. To achieve this, further numerical and empirical validation on a broader range of joint geometries and loading conditions is however required.

7. CONCLUSIONS

The main aim of this study was to develop a practical and effective CFRP retrofit design for realistic full-scale pre-1970's RC beam-column joints to achieve an adequate seismic behaviour with respect to modern capacity design principles.

To achieve this, a research program comprising an in-depth analysis of the state-of-the-art, the development of finite element models of the joints, the design of three retrofit and repair schemes, as well as a series of fourteen full-scale experiments to assess these schemes, was developed.

The brittle failures of existing RC structures, built before the introduction of modern seismic codes, resulted in significant human and financial losses after many recent seismic events. These structures are of particular concern, as they constitute a large proportion of the existing building stock in many earthquake-prone countries, encompassing commercial and residential properties, but also more critical structures, including schools and hospitals. The vulnerability of pre-1970's or 80's RC frames is a result of their lack of seismic detailing, leading to an inadequate hierarchy of strengths between the lateral load carrying members at beam-column connections. Following the principle of capacity design, joint shear failures and weak-column/strong-beam failure mechanisms lead to a non-ductile structural behaviour that needs to be prevented.

Demolition of deficient structures at scale is neither feasible, nor is it economical or sustainable. Instead, these structures can be retrofitted to improve their seismic behaviour. Traditional retrofit methods, including steel or RC-jacketing, are common interventions, however, they often require significant intrusive work that can leave buildings unoccupied for longer periods of time. The added weight of such retrofits and their susceptibility to corrosion are further shortcomings. Better retrofit options are hence required to mitigate against the risk of further pre-1970's RC failures. Fibre-reinforced polymer sheet has crystallised as ideal retrofit material, as it benefits from a high strength-to-weight ratio, corrosion-resistance and low labour cost. FRP retrofits can be applied quickly and without disrupting building occupancy, which can reduce down-time in businesses and the need of relocating inhabitants in residential properties.

The implementation of FRP retrofit schemes for individual members is already common in many countries, such as Italy or New Zealand. Moreover, a review of the state-of-the-art of FRP retrofitting of beam-column joint subassemblies, presents numerous successful implementations that address various retrofit objectives.

A detailed analysis of previously tested retrofit solutions and a compilation of a database of all previous experiments allows a number of important conclusions to be drawn from this review. Despite the large number of conducted studies, a strong bias towards scaled, cruciform test specimens is observed, which presents a major shortfall in many existing studies. An analysis of the compiled database shows that the lack of slabs and transverse beams, as well unrealistic

specimen dimensions and loading conditions significantly affect the effectiveness of retrofit schemes. There is hence a significant need in testing FRP retrofits for realistic RC beam-column joints to feed into the design of adequate design guidelines. This will ultimately ensure the wider acceptance and practical implementation of suitable, fast and efficient retrofits to address the constant threat of inadequate seismic behaviour of existing RC frames.

- Objective 1: to design and model three realistic FRP retrofit and repair schemes

Using the knowledge drawn from the literature review, as a first step, it was hence an objective to design and model three FRP retrofit and repair schemes with different strengthening aims for realistic full-scale beam-column joints with slabs and transverse beams.

The aim of designing retrofit schemes with different strengthening objectives is achieved by drawing on the knowledge gained from the literature survey. For instance, the use of CF-anchors is shown to be a viable solution to achieve continuous retrofit of columns. The potential of using selective weakening of slabs to promote a beam hinging failure mode in specimens with slabs is another crucial outcome from the literature survey. Moreover, using FRP to strengthen the beam ends to potentially relocate the plastic hinge away from the joint interface, allows to protect the joint from unwanted damage.

Three retrofit schemes with increasing complexity are developed in this study and are designed to address different objectives. The schemes are designed to take into account practical limitations. Excessive removal of concrete, full wrapping of inaccessible members, ignoring slabs or transverse beams, were hence not considered. Retrofit scheme A is the simplest design, using FRP strands for strengthening of the columns through the slab. It aims to improve the strength of the specimen by increasing the moment capacity of the deficient columns and increase the global displacement capacity of the specimen by connecting the flexural strengthening of the superior and inferior columns. Scheme A-sw, adds selective weakening (sw) of the slab with the aim of promoting a more ductile beam hinging failure mechanism. Finally, scheme B-sw aims to increase strength and ductility of the specimen to achieve a behaviour comparable to specimens designed to modern design codes. This is the most intricate scheme including a combination of FRP strengthening of columns, beams and joint, as well as selective weakening of the slab.

The proposed retrofit schemes are compliant with current design recommendations (CNR, 2013) and the relative capacities of the strengthened members are evaluated using existing design equations. The design methodology for the retrofit schemes is based on FE models developed for this study, which are initially calibrated on a set of small-scale beam tests. The FE models are first used to evaluate potential design deficiencies of realistic pre-1970's specimens. To improve the confidence in the schemes before testing, the expected failure mechanism for each retrofitted specimen is initially established by numerical modelling. The results from the models is then used

to inform the design of the subsequent retrofit schemes of increased complexity, which are adapted to a new retrofit objective to improve the global behaviour of the specimen.

Undoubtedly, the analysis of the existing literature was crucial for developing the proposed schemes. A number of innovations were however introduced in this thesis. The presented retrofit schemes are the first to use FRP strands, made from simple CFRP sheets, for continuous flexural strengthening of columns on full-scale specimens with slabs and transverse beams. The design of RT-B-sw also includes the first effort of joint shear strengthening applied through transverse beams. Flexural strengthening of beams for plastic hinge relocation using FRP anchor strands is proposed for the first time. Finally, a combined retrofit following the principles of capacity design and using FRP strands in beams, joints and columns, together with selective weakening is proposed and tested for the first time.

The shortfalls in terms of joint geometry, scale and loading arrangements, identified from the existing literature is used to design an innovative testing set-up for realistic full-scale joints with slabs and transverse beams. In total, twelve full-scale beam-column joints, as well as two column-only tests, were carried out. To the best knowledge of the author, these correspond to the first full-scale cyclic tests of realistic interior beam-column joints with slab and transverse beams, strengthened with FRP.

The results from experimental testing show that the FE models used for the design of the three FRP retrofits are very useful in determining the retrofit objectives. The failure mechanisms of all modelled specimens are accurately predicted, with the correct damage location validated by the experiments for control specimens C1, C-EC8, C-noSLT, as well as for retrofit specimen C1-RT-A. The damage evolution in the beams is also accurately predicted for specimens C1-sw, C1-RT-A-sw and C1-RT-B-sw. Overall, the step-wise retrofit design method using FE modelling to update the retrofit objectives is hence confirmed.

- Objective 2: To evaluate the influence of slab and transverse beams

An important outcome of the analysis of the experimental database is that the slab and transverse beams, which are often omitted from experimental studies, may significantly influence the effectiveness of retrofit schemes. As a second objective of this study, this influence was hence evaluated both numerically and experimentally.

As a first step the developed FE models were used to assess the influence of slab and transverse beams individually. It was shown that the slab significantly alters the hierarchy of strength within a structure, by increasing the moment capacity of the beams. The transverse beams alone, in turn, contribute to the joint confinement and can prevent joint shear failure, which is typically observed for cruciform joint specimens.

Full-scale experimental testing of specimens with and without slab and transverse beams confirms the observations from numerical modelling. The effect of slab and transverse beams is shown to be significant in terms of load carrying capacity and failure mechanism of the specimens. The different failure mechanism obtained affects the design of FRP retrofit strategies, as the specimen with slab needs retrofitting of the column to increase its confinement and flexural capacity, while the cruciform specimen, instead, mainly requires shear strengthening of the joint.

To assess the consequence of slab and transverse beams on the retrofit effectiveness, retrofit layout B is applied for specimens with and without slab. As expected from the analysis of the literature database, a higher strength increase is observed for the cruciform specimen C-noSLT-RP-B. In terms of ductility and softening behaviour, the opposite effect is observed. Overall, the numerical and experimental results confirm that considering a realistic geometry is of outmost importance to assess FRP retrofits of beam-column joints. The results from this study also strengthen the hypothesis that many past tests on cruciform-specimens may hence overestimate the effectiveness of retrofit schemes.

- Objective 3: to identify an optimal FRP retrofit design for realistic structures

The main target of the series of full-scale tests was to establish and compare the effectiveness of the three FRP retrofit schemes, in order to identify an optimal FRP retrofit design for realistic structures. Through initial trialling of the retrofit schemes as repair interventions, their applicability on pre-damaged structures is also validated.

The retrofit of columns is shown to improve ductility and softening for all retrofits. On the one hand, this is a consequence of the applied FRP confinement wrapping, which successfully prevents rebar buckling. On the other hand, the use of FRP strands between the superior and inferior columns successfully prevents the single-storey failure observed for the control specimens, and improves the ductility of the specimens.

The three retrofit schemes are also judged in their ability to move damage to the beams and the success of selective weakening is highlighted by the increased beam rotation for retrofits A-sw and B-sw. Due to the selective weakening, retrofit A-sw is shown to be most effective in increasing ductility. Moreover, the relocation of damage within the beams to protect the joint in retrofit B-sw is also successfully implemented and leads to the most dissipative mechanism, reaching the target performance of 80% of EC8 in terms of dissipated energy.

Finally, in terms of strength enhancement, retrofits RT-A and RT-B-sw are most effective, with an increase in strength close to 40% compared to C1. While this corresponds to a capacity close to 70% of the EC8 specimen, which is lower than anticipated (80% of EC8), the increase in strength is still substantial when compared to other proposed retrofits for specimens with slab

(26% average strength increase). For retrofit RT-A-sw, for which the beams are not strengthened, only a 13.5% increase in strength is observed.

Overall, retrofit RT-B-sw can be seen to achieve a good balance compared to retrofits A and A-sw. It is the most effective in terms of increasing lateral load capacity, ductility and post-peak softening. While increased damage along the length of the beams is achieved with the proposed retrofit, full relocation of the ultimate failure to a beam-only mechanism is not accomplished. Still, a strongly improved seismic performance is observed by all relevant diagnostics for RT-B-sw, which even outperforms the EC8 specimen in many cases.

- Objective 4: to devise design equations for potential future implementations

The final objective of this study was to devise a methodology for the retrofit scheme to be potentially implemented in future applications. Based on observations from the experimental study, a full retrofit methodology and design equations based on the CNR design guidelines is indeed proposed and validated in this thesis.

An important outcome of the testing campaign was that the capacity of the columns is not suitably predicted using existing design equations. This is a result of a lower effective strain in the non-bonded FRP strands compared to fully bonded FRP assumed in the strain calculations from the CNR guidelines. This is only observed due to the realistic test set-up, as for tests with similar FRP anchors tested on column bases, much larger strain was reported. To address this, a new equation for predicting strain in the FRP strands was developed in this thesis.

Based on the results from five specimens, it is shown that suggested equations are significantly more accurate in predicting FRP strain. Crucially, it was also confirmed that the newly developed equations can be used successfully in conjunction with the existing CNR guideline equations to accurately predict the moment capacities of retrofitted RC columns.

Furthermore, the design methodology for beams and joint, which also uses FRP strands, is also validated experimentally, albeit only for one specimen. Again, only slight modification of existing guideline equations is needed, which makes the implementation of the proposed retrofit easier to adopt in future design guidelines.

It is envisaged that the proposed retrofit methodology can be implemented in real structural retrofits. To ensure that the retrofit maintains all benefits of general FRP retrofits, it was designed so as not to require excessive removal of material and to only use readily available materials (FRP sheets). The proposed repair schemes are also based on commonly used methods, which facilitates the implementation in the field.

It is conceivable that the effective strain calculation, as well as the design philosophy could be integrated within an existing and approved framework, facilitating the potential for future

implementation. Still, further work is required to eventually implement the proposed retrofits in real structures, including further numerical and empirical ratification of the design.

7.1. CONTRIBUTIONS TO THE RESEARCH FIELD

A number of contributions to the research field are made by the work presented in this thesis. The main contributions to the research community are summarised below.

- Creation of a full database of all experimental work on FRP strengthened RC joints.
  This database is not only useful in assessing the current state-of-the-art, but also allows to identify the factors affecting retrofit effectiveness. Moreover, the compiled database can also be used to assess existing design guidelines (e.g.: Pohoryles and Rossetto, 2014) or validate new empirical design equations.
- Quality of experimental data.
  The conducted experiments are a significant contribution to the research community, as the loading and test set-up, as well as specimen geometry, are highly realistic. The empirical data gathered from the experiments is hence valuable to assess not only FRP retrofit design equations, but also the behaviour of RC structures in general. During the experimental testing, unprocessed digital image correlation (DIC) was also collected, which can serve as high quality data for calibration and refinement of FE models.
- Proposed design methodology.
  The proposed design methodology for retrofit B-sw is a significant contribution to the field, as it enables the proposed retrofit to be implemented in real structures. The proposed design equations for columns, beams and joint were formulated so as to be used with existing FRP guidelines (CNR), which would ease their future adoption. Still, further validation of the equations, both numerically and experimentally is first required.

7.2. AVENUES FOR FUTURE RESEARCH

Overall, the outcomes of the research presented in this thesis provide a series of avenues for future research that are discussed in this section. The proposed design methodology was only confirmed based on a limited number of experiments, and hence requires additional support.

As with any experimental study, the presented work also suffers from some limitations. While the tests were conducted on realistic full-scale joint specimens, the tests are still limited to one specimen geometry in terms of column and beam cross-sections. The applied loading is an attempt to replicate real conditions, still, bi-directional loading would be more realistic. As a first step, further numerical validation is hence suggested. This could be based on the FE models presented in this thesis. While the models are useful in assisting the retrofit design process, it was not within the context of this thesis to further refine them. It is, however, in the scope of future work to develop the FE models further, in order to conduct parametric studies that can be used to develop

or verify design equations to ensure implementation of the proposed FRP retrofits in future guidelines. This would require expanding the FE models to assess a broader range of geometries, reinforcement and more realistic loading conditions. Moreover, a numerical study on the effect of the retrofit schemes on the behaviour of full structures is required. Future numerical work will benefit from the available test data, including the DIC data not analysed in this thesis. This can be used to improve calibration and validation of the FE models.

In terms of retrofit design, it is envisaged that the retrofit B-sw may be further improved. The effectiveness of the proposed FRP retrofit schemes depends strongly on the strain reached in the FRP strands. To reach higher retrofit effectiveness, anchoring the FRP strands in the joint region to reduce the free, non-bonded length, could be beneficial. The strands should however not be bonded along the full length, as it was shown for specimen C0-RP-A-gs that very high local strain at the column/slab interface develops and leads to rupture of the strands. A possibility may be to anchor the strands at their midpoint, however, to achieve an effective bonding, the length may be to short and a special anchorage solution would need to be explored.

Finally, as the behaviour of a full frame under dynamic seismic loading is not fully replicated by pseudo-static tests on isolated joints, ultimately, a full-scale shaking table test of a realistic structure retrofitted to an improved scheme B-sw would allow a final validation, ensuring all potential interactions are considered.

BIBLIOGRAPHY

ABAQUS. (2011). "Theory Manual Version 6.11." ABAQUS Inc., USA.

Abbasnia, R., Hosseinpour, F., Rostamian, M., and Ziaadiny, H. (2012). "Effect of corner radius on stress–strain behavior of FRP confined prisms under axial cyclic compression." *Engineering Structures*, 40, 529–535.

ACI. (2002). *ACI 440.2R-02 - Guide for the design and construction of externally bonded FRP systems for strengthening concrete structures*. American Concrete Institute.

ACI (Ed.). (2008a). *ACI 318-08 - Building Code Requirements for Structural Concrete and Commentary*. American Concrete Institute.

ACI. (2008b). *ACI 440.2R-08 - Guide for the design and construction of externally bonded FRP systems for strengthening concrete structures*. American Concrete Institute, Farmington Hills, Mich.

ACI. (2014). *ACI 440-F - Seismic Strengthening of Concrete Buildings Using FRP Composites (draft)*.

ACI Committee 352 (Ed.). (2002). *ACI 352R-02 - Recommendations for Design of Beam-Column Connections in Monolithic Reinforced Concrete Structures*. American Concrete Institute.

Agarwal, P., Gupta, A., and Angadi, R. G. (2014). "Effect of FRP wrapping on axial behavior of concrete and cyclic behavior of external RC beam column joints." *KSCE Journal of Civil Engineering*, 18(2), 566–573.

Akguzel, U., and Pampanin, S. (2007). "Experimental behaviour of exterior beam-column joint subassemblies retrofitted using GFRP composites." Palmerston North, New Zealand.

Akguzel, U., and Pampanin, S. (2009). "Analytical model for shear strengthening of RC beam-column joints using composite materials." Christchurch, New Zealand.

Akguzel, U., and Pampanin, S. (2010). "Effects of Variation of Axial Load and Bidirectional Loading on Seismic Performance of GFRP Retrofitted Reinforced Concrete Exterior Beam-Column Joints." *Journal of Composites for Construction*, 14(1), 94–104.

Akguzel, U., and Pampanin, S. (2012a). "Recent Developments in Seismic Strengthening of RC Beam-Column Joints with FRP Materials." *Proceedings of the 15th world conference on earthquake engineering*, Lisbon, Portugal.

Akguzel, U., and Pampanin, S. (2012b). "Assessment and Design Procedure for the Seismic Retrofit of Reinforced Concrete Beam-Column Joints using FRP Composite Materials." *Journal of Composites for Construction*, 16(1), 21–34.

Akguzel, U., Quintana Gallo, P., and Pampanin, S. (2011). "Seismic strengthening of a non-ductile RC frame structure using GFRP sheets." *Proceedings of the Ninth Pacific Conference on Earthquake Engineering*, Auckland, New Zealand.

Almusallam, T., and Al-Salloum, Y. (2007). "Seismic Response of Interior RC Beam-Column Joints Upgraded with FRP Sheets. II: Analysis and Parametric Study." *Journal of Composites for Construction*, 11(6), 590–600.

Al-Salloum, Y., and Almusallam, T. (2007). "Seismic Response of Interior RC Beam-Column Joints Upgraded with FRP Sheets. I: Experimental Study." *Journal of Composites for Construction*, 11(6), 575–589.

Alsayed, S. H., Al-Salloum, Y. A., Almusallam, T. H., and Siddiqui, N. A. (2010). "Seismic Response of FRP-Upgraded Exterior RC Beam-Column Joints." *Journal of Composites for Construction*, 14(2), 195–208.

Antonopoulos, C., and Triantafillou, T. (2002). "Analysis of FRP-Strengthened RC Beam-Column Joints." *Journal of Composites for Construction*, 6(1), 41–51.

Antonopoulos, C., and Triantafillou, T. (2003). "Experimental Investigation of FRP-Strengthened RC Beam-Column Joints." *Journal of Composites for Construction*, 7(1), 39–49.

Aranda, C., Vidal, F., Alguacil, G., Navarro, M., and Valverde-Palacios, I. (2014). "Fundamental period and earthquake damage in RC buildings of Viña del Mar (Chile)." *Proceedings of the 9th International Conference on Structural Dynamics, EURODYN 2014*, Porto, Portugal.

Arya, C. (2009). *Design of Structural Elements: Concrete, Steelwork, Masonry and Timber Designs to British Standards and Eurocodes, Third Edition*. CRC Press.

Asaei, S. M. S., Lau, T. L., and Bunnori, N. M. (2012). "Experimental and Numerical Verification of the Retrofitted RC Columns using FRP-A State of the Art Review." *Caspian Journal of Applied Sciences Research*, 1(9), 38–55.

ASCE (Ed.). (2014). *41-13 - Seismic Evaluation and Retrofit of Existing Buildings*. American Society of Civil Engineers, Reston, VA.

Au, C., and Büyüköztürk, O. (2006). "Debonding of FRP plated concrete: A tri-layer fracture treatment." *Engineering Fracture Mechanics*, 73(3), 348–365.

Barros, J. A. O., Ferreira, D. R. S. M., Fortes, A. S., and Dias, S. J. E. (2006). "Assessing the effectiveness of embedding CFRP laminates in the near surface for structural strengthening." *Construction and Building Materials*, 20(7), 478–491.

Barros, J. A. O., Varma, R. K., Sena-Cruz, J. M., and Azevedo, A. F. M. (2008). "Near surface mounted CFRP strips for the flexural strengthening of RC columns: Experimental and numerical research." *Engineering Structures*, 30(12), 3412–3425.

Belouar, A., Laraba, A., Benzaid, R., and Chikh, N. (2013). "Structural Performance of Square Concrete Columns Wrapped with CFRP Sheets." *Procedia Engineering*, 54, 232–240.

Beres, A., Pessiki, S. P., White, R. N., and Gergely, P. (1996). "Implications of experiments on the seismic behavior of gravity load designed RC beam-column connections." *Earthquake Spectra*, (122), 185–198.

Beres, A., White, R. N., and Gergely, P. (1992). *Seismic Behavior of Reinforced Concrete Frame Structures with Nonductile Details Part I: Summary of Exp Findings of Full-Scale Beam-Column Joint Tests*. 88.

Berry, M., Parrish, M., and Eberhard, M. (2004). "PEER Structural Performance Database User's Manual (Version 1.0)." *University of California, Berkeley*.

Beydokhti, E. Z., and Shariatmadar, H. (2016). "Strengthening and rehabilitation of exterior RC beam–column joints using carbon-FRP jacketing." *Materials and Structures*, 1–17.

Birtel, V., and Mark, P. (2006). "Parameterised finite element modelling of RC beam shear failure." *2006 ABAQUS User's Conference. Taiwan*, 95–108.

Bournas, D. A., Pavese, A., and Tizani, W. (2015). "Tensile capacity of FRP anchors in connecting FRP and TRM sheets to concrete." *Engineering Structures*, 82, 72–81.

Bournas, D. A., and Triantafillou, T. C. (2009). "Flexural Strengthening of Reinforced Concrete Columns with Near-Surface-Mounted FRP or Stainless Steel." *ACI Structural Journal*, 106(4), 495–505.

Bousias, S. N., Spathis, A.-L., and Fardis, M. N. (2006). "Concrete or FRP Jacketing of Columns with Lap Splices for Seismic Rehabilitation." *Journal of Advanced Concrete Technology*, 4(3), 431–444.

Bousselham, A. (2010). "State of Research on Seismic Retrofit of RC Beam-Column Joints with Externally Bonded FRP." *Journal of Composites for Construction*, 14(1), 49–61.

Box, G. E. P., and Draper, N. R. (1986). *Empirical Model Building and Response Surfaces*. Wiley-Blackwell, New York.

CEN. (2004). "BS EN 1998-1:2004 Eurocode 8. Design of structures for earthquake resistance. General rules, seismic actions and rules for buildings."

CEN. (2006). "BS EN 1998-3:2005 - Eurocode 8. Design of structures for earthquake resistance. Assessment and retrofitting of buildings." BSI.

CEN. (2008). *BS EN 1992-1-1:2004 Eurocode 2. Design of concrete structures. Part 1-1*. BSI, London.

Chen, G. M., Chen, J. F., and Teng, J. G. (2012). "On the finite element modelling of RC beams shear-strengthened with FRP." *Construction and Building Materials*, 32, 13–26.

Cheung, P. C., Paulay, T., and Park, R. (1991a). "Mechanisms of Slab Contributions in Beam-Column Subassemblages." *Special Publication*, 123, 259–290.

Cheung, P., Paulay, T., and Park, R. (1991b). "New Zealand Tests on Full-Scale Reinforced Concrete Beam-Column-Slab Subassemblages Designed for Earthquake Resistance." *Special Publication*, 123, 1–38.

Chiu, C.-K., Hsiao, F.-P., and Jean, W.-Y. (2013). "A novel lifetime cost-benefit analysis method for seismic retrofitting of low-rise reinforced concrete buildings." *Structure and Infrastructure Engineering*, 9(9), 891–902.

Choudhury, A. M., Deb, S. K., and Dutta, A. (2013). "Study on size effect of fibre reinforced polymer retrofitted reinforced concrete beam–column connections under cyclic loading." *Canadian Journal of Civil Engineering*, 40(4), 353–360.

CNR. (2013). "DT 200.R1/2013 - Guide for the Design and Construction of Externally Bonded FRP Systems for Strengthening Existing Structures - Materials, RC and PC structures, masonry structures." CNR.

Coburn, A., and Spence, R. (2006). "Front Matter." *Earthquake Protection*, John Wiley & Sons, Ltd, i–xvi.

Comartin, C., Bonowitz, D., Greene, M., McCormick, D., May, P., and Seymour, E. (2011). *The Concrete Coalition and the California Inventory Project: An Estimate of the Number of Pre-1980 Concrete Buildings in the State*. Concrete Coalition.

CSA A23.3 (Ed.). (1994). *Design of Concrete Structures*. Canadian Standards Association, Rexdale, Ontario, Canada.

D'Ayala, D., Penford, A., and Valentini, S. (2003). "Use of FRP fabric for strengthening of reinforced concrete beam-column joints." *Proceedings of the 10th International conference on structural faults and repair, London*.

Del Vecchio, C., Di Ludovico, M., Balsamo, A., Prota, A., Manfredi, G., and Dolce, M. (2014). "Experimental Investigation of Exterior RC Beam-Column Joints Retrofitted with FRP Systems." *Journal of Composites for Construction*, 18(4).

Dilley, M. (2005). *Natural Disaster Hotspots: A Global Risk Analysis*. World Bank Publications.

Doğangün, A. (2004). "Performance of reinforced concrete buildings during the May 1, 2003 Bingöl Earthquake in Turkey." *Engineering Structures*, 26(6), 841–856.

Dritsos, S. E. (2005). "Seismic retrofit of buildings a greek perspective." *Bulletin of the NZ Society of Earthquake Engineering*, 38(3), 165–181.

El-Amoury, T., and Ghobarah, A. (2002). "Seismic rehabilitation of beam–column joint using GFRP sheets." *Engineering Structures*, 24(11), 1397–1407.

Engindeniz, M. (2008). "Repair and Strengthening of Pre-1970 Reinforced Concrete Corner Beam-column Joints Using CFRP Composites." PhD, Georgia Institute of Technology.

Engindeniz, M., Kahn, L. F., and Zureick, A. (2008a). "Pre-1970 RC corner beam-column-slab joints: Seismic adequacy and upgradability with CFRP composites." *Proceedings of the 14th World Conf. on Earthquake Engineering*, Beijing, China, 12–17.

Engindeniz, M., Kahn, L. F., and Zureick, A. H. (2008b). "Performance of an RC corner beam-column joint severely damaged under bidirectional loading and rehabilitated with FRP composites." *Seismic Strengthening of Concrete Buildings Using FRP Composites*, 25.

Engindeniz, M., Kahn, L. F., and Zureick, A.-H. (2005). "Repair and strengthening of reinforced concrete beam-column joints: State of the art." *ACI structural journal*, 102(2), 187–197.

Eslami, A., Dalalbashi, A., and Ronagh, H. R. (2013). "On the effect of plastic hinge relocation in RC buildings using CFRP." *Composites Part B: Engineering*, 52, 350–361.

Eslami, A., and Ronagh, H. (2014). "Experimental Investigation of an Appropriate Anchorage System for Flange-Bonded Carbon Fiber–Reinforced Polymers in Retrofitted RC Beam–Column Joints." *Journal of Composites for Construction*, 18(4), 4013056.

Fardis, M. N. (2009). *Seismic Design, Assessment and Retrofitting of Concrete Buildings: based on EN-Eurocode 8*. Springer.

Feenstra, P. H., and de Borst, R. (1995). "A Constitutive Model for Reinforced Concrete Based on Stress Decomposition." *Engineering Mechanics*, ASCE, 643–646.

FEMA (Ed.). (1999). *FEMA 356 Handbook for the Seismic Evaluation of Buildings*. DIANE Publishing.

Fernandes, C., Melo, J., Varum, H., and Costa, A. (2011). "Comparative analysis of the cyclic behaviour of beam-column joints with plain and deformed reinforcing bars."

fib. (1990). "CEB-FIP model code for concrete structures." Thomas Telford, London, UK.

fib. (2006). *fib Bulletin 35 - Retrofitting of concrete structures by externally bonded FRPs, with emphasis on seismic applications*. fib, Lausanne.

Gallo, P. Q., Akguzel, U., Pampanin, S., Carr, A. J., and Bonelli, P. (2012). "Shake table tests of non-ductile RC frames retrofitted with GFRP laminates in beam column joints and selective weakening in floor slabs." Christchurch, NZ.

Garcia, R., Hajirasouliha, I., and Pilakoutas, K. (2010). "Seismic behaviour of deficient RC frames strengthened with CFRP composites." *Engineering Structures*, 32(10), 3075–3085.

Garcia, R., Jemaa, Y., Helal, Y., Guadagnini, M., and Pilakoutas, K. (2014). "Seismic Strengthening of Severely Damaged Beam-Column RC Joints Using CFRP." *Journal of Composites for Construction*, 18(2), 4013048.

Garcia, R., Jemaa, Y., Helal, Y., Pilakoutas, K., and Guadagnini, M. (2012). "FRP Strengthening of Seismically Deficient Full-Scale RC Beam-Column Joints." *Proceedings of the 15th world conference on earthquake engineering*, Lisbon, Portugal.

Genesio, G., Eligehausen, R., Sharma, A., and Pampanin, S. (2010). "Experimental and numerical study towards a deformation-based seismic assessment of substandard exterior RC beam-column joints." *Proceedings of the 7th Int. Conf. on Fracture Mechanics of Concrete and Concrete Structures (FRAMCOS-7), Jeju, Korea*.

Gergely, J., Pantelides, C., and Reaveley, L. (2000). "Shear Strengthening of RCT-Joints Using CFRP Composites." *Journal of Composites for Construction*, 4(2), 56–64.

Ghobarah, A., and El-Amoury, T. (2005). "Seismic Rehabilitation of Deficient Exterior Concrete Frame Joints." *Journal of Composites for Construction*, 9(5), 408–416.

Ghobarah, A., and Said, A. (2002). "Shear strengthening of beam-column joints." *Engineering Structures*, 24(7), 881–888.

Ghosh, K. K., and Sheikh, S. A. (2007). "Seismic upgrade with carbon fiber-reinforced polymer of columns containing lap-spliced reinforcing bars." *ACI structural journal*, 104(2), 227.

Global Risk Miyamoto. (2009). *2009 M6.3 L'Aquila, Italy, Earthquake Field Investigation Report*.

Hadi, M. N. S., and Tran, T. M. (2014). "Retrofitting nonseismically detailed exterior beam–column joints using concrete covers together with CFRP jacket." *Construction and Building Materials*, 63, 161–173.

Hadi, M. N. S., and Tran, T. M. (2015). "Seismic rehabilitation of reinforced concrete beam–column joints by bonding with concrete covers and wrapping with FRP composites." *Materials and Structures*, 1–19.

Hakuto, S., Park, R., and Tanaka, H. (2000). "Seismic load tests on interior and exterior beam-column joints with substandard reinforcing details." *ACI Structural Journal*, 97(1).

Hasan, Q. F., Tekeli, H., and Demir, F. (2016). "NSM Rebar and CFRP laminate strengthening for RC columns subjected to cyclic loading." *Construction and Building Materials*, 119, 21–30.

Hillerborg, A. (1983). "Analysis of one single crack." *Fracture Mechanics of Concrete (Developments in civil engineering)*, 223–249.

Hillerborg, A. (1986). "The theoretical basis of a method to determine the fracture energy Gf of concrete, Matériaux et Struct." *RILEM*, 18, 106.

Hordijk, D. A. (1992). "Tensile and tensile fatigue behaviour of concrete; experiments, modelling and analyses." *Heron*, 37(1).

Ibrahim, A. M., and Mahmood, M. S. (2009). "Finite element modeling of reinforced concrete beams strengthened with FRP laminates."

Ilki, A., Bedirhanoglu, I., and Kumbasar, N. (2011). "Behavior of FRP-Retrofitted Joints Built with Plain Bars and Low-Strength Concrete." *Journal of Composites for Construction*, 15(3), 312–326.

Inel, M., Ozmen, H. B., and Akyol, E. (2013). "Observations on the building damages after 19 May 2011 Simav (Turkey) earthquake." *Bulletin of Earthquake Engineering*, 11(1), 255–283.

Jankowiak, T., and Lodygowski, T. (2005). "Identification of parameters of concrete damage plasticity constitutive model." *Foundations of civil and environmental engineering*, 6, 53–69.

Jiang, C., Wu, Y.-F., and Wu, G. (2014). "Plastic Hinge Length of FRP-Confined Square RC Columns." *Journal of Composites for Construction*, 18(4), 4014003.

Joh, O., Goto, Y., and Shibata, T. (1988). "Behavior of three-dimensional reinforced concrete beam-column subassemblages with slabs." *北海道大學工學部研究報告= Bulletin of the Faculty of Engineering, Hokkaido University*, 145, 41–52.

Kalfat, R., Al-Mahaidi, R., and Smith, S. (2013). "Anchorage Devices Used to Improve the Performance of Reinforced Concrete Beams Retrofitted with FRP Composites: State-of-the-Art Review." *Journal of Composites for Construction*, 17(1), 14–33.

Kam, W. Y., Bull, D., and Pampanin, S. (2009). "Experimental Validation of Selective Weakening Approach for the Seismic Retrofit of Exterior Beam-Column Joints."

Kam, W. Y., and Pampanin, S. (2009). "Experimental and numerical validation of selective weakening retrofit for existing non-ductile RC frames." *Proc. of ATC-SEI Conf on Improving the Seismic Performance of Existing Buildings and Other Structures*, 9–11.

Kam, W. Y., Pampanin, S., and Elwood, K. (2011). "Seismic performance of reinforced concrete buildings in the 22 February Christchurch (Lyttelton) earthquake." *Bulletin of the New Zealand Society for Earthquake Engineering*, 44(4), 239–278.

Kam, W. Y., Quintana Gallo, P., Akguzel, U., and Pampanin, S. (2010). "Influence of slab on the seismic response of sub-standard detailed exterior reinforced concrete beam column joints." Toronto, Canada:

Kaplan, H., Bilgin, H., Yilmaz, S., Binici, H., and Öztas, A. (2010). "Structural damages of L'Aquila (Italy) earthquake." *Natural Hazards and Earth System Science*, 10(3), 499–507.

Kappos, A. J. (2007). "Seismic vulnerability and risk assessment of urban habitat in Southern European cities." *Proceedings of the Urban Habitat Constructions under Catastrophic Events Workshop (COST C26), Prague*, 115–129.

Kappos, A., and Panagopoulos, G. (n.d.). *WHE-Pager project: Building construction vulnerability and inventory*. EERI and IAEE.

Kappos, A., and Penelis, G. G. (1996). *Earthquake Resistant Concrete Structures*. CRC Press, London ; New York.

Karayannis, C. G., and Sirkelis, G. M. (2008). "Strengthening and rehabilitation of RC beam–column joints using carbon-FRP jacketing and epoxy resin injection." *Earthquake Engineering & Structural Dynamics*, 37(5), 769–790.

Kazuhiro, K., Shunsuke, O., and Hiroyuki, A. (1991). "Development of design criteria for RC interior beam-column joints." *ACI Special Publication*, 123.

Kmiecik, P., and Kamiński, M. (2011). "Modelling of reinforced concrete structures and composite structures with concrete strength degradation taken into consideration." *Archives of civil and mechanical engineering*, 11(3), 623–636.

Krätzig, W. B., and Pölling, R. (2004). "An elasto-plastic damage model for reinforced concrete with minimum number of material parameters." *Computers & Structures*, 82(15–16), 1201–1215.

Lee, J., and Fenves, G. (1998). "Plastic-Damage Model for Cyclic Loading of Concrete Structures." *Journal of Engineering Mechanics*, 124(8), 892–900.

Lee, W. T., Chiou, Y. J., and Shih, M. H. (2010). "Reinforced concrete beam–column joint strengthened with carbon fiber reinforced polymer." *Composite Structures*, 92(1), 48–60.

Lehman, D., Stanton, J., Anderson, M., Alire, D., and Walker, S. (2004). "Seismic performance of older beam-column joints." *Proc. 13th world conf. earthquake engineering*, Vancouver, Canada.

Le-Trung, K., Lee, K., Lee, J., Lee, D. H., and Woo, S. (2010). "Experimental study of RC beam–column joints strengthened using CFRP composites." *Composites Part B: Engineering*, 41(1), 76–85.

Li, X., Lv, H.-L., Zhang, G.-C., Sha, S.-Y., and Zhou, S.-C. (2013). "Seismic retrofitting of rectangular reinforced concrete columns using fiber composites for enhanced flexural strength." *Journal of Reinforced Plastics and Composites*, 32(9), 619–630.

López-Almansa, F., Alfarah, B., and Oller, S. (2014). "Numerical simulation of RC frame testing with damaged plasticity model. Comparison with simplified models." Istanbul, Turkey.

Lubliner, J., Oliver, J., Oller, S., and Oñate, E. (1989). "A plastic-damage model for concrete." *International Journal of Solids and Structures*, 25(3), 299–326.

Luk, S., and Kuang, J. (2012). "Seismic behaviour of RC exterior wide beam-column joints." *Proceedings of the 15th world conference on earthquake engineering*, Lisbon, Portugal.

Mahini, S. S., and Ronagh, H. R. (2007). “A new method for improving ductility in existing RC ordinary moment resisting frames using FRPs.” *Asian Journal of Civil Engineering (Building and Housing)*, 8(6), 581–595.

Mahini, S. S., and Ronagh, H. R. (2011). “Web-bonded FRPs for relocation of plastic hinges away from the column face in exterior RC joints.” *Composite Structures*, 93(10), 2460–2472.

Malm, R. (2009). “Predicting shear type crack initiation and growth in concrete with non-linear finite element method.”

Mark, P., and Bender, M. (2010). “Computational modelling of failure mechanisms in reinforced concrete structures.” *Facta universitatis-series: Architecture and Civil Engineering*, 8(1), 1–12.

Melo, J. (2014). “Characterisation of the cyclic response of reinforced concrete elements with plain bars.” PhD, Universidade de Aveiro, Portugal.

Melo, J., Varum, H., and Rossetto, T. (2015). “Cyclic behaviour of interior beam–column joints reinforced with plain bars.” *Earthquake Engineering & Structural Dynamics*, 44(9), 1351–1371.

Mosallam, A. . (2000). “Strength and ductility of reinforced concrete moment frame connections strengthened with quasi-isotropic laminates.” *Composites Part B: Engineering*, 31(6–7), 481–497.

Motavalli, M., and Czaderski, C. (2007). “FRP composites for retrofitting of existing civil structures in Europe: state-of-the-art review.” *International Conference of Composites & Polycon., American Composites Manufacturers Association. Tampa, FL, USA*.

Mukherjee, A., and Joshi, M. (2005). “FRPC reinforced concrete beam-column joints under cyclic excitation.” *Composite Structures*, 70(2), 185–199.

Noor, F. A., and Boswell, L. F. (1992). *Small scale modelling of concrete structures*. Elsevier applied science.

Obaidat, Y. T., Heyden, S., and Dahlblom, O. (2010). “The effect of CFRP and CFRP/concrete interface models when modelling retrofitted RC beams with FEM.” *Composite Structures*, 92(6), 1391–1398.

Ozcan, O., Binici, B., and Ozcebe, G. (2010). “Seismic strengthening of rectangular reinforced concrete columns using fiber reinforced polymers.” *Engineering Structures*, 32(4), 964–973.

Pampanin, S. (2006). “Controversial aspects in seismic assessment and retrofit of structures in modern times: Understanding and implementing lessons from ancient heritage.”

Pampanin, S., and Akguzel, U. (2011). “Performance-Based Seismic Retrofit of Existing Reinforced Concrete Frame Buildings using Fibre-Reinforced Polymers: Challenges and Solutions.” *Structural Engineering International*, 21(3), 260–270.

Pampanin, S., Bolognini, D., and Pavese, A. (2007). “Performance-Based Seismic Retrofit Strategy for Existing Reinforced Concrete Frame Systems Using Fiber-Reinforced Polymer Composites.” *Journal of Composites for Construction*, 11(2), 211–226.

Pampanin, S., Bolognini, D., Pavese, A., Magenes, G., and Calvi, G. M. (2004). “Multi-level seismic rehabilitation of existing frame systems and subassemblies using FRP composites.” *Proceedings of the 2nd International Conference on FRP Composites in Civil Engineering*, Adelaide, Australia.

Pampanin, S., Calvi, G. M., and Moratti, M. (2002). “Seismic Behavior of R.C. Beam-Column Joints Designed for Gravity Only.”

Pantazopoulou, S. j., Tastani, S. p., Thermou, G. e., Triantafillou, T., Monti, G., Bournas, D., and Guadagnini, M. (2015). “Background to European seismic design provisions for the retrofit of R.C. elements using FRP materials.” *Structural Concrete*, n/a-n/a.

Pantelides, C., Okahashi, Y., and Reaveley, L. (2008). “Seismic Rehabilitation of Reinforced Concrete Frame Interior Beam-Column Joints with FRP Composites.” *Journal of Composites for Construction*, 12(4), 435–445.

Park, R., and Paulay, T. (1973). “Behaviour of reinforced concrete external beam-column joints under cyclic loading.” *Proceedings*.

Park, S., and Mosalam, K. M. (2013). “Experimental Investigation of Nonductile RC Corner Beam-Column Joints with Floor Slabs.” *Journal of Structural Engineering*, 139(1), 1–14.

Park, Y. J., Ang, A. H., and Wen, Y. K. (1987). "Damage-limiting aseismic design of buildings." *Earthquake spectra*, 3(1), 1–26.

Paulay, T. (1986). "A Critique of the Special Provisions for Sesmic Design of the Building Code Requirements for Reinforced Concrete (ACI 318-83)." *Journal Proceedings*, 83(2), 274–283.

Paulay, T., and Priestley, M. J. N. (1992). "Seismic design of concrete and masonry structures." *John Wilev and Sons. New York*.

Perrone, M., Barros, J., and Aprile, A. (2009). "CFRP-Based Strengthening Technique to Increase the Flexural and Energy Dissipation Capacities of RC Columns." *Journal of Composites for Construction*, 13(5), 372–383.

Pohoryles, D. A., Melo, J., Rossetto, T., Fabian, M., McCague, C., Stavrianaki, K., Lishman, B., and Sargeant, B. (2016). "Use of DIC and AE for Monitoring Effective Strain and Debonding in FRP and FRCM-Retrofitted RC Beams." *Journal of Composites for Construction*, 0(0), 4016057.

Pohoryles, D. A., and Rossetto, T. (2014). "A critical evaluation of current design guidelines for the seismic retrofit of beam-column joints with FRP." *Proceedings of the 2nd Second European Conference on Earthquake Engineering and Seismology*, Istanbul, Turkey.

Prota, A., Nanni, A., Manfredi, G., and Cosenza, E. (2004). "Selective upgrade of underdesigned reinforced concrete beam-column joints using carbon fiber-reinforced polymers." *ACI structural journal*, 101(5), 699–707.

Realfonzo, R., Napoli, A., and Pinilla, J. G. R. (2014). "Cyclic behavior of RC beam-column joints strengthened with FRP systems." *Construction and Building Materials*, 54, 282–297.

Reinhardt, H., Cornelissen, H., and Hordijk, D. (1986). "Tensile Tests and Failure Analysis of Concrete." *Journal of Structural Engineering*, 112(11), 2462–2477.

Restrepo-Posada, J. I. (1992). "Seismic behaviour of connections between precast concrete elements." PhD, University of Canterbury, Christchurch, New Zealand.

Ricci, P., De Luca, F., and Verderame, G. M. (2011). "6th April 2009 L'Aquila earthquake, Italy: reinforced concrete building performance." *Bulletin of Earthquake Engineering*, 9(1), 285–305.

Rocca, S., Galati, N., and Nanni, A. (2008). "Review of Design Guidelines for FRP Confinement of Reinforced Concrete Columns of Noncircular Cross Sections." *Journal of Composites for Construction*, 12(1), 80–92.

Rodrigues, H., Furtado, A., Arêde, A., Pouca, N., and Varum, H. (n.d.). "Experimental study of repaired RC columns subjected to uniaxial and biaxial horizontal loading and variable axial load with longitudinal reinforcement welded steel bars solutions." *Engineering Structures (under review)*.

Rossetto, T., and Elnashai, A. (2003). "Derivation of vulnerability functions for European-type RC structures based on observational data." *Engineering Structures*, 25(10), 1241–1263.

Russo, G., and Pauletta, M. (2012). "Seismic Behavior of Exterior Beam-Column Connections with Plain Bars and Effects of Upgrade." *ACI Structural Journal*, 109(2), 225.

Said, A. M., and Nehdi, M. L. (2004). "Use of FRP for RC Frames in Seismic Zones: Part I. Evaluation of FRP Beam-Column Joint Rehabilitation Techniques." *Applied Composite Materials*, 11(4), 205–226.

Sezen, H., Whittaker, A. S., Elwood, K. J., and Mosalam, K. M. (2003). "Performance of reinforced concrete buildings during the August 17, 1999 Kocaeli, Turkey earthquake, and seismic design and construction practise in Turkey." *Engineering Structures*, 25(1), 103–114.

Shiohara, H. (1998). "A new model for joint shear failure of reinforced concrete interior beam-to-column joint." *Journal of the School of Engineering, the University of Tokyo*, 45, 15–40.

Shiohara, H. (2001). "New model for shear failure of RC interior beam-column connections." *Journal of Structural Engineering*, 127(2), 152–160.

Shiohara, H., Kusuhara, F., Tajiri, S., and Fukuyama, H. (2009). "Seismic Retrofit of Reinforced Concrete Beam-Column Joints with CFRP Composites." *Improving the*

Seismic Performance of Existing Buildings and Other Structures, American Society of Civil Engineers, San Francisco, California, 1449–1459.

Sinaei, H., Shariati, M., Abna, A. H., Aghaei, M., and Shariati, A. (2012). "Evaluation of reinforced concrete beam behaviour using finite element analysis by ABAQUS." *Scientific Research and Essays*, 7(21).

Smith, S. T., Hu, S., Kim, S. J., and Seracino, R. (2011). "FRP-strengthened RC slabs anchored with FRP anchors." *Engineering Structures*, 33(4), 1075–1087.

Smyth, A. W., Altay, G., Deodatis, G., Erdik, M., Franco, G., Gulkan, P., Kunreuther, H., Lus¸, H., Mete, E., Seeber, N., and Yuzugullu, O. (2004). "Probabilistic Benefit-Cost Analysis for Earthquake Damage Mitigation: Evaluating Measures for Apartment Houses in Turkey." *Earthquake Spectra*, 20(1), 171–203.

Swiss RE. (2016). "Preliminary sigma estimates for 2015." <http://www.swissre.com/media/news_releases/Preliminary_sigma_estimates_for_2015.html> (Sep. 28, 2016).

Thermou, G. E., and Elnashai, A. S. (2006). "Seismic retrofit schemes for RC structures and local-global consequences." *Progress in Structural Engineering and Materials*, 8(1), 1–15.

Tsonos, A. G. (2008). "Effectiveness of CFRP-jackets and RC-jackets in post-earthquake and pre-earthquake retrofitting of beam–column subassemblages." *Engineering Structures*, 30(3), 777–793.

USGS. (2016). "Earthquake Statistics." <https://earthquake.usgs.gov/earthquakes/browse/stats.php> (Sep. 28, 2016).

Varum, H. (2003). "Seismic Assessment, Strengthening and Repair of Existing Buildings." PhD Thesis, University of Aveiro, Portugal.

Vonk, R. A. (1993). *A Micromechanical Investigation of Solftening of Concrete Loaded in Compression*. Stevin-Laboratory of the Faculty of Civil Engineering, University of Technology.

Vrettos, I., Kefala, E., and Triantafillou, T. C. (2013). "Innovative flexural strengthening of reinforced concrete columns using carbon-fiber anchors." *ACI Structural Journal*, 110(1), 63.

Wang, Q., Liu, Y. Q., and Lebet, J. P. (2012). "Nonlinear Finite-Element Analysis of the Shear Behaviour of Stud Connectors."

Yakut, A. (2004). *World Housing Encyclopedia–Reinforced concrete frame construction*. EERI and IAEE, 9–1.

Yu, J., Shang, X., and Lu, Z. (2016). "Efficiency of Externally Bonded L-Shaped FRP Laminates in Strengthening Reinforced-Concrete Interior Beam-Column Joints." *Journal of Composites for Construction*, 20(3), 4015064.

Yurdakul, Ö., and Avşar, Ö. (2015). "Structural repairing of damaged reinforced concrete beam-column assemblies with CFRPs." *Structural Engineering and Mechanics*, 54(3), 521–543.

Appendix A. DATABASE OF EXISTING EXPERIMENTAL STUDIES

Author	Number of specimens				Specimen	Type of design deficiency										Materials			Experimental set-up					Results	
	Total	Control	Retrofit	Repaired		JTR	WC/SB	CTR	LSC	EC	BTR	BLR	BA	LC	PB	PED	f'ck (MPa)	fy main (MPa)	FRP type	Anchors	Type of Joint	Slab	Transv. beam	Scale	norm. ax. load (v=N/Acfc)	Fmax (kN)	ΔF max
Gergely et al. (2000)	14	4	10	0																						
		1			1	✓					✓						12.0	414			T			1/3	0.00	129.0	
		1			2	✓					✓						12.0	414		F	T			1/3	0.00	129.0	
			1		3	✓					✓						12.0	414	C	F	T			1/3	0.00	182.0	41.1%
			1		4	✓					✓						12.0	414	C	F	T			1/3	0.00	187.0	45.0%
			1		5	✓					✓						12.0	414	C	F	T			1/3	0.00	161.0	24.8%
			1		6	✓					✓						12.0	414	C	F	T			1/3	0.00	158.0	22.5%
			1		7	✓					✓						12.0	414	C	F	T			1/3	0.00	156.0	20.9%
			1		8	✓					✓						12.0	414	C	F	T			1/3	0.00	187.0	45.0%
			1		9	✓					✓						12.0	414	C	F	T			1/3	0.00	216.0	67.4%
		1			10	✓					✓						26.0	414			T			1/3	0.00	126.0	
		1			11	✓					✓						26.0	414			T			1/3	0.00	148.0	
			1		12	✓					✓						26.0	414	C	F	T			1/3	0.00	184.0	46.0%
			1		13	✓					✓						26.0	414	C	F	T			1/3	0.00	204.0	61.9%
			1		14	✓					✓						26.0	414	C	F	T			1/3	0.00	229.0	81.7%
Pantelides et al. (2000)	2	1	1	0																						
		1				✓			✓				✓				37.5	469			Ext			1/2	0.10	218.0	
			1			✓			✓				✓				37.5	469	C		Ext			1/2	0.10	261.0	19.7%
El-Amoury and Ghobarah (2002)	3	1	1	1																						
		1			T0	✓							✓				22.6	425			Ext		1		0.20	86.0	
			1		TR1	✓							✓				35.5	425	G	S	Ext		1		0.20	120.0	39.5%
				1	TR2	✓							✓				31.5	425	G	S	Ext		1		0.20	131.0	52.3%

Author	Total	Control	Retrofit	Repaired	Specimen	JTR	WC/SB	CTR	LS	EC	BTR	BLR	BA	LC	PB	PED	f'ck (MPa)	fy main (MPa)	FRP type	Anchors	Type of Joint	Slab	Transv. beam	Scale	norm. ax. load	Fmax (kN)	ΔF max
Ghobarah and Said (2002)	6	2	2	2																							
		1			T1	✓	✓						✓				22.8	425			Ext			1	0.19	116.1	
		1			T2	✓	✓						✓				22.8	425			Ext			1	0.10	110.0	
				1	T1R	✓	✓						✓			✓	22.6	425	G	S	Ext			1	0.20	126.2	8.7%
				1	T2R	✓	✓						✓			✓	30.0	425	G	S	Ext			1	0.16	129.9	18.1%
			1		T4	✓	✓						✓				22.8	425	G		Ext			1	0.19	110.0	0.0%
			1		T9	✓	✓						✓				17.1	425	G		Ext			1	0.24	129.5	11.5%
Antopoulos and Triantafillou (2003)	18	4	13	1																							
		1			C	✓											9.9	585			Ext			2/3	0.06	30.1	
		1			C	✓											9.9	585			Ext			2/3	0.06	30.1	
			1		S33	✓											13.6	585	C		Ext			2/3	0.05	35.0	16.3%
			1		S63	✓											12.1	585	C		Ext			2/3	0.06	39.8	32.2%
			1		S33L	✓											13.8	585	C	S	Ext			2/3	0.05	42.5	41.2%
			1		F11	✓											10.9	585	C		Ext			2/3	0.06	42.6	41.5%
			1		F22	✓											14.6	585	C		Ext			2/3	0.05	49.6	64.8%
			1		F21	✓											14.4	585	C		Ext			2/3	0.05	50.7	68.4%
			1		F12	✓											16.5	585	C		Ext			2/3	0.05	44.4	47.5%
			1		F22A	✓											15.1	585	C		Ext			2/3	0.12	55.0	82.7%
			1		F22W	✓											16.2	585	C	F	Ext			2/3	0.05	55.4	84.1%
				1	F22in	✓										✓	9.4	585	C		Ext			2/3	0.07	41.8	38.9%
			1		GL	✓											8.2	585	G		Ext			2/3	0.07	43.6	44.9%
		1			S-C												8.0	585			Ext			2/3	0.07	32.7	
			1		S-F22												7.8	585	C		Ext			2/3	0.07	43.7	33.6%
		1			T-C	✓											12.4	585			Ext		✓	2/3	0.06	34.9	
			1		T-F33	✓											13.6	585	C		Ext		✓	2/3	0.05	44.4	27.2%
			1		T-F22S2	✓											10.3	585	C		Ext		✓	2/3	0.06	39.9	14.3%

Author	Total	Control	Retrofit	Repaired	Specimen	JTR	WC/SB	CTR	LS	EC	BTR	BLR	BA	LC	PB	PED	f'ck (MPa)	fy main (MPa)	FRP type	Anchors	Type of Joint	Slab	Transv. beam	Scale	norm. ax. load	Fmax (kN)	ΔF max
D'Ayala (2003)	16	4	8	4																							
		1			WB-S1-U	✓						✓			✓		20.0	353			Int			1	0.04	28.6	
				1	WB-S1-R-C1	✓						✓			✓		20.0	353	C	F	Int			1	0.04	30.4	6.3%
			1		WB-S3-C1	✓						✓			✓		20.0	353	C	F	Int			1	0.04	33.6	17.5%
			1		WB-S5-C1	✓						✓			✓		20.0	353	C	F	Int			1	0.04	29.1	1.7%
		1			WB-S2-U	✓						✓			✓		20.0	353			Int			1	0.04	30.0	
				1	WB-S2-R-C5	✓						✓			✓		20.0	353	C	F	Int			1	0.04	37.7	25.7%
			1		WB-S4-C5	✓						✓			✓		20.0	353	C	F	Int			1	0.04	40.0	33.3%
			1		WB-S6-C5	✓						✓			✓		20.0	353	C	F	Int			1	0.04	38.7	29.0%
		1			SB-S1-U	✓	✓							✓	✓		15.0	353			Int			1	0.05	28.9	
				1	SB-S1-R-W1	✓	✓							✓	✓		15.0	353	C		Int			1	0.05	27.4	-5.2%
			1		SB-S3-W1	✓	✓							✓	✓		15.0	353	C	F	Int			1	0.05	33.9	17.3%
		1			SB-S2-U	✓	✓							✓	✓		10.0	353		F	Int			1	0.06	20.4	
				1	SB-S2-R-W2	✓	✓							✓	✓		10.0	353	C	F	Int			1	0.06	20.8	2.0%
			1		SB-S4-W2	✓	✓							✓	✓		15.0	353	C	F	Int			1	0.05	39.3	92.6%
			1		SB-S5-W3	✓	✓							✓	✓		10.0	353	C	F	Int			1	0.06	29.8	46.1%
			1		SB-S6-W2	✓	✓							✓	✓		10.0	353	C	F	Int			1	0.06	26.9	31.9%
Prota et al. (2004)	10	2	8	0		✓	✓																				
		1			L1	✓	✓										30.9	511			Int			1/2	0.08	41.2	
			1		L2	✓	✓										31.8	511	C	F	Int			1/2	0.08	44.2	7.4%
			1		L3	✓	✓										30.9	511	C	F	Int			1/2	0.08	57.2	39.0%
			1		L4	✓	✓										28.5	511	C	F	Int			1/2	0.09	56.6	37.4%
		1			H1	✓	✓										23.7	511			Int			1/2	0.20	38.5	
			1		H2	✓	✓										28.5	511	C	F	Int			1/2	0.17	49.7	29.3%
			1		H2U	✓	✓										28.5	511	C	F	Int			1/2	0.17	51.2	33.1%
			1		H3	✓	✓										23.7	511	C	F	Int			1/2	0.20	62.4	62.2%

Author	Total	Control	Retrofit	Repaired	Specimen	JTR	WC/SB	CTR	LS	EC	BTR	BLR	BA	LC	PB	PED	f'ck (MPa)	fy main (MPa)	FRP type	Anchors	Type of Joint	Slab	Transv. beam	Scale	norm. ax. load	Fmax (kN)	ΔF max
Prota (cont.)			1		H4	✓	✓										31.8	511	C	F	Int			1/2	0.16	70.4	83.1%
			1		M3	✓	✓										31.8	511	C	F	Int			1/2	0.23	56.2	
Pampanin et al. (2004)	6	3	3	0																							
		1			T1	✓			✓				✓		✓		17.0	430			Ext			2/3	0.10	11.0	
			1		T1B	✓			✓				✓		✓		17.0	430	C		Ext			2/3	0.10	18.0	63.6%
		1			T2	✓			✓				✓		✓		17.0	430			Ext			2/3	0.10	12.0	
			1		T2B	✓			✓				✓		✓		17.0	430	C		Ext			2/3	0.10	14.5	20.8%
		1			C4	✓			✓						✓		17.0	430			Int			2/3	0.10	18.0	
			1		C3	✓			✓						✓		17.0	430	C		Int			2/3	0.10	25.5	41.7%
Ghobarah and El-Amoury (2005)	3	1	2	0																							
		1			T-B10								✓				22.0	425			Ext			1	0.20	61.5	
			1		T-B12								✓				22.0	425	C	S	Ext			1	0.20	55.0	-10.6%
			1		T-B11								✓				22.0	425	C	S	Ext			1	0.20	86.0	39.8%
Mukherjee and Joshi (2005)	13	2	10	1																							
		1			D-1	✓						✓	✓				22.0	275			Int			1/3	0.33	3.8	
		1			ND-1	✓					✓						22.0	275			Int			1/3	0.33	3.7	
			1		G1L-D	✓						✓	✓				22.0	275	G		Int			1/3	0.33	4.5	18.4%
			1		G2L-D	✓						✓	✓				22.0	275	G		Int			1/3	0.33	5.8	52.6%
			1		C1L-D	✓						✓	✓				22.0	275	C		Int			1/3	0.33	4.2	9.2%
			1		C2L-D	✓						✓	✓				22.0	275	C		Int			1/3	0.33	6.0	57.9%
			1		CP1-D	✓						✓	✓				22.0	275	C		Int			1/3	0.33	8.1	113.2%
				1	Rehab.	✓					✓					✓	22.0	275			Int			1/3	0.33	6.3	66.1%
			1		G1L-ND	✓					✓						22.0	275	G		Int			1/3	0.33		
			1		G2L-ND	✓					✓						22.0	275	G	F	Int			1/3	0.33	7.4	99.2%
			1		C1L-ND	✓					✓						22.0	275	C	F	Int			1/3	0.33	4.1	11.0%
			1		C2L-ND	✓					✓						22.0	275	C	F	Int			1/3	0.33	6.7	78.8%

Author	Total	Control	Retrofit	Repaired	Specimen	JTR	WC/SB	CTR	LS	EC	BTR	BLR	BA	LC	PB	PED	f'ck (MPa)	fy main (MPa)	FRP type	Anchors	Type of Joint	Slab	Transv. beam	Scale	norm. ax. load	Fmax (kN)	ΔF max
			1		CP1-ND	✓					✓						22.0	275	C	F	Int			1/3	0.33	6.3	68.4%
Akguzel and Pampanin (2007)	4	2	2	0													0.0	430							0.00		
		1			2DB	✓							✓		✓		17.0	430			Cor			2/3	0.09	14.9	
			1		2D-GF1												23.2	430	G		Cor			2/3	0.08	26.0	74.5%
		1			3DB												16.8	430			Cor		✓	2/3	0.10	14.0	
			1		3D-GF1												22.1	430	G		Cor		✓	2/3	0.08	22.5	60.7%
Al-Salloum and Almusallam (2007)	6	2	2	2																							
		1			IC1	✓											22.0	420			Int	✓		1/2	0.20	71.0	
				1	IR1	✓										✓	22.0	420	C		Int	✓		1/2	0.20	64.1	-9.6%
			1		IS1	✓											22.0	420	C		Int	✓		1/2	0.20	85.2	20.0%
		1			IC2	✓											17.0	420			Int	✓		1/2	0.20	59.1	
				1	IR2	✓										✓	17.0	420	C	S	Int	✓		1/2	0.20	66.8	13.0%
			1		IS2	✓											17.0	420	C	S	Int	✓		1/2	0.20	63.3	7.0%
Mahini and Ronagh (2007)	2	1	1	0																							
		1			CSC1								✓				32.7	500			Ext			1/2	0.19	19.5	
			1		RSC1								✓				28.4	500			Ext			1/2	0.21	21.3	9.2%
Engindeniz et al. (2008)	6	2	2	2																							
		1			Specimen 1	✓	✓		✓				✓				13.4	315			Cor	✓	✓	1	0.10	50.0	
		1			Specimen 2	✓	✓		✓				✓				20.7	315			Cor	✓	✓	1	0.10	52.5	
			1		Specimen 3	✓	✓		✓				✓				20.1	315	C	F	Cor	✓	✓	1	0.10	68.0	36.0%
			1		Specimen 4	✓	✓		✓				✓	✓			4.8	315	C	F	Cor	✓	✓	1	0.10	50.0	-4.8%
				2	Repaired 1/2	✓	✓		✓				✓			✓	13.4	315	C	F	Cor	✓	✓	1	0.10		

Author	Total	Control	Retrofit	Repaired	Specimen	JTR	WC/SB	CTR	LS	EC	BTR	BLR	BA	LC	PB	PED	f'ck (MPa)	fy main (MPa)	FRP type	Anchors	Type of Joint	Slab	Transv. beam	Scale	norm. ax. load	Fmax (kN)	ΔF max
Karayannis and Sirkelis (2008)	6	2	2	2																							
		1			A2	✓											28.4	574			Ext			1/2	0.05	21.5	
				1	A2R	✓										✓	28.4	574	C	F	Ext			1/2	0.05	40.5	88.4%
			1		A3	✓											28.4	574	C	F	Ext			1/2	0.05	40.0	86.0%
		1			B2						✓		✓				28.4	574			Ext			1/2	0.05	24.5	
				1	B2R						✓		✓			✓	28.4	574	C	F	Ext			1/2	0.05	39.5	61.2%
			1		B3						✓		✓				28.4	574	C	F	Ext			1/2	0.05	40.5	65.3%
Pantelides et al. (2008)	8	3	5	0																							
		1			24-1	✓	✓	✓					✓				35.0	454			Int			1	0.10	144.0	
		1			24-2	✓	✓	✓					✓				35.0	454			Int			1	0.10	144.0	
			1		R24-3	✓	✓	✓					✓				35.0	454	C		Int			1	0.10	216.0	50.0%
			1		R24-4	✓	✓	✓					✓				35.0	454	C		Int			1	0.10	200.0	38.9%
		1			16-1			✓					✓				35.0	454			Int			1	0.10	84.0	
			1		R16-2			✓					✓				35.0	454	C		Int			1	0.10	115.0	36.9%
			1		R16-3			✓					✓				35.0	454	C		Int			1	0.10	125.0	48.8%
			1		R16-4			✓					✓				35.0	454	C		Int			1	0.10	130.0	54.8%
Tsos (2008)	3	1	0	2		✓	✓	✓								✓											
		1			F1	✓	✓	✓									14.0	540			Cor	✓	✓	1/2	0.17	50.0	
				1	FRPS1	✓	✓	✓									13.8	540	C	F	Cor	✓	✓	1/2	0.17	85.0	70.0%
				1	FRPF1	✓	✓	✓									14.0	540	C	F	Cor	✓	✓	1/2	0.17	80.0	60.0%
Li and Chua (2009)	6	3	3	0																							
		1			E1C	✓				✓							10.4	510			Int			1	0.35	15.8	
			1		SE1C	✓				✓							10.8	510	G	FA	Int			1	0.35	36.9	133.5%
		1			C1C	✓											11.0	510			Int			1	0.35	15.5	
			1		SC1C	✓											10.5	510	G	FA	Int			1	0.35	31.8	105.2%
		1			C2C	✓											12.0	510			Int			1	0.35	139.0	

Author	Total	Control	Retrofit	Repaired	Specimen	JTR	WC/SB	CTR	LS	EC	BTR	BLR	BA	LC	PB	PED	f'ck (MPa)	fy main (MPa)	FRP type	Anchors	Type of Joint	Slab	Transv. beam	Scale	norm. ax. load	Fmax (kN)	ΔF max
			1		SC2C	✓											10.4	510	G	FA	Int			1	0.35	214.0	54.0%
Shiohara et al. (2009)	4	2	2	0																							
		1			C01	✓											23.0	378		F	Int			1/3	0.00	73.4	
			1		C02	✓											23.0	378	C	F	Int			1/3	0.00	77.8	6.0%
		1			C03	✓											23.0	378		F	Int			1/3	0.00	65.8	
			1		C04	✓											23.0	378	C	F	Int			1/3	0.00	74.2	12.8%
Akguzel and Pampanin (2010)	10	4	6	0																							
		1			2DB1	✓						✓			✓		17.0	430			Cor			2/3	0.06	16.2	
		1			3DB1	✓						✓			✓		16.2	430			Cor		✓	2/3	0.06	12.6	
			1		2DR1	✓						✓			✓		16.8	430	G	F	Cor			2/3	0.06	26.2	61.5%
			1		3DR1	✓						✓			✓		23.2	430	G	F	Cor		✓	2/3	0.05	23.2	83.9%
		1			2DB2	✓						✓		✓	✓		9.9	430			Cor			2/3	0.12	18.9	
			1		2DR2	✓						✓		✓	✓		10.9	340	G	F	Cor			2/3	0.11	23.9	26.3%
			1		2DR3	✓						✓		✓	✓		10.0	340	G	F	Cor			2/3	0.12	26.8	41.5%
			1		2DR4	✓						✓		✓	✓		10.7	340	G	F	Cor			2/3	0.11	23.9	26.3%
		1			3DB2	✓						✓		✓	✓		9.4	340			Cor		✓	2/3	0.12	18.8	
			1		3DR2	✓						✓		✓	✓		8.9	340	G	F	Cor		✓	2/3	0.12	20.5	8.8%
Alsayed et al. (2010)	4	2	2	0																							
		1			EC1	✓											22.0	420			Ext	✓		1/2	0.20	47.1	
		1			EC2	✓											22.0	420			Ext	✓		1/2	0.20	45.8	
			1		ES1	✓											22.0	420	C		Ext	✓		1/2	0.20	62.3	32.4%
			1		ES2	✓											22.0	420	C	S	Ext	✓		1/2	0.20	58.1	26.9%
Attari et al. (2010)	3	1	1	1																							
		1			NC								✓				30.0	580			Int			1/3	0.18	25.0	
			1		NA1								✓				30.0	580	C		Int			1/3	0.18	31.0	24.0%
				1	NR1								✓			✓	30.0	580	G		Int			1/3	0.18	36.0	44.0%

Author	Total	Control	Retrofit	Repaired	Specimen	JTR	WC/SB	CTR	LS	EC	BTR	BLR	BA	LC	PB	PED	f'ck (MPa)	fy main (MPa)	FRP type	Anchors	Type of Joint	Slab	Transv. beam	Scale	norm. ax. load	Fmax (kN)	ΔF max
Lee et al. (2010)	3	1	2	0																							
		1			JI0		✓	✓									19.0	456			Int			1	0.19	134.0	
			1		JI1		✓	✓									19.0	456	C		Int			1	0.19	139.0	3.7%
			1		JI2		✓	✓									19.0	456	C	S	Int			1	0.19	182.0	35.8%
Le-Trung et al. (2010)	8	2	6	0																							
		1			NS	✓											25.8	324			Ext			1/3	0.00	8.6	
		1			SD												25.8	324			Ext			1/3	0.00	10.4	21.7%
			1		RNS-1	✓											25.8	324	C	F	Ext			1/3	0.00	10.1	18.0%
			1		RNS-2	✓											25.8	324	C		Ext			1/3	0.00	9.9	15.3%
			1		RNS-3	✓											25.8	324	C		Ext			1/3	0.00	10.1	17.5%
			1		RNS-4	✓											25.8	324	C		Ext			1/3	0.00	9.9	15.7%
			1		RNS-5	✓											25.8	324	C	F	Ext			1/3	0.00	9.5	11.2%
			1		RNS-6	✓											25.8	324	C	F	Ext			1/3	0.00	11.3	31.7%
Ilki et al. (2011)	7	2	1	4																							
		1			JO	✓								✓	✓		8.3	333			Ext	✓	✓	1	0.13	53.3	
			1		JC-F-3	✓								✓	✓		8.3	333	C	F	Ext	✓	✓	1	0.13	63.3	18.8%
		1			JW	✓								✓	✓		8.3	333	C		Ext	✓	✓	1	0.13	73.0	
				1	JWC-F-3	✓								✓	✓		8.3	333	C		Ext	✓	✓	1	0.13	86.6	18.6%
				1	JWC-D-2	✓								✓	✓		8.3	333	C		Ext	✓	✓	1	0.13	87.6	20.0%
				1	JWC-D-5	✓								✓	✓		8.3	333	C		Ext	✓	✓	1	0.13	71.4	-2.2%
				1	JWCP-D-(1+1)	✓								✓	✓		8.3	333	C		Ext	✓	✓	1	0.13	89.0	21.9%

Author	Total	Control	Retrofit	Repaired	Specimen	JTR	WC/SB	CTR	LS	EC	BTR	BLR	BA	LC	PB	PED	f'ck (MPa)	fy main (MPa)	FRP type	Anchors	Type of Joint	Slab	Transv. beam	Scale	norm. ax. load	Fmax (kN)	ΔF max
Akguzel and Pampanin (2012) (Kam et al., 2010)	4	2	2	0																							
		1			2DB	✓									✓		9.9	430			Cor			2/3	0.12	17.9	
		1			3DB	✓									✓		9.4	430			Cor		✓	2/3	0.12	17.4	
			1		3DF	✓									✓		13.3	430	G	FA	Cor		✓	2/3	0.10	23.4	34.5%
			1		3DSF	✓									✓		11.4	430	G	FA	Cor	✓	✓	2/3	0.11	21.4	28.1%
	1	1			3DS	✓									✓		11.4	430			Cor	✓	✓	2/3	0.11	16.7	
Garcia et al. (2012)	6	3	0	3																							
		1			JA-2	✓			✓				✓				24.0	551			Ext			1	0.07	57.0	
		1			JB-2	✓			✓				✓				23.3	551			Ext			1	0.07	58.0	
		1			JC-2	✓			✓				✓				24.0	551			Ext			1	0.07	54.5	
				1	JA-2RF	✓			✓				✓			✓	46.2	551	C	FA	Ext			1	0.04	86.2	51.2%
				1	JB-2RF	✓			✓				✓			✓	47.3	551	C	FA	Ext			1	0.04	120.0	106.9%
				1	JC-2RF	✓			✓				✓			✓	48.9	551	C	FA	Ext			1	0.04	119.4	119.1%
Russo and Pauletta (2012)	11	5	1	5																							
		1			12-6	✓							✓		✓		14.2	315			Ext			2/3	0.05	6.0	
				1	12-6-upgraded	✓							✓		✓		14.2	315	C	S	Ext			2/3	0.05	22.0	266.7%
		1			12-8	✓							✓		✓		14.2	315			Ext			2/3	0.05	11.7	
				1	12-8-upgraded	✓							✓		✓		14.2	315	C	S	Ext			2/3	0.05	22.0	88.0%
		1			16-6	✓							✓		✓		14.2	315			Ext			2/3	0.05	14.0	
				1	16-6-upgraded	✓							✓		✓		14.2	315	C	S	Ext			2/3	0.05	33.0	135.7%
		1			16-8	✓							✓		✓		14.2	315			Ext			2/3	0.05	14.0	
				1	16-8-upgraded	✓							✓		✓		14.2	315	C	S	Ext			2/3	0.05	34.0	142.9%
		1			8-8A	✓							✓		✓		12.2	315			Ext			1	0.04	14.0	
				1	8-8A-upgraded	✓							✓		✓		12.2	315	C	S	Ext			1	0.04	20.2	44.3%
			1		8-8B	✓							✓		✓		12.2	315	C	S	Ext			1	0.04	20.8	48.6%

Author	Total	Control	Retrofit	Repaired	Specimen	JTR	WC/SB	CTR	LS	EC	BTR	BLR	BA	LC	PB	PED	f'ck (MPa)	fy main (MPa)	FRP type	Anchors	Type of Joint	Slab	Transv. beam	Scale	norm. ax. load	Fmax (kN)	ΔF max
Choudhury et al. (2013)	12	6	6	0																							
		1			BWFLC							✓					22.0	500			Ext			1	0.10	73.3	
			1		BWFLR							✓					22.0	500 C		F	Ext			1	0.10	77.2	5.3%
		1			BWFMC							✓					22.0	500			Ext			2/3	0.10	32.9	
			1		BWFMR							✓					22.0	500 C		F	Ext			2/3	0.10	40.2	22.0%
		1			BWFSC							✓					22.0	500			Ext			1/3	0.10	8.8	
			1		BWFSR							✓					22.0	500 C		F	Ext			1/3	0.10	10.9	23.6%
		1			BWSLC						✓						22.0	500			Ext			1	0.10	69.6	
			1		BWSLR						✓						22.0	500 C		F	Ext			1	0.10	78.1	12.2%
		1			BWSMC						✓						22.0	500			Ext			2/3	0.10	34.1	
			1		BWSMR						✓						22.0	500 C		F	Ext			2/3	0.10	41.3	21.1%
		1			BWSSC						✓						22.0	500			Ext			1/3	0.10	10.0	
			1		BWSSR						✓						22.0	500 C		F	Ext			1/3	0.10	12.7	26.9%
Agarwal et al. (2014)	4	2	0	2																							
		1			BCJ1-U	✓											19.0	415			Ext			1	0.00	53.7	
				1	BCJ1-U-R	✓										✓	19.0	415 G			Ext			1	0.00	36.5	-32.0%
		1			BCJ2-C												19.0	415			Ext			1	0.00	61.7	
				1	BCJ2-C-R											✓	19.0	415 G			Ext			1	0.00	52.2	-15.4%
Del Vecchio et al. (2014)	6	3	3	0																							
		1			T_C1	✓	✓										4.6	470			Ext	✓		1	0.20	33.2	
		1			T_C2	✓	✓										8.4	470			Ext	✓		1	0.20	42.6	
		1			T_C3	✓	✓										8.3	470			Ext	✓		1	0.20	43.8	
			1		T_FL1	✓	✓										5.6	470 C			Ext	✓		1	0.20	38.8	17%
			1		T_FS1	✓	✓										9.7	470 C			Ext	✓		1	0.20	56.1	32%
			1		T_FS2	✓	✓										8.4	470 C			Ext	✓		1	0.20	65.3	49%

Author	Total	Control	Retrofit	Repaired	Specimen	JTR	WC/SB	CTR	LS	EC	BTR	BLR	BA	LC	PB	PED	f'ck (MPa)	fy main (MPa)	FRP type	Anchors	Type of Joint	Slab	Transv. beam	Scale	norm. ax. load	Fmax (kN)	ΔF max
Eslami and Ronagh (2014)	3	1	2	0																							
		1			CS-C							✓					38.6	521			Ext			1/3	0.17	22.9	
			1		HSG-C							✓					38.6	521	C	F	Ext			1/3	0.17	30.1	31.4%
			1		RSG-C							✓					38.6	521	C	F	Ext			1/3	0.17	33.3	45.4%
Hadi and Tran (2014)	2	0	1	1																							
			1		TS	✓											42.0	550	C		Ext			1	0.00	84.9	137.2%
				1	TR	✓										✓	41.0	550	C	F	Ext			1	0.00	77.5	116.5%
Realfonzo et al. (2014)	8	2	6	0																							
		1			J-01	✓	✓										16.0	540			Ext			1	0.21	65.8	
			1		J-02	✓	✓										16.0	540	C		Cor			1	0.21	80.7	22.6%
			1		J-03	✓	✓										16.0	540	C		Ext			1	0.21	118.8	
			1		J-04	✓	✓										16.0	540	C	S	Ext			1	0.21	130.3	98%
		1			J-05	✓											16.0	540			Ext			1	0.21	70.1	
			1		J-06	✓											16.0	540	C	S	Ext			1	0.21	108.2	54.2%
			1		J-07	✓											16.0	540	C	S	Ext			1	0.21	109.7	56.4%
			1		J-08	✓											16.0	540	C	S	Ext			1	0.21	122.6	74.8%
Hadi and Tran (2015)	3	1	2	0																							
		1			T0	✓											33.0	550			Ext			1	0.00	35.8	
			1		TS1	✓											33.0	550	C	F	Ext			1	0.00	65.8	83.8%
			1		TS2	✓											36.0	550	C	F	Ext			1	0.00	84.9	137.2%
Yu et al. (2015)	14	4	2	8																							
		1			J-1		✓										13.5	387			Int	✓	✓	1/2	0.23	55.7	
				1	J-2		✓									✓	13.5	387	C		Int	✓	✓	1/2	0.23	70.2	26.0%
				1	J-3		✓									✓	13.5	387	C		Int	✓	✓	1/2	0.23	69.5	24.8%
				1	J-4		✓									✓	13.5	387	C		Int	✓	✓	1/2	0.14	67.5	21.2%
			1		J-5		✓										13.5	387	C		Int	✓	✓	1/2	0.14	68.5	23.0%

Author	Total	Control	Retrofit	Repaired	Specimen	JTR	WC/SB	CTR	LS	EC	BTR	BLR	BA	LC	PB	PED	f'ck (MPa)	fy main (MPa)	FRP type	Anchors	Type of Joint	Slab	Transv. beam	Scale	norm. ax. load	Fmax (kN)	ΔF max
Yu (cont.)		1			J-6		✓										16.2	375			Int	✓	✓	1/2	0.20	71.4	
				1	J-7		✓									✓	16.2	375	B		Int	✓	✓	1/2	0.20	75.8	6.2%
				1	J-8		✓									✓	16.2	375	B		Int	✓	✓	1/2	0.20	75.8	6.2%
				1	J-9		✓									✓	16.2	375	B		Int	✓	✓	1/2	0.20	72.6	1.7%
			1		J-10		✓										16.2	375	B		Int	✓	✓	1/2	0.20	79.6	11.5%
Yurdakul and Avsar (2015)	4	2	0	2																							
		1			E001							✓					11.1	522			Ext			1	0.10	117.0	
				1	E001-R							✓				✓	11.1	522	C	F	Ext			1	0.10	117.3	0.3%
		1			E002	✓								✓	✓		8.1	293			Ext			1	0.10	47.7	
				1	E002-R	✓								✓	✓	✓	8.1	293	C	F	Ext			1	0.10	37.4	-21.7%
Beydokhti and Shariatmadar (2016)	6	2	0	4																							
		1			NS5												30.5	533			Ext			2/3	0.02	118.0	
				1	NS1R	✓										✓	30.9	533	C	F	Ext			2/3	0.01	121.0	2.5%
				1	NS2R	✓										✓	30.6	533	C	F	Ext			2/3	0.02	125.0	5.9%
				1	NS3R	✓										✓	30.6	533	C	F	Ext			2/3	0.02	95.0	-19.5%
				1	NS5R	✓										✓	30.5	533	C	F	Ext			2/3	0.02	100.0	-15.3%
		1			S												30.6	533			Ext			2/3	0.02	120.0	1.7%

Appendix B. LIST OF PUBLICATIONS

B.1 PEER-REVIEWED JOURNAL PAPERS

Pohoryles, D. A., Melo, J., Rossetto, T., Fabian, M., McCague, C., Stavrianaki, K., Lishman, B., and Sargeant, B. (2016a). "Use of DIC and AE for Monitoring Effective Strain and Debonding in FRP and FRCM-Retrofitted RC Beams." *Journal of Composites for Construction*, 0(0), 4016057.

B.2 PEER-REVIEWED PUBLISHED CONFERENCE PAPERS

Pohoryles, D. A., Melo, J., Rossetto, T., and Varum, H. (2015b). "Experimental investigation on the seismic FRP retrofit of full-scale RC beam-column joints." *Improving the Seismic Performance of Existing Buildings and Other Structures*, ASCE, San Francisco, California, pp. 619–631.

B.3 PRESENTED CONFERENCE PAPERS

Pohoryles, D. A., and Rossetto, T. (2014). "A critical evaluation of current design guidelines for the seismic retrofit of beam-column joints with FRP." *The 2nd European Conference on Earthquake Engineering and Seismology*, Istanbul, Turkey.[1]

Pohoryles, D. A., Melo, J., and Rossetto, T. (2015a). "Numerical modelling of FRP-strengthened RC beam-column joints." *2015 SECED Conference*, Cambridge, UK.[1]

Pohoryles, D. A., Rossetto, T., Melo, J., and Varum, H. (2016b). "A combined FRP and selective weakening retrofit for realistic pre-1970's RC structures." Chania, Greece. [1, 2]

Pohoryles, D. A., Melo, J., Rossetto, T., Varum, H., and D'Ayala, D. (2017). "A realistic full CFRP retrofit of RC beam-column joints compared to seismically designed specimens." *The 16th World Conference on Earthquake Engineering*, Santiago, Chile.

Rossetto, T., Pohoryles, D. A., Melo, J., and Varum, H. (2017). "The effect of slab and transverse beams on the behaviour of full-scale pre-1970's RC beam-column joints." *The 16th World Conference on Earthquake Engineering*, Santiago, Chile.

Melo, J., Pohoryles, D. A., Rossetto, T., and Varum, H. (2017). "Performance comparison of RC retrofitted interior beam-column joints with CFRP and steel plates." *The 16th World Conference on Earthquake Engineering*, Santiago, Chile.

[1] Available on Researchgate.
[2] Recipient of the Student Paper Award for best paper.

B.4 DISSEMINATION PLAN

Planned future publications:

1. The effect of slab and transverse beams on the effectiveness of seismic retrofits of full-scale beam column joints with FRP.
2. An experimental comparison of CFRP retrofit and repair schemes for realistic full-scale RC beam-column joints.
3. A novel capacity designed FRP seismic retrofit methodology for realistic beam-column joints.
4. A parametric study on CFRP retrofitted RC beam-column joints.

Appendix C. DESIGN GUIDELINES

C.1 EXISTING GUIDELINES

In the U.S. and in Europe, four major bodies have published design guidelines on the seismic retrofit of RC structures with FRP. These guidelines are summarised in Table C.1 below. Only design guidelines that specifically address seismic retrofit are considered. The design guidelines and their equations for joint shear strengthening with FRP are outlined in this chapter. Please refer to the glossary of terms provided at the end of this thesis for commonly used symbols.

Table C.1 Analysed design guidelines.

Publisher	*Name*	*Country*	*Year*
ACI	440 F - Seismic Strengthening of Concrete Buildings Using FRP Composites	U.S.	2009
fib	*fib* Bulletin 35 - Retrofitting of concrete structures by externally bonded FRPs, with emphasis on seismic applications	Europe	2006
CNR	DT 200.R1/2012 - Guide for the Design and Construction of Externally Bonded FRP Systems for Strengthening Existing Structures	Italy	2012
CEN	Eurocode 8: Design of structures for earthquake resistance – Part 3: Assessment and retrofitting of buildings - ANNEX A.4.	Europe	2013

C.1.1 EUROCODE 8 – PART 3

Eurocode 8 (EC8) Part 3 deals with the assessment and retrofit of buildings and in its Annex A.4.4., it gives informative design guidance for the FRP retrofit of RC members. Joint strengthening is not explicitly addressed, however equations for the shear strengthening of rectangular sections are provided.

To calculate the required amount of FRP, first the shear demand on the joint is to be evaluated according to EC8 Part 1 cl. 5.5.2.3, and then the capacity of the as-built joint is to be evaluated according cl. 5.5.3.3. The horizontal joint shear capacity, V_{jh}, is expressed in equation 5.33 for interior joints, or 80% of that value for exterior joints (cl. 5.5.3.3.2(b)):

$$V_{jhd} \leq \eta \cdot f_{cd} \sqrt{1 - \frac{\nu_d}{\eta}} \cdot b_j \cdot h_{jc} \tag{C.1}$$

where $\eta = 0.6(1-f_{ck}/250)$, h_{jc} is the distance between extreme layers of column reinforcement, b_j is the effective joint width defined in expressions 5.34 (cl. 5.5.3.3); ν_d is the normalised axial force in the column above the joint; and f_{ck} is the characteristic cylinder strength given in MPa.

To enhance shear capacity, it is suggested that FRP is placed with fibres in the direction of hoops (cl. 4.4.1(1)), while ductility of framing members should be enhanced by longitudinal FRP. From the difference of demand and capacity, the gap to be filled by the FRP sheets is hence found. The

contribution of FRP, $V_{Rd,f}$, can be calculated according to equations A.22 (eq. C.2) and A.23 (eq. C.3) of EC8 Part3:

For full wrapping with FRP, or for U-shaped FRP strips or sheets:

$$V_{Rd,f} = 0.9 \cdot d \cdot f_{fdd,e} \cdot 2 \cdot t_f \cdot \left(\frac{w_f}{s_f}\right)^2 \cdot (\cot\theta + \cot\beta) \cdot \sin\beta \quad \text{(C.2)}$$

For side bonded FRP strips or sheets as:

$$V_{Rd,f} = 0.9 \cdot d \cdot f_{fdd,e} \cdot 2 \cdot t_f \cdot \frac{\sin\beta}{\sin\theta} \cdot \left(\frac{w_f}{s_f}\right) \quad \text{(C.3)}$$

Where β is the angle of the fibres to the axis of the column, θ is the angle of the principal stress in the joint (assumed to be the angle of the diagonal) to the axis of the column. w_f is the width of FRP sheet or strip, measured in the orthogonal direction to the fibres, s_f the spacing between the strips of FRP (equal to w_f for sheets), d is the effective depth and t_f is the thickness of the FRP jacket. The effective debonding strength, $f_{fdd,e,}$ is calculated with reference to cl.A.4.4.2(5) for fully wrapped or properly anchored jackets, cl.A.4.4.2(6) for U-wraps, and cl.A.4.4.2(7) for side-bonded sheets and strips. The equations to calculate $f_{fdd,e}$ take into account the design debonding strength, f_{fdd}, which is found using a partial factor for FRP debonding, γ_{fd}, taken as 1.5, as well as the concrete tensile strength. Other factors used for calculation are the FRP ultimate tensile strength, the corner radius of the element, as well as efficient bond length.

FRP sheets used for strengthening of adjacent member need to be applied with an effective bond length for FRP sheets, determined according to equation A.28 of EC8:

$$L_e = \sqrt{\frac{E_f t_f}{\sqrt{4\tau_{max}}}} \quad \text{(C.4)}$$

Where L_e is the effective bond length in mm and $\tau_{max} = 1.8\, f_{ctm}\, k_b$ is the maximum bond strength. While flexural strengthening of beams and columns is not addressed, confinement of the plastic hinge region of the column is suggested. No specific value for a minimum corner radius is suggested, but the effect of rounding corners is explicitly mentioned in the equations for strengthening.

The strong points of the EC8 guidelines are that the angle of fibres is explicitly taken into account and that FRP rupture strain is not used explicitly, as the strength of FRP is calculated according its effective debonding strength, which in turn is related to the geometry and anchorage. However, the design requires a large number of different equations that are interrelated, which renders the overall design process tedious and complicated.

C.1.2 CNR DT 200.R1/2012

Initially published in 2004, the Italian guidelines (CNR, 2012) for the FRP strengthening of structures published by the National Research Council (CNR), is a very complete set of regulations for non-seismic and seismic retrofit. The section on seismic strengthening of RC structures, chapter 4.7, addresses specific issues relevant to seismic loading, such as joint retrofitting but refers to previous chapters for design equations.

C.1.2.1 JOINT STRENGTHENING

Most importantly, the guidelines state that for seismic applications the principles of capacity design have to be followed; hence the formation of plastic hinging in the column before the beam is to be avoided (clause 4.7.2.3.2 (1)P). The implications of flexural strengthening of members should be considered, and shear strengthening may be required to avoid brittle collapse mechanisms (clause 4.7.2.3.2 (2)P) that might arise due to alterations of the hierarchy of strengths and sequence of damage events.

More specifically, for the shear strengthening of RC joints, clause 4.7.2.1.4 (1) applies, which states that FRP should be placed "with the fibres running in the direction of principal tensile stresses", rather than the hoop direction, as suggested by EC8 and ACI 440-F. Anchorage is explicitly addressed and "FRP strengthening shall not be considered effective" (clause 4.7.2.1.4 (1)) if proper anchorage is not provided, which is consistent with literature (Antonopoulos and Triantafillou, 2003; Ghobarah and Said, 2002). The problem bond between the FRP and concrete is specifically addressed in Annex D of the guidelines. Finally, it is stated that the maximum tensile strain of FRP wraps in RC joint strengthening shall not exceed 4‰, which is in line with ACI-440F and *fib* 35.

For the design of shear strengthening interventions, the designer is referred to section 4.3.3. The shear capacity and demand of the joint can be assessed using the equations in EC8. The contribution of FRP to the shear capacity of elements with rectangular cross-sections is then calculated using equation 4.19 of CNR DT-200, which is similar to the formula in EC8 Part 3. It differs from EC8, however, as it omits the sin β term and includes a partial factor γ_{Rd}, equal to 1.2 according to Table 3-1 of CNR DT 200. For fully-wrapped or U-wrapped sections, this yields:

$$V_{Rd,f} = \frac{1}{\gamma_{Rd}} \cdot 0.9 \cdot d \cdot f_{fed} \cdot 2 \cdot t_f \cdot (\cot\theta + \cot\beta) \cdot \frac{w_f}{s_f} \tag{C.5}$$

It is highlighted that in the new CNR guidelines only U-wrapped or fully wrapped configurations are allowed for shear strengthening. The equation for side-bonded sheets or strips for shear strengthening is hence taken from equation 4.25 of the 2004 edition (CNR, 2004):

$$V_{Rd,f} = \frac{1}{\gamma_{Rd}} \cdot 0.9 \cdot d \cdot f_{fed} \cdot 2 \cdot t_f \cdot \frac{\sin\beta}{\sin\theta} \cdot \left(\frac{w_f}{s_f}\right) \tag{C.6}$$

Here, f_{fed} is equivalent to $f_{fdd,e}$ in EC8. The other factors are defined as for EC8 in equation C.4. The procedure for calculating f_{fed} (cl. 4.3.3.2, 2004 edition) is similar to that of EC8 as it has

equations for fully wrapped or properly anchored jackets (equation 4.31), for U-wraps (equation 4.30) and for side-bonded sheets and strips (equation 4.28). However, the specific equations vary slightly from the ones in EC8.

When calculating the debonding strength f_{fdd} (equation 4.4) required to compute f_{fed}, as in EC 8, a partial factor for debonding, γ_{fd}, taken as 1.5 (or 1.2 for "certified" retrofits), is used. Again factors such as concrete tensile strength, FRP ultimate tensile strength, the corner radius of the element, as well as efficient bond length are used in the equations required to calculate f_{fed} (equations 4.1 – 4.4).

C.1.2.2 FRP IN ADJACENT MEMBERS

FRP shall be applied in longitudinal direction for adjacent members to enhance the flexural capacity to a length until the required member capacity is achieved. Care should be taken to ensure capacity design principles are followed.

In all cases, the optimal bonded length of FRP sheets is determined according to equation 4.1 of CNR DT-200:

$$l_e = \sqrt{\frac{E_f \cdot t_f}{2 \cdot f_{ctm}}} = \sqrt{\frac{E_f \cdot n_f \cdot t_{f,1}}{2 \cdot f_{ctm}}} \qquad \text{(C.7)}$$

For anchorage, a minimum of 200mm shall be added unless mechanical anchors are used (cl. 4.8.2.2(1)).

For confinement of columns over the plastic hinge length, the amount of required FRP can be calculated according to equation 4.59:

$$t_f = \frac{0.45 \cdot n \cdot f_y^2 \cdot d}{4 \cdot E_{ds} \cdot E_f} \approx \frac{10 \cdot n \cdot d}{E_f} \qquad \text{(C.8)}$$

Where n is the number of bars subjected to buckling, d the cross section size parallel to the bending plane and E_{ds} representing a reduced modulus according to equation 4.60.

In all cases, to ensure good bond, a minimum 20 mm radius is required when the sheet is wrapped around corners.

C.1.3 FIB BULLETIN 35

The International Federation for Structural Concrete (*fib*) has published guidelines on the seismic retrofit of concrete structures with FRP in the form of Bulletin 35 (fib, 2006). Chapter 8 of the publication focuses on beam-column joints (Mosalam, 2006). In his chapter, Mosalam first describes the deficiencies in inadequate RC beam-column joints with respect to seismic loading and their analytical modelling. Next, experimental work on FRP retrofit is presented, leading to

design equations based on previous research on GFRP retrofit of exterior beam-column joints by El-Amoury and Ghobarah (2002).

The retrofit design approach described in the *fib* Bulletin 35 consists of two steps for flexural and shear enhancement. The amount of FRP needed is based on desired moment and shear capacities of the members. The shear strengthening procedures is explained here.

For FRP shear strengthening of the joint panel, first the shear force developed in the joint is calculated assuming the ultimate capacity of the framing members are reached. The amount of FRP required is calculated by comparing the shear force to the total shear resistance of the joint, V_j:

$$V_j = V_c + V_s + V_{frp} \tag{C.9}$$

Where V_c, V_s , V_{frp} are the shear resistance contribution of concrete, steel and FRP, respectively. The contribution of steel is ignored, and the contribution of concrete is calculated according to ACI 352 guidelines from 1976 (ACI Committee 352, 1976):

$$V_c = \ 0.3\sqrt{f_c'(1 + 0.3f_{col})}\, b_j \cdot d_j \ \ (f_c' \text{ in MPa}) \tag{C.10}$$

where f_{col} is the axial stress applied to the column, b_j is the joint width, and d_j is the joint effective depth. V_{frp}, similarly to in ACI 440-F, can be related to the cross sectional area of FRP, A_{frp}, its elastic modulus, E_{frp}, and its design strain, ε_{frp}:

$$V_{frp} = A_{frp}\varepsilon_{frp}E_{frp} \tag{C.11}$$

The design strain should not be greater than 2/3 of the rupture strain (which is lower than the value in ACI 440-F), or if no anchorage is provided, no greater than the debonding strain of FRP laminates (assumed to be 0.004), which is usually much lower than its rupture strain. According to *fib* 35, the FRP sheets or strips for joint shear strengthening have to be anchored with steel or polymeric composite anchors at the beam-column interface to prevent early debonding. This is heavily supported by many research groups (Antonopoulos and Triantafillou, 2003; Ghobarah and Said, 2002) and can also be found as a recommendation in other guidelines (e.g.CNR).

Furthermore, FRP wrapping of the column potential plastic hinge region is also recommended for all FRP interventions. Retrofitting the beam near the joint should however be avoided.

Albeit being a good exposé on the need for beam-column retrofit and the mechanisms involved, the retrofit design guidelines have limited experimental foundation. They are based on one experimental campaign only that focusses on a specific joint geometry and only one type of fibre (GFRP). Furthermore, only exterior beam-column joints without slabs are investigated in the experimental campaign used. Overall, a synthesis of experimental results and observations from several studies would give the design approach more validity.

C.1.4 ACI 440F

The FRP retrofit guidelines of the American Concrete Institute (ACI 440-F, 2009) focus on two upgrade objectives to deal with the issues of low joint shear capacity and pull-out of non-continuous beam and/or column longitudinal bars. The joint shear strengthening procedure for joints in ACI 440-F is similar to the one outlined in *fib* 35. The main differences lie in the determination of the shear capacity of the unstrengthened joint and in the factors for calculating FRP design strain.

C.1.4.1 SHEAR STRENGTHENING

First the shear demand is determined based on the moment capacity of the beam, and then the shear capacity of the deficient joint is found according to equation 4.7 in ACI 352R-02:

$$V_N = 0.083\gamma\sqrt{f_c'}b_{je}h_c \quad (f_c' \text{ in MPa}) \tag{C.12}$$

where V_N is the nominal joint shear capacity and γ can be found from Table 1 in Section 4.3 of ACI 352R-02. It is noted that connection type 2 should be assumed for all joints subjected to seismic loading, even if they were not originally designed for it (Beres *et al.*, 1996).

If the nominal shear strength times a factor of φ (=0.85) does not exceed the horizontal shear V_{jh} in the joint, then shear strengthening of the joint is required. The retrofit is based on the conservative assumption that the FRP is to resist the entire shear force acting on the joint. Shear strengthening is provided by horizontal FRP in the joint panel, i.e. in the direction of the missing hoops. The number of horizontal layers of FRP on the joint panel, n_{jh}, required is given by equation 3-38 in ACI-440F:

$$n_{jh} = \frac{V_{jh}}{h_j t_f f_{fe}} \tag{C.13}$$

where h_j is the height of the joint, t_f, the thickness of one layer of FRP and f_{fe} the effective tensile stress per layer of FRP, given by:

$$f_{fe} = \varepsilon_{fe} E_f \tag{C.14}$$

The effective design strain of FRP, ε_{fe}, should be limited to 75% of its ultimate strain value for full wraps and be reduced further by a factor κ_v otherwise. However, it should never exceed 0.004 according to equations 11-6 (a) and (b) in ACI 440 (ACI 440, 2008), which corresponds to the debonding strain suggested by fib 35 and the Italian guidelines (CNR, 2012). The bond-reduction coefficient κ_v depends on concrete strength, the type of wrapping scheme used and properties of the FRP. It is determined from equations 11-7 to 11-10 of ACI 440 (2008) for U-wraps and sheets bonded to a single face. It is however not mentioned whether appropriate anchorage (e.g. with steel anchors) would permit the designer to use larger values of strain in the design of the retrofit. It is noted that mechanical anchorage is generally not addressed in ACI 440-F.

C.1.4.2 FRP IN ADJACENT MEMBERS

Longitudinal FRP sheets for flexural strengthening along the plastic length of the column and beams are also suggested in ACI 440-F. This is done in order to increase their moment capacities, but attention should be paid to capacity design principles to force hinging to form in the beams (section 13.4). ACI 440-F also recommends a minimum of two additional vertical layers of FRP in the joint area, which should extend into the column in both directions by a length not less than the height of the joint, in order to provide appropriate anchorage. The sheets should run continuously through the joint, possibly requiring cut-outs at the corners of the slab.

For improved anchorage, transversal FRP sheet should be applied above the longitudinal sheets over a length $l_{d,E}$ which depends on the development length of the system, l_{df}, and l_0, as defined in section 21.6.4.1 in ACI 318.

$$l_{d,E} > l_{df} + l_0 \tag{C.15}$$

The development length for FRP is given by equation 13-2 (ACI 440, 2008):

$$l_{df} = \sqrt{\frac{nE_f t_f}{\sqrt{f_c'}}} \tag{C.16}$$

And l_0 is determined as the minimum of: (a) The depth of the member at the joint face; (b) One-sixth of the clear span of the member; and (c) 460 mm.

Furthermore, transversal FRP confinement wraps are also recommended for ductility enhancement in the column and beams. This may be provided by the transversal sheets already used for anchorage of the longitudinal sheets. The length of the confinement wraps is to be determined by evaluating the plastic hinge length of the member.

For beams:

$$L = 2h$$

For columns:

$$L_p = g + 0.044\, f_y d_{bL}$$

where d_{bl} and f_y are, respectively, the diameter and yield stress of the longitudinal steel, and g is the clear gap to adjacent members, but no more than 50.8mm.

The number of layers required for confinement for rectangular sections is determined by equation 13-5:

$$n_f t_f = 1{,}500 \times \frac{D}{E_f} \tag{C.17}$$

Where D is the greater dimension of the rectangular member.

A conceptual beam-column joint upgrade according to the latest draft version of the ACI-440 F guidelines is shown in Figure C.1.

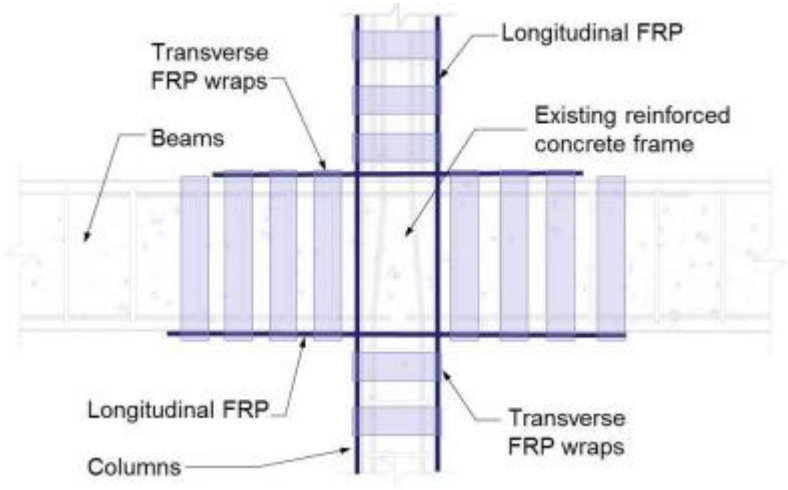

Figure C.1. Conceptual retrofit according to ACI-440 F 2014 draft

Note that transverse FRP wraps can be continuous sheets or strips. In all cases, to ensure good bond, a minimum 13 mm radius is required when the sheet is wrapped around corners. An overlap of 150 mm is required when lapping FRP sheets or when multiple layers are applied.

C.1.5 SUMMARY OF THE GUIDELINES

The different factors taken into account by the four guidelines presented before are summarised in Table C.2. The table highlights the differences between the equations used to determine shear strength in the four guidelines. It can be seen that EC8 and CNR DT 200 are the most "complete" and take into account factors such as bond strength and angle of fibres. Moreover, the design strain of FRP is evaluated in the equations rather than a maximum imposed. This has important implications for the values of capacity enhancement and highlights the importance of appropriate strain monitoring during experiments to improve design guidelines.

Table C.2. Comparison of the factors taken into account by the four guidelines

	ACI 440 F Seismic Strengthening of Concrete Buildings Using FRP Composites (2009)	***fib* Bulletin 35** Retrofitting of concrete structures by externally bonded FRPs, with emphasis on seismic applications (2006)	**CNR DT 200.R1/2012** Guide for the Design and Construction of Externally Bonded FRP Systems for Strengthening Existing Structures (2012)	**Eurocode 8**: Design of structures for earthquake resistance – Part 3: Assessment and retrofitting of buildings - ANNEX A.4. (2013)
Height of joint	✓		✓	✓
FRP thickness	✓	✓	✓	✓
Area of FRP	✓	✓	✓	✓
FRP design strain	75% of ultimate strain	2/3 of rupture strain	calculated	calculated
Angle of fibres			✓	✓
FRP ult. strength	✓		✓	✓
Bond strength			✓	✓
Anchorage	recommended	recommended	✓	✓
Corner radius			✓	✓

C.2 EVALUATION OF FRP DESIGN GUIDELINES

C.2.1 ANALYSED DATA

Based on the experimental database compiled from research papers looking at shear strengthening of deficient joints with FRP, the FRP contribution to the joint shear capacity is estimated using the expressions contained in EC8, CNR DT-200, *fib* 35 and ACI 440-F. For the purpose of this analysis, from the database described in the literature review, only specimens that failed in joint shear were selected. Specimens of all scales were used in this analysis as the data of full-scale specimens alone would not be sufficient for statistical analysis. This results in a total of 61 specimens from twelve research papers (Akguzel and Pampanin, 2010; Al-Salloum and Almusallam, 2007; Alsayed et al., 2010; Antonopoulos and Triantafillou, 2003; Del Vecchio et al., 2014; El-Amoury and Ghobarah, 2002; Engindeniz et al., 2008a; Ghobarah and Said, 2002; Ilki et al., 2008; Pantelides et al., 2008, 2000; Realfonzo et al., 2014). Of the 61, 25 are control specimens and 36 are retrofitted ones. While a majority of specimens in the database are exterior joints without slab or transverse beams, the selected specimens are still diverse in geometry, size and set-up. This gives this study a wider outlook on the issue of joint shear strengthening equations, as it allows testing the equations for different circumstances.

C.2.2 METHODOLOGY

To determine the experimental shear capacities of joints, the published values of ultimate force acting on beam or column (depending on the experimental set-up) are used. Only experimental specimens that failed in shear are evaluated for this study.

The horizontal shear acting at the centre of the joint, V_{jh}, is evaluated by equilibrium considerations. The shear is caused by the tension force in the beam bars framing into the joint (one or two forces depending on the exterior or interior joints) and the shear force from the column, V_{col}, in the opposite direction. This is in accordance with EC8 and ACI 352 for the evaluation of joint shear demand:

$$V_{jh} = T_{s1}(+T_{s2}) - V_{col} \tag{C.18}$$

The tension in the bars, T_{s1} and T_{s2}, at the ultimate load (P_i) at the tip of the beam or column is easily evaluated by determining the moment in the beam at the beam-joint interface, M_{bi}, and dividing it by the lever between the centroid of compression forces and the tension forces acting in the joint, *jd*. In the absence of more in depth analysis of all the different joint set-ups in the literature, a value of *jd* can be assumed to be 0.9 d_{eff} (Hakuto *et al.*, 2000) or 0.75 h_b (Bousselham, 2010). The latter was chosen in this paper. Hence:

$$V_{jh,exp} = \frac{M_{b1}}{jd_1}(+\frac{M_{b2}}{jd_2}) - V_{col} \tag{C.19}$$

Where M_{b1} and M_{b2} are assumed to be equal for symmetrical interior joints and M_{b1} can be found from:

$$M_{b1} = P_{b1} \cdot l_{b1} \quad \text{(C.20)}$$

P_{b1} being the ultimate force acting at the beam tip and l_{b1} the distance between the point the force is acting on and the joint interface. If the load is applied at the column, P_{b1} can be evaluated from P_c, the ultimate force at the column tip, as:

$$P_{b1} = P_c \cdot l_c / W_b \quad \text{(C.21)}$$

Where l_c is the total height of the test set-up (i.e. from pin at bottom column to pin at top column) and W_b is the total width of set-up (i.e. length of one beam and half-width of column for exterior joint or total length of both beams and column width for interior joint).

The horizontal shear force from the column V_{col}, is equal to P_c if the force is applied at the column tip or can be determined from equilibrium conditions if the force is applied at the beam tip:

$$V_{col} = P_{b1} \cdot W_b / l_c \quad \text{(C.22)}$$

C.2.3 RESULTS

The experimental values of $V_{jh,exp}$ are computed for all specimens that failed in joint shear and compared to those calculated with the equations from the different design guidelines. This is done both for control specimens and retrofitted specimens. The control specimens are compared to the shear capacities of concrete from the related codes of practices (i.e. EC8-Part 1 for EC8-Part 3, ACI 352 (2002) for ACI 440-F and ACI 352 (1976) for fib 35). It is highlighted that for some retrofitted specimens two types of FRP material (e.g. CFRP and GFRP) or forms (e.g. sheet and strips) were used. In the latter cases, contributions of both types of FRP are calculated separately. In all cases, when the characteristic concrete strength, f'_c, is needed, the reported mean cylinder strength value minus 8 MPa is used according to EC 2 Table 3.1 (CEN, 2008).

The results of predicted to experimental joint shear strength for the three guidelines are shown in Figure C.2 and summarised in Table C.3. For ease of analysis the ratio of predicted joint shear capacity to experimental joint shear capacity is referred to as ρ_V.

$$\rho_V = \frac{V_{jh,predicted}(codes)}{V_{jh,experimental}} \quad \text{(C.23)}$$

Figure C.2 shows the predicted values of the codes against experimental values of shear capacity, where the dotted lines represent the median values of ρ_V for the guidelines and the black line the ideal line of predicted results matching experiments (ρ_V=1).

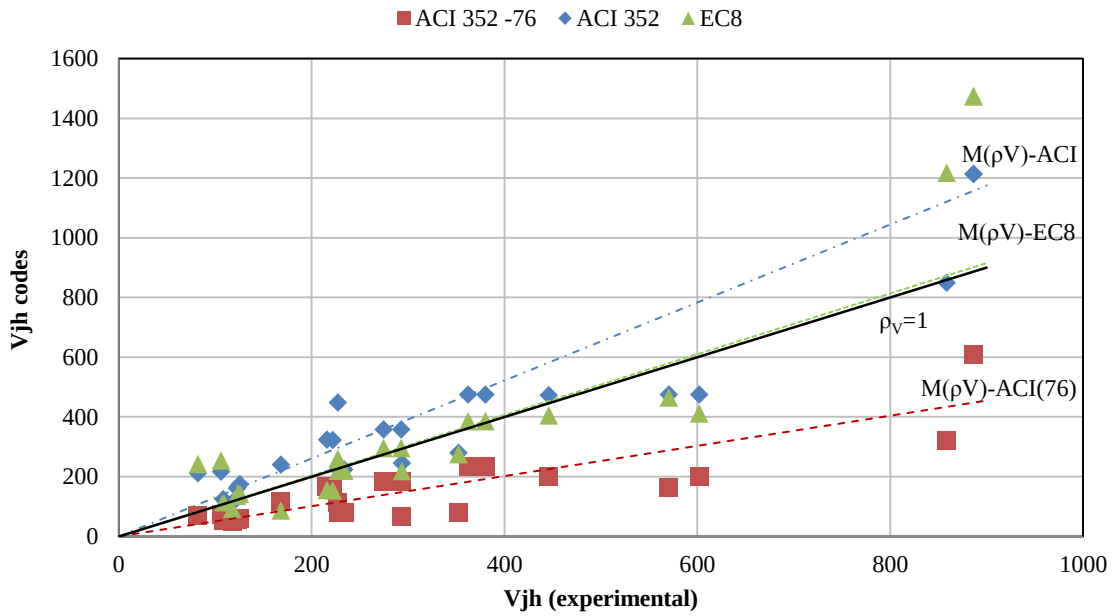

Figure C.2. Comparison of predicted joint shear to experimental results for the as-built joints (in black – 1:1 line).

Table C.3 presents the mean and median values, as well as standard deviation and coefficient of variation for ρ_V. It can be seen that EC8 offers the closest match to experimental values, with a mean value of ρ_V of 1.14. The new ACI-352 code generally overestimates the joint shear capacity while the ACI 352 (1976) strongly underestimates it. The latter confirms the major point of criticism mentioned in the description for the *fib* 35 guidelines, which use an out-of-date code of practice to evaluate the concrete contribution to joint shear capacity.

Table C.3. Summary of results for as-built joints for the three design guidelines

	ACI 352 -76	**ACI 352**	**EC8**
mean, μ(ρ_V)	0.53	1.29	1.14
median, *M*(ρ_V)	0.51	1.31	1.02
standard deviation, σ(ρ_V)	0.18	0.41	0.54
coeff. of variation, c_v(ρ_V)	0.33	0.32	0.47

Despite not giving very accurate results, underestimating the contribution of concrete is conservative, and the results of ACI 352-76 are relatively consistent, with a low standard deviation. The standard deviation and coefficient of variance is the largest for EC8, indicating a large variability in the accuracy of predicting joint shear capacity. In Figure C.2, it can also be seen that large variance is particularly striking for low values of joint shear capacity. This trend is however inconclusive as a lot of small scale specimens are found in the database, the joint shear capacities of the specimens hence being also relatively low, which explains the clustering of data points at the lower end of $V_{jh,exp}$. More data for larger values of V_{jh} would be needed to get a better understanding of how accurate the predictions are for large scale specimens.

For the retrofitted specimens, Figure C.3 presents the comparison of the predicted and experimental. It is shown that EC8 again gives the best results for predicting the joint shear capacity, with a close match on average (ρ_V =1.12). The predicted results for *fib*35 are fairly similar, as shown in Figure C.3 by the line of median values of ρ_V for EC8 and *fib*35 nearly super-imposed. It can however be seen that the spreads of values is much larger for *fib*35, which is also confirmed by the statistical analysis of the data.

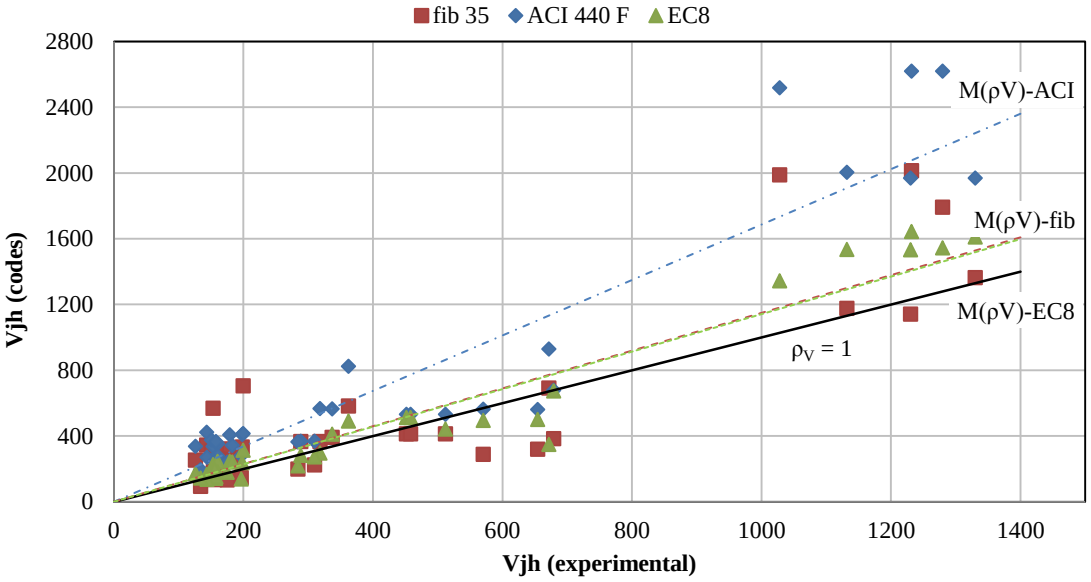

Figure C.3. Comparison of predicted joint shear to experimental results for the retrofitted specimens (in black – 1:1 line).

The results are summarised in Table C.4, highlighting that EC8 and CNR DT-200 give a very good match to experimental data, with relatively low variance, while the opposite is true for *fib* 35 and ACI 440-F, which greatly overestimate the contribution of FRP.

Table C.4. Summary of results for retrofitted joints for the four design guidelines.

	ACI 440-F	**fib 35**	**EC8**	**CNR**
mean, $\mu(\rho_V)$	1.74	1.34	1.12	1.06
median, $M(\rho_V)$	1.69	1.15	1.14	1.05
standard deviation, $\sigma(\rho_V)$	0.51	0.72	0.24	0.22
coeff. of variation, $c_v(\rho_V)$	0.29	0.54	0.21	0.21

For *fib* 35 and ACI 440-F, the standard deviation in ρ_V is larger for the retrofitted specimens then for the as-built joints and the predictions are not very accurate. This is particularly true for low values of V_{jhd}.

The results seem to indicate that the complexity and detail included in the equations of EC8 Part 3 and CNR DT-200 do result in a better prediction of the FRP contribution in joint shear retrofit. Evaluating the bonding strength of FRP to concrete, explicitly taking into account anchorage, means that even for badly designed retrofits without anchorage, the equations in EC8 permit a relatively accurate estimation of the retrofitted joint shear capacity without overestimating the contribution of FRP. Furthermore, by taking into account both the angle of principal stress and the angle of fibres allows a more accurate representation of how much the fibres actually work tension. Ignoring this, leads to an overestimation of the FRP contribution as seen for ACI 440-F and *fib* 35. For the latter two guidelines, a major downside can be found in the calculations for the FRP contribution to joint shear. The angle of fibres is not taken into account in the equations and the FRP strain used for calculating its contribution, is based on assumed values (2/3 or 75%) of its rupture strain, for which no reasoning is provided.

Analysis of the equations in EC8 and CNR DT-200 shows that there are only small differences between them. It is not therefore surprising that the joint shear capacities predicted by the two guidelines are very similar. As shown in Figure C.4, the ratio of the predicted capacities of CNR DT-200 to EC8 is on average very close to 1 (0.94), with a small standard deviation. In some instances a difference of close to 20% can be observed, which demonstrates that overall there is a slight difference in performance between the two codes. As shown in Table C.4, EC8 is in general slightly less accurate than the CNR guidelines. Again, this observation is based on a limited data-set, and more experiments are needed in the future to get a more reliable proof of the effectiveness of code expressions.

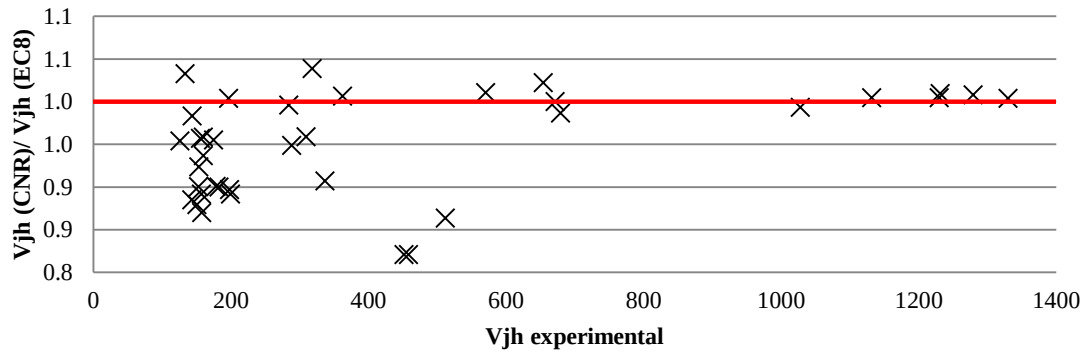

Figure C.4. Comparison of predicted values of CNR DT-200 to EC8 with respect to experimental results.

C.3 CONCLUSIONS

Based on a database of as-built and retrofitted beam-column joint specimens that failed in shear, a comparative study of the ability of four major design guidelines to predict joint shear capacity was conducted. Results of this analysis indicate a large variation in the predicted joint shear capacity contribution of FRP between the guidelines. It is found that the equations of Eurocode 8

and CNR DT-200 are the most accurate with lowest variance in their predictions. The sophisticated equations used in these guidelines are seen to provide advantages over simpler expressions proposed in other codes. Still, even these guidelines show a relatively large variance in their ability to predict joint shear capacity and hence leave room for improvement of the design equations based on more empirical evidence.

The results of this analysis hence highlight once more the importance of further full-scale testing of realistic structures, as new empirical data can help providing evidence for improved design guidelines. Moreover, effective strain in the FRP was a major difference in the design guidelines that was highlighted in the review.

Appendix D. EUROCODE 8 DESIGN CALCULATIONS

In this section the design calculation for specimen C-EC8, a first to second-storey beam-column joint in a four-storey structure is presented. Seismostruct was used for the structural analysis of the building.

D.1 GENERAL DESCRIPTION OF THE STRUCTURE

D.1.1 MAIN GEOMETRY DESCRIPTIONS

- The structure has 4 storeys, with storey heights of 3m.
- There are 3 bays of 4 m in the x-direction and 4 bays of 4 m in the y-direction. The total floor area in each storey is hence 12x16=192m².
- The structure has in-plane and elevation regularity.
- The slab thickness is 150mm; the dimensions of all columns is 300x300 mm and the beams are 450 mm deep.
- The cross-sectional dimensions for all elements are detailed in Chapter 3.

D.1.2 DESIGN CONSIDERATIONS:

- Subsoil Class: D (soft-to-firm cohesive soil) (**cl. 3.1.2- EC8**)
- Ductility Level: DCH – high ductility
- The relative design ground acceleration for the reference return period is pga=0.36g according to a location of high seismicity (zone 3) in a typical Southern European country.
- Importance category of the building is "II" → ordinary building and $\gamma I = 1$.
- The non-structural elements of the building are assumed to be fixed so as not to interfere with structural deformations.
- The structure is rigidly fixed in non-deformable foundations.

D.1.3 MATERIALS

- Concrete class: → C30/37
- Steel grade: S500

D.1.4 STRUCTURAL REGULARITY

According to **Section 4 – EC8**, regularity in plan and elevation make a structure safer and more efficient under seismic conditions.

- The building has structural regularity in plan according to cl. **4.2.3.2 – EC8** [3], as the building structure is symmetrical in plan with respect to two orthogonal directions.

- The building has structural regularity in elevation according to cl. **4.2.3.3 – EC8**, as all the lateral resisting systems run without interruption from the foundations to the top of the structure.

D.2 STRUCTURAL ANALYSIS USING SEISMOSTRUCT

The 3D structural analysis was carried out using Seismostruct. The structure to design is displayed in Figure D.1.

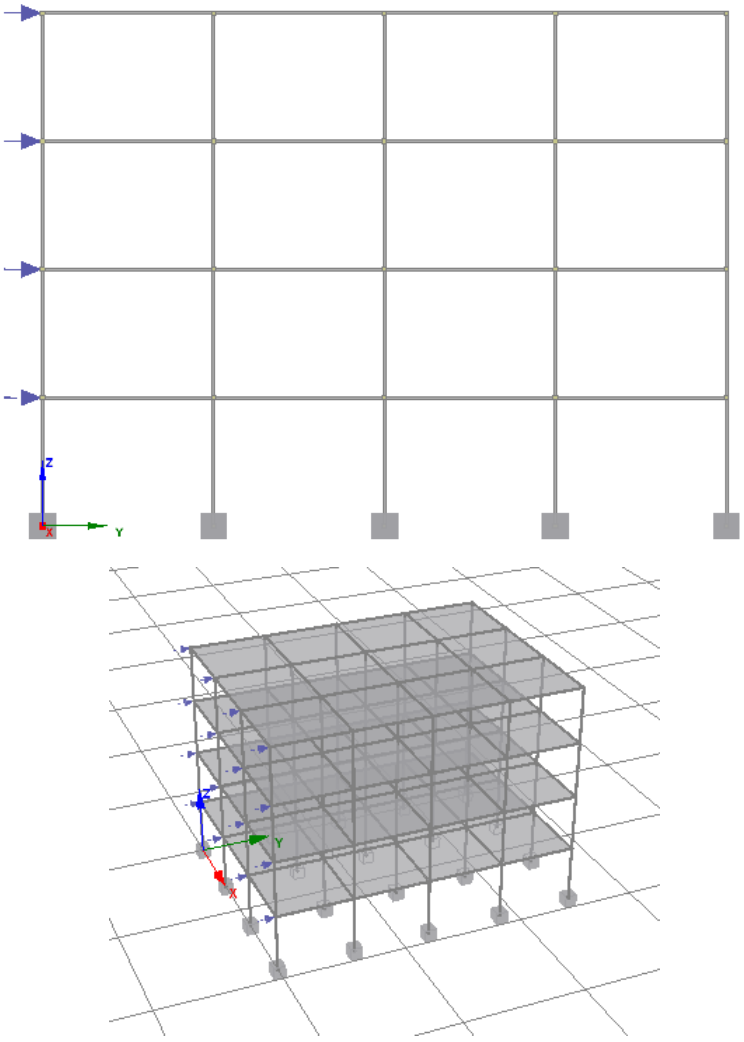

Figure D.1 – Elevation and 3D model in Seismostruct of the model structure.

D.3 PRE-DESIGN

D.3.1 BASE SHEAR FORCE

In order to calculate the seismic base shear force, for the direction in which the building is analysed, the following equation is used (cl. 4.3.3.2.2. (1) – EC8):

$$F_b = S_d(T_1) \times m \times \lambda$$

Where:

- S_d (T_1) - ordinate of the design spectrum at period T_1 – cl 3.2.2.5 –EC8;
- T_1 - fundamental period of vibration of the building for lateral motion in the considered direction;
- m - total mass of the building, above the foundation or above the top of a rigid basement - cl. 3.2.4(2) – EC8;
- λ - correction factor, with λ = 0.85 if $T_1 < 2\ T_C$ and the building has more than two storeys, or λ = 1.0 otherwise.

The fundamental period of vibration T_1, for buildings with heights of up to 40 m the value of T_1 (in s) may be approximated by the following expression (Cl. 4.3.3.2.2 – EC8):

$$T_1 = C_T \times h^{3/4} = 0.075 \times 12^{3/4} = 0.48s$$

Where:

- C_t – 0.075 for moment resistant space concrete frames;
- h - height of the building, in m, from the foundation or from the top of a rigid basement, hence 16m in this case.

For a Type 1, ground type D, the following factors are obtained from Table 3.2.2.2 – EC8:

Ground	S	T_B (s)	T_C (s)	T_D (s)
D	1.35	0.20	0.8	2.0

Where:

- T - vibration period of a linear single-degree-of-freedom system;
- T_B - lower limit of the period of the constant spectral acceleration branch;
- T_C - upper limit of the period of the constant spectral acceleration branch;
- T_D - value defining the beginning of the constant displacement response range of the spectrum;
- S is the soil factor;

Hence $T_B \leq T_1 \leq T_C$

<u>Design spectrum</u>

This means, according to cl. 3.2.2.5 (4) – EC8, that:

$$S_d\ (T_1) = \alpha_g \times S \times \frac{2.5}{q}$$

And we have:

$$pga = \alpha_g\ = 0.36g$$

The behaviour factor q, can be calculated for a concrete moment resisting frame and high ductility class according to cl. 5.2.2.2. – EC8:

$$q = q_o k_w$$

- q_0 can be found from Table 5.1. – EC8 and is 4.5 α_u/α_1
- k_w is the factor reflecting the prevailing failure mode in structural systems with walls. According to cl. 5.2.2.2 (11) – EC8: $k_w = 1.0$

- the ratio α_u/α_1, can be found from cl. 5.2.2.2. (5a) – EC8, for a multi-storey, multi-bay frames or frame-equivalent dual structures:

$$\frac{\alpha_u}{\alpha_1} = 1.3$$

Hence:

$$q0 = 4.5\alpha_u/\alpha_1 \times k_w = 4.5 \times 1.3 \times 1 = 5.85$$

This allows the calculation of $S_d(T_1)$:

$$S_d\ (T_1) = \alpha_g \times S \times \frac{2.5}{q} = 0.36 \times 1.35 \times \frac{2.5}{5.85} = 2.04$$

Total mass of the structure

The inertial effects of the design seismic actions are to be evaluated by taking into account the masses associated to all gravity loads according to the combination of actions in cl. 3.2.4 - EC8:

$$m = \sum G_{k,j} + \sum \psi_{E,i}\, Q_{k,i}$$

- $\psi_{E,i}$ – combination coefficients, according to cl. 4.2.4 – EC8: $\psi_{E,i} = \varphi \cdot \psi_2$
  - φ is taken from to be from table 4.2 in cl. 4.2.4 – EC8:
    - $\varphi = 1.0 \rightarrow$ for the roof
    - $\varphi = 0.8 \rightarrow$ for storeys with correlated occupancies
  - $\psi_2 = 0.3$ for residential areas – EC0 Annex A1

Hence

- $\psi_{E,i} = 0.3 \rightarrow$ for the roof
- $\psi_{E,i} = 0.24 \rightarrow$ for storeys with correlated occupancies

Loads:

- *Dead load G*

Reinforced concrete density = density of concrete + normal % of rebar and pre-stressing steel = 25 kN/m³ (Cl. 4.1 EC1)

Hence, dead load=slab height (0.150m) x reinforced concrete density (25 kN/m³) = 3.75 kN/m²

- *Live load Q*

For apartments (Category A, residential), according to table 6.2 - EC1:

Live load = 2 kN/m² for the storeys and 0.6 kN/m² for the roof.

- *"Superimposed load"- (taken into account like dead load)*

I.e. partitions, façade, flooring, services – assumed 3 kN/m²

Cross sectional area		m²	m²
Columns	A(col)	0.3*0.3	0.09
Beams	A(beam)	0.30*0.45	0.135
Slab	A(slab)	0.15*16	2.4
Floor Area	A(floor)	12*16	192

Tributary Weight Calculations:

Dead loads are obtained from material volume time's concrete density, e.g. by multiplying cross sectional area of the different members by their lengths and the number of members per storey.

Live load and super-imposed values are obtained by multiplying load per meter square by the area.

To illustrate, e.g. for floor 1:

Dead load = [A(col)*3*20 + A(beams)*109 + A(slab)*9]*(density of material)=980kN

Note:

- tributary storey height= 4m/2 (ground floor height/2) + 3m/2 (first floor height/2) = 3.5m
- 20 columns per storey;
- Total beam length = 124 m per floor.
- Slab volume = height*length*depth = A(slab)*0.15m
- The density of material is 25 kN/m³

Live load = 2kN/m³ * A(floor)

Super-imposed load = 3kN/m³ * A(floor)

	Dead load (kN)	Live load (kN)	Superimposed load (kN)	Total Tributary Weight (kN) = G+Q*ψ
Floor 1	1274	384	576	1941.7
Floor 2	1274	384	576	1941.7
Floor 3	1274	384	576	1941.7
Roof	1206	115.2	576	1816.6
ground floor columns	67.5	0	0	67.5
TOTAL				**7709.0**

This gives the tributary weight W, to get the tributary mass, m, we need to divide this value by g. Re-call the formula for the base shear calculation:

$$F_b = S_d(T_1) \times m \times \lambda$$

$$F_b = 2.04 \times \frac{7709.0}{\mathrm{g}} \times 0.85 = \mathbf{1360.9\ kN}$$

D.3.2 SEISMIC LOAD DISTRIBUTION

To determine the seismic load distribution per floor and hence per node for each floor, the horizontal forces have to be calculated according to cl. 4.3.3.2.3 (3) – EC8:

$$F_i = F_b \frac{z_i \cdot m_i}{\sum z_j \cdot m_j}$$

- F_i - horizontal force acting on storey i;
- F_b - seismic base shear defined earlier;
- z_i, z_j - heights of the masses m_i and m_j above the level of application of the seismic action (foundation or top of a rigid basement).
- m_i, m_j - storey masses computed in accordance with 3.2.4(2) – EC8.

Instead of converting the tributary weights calculated earlier into masses, the tributary storey weights w_i, w_j will be used, as g will cancel out and give the same result as when using m_i, m_j.

The force per node was obtained by dividing the seismic force of the relevant floor by four, as there are four nodes on the side of each floor.

	Tributary weight, w_i (kN)	**Height of floor, z_i (m)**	**Seismic Force $F_i = F_b * z_i * w_i / \Sigma(z_j * w_j)$ (kN)**	**Per node (kN)**
Floor 1	1941.7	3	139.7	34.92
Floor 2	1941.7	6	279.4	69.85
Floor 3	1941.7	9	419.1	104.77
Roof	1816.6	12	522.8	130.69
Total=	7709.0	12	**1360.9**	

D.4 BEAM DESIGN ACCORDING TO EC 8 AND EC 2

The first-floor beam will be designed for the specimen.

Design action effects

According to cl. 5.5.2.1 (2)P, (i.e. 5.4.2.2 (1)P) – EC8, seismic beams the design shear forces shall be determined in accordance with the capacity design rule. This should be done considering the equilibrium of the beam under:

- the transverse load acting on it in the seismic design situation and
- end moments Mi,d (with i=1,2 denoting the end sections of the beam), corresponding to plastic hinge formation for positive and negative directions of seismic loading.

The plastic hinges should be considered to form either at the end of the beam or the vertical elements connected to the joints into which the beam ends frame, depending on which ever takes place first.

D.4.1 ACTIONS

Gravity Actions
Dead Load: DL
Live Load: LL
Seismic Actions
Lateral seismic forces in either direction.

Action combinations

There are three load cases according to EC8:

I. Gravity load combination from EC1 and EC2: **1.35DL + 1.5LL**
II. Seismic combination 1 (from EC8): **DL+0.3LL+Seismic**
III. Seismic combination 2 (from EC8): **DL+0.3LL+Seismic (opposite direction)**

Internal forces

The internal forces were determined using Seismostruct, structural analysis suite to determine applied bending moments and shear forces.

GEOMETRICAL RESTRAINTS OF THE BEAM

Effective flange width:
According to cl**. 5.5.3.1.1(3) – EC8**, the effective flange width has to be determined. For primary seismic beams framing into **interior columns** the above width may be increased by $2h_f$ on each side of the beam. Where h_f is the flange height and b_c the column width. The effective flange width of beams framing to the interior columns is:

$b_c = 300\ mm$; $h_f = 150\ mm \rightarrow b_{eff} = b_c + 2 \times 4 \times h_f = 1500mm$

Limitation to width of the beams:

- To use the favourable effect of column compression on the bond of horizontal bars passing through the joint, the width *b*w of a primary seismic beam has to follow:
  $b_w \leq min\{b_c + h_w ; 2b_c\}$ – **cl. 5.5.1.2.1** (see cl. 5.4.1.2.1 (3) P) – EC8

Where h_w is the depth of the beam.

- This is satisfied as $b_w = 300mm \leq \begin{cases} 300 + 450 = 750mm \\ 2 * 300 = 600mm \end{cases}$ **OK**
- Also, according to 5.5.1.2.1 (1)P, $b_w = 300mm > 200mm$ **OK**

D.4.2 FLEXURAL REINFORCEMENT – ULTIMATE LIMIT STATES

The reinforcement of the beam will be calculated according to EC2.

FLEXURAL REINFORCEMENT

The need for flexural reinforcement will be assessed for the highest hogging and sagging moments (M^+ and M^-) in the beam obtained from the Seismostruct model.

Maximum moments acting on the beam:

M^+ = 138.9 kNm

M^- = -71.0 kNm

Cover

According to 4.4.1 – EC2, the concrete cover is the distance between the surface of the reinforcement closest to the nearest concrete surface and the nearest concrete surface. The nominal cover is specified as:

$c_{nom} = c_{min} + \Delta c_{dev}$ (cl.4.4.1.1 (2)P – EC2)

Where,

- c_{min} – minimum concrete cover, to ensure safe transmission of bond forces, protection of the steel against corrosion, adequate fire resistance; $c_{min} = max[c_{min,b}; c_{min,dur}; 10mm]$ (cl. 4.4.1.2 (2)P – EC2)
- $c_{min,b}$ - minimum cover due to bond requirement; $c_{min,b}$ = diameter of bar. Assume 16 mm bars and 6 mm hoops - Table 4.2 – EC2.
- $c_{min,\ dur}$ = minimum cover due to environmental conditions (cl.4.4.1.2 (5)). Assuming that Exposure class is XC1 and Structural Class is S4 → $c_{min,dur}$ = 15mm
- Δc_{dev} = 10 mm, this the allowance for negative deviation, 10 mm is a recommended value.

Hence $c_{nom} = c_{min} + \Delta c_{dev}$ = 16 + 10 = 26 mm

Effective depth

Assuming the diameter of the main bar to be ϕ = 16 mm and 6 mm hoops (ϕ_h=6mm):

$$d = h - c - \frac{\phi}{2} - \phi_h = 450 - 26 - \frac{16}{2} - 6 = 410\ mm$$

Effective width

This was determined previously as:

$$b_{eff} = b_c + 4 \times 2 \times h_f = 150\ mm$$

For M^+ = 138.9 kNm:

Area of flexural reinforcement steel

To determine the flexural reinforcement, **Cl. 6.1** – EC2 is used. The ultimate moment of resistance of the concrete cross-section can be determined from the assumptions listed in **cl. 6.1 (2)**P:

- Plane sections remain plane.
- Strain in bonded reinforcement, in tension or in compression, is the same as that in the surrounding concrete.
- Concrete has zero tensile strength.
- Stresses in the concrete in compression are derived from the design stress/strain relationship given in **cl. 3.1.7 –EC2**;
- the stresses in the reinforcing steel are derived from the design curves **in cl. 3.2 and 3.3** – EC2.

From "Design of Structural Elements" (Arya, 2009), using rectangular stress blocks and applying the assumptions from EC2 mentioned above, the moment of resistance of the section can be found.

Area of tensile steel A_{s1} :

First the lever arm is determined from equilibrium:

$$z = d \times \left[0.5 + \sqrt{0.25 - 3K/3.4}\right]$$

Where $K = \frac{M_{Ed}}{f_{ck} b_{eff} d^2} = \frac{138.9 \times 10^6}{35 \times 300 \times 410^2} = 0.092$

$$z = 410 \times \left[0.5 + \sqrt{0.25 - 3 \times 0.092/3.4}\right] = \mathbf{373.5\ mm} \leq 0.95d = 389.5\ mm$$

The neutral axis depth is then found:

$x = 2.5(d - z) = 2.5(410 - 373.5) = 91.25\ mm < 1.25h_f = 1.25 \times 150 = 187.5mm$

OK

The moment of resistance can then be found from:

$$M_{Rd} = A_s f_{yd} z$$

As we want $M_{Rd} \geq M_{Ed}$, we have:

$$A_s \geq \frac{M_{Ed}}{f_y z} = \frac{138.9 \times 10^6}{530 \times 373.5} = 699.1\ mm^2$$

Choose **2 ϕ 16** and taking into account the additional reinforcement in the flange (8 ϕ8) for flexural reinforcement (A_S=804 mm²).

The over-strength factor can be calculated from the ratio of the moment of resistance and the design moment, where

$$M_{Rd} = A_s f_{yd} z = 804 \times 530 \times 373.5 \times 10^{-6} = 166.0\ kNm$$

Hence the over-strength factor is: $\frac{166.0}{138.9} = 1.19$

Ratio of longitudinal reinforcement

$$\rho_l = \frac{A_s}{b_w d} = \frac{804}{300 \times 410} = 0.0065$$

***For M⁻* = -71.0 kNm**

Area of tensile steel A_{s1} :

$$z = d \times \left[0.5 + \sqrt{0.25 - 3K/3.4}\right]$$

Where $K = \frac{M_{Ed}}{f_{ck} b_{eff} d^2} = \frac{\mathbf{71.0} \times 10^6}{30 \times 1500 \times 410^2} = 0.009$

$$z = 410 \times \left[0.5 + \sqrt{0.25 - 3 \times 0.009/3.4}\right] = 402.1\ mm \leq 0.95d = \mathbf{389.5\ mm}$$

$x = 2.5(d - z) = 2.5(410 - 389.5) = 51.25\ mm < 1.25h_f = 1.25 \times 150 = 187.5mm$

OK

$$M_{Rd} = A_s f_{yd} z$$

As we want $M_{Rd} \geq M_{Ed}$, we have:

$$A_s \geq \frac{M_{Ed}}{f_y z} = \frac{71.0 \times 10^6}{530 \times 389.5} = 343.9\ mm^2$$

We choose **2 ϕ 16** (A_S=402 mm²) for flexural reinforcement.

The over-strength factor can be calculated from the ratio of the moment of resistance and the design moment, where

$$M_{Rd} = A_s\, f_{yd}\, z = 402 \times 530 \times 389.5 \times 10^{-6} = 86.6\ kNm$$

Hence the over-strength factor is: $\frac{86.6}{71.0} = 1.22$

Ratio of longitudinal reinforcement

$$\rho_l = \frac{A_s}{b_w d} = \frac{410}{300 \times 410} = 0.0032$$

FURTHER CHECKS

Spacing

The spacing of the bars has to be more than the minimal spacing in **cl. 8.2(2)** - EC2:

$$\min spacing = max \begin{cases} bar\ diameter = 16mm \\ aggregate\ size + 5mm = \mathbf{30\ mm} \\ 20\ mm \end{cases}$$

The actual spacing is given by finding the average space between bars:

$$\frac{b_w - 2c_{nom} - 2\phi_h - 4\phi}{3} = \frac{300 - 2 \times 26 - 2 \times 6 - 4 \times 16}{3} = 172\ mm > 30\ mm\ \ \boldsymbol{OK}$$

Deflection check

According to **cl. 7.4 – EC2**, the deflection needs to be controlled. The limit state of deformation may be checked by limiting the span/depth ratio, according to **cl. 7.4.2-EC2**.

First it needs to be determined which of ρ and ρ_0 is the bigger, where is the reference reinforcement ratio:

$$\rho_0 = 10^{-3} \sqrt{f_{ck}} = 10^{-3} \sqrt{30} = 0.0055 > \rho = 0.0032$$

As **ρ<ρ₀** the maximum allowable span to depth (l/d) ratio is found from:

$$\frac{l}{d} = K\left[11 + 1{,}5\sqrt{f_{ck}}\frac{\rho_0}{\rho} + 3{,}2\sqrt{f_{ck}}\left(\frac{\rho_0}{\rho} - 1\right)^{3/2}\right] \quad \text{if } \rho \leq \rho_0$$

- K is the factor to take into account the different structural systems, 1.3 in this case
- ρ is the required tension reinforcement ratio
- ρ′ is the required compression reinforcement ratio

The value obtained is:

$$\frac{l}{d} = 60.5 > actual\,\frac{l}{d} = \frac{4000}{410} = 8.9\ \boldsymbol{OK}$$

SPECIFIC MEASURES FOR THE FLEXURAL REINFORCEMENT FROM EC8

According to EC8, to satisfy the necessary ductility conditions, the following conditions shall be satisfied along the entire length of a primary seismic beam.

Min/max reinforcing steel

To satisfy cl. **5.5.3.1.3 (5)P – EC8**, (see cl.5.4.3.1.2 (5)P – EC8), along the entire length of a primary seismic beam, the reinforcement ratio of the tension zone, should be more than:

$$\rho_{min} = 0.5\left(\frac{f_{ctm}}{f_y}\right) = 0.5\left(\frac{2.9}{530}\right) = 0.0027 < \rho = 0.0032\ \boldsymbol{OK}$$

On the other, hand, it should not exceed the value given in **cl. 5.5.3.1.3 (4)** (see cl. 5.4.3.1.2 (4) b) – **EC8**

$$\rho_{max} = \rho' + \frac{0.0018}{\mu_\phi \times \varepsilon_{sy,d}} \times \frac{f_{cd}}{f_{yd}}$$

Where μ_φ is the curvature ductility factor, which according to cl. **5.2.3.4(3),** shall be at least equal to:

$$\mu_\varphi = 1 + 2(q_o - 1)\frac{T_C}{T_1} if\ T_1 < T_C \text{ (which is the case here)}$$

Where the factors were explained in the section on seismic force calculations:

$$q_o = 1.3$$
$$T_1 = 0.48s$$
$$T_C = 2s$$

Hence:

$$\mu_\varphi = 1 + 2(q_o - 1)\frac{T_C}{T_1} = 3.5$$

And:

$$\varepsilon_{sy,d} = \frac{f_y}{E_s} = \frac{530}{200000} = 0.00265$$

For all cases, as the longitudinal reinforcement is the same at the top and bottom and left and right:

$$\rho_{max} = \rho' + \frac{0.0018}{\mu_\phi \times \varepsilon_{sy,d}} \times \frac{f_{cd}}{f_{yd}} = 0.0032 + \frac{0.0018}{3.5 \times 0.00265} \times \frac{30}{530} = 0.0143 > \rho = 0.0065\ \boldsymbol{OK}$$

Furthermore, according to cl. **5.5.3.1.3 (5)P – EC8**

- at least two high bond bars with d_b = 14 mm shall be provided both at the top and the bottom of the beam that run along the entire length of the beam; - SATISFIED

- one quarter of the maximum top reinforcement at the supports shall run along the entire beam length. - SATISFIED

D.4.3 SHEAR RESISTANCE

Design shear

The design shear force from capacity design is evaluated for DCH according to cl.5.5.2.1 – EC8. The beam shear demand was calculated as follows:

$$V_{A,s1} = \frac{wl}{2} + \gamma_{Rd}\frac{|M_{Ar}^{-}| + ||M_{Br}^{+}|}{l} = 112kN$$

$$V_{B,s1} = \frac{wl}{2} - \gamma_{Rd}\frac{|M_{Ar}^{-}| + ||M_{Br}^{+}|}{l} = -40\ kN$$

$$V_{A,s2} = \frac{wl}{2} - \gamma_{Rd}\frac{|M_{Ar}^{+}| + ||M_{Br}^{-}|}{l} = -40\ kN$$

$$V_{B,s2} = \frac{wl}{2} + \gamma_{Rd}\frac{|M_{Ar}^{+}| + ||M_{Br}^{-}|}{l} = 112kN$$

$$\gamma_{Rd} = 1.2\ for\ DC\ H$$

Where wl/2 = 36.15 kN.

Note: There is no difference in shear at support A and B, the possibility of modifying the shear reinforcement between A and B is hence neglected.

The critical factor of shear strength verification is ζ, it indicates the degree of shear reversal under seismic loading.

$$\zeta = \frac{V_{A,s2}}{V_{A,s1}} = -0.35 < -0.5$$

As ζ < -0.5, almost full reversal of shear forces is expected, this means, according to cl. 5.5.3.1.2 (3) a – EC8, a limit on allowable shear is imposed. The following limit needs to be verified to decide whether shear resistance can be computed using EC2 or not:

$$|V|_{max} \leq (2 + \zeta) \times f_{ctd} \times b_w \times d$$

At A: $|V|_{max} = 112\ \text{kN} \leq (2 - 0.35) \times 1.9 \times 300 \times 410 = 390\ \text{kN}$ OK

Hence, the shear resistance provided by the reinforcement should be computed in accordance with EC2.

Length of critical zone

In order to satisfy the local ductility requirements, according to EC8, outside the critical zone, the shear loops are designed to EC2, while inside the critical zone, they are designed to EC8. The length of critical zone can be determined for a high ductility class according to cl. 5.5.3.1.3 (1)P – EC8:

$$l_{cr} = 1.5h_w = 1.5 \times 450mm = 675mm$$

l_{cr} is given from the column-beam connection.

Shear resistance outside the critical region (according to EC2)

Here confinement and anti-buckling are not relevant, hence shear is checked per EC2.

$$V_{Cd} = V_{Rd,1}$$

The design value for the shear resistance of concrete can be calculated from Cl . 6.2.2 (1) - EC2:

$$V_{Rd,c} = [C_{Rd,c}k(100\,\rho_l\ f_{ck})^{1/3} + k_1\,\sigma_{cp}]\,b_w d$$

With a minimum of:

$$V_{Rd,c,min} = (v_{min} + k_1\sigma_{cp})\ b_w d$$

Where:

- The recommended value for $C_{Rd,c}$ is $0.18/\gamma_c$=0.18/1.5=0.12
- f_{ck} is in MPa
- $k = 1 + \sqrt{\frac{200}{d}} = 1 + \sqrt{\frac{200}{410}} = 1.7 \leq 2.0$ with d in mm
- $\rho_l = \frac{A_{sl}}{b_w d} = 0.0065 \leq 0.02$; Asl is the area of the tensile reinforcement
- b_w is the smallest width of the cross-section in the tensile area, i.e. 300 mm; and d is the 410 mm
- neglecting the axial force influence, i.e. N_{Ed} = 0 for the beam; $\sigma_{cp} = N_{Ed}/A_c$ =0, where N_{Ed} is the axial force in the cross-section;
- $v_{min} = 0.035\,k^{3/2} \times {f_{ck}}^{1/2} = 0.035 \times 1.7^{3/2} \times 30^{1/2} = 0.42$

Hence:

$$V_{Rd,c} = \left[C_{Rd,c}k(100\,\rho_l\ f_{ck})^{\frac{1}{3}} + k_1\,\sigma_{cp}\right] b_w d = \mathbf{54.0}\boldsymbol{kN}$$

$$\geq V_{Rd,c,min} = \left(v_{min} + k_1\sigma_{cp}\right) b_w d = 52\ kN$$

Hence the shear resistance of concrete is lower than the design shear (V=112 kN), shear reinforcement needs to be provided.

According to cl. 6.2.1(2) – EC2, for a member with shear reinforcement, the shear resistance is equal to:

$$V_{Rd} = V_{Rd,s} + V_{ccd} \geq |V|_{max} = 112\ kN$$

V_{ccd} is the concrete contribution and $V_{Rd,s}$ is the shear carried by the shear reinforcement. For vertical shear reinforcement (cl. 6.2.3 (3) - EC2):

$$V_{Rd,s} = \frac{A_{sw}}{s} z f_{ywd} cot\theta$$

Of which the maximum value is:

$$V_{Rd,max} = b_w\, z\, \nu_1\, f_{cd}/(cot\theta + tan\theta)$$

where:

- A_{sw} is the cross-sectional area of the shear reinforcement
- s is the spacing of the stirrups
- ν_1 is a strength reduction factor for concrete cracked in shear, recommended value, v (cl. 6.2.2 (6)-EC2):

$$v = 0.6\left(1 - \frac{f_{ck}}{250}\right) = 0.6\left(1 - \frac{30}{250}\right) = 0.55$$

- z is the inner lever arm; as axial force is ignored, the approximate value z = 0.9d may be used.
- θ is the angle between the concrete compression strut and the beam axis perpendicular to the shear force; $1 \leq cot\theta \leq 2.5$, for vertical hoops, $cot\theta=2.5$

$$V_{Rd,s} = \frac{A_{sw}}{s} z f_{ywd} cot\theta = \frac{A_{sw}}{s} 0.9d \times 570 \times 1 \geq |V|_{max} - V_{ccd} = 112.0 - 54.0$$
$$= 58.0\ kN$$

$$\therefore \frac{A_{sw}}{s} = \frac{58.0 \times 10^3}{0.9 \times 369 \times 570 \times 2.5} = 0.11$$

Hence provide **H6@200 centres** ($A_{sw}/s=0.28$) outside the critical region. This means the ratio of shear reinforcement is, according to 9.2.2 (5) - EC2:

$$\rho_w = \frac{A_{sw}}{s} \times \frac{1}{b_w \times sin\alpha} = 0.19 \times \frac{1}{300} = 0.00094$$

Where $sin\alpha=1$, as α is the angle between the hoops and the longitudinal axis, i.e. 90°.

Minimal shear reinforcement needs to be provided, according to 9.2.2 (5) - EC2:

$$\rho_{w,min} = \frac{0.08\sqrt{f_{ck}}}{f_{yk}} = \frac{0.08\sqrt{30}}{530} = 0.00082$$

Hence the shear reinforcement provided is enough.

It must be checked that $V_{Rd,\ max}$ is not exceeded by $|V|_{max}$. $V_{Rd,\ max}$ is the design value of the maximum shear force which can be sustained by the member, limited by crushing of the compression struts.

$$V_{Rd,max} = b_w\, z \frac{\nu_1 f_{cd}}{cot\theta + tan\theta} = 300 \times 0.9 \times 410 \times \frac{0.528 \times 30}{2.5 + 0.4} = 604.6\text{kN} > |V|_{max}$$ **OK**

Shear resistance inside the critical region (according to EC8)

$$V_{Rd} = V_{Rd,s} + V_{ccd} \geq |V|_{max}$$

For DCH, V_{ccd}=0 inside the critical region. In order not to crush the concrete struts between adjacent shear cracks, the maximum allowable shear force is:

$$V_{Rd,2} = 0.5 \times v \times f_{cd} \times b_w \times 0.9\, d$$

- $v = \left(0.7 - \frac{f_{ck}}{200}\right) = 0.55$

$$V_{Rd,2} = 0.5 \times 0.55 \times 30 \times 300 \times 0.9 \times 410 = 913.3\, kN \geq |V|_{max}$$ **OK**

To find the shear reinforcement in the critical area, we apply:

$$V_{Rd} = \frac{A_{sw}}{s} 0.9 d f_{ywd} cot\theta \geq |V|_{max}$$

$$\therefore \frac{A_{sw}}{s} = \frac{112.0 \times 10^3}{0.9 \times 369 \times 570 \times 2.5} = 0.21$$

Provide **H6@ 100 centres** (A_{sw}/s=0.56).

According to cl.5.5.3.1.3 (6)P – EC8, the following requirements must be satisfied for hoops in the critical regions of primary seismic beams:

- The diameter d_{bw} of the hoops has to be at least 6mm.
- For DCH, the spacing, s, of hoops (in mm) should not exceed:

$$s = min \begin{cases} \frac{h_w}{4} = 112.5mm \\ 24d_{bw} = 24 \times 6 = 144mm \\ 175mm \\ 6d_{bL} = 96\, mm \end{cases}$$

$$\therefore s = 100\, mm \sim 96\, mm\ OK$$

Where

d_{bL} is the minimum longitudinal bar diameter, i.e. 16 mm; and h_w the beam depth, i.e. 450 mm.

The first hoop shall be placed not more than 50 mm from the beam end section.

D.5 COLUMN DESIGN ACCORDING TO EC 8 AND EC 2

According to cl**. 5.5.1.2.2 (1P) – EC8**, the minimum cross-sectional dimension of primary seismic columns has to be over 250 mm. This condition is met as the external columns in the second floor are 300x300mm.

D.5.1 DESIGN ACTION EFFECTS

Design action effects will be considered to **cl. 5.5.2.2 – EC8** for DCH. Column design action effects include capacity design for DCH, which dictates the strength hierarchy between column and beams at the joints. The principle of strong columns - weak beams applies.

Design column moments

According to **cl. 4.4.2.3 (3)P – EC8**, in multi-storey buildings, formation of a soft storey plastic mechanism should be prevented, to make sure there is no excessive local ductility demands in the columns of the soft storey.

In order to satisfy this requirement:

$$\Sigma M_{Rc} \geq 1.3 \Sigma M_{Rb}$$

Hence $\Sigma M_{Rc} \geq 1.3 \times (166 + 86.6) = 252.6$ kNm

ΣM_{Rc}, the sum of the moments of resistance in the columns, is made up from the moment at the bottom of the second-floor column and the moment at the top of the first-floor column. The ratio of moments from the Seismostruct model will be maintained, but the individual moments are scaled up for capacity design by 1.3. Hence the ratio of the actual moments of these columns can be obtained to understand what part of the sum of moments is at the top of the first-floor column, i.e.:

Direction 1 >	Worst case	
MCSd1	118	kNm
MDSd1	122	kNm
MDSd1 % of sum	51%	

Hence the capacity derived design moment at the top of the second floor column, $M_{Rc,top,CD}$, can be found from:

$$M_{Rc,top,CD} = 51\% \times 252.6 = 166.8 \text{ kNm}$$

COLUMN FLEXURAL REINFORCEMENT – EC2

Design Moments

According to **cl. 6.1 – EC2,** the column only to be designed to the applied axial action, N_{Ed}, and the moment from first order effects, M_{Ed}. Where M_{Ed} can be found from the sum of the largest design end moment, M_{02} or $M_{Rc,top,CD}$ and any moment due to geometric imperfections, $N_{Ed}.e_i$:

$$M_{Ed} = M_{02} + N_{Ed} \times e_i$$

Where e_i is the geometric imperfection factor, which can be taken as, according to **cl. 5.2(7) – EC2**:

$e_i = \frac{\theta_i l_0}{2} = \frac{1840}{200 \times 2} = 4.6mm$ with θi=1/200.

However, this has a minimal value of e_0 = h/30 or 20mm, according to **cl.6.1(4) – EC2**:

$$e_0 = \min \begin{cases} \frac{h}{30} = \frac{300}{30} = 10mm \\ 20mm \end{cases}$$

Hence e_i is taken as 20mm. Which gives the minimum moment due to geometric imperfections:

$$N_{Ed} \times e_0 = 425 \times 0.02 = 8.5\ kNm$$

The design moment is hence:

$$M_{Ed} = 166.8 + 8.5 = 175.3\ \text{kNm}$$

Cover

According to **4.4.1 – EC2**, the concrete cover is the distance between the surface of the reinforcement closest to the nearest concrete surface and the nearest concrete surface. The nominal cover is specified as:

$c_{nom} = c_{min} + \Delta c_{dev}$ (**cl.4.4.1.1 (2)P – EC2**)

- c_{min} = max [$c_{min,b}$; $c_{min,dur}$;10mm] (**cl. 4.4.1.2 (2)P – EC2**)
- $c_{min,b}$ - minimum cover due to bond requirement; $c_{min,b}$ = diameter of bar. Assume 25mm bars and 8 mm hoops
- $c_{min,\ dur}$ = minimum cover due to environmental conditions (**cl.4.4.1.2 (5)**). Assuming that Exposure class is XC1 and Structural Class is S4 → $c_{min,dur}$ = 15mm
- Δc_{dev} = 10mm, this the allowance for negative deviation, 10mm is a recommended value.

Hence c_{nom} = 25 mm

Longitudinal steel area

The area of steel required can be obtained from the design charts given, for instance provided by the Reinforced Concrete Council in the UK.

According to **cl.5.5.3.2.2** (2)P – EC8 at least one intermediate bar shall be provided between corner bars along each column side, i.e. at least 3 bars should be provided at each side of the column. This is to ensure the integrity of the beam-column joints. Hence at least 8 bars should be provided. With accordance to the design charts, provide 8H25 (A_s= 3930mm²). Accordingly, a moment resistance of 185.7 kNm can be achieved in the column.

EC8 – RESTRICTIONS

Maximum normalised axial force

According to **cl. 5.5.3.2.1 (3)P** – EC8, for DCH, the value of the normalised axial force ν_d shall not exceed:

$$v_d = \frac{N_d}{A_g f_{cd}} \leq v_{d,\max} = 0.55$$

The axial load, N_d is 425 kN, hence:

$$v_d = \frac{425 \times 10^3}{300 \times 300 \times 30} = 0.16 \leq v_{d,\max} = 0.55 \textbf{ OK}$$

Minimum and maximum longitudinal reinforcement ratio

According to **cl. 5.5.3.2.2** (1)P – EC8 (see 5.4.3.2.2(1)P), the total longitudinal reinforcement ratio ρ_l shall limited to:

$$\rho_{l,min} = 0.01 \leq \rho_{tot} \leq \rho_{l,max} = 0.04$$

This is done to avoid congestion of reinforcement and at the same time increase ductility and reduce shear.

$$\rho_{tot} = \frac{A_{s,tot}}{bh} = \frac{3930}{300 \times 300} = 0.04 \textbf{ OK}$$

Shear resistance

Column shear demand

According to **cl.5.5.2.2** (see cl.5.4.2.1(1)P) - EC8 the design values of bending moments and axial forces are obtained from structural analysis in the seismic design situation in accordance with cl. **6.4.3.4 – EC0** and from the capacity design requirements in **5.2.3.3(2)-EC8**.

According to **cl. 5.5.2.2 (2)P –EC8** (see 5.4.2.3(1)P), in primary seismic columns the design values of shear forces shall be determined in accordance with the capacity design rule. This is done on the basis of the equilibrium of the column under end moments Mi,d (with i=1,2 are ends of the column), corresponding to plastic hinge formation for positive and negative directions of

seismic loading. As mentioned before, the plastic hinges should form at the ends of the beams to satisfy the weak beam – strong column rules.

This implies that:

$$M_{i,d} = \gamma_{Rd} M_{Rc,i} \min(1, \frac{\sum M_{Rb}}{\sum M_{Rc}})$$

Where

- γ_{Rd} is the factor accounting for over strength due to steel strain hardening and confinement of concrete of the compression zone of the section, taken as being equal to $\gamma_{Rd} = 1.3$
- $M_{Rc,i}$ is the design value of the column moment of resistance at end *i* in the sense of the seismic bending moment under the considered sense of the seismic action;
- ΣM_{Rc} and ΣM_{Rb} are the sum of the design values of the moments of resistance of the columns and the sum of the design values of the moments of resistance of the beams framing into the joint, respectively.

$$M_{i,d} = 164\ kNm$$

The design shear force is then:

$$\mathrm{V} = \frac{2M_{1,d}}{l_{\mathrm{cl}}} = \frac{2 \times 164}{3} = 109.5\ kN$$

Length of critical zone

In order to satisfy the local ductility requirements, according to EC8, outside the critical zone, the shear loops are designed to EC2, while inside the critical zone, they are designed to EC8. The length of critical zone can be determined for a high ductility class according to cl. **5.5.3.2.2** (4) – EC8:

$$l_{cr} = \max \begin{cases} 1.5h_c = 1.5 \times 0.30m = 0.50\mathrm{m} \\ \frac{l_{\mathrm{cl}}}{6} = \frac{3}{6} = 0.5\mathrm{m} \\ \mathbf{0.60m} \end{cases}$$

where

- hc is the largest cross-sectional dimension of the column (in metres); and
- l_{cl} is its clear length (in metres).

According to cl. **5.5.3.2.2** (5)P – EC8, the column needs to be checked for short column effects, i.e. if:

$$l_c/h_c < 3$$

the entire height of the primary seismic column shall be considered as being a critical region and shall be reinforced accordingly.

$$\frac{l_{\mathrm{cl}}}{h_c} = \frac{3}{0.3} = 10 > 3$$

Hence, this clause does not apply.

For columns, the same provisions apply inside and outside the critical region due to favourable effects from compressive axial loads with regard to shear. As for the beam, V_{Rd} needs to be evaluated. In the case of the column however, this time $\sigma_{cp} = N_{Ed}/A_c$ is non-zero. The design value for the shear resistance of concrete can be calculated from **Cl . 6.2.2 (1) - EC2**:

$$V_{Rd,c} = [C_{Rd,c} k (100\, \rho_l\ f_{ck})^{1/3} + k_1\, \sigma_{cp}]\, bh$$

With a minimum of:

$$V_{Rd,c,min} = (v_{min} + k_1 \sigma_{cp})\ bh$$

Where:

- The recommended value for $C_{Rd,c}$ is $0.18/\gamma_c = 0.18/1.5 = 0.12$
- f_{ck} is in MPa
- $k = 1 + \sqrt{\frac{200}{d}} = 1 + \sqrt{\frac{200}{300}} = 1.82 \leq 2.0$ with d in mm
- $\rho_l = \frac{A_{sl}}{\mathrm{bh}} = 0.03275$;
- b_w is the smallest width of the cross-section in the tensile area, i.e. 300 mm; and h is the beam depth 450 mm;
- N_{Ed} = 425 kN for the column; $\sigma_{cp} = N_{Ed}/A_c = 4.72$, where N_{Ed} is the axial force in the cross-section;
- $v_{min} = 0.035\, k^{3/2} \times {f_{ck}}^{1/2} = 0.035 \times 1.82^{3/2} \times 30^{1/2} = 0.47$

Hence:

$$V_{Rd,c} = \left[C_{Rd,c} k (100\, \rho_l\ f_{ck})^{\frac{1}{3}} + k_1\, \sigma_{cp}\right] bh = \mathbf{163.0\ kN}$$

$$\geq V_{Rd,c,min} = \left(v_{min} + k_1 \sigma_{cp}\right) bh = 106.0\ kN$$

As for the beams, the amount of shear reinforcement is determined for the critical and non-critical sections. However, the strict minimum reinforcement detailing rules from EC8 govern the amount required.

<u>EC8 transverse detailing requirements:</u>

According to **5.2.3.4 (11)P** , within the critical regions of the primary seismic columns, hoops of at least 6 mm in diameter shall be provided at spacing such that a minimum ductility is ensured and local buckling of longitudinal bars is prevented, more precisely:

a) The diameter dbw of the hoops is at least:

$$dbw \geq 0.4 \cdot dbL,max \cdot \frac{fydL}{fydw} \sim 8\,mm$$

b) The spacing s of hoops (in millimetres) does not exceed:

$$s = \min \begin{cases} \frac{bo}{3} = \frac{242}{3} = 80\,mm \\ 125mm \\ 6dbL = 6 \times 25 = 150mm \end{cases} \quad \therefore s = 80\,mm$$

Where b_o (in millimetres) is the minimum dimension of the concrete core (to the inside of the hoops); and d_{bL} is the minimum diameter of the longitudinal bars (in millimetres).

c) The distance between consecutive longitudinal bars restrained by hoops does not exceed 150 mm, hence requiring 3 legs of hoops.

Hence hoops of **H8 will be provided at 80mm** ($A_{sw}/s = 0.62$) centres in the critical region, with crossties linking the longitudinal reinforcement. Outside the critical zone, this is extended to H8 @150mm ($A_{sw}/s = 0.34$).

EC2 minimum reinforcement

Cross-checking with the minimal shear reinforcement rules according **to 9.2.2 (5) - EC2** is:

$$\rho_w = \frac{A_{sw}}{s} \times \frac{1}{b \times sin\alpha} > \rho_{w,min} = \frac{0.08\sqrt{f_{ck}}}{f_{yk}} = 0.0008$$

$$\frac{A_{sw}}{s} > 0.0008 \times b = 0.23$$

The amount of reinforcement is hence ok.

CONFINEMENT

Finally, the confinement checks of EC8 are applied.

Minimum value of the curvature ductility factor

The minimum value of the curvature ductility factor, μ=10.5 for DCH, according to **5.2.3.4(3).**

Mechanical volumetric ratio of confinement reinforcement

According to **5.2.3.4 (10)** The minimum value of ω_{wd} (the mechanical volumetric ratio of confining hoops within the critical regions) to be provided is 0.12 within the critical region at the base of the column, or 0.08 in all column critical regions above the base:

$$\omega_{wd} = \frac{\text{volume of confining hoops}}{\text{volume of concrete core}} \times \frac{f_{yd}}{f_{cd}} = 0.29 \geq \omega_{wd,min} = 0.12 - \boldsymbol{OK}$$

Appendix E. BEAM TESTS

E.1 OBJECTIVES

A series of small scale experiments was designed in order to investigate the materials used and devise finite-element models to design the large-scale test specimens. In this Appendix the preliminary experiment and monitoring system is introduced and the results are presented. In particular, this study aimed at obtaining experimental data for calibration and comparison of ABAQUS finite-element models. The following sections introduce the FRP strengthening of beams, describe the tests carried out and the result obtained.

E.2 CONCISE REVIEW OF RECENT LITERATURE ON FRP STRENGTHENED RC BEAMS

The FRP retrofit of RC beams is a well-studied area of research and in particular for monotonic loading, a large number of experimental campaigns has been carried out. Compared to the seismic retrofit of beam-column joints discussed earlier, there is a wealth of design guidelines for RC beam strengthening focussing on shear and flexural strengthening as well as bond properties of FRP to concrete. The guidelines include the American ACI-440.2R-08 (ACI 440, 2008), the Canadian CSA-S806 (CSA, 2012), the fib Bulletin 14 (fib, 2001), the Italian CNR-DT-200 (CNR, 2012),the Australian HB 305 (Standards Australia Limited, 2008) and the German code (DAfStb, 2012).

E.2.1 SHEAR STRENGTHENING OF RC BEAMS WITH FRP

A thorough review of FRP design guidelines (Mofidi and Chaallal, 2014) has shown that the design of transversal FRP strengthening in most design codes depends largely on an FRP to concrete bond model, effective strain of FRP and the width to spacing ratio of FRP strips, while factors such as anchorage length and crack angle are only considered by the Italian and Australian guidelines.

Furthermore, based on experimental evidence, crack patterns and the adverse effect of transverse steel reinforcement on the effectiveness of FRP strengthening have been identified as important parameters that are not yet included in any guidelines. Models including such features have been proposed by (Chen et al., 2013; Mofidi and Chaallal, 2014, 2011).

Other factors that have been experimentally shown to have an adverse influence on the shear capacity of strengthened beams, which have not yet been addressed by design guidelines, are the size of the beam (Ashour and Kara, 2014; Bousselham and Chaallal, 2013) and the amount of flexural FRP strengthening (El-Sayed, 2014).

A topic of particular importance that has been increasingly studied in recent years is the evaluation of effective strain in FRP sheets and strips. The value of effective strain is used by all guidelines

to determine the contribution of FRP to shear strength and flexural capacity in particular, but also to anchorage. The aim of most researchers is to determine the actual effective strain in FRP sheets and to compare it to values determined by code equations. Recent efforts looking at the effective strain of FRP sheets in beam tests rather than the bond properties of FRP include (Lee et al., 2012; Lu et al., 2009; Sayed et al., 2014; Teo and Yin, 2014).

E.2.2 Flexural strengthening of RC beams with FRP

Esfahani et al. evaluated the effect of the longitudinal steel reinforcement ratio on the flexural strength of FRP retrofitted beams and compared experimental results to predictions by the ACI and ISIS Canada guidelines, which they found to overestimate the effect of FRP strengthening for beams with low reinforcement ratio (Esfahani et al., 2007). The performance of the ACI and fib guidelines were assessed for flexural strengthening and found to overestimate the contribution of FRP in particular due to overestimated values of effective strain. For shear strengthened beams the ACI, fib and CNR guidelines were assessed, and it was found that the CNR code gave the safest results as it predicted the lowest values of effective strain (Barros et al., 2007).

E.2.3 Combined strengthening schemes

While most studies analysed the effects of shear and flexural strengthening separately, it was shown that the flexural strengthening positively affects shear strengthening (El-Sayed, 2014) and vice-versa (Sharkawi and Etman, 2007). Flexural strengthening increases the shear strength of beams as it increases the neutral axis depth of the beam, hence increasing the area of concrete in the compression zone that can resist shear. Shear strengthening schemes, especially with U-wraps, help delaying common premature failure modes of flexural FRP strengthening, such as end peeling of the sheet or of the concrete cover, which hence increases the moment capacity of the beam.

While transversal strengthening for anchorage of flexural FRP is recommended by most guidelines, the effect that two strengthening schemes have on each other is often ignored. The ACI 440 guidelines states that if transversal shear strengthening is applied, it can serve as anchorage for the longitudinal FRP sheet and can be counted towards the area of FRP needed for anchorage. In clause 10.2.10, it is stated that a factor of 1.3 can be applied to the debonding strain of the flexural sheet if transversal sheets are used for anchorage, which affects the amount of flexural strengthening significantly.

Combined CFRP strengthening of RC beams in flexure and shear has been analysed by El-Ghandour and compared to predictions by the ACI guidelines (El-Ghandour, 2011). It was found that the guidelines are accurate for singly strengthened beams, but not for combined ones, as the enhancement in capacity depended strongly on the cracking and damage patterns observed. A

similar study by Dong et al. (2013) has shown that combined strengthening was more effective in increasing the capacity of a beam than flexural strengthening alone.

This short review has shown that combined strengthening of beams can increase effectiveness of the retrofit, but is still an area in which further experimental data is needed. In particular, effective FRP strain data is still needed to derive better empirical strengthening equations. The strengthening equations from ACI have proven to be relatively accurate for flexural strengthening and are used for the design of this experimental study. Additionally, the instrumentation provided will produce more empirical data on the strain in FRP for strengthened beams.

E.3 EXPERIMENTAL STUDY

Three T-beam specimens were tested under monotonic loading in a four-point bending instrument at the concrete laboratory at University College London. The specimen geometry investigated is shown in Figure E.1. The reinforcement detailing was the same for all specimens and was designed to achieve flexural failure according to EC2 design equations. FRP was applied for flexural strengthening to the bottom face of the beam and as U-strips for anchorage and shear strengthening. This pilot study was carried out from May to July 2014.

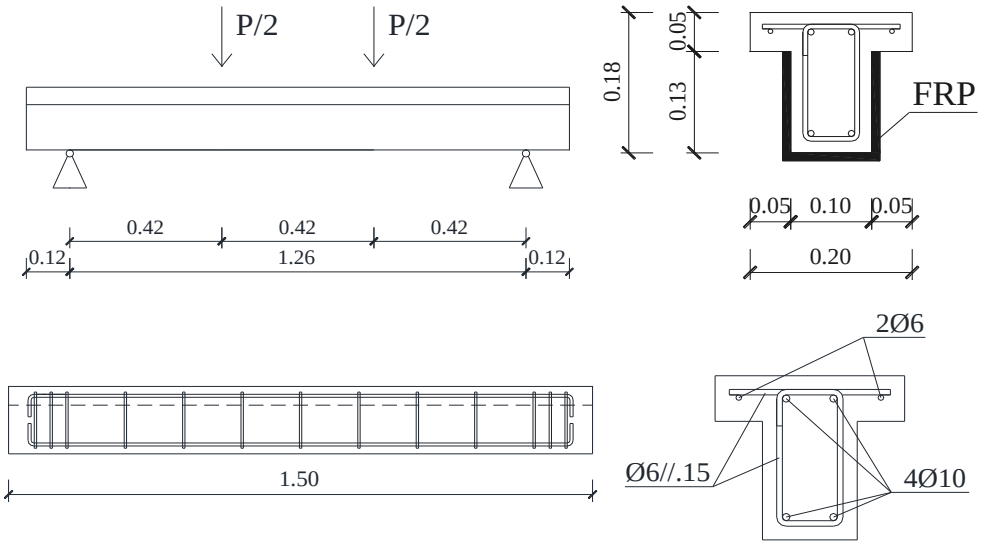

Figure E.1. Beam specimens tested at the UCL concrete lab (dimensions in meters)

A summary of the tested specimens, the instrumentation used for each test and concrete strength from three standard cube tests (f_{cu}) and the converted mean cylinder strength (f_{cm}) can be found in Table E.1. The steel reinforcement used consisted of 10mm longitudinal bars (yield stress = 550 MPa) and 6mm smooth transverse bars (yield stress = 400MPa).

The unidirectional CFRP sheets used in this experiment were S&P C-Sheet provided by S&P reinforcement. The main properties are found in Table E.2. The epoxy resin to apply the CFRP sheets was the recommended S&P resin 55. The FRP composite was applied to the surface of the concrete specimen using the wet-layup procedure recommended by the manufacturer.

Table E.1. Summary of beam tests conducted at UCL

#	*Strengthening*	f_{cu} *(MPa)*	f_{cm} *(MPa)*
C	control	30.7	25.5
FRP1-A	FRP - 1 layer	30.1	25
FRP2	FRP - 2 layers	24.8	20.6

Table E.2. Material properties of CFRP sheets used as stated in technical data sheet

	Fibre weight $[g/m^2]$	*Elastic modulus* $[kN/mm^2]$	*Tensile strength* $[N/mm^2]$	*Rupture strain [%]*	*Thickness [mm]*
S&P C-sheet 240	400	> 240	> 4300	1.7	0.223

E.3.1 INSTRUMENTATION

The full test set-up is shown in Figure E.2. The four-point bending testing rig, load cell and ADVANTEST 9 command system are shown as well as the monitoring set-up. Load was applied linearly up to failure of the beam with a rate of 0.2kN/s using a 300kN AEP TC4 load cell.

The monitoring set-up consisted of three LVDTs for measuring displacements at mid-span (50mm stroke) and the locations of applied load (25mm), the integrated load sensor of the load cell, two cameras used for digital image correlation (DIC), three strain gauges placed on the concrete surface and up to six fibre-optics placed on the concrete and FRP surfaces. The instrumentation for strain measurement is described in more detail below.

Figure E.2. Full UCL Beam test set-up

The cameras used for DIC were two IDS 5MP sensors equipped with 8mm focal length lenses with an angle of view of 45°. The pixel size of the sensors was 2.2µm. The cameras were interface with a PC using a netgear Ethernet box. In order to acquire pictures from both cameras simultaneously at set intervals of about 1Hz, the VMSCapture software developed by Prof. Stuart

Robson from the UCL Civil, Environmental and Geomatic Engineering department was used. To analyse the images taken and extract strain data, the commercial software DaVis 8.2.1 by LaVision was used.

In order to obtain more accurate strain readings, engineers at LaVision recommended to paint the investigated surface with a high contrast random pattern. This was obtained by spraying the FRP and the concrete surfaces with black paint followed by a white mist of paint to create the speckles. To improve the readings further, the specimen was illuminated using a strip of LEDs placed below the specimen which provided uniform light intensity across the surface.

The cameras were placed at 750 mm at an angle of about 45° to the side face of the beam, to test the effectiveness at an angle and distance similar to the full-scale tests. It was planned to measure strains on two faces simultaneously, however this was not possible due to a calibration issue. For the full-scale tests, multiple calibrations will be conducted before each test in order to measure strains on two perpendicular faces with the cameras again positioned at 45°.

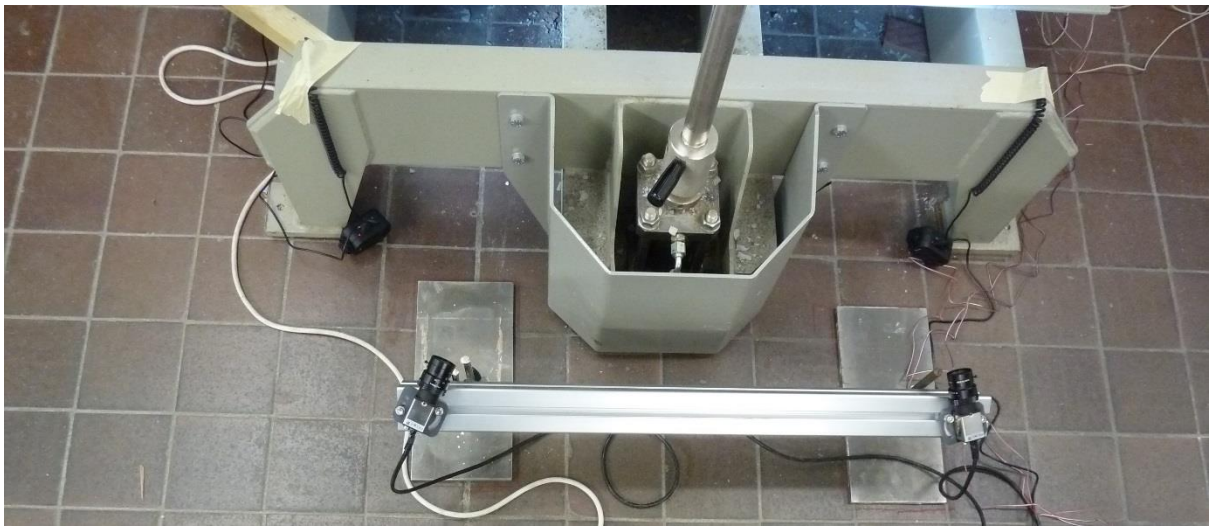

Figure E.3. DIC camera set-up

The strain gauges and fibre-optics were placed parallel to each other along the beam bottom face. There were three strain gauges placed at the centre of the beam and below the locations of applied load. It was ensured that the bragg gradings of the fibre-optics were aligned with the centres of the strain gauges, as shown in Figure E.4. The strain gauges used in the experiments were foil gauges by Micro-measurements with ±0.6% accuracy. The fibre-optics were produced by Dr Matthias Fabian from the Civil Engineering department at City University London. Two different kinds of fibre-optics were produced. The “long” fibre-optics were 500 mm long and were placed along the length of the beam with 5 bragg gradings spaced at 100 mm.

Figure E.4. Fibre-optics and strain gauge set-up on bottom beam face

In more detail, for control beam C and beam FRP1-A with one layer of FRP, three strain gauges were placed on the concrete surface and DIC was used. For beam FRP2 DIC was used for the FRP surface, fibre-optics were used on the concrete and on the FRP surface, and strain gauges were used on the concrete surface.

E.3.2 EXPERIMENTAL RESULTS

For the retrofit of the beams, one and two layers of 80mm wide FRP sheet were placed along the bottom face of the beam. The guidelines of ACI 440.2R-08 were followed to determine the transversal anchorage area required for bottom longitudinal sheets. For beam FRP1-A with one layer of FRP, three 4cm U-strips with 140mm separation were used for shear strengthening and anchorage, while for beam FRP2 with two layers of bottom FRP, a full U-wrap along the length requiring anchorage was provided. ACI 318.R-08 (ACI Committee 318, 2008) and sections 10 and 11 of ACI 440.2R-08 (ACI 440, 2008) were used to evaluate the expected failure patterns and capacities of the control and retrofitted beams.

The experimental results for the three beams are shown in Figure E.5. It can be seen that the increase in strength for the retrofitted beams is relatively low, about 9kN for beam FRP1-A and 6kN for beam FRP2. Moreover, an increase in stiffness with increase in number of FRP layers was observed.

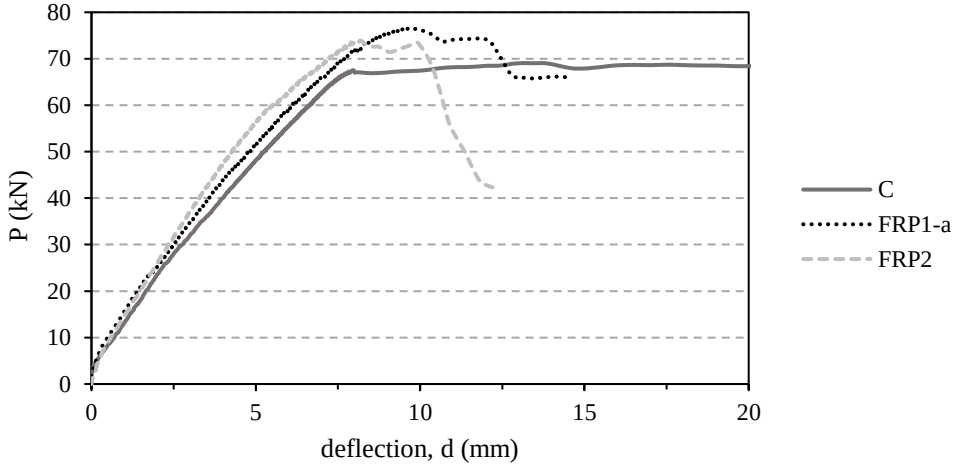

Figure E.5. Experimental results from four point bending test of three beams in the UCL lab

The results expected by the design equations from the ACI guidelines compared to experimental results are shown in Table E.3. The predicted bending capacity of the control beam C is underestimated, so it is not surprising that for beam FRP1-A with one layer, the capacity is underestimated too. However, the equations accurately predict that failure occurs in shear, and the increase in strength of about 9 kN was relatively consistent, albeit overestimated (about 12 kN). For beam FRP2, the increase in strength was even lower than expected.

Table E.3. Estimated and experimental capacities of the FRP strengthened beams

		ACI				*Experimental*	
Specimen	f'_c	V_u *(kN)*	M_u *(kNm)*	P_u *(kN)*	*Failure*	P_{exp} *(kN)*	*failure*
C	25.5	29.3	12	55.2	bending	67	bending
FRP1-A	25	33.7	17.5	67.5	shear	76	shear
FRP2	20.6	42.2	18.6	84.4	shear	73	shear

The reason for the lower increase in strength can be associated to premature failure in shear and FRP U-strip debonding occurred for the retrofitted beams. The flexural capacity of the beams was enhanced as the longitudinal FRP along the bottom of the beam contributed in the resisting tension along the bottom of the beam. This observation is confirmed by strain readings at bottom of beams at midspan, as strain on the concrete surface decreased from control (4800με at midspan) to 1 layer of FRP (3200 με) to 2 layers (ca. 2900με).

In both retrofitted beams, shear failure to the right hand side of the support is observed, despite the transverse reinforcement being strongly increased for the second beam (full U-wrap instead of strips). As shown in Figure E.6 and Figure E.7, a large shear crack formed between the end of the FRP layer and the point of load application. In both cases a large increase in strain at the right strain gauge compared to the left one was observed.

Figure E.6. Shear crack in Beam FRP1-A

Figure E.7. Shear crack in beam FRP2

Debonding of the transversal U-wraps was observed for both retrofitted specimens, indicating that anchorage of the U-wraps would be required, but no debonding of the bottom sheets was observed. Instead, peeling of the concrete cover was strongly observed from the ends of the FRP sheet. Both debonding mechanisms are clearly visible in Figure E.8. The former is referred to as FRP end peeling in clause 13.1.2 in ACI 440.2R-08. The internal steel reinforcement acts as bond breaker in the horizontal plane and the concrete cover is hence pulled away.

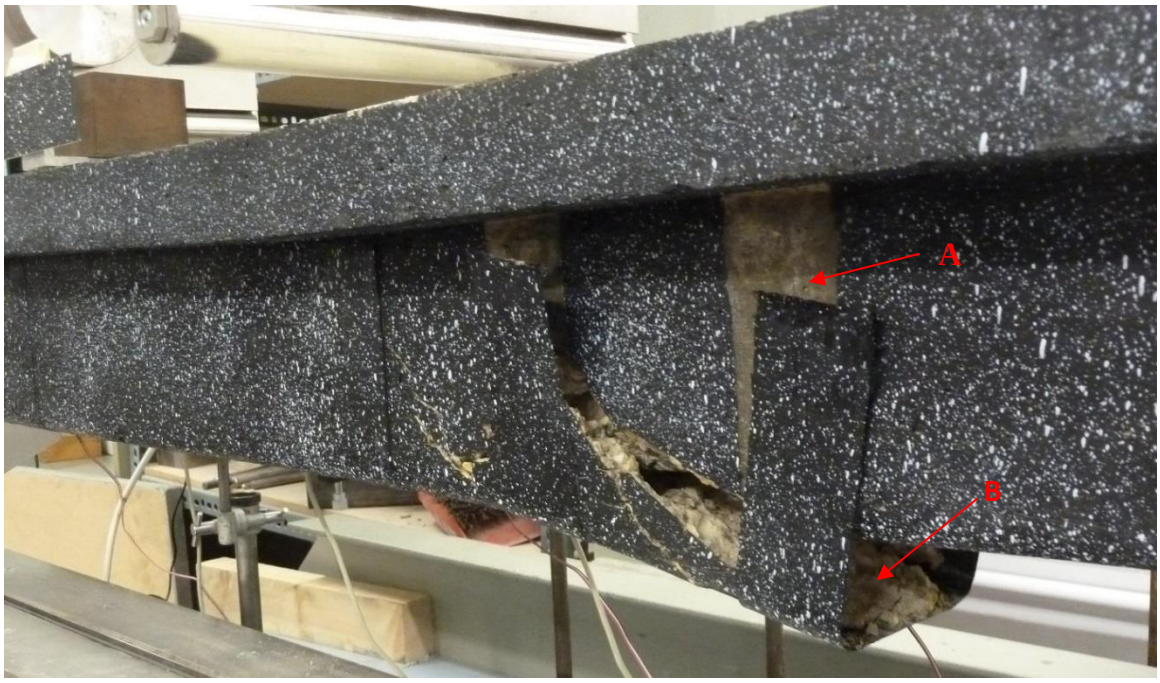

Figure E.8. FRP delamination of the transverse strips (A) and end peeling of the bottom strip (B) in Beam FRP1-A.

Appendix F. RETROFIT METHOD B-SW

This appendix presents the design approach and calculations for a CFRP retrofit scheme for interior beam-column joints with slab and transverse beams. The retrofit scheme aims to increase the strength, as well as to improve the ductility of the sub-assembly, by promoting a beam hinging mechanism. To increase the energy dissipation and reduce the risk of joint damage, plastic hinge relocation within the beam is also addressed. The final retrofit is shown in Figure F.1.

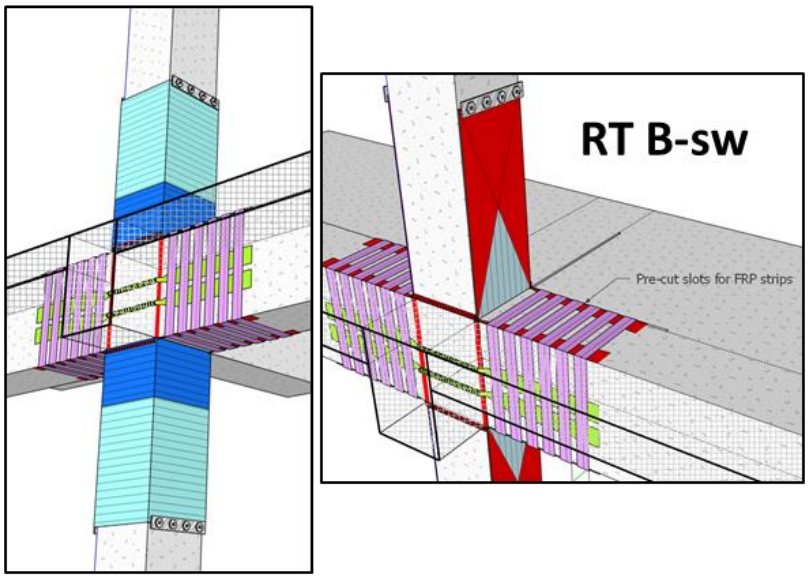

Figure F.1. Schematic illustration of full Retrofit B-sw.

To ease the practical implementation of retrofit B-sw, the existing CNR-DT 200 R1/2013 design guidelines (CNR 2013), are used for the retrofit design. The step-wise design process outlined below hence refers to equations (eqs.) within these guidelines, but does not reprint the detailed equations that can be found within CNR-DT 200 R1/2013.

Step 0. Analysis of the existing structure.

First, a seismic analysis according to EC8 needs to be conducted to determine the target base shear for the structure to be retrofitted. Then the distribution of moments and shear forces in the structure and the shear and moment capacities of the structure are determined following the procedures in EC2 and EC8.

If strengthening of the structure is required, the following steps are proposed for designing and FRP retrofit.

Step 1. Selective weakening of slab.

To reduce the contribution of the slab to the beam hogging moment capacity, and hence reduce the effect of asymmetric moment capacities in the beam, the slab reinforcement bars are cut along the beams for a distance of two column depths ($2 \cdot h_c$), as shown in Figure F.2.

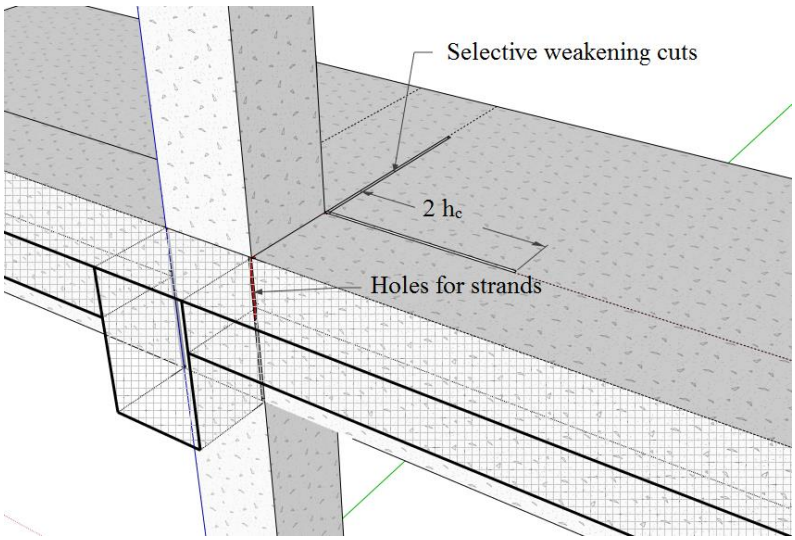

Figure F.2. Selective weakening cuts in the slab.

The hogging and sagging moments of resistance, $M_{Rb,sw}$, are then re-evaluated in the weakened section using the equations in cl. 6.1 of EC2, but with a reduced effective width for hogging moment:

$$b_{eff,sw} = b_{eff} - 2 \cdot 2h_c \qquad \text{(F.1)}$$

Where b_{eff} is the flange width to be considered in beam design according to cl. 5.5.3.1.1(3) – EC8, and $b_{eff,sw}$ the reduced width for the selectively weakened section.

Step 2. Design FRP retrofit of beam ends.

As shown in Figure F.3, the flexural strengthening consists of FRP strands along the joint splayed out and extending for a distance of h_b along the beams.

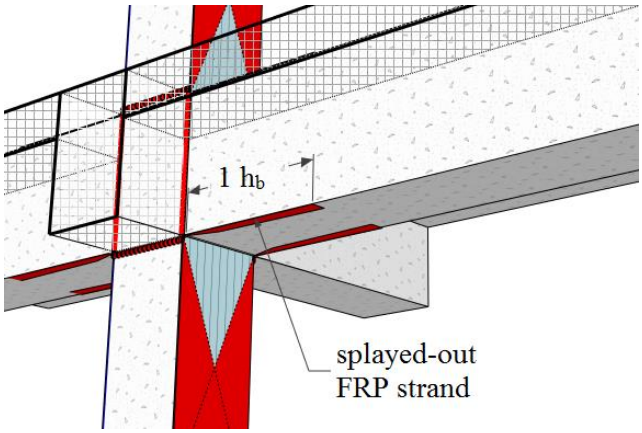

Figure F.3. Beam strengthening for plastic hinge relocation

Figure F.4 illustrates the design concept to promote plastic hinge (PH) formation away from the joint. It is important to ensure that the moment capacity at the retrofitted beam ends, $M_{Rb,FRP}$, is hence larger than the evaluated design moment at beam ends, $M_{Rd,b}$, based on $M_{Rb,sw}$ (step1) in hogging and sagging:

$$M_{Rd,b} = \gamma_{Rd} \cdot \frac{M_{Rb,sw} \cdot L_b}{(L_b - h_b)} \quad \text{(F.2)}$$

Where L_b is the length of the beam between the support and the point of contra-flexure determined in step 0. In line with EC8, the reduction factor for beam flexure, γ_{Rd} is taken as 1.2 for DCH.

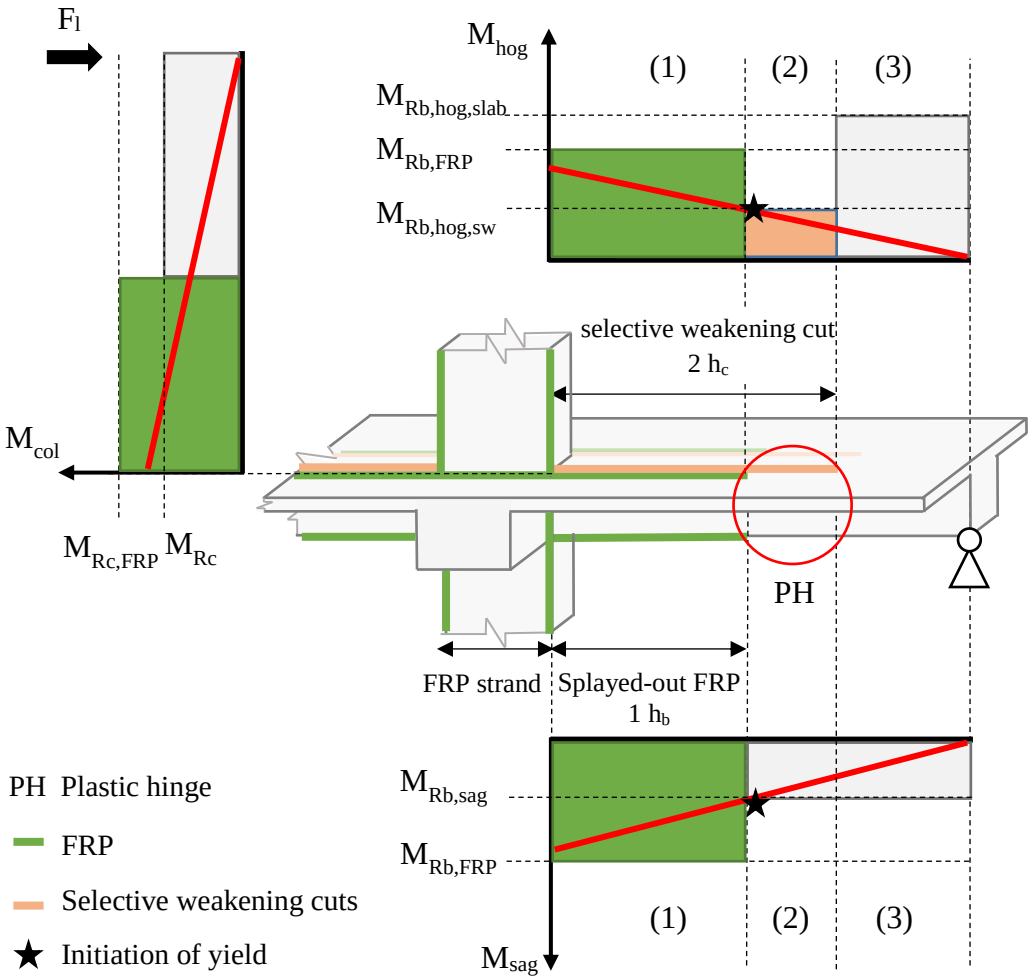

Figure F.4. Conceptual design of Retrofit B-sw with moment diagrams for hogging (M_{hog}) and sagging (M_{sag}) with indication of the non-retrofitted capacities (M_{Rb}), with ($M_{Rb,slab}$) and without slab contribution ($M_{Rb,sw}$), as well as the retrofitted capacity ($M_{Rb,FRP}$).

The procedure outlined in cl. 4.2.2 of CNR-DT 200 R1/2013 is used to evaluate the amount of FRP required for the beams in the end section to withstand $M_{Rd,b}$. As the FRP is applied as strands in the joint region and then splayed-out to the beam face, an equivalent thickness and width of FRP with the same cross-sectional area as a rectangular FRP sheet is needed to comply with the CNR design equations. This can be done using the procedure illustrated in Figure F.5.

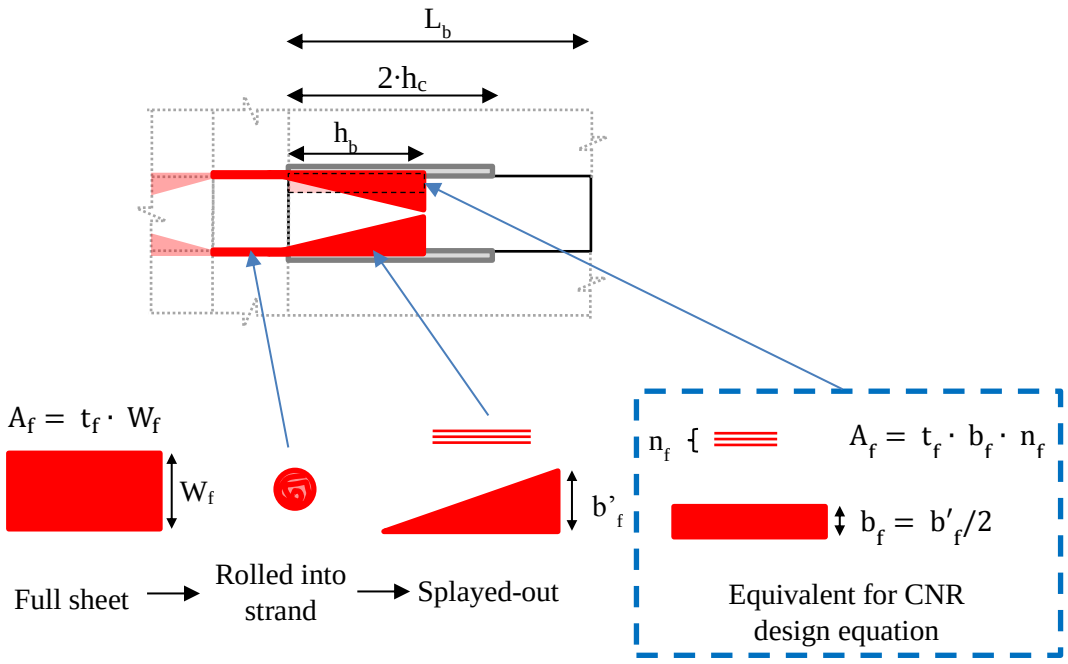

Figure F.5. Equivalent width and thickness of FRP for beam strengthening

Step 3. Design shear strengthening for the beam end sections.

To evaluate the capacity design shear demand in the section, EC8 cl. 5.4.2.2(2) is used based on the design moment at the beam ends, $M_{Rd,b}$, in combination with the shear force from the gravity load case.

If strengthening is required, FRP shear strengthening can be designed following section 4.3 of CNR-DT 200 R1/2013. It is recommended to apply shear strengthening FRP strips as full wraps by drilling holes through the slab (Figure F.6). The lap length of the full wrap should exceed a distance of h_b. Eq. 4.22 (CNR) is then used to calculate the effective stress in the FRP wrap for the shear calculation in eq. 4.19 (CNR).

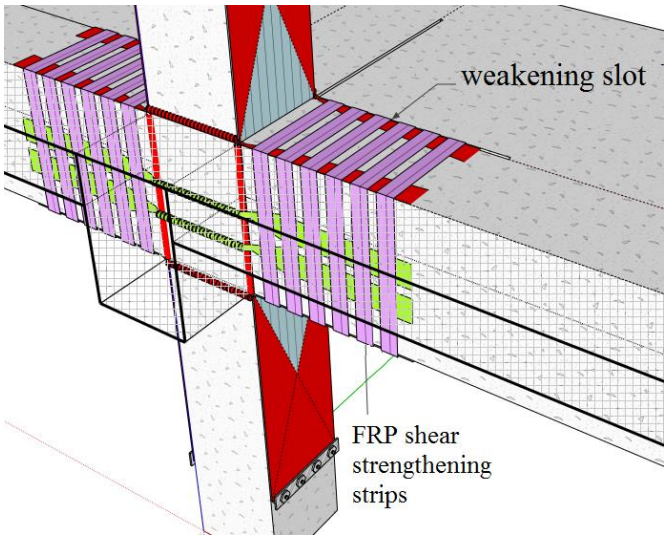

Figure F.6. FRP shear strengthening strips wrapped though selective weakening cut.

Step 4. Design the column confinement.

The amount of FRP confinement wrapping is determined according to 4.5 of CNR-DT 200 R1/2013, considering:

- Axial load capacity (eqs. 4.29-4.40), ensuring the confinement is effective according to cl. 4.5.2 (7)
- In the case of an inadequate lap-splice length of the column longitudinal bars, confinement against bar slippage should be checked according to eq. 4.43 and 4.44.
- In the case of inadequate spacing between the transverse steel reinforcement, confinement FRP against bar buckling should be checked according to eq. 4.45 and 4.46

Based on the design of the confinement wraps, the confined design concrete strength, f_{ccd}, should be calculated according to eq. 4.31 and used within the following design steps.

Step 5. Design the column flexural strengthening.

The flexural strengthening consists of FRP strands passed through tubes in the joint region and splayed-out on the columns. The capacity design moment in the columns, $M_{Rd,c}$, is evaluated according to EC8 cl.4.4.2.3(4) and 5.4.2.3 (2), using the retrofitted beam end moment $M_{Rb,FRP}$.

The procedure detailed in Appendix E of CNR-DT 200 R1/2013 is then used to determine the amount of FRP required for flexural strengthening of the columns. Assuming a width of the FRP sheet, b_f, shown in Figure F.7, of maximum:

$$b_f \leq b_c - 2\,r_c \qquad \text{(F.3)}$$

Where b_c is the column width and r_c the corner radius of the rounded column edges.

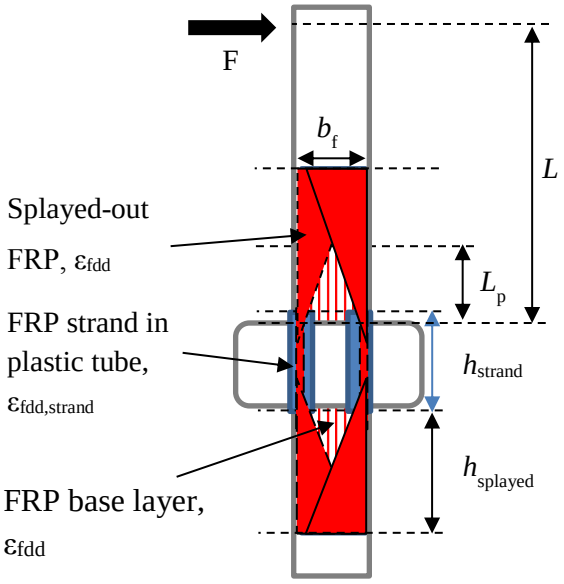

Figure F.7. Definition of geometric parameters for the FRP strands in the tubes and splayed-out.

As shown in Figure F.7, the FRP strands are splayed-out and some fibres are at an angle with respect to the longitudinal axis of the column. To ensure the same equivalent amount of strength provided by the splayed-out fibres and the FRP strand, one extra layer of FRP in the longitudinal direction is applied as a base layer on the column (Figure F.8).

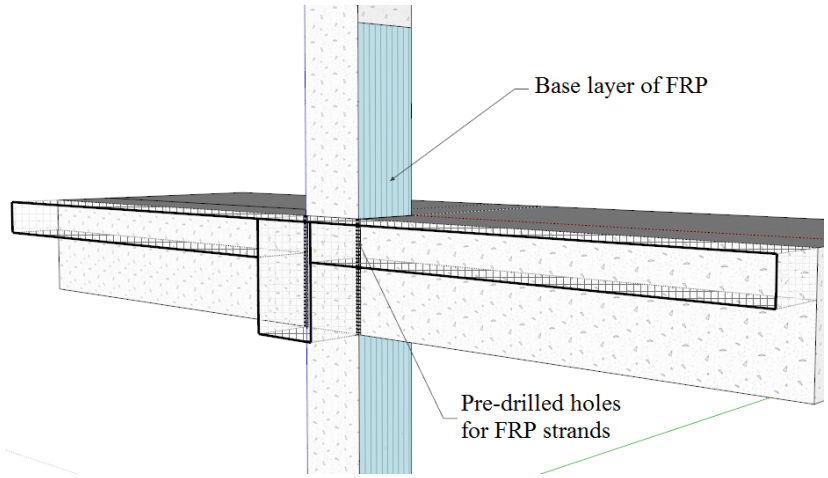

Figure F.8. Base layer of column FRP.

Next, to evaluate the effective strain, ε_{fdd} in the FRP fibres, to eq. 4.6 (CNR) is used. As shown in Figure F.7, the FRP strands are placed in plastic tubes and passed through holes in the slab between the superior and inferior columns. The strain in the FRP strands is not the same as in the splayed-out FRP, as it is not bonded to concrete. It is hence required to determine the equivalent effective strain $\varepsilon_{fdd,strands}$ in the FRP strands passed though plastic tubes.

First, the non-bonded, free length of the FRP, h_{strand}, is defined as the height of the beam plus the protrusion of the strand, $h_{protrusion}$, on either side, to allow for the length of the plastic tubes not finishing exactly at the joint-column interface:

$$h_{strand} = h_b + 2 \cdot h_{protrusion} \ \ (mm) \tag{F.4}$$

An empirical value of 30 mm is recommended for $h_{protrusion}$, but its value will depend on the specific application on site.

To determine the strain in the strands, the length of the FRP confined plastic hinge length first needs to be determined. With no slippage and debonding, it is assumed that at the level of maximum moment in the column, the effective maximum FRP strain, ε_{fdd}, will be fully developed along the plastic hinge length, L_p. The length of the FRP confined plastic hinge is determined using the equations tested and proposed by Jiang et al. (2014):

$$L_p = L_{p0} + \left(\frac{2r_c}{b}\right)^{0.72} \cdot L_{pc} \tag{F.5}$$

Where L_{p0} is the unconfined plastic hinge length determined according to the well-established equation by Paulay and Pristley (1992):

$$L_{p0} = 0.08L + 6\,d_b \quad \text{(F.6)}$$

With the L, the column shear span, and d_b being the bar diameter of the longitudinal steel.

Finally, L_{pc} is the plastic hinge length due to the confinement effect for circular columns, reduced by the $k_s = \left(\frac{2r_c}{b}\right)^{0.72}$ factor, dependent on the corner radius, r_c, and the column width, b, to account for square column geometries:

$$\begin{cases} L_{pc} = 3.028\,\lambda_f & when\ \ 0 \le \lambda_f < 0.1 \\ L_{pc} = \left(0.51 - 2.3\,\lambda_f + 2.28\,{\lambda_f}^2\right)L & when\ \ 0.1 \le \lambda_f < 0.5 \end{cases} \quad \text{(F.7)}$$

With λ_f defined as the confinement ratio, calculated as in cl. 4.5.2 (7) of CNR-DT 200 R1/2013:

$$\lambda_f = f_{1,eff} / f_{cd} \quad \text{(F.8)}$$

Based on the plastic hinge length, the strain in the strand is then determined by calculating the fixed end deformation along the plastic hinge from the effective strain in the bonded FRP, ε_{fdd}, and dividing this by the free length of the FRP in the plastic tube, i.e.:

$$\varepsilon_{fdd,strand} = \frac{(\varepsilon_{fdd} \cdot L_p)}{h_{strand} + 2\,x_i} \quad \text{(F.9)}$$

As illustrated in Figure F.9, x_i is an empirical variable to account for part of the splayed-out FRP not adequately bonded to the concrete surface at the transition to the plastic tubes. An average value for x_i of 20 mm is suggested.

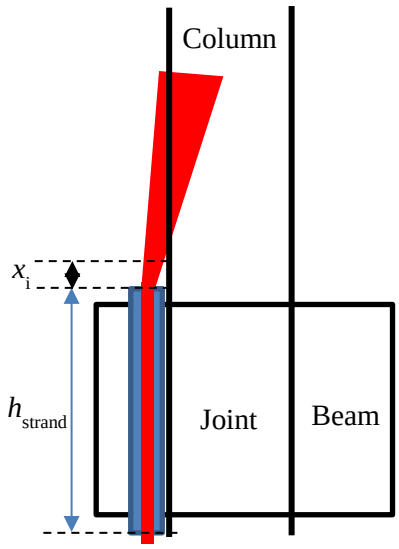

Figure F.9. Schematic representation of empirical factor x_i.

The moment capacity at the column/joint interface needs then to be re-evaluated using the design strain of the FRP strands in the equations of in Appendix E of CNR-DT 200 R1/2013. If the capacity at the interface does not exceed the design moment, $M_{Rd,c}$, increase the amount of FRP in the strands and repeat step 5.

Next, the bonded length of FRP, $h_{splayed}$, needs to be evaluated with respect to the moment capacity of the strengthened, $M_{Rc,FRP}$, and unstrenghtened, M_{Rc}, column sections to ensure the flexural capacity along the entire length of the column is sufficiently large to allow the moment capacity at the column/joint interface to develop (see Figure F.10):

$$h_{splayed} > \frac{M_{Rc}}{M_{Rc,FRP}} \cdot L_c \qquad \text{(F.10)}$$

Where L_c is the column length. The bonded length however also needs to exceed the optimal bond length according to eq. 4.1 of of CNR-DT 200 R1/2013.

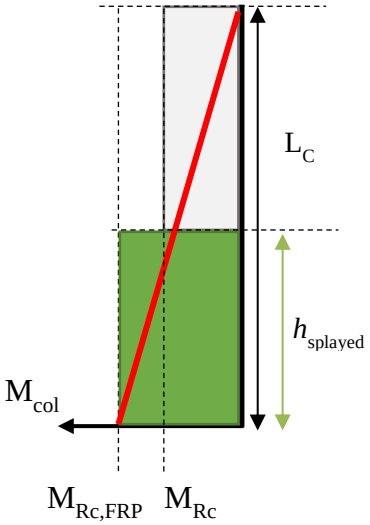

Figure F.10. Moment capacity and applied moment (red) along the column.

Finally, it is recommended to anchor the splayed out FRP strands at their ends by means of steel anchors. The full flexural column retrofit is shown in Figure F.11.

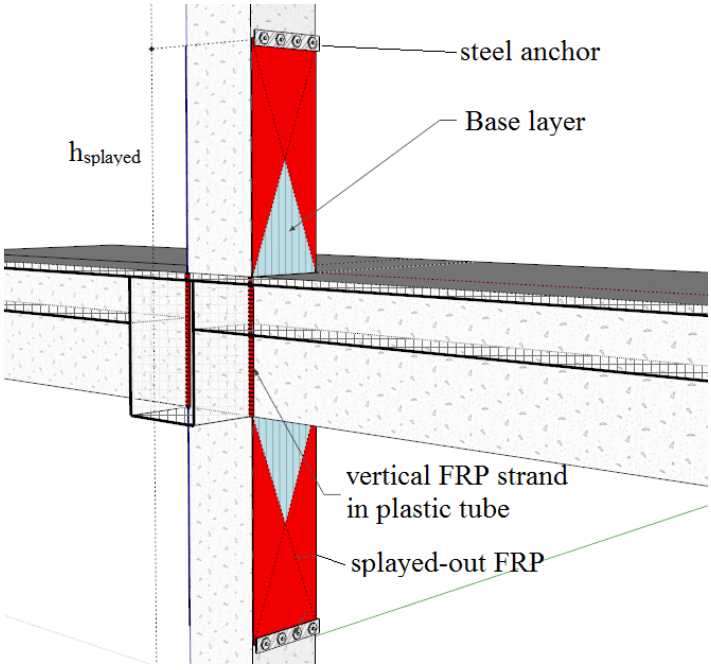

Figure F.11. Flexural retrofit of columns.

Step 6. Design shear strengthening for the column end sections.

To evaluate the capacity design shear demand in the column ends based on $M_{Rd,c}$, EC8 cl. 5.4.2.3(3) is used. If required, the FRP shear strengthening is then designed following section 4.3 of CNR-DT 200 R1/2013. It is recommended to apply shear strengthening FRP as full wraps (Figure F.12). The lap length of the full wrap should exceed a distance of h_c. Eq. 4.22 (CNR) is then used to calculate the effective stress in the FRP wrap for the shear calculation in eq. 4.19 (CNR).

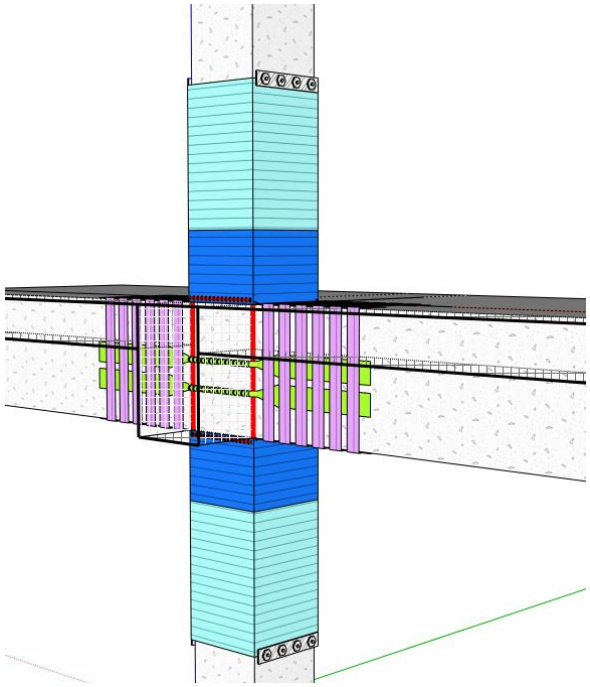

Figure F.12. Confinement and shear strengthening wraps for the columns.

Step 7. Design of Joint shear strengthening.

First, it is important to check if joint shear strengthening is required by determining if the design horizontal joint shear force V_{jhd} in EC8 eq. 5.22 satisfies the condition in eq. 5.33. If it does not, strengthening is required. The required joint shear strength enhancement from the FRP retrofit, $V_{Rd,f,joint}$, is calculated from:

$$V_{Rd,f,joint} = V_{jhd} - V_{jRc} \quad \text{(F.11)}$$

Where V_{jRc} corresponds to the joint shear capacity of the unstrenghtened joint determined using the RHS of eq. 5.33 (EC8).

The amount of shear strengthening required to reach $V_{Rd,f,joint}$, is then evaluated following the shear strengthening calculations for rectangular sections in 4.3 of CNR-DT 200 R1/2013. As the joints cannot be fully wrapped, eq. 4.21 (CNR) is used to calculate the effective stress in the FRP wrap for the shear calculation in eq. 4.19 (CNR). The shear strengthening is applied in the form of two thin FRP strips rolled into strands and passed through pre-drilled holes through the beams

at the joint (Figure F.13). Again a modification of the FRP width and area of FRP is required to account for the different geometry between the strands and the rectangular section (see Figure F.5).

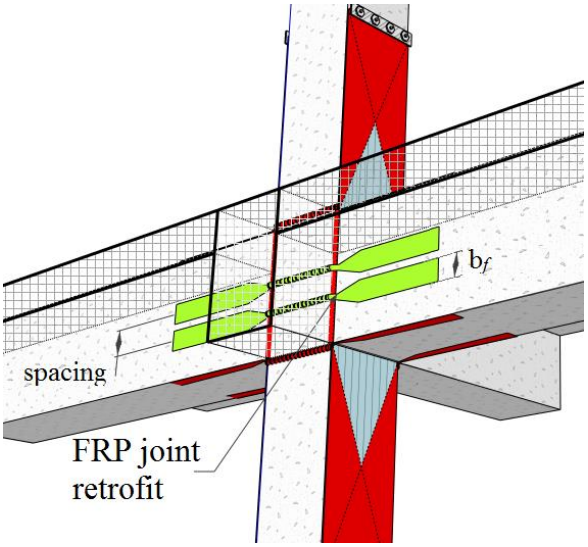

Figure F.13. Joint shear retrofit using FRP strands.

On the following pages, pictures from the actual retrofit application in the laboratory are presented.

Figure F.14. Holes drilled for FRP strands.

Figure F.15. Selective weakening cuts and holes for transverse FRP.

Figure F.16. Holes for joint FRP strands

Figure F.17. Application of base layer of FRP on columns.

Figure F.18. Application of FRP strands - splaying out on column step 1.

Figure F.19. Application of FRP strands - splaying out on column step 2.

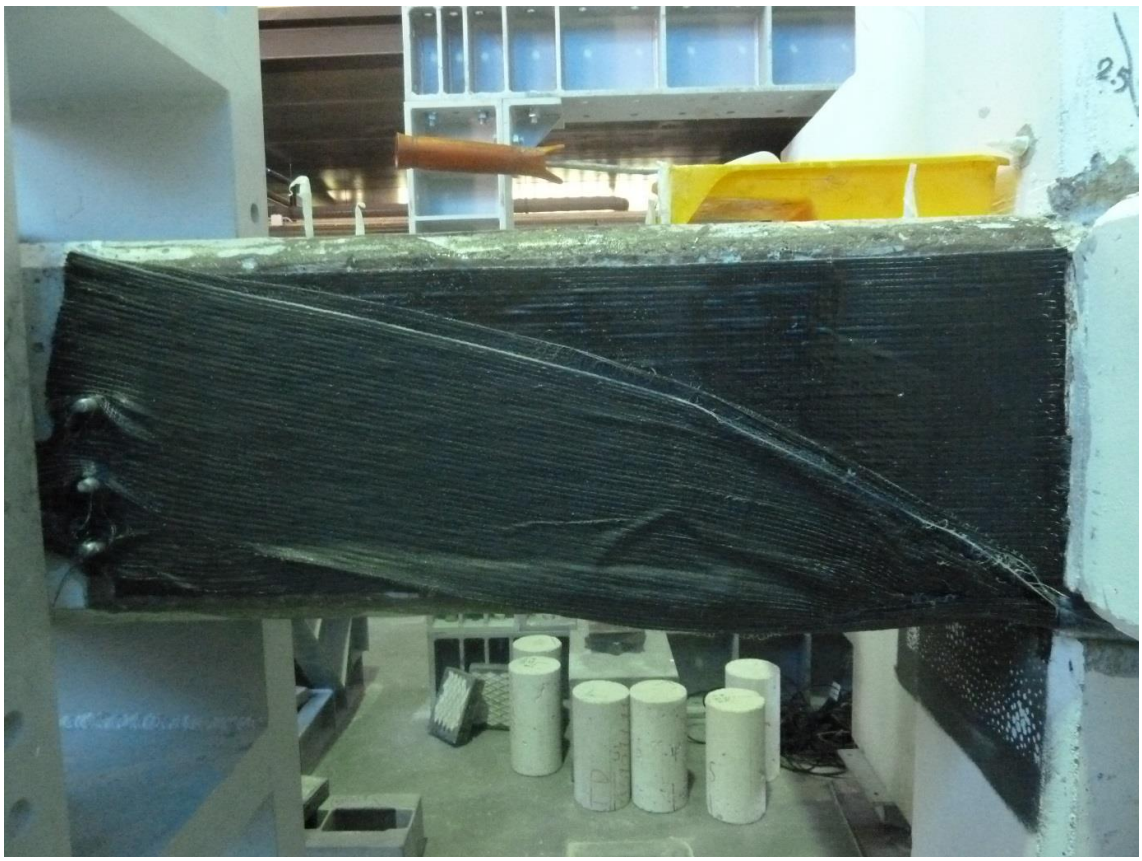

Figure F.20. Application of FRP strands - splaying out on column step 3.

Figure F.21. Application of FRP strands – anchoring.

Figure F.22. Application of FRP confinement wraps for columns.

Figure F.23. Application of FRP strands for joint shear strengthening.

Figure F.24. Application of beam FRP strands splayed out on beams.

Figure F.25. Splaying out of joint shear FRP strands onto beams.

Figure F.26. Final FRP retrofit B-sw - superior column view.

Figure F.27. Final FRP retrofit B-sw - inferior column view.